Enhancing inter-layer bond strength in 3D Concrete Printing using topological design principle

Research on effect of topological interlocking in extrusion-based 3D printable concrete

Nitesh Mithapelli

TU Delft

Enhancing inter-layer bond strength in 3D Concrete Printing using topological design principle

Research on effect of topological interlocking in extrusion-based 3D printable concrete

by

Nitesh Mithapelli

to obtain the degree of Master of Science
at the Delft University of Technology

Student number:	5016215	
Project duration:	November, 2020 - March, 2023	
Thesis committee:	Dr. Branko Šavija,	TU Delft (Committee Chair)
	Dr. S. C. Barbosa Nunes	TU Delft (Committee member)
	Dr. Ir. H. R. Schipper	TU Delft (Committee member)
	Ir. A. L. van Overmeir	TU Delft (Committee member)

TU Delft

Preface

After three intriguing years in the engineering and consulting industry and having a good outlook on various aspects of Structural Engineering, I decided to challenge myself further by taking up the Master's Program, at TU Delft with a view to gaining advanced knowledge related to Structural Engineering. The Master thesis titled - 'Research on the effect of topological interlocking in extrusion-based 3D printable concrete' has been performed to fulfil the graduation requirements of the Structural Engineering Track at the TU Delft's Faculty of Civil Engineering and Geosciences. I was engaged in researching and writing a thesis from November 2020 to November 2022.

I developed a keen interest in innovations in 3D concrete printing whilst working as an intern at firms like Cybe Constructions B.V. and Vertico. Through my experience, I found the aspects of pursuing research relevant to the industry as an endeavour and became fascinated by this innovative technology and its ability to outperform traditional construction methods in the foreseeable future. I was motivated and driven to address the lack of strength-related issues encountered in 3D concrete printed structures through my Master thesis. Whilst transitioning from professional setup to academics was a huge adventure, the academic research experience has been unique as it demanded not only the technical expertise of an engineer but also the managerial acumen of a businessperson in ensuring organisation and execution. I have learnt that struggling is part of the process and that it is important to trust the process.

I would like to express my gratitude to my supervisor, Dr. Branko Šavija who guided me throughout the thesis time frame. Your knowledge in the field of 3D concrete printing is extraordinary and I chose you to be my supervisor because I knew you would provide me with the right challenges that would not only help me solve the problem but grow immensely in the process. I would also like to thank Prof. Sandra Barbosa Nunes from Concrete Structures whose knowledge and guidance helped me steer in the right direction. I am immensely grateful for the support from Anne Linde van Overmier and especially her knowledge in the field of 3D concrete printing with SHCC-based mix that helped me gain a good perspective on the topic. She has been a constant source of motivation in the toughest times. I would like to thank Maiko van Leeuwen and Ton Blom for assisting me and facilitating my experiments in the Microlab and Stevin Laboratory.

Finally, I would like to dedicate this thesis to my late mother Shobha Mithapelli who lost her battle with cancer during my thesis. She was a strong, brave and kind woman to have graced our family. Words cannot express my gratitude for the constant support and motivation received by my father and brother in times of such difficult circumstances. Their grit and determination to support my mom to fight cancer and at the same time encourage me to pursue my ambitions are unparalleled. Lastly, I would like to mention my family away from home - my friends here in the Netherlands who always made me feel at home and kept me motivated throughout my Master's Program. Thank you to the reader, I hope you enjoy reading it.

Nitesh Mithapelli
Delft, March 2023

Summary

Various problems faced by conventional construction techniques like those of longer construction time, being labour intensive and using formwork make the process highly unsustainable and expensive. Due to its novelty and benefits, 3D concrete printing (3DCP) is looked at as a good substitute to overcome these problems and hence, is gaining interest in the research field.

One of the major issues within extrusion-based 3D concrete printed structures is that they exhibit a weak inter-layer bond in their hardened state. Various aspects like that of under-filling, layer time gaps, surface moisture, extrusion parameters and mix composition affect the inter-layer bond. Previously researchers have tried to address this problem by techniques which involved placing a cement mortar layer between the successive extruded layers, using a different set of nozzle and brushes to induce surface roughness and by placing vertical steel reinforcement between the extruded layers. Options like surface roughening and the addition of concrete mortar between layers have shown considerable improvement in inter-layer bond.

The research herein focuses on addressing the problem of the weak inter-layer bond by implementing the phenomenon of 'topological interlocking'. This involves the modification of extruded layer from a planar to an osteomorphic block-inspired shape. The aim of which is to help increase the mechanical interlocking between the layers solely by the topological modifications without the use of any binders or connectors. Previous research has highlighted the benefits of using this principle like that of achieving high resistance to crack propagation, large energy absorption capacity and remarkable tolerance to local failures exhibited by these structures. An extensive literature study was performed which highlighted various use cases of this principle in terms of glass and concrete blocks for loading in the out-of-plane direction of the structure. The research herein is the first of its kind and aims to study the effect of implementing such a non-planar shape in extrusion-based 3D concrete printing on the inter-layer bond strength with Strain hardening cementitious concrete (SHCC).

Since, at the time of conducting this research, the printing equipment required to produce such a non-planar shape was nonexistent, so a more reasonable approach was adopted to narrow down the printing parameters and perform scale model printing in the form of mould-casting and caulk-gun extrusion to produce specimens. First, the effect of 'topological interlocking was to be analysed independently and hence, the mould-casting specimens served the purpose of studying the effect of grooving whereas later the caulk-gun extrusion specimens were produced in order to study the effect of grooving in terms of extrusion parameters in a combination with different time-gaps.

The specimens were tested for a tensile inter-layer bond test under an Instron test setup. Furthermore, owing to the non-uniform bond observed in the inter-layer of caulk-gun extruded specimens, image analysis was performed on the fractured inter-layer. The caulk-gun specimens were additionally subjected to surface moisture content measurements for different adopted time-gaps. The bond test results along with the image analysis and surface moisture content data were further analysed in detail.

Based on the reliability analysis of tests and their correlation to the image analysis results it could be concluded that the results for the specimens in terms of the grooving effect were counter-intuitive to the one observed in previous research. The specimen with shallower grooves tends to perform better than the deeper ones. The inverse relationship between surface moisture content and time-gaps as suggested in previous research could be proven. However, as the effect of specimen dimensions, notching, asymmetry, under-filling and surface roughness interfered greatly, a similar inverse relationship between the tensile inter-layer bond strength and time-gap could not be confirmed. The research though inconclusive in proving the initially stated hypothesis manages to successfully provide a detailed insight into the issues that should be expected in further similar studies and provides recommendations to avoid them in future research.

List of Figures

1.1 (Right) Good quality sample with an identifiable outline of each filament, interspersed with voids (Left) Poor quality sample with the indiscernible filaments [1] 1
1.2 Proposed approach on extruding the layers 3
1.3 (Left picture) Osteomorphic blocks and their interlocking within a planar structure. (Right picture) Principle building block geometries of an osteomorphic block. 3
1.4 Research Flow Chart 5

2.1 Schematic representation of 3DCP process [3] 7
2.2 Schematic representation of Literature Review 8
2.3 Extrusion defects in 3D printed specimen [1] 9
2.4 (a) Voids formation between 4 filaments (b) Poor printing parameters leading to the formation of voids in the specimen [19] 10
2.5 Voids structure in three specimens [19] 10
2.6 Slice image of different specimens. (a) Cast specimen; (b) Printed specimen within the filaments; (c) Printed specimen between filaments. [22] 11
2.7 Voids structure in poor and good printed specimens [20] 11
2.8 Under-filling due to nozzle direction change [1] 12
2.9 Performance of tool-path highlighting Under-filling and over-filling aspects [25] 12
2.10 Comparison of conventional and double offset algorithms used for slicing on a 2-D specimen [25] 13
2.11 SEM images showing cold-joint formations due to lack of layer inter-mixing [27] 13
2.12 SEM images showing cold-joint formations due to cavities induced via “air enclosure” [27] 13
2.13 SEM image of the specimen with a mix including fly ash and silica and 1 day TG - visible cavities at interface[27] 14
2.14 Specimen under SEM image investigation [27] 14
2.15 Inter-layer Bond Strength for specimens with printed with different time-gaps and printing speeds [6] 14
2.16 Fracture surface of 3D printer UHDC-based mix after inter-layer bond test [30] 15
2.17 Fracture surface of 3D printer normal concrete-based mix after inter-layer bond test [8] . 15
2.18 Modes of Fracture Failure [31] 15
2.19 (a) Open loop control (OLC’s) (b) Closed loop control (CLC’s) [33] 16
2.20 Load-deformation relations for concrete bar under uni-axial tensile loading [34] 17
2.21 Deformation distribution for Specimen type A (250x60x50 mm^3) [34] 17
2.22 Average stress-deformation relationship [34] 17
2.23 Stress-deformation relationship for front and rear sides of the specimen type A [34] . . . 17
2.24 Deformation distribution for Specimen type C (50x60x50 mm^3) [34] 17
2.25 Stress-deformation relations for different specimen length [34] 18
2.26 Uni-axial tensile test of a concrete specimen with different rotational stiffness exhibiting bump effect [36] 19
2.27 Progressive crack penetration for (a) rotational boundary conditions and (b) fixed boundary conditions [37] 19
2.28 Tensile Stress Vs. Strain response of SHCC showing a tight crack width (below 100 µm) [40] 20
2.29 Tensile Stress Vs. Strain response of Printable SHCC with different fibre content [43] . . 21
2.30 Representative crack patterns of specimen C-print after failure in uni-axial tension tests [43] 21
2.31 Stress Vs. Strain Graph for Bond Strength of Specimen X (mix composed of Portland cement (OPC), blast furnace slag (BFS) and limestone powder(LP)) [44] 21
2.32 Stress Vs. Strain Graph for Bond Strength of Specimen Y2T (mix composed of OPC, fly ash (FA) and sand) [44] 21
2.33 Load-displacement curve for smooth layered specimen printed with PVA fibre-based mix [3] 22
2.34 Fracture behaviour of interface for smooth layering in specimen printed with PVA fibre-based mix [3] 22

2.35 Load-displacement curve for groove layered specimen printed with PVA fibre-based mix [3] . . . 22
2.36 Fracture behaviour of interface for groove layered specimen printed with PVA fibre-based mix [3] . . . 22
2.37 Preliminary study on the size of interlocking [24] . . . 23
2.38 Comparison of bond interface for four types of interlock [24] . . . 23
2.39 28 days' strength development of four types of interlock [24] . . . 23
2.40 Fracturing of the assembly of interlocked blocks in concentrated load tests as compared to a solid plate of the same dimensions made from the same material (polyester casting resin): (a) localised fracture in interlocking assembly and (b) global fracturing of the solid plate [13]. . . . 24
2.41 Failure in (a) Hybrid plate (interfaces between bricks are filled with silicon-based rubber) (b) assembly plate (c) monolithic plate under quasi-static load [46] . . . 25
2.42 Assembly of Osteomorphic block for axial compression test [47] . . . 26
2.43 Identification of crack formation in the osteomorphic block after compression test [47] . . . 26
2.44 Moisture Content of a printed element measured at different time gaps [48] . . . 27
2.45 Relation between Inter-layer bond Strength and Time-gaps for 3D printed specimens (V represents the print speeds) [48] . . . 27
2.46 Inter-layer strength of the printed concrete [8] . . . 27
2.47 Bleeding rate from the surface of the printed concrete [8] . . . 27
2.48 Results of application of colour thresholding. (a) Top Image before thresholding, (b) Top Image after thresholding, (c) Bottom Image before thresholding, (d) Bottom Image after thresholding. [9] . . . 28

4.1 Dimension of the groove-size for the topology (to be referred in accordance with Table 4.2) . . . 37
4.2 (Left) Roughneck mortar gun used for scale model 3D concrete printing for extrusion (Right) Brennenstuhl 1298680 Moisture meter MD . . . 37
4.3 Expected moisture migration in the extruded layer (as seen in blue) due to topology . . . 38
4.4 Positions at which the specimens were sawn and extracted for further testing (For the overall height of sawn specimen (H) refer Figure 4.11 and Table 4.4) . . . 39
4.5 Positions at which SMC was measured representative in terms of sawn specimens. Points I, II and III represent positions of Surface Moisture Content (SMC) measurement at different time-gaps on the first extruded layer . . . 40
4.6 Casted specimens (cut along the length) (Red encircled regions) show few air voids induced due to the process of casting which were neglected (Green encircled regions) show black marks on the cut surface which is due to grease from the diamond cutter and is considered to have no effect on the results . . . 40
4.7 Setup used for extruding specimens in-order to have the extrusion at constant speed and height (Left: Side view; Right: Top view) . . . 41
4.8 Casting of first layer using caulk-gun on the base blocks (Positions 1, 2, 3 indicate the positions at which samples were sawn at a later stage for further testing) . . . 42
4.9 Measurement of surface moisture content on the first extruded layer using moisture measuring device . . . 42
4.10 Grinding/cutting and glueing of the specimens to achieve flat surface . . . 43
4.11 Overall height of the sawn specimens after grinding/cutting the curved surface . . . 44
4.12 Example of Instron inter-layer bond test setup for a specimen . . . 45

5.1 Flow chart illustrating steps followed in the data analysis . . . 50
5.2 Uniform debonding occurring in Specimen A-2 . . . 51
5.3 Average (green curve) and LVDT specific (red and blue curves) Stress-strain curves for Specimen A-2 . . . 51
5.4 Non-Uniform debonding occurring in Specimen A-1 . . . 52
5.5 Average (green curve) and LVDT specific (red and blue curves) Stress-strain curves for Specimen A-1 . . . 52
5.6 Stress-Strain Curve for Fixed-Rotational boundary conditions with no bumps . . . 53

5.7 Stress-Strain Curve for Fixed-Fixed boundary conditions showcasing bumps in the softening curve . . . 53
5.8 Specimen TG20-B-3 after failure: The thickness of the upper layer is less as compared to bottom extruded layer . . . 54
5.9 Specimen TG5-B-3 after failure: The thickness of the bottom layer is less as compared to upper extruded layer . . . 54
5.10 Inter-layer surface of Casted Specimen B-2 after failure with clustered voids (depicted by green regions) and mould-induced discontinuity (depicted by yellow) . . . 55
5.11 Inter-layer surface of Casted Specimen C-2 after failure with clustered voids (depicted by green regions) and mould-induced discontinuity (depicted by yellow) . . . 55
5.12 Extruded second layer on the first layer (Regions highlighted with red show defects in the specimens related to non-uniform contact between layers and non-uniform layer thickness induced due to the caulk gun extrusion process) . . . 55
5.13 Inter-layer surface after failure for Specimen TG10-A-1 with visible under-filling effects like lack of inter-layer mixing (regions marked in blue) . . . 56
5.14 Mould-induced discontinuity (Specimen A-2) in the inter-layer (encircled yellow) when specimen is in the test setup . . . 56
5.15 Cold joint formation in the inter-layer of saw-cut caulk-gun based-specimen . . . 56
5.16 Post-peak cyclic tensile behaviour observed in stress-strain curve [34] . . . 58
5.17 Post-peak cyclic tensile behaviour observed in the stress-strain curve of Specimen A-2 58
5.18 Post-peak cyclic tensile behaviour observed in the stress-strain curve of Specimen A-1 58
5.19 Strain rate sensitivity observed in stress-strain curves for different strain rates [57] . . . 59
5.20 Tensile inter-layer bond strength results for Mould-Casted Specimens (refer Appendix E) 60
5.21 Plot of SMC Measurements against Bond Strength of different Time-gaps (TG's) based -**Caulk-gun specimens** . . . 62
5.22 Plot of SMC Measurements against Bond Strength of different Time-gaps (TG's) based - **Caulk-gun specimens (Reliable)** . . . 64
5.23 Plot of Bonding acquired from Image analysis Vs. Average Bond Strength for (reliable) caulk-gun specimens . . . 64
5.24 Image analysis results performed on fractured inter-layer surface: (Top) Original Image (Middle) Threshold image representing weak bond (Bottom) Threshold image representing good bond . . . 65
5.25 Failure of Specimen TG5-C-3 influenced by asymmetry (bottom layer) . . . 66
5.26 Overall comparison of bond strength results for samples with reliable test results . . . 67
5.27 Fractured (bottom) inter-layer surface of mould casted specimen: exhibiting (green regions) clustered voids in the interface (yellow regions) mould induced-discontinuity (red regions) showing fibre dispersion in the layer . . . 68

List of Tables

4.1 Mix Proportions for 1 Litre of Mix 36
4.2 Groove-size adopted for investigation (refer table in accordance to Figure 4.1) 36
4.3 Reference and Adjusted scaled values of moisture content (as indicated in the manual of Moisture meter) measurement 39
4.4 Overall height of the specimens to be used for inter-layer bond test 44

5.1 Failure mechanism observed in specimens tested for the inter-layer bond test (refer Appendix - E) 50
5.2 Boundary conditions of Specimens during the inter-layer bond test-based on softening curves 53
5.3 Specimens with reliable test results 63

Contents

Summary **v**

List of Figures . . . vi

List of Tables . . . ix

1 Introduction **1**

1.1 Problem Statement . . . 2

1.2 Research Outline . . . 2

1.3 Scope of Research . . . 4

2 Literature Review **7**

2.1 Extrusion based 3D concrete printing . . . 7

2.2 Inter-layer bonding in 3D Concrete Printing . . . 13

2.3 Reliability of results in tensile tests . . . 15

2.4 Strain Hardening Cementitious Composite (SHCC) . . . 19

2.5 Concept of topological interlocking . . . 22

2.6 Surface Moisture Content and Time-Gap . . . 26

2.7 Image Analysis of Fractured Inter-layer . . . 28

3 Research Framework **31**

3.1 Research Justification . . . 31

3.2 Research Objective . . . 32

3.2.1 Preparation of specimens . . . 32

3.2.2 Performing bond strength tests and analysing results . . . 33

4 Research Setup **35**

4.1 Design Parameters . . . 35

4.1.1 Mix Design and Mixing Procedure . . . 35

4.1.2 Groove-Size Investigations . . . 36

4.1.3 Time Gap Investigations . . . 37

4.1.4 Surface Moisture Content (SMC) Characterisations . . . 38
4.1.5 Measurement of surface moisture content . . . 39
4.2 Sample Preparation . . . 40
4.2.1 Casting the specimens . . . 40
4.2.2 Caulk-gun extrusion technique . . . 41
4.3 Test Methods . . . 43
4.3.1 Inter-layer Bond Test . . . 43
4.3.2 Image Analysis of Debonded Inter-layer Surface . . . 46

5 Laboratory Results, Analysis and Discussions 49

5.1 Pure-Tension Failure . . . 51
5.2 Tension-Bending Failure . . . 51
5.3 Factors influencing failure mechanism . . . 52
5.3.1 Effect of boundary conditions of test specimen . . . 52
5.3.2 Effect of specimen dimensions . . . 53
5.3.3 Effect of notching and symmetry of test specimen . . . 54
5.3.4 Effect of under-filling in the inter-layer . . . 54
5.3.5 Effect of roughness in inter-layer . . . 56
5.3.6 Effect of non-uniform glueing . . . 57
5.4 Characteristics of stress-strain curve . . . 57
5.4.1 Post-peak unloading-reloading . . . 57
5.4.2 Influence of displacement-rate . . . 58
5.5 Overview on Bond Tests for Mould Casting based-specimens . . . 60
5.6 Overview on Bond Tests for Caulk-Gun based-specimens . . . 62
5.7 Overview on Bond Tests for Reliable Specimens . . . 67

6 Conclusion and Recommendations 69

6.1 Detailed Conclusions . . . 69
6.1.1 Mould-casting method . . . 69
6.1.2 Caulk-gun extrusion method . . . 70
6.2 General Conclusions . . . 71
6.3 Recommendations . . . 71

Bibliography **73**

A Appendix-A **77**

A.1 Designing and Testing a Dynamic Nozzle 77

A.1.1 Nozzle Design 77

A.1.2 Conventional Nozzle 78

A.1.3 Modified Nozzle. 79

A.1.4 Code to be uploaded on Arduino UNO for synchronous run of stepper motors . . . 82

A.1.5 G-Code for Modified Nozzle based Printing 83

B Appendix-B **85**

B.1 Detailed analysis of Bond test results 85

B.1.1 Caulk-gun Specimens 85

B.1.2 Casting based Specimens 160

C Appendix-C **187**

C.1 Images of failed specimens post Inter-layer Bond Test 187

C.1.1 Failed specimens from Caulk-gun extrusion 187

C.1.2 Failed specimens from Casting method 194

D Appendix-D **197**

D.1 Images analysis of Inter-layer surface of failed specimens. 197

D.1.1 Specimen Type-A. 197

D.1.2 Specimen Type-B. 252

D.1.3 Specimen Type-C 312

D.1.4 Inter-layer surface of Casting based - Failed Specimens. 362

E Appendix-E **365**

E.1 Failure Mechanism in tested Specimens 365

E.1.1 Failure Mechanism in Caulk-gun extrusion-based specimens 365

E.1.2 Failure Mechanism in Mould-Casted-based specimens 379

1

Introduction

The concept of 3D concrete printing (3DCP) involves layer-by-layer extrusion of concrete through a digitally controlled nozzle and works on similar lines as large-scale additive manufacturing. The nozzle may be mounted either on a gantry or a robotic arm that precisely controls the concrete extrusion process [1]. The thickness of these layers is generally on the order of a few centimetres. The material used in this process includes concrete used in conventional construction processes with changes to its composition specifically with the aim of achieving a high cement content mortar or fibre-reinforced cement mortar which can be mixed and pumped through a hose and further extruded through a nozzle. The material in its fresh state must satisfy the minimum requirements of pumpability (which describes the ease with which the fresh mix is transported from the pump to the extrusion nozzle [1]), extrudability (the ability to extrude the mix through a nozzle without considerable cross-sectional deformation and with an acceptable degree of splitting/tearing of filament [1]) and buildability (characteristics to enable it to lay down correctly, remain in position, be stiff enough to support further layers without collapsing and yet still be suitable to provide a good bond between layers [2]). Due to differences between 3DCP and conventional construction process, it is crucial to examine the printed structure in its hardened state for layer adhesion, bulk density and under-filling (that is existence of voids within components as shown in Figure 1.1 reducing the effective density and potentially to the detriment of durability), tensile strength and shrinkage [1].

Figure 1.1: (Right) Good quality sample with an identifiable outline of each filament, interspersed with voids (Left) Poor quality sample with the indiscernible filaments [1]

Over the recent past, cementitious composites have been developed that exhibit high tensile strain capacity [3], [4] which are termed as Engineered Cementitious Composites (ECC) or Strain Hardening Cementitious Composites (SHCC). In terms of Strain Hardening Cementitious Composites (SHCC), while strength characteristics in the direction parallel to the print direction are strong (in terms of tensile ductility) the same does not hold true for the direction perpendicular to the printing direction (vertical direction). As per ongoing research in the field of 3DCP, this discrepancy in ductility is associated with inter-layer adhesion between two extruded layers of material which remains to be the weakest aspect in a printed structure. This has been addressed by researchers in either of the following ways: by introducing vertical reinforcement in the inter-layer [5], surface roughening [6], [7], using concrete mortar between layers [8] or by changing nozzles used for extrusion process [5]. While some options like surface roughening and the addition of concrete mortar between layers [9] have shown considerable improvement in inter-layer bonding, others such as vertical reinforcement and nozzle changes have not been effective.

1.1. Problem Statement

The thesis's approach herein intends to address the problem of inter-layer bond by concentrating on the design principle of 'topological interlocking'. The mechanisms behind the formation of inter-layer bond strength between two layers of concrete can be divided into three groups: mechanical interlocking, chemical bonding (involving processes like that of demulsification of bonding agent and cement hydration [10]) and physical bonding [11]. Inter-layer adhesion models can be introduced as the interaction of the layers on both micro and macro scales. In the micro-scale, chemical forces, and the macro-scale layer configurations interlocking and surface roughness are responsible for bonding between layers [12]. Through this thesis, the concept of topological interlocking, which, has its focus on the macro scale aspects would be realised by introducing an osteomorphic block-inspired shape of the extruded layer as shown in Figure 1.3. Topological interlocking is a design principle by which elements (blocks) of special shape are arranged in such a way that the whole structure can be held together by a global peripheral constraint, while locally the elements are kept in place by kinematic constraints imposed through the shape and mutual arrangement of the elements [11], [13]. Based on the presently available literature, this, if successful will give a new perspective in addressing the problem of weak inter-layer bond between layers of extruded 3D-printed concrete structures. In this type of arrangement, structural integrity between elements is ensured solely by the topological modifications without the use of any binders or connectors [11]. The benefits of using this principle are the high resistance to crack propagation, large energy absorption capacity and remarkable tolerance to local failures exhibited by these structures [13]. Except for in the research of Estrin *et al.* et al.[11] this has been examined in terms of fragmented block elements as shown in Figure 1.3 which offers enhanced strength and structural stability as the block elements prevent crack propagation due to a discontinuous medium and hence, are subjected to local failures as seen in Figure 2.40. When implementing the topological interlocking phenomenon in terms of 3DCP these fragmented elements would cease to exist due to continuous layer extrusion as shown in Figure 1.2. This is further expected to ensure a continuous medium for crack propagation and facilitate seamless chemical reaction (in relation to cement hydration and layer inter-mixing) between the layers resulting in a good bond. However, the most important aspect of interest amidst this thesis approach would be to look at improvements in the strength and ductility performance of the printed structure, specifically in the direction perpendicular to the printing direction.

1.2. Research Outline

The research flow process as observed in Figure 1.4 was followed throughout. The focus of this research is to assess the influence of adopting an osteomorphic (literally meaning interlocking by non-planar surfaces) block-inspired shape on inter-layer bond in extrusion-based 3D concrete printable structures. Since, at the time of conducting this research, the printing equipment required to produce such a non-planar shape was non-existent, a more reasonable approach was to narrow down the print-

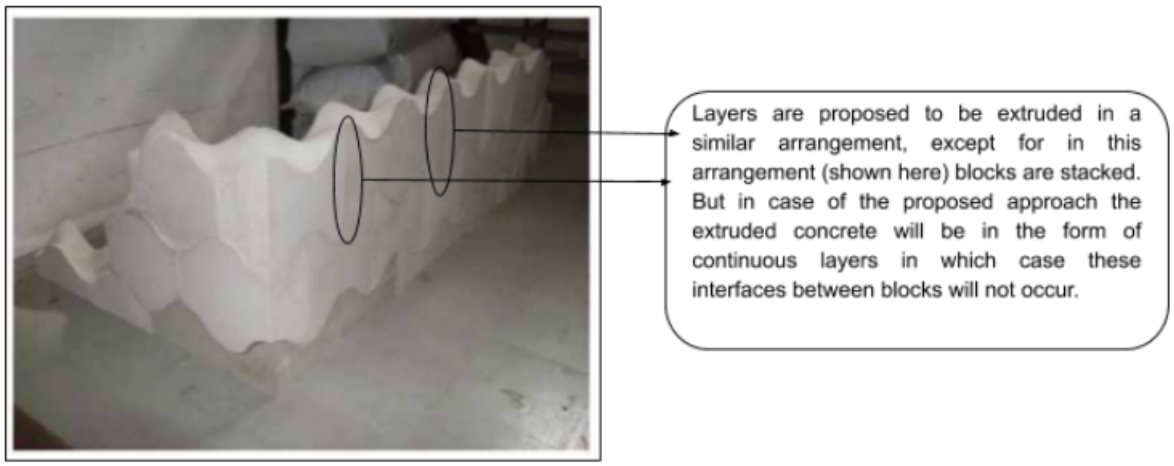

Figure 1.2: Proposed approach on extruding the layers

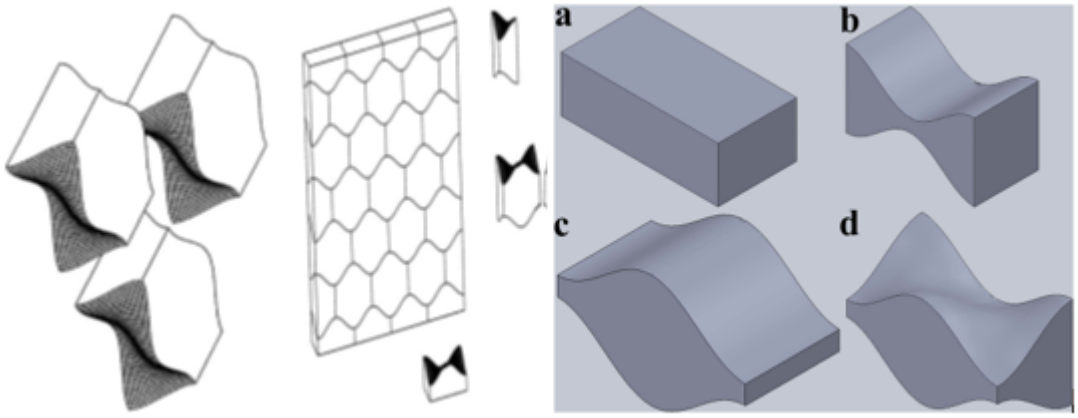

Figure 1.3: (Left picture) Osteomorphic blocks and their interlocking within a planar structure. (Right picture) Principle building block geometries of an osteomorphic block.

ing parameters and to use primary techniques like caulk-gun extrusion and mould-casting to produce the specimens which could be further tested for inter-layer bond strength.

Firstly, the mould-casting method was used to produce the specimens. This method was adopted from the perspective of narrowing down and eliminating the printing parameters which helped focus solely on the problem statement at hand as described in detail in Section 1.1. Simultaneously, a set of groove sizes is ascertained in order to investigate and identify the most effective dimension of topology that ensures that topological interlocking can be achieved solely by layer-over-layer extrusion without the use of additives, glues or mechanical connections. The specimens were sawn, cured and further tested for the inter-layer bond.

In order to further understand the implications in terms of the extrusion process in the specimens it was then decided to include printing parameters like extrusion from the nozzle from a constant height and speed so as to simulate the extrusion process involved in 3D concrete printing. This was achieved by using a manually operated caulk gun in combination with a setup which ensured that the extrusion occurs from a constant height and speed. At this stage, for the purpose of groove-size investigation, different dimensions of the topology were selected and additionally, the layer-on-layer extrusion for these specimens was carried out with different time-gaps in-order to investigate its effect on inter-layer bond strength. The specimens were then sawn, cured and inter-layer bond tests were carried out. After completion of the tensile bond test, the fracture surfaces of these specimens were analysed using an image analysis tool to assess the effective bond surface.

1.3. Scope of Research

In order to account for the limitations of time and resources and keep the research topic concise the following assumptions are considered right from the initial phase of research:

- The research is based on the extrusion-based-3D printable concrete and is limited to SHCC-based mix.
- The mould-casted samples are cast using the printable SHCC-based mix using a silicon rubber mould.
- All the mould-casted samples were cast within one day over a time of 2-3 hours in order to keep minimum deviations in the surrounding conditions.
- The caulk gun-based specimens were prepared over a period of 2-3 days without any gap in-order to keep minimum deviations in the surrounding conditions.
- The fractured inter-layer images were clicked with the help of a 12.2-megapixel rear camera of a smartphone immediately after the test termination and demounting of loading plates from the test setup. Although no intricate studies are performed, this procedure is assumed to produce images with similar quality and accuracy as that with the help of a flatbed scanner.
- Based on the literature review and the process of digital image processing it is assumed that the dark and light grey patches observed in the fractured inter-layer of the specimen are said to represent the corresponding regions of weak and strong bond respectively.
- The open time of the mix i.e. the time between mixing it and pumping or casting was kept as minimum as possible and was not more than 5 minutes.

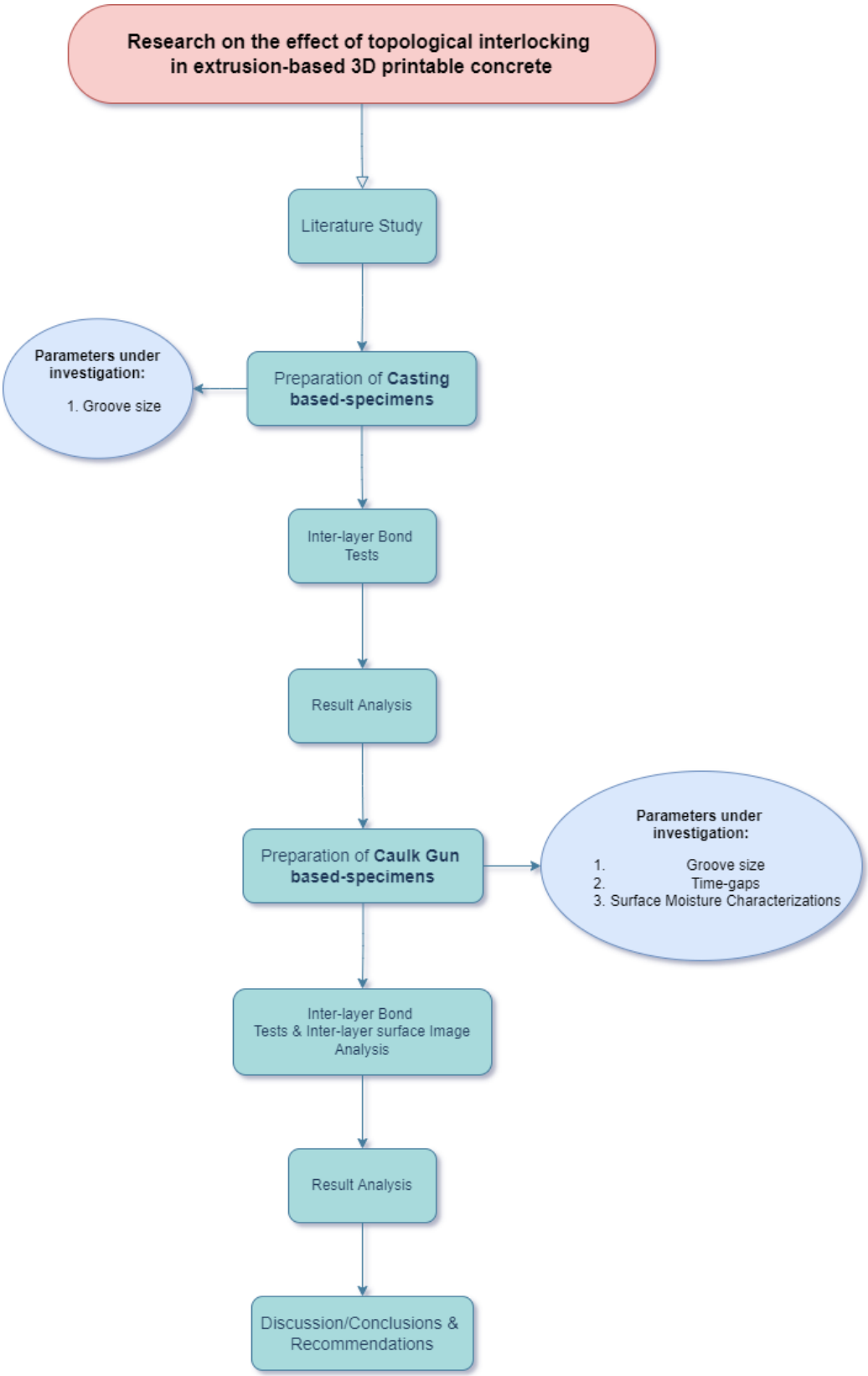

Figure 1.4: Research Flow Chart

2

Literature Review

An extensive literature review was performed prior to confirming the research framework and throughout the result analysis phase. Figure 2.2 shows a schematic representation of the literature reviewed in the entire research. The topics herein involve a summary of the research work along with important conclusions from the literature which are most relevant to the research presented in the thesis.

2.1. Extrusion based 3D concrete printing

Concrete has numerous benefits over other building materials such as the raw materials being cheap and readily available, good mechanical characteristics like high compressive strength and durability and abilities to mould and cast it in any shape and form. The term concrete as such is extensive and the use of additional binders, fibres, additives and admixtures is common to achieve specific properties for various special intended purposes. However, the current problems faced in the construction of conventional concrete structures like those of longer construction time, being labour intensive and the need for form-work make the process highly unsustainable and expensive [14]. Owing to the limitations of the traditional construction processes the concept of additive manufacturing (AM) is gaining interest in the research field and is looked after as an excellent substitute which would help solve all the aforementioned problems associated with the current construction processes.

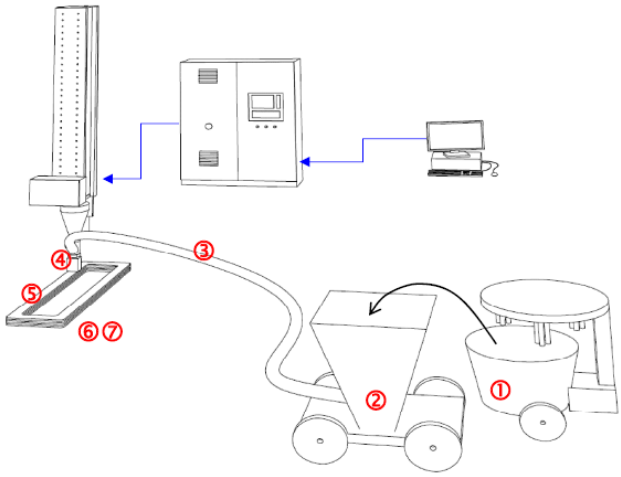

Figure 2.1: Schematic representation of 3DCP process [3]

Typically, AM processes involve the creation of 2D/3D models in computer-aided design (CAD) software which are converted into a numerical control programming language such as GCODE/Rapid Code which is further fed to the robot to fabricate 2D/3D design models in a layer-by-layer manner [15].

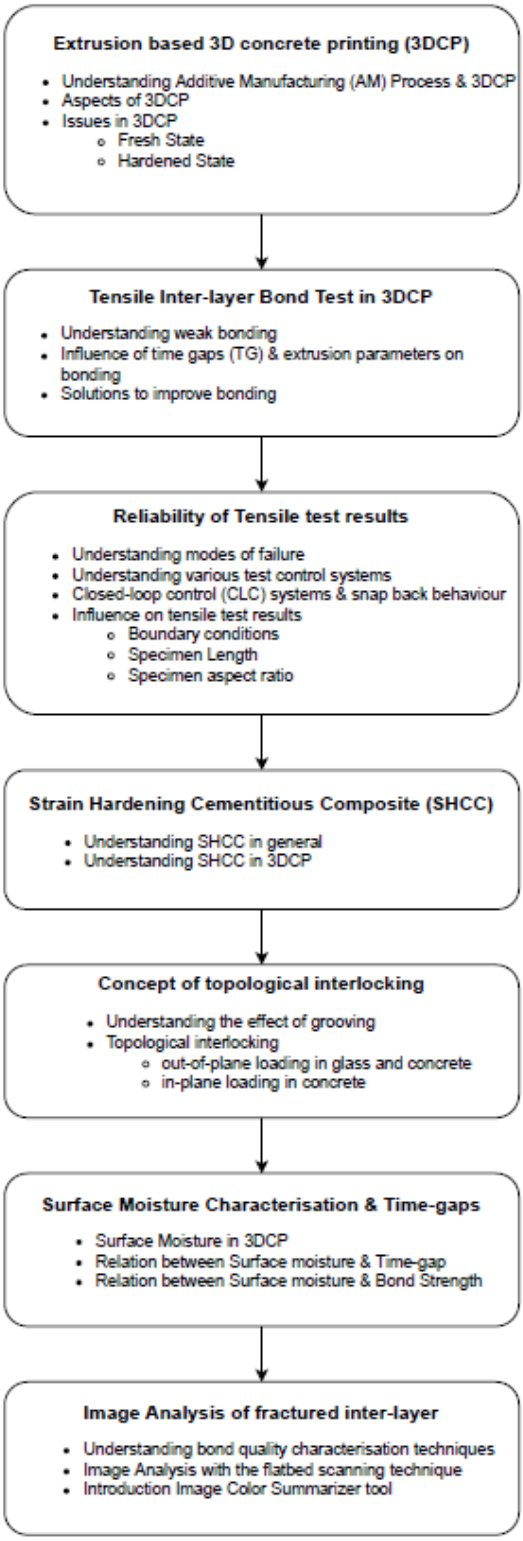

Figure 2.2: Schematic representation of Literature Review

In terms of the extrusion-based 3D concrete printing (3DCP) process the fabrication occurs by layer-by-layer extrusion of concrete through a nozzle (connected to a mixing pump) fixed to the robotic arm. The nozzle then follows the tool path while extruding the concrete in a layer-by-layer manner to produce a concrete structure. Figure 2.1 gives a schematic representation of the concrete 3D printing process. The numbers in Figure 2.1 correspond to various aspects of 3DCP which are as follows:

1. Mixing
2. Pumping
3. Transporting
4. Extruding
5. Building
6. Curing

Although 3D concrete printing helps overcome problems of the traditional construction methods, since, the technology is in its nascent stage it does come with technical issues, which need to be addressed before the technology can be completely put to use in the mainstream construction sector. These problems have been extensively researched and identified by Buswell *et al.* [1]. The research tries to classify them as follows:

1. **Fresh State Issues**
    - **Pumpability**: It describes the ease with which the fresh mix is transported from the pump to the extrusion nozzle. Problems such as particle segregation due to insufficient mixing prior to pumping can cause blockages in the hose.
    - **Extrudability**: It is defined as the ability to extrude the mix through a nozzle without considerable cross-sectional deformation and with an acceptable degree of splitting/tearing of filament [16]. It is governed by the critical yield stress value, beyond which, the filament displays high levels of defects and discontinuities.

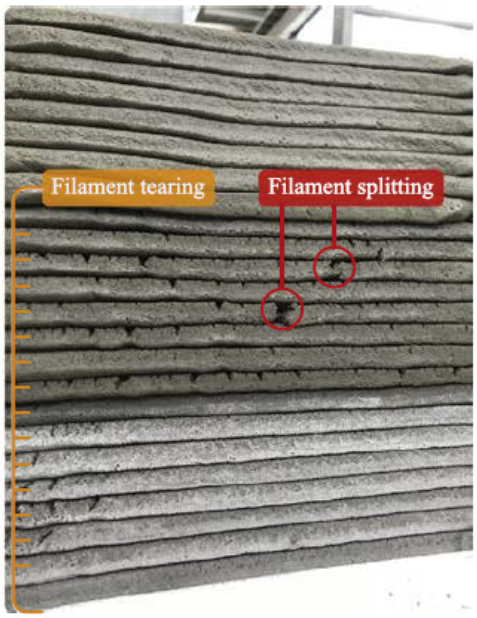

Figure 2.3: Extrusion defects in 3D printed specimen [1]

- **Buildability**: It is the ability to 3D print by adding concrete layer by layer continuously to the required level without significant deformation or collapse of the freshly printed component. Poor buildability results in the collapse of the print which occurs due to three mechanisms: plastic collapse, elastic buckling, and a combination of both [17].
- **Open Time**: The time during which a material may be used in 3DCP, and its influence on pumping and extrusion. It is associated to the maintenance of the viscosity and yields stress of the mix which is critical to the process [1].

2. **Hardened State Issues**

- **Layer Adhesion**: Creation of cold joints between layers where the time-gap is too great [18], [19] is responsible for this problem.
- **Under-filling**: Under-filling can create voids within components reducing the effective density and potentially to the detriment of durability [1], [19], [20]. The concrete extrusion process has the potential of creating small voids in the interstices between the filaments as observed in Figure 2.4. Careful design and control of mix rheology and printing process can avoid such macro effects [19].

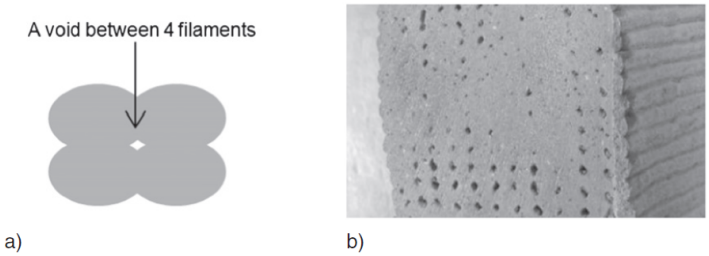

Figure 2.4: (a) Voids formation between 4 filaments (b) Poor printing parameters leading to the formation of voids in the specimen [19]

A study on the void structure was further carried out in the research of Le *et al.* between mould-cast, poorly printed and well-printed specimens and it was concluded that the poorly printed specimens had more number of voids as compared to mould-casted and well-printed specimens as observed in the Figure 2.5. This provides an important insight into the nature of the concrete extrusion process and the influence on the void structure of the resulting matrix and hence, mechanical performance [19].

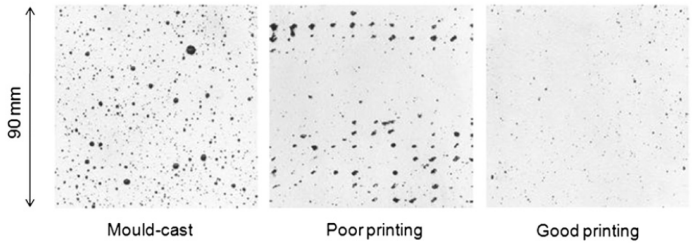

Figure 2.5: Voids structure in three specimens [19]

The research of Rahul *et al.* [21] further explores this in detail in terms of mould-casted specimens and infers that the formation of voids causes higher porosity and hence, reduction of the effective density leading to the formation of a weaker interface. On the other hand, The extrusion process in 3D-printed concrete facilitates specimens to have low porosity and higher effective density. This might not always be the case as sometimes the printing process induces a more porous material which is interdependent on both the material and the printing equipment. The results from the research of Liu *et al.* [22] explain this through a detailed study on pore structures of 3D concrete printed and cast specimens. This research

concludes that the internal pore structure of 3D printed concrete specimens was different from that of cast concrete, showing irregular shapes of voids as compared to spherical in the cast specimens. These pores are prone to stress concentration, resulting in the split tensile strength of 3D printed specimen being generally higher than that of cast specimens as observed in Figure 2.6

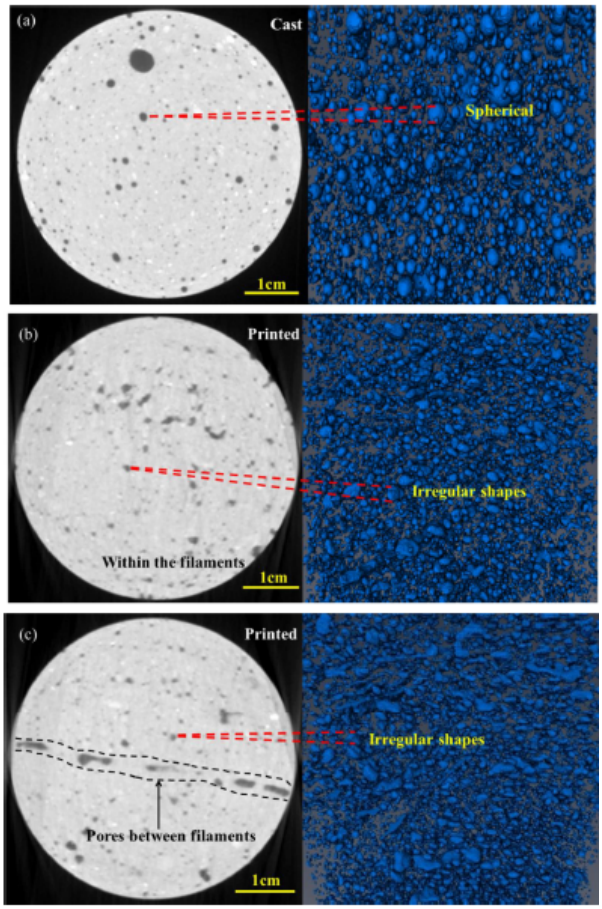

Figure 2.6: Slice image of different specimens. (a) Cast specimen; (b) Printed specimen within the filaments; (c) Printed specimen between filaments. [22]

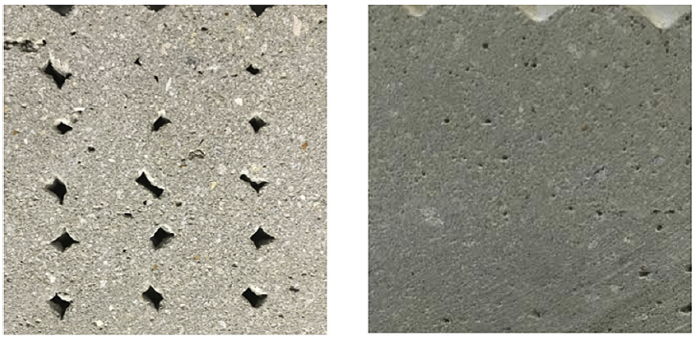

Figure 2.7: Voids structure in poor and good printed specimens [20]

The research of Le *et al.* [19] was also confirmed by Panda *et al.* [20] in terms of geopolymer mix and associated the good printing specimen characteristics to the pressure exerted by the

pump on the material during extrusion helping avoid under-filling and hence, increase density of the specimen (refer Figure2.7) [20]. Furthermore, the research identifies the proper selection of nozzle and high pump pressure to help reduce the voids in the printed specimen.

In an attempt to achieve mechanical inter-locking by increasing the contact surface between the layers Zareiyan *et al.* [24] carried out a study on different groove sizes as seen in Figure 2.37 and inferred that deeper grooving can potentially cause problems of under-filling and lead to voids and non-uniform contact. Furthermore, in regards to this, the research of Buswell *et al.* [1] states that for a given material formulation and nozzle geometry the tool path has an influence over the under-filling implying that the filament is limited to following the radius of a curve during a direction change. The radii that can be accommodated without fracturing or creating a defect is a function of the wet properties, the size and geometry of the nozzle and the speed of deposition and the effects of such direction change can be observed in Figure 2.8

Figure 2.8: Under-filling due to nozzle direction change [1]

In the research of Bi *et al.* [25] the authors assess the performance of constructed tool-path in Large format additive manufacturing (LFAM) based on four aspects: under-filling, over-filling, number of sharp corners and total path length as illustrated in Figure 2.9. They identified under-filling areas where the printed material cannot reach resulting in voids and hence, loss of stiffness. The problem is further dealt with in depth by using the conventional offset algorithm (a slicing method) commonly used in additive manufacturing and points out the problems it possesses in terms of under-filling, over-filling and having bottle-neck effect as seen in Figure 2.10. A double offset algorithm is suggested which helps eliminate issues of over-filling and sharp corners but under-filling still prevails.

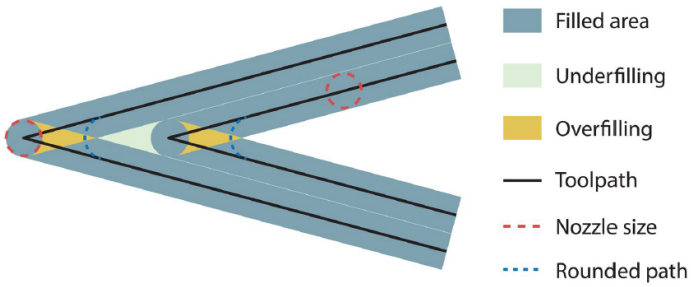

Figure 2.9: Performance of tool-path highlighting Under-filling and over-filling aspects [25]

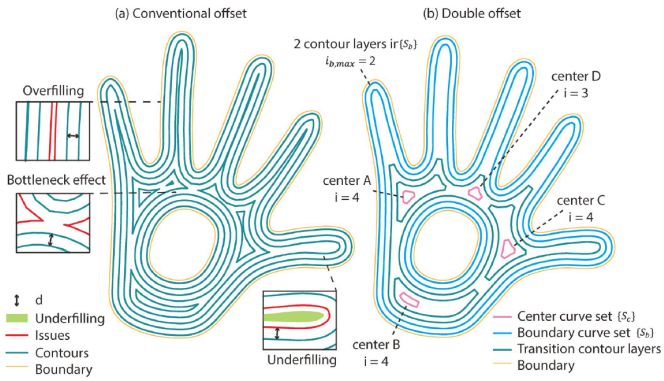

Figure 2.10: Comparison of conventional and double offset algorithms used for slicing on a 2-D specimen [25]

- **Shrinkage and durability**: The combination of a greater exposed surface with low water-cement ratios in 3D printable concrete increase the likelihood of cracking due to drying shrinkage [1]. When compared to conventional cast specimens the drying shrinkage for the 3D printable mortar is observed to be decreased (at 28 days). This decrease is associated with excessive moisture loss at an early age which results from a higher surface exposure [26]

2.2. Inter-layer bonding in 3D Concrete Printing

The inter-layer bond strength between extruded layers in the 3DCP process is considered the weakest spot due to the weak bonding. Buswell *et al.* [1], gives a structured insight into the technical issues surrounding 3DCP and mentions layer adhesion as one of the hardened state issues. Various aspects affecting the layer adhesion, for example, the formation of cold joints between layers (Figure 2.13 and 2.14), sand particle size, shrinkage and carbonation are discussed in this review paper.

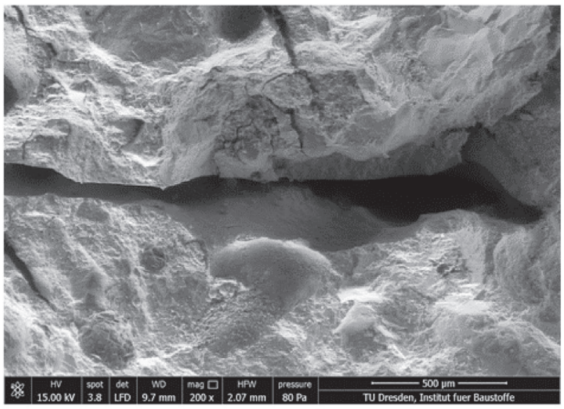

Figure 2.11: SEM images showing cold-joint formations due to lack of layer inter-mixing [27]

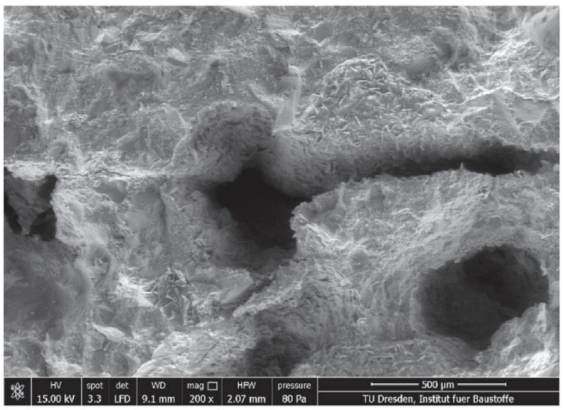

Figure 2.12: SEM images showing cold-joint formations due to cavities induced via “air enclosure” [27]

Time-gap (also referred to as cycle time) refers to the time delay between fresh mortar being placed in the same location on top of the previous extruded layer. If these time-gaps are kept longer, then, there is a potential for the formation of cold joints between the layers resulting in an adverse effect on the layer adhesion [28]. This was further confirmed from a microscopic investigation which was carried in the research of Nerella *et al.* [27] with 2 mixture compositions, one with fly ash and silica and the other without. The printed specimens had a layer time-gap of 1-minute, 10-minutes and 1 day. The research

concluded that the time-gap (TG) between placements of consequent layers considerably influences the interface bond quality. Especially, specimens produced with 1 day TG showed clear separations of concrete layers [27]. These cold joints are considered temporary as inter-layer adhesion is said to increase with the progress of cement hydration [1]

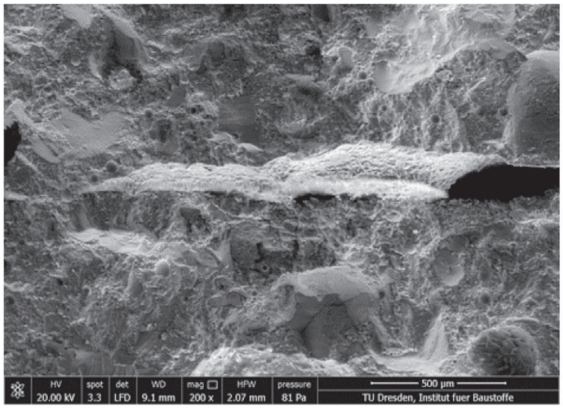

Figure 2.13: SEM image of the specimen with a mix including fly ash and silica and 1 day TG - visible cavities at interface[27]

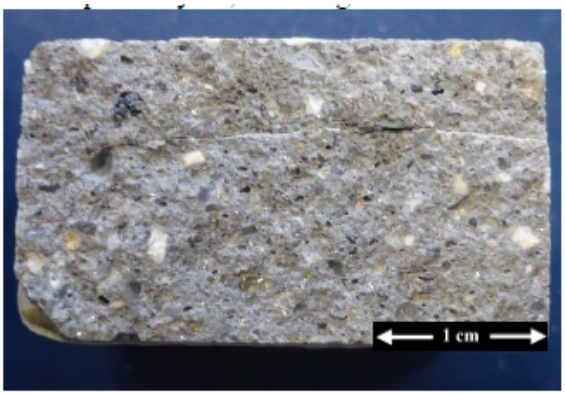

Figure 2.14: Specimen under SEM image investigation [27]

Another micro-structure investigation carried out in the research of Putten *et al.* [6], resulted in higher inter-layer bond strength at lower speeds and time-gaps as seen in Figure 2.15. Hence, it is essential to keep layer time-gaps short in order to achieve a higher inter-layer bond strength.

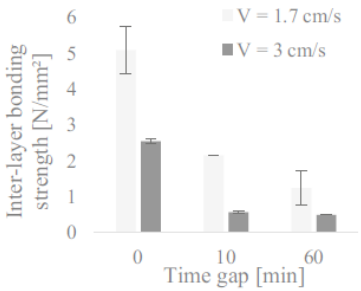

Figure 2.15: Inter-layer Bond Strength for specimens with printed with different time-gaps and printing speeds [6]

The effect of surface roughness on the bonding between old and new cast (conventional) concrete has been explored in terms of concrete repairs. The bonding, in this case, is concluded to have a more stable fracture and ductile performance under the uni-axial tension test indicating an increase in the ductility behaviour of the interface [7]. This research was in terms of bonding in concrete surfaces in repair systems. Another similar experimental research in terms of 3D concrete printing was performed by Van Der Putten *et al.* [29] wherein the surface roughness was measured and the effect of the modification technique on the inter-layer bond strength was investigated. The research concluded that the inter-layer bond strength is positively influenced by surface modifications done using a comb which eventually increases the interlocking effect that is created between the two layers. In the research of van Overmeir et al.[5], this was further addressed by performing experiments on Strain Hardening Cementitious Composites (SHCC) based 3D printed specimen in the form of roughening the surface by brushing and results indicated an increase in the inter-layer bond but at the expense of reduction of the tensile strain-hardening capacity in the direction parallel to the printing layer.

In the research of Ye *et al.* [30], a novel ultra-high ductile concrete (UHDC) for 3D concrete printing was developed which was further modified by crumb rubber to possess high ductility. The experimental results of mechanical anisotropy indicated that the inter-layer bond property had a non-negligible influence on the mechanical property of printed UHDC specimens. As seen in Figure 2.16, a fibre pull-out was observed on the fracture surface which is different from that observed in the research of Sanjayan *et al.* [8] which was a specimen based on normal concrete based-mix.

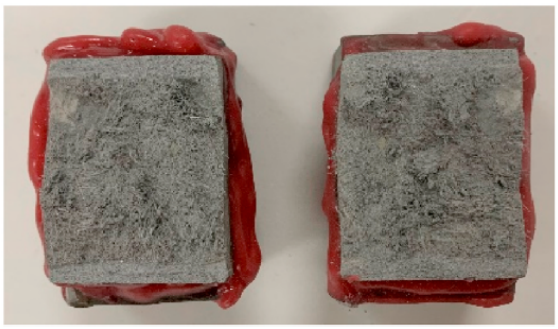

Figure 2.16: Fracture surface of 3D printer UHDC-based mix after inter-layer bond test [30]

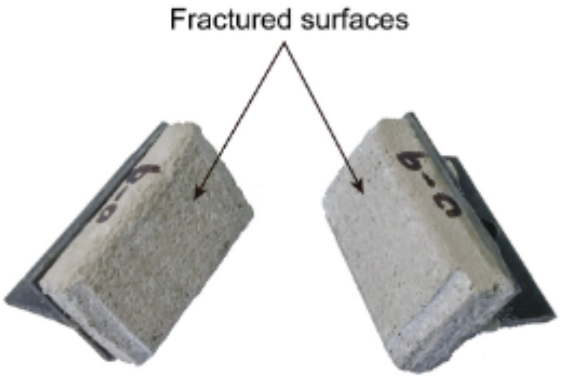

Figure 2.17: Fracture surface of 3D printer normal concrete-based mix after inter-layer bond test [8]

2.3. Reliability of results in tensile tests

Fracture is the total or partial separation of an originally intact body or structure by the propagation of one or more cracks, under loading. Fracture mechanics involves quantitatively assessing crack characteristics in relation to the material's inherent resistance to these cracks [31]. There are 3 ways to apply loading in order to ensure the propagation of a crack in a structural component [31]:

- Mode I: Crack opening mode when the displacement is normal to the crack surface
- Mode II: Crack sliding mode when the displacement is in-plane of the component resulting in an anti-symmetric separation and with the relative displacement normal to the crack front
- Mode III: Crack sliding mode but with displacement occurring normally to the crack front resulting in tearing.

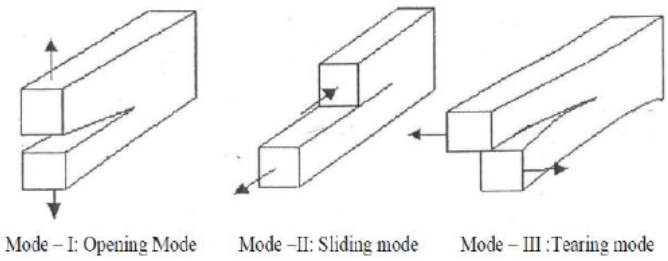

Figure 2.18: Modes of Fracture Failure [31]

The assessment of Mode I properties of concrete needs to be done in a reliable and reproducible test method. The gripping problems (attachment of the specimen to the loading platens) along with the selection of a proper test control system are the most basic aspect that need addressing in order

for the test results to be reliable [32]. The focus here is first placed on issues related to testing control systems that are relevant to the current research program.

The test control systems can be classified as open-loop control (OLC) and closed-loop control (CLC). The main difference in these two systems is that of the system output. In OLC the system output is not used by the controller and the process solely depends on the system inputs whereas in CLC the output of the controlled variable is directly monitored by the controller. In CLC the output is fed back to the controller, compared to the reference input signal and the difference between both is then used as the input variable to manipulate the actuator [33]. The control variable in CLCs can be any quantity that is accessible to a controller such as a displacement, strain or crack control. Since the range of control variables in CLC's is greater it finds a wider application in the test control over OLC's. However, CLC's come with limitations which concern mainly the high initial costs, requirements of precise operator skills and a lag between actual response and corrective action of the controller, which may cause issues in performing the test in the form of loss of control, over-correction or under-correction [33]. To avoid these issues it is suggested to perform a loop shaping with a dummy specimen having characteristics similar to the test specimen, the procedure for which is recommended by the manufacturer.

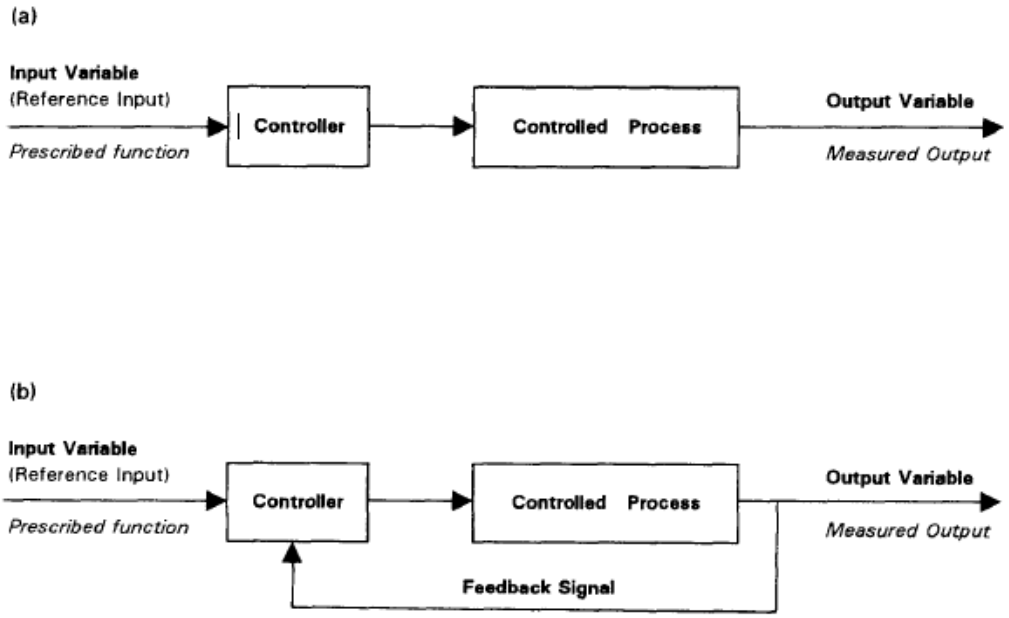

Figure 2.19: (a) Open loop control (OLC's) (b) Closed loop control (CLC's) [33]

One of the drawbacks of CLC-based tensile testing equipment which is that of a lag between actual response and corrective action mentioned in the research of Gettu *et al.* [33] has been addressed extensively by researchers and is discussed herein. In the research of Hordijk [34], the behaviour of a concrete bar under a deformation-controlled uni-axial tension test is explained. As seen in Figure 2.20, at first the deformation of the bar increases homogeneously, later as the peak load is reached strains start to localise within a narrow zone of micro-cracks (known as process zone which occurs in the weakest section of the bar) after which a continuous macro-crack will develop. If the process zone falls within the measuring length whose deformation is used as a control parameter, then a load-deformation relation as indicated by line I in Figure 2.20 will be obtained [34]. With an increasing deformation of the process zone the load transfer capacity of the bar decreases which results in the unloading of the concrete outside this zone and leads to load-deformation relation as indicated by line II. This behaviour of the load-deformation curve is termed as 'snap-back' behaviour [32], [34]. This occurs as a result of the equipment in the experimental setup not being fast enough to overcome a sudden jump in the deformation (after reaching the peak).

These snap-back behaviours were further confirmed by performing a uni-axial tensile test using

CLC based experimental setup on a specimen of dimension 250x60x50 mm^3 as seen in Figure 2.21 to 2.24. The curve in Figure 2.22 indicates two parts wherein no data points are observed despite regular intervals for these measurements which confirms the snap-back behaviour. Hordijk [34] also performed the same tests on different specimen dimensions inferring that the specimen with shorter dimensions have higher rotational stiffness i.e. the non-uniform crack opening is less pronounced as observed from Figure 2.21 and 2.24 and hence, is less susceptible to tension-bending failure.

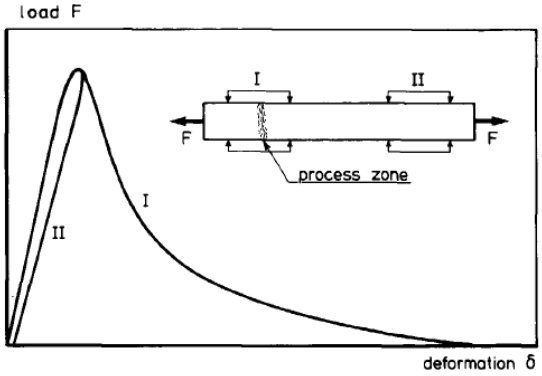

Figure 2.20: Load-deformation relations for concrete bar under uni-axial tensile loading [34]

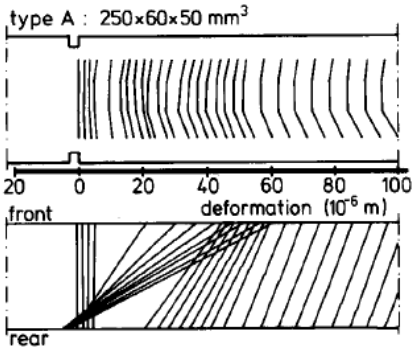

Figure 2.21: Deformation distribution for Specimen type A (250x60x50 mm^3) [34]

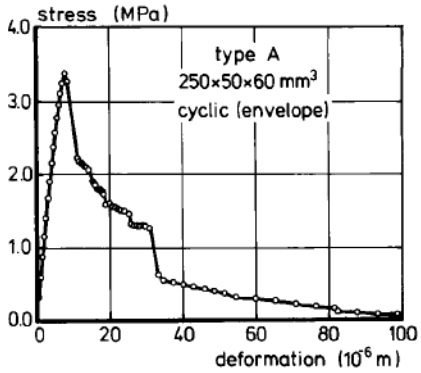

Figure 2.22: Average stress-deformation relationship [34]

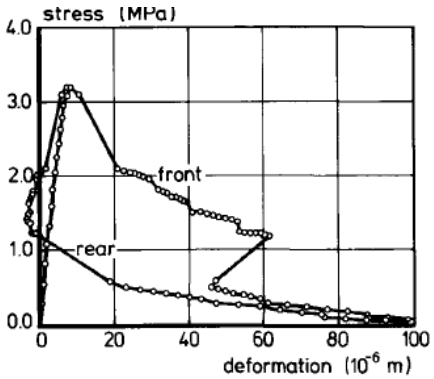

Figure 2.23: Stress-deformation relationship for front and rear sides of the specimen type A [34]

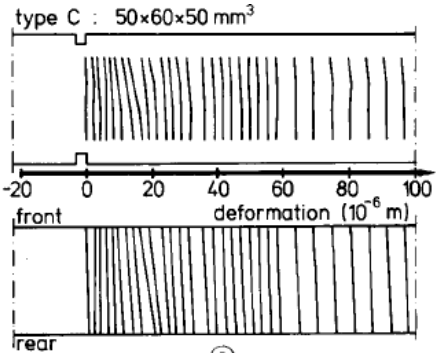

Figure 2.24: Deformation distribution for Specimen type C (50x60x50 mm^3) [34]

Hordijk [34] also showed the effect of choice of measuring length on snap-back behaviour as observed from Figure 2.25 which suggested that the descending branch becomes steeper with increasing length. It is also notable to observe that the specimen with the lowest measuring length has a steep ascending curve suggesting that the deformation capacity of the specimen is less.

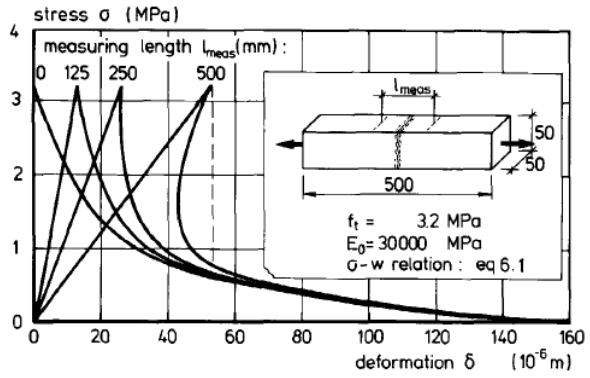

Figure 2.25: Stress-deformation relations for different specimen length [34]

As these snap-back behaviours result in an unstable/eccentric increase of deformation within the damage zone they are said to impair the stability of the experiment [32]. There are several measures that can be taken to avoid the snap-back and ensure stable controlled tests some of which include:

- The length of the LVDT's selected for test control should be selected as small as possible. However, if the specimen is too small then this would be impossible.

- Creating a notch is a workaround for long prismatic specimens wherein the location of the crack is not known prior.

- As suggested by Li *et al.* [35] testing of un-notched concrete specimens can also yield stable controlled tests which can be achieved by placing a number of LVDT's with small measuring length over the length of the specimen and selecting the critical deformation of all the LVDT's and feeding it back to the controller by manipulating it to stabilise the upcoming input.

The boundary conditions of the specimen under uni-axial tensile loading is significantly said to affect the shape of the strain- softening curve and has a similar effect as that of rotation induced due to unsymmetrical specimen [34]. In uni-axial tensile tests, the crack usually propagates from one side and eventually as the test progresses the specimen is eccentrically loaded. If the specimen has fixed boundary conditions a counteracting bending moment will develop to overcome these eccentricities, however, in the case of free rotating boundary conditions, this bending moment is unable to develop [32]. This results in the softening part of the stress-deformation curve having bumps in the fixed boundary conditions as compared to no bumps in the rotational boundary conditions which was confirmed in the research of Zhou [36] as observed in the Figure 2.26.

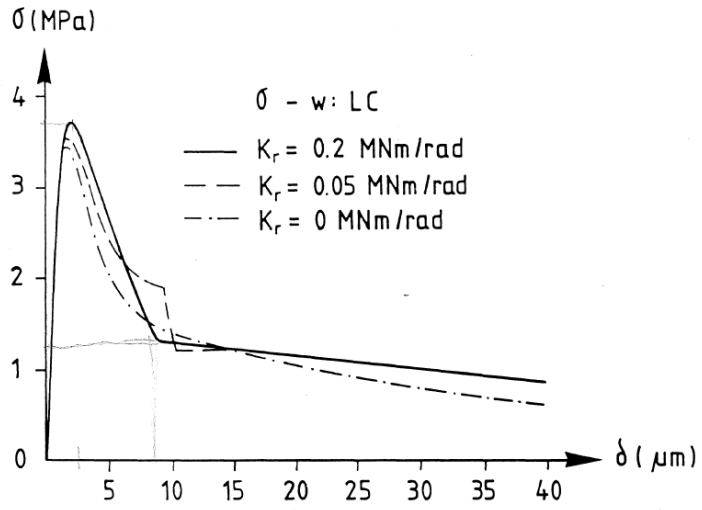

Figure 2.26: Uni-axial tensile test of a concrete specimen with different rotational stiffness exhibiting bump effect [36]

Further, the research of Cattaneo *et al.* [37] concluded that the fixed boundary conditions resulted in a more stable crack propagation in the critical cross-section as compared to the rotational boundary conditions of the specimen as observed in the Figure 2.27. The decrease in fracture energy is about 40% in rotational as compared to that of fixed boundary conditions [38].

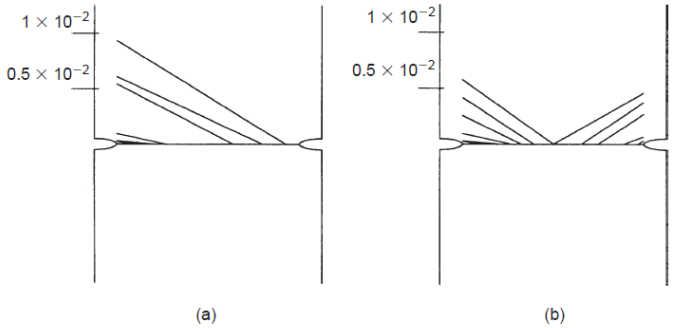

Figure 2.27: Progressive crack penetration for (a) rotational boundary conditions and (b) fixed boundary conditions [37]

Van Mier *et al.* [32] state in their research that if fracture properties are dependent on boundary conditions they cannot be regarded as the true property of the material under consideration. Therefore, in-order to ensure reliable and stable tensile tests on un-notched specimens it is essential to use several LVDT's to measure deformation [35] and a CLC-based testing equipment [33] having a feedback manipulator [35] which will help eliminate snap-back behaviour. After ensuring stable deformation-controlled tests it is also important to ensure that the boundary conditions of the specimen are fixed [37] and the specimen is as symmetrical as far as possible in-order to eliminate problems of unstable fracture propagation [37] and rotation due to unsymmetrical specimen [34].

2.4. Strain Hardening Cementitious Composite (SHCC)

Strain Hardening Cementitious Composite (SHCC) (also known as Engineered Cementitious Composite (ECC)) mixes are said to exhibit high tensile ductility (several hundred times that of normal concrete), intrinsically tight crack width (as seen in Figure 2.28), self-reinforcing characteristic and are

well-equipped to absorb impact energy [3]. A range of studies suggests that SHCC has the potential to overcome the brittle behaviour of ordinary (non-fibre reinforced concrete). The ductility associated with the SHCC composites is attributed to the formation of multiple micro-cracks which do not increase the permeability of the material substantially and may also exhibit some self-healing capabilities [12]. The tight crack width in the SHCC-based composites as spotted in Figure 2.28 can help address the aspects of maintenance and rehabilitation in the life-cycle of the structure by enhancing their durability as moisture, gas and salt ingress in the cement-based materials are major factors responsible for degradation of the structures [39].

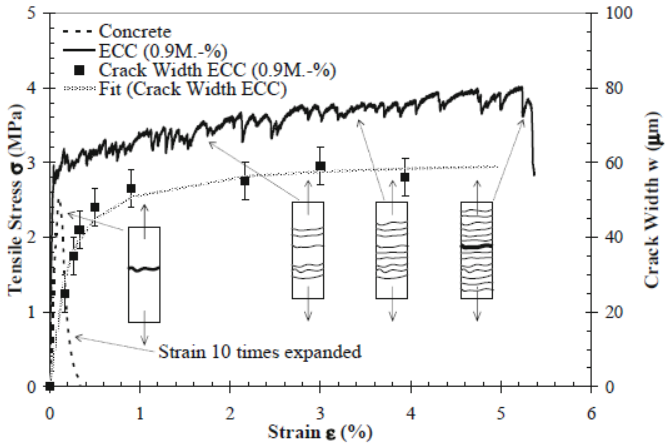

Figure 2.28: Tensile Stress Vs. Strain response of SHCC showing a tight crack width (below 100 µm) [40]

An experimental study based on fundamental rheological properties was carried out by Figueiredo *et al.* [4], which presented a methodology to develop mix-designs for printable cementitious composites. The study focuses on two SHCC mixtures one composed of Portland cement (OPC), blast furnace slag (BFS) and limestone powder (LP), while the second is composed of OPC, fly ash (FA) and sand. The research concluded that the mixtures with high fibre content exhibited high mechanical performance and superior printing quality and therefore, must be considered for further developments in the construction printing industry [4].

From the research of Panda *et al.* [41] it was concluded that the addition of fibres to printable mortar improves flexural and tensile strength. The research of Nematollahi *et al.* [42], further investigates the effect of fibre content through a comparative study between 3D-printed geopolymer without fibres and the other with fibres and this reported increase in flexural and tensile strength when compared to reference geopolymer without fibres. These investigations confirm the feasibility of using dispersed fibre reinforcement as an approach to integrate reinforcement into the 3D-printing processes. Based on these findings printable SHCC with High-density polyethylene micro-fibres were chosen in the study of Ogura *et al.* et al. [43]. The specimens extracted from the SHCC-based printed walls in this research exhibited pronounced strain-hardening behaviour under uni-axial tensile loading for fibre concentrations as low as 1%. Also as can be spotted in Figure 2.29, for a fibre content of 1.5%, strain capacity was considerably higher, and very uniformly distributed fine multiple cracks were observed (Figure 2.30) eventually contributing to enhanced inter-layer bond strength.

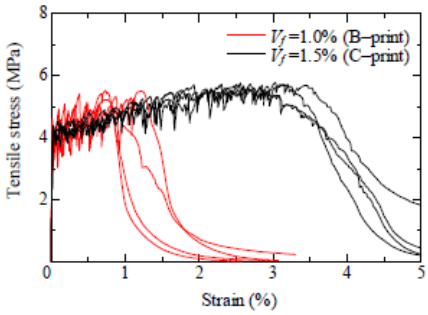

Figure 2.29: Tensile Stress Vs. Strain response of Printable SHCC with different fibre content [43]

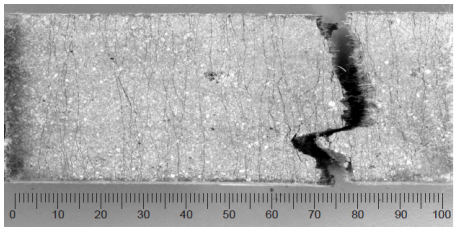

Figure 2.30: Representative crack patterns of specimen C-print after failure in uni-axial tension tests [43]

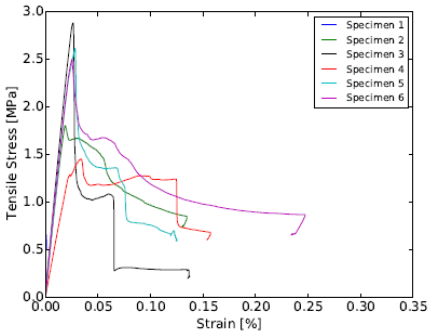

Figure 2.31: Stress Vs. Strain Graph for Bond Strength of Specimen X (mix composed of Portland cement (OPC), blast furnace slag (BFS) and limestone powder(LP)) [44]

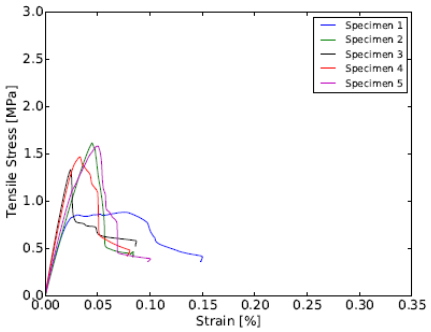

Figure 2.32: Stress Vs. Strain Graph for Bond Strength of Specimen Y2T (mix composed of OPC, fly ash (FA) and sand) [44]

The research of Figueiredo *et al.* [4] was further extended with the 2 mixtures and after analysing tensile bond strength of the interface it was inferred that all the specimens showed little ductility and no strain hardening due to lack of fibre bridging in the fracture surface [44] as can be observed from Figures 2.31 and 2.32. The research also confirms that the printing technique leads to intrinsic anisotropy from the observation that strain hardening behaviour was achieved in two directions with minor ductility in the third direction.

In the research of Li *et al.* [3], an attempt was made to study the interface in a specimen 3D printed using a PVA fibre-based mix through single notch fracture tests. These specimens show an initial brittle failure with a residual strength after a sudden drop post-peak stress is reached which is associated with the fibre penetration in the interface.

The study further investigated the grooving effect in the interlocking through similar tests and the results conclude that the inter-facial crack bifurcates which results in a subsequent rise in post-peak loading.

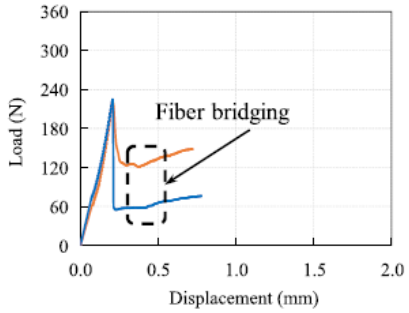

Figure 2.33: Load-displacement curve for smooth layered specimen printed with PVA fibre-based mix [3]

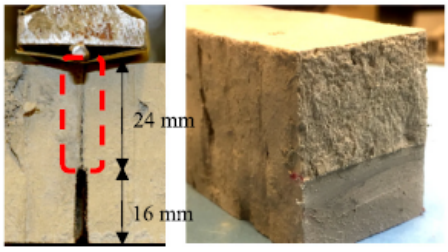

Figure 2.34: Fracture behaviour of interface for smooth layering in specimen printed with PVA fibre-based mix [3]

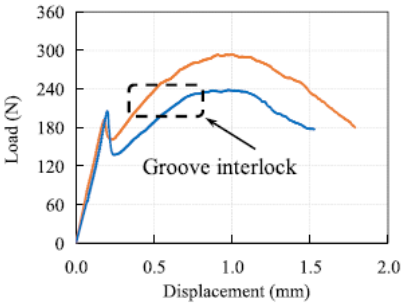

Figure 2.35: Load-displacement curve for groove layered specimen printed with PVA fibre-based mix [3]

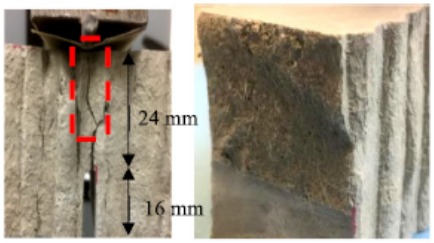

Figure 2.36: Fracture behaviour of interface for groove layered specimen printed with PVA fibre-based mix [3]

2.5. Concept of topological interlocking

In the research of Hamilton *et al.* [45], the potential of mechanically interlocking micro-structured adherents to increase the strength and toughness of single lap joints is investigated. Compared to the planar roughened joints, results for the micro-structured joints revealed an increase of up to 95.9% for strength.

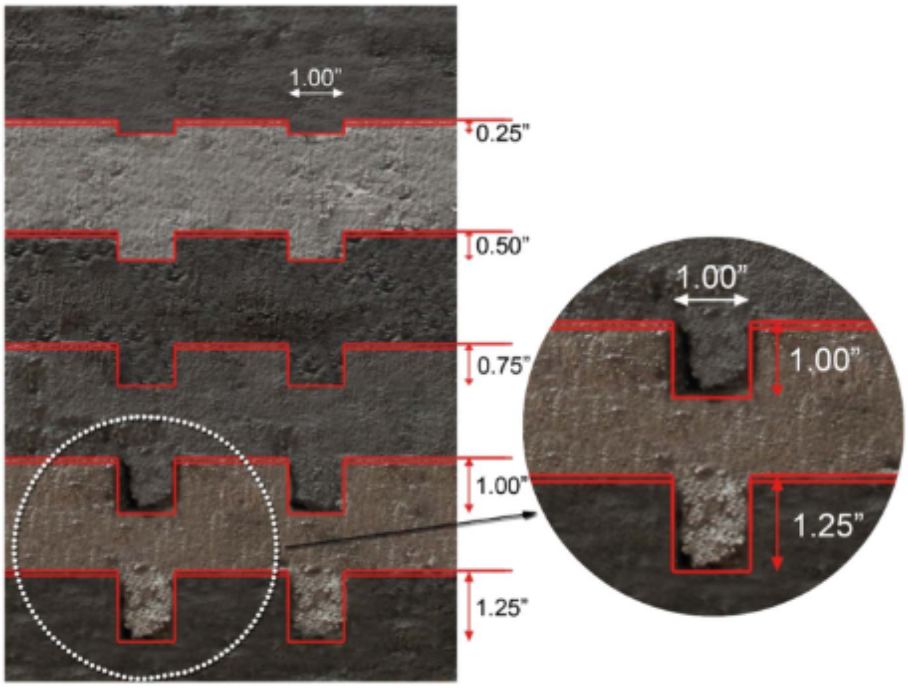

Figure 2.37: Preliminary study on the size of interlocking [24]

Further research in terms of the effects of interlocking attributed the increase in the bond strength to the increase in the contact surface of layers [24]. The results show that bonding strengths are sensitive to interlocking and it can be increased by an average of 26% as shown by splitting test results in Figure 2.38 and 2.39. As observed from Figure 2.37 the groove size of more than 3/4”(19 mm.)in the interface can cause a non-uniform distribution of material into the groove. Hence, this research serves as a good basis for the choice of groove sizes to be ascertained herein the research to ensure interlocking.

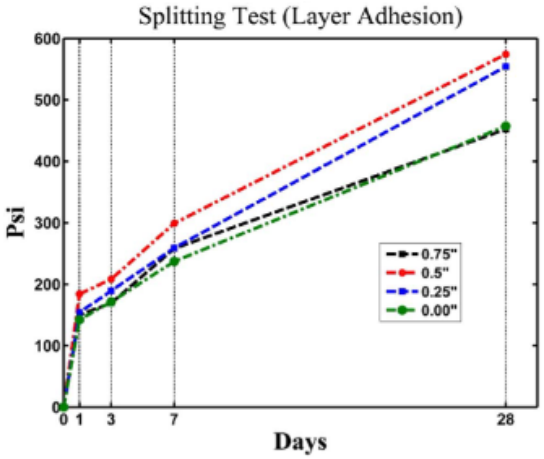

Figure 2.38: Comparison of bond interface for four types of interlock [24]

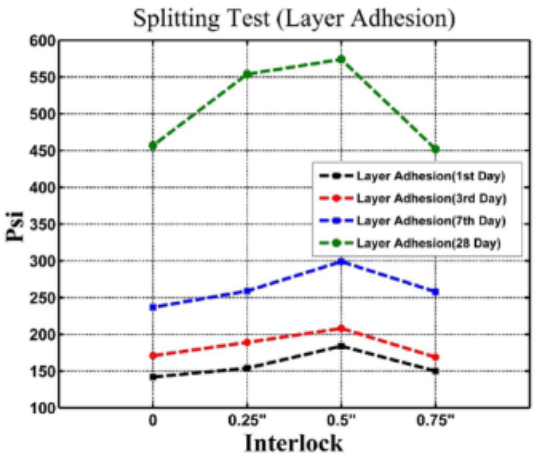

Figure 2.39: 28 days’ strength development of four types of interlock [24]

Taking these aspects into account the design principle of topological interlocking is proposed in this research wherein the elements are held together purely by geometrical constraints without the use of

mortar-based binder or connector [11]. Concentrated (out-of-plane) load tests have been carried out in previous literature on a plate made of osteomorphic block elements and compared to similar tests on a solid plate which resulted in localised failure of elements in the former as compared to the global failure of solid plate [13] as shown in Figure 2.40.

The block assembly suggested in these literature studies [11], [13] is said to exhibit a small-scale crack propagation across the assembly because the elements are not connected which would otherwise help form a medium for cracks to propagate. Simulations have been performed on these block assemblies and it is concluded that loss of nearly 25% of the constituent elements would still suffice to maintain the structural integrity. In the research of Molotnikov *et al.* [13], the load was applied in a plane perpendicular to the specimen as shown in Figure 2.40 and results were analysed. This study further goes to show how promising the concept of mechanical interlocking can be and the benefits it has to offer. Though this study has been in the direction out-of-plane of the specimen it forms a good basis for understanding the concept of mechanical interlocking hereon.

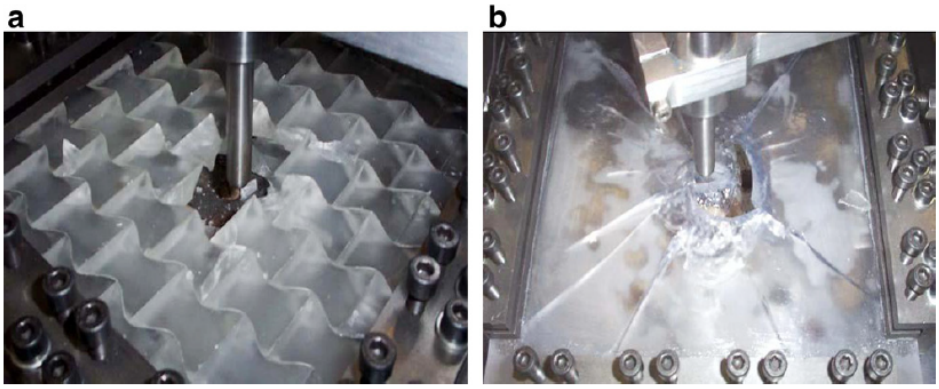

Figure 2.40: Fracturing of the assembly of interlocked blocks in concentrated load tests as compared to a solid plate of the same dimensions made from the same material (polyester casting resin): (a) localised fracture in interlocking assembly and (b) global fracturing of the solid plate [13].

Furthermore, similar research is carried out in terms of concrete bricks by Javan *et al.* [46]. In this research, a comparative study of the mechanical behaviour of a hybrid assembly plate (which is made of a combination of topologically interlocking concrete bricks and rubber interfaces), an assembly plate and a monolithic plate are investigated under quasi-static load. Failures occurring in different plates are shown in Figure 2.41. The results show that the hybrid assembly plate has remarkable flexural compliance with less damage in the bricks [46].

As can be observed from Figure 2.41, the hybrid plate experiences a push-out of the brick. On the other hand, the assembly plate experiences cracking of the centre brick. The monolithic plate cracks entirely and the crack propagates towards the corner of the plate. In both hybrid and assembly plates, however, the integrity of the structure is maintained with some exceptions of minor cracks propagating in the surrounding region of the assembly plate.

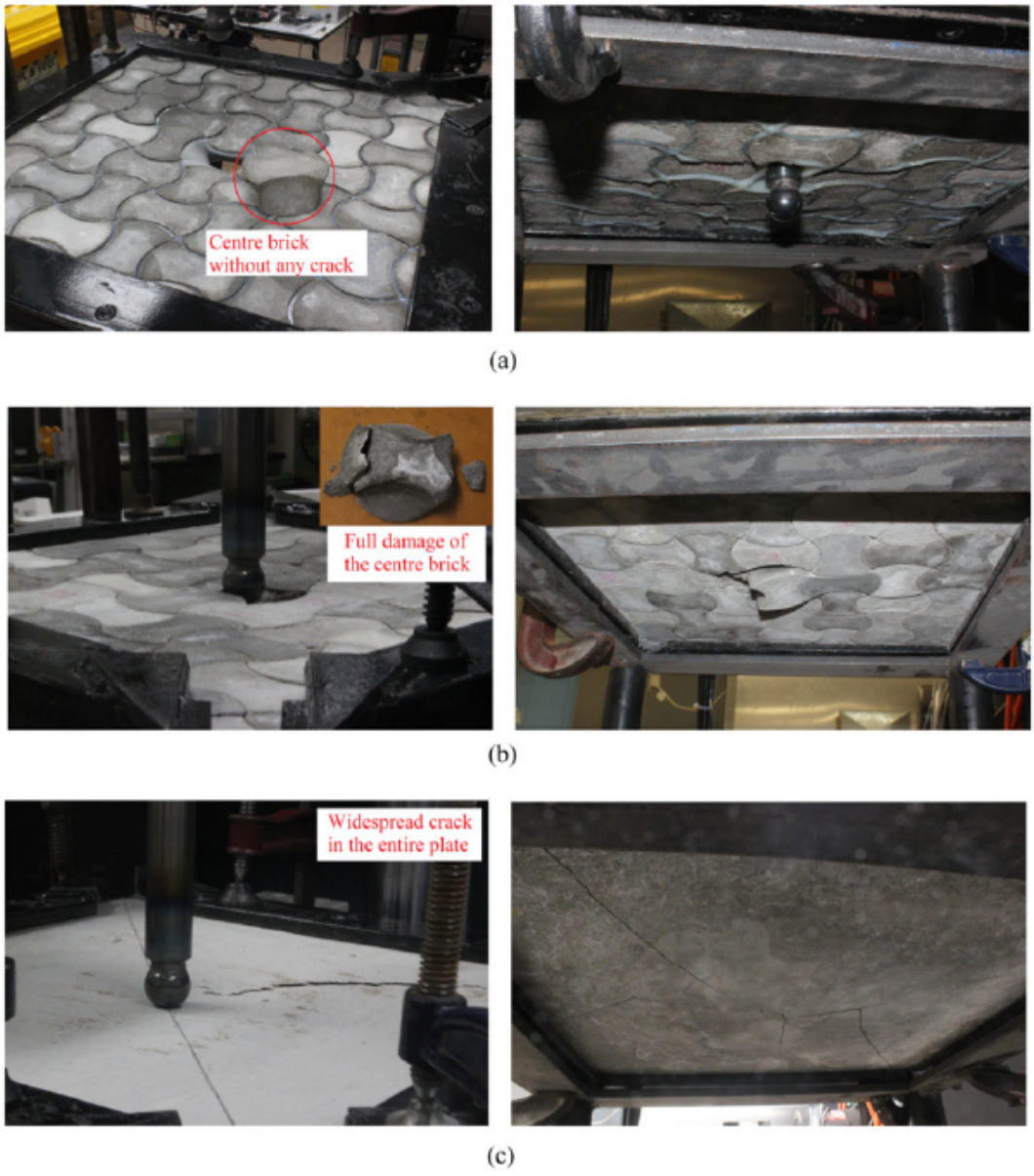

Figure 2.41: Failure in (a) Hybrid plate (interfaces between bricks are filled with silicon-based rubber) (b) assembly plate (c) monolithic plate under quasi-static load [46]

In the research of Yong [47] an experimental study was carried out which involved testing the axial compression of osteomorphic block assembly manufactured from plain dental gypsum stone, comprising a full block capped with 2 half blocks. A Baldwin universal testing machine was used for the test and after the failure, a photographic assessment of the crack formation is carried out which can be seen in Figure 2.42 and 2.43.

The results conclude that interface friction is a stabilising factor, and when the stacked blocks are axially compressed, interface sliding occurs which further causes outward displacement of the interlocking crests thus, inducing tensile stresses within the block which results in premature load-bearing failure before the full material compressive strength can be mobilised. The shear stress due to induced interface friction can limit this interface sliding, thus reducing the formation of tensile stress and subsequently increasing the compressive strength [47].

Figure 2.42: Assembly of Osteomorphic block for axial compression test [47]

Figure 2.43: Identification of crack formation in the osteomorphic block after compression test [47]

There has been extensive research in terms of the use and applications of osteomorphic blocks as a form of mechanical interlocking. Most of the research is focused on other materials, namely glass [11], brick masonry and conventional concrete (which does not contain fibres) [46]. Also, the experimental studies conducted involve testing of the specimens by out-of-plane application of loads [11], [46] and there has been very less focus in terms of testing these specimens for in-plane loading except for a few axial compression studies [47].

2.6. Surface Moisture Content and Time-Gap

The exposure of extruded layers to the environment results in loss of moisture on the surface of these layers. The time-gap between the extrusion of one layer on the underlying layer and the surface water evaporation from the underlying layer together results in inadequate moisture exchange and eventually can result in a weak inter-layer bond [8]. The surface water evaporation also leads to non-uniform distribution of contact between the layers and eventually results in the formation of voids between the printed layers which is a common phenomenon in 3D concrete printing. These voids can negatively affect the durability of the printed structures [48] resulting in a weak inter-layer bond. In the research of Van Der Putten *et al.* [48] the results of mechanical performance were correlated to process parameters like printing speed and time-gaps. The surface moisture content changes were measured by pressing the blotting paper strips on the layers at pre-defined time-steps of 0, 10, 30 and 60 minutes after printing (as shown in Figure 2.44).

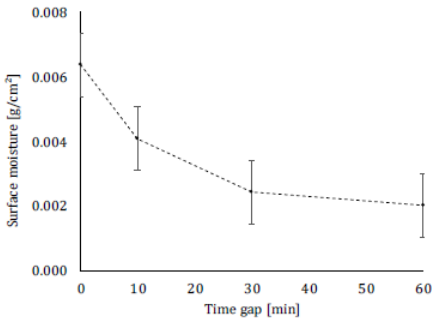

Figure 2.44: Moisture Content of a printed element measured at different time gaps [48]

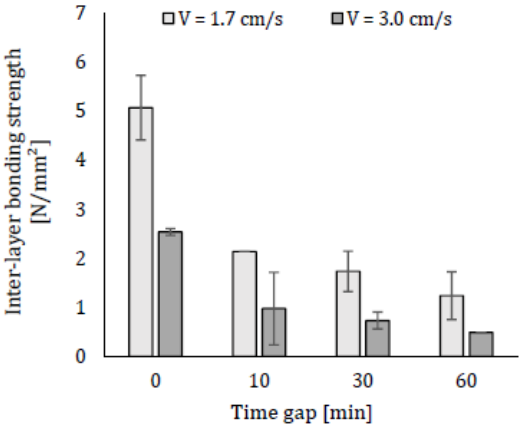

Figure 2.45: Relation between Inter-layer bond Strength and Time-gaps for 3D printed specimens (V represents the print speeds) [48]

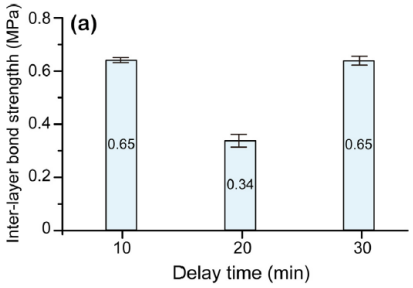

Figure 2.46: Inter-layer strength of the printed concrete [8]

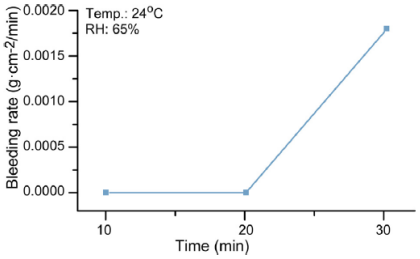

Figure 2.47: Bleeding rate from the surface of the printed concrete [8]

The mass change of the blotting paper was calculated and the mass of absorbed fluid was determined. The specimens of different time-gap were then tested for inter-layer bond strength (as seen in Figure 2.45) and a relation between surface moisture content, time-gaps and inter-layer bond strength was established. As can be inferred from Figure 2.44 & 2.45 the inter-layer bond strength and surface moisture for specimens with smaller time-gap is higher than that for the specimens with larger time-gap. In the research of Wang *et al.* [49] it is observed that the exposure of the concrete surface to the atmosphere leads to the evaporation of water which is further replaced by the migration of water from the inside to the top surface generating a gradient of relative humidity over the height of the concrete layer.

The research of Sanjayan *et al.* [8] is on similar lines but is performed for extended time-gaps as compared to smaller time-gaps in the case of the research of Van Der Putten *et al.* [48]. This experimental study suggests that the inter-layer bond decreases for certain time-gaps and later increases as shown in Figure 2.46. The reason identified for these discrepancies in the results is that moisture is brought to the surface by the bleeding of water from the concrete when the delay time is sufficiently larger as seen in Figure 2.47. One of the main conclusions to draw attention to in this research is that the major factor affecting the inter-layer strength is the moisture level at the surface between the layers. If the surface is dry, it does not have the workability (or malleability) for the bond to develop [8]. However, this research also infers that the moisture level between the layers is a function of the printing process, evaporation rate and bleeding rate of the mixes and moreover, also depends on the level of

moisture expelled to the surface during the extrusion process which helps in explaining the discrepancies in the findings in the two research studies. However, the relationship between moisture level and inter-layer strength is universal (implying that dry surface has a decreased capability to develop bond) [8].

2.7. Image Analysis of Fractured Inter-layer

Image analysis tools have been widely adopted in material research and aid the purpose of visualisation and quantification of results. There are various alternatives that can be implemented in-order to characterise the quality of bond in the inter-layer, the most common being micro-structural analysis techniques like that of the scanning electron microscope (SEM) and Maximum intensity projection (MIP) or image analysis techniques like X-Ray or computed tomography scans (CT) [50] [6]. These techniques have the benefit of providing detailed information on the inter-layer at the cost of being time-consuming and cost-intensive.

Image analysis is an alternative approach used in concrete research for applications ranging from damage characterisation [51] to air void determination [19] (as seen in Figure 2.5). Image analysis involves a crucial step which is that of acquiring a high-resolution image for processing at a later stage. In the research of Miriello *et al.* [52], flatbed scanners (which has a flat surface on which the printed image or document is scanned and stored) were used for image acquisition which was a cheap and effective alternative to get fast and high-quality images. Furthermore, in the research of Peterson *et al.* [53], acquired images from a flatbed scanner to quantify air void characteristics in the hardened concrete surface. In the research of Marchment *et al.* [9], image analysis of the fractured inter-layer of 3D concrete printed sample was carried out using images acquired from flatbed scanners. The top and bottom images of the inter-layer acquired were first put through the process of 'CIELAB colour space thresholding' wherein the coloured flatbed scanner images were converted to black and white images as seen in Figure 2.48. The number of black pixels in both images was then used to quantify the effective bond area in percentage as illustrated below:

$$\text{Effective Bond Area (in \%)} = Total - \frac{(Bottom - Top)}{Total} x100\%$$

where, Total - Total number of pixels

Bottom - Number of black pixels of bottom image

Top - Number of black pixels of top image

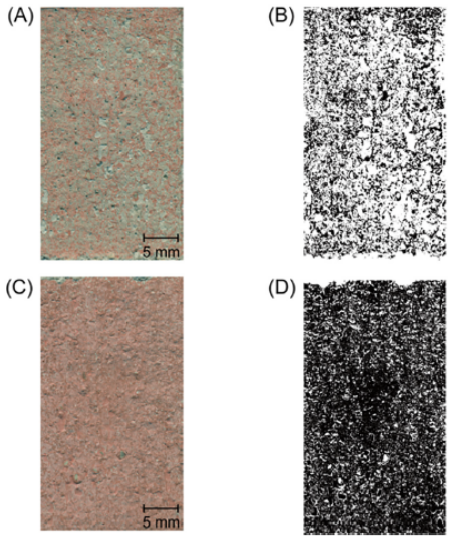

Figure 2.48: Results of application of colour thresholding. (a) Top Image before thresholding, (b) Top Image after thresholding, (c) Bottom Image before thresholding, (d) Bottom Image after thresholding. [9]

Image colour summarizer is an open-source tool based on the concept of 'Digital Image Processing' wherein the image pixels are analyzed with an algorithm and provides statistics for that image. The Image colour summarizer tool creates a set of clusters of similar colours from an image which is representative of the image. The method works well on images with relatively well-defined colour boundaries. Based on the inputs given by the user, such as output format, statistics, colour clusters, delimiter and precision control, the summarizer reports the average, median, minimum and maximum values for each component in different colour models namely, RGB, HSV, Lab and LCH. This tool has found scientific applications in cancer research and genome analysis which helps understand its credibility and hence has been preferred for the research herein. A similar strategy to quantifying inter-layer bond as observed in the research of Marchment *et al.* [9] is attempted in the research herein using the image summarizer tool.

3

Research Framework

3.1. Research Justification

The literature is extensive in terms of improving the bonding between the layers with the help of additives, glue and mechanical additions. At the stage of writing this research, there hasn't been any significant study in terms of improving the inter-layer bond, solely, by ensuring topological inter-locking by changing the shape of the extruded layer. However, there has been considerable research [11], [46] which focuses on the benefits of topological interlocking for developing and strengthening architecturally engineered materials and structures for out-of-plane loading directions which has shown promising results in improving mechanical inter-locking. The benefits of this concept which include high resistance to crack propagation, large energy absorption capacity and tolerance to local failures have been less explored in regard to 3D concrete printing structures. This research intends to focus on altering the shape of extruded layers from planar to those inspired by osteomorphic block elements in-order to achieve interlocking between consecutive layers without the use of additives, glue and mechanical modifications. Additionally, combining this concept with fibre based-mix can be insightful as most of the current literature's [3], [8], [30] suggest showing fibre bridging in fracture surface of the specimens tested for inter-layer bonding that are printed using fibre based-mixes. Hence, given the modification of the extruded layer, the material and the in-plane load application, differences in the results in terms of the 3D concrete printed specimen could be interesting to analyse.

However, the current advancements in 3D concrete printing technology do not have enough degree of freedom (DOF) in the extruding arm in-order to modify the planar shape to that proposed herein and the mixing pump limitations to extrude fibre-based mix without clogging issues further make it impossible to extrude this proposed osteomorphic block inspired shape. This further makes it complicated to achieve the osteomorphic block-inspired shaped specimens required for inter-layer bond testing which forms the main part of the research scope herein. To overcome this hurdle it is proposed to use a manual caulk-gun extrusion technique in combination with casted osteomorphic blocks inspired by the shape of concrete base-blocks and mould-casting technique to extrude/cast the specimens. The samples are then derived from the extruded/casted specimens by sawing which are further cured and tested in the available test setups (without making excess modifications to the current test setup) that yield results which can be helpful to analyse the effectiveness of interlocking between successive layers. Given the outcomes in the literature based on moisture migration and time gap investigations in terms of 3D printable concrete [8], [48], [49] an intermediate study focusing on correlation of time-gap in terms of moisture migration in the layer with inter-layer bond test results is also proposed and executed.

3.2. Research Objective

This research aims at addressing the problem of weak inter-layer bonding in printable SHCC-based mix by incorporating the concept of topological interlocking in the extrudable 3D printable concrete layers. This is mainly achieved by altering the general planar shape of extruded 3D printable concrete layers by incorporating an osteomorphic block-inspired shape. Hence, with a combination of the random orientation of fibres this concept is expected to impart an enhanced mechanical interlocking between two extruded layers leading to an increase in inter-layer bond within extrudable 3D printable concrete structures. Hence, the research aims at answering the following main question:

What is the effect in the inter-layer bond when the prevalent planar geometry of SHCC-based extruded layers is modified to one inspired by osteomorphic blocks in extrusion-based 3D concrete printing?

In order to achieve the research objective the research tasks are divided into two main parts as below:

- **Analysing the grooving effect**: In the first part, the focus is on the preparation of mould-cast specimens with different groove sizes and testing them for tensile bond strength and analysing the results to study the effect of grooving.
- **Analysing grooving effect in combination with time-gap and extrusion parameters**: The second part intends to focus on the preparation of caulk-gun specimens with an intention of inclusion of extrusion parameters along with different time-gaps and testing these for tensile bond strength. Further, image analysis is performed on the fractured inter-layer surface, the results of which are then correlated with bond test results and surface moisture to draw conclusions.

3.2.1. Preparation of specimens

At this point in time, the 3D concrete printing technology works on the basis of additive manufacturing which involves extruding planar layers in a layer-over-layer form in order to construct a 3D concrete element. This method is convenient given the availability of as many as seven/six degrees of freedom operable in a robotic arm in the present-day robotics infrastructure. The problem which is still not addressed convincingly in the layer-over-layer extrusion of 3D concrete printing technique is that of weak inter-layer bond in the printed concrete elements.

In order to address this issue a new shape of the layer is proposed to be extruded which is inspired by the osteomorphic block shape which is hypothesised to increase the inter-layer bond by providing topological interlocking between the extruded layers. The problem then lies in devising a technique to extrude this non-planar shape using the available robotic infrastructure since, doing so would require not only making changes at the level of providing instructions to the robot but also at the nozzle level in terms of regulating the flow to extrude the right amount of concrete and providing the nozzle with additional degrees of freedom which has to be done simultaneously with the robotic arm movement to achieve the osteomorphic block inspired shape of the layer.

In this research, methods to extrude the proposed non-planar shape of the layer were explored and attempted (which are further described and explained in detail in Appendix - A from the point of view of extracting a sample from these extruded specimens which can be then further tested in the Instron test setup for inter-layer bond test available at Delft University of Technology's MicroLab. However, since the current technological advancements in 3D concrete printing are not suitable to extrude the proposed layer and due to the limited availability of time for the research to devise and develop such equipment, it was decided to adopt the methods of mould-casting and caulk-gun extrusion (which are explained in brief below) to obtain the specimens required for further investigation.

- **Casting the specimens using silicon-rubber moulds:** In order to keep the problem simple and

eliminate the extrusion parameters altogether, it was decided to mould-cast the specimens. This helped to concentrate solely on investigating the influence of adopting an osteomorphic block-inspired shape on the inter-layer bond between extruded specimens. Simultaneously multiple groove sizes were selected to cast these specimens which would help to understand the approximate depth of the groove required in the topology to ensure interlocking between the layers. The procedure and detailed explanation for the preparation of specimens using this method can be found in Sub-section 4.2.1.

- **Caulk gun extrusion technique:** A manually operated caulk gun was used to extrude layers in-order to simulate process parameters of 3D concrete printing such as nozzle extrusion from a constant height and speed to obtain specimens which have an osteomorphic block-inspired shape (as seen in Figure 1.3). Samples were sawn from these specimens which were further used to test the inter-layer bonding. At the time of preparation of the specimens, the time-gap between the extruded layers and the surface moisture content parameters was accounted for in order to study their influence on inter-layer bond strength. The parameter of groove sizes selected at the time of mould-casting the specimens was also retained at the time of caulk-gun extrusion of specimens. The detailed procedure followed for the same is covered in Sub-section 4.2.2.

3.2.2. Performing bond strength tests and analysing results

Specimens were produced using caulk-gun and from the mould-casting methods were sawn and then cured for 28 days. The samples were then tested under the Instron test set-up (as seen in Figure 4.12) for the inter-layer bond test available at the Micro-Lab at Delft University of Technology's faculty of Civil Engineering. A detailed description of the test setup is given in Section 4.3.1. Furthermore, the results were analyzed and a correlation was found between groove size, time gap, and surface moisture content. Detailed analysis of test results for each specimen is covered in Appendix - B for Mould-casted and Caulk-gun-based specimens.

4

Research Setup

The previous chapter gives an overview of the research that has been carried out during the entire tenure of the thesis. The intention of this chapter is to elaborate on each aspect of the research in detail. This is done by first discussing comprehensively the methods adopted to cast/print the specimens which are then followed by a brief description of the test methods adopted. Furthermore, the chapter also addresses on few other details followed along the research like that of design parameters, mix design and printing facilities.

4.1. Design Parameters

4.1.1. Mix Design and Mixing Procedure

As the research involves extruding concrete in the form of a newly proposed topology, this requires that the mix used should have a stiffness of the order such that it can exhibit shape retention capabilities in-order to facilitate the printing in a non-planar fashion. The research focuses on studying the interlocking between layers due to the topology which is created as a result of non-planar layer extrusion and as most of the research [42]–[44] suggest the orientation of fibres used in the mix might help in enhancing this interlocking effect. This makes it relevant to use a Strain-Hardening Cementitious Mix for this research. The mix chosen for this research was developed by Anne Linde Van Overmier and covered extensively in the article titled 'Consistency of Mechanical Properties of 3D Printed Strain Hardening Cementitious Composites Within One Printing System' [54]. The mix demonstrated good results during 3D concrete printing sessions at the Eindhoven University of Technology in terms of being adequately stiff which made it compatible with this research. To understand if the extrusion of this mix was possible with the printing facilities available at Stevin Lab in the Delft University of Technology a printing session was carried out in which the results were positive in the sense that it could be extruded well and hence, it was decided to proceed with this mix for the research.

For the caulk-gun extrusion technique, 3 batches (resulting in a total volume of 10.5 litres) each weighing 3.5 litres were mixed in a Hobart mixer. For the mould-casting technique through 4 batches (resulting in a total volume of 14 litres) were used being mixed in groups of 2 batches (one after the other) at a time. The mixing procedure described below is followed to keep consistency between different mix batches throughout the extrusion/casting session. The mix proportions are given the Table 4.1 below.

Table 4.1: Mix Proportions for 1 Litre of Mix

Mix Constituents	Quantity (grams/litre)
BFS - eco2cem	262.34
CEM-1 42.5	469.51
SF	32.87
LS Inducal 105	582.77
Sand 125-250	316.92
Water	366.17
VMA	3.44
Superplasticiser	3.06
PVA	26.00

Dry mix all the materials including fibres, superplasticizer (powder-based) and one-third of the total volume of viscosity modifier (also powder-based) for 2 minutes at moderate speed. After 2 minutes of dry mixing, slowly add water to the mix for a duration of 1 minute (while continuing to mix at low speed). Continue mixing for another 2 minutes until a dough-like mixture is formed. Add the remaining two-thirds of the viscosity modifier (while continuing to mix at a moderate speed). Continue mixing for another 4 minutes until the mixture is well mixed and fibres are distributed evenly in the mix.

4.1.2. Groove-Size Investigations

The proposed non-planar osteomorphic block-inspired shape of the extruded layer is said to create a topology that would facilitate interlocking between 2 successive extruded layers. The groove size is associated with the size of this topology. So as to ensure that the interlocking effect is adequate, such that the inter-layer bond between the layers is enhanced, an appropriate size of the topology had to be identified and adopted as studied in the research of Zareiyan *et al.* [24]. For this purpose, the groove size parameter was established. The groove size was calculated to eliminate the problems of under-filling, air void, cold joints and non-uniform contact between the extruded layers. The groove sizes selected (as seen in Table 4.2) were such that the minimum and maximum values considered were based upon the shape retention capabilities of the mix which was judged from prior printing sessions.

Table 4.2: Groove-size adopted for investigation (refer table in accordance to Figure 4.1)

Sr. Nr.	Specimen	Groove size dimension (X in mm.)
1	Specimen 'A'	20
2	Specimen 'B'	30
3	Specimen 'C'	40

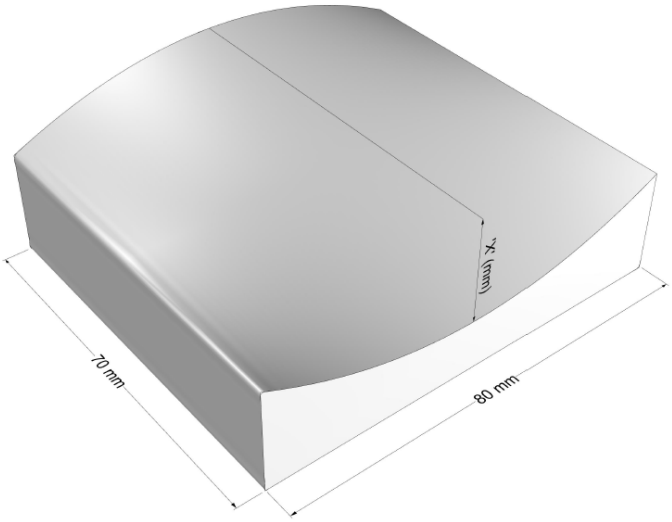

Figure 4.1: Dimension of the groove-size for the topology (to be referred in accordance with Table 4.2)

4.1.3. Time Gap Investigations

The time gap investigations were usually done to study the effect of moisture migration on the surface and its evaporation to the surrounding exposed atmosphere. This is further used as a basis to assess the changes over a period of time in the strength characteristics mainly inter-layer bond.

Figure 4.2: (Left) Roughneck mortar gun used for scale model 3D concrete printing for extrusion (Right) Brennenstuhl 1298680 Moisture meter MD

At this stage a scale model 3D concrete printing methodology was adopted which used caulk-gun (as shown in Figure 4.2 below) to extrude the mix on the base blocks which immensely helped eliminate the human and mechanical dependencies involved in using the gantry based 3D concrete printer. This scale model printing methodology involved a pump which was used to mix and fill the barrel of the caulk gun with the concrete mix. To avoid air voids formation in the caulk gun the hose was placed at the bottom-most point of the barrel by closing the nozzle extrusion end. The concrete mix was then extruded through the hose and as the mix filled the barrel the hose was pushed up automatically and eventually the barrel was filled. Later the mix in the barrel was tamped and the excess mix at the plunger end was cleared to fit the plunger in place. The time-gaps adopted to study the strength characteristics of the specimen were 5-, 10- and 20-minutes.

In-order to allow for a better comparison of the strength test results it was essential to cast/extrude

the specimens under similar room conditions. Owing to this, specimens having the same time-gaps were printed together i.e. for a 5-minute time-gap specimen A, B and C (having different groove-size) were printed which was then similarly followed by 10- and 20-minutes specimen.

4.1.4. Surface Moisture Content (SMC) Characterisations

The moisture content measurement is carried out simultaneously with the time-gap investigations on the surface of the first extruded layer. The main aim of carrying out such investigations is to study the surface water evaporation to the atmosphere along with moisture migration in the extruded layer due to the unevenness of the topology. These two parameters are predicted to have a direct impact on the inter-layer bond strength results as suggested in the research of Van Der Putten *et al.* [48] wherein mechanical strength test results were correlated to the process parameters like print speed and time through moisture content changes on the surface of extruded layers. As shown in Figure 4.3 and on similar lines as in the research of Wang *et al.* [49], in the research herein, it is predicted that the moisture migration may occur towards the grooves due to the slopes present in the topology. This may cause an increase in the water-cement ratio at these spots leading to weaker inter-layer bonding.

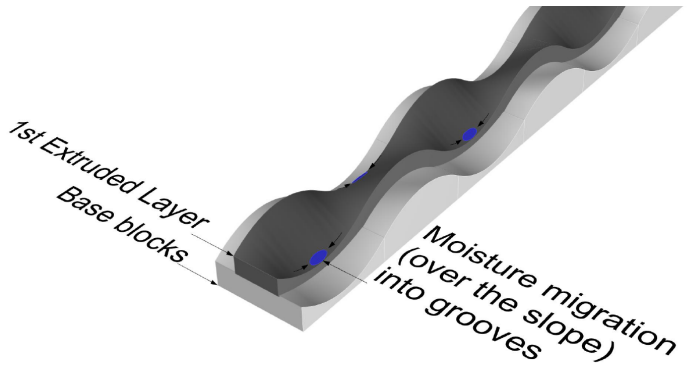

Figure 4.3: Expected moisture migration in the extruded layer (as seen in blue) due to topology

The surface moisture measurement was carried out on similar lines as performed in the research of Pan *et al.* [55], the moisture content measuring device used for surface moisture measurement was 'Brennenstuhl 1298680 Moisture meter MD' as shown in Figure 4.2 (Right). This device uses the principle of electrical resistance which implies that the electricity is transmitted between pins using moisture as a medium of conduction. The moisture content meter shows a reference value of 1.5-33% for concrete surfaces. The values shown on a reference scale do not represent the moisture content of the material under test. Instead, these are estimates where high values signify high moisture levels and low values signify low moisture levels i.e. if the reference scale shows a reading of 33%, it does not mean that 33% of the dry weight of the tested material is water. Instead, it just means that the moisture content of the material represents 33% of the reference scale. It is a qualitative value. In order to quantify these measurements and for the purpose of further analysis the reference values provided with the moisture measuring device were scaled and adjusted between 0 to 100% as can be observed in Table 4.3.

Note: The moisture content measurement was only done in the case of caulk-gun extruded specimens and not for the mould-cast specimens as the sole purpose of the latter was to investigate the effect of the mechanical interlocking with groove size as the only parameter.

Table 4.3: Reference and Adjusted scaled values of moisture content (as indicated in the manual of Moisture meter) measurement

Moisture Content	Reference Values (For Concrete Surface)	Adjusted & Scaled Values
Low	1.5 - 16.9%	0 - 48.75%
Medium	17 - 19.9%	48.89 - 58.10%
High	20 - 33%	58.41 - 100%

4.1.5. Measurement of surface moisture content

At the initial stage, the moisture content is set to always display a reference moisture content value of 33% which is the maximum that can be displayed by this meter for the construction materials (which includes concrete surface) (Refer Table D.33).

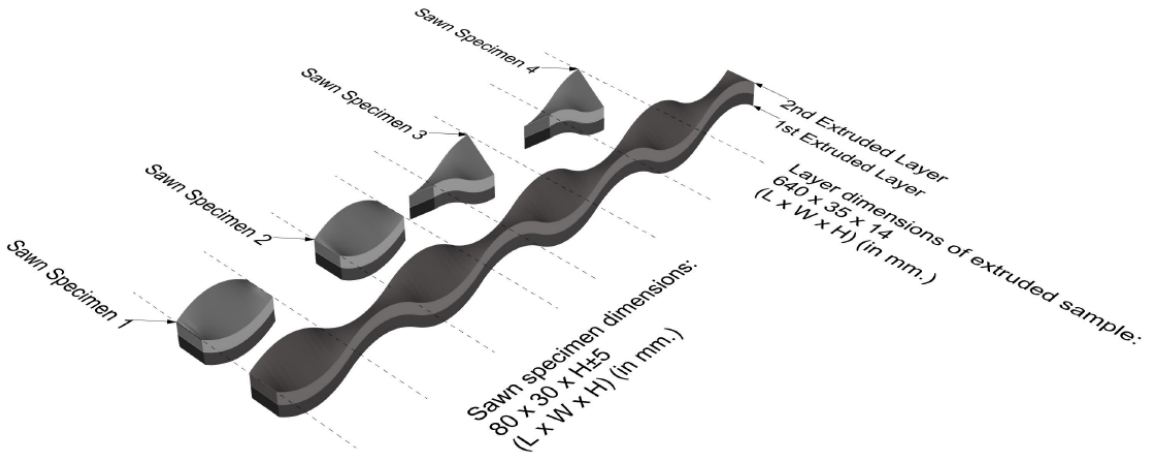

Figure 4.4: Positions at which the specimens were sawn and extracted for further testing (For the overall height of sawn specimen (H) refer Figure 4.11 and Table 4.4)

The data points selected for measuring the moisture content on the surface of the extruded layers can be seen in Figure 4.5. The specimens were sawn at 4 positions (tagged as 1, 2, 3 and 4) such that 2 of them have identical shapes. Figure 4.4 shows an entire sample extruded and indicates the position at which these specimens for the inter-layer bond test were extracted. Hence, the moisture content measurements are done at 3 data points along these blocks (labelled as I, II & III). The reading is taken by piercing the pins of the moisture meter at a shallow depth (approx. 0.5cm) into the surface of the extruded layer as shown in Figure 4.9. As the moisture meter reads the moisture content by passing electricity between 2 pins to have an accurate reading at points where there exists a groove the readings were taken towards the groove side and at the crest points, these readings were taken towards the higher side eventually giving a good idea of moisture migration.

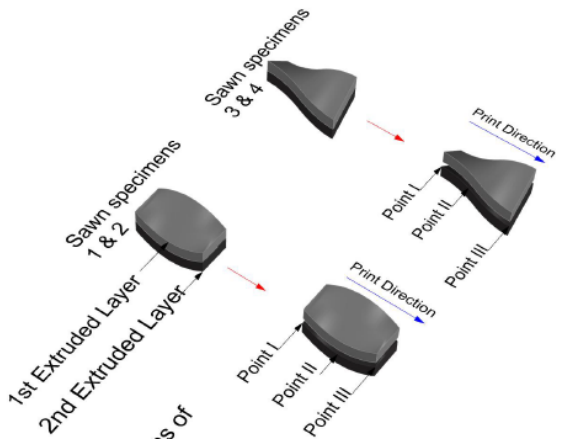

Figure 4.5: Positions at which SMC was measured representative in terms of sawn specimens.
Points I, II and III represent positions of Surface Moisture Content (SMC) measurement at different time-gaps on the first extruded layer

4.2. Sample Preparation

4.2.1. Casting the specimens

The casting of the specimens was a fairly simple process as it involved firstly, casting silicon-rubber moulds which had the shape of the sample to be cast later. Secondly, once the moulds were ready the mix was poured into these moulds to cast the first layer of the samples. The base layer for all the samples (i.e. Specimens i.e. A, B and C) were cast in one go. After waiting for 3-4 minutes and examining the casted base layer for hardening the base layer was de-moulded and the empty silicon-rubber mould was then used to cast the second layer. Once the second layer was done casting it was then pressed gently by the base layer in-order that the interface attains the topology shape. Figure 4.6 shows the finished casted samples.

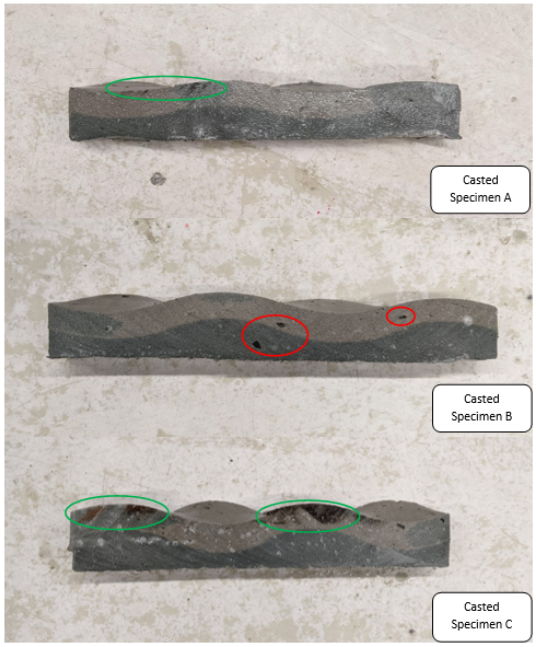

Figure 4.6: Casted specimens (cut along the length) (Red encircled regions) show few air voids induced due to the process of casting which were neglected (Green encircled regions) show black marks on the cut surface which is due to grease from the diamond cutter and is considered to have no effect on the results

4.2.2. Caulk-gun extrusion technique

For the caulk-gun extrusion technique, the mix was manually pushed into the pump reservoir in-order to avoid air entrapment. To minimise the water loss to the surroundings the mix in the pump reservoir was covered with a plastic sheet. Before the extrusion process, the mix was pumped through the hose and the mix was allowed to extrude until a smooth flow (devoid of entrapped air) was observed. After a constant uniform flow of the mix was achieved the caulk-gun barrel was filled by placing the hose at the bottom-most part of the barrel.

The extrusion of all specimens (i.e. Specimen A, B & C) for a single time-gap was done in one printing session. This also meant that multiple printing sessions were required to extrude specimens of all the time-gaps which was therefore done over a period of 3-4 days to ensure that the deviations in room conditions are minimum and had no effect on the final outcomes. Each specimen extruded had a length of 650mm and 2 layers with layer width and thickness (applicable to both the first and second layer) of 35 and 14mm respectively.

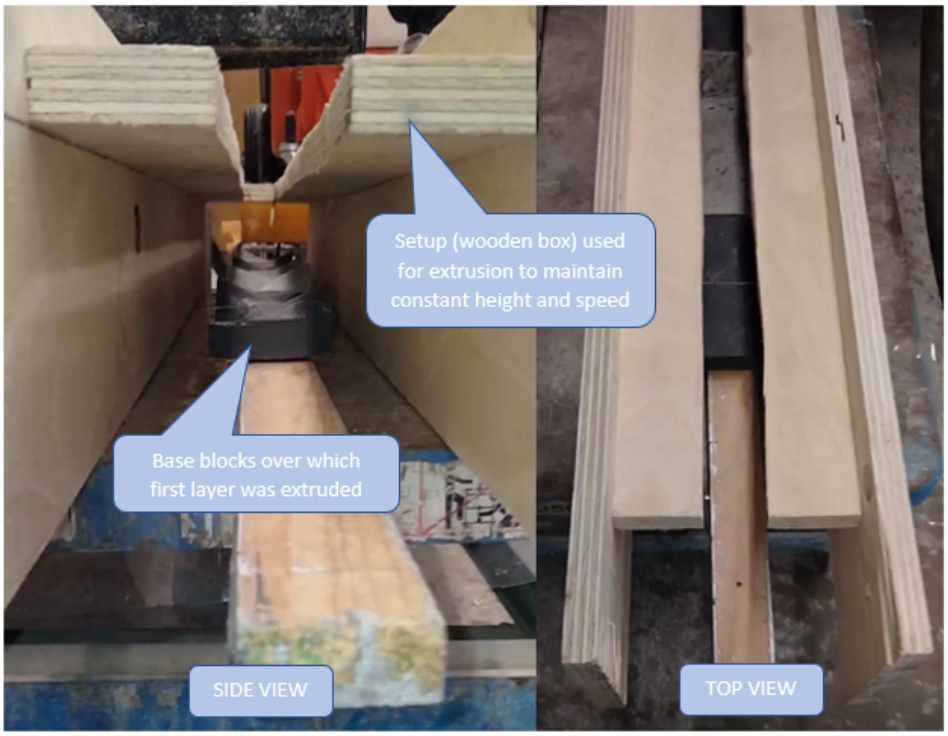

Figure 4.7: Setup used for extruding specimens in-order to have the extrusion at constant speed and height (Left: Side view; Right: Top view)

Figure 4.7 shows the setup used to extrude the layers of the specimen. The caulk gun nozzle was rested in the gap of this setup during extrusion, this was done in-order to have a constant height and speed during extruding the mix (which also helps to simulate the 3D concrete printing process parameters). The distance between the nozzle and base blocks was kept to 20mm and it was ensured that the nozzle was held at an angle of 45°to the flat top.

The procedure followed to produce the samples in the caulk-gun extrusion technique was as follows (explained from the perspective of producing samples for a single time-gap):

- **Extruding first layer over the base blocks for all specimens - A, B and C**

Figure 4.8: Casting of first layer using caulk-gun on the base blocks (Positions 1, 2, 3 indicate the positions at which samples were sawn at a later stage for further testing)

- **First set of SMC data measurement (1-min gap):** This involves the time required for preparation of the moisture content meter and up to the point of taking the first set of readings with the same on the first extruded layer.

Figure 4.9: Measurement of surface moisture content on the first extruded layer using moisture measuring device

- **Second set of SMC data measurement (for single time-gap):** This corresponds to the time-gap at which the strength characteristics of the specimens are to be investigated further and hence, also marks the point of taking the second set of readings.

- **Extrusion of second layer (1-min gap):** This involves the time required for preparation of the caulk gun for casting the second layer and up to the point of starting to extrude the second layer.

4.3. Test Methods

Both the extruded and casted specimens were cured in similar room conditions (as were while casting/extruding) for a period of 24 hours by covering them with a wet cloth. The specimens were then shifted to the humidity chamber where they were kept under a constant temperature of 20°C and relative humidity of approx. 98%. The specimens were then allowed to cure for 27 days in the humidity chamber after which they were taken out and dried at room temperature for 1 day prior to the tests.

4.3.1. Inter-layer Bond Test

Detailed Procedure for Test Performance

After a week of curing, the specimens were sawn at the positions as depicted in Figure 4.4. The sawn specimens were then cleaned and cured for the remaining duration (27 days) in the humidity chamber. The specimens were taken out of the humidity chamber, dried with a dry cloth and kept to dry overnight the day before the test was to be performed. For the inter-layer bond test, the specimens were to be positioned between the flat plates as shown in Figure 4.12. However, the specimens had a curved surface instead of a flat as can be seen from Figure 4.4 and 4.5 which made it difficult to position them in the available test setup. This required that the curved surface of the specimen had to be grinded/cut and then applied with glue such that it achieved a flat surface to make good contact with the steel plates (as explained in Figure 4.10).

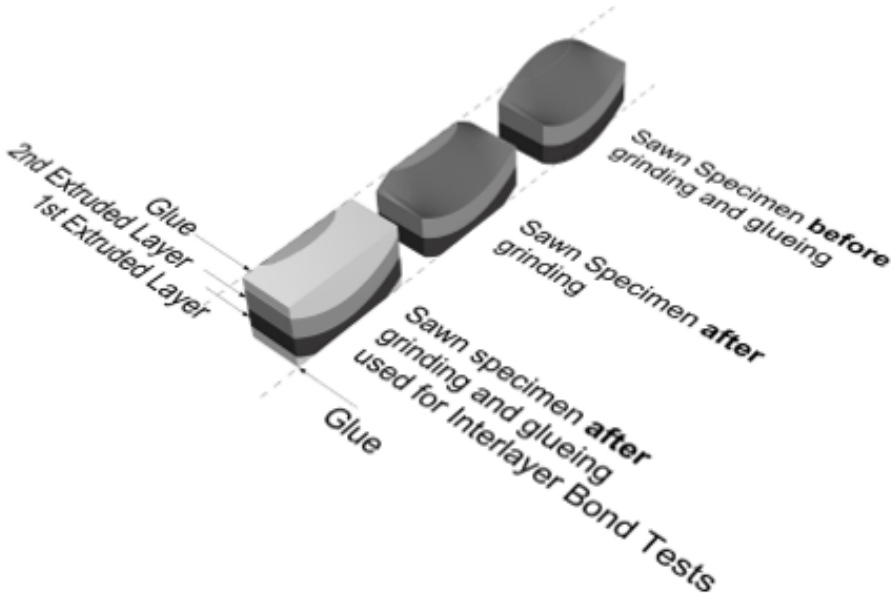

Figure 4.10: Grinding/cutting and glueing of the specimens to achieve flat surface

The overall size of the sawn specimen was 80 (L) x 30 (B) mm. The calculation of the height (H) of the specimens after grinding/cutting is as depicted in Figure 4.11 and Table 4.4. The thickness of the glue is not accounted for in calculating the height of the specimen as the glue distribution was not uniform and with regards to the specimen length, including the glue thickness in the height wouldn't affect the aspect ratio as the specimen length is too long. The inter-layer of the specimen had a curved shape and hence, notching of the specimen was not possible. The specimens were subject to closed-loop displacement-controlled tests with a displacement rate of 0.1 µm/s which was ascertained by

performing prior bond tests on dummy planar specimens of similar material and length dimensions. Linear variable differential transformer (LVDT) sensors were attached to the steel plates at the start and end of specimen length and were utilized to control the vertical displacement during the tensile test. The final bond test set-up is as seen in Figure 4.12. The upper loading plate was glued with the specimen and then screwed tightly to the rod of the Instron testing machine and hence, is assumed to have fixed boundary conditions. In the case of most of the specimens, the lower loading plate had to be adjusted and hence, was not completely screwed. This was done in-order to setup the LVDT's in their initial position and give a zero reading which meant the lower loading plate had a semi-fixed or rotating boundary condition.

Table 4.4: Overall height of the specimens to be used for inter-layer bond test

Sr. Nr.	Specimen 'type'	Groove size dimension (y in mm.)	Overall height of specimen (in mm.)
1	Specimen 'A'	20	38
2	Specimen 'B'	30	43
3	Specimen 'C'	40	48

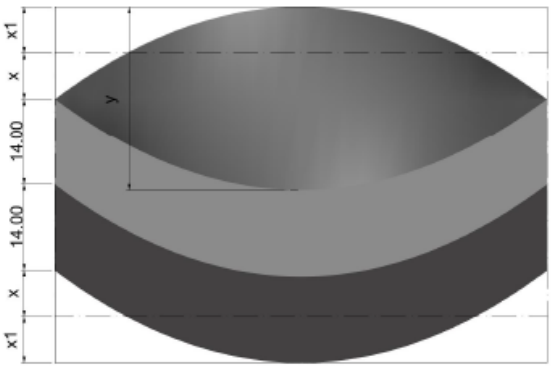

where,

y - Groove height of samples(viz. A(20)/B(30)/C(40) (in mm.))

x, x1 - Aprrox. 50% of (y/2)

x1 - Part chipped off for alignment of the sawn specimen with flat steel plates of instron machine

Figure 4.11: Overall height of the sawn specimens after grinding/cutting the curved surface

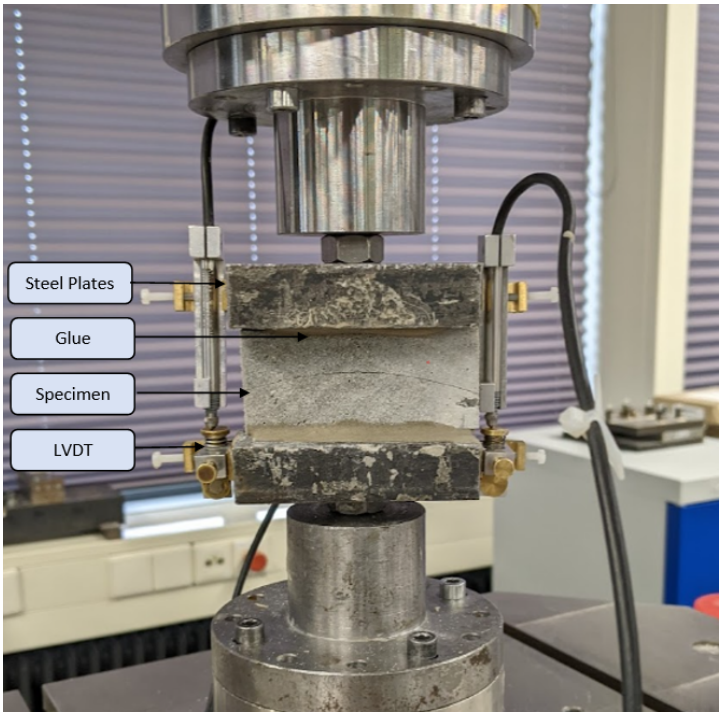

Figure 4.12: Example of Instron inter-layer bond test setup for a specimen

Detailed Analysis of Test results

A similar procedure is applied for analysing the results of both the mould-casted and caulk-gun extrusion-based specimens. The output data received from the Instron machine was further analysed using MS Excel software to plot relevant graphs and analyse the data in-depth. Herein the analysis is explained in terms of Specimen TG5-A-2 and where necessary the corresponding specimens are referenced in order to explain the context.

First and foremost, if required, the bond test results for a specimen were offset so that the curve could start from the origin. Secondly, a Load Vs. Displacement and Stress Vs. Strain graphs (refer Figures B.9 and B.10) were plotted for the entire test duration from the perspective of identifying the 'snap-back' behaviour in the specimen (if any). If the snap-back occurred then this was considered the point at which the majority of debonding in the specimen has occurred and as stated in the literature [34], [32] the test is considered to be unstable from this point on-wards and further test data is not considered for analysis. This was further confirmed by plotting a graph of Time Vs. Displacement (refer Figure B.11) for entire test duration which was further sampled (refer Figure B.11 and B.12) to correlate and analyse the point of snap-back in these graphs with the one found in the previous one which is one and the same. With an increase in time, the displacement increases linearly (refer Figure B.11) and at the point where a majority of debonding occurs and the peak is achieved, this step-wise trend in the curve shows an unusual behaviour and from this point onwards any further increase in displacement causes unstable loading and hence, the test data is not analysed beyond this snap-back point. From the sampled data of displacement and loads the strain and bond stress were calculated as follows:

$$\epsilon_{(1/2)} = \frac{Z_{filtered}}{H_{specimen}} \text{ and } \sigma_{bond} = \frac{F_{filtered}}{A_{specimen}}$$

where,

$\epsilon_{(1/2)}$ - Strain (filtered) for LVDT1/LVDT2

$Z_{filtered}$ - Displacement (filtered for LVDT1/LVDT2)

$H_{specimen}$ - Height of the specimen (Refer Table 4.4)

σ_{bond} - Bond Stress (filtered)

$F_{filtered}$ - Load (filtered)

$A_{specimen}$ - Area of specimen

Further a final Load Vs. displacement graph (refer Figure B.13) is plotted for confirmation of the test interval to be analysed and then a Stress Vs. Strain graph (refer Figure B.14) is plotted for the sampled interval to identify the peak stress and, finally, to understand the problems of bending of the specimen within the test setup (due to boundary conditions), nozzle extrusion induced roughness in the inter-layer, glue distribution, mould induced discontinuity and long clustered cavities a plot of Stress Vs. Strain graph (refer Figure B.15) for the 2 LVDT's is plotted and the bending (usually in terms of strains)in the curve are studied by plotting it in a representative test-setup graph. Overall a set of 7-8 graphs need to be chronologically analysed as mentioned above herein. In some specimens (e.g. Specimen TG10-B-1) in order to confirm the test run interval the Time Vs. The displacement graph is required to be plotted multiple times than usual so as to fine-tune the sampling in which case there are overall 9 graphs that need to be analysed.

From the data analysed, the maximum bond stress and strain were identified for each specimen and then compared. In order to identify the quality of the bond between the inter-layers the images of the inter-layer surface of the samples from the caulk-gun extrusion method (after failure in the bond test) were analysed using a reliable online image analysis and summarizer tool.

4.3.2. Image Analysis of Debonded Inter-layer Surface

The inter-layer surface of the mould-casted specimens showed characteristics of uniform bond in inter-layer as compared to the caulk-gun extruded specimens with an exception of a few clustered voids. The inter-layer surface of the debonded caulk-gun-based specimens had defects related to under-filling like that of non-uniform contact and cold joints which can be confirmed from the fractured inter-layer surface as seen Appendix-D.

The fact that specimens were air dried before the test, facilitates the escape of any excess moisture to the surrounding. Also, as pointed out in the research of Van Der Putten *et al.* [48], the speed of extrusion is inversely related to the surface roughness of the inter-layer which further affects the bond strength as can be observed in Figure 2.45. In the research herein, even though the height of extrusion from the nozzle point of view was kept constant with the help of setup, it was variable owing to the other end i.e. the wavy surface on which the extruded layer rested after extrusion. Also, given that it was not possible to achieve precise control over the speed of extrusion due to the manual operation of the caulk gun, the speed was kept as low as possible in-order to counter-balance the effect of variable height. This resulted in a surface roughness that was variable throughout the specimens which can be confirmed from the images of the fractured inter-layer surface as observed in Appendix-D. This surface roughness [48] and the effects of under-filling [24], [20], [27], [19] lead to a non-uniform contact and cold-joints between the successive layers and owing to this it is assumed that the dark grey patches are regions of good bonding wherein the moisture gets trapped as opposed to the light grey patches where the bonding is weak and moisture escapes and hence, it appears relatively drier. This assumption is based on similar lines which suggest that due to the absence of form-work and exposure of 3D printed concrete to the atmosphere the sides of the printed layers are insufficiently protected resulting in evaporation of water from the concrete surfaces [6]. The fractured inter-layer surface exhibiting regions of wetter and drier patches helps classify the entire inter-layer surface into 2 distinctive colour clusters. It was hence, convenient to quantify and understand the bond quality between the layers of the caulk-gun specimens which was done with the help of an online open-source image colour summarizer tool as was followed in the research of Marchment *et al.* [9].

After the bond test, images of the failed inter-layer surface (classified as top and bottom de-bonded part in Appendix - C) were photographed with a high-resolution smartphone camera application and further cropped and adjusted to focus only on the inter-layer surface (eliminating other details such as test plates and glue lines). This process is similar to the flatbed scanner technique as followed in

the research of Miriello *et al.* [52] except that the precision in terms of height from where the images were clicked could not be maintained repetitively. Further, the image was uploaded to the image colour summarizer tool and inputs such as output format, statistics, colour clusters, delimiter and precision controls are specified. The output format selected is as HTML and provides a detailed image analysis report and can be found in Appendix-D. The statistics are provided as colour clusters which helps us to mention the number of colour clusters in the next input which is 2 in this case given the fact that the wet regions have a dark grey colour and the dry regions a light grey. The delimiter input helps to separate the various colour tags identified by the tool in the image. The precision input controls the extent to which the image will be resized before sampling. The idea behind it is that a lower precision control divides the image into a lower amount of pixels which helps process the image faster and reduces the computation time. Herein, given the extent of the research, a high-precision input is considered.

After processing the image, the tool then generates statistical colour summaries of the image and reports average RGB and HSV colour components as well as histograms and individual pixel values for these colour spaces. Basically, it divides the pixels in the uploaded image into a number of specified colour clusters and provides statistics for further analysis. The data which is of more interest is that of the one under the ”pixels” column in the table provided in the resulting output. The light coloured cluster being relatively drier has negligible moisture and hence, is identified as a weak-bonding region and the dark coloured cluster being relatively wetter has adequate moisture and is associated to have a good-bonding region as explained above herewith. An average from the top and bottom debonded inter-layer surface is obtained and the quality of the bond is ascertained. Thus, for each failed specimen in the inter-layer bond test, we can analyse the inter-layer surface and identify the bond quality. This can further be correlated to the results from the inter-layer bond test and would help analyse the results better.

5

Laboratory Results, Analysis and Discussions

Both the mould-casted specimens and the caulk-gun extruded specimens were tested for a tensile inter-layer bond. The inter-layer bond test results for some of the specimens exhibited the phenomenon of non-uniform debonding of the inter-layer as identified in the research of Van Mier *et al.* [32] while some specimens were devoid of it. This non-uniform debonding results in load eccentricities during test progress and hence is responsible for impairing the stability of the tests [32]. Therefore, it becomes an important aspect in the research herein to identify the stability of the tests for every specimen which further decides the reliability of the results acquired in-order to consider these for further analysis to make overall conclusions on the research question. The steps followed in processing and analysing the data is as illustrated in the flow chart in Figure 5.1.

Given the phenomenon of non-uniform debonding as will be explained hereon, all the specimens are categorised based on two types of failure mechanisms observed in them, namely, pure tension (near-uniform debonding) and tension-bending failure (non-uniform debonding) as illustrated in the Table 5.1.

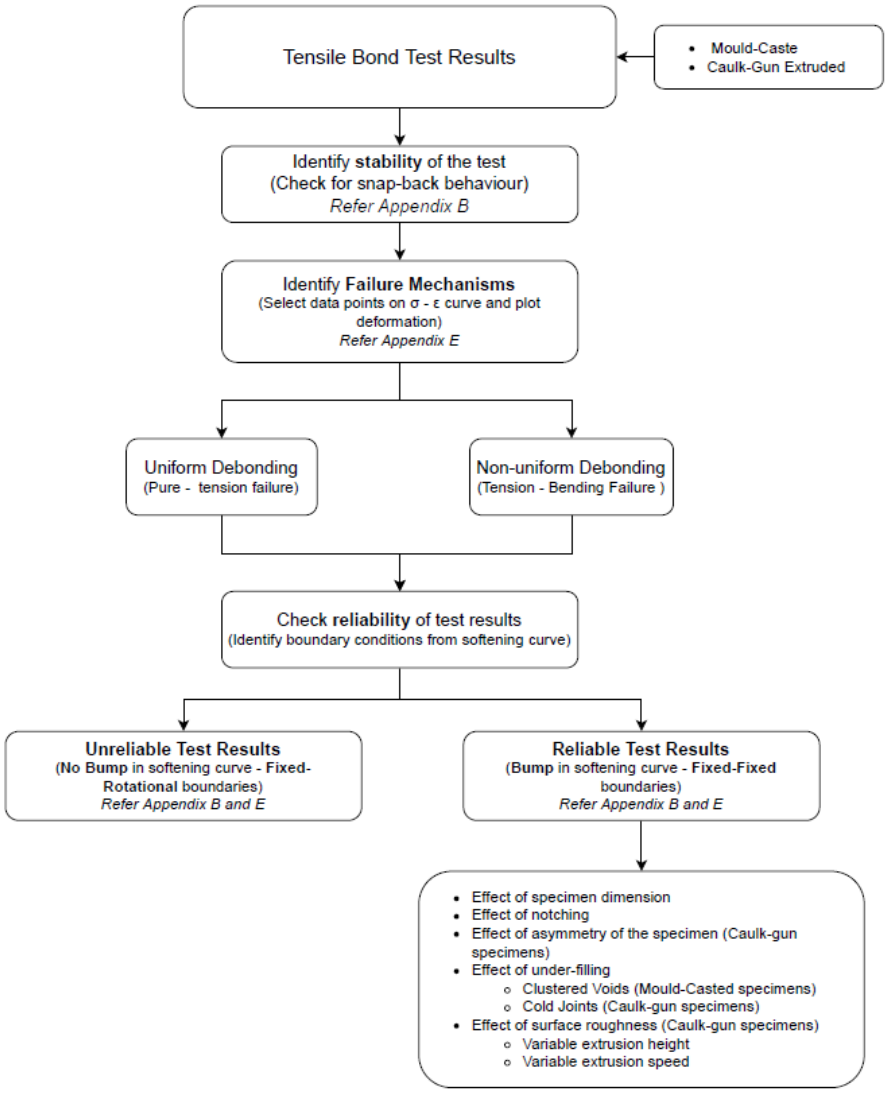

Figure 5.1: Flow chart illustrating steps followed in the data analysis

Table 5.1: Failure mechanism observed in specimens tested for the inter-layer bond test (refer Appendix - E)

Specimen Type		**Failure Mechanism**	
Preparation method		**Pure Tension Failure**	**Tension-Bending Failure**
Mould-Casting Based		A-2	A-1, A-3 and A-4
		B-1 and B-4	B-2 and B-3
			C-1, C-2, C-3 and C-4
Caulk-gun Based	Time-gap		
	5-mins	5-A-1 and 5-A-2	5-A-3 and 5-A-4
		5-B-2	5-B-1, 5-B-3 and 5-B-4
		5-C-2 and 5-C-4	5-C-1 and 5-C-3
	10-mins		10-A-1, 10-A-2, 10-A-3 and 10-A-4
		10-B-1	10-B-2, 10-B-3 and 10-B-4
		10-C-2 and 10-C-4	10-C-1 and 10-C-3
	20-mins	20-A-4	20-A-1, 20-A-2 and 20-A-3
		20-B-2 and 20-B-4	20-B-1 and 20-B-3
		20-C-4	20-C-1, 20-C-2 and 20-C-3

5.1. Pure-Tension Failure

The pure-tension failure (uniform debonding) observed in the test results of some specimens is illustrated and explained below with an example of mould-casted specimens, the same applies to the behaviour observed in the caulk-gun-based specimens. The state of deformation of the Specimen A-2 occurring throughout the test progress is shown in Figure 5.2 for the data points of interest marked in Figure 5.3. As can be observed from these figures the loading is centric throughout the test progress.

A difference is observed in the deformation at the peak (i.e. data point 2) and at the stage where full unloading has occurred and the test is stopped (i.e. data point 3). This is the part in the post-peak curve where no measurements are plotted despite the regular increase of deformation. This is similar behaviour as the one observed in the research of Hordijk [34] seen in Figure 2.22 and is associated to the snap-back behaviour due to CLC-based deformation-controlled tests and occurs as a result of the equipment in the test setup not being fast enough to overcome sudden stress drop, which results in unstable test progress thereon. This phenomenon has been observed in all the specimens tested for inter-layer bond within this research. The occurrence of snap-back behaviour like these does not always mean that the test results are entirely unreliable, it is an indication that in the analysis of the results the unstable part of the test needs to be separated from the stable part for accurate assessments.

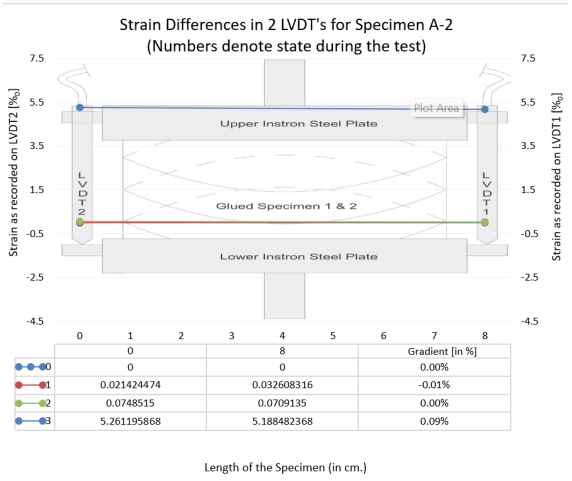

	0	8	Gradient [in %]
0	0	0	0.00%
1	0.021424474	0.032608316	-0.01%
2	0.0748515	0.0709135	0.00%
3	5.261195868	5.188482368	0.09%

Figure 5.2: Uniform debonding occurring in Specimen A-2

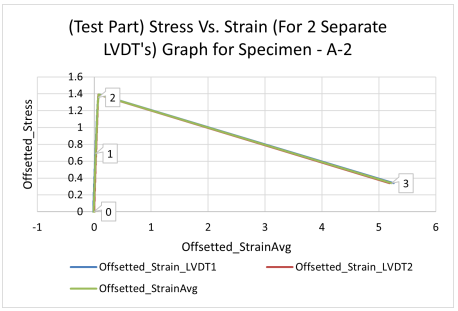

Figure 5.3: Average (green curve) and LVDT specific (red and blue curves) Stress-strain curves for Specimen A-2

5.2. Tension-Bending Failure

Figure 5.4 and 5.5 represent the non-uniform debonding and the stress-strain curve for Specimen A-1 respectively. As observed from these Figures the debonding at the side of LVDT2 for the specimen keeps on increasing until the peak stress is achieved and it decreases thereon reaching a negative value, whereas, the debonding on the other side i.e. at LVDT1 keeps on increasing uniformly until the peak stress, and post-peak stress the increase in the strain value is enormous. On comparison of strain values in terms of gradient (expressed in % in Figure 5.4) on both sides of the specimen it can be concluded that the specimen is undergoing minor non-uniform debonding right from the start of the test and post-peak stress this debonding intensifies.

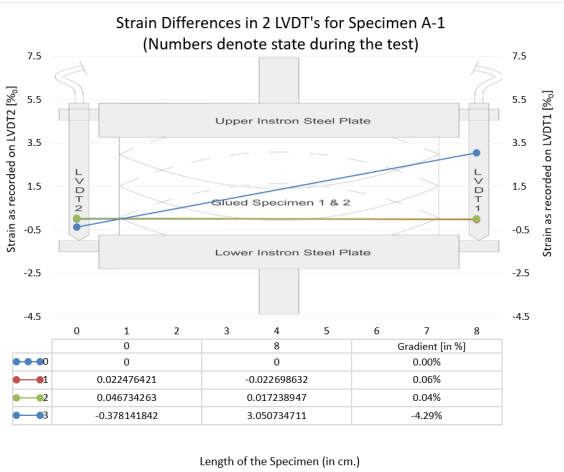

Figure 5.4: Non-Uniform debonding occurring in Specimen A-1

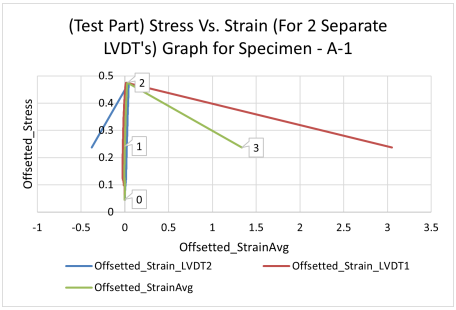

Figure 5.5: Average (green curve) and LVDT specific (red and blue curves) Stress-strain curves for Specimen A-1

5.3. Factors influencing failure mechanism

Non-uniform debonding which results in load eccentricities during the test progress is a possible consequence of several factors such as boundary conditions, specimen dimensions, and asymmetrical and un-notched specimens. The non-uniform bonding within the specimen, resulting under-filling and surface roughness in the inter-layer, is an additional factor responsible for these load eccentricities.

5.3.1. Effect of boundary conditions of test specimen

It is important to understand the procedure of mounting the specimen in the test setup to understand the influence of boundary conditions on loading. The surface of the loading plates was cleaned and later, the LVDT-sensor placeholders were glued on the sides of the plates. Further, the specimen was glued to the upper loading plate and after drying for about approx. 5 minutes the plate along with the glued specimen was screwed into the Instron test setup. Later, the lower plate was screwed in the test setup and aligned with the upper loading plate in such a manner that the plates and glued specimens are aligned horizontally parallel to each other. While doing so adjustments were made in terms of slight loose screwing of the lower loading plate to account for two things: firstly, in order to make up for the non-uniform glueing of the specimen with the upper plate which resulted in the specimen not being parallel between the plates. Secondly, to ensure that the LVDT-sensor placeholders of the upper and lower loading plates are aligned vertically with each other. This setup had a disadvantage since it affected the boundary condition of the lower loading plate which was now rotational as opposed to being fixed. During the test progress, the debonding in the majority of the specimens occurred non-uniformly, identical to one observed in Figure 5.4 which resulted in the specimen being loaded eccentrically as the test progressed. As suggested in the literature [32], fixed boundary conditions of the specimens have the ability to develop a counteracting bending moment whereas the same is not possible in the case of rotational boundary conditions. This results in the softening part of the stress-strain curve having bumps in the case of the former which is confirmed in the research of [36] as observed in Figure 2.26. Previous researchers concluded that a decrease in the fracture energy is observed in rotational boundary conditions as compared to that of fixed boundary conditions [37] and hence, it is said that the results do not exhibit the true property of the material under consideration [32]. These bumps can be seen in approximately one-third of the tested specimens as observed in Table 5.2 suggesting that the boundary conditions were fixed-rotational almost always instead of fixed-fixed and the difference of which can be observed in the Figures 5.6 and 5.7 in the softening part of the curve. Hence, the

boundary conditions of the specimen play a vital role in deciding the reliability of the results and the conclusions drawn from it. This should also explain the discrepancies in the softening curves for SHCC-based specimens observed in the literature (Figure 2.31 and 2.32 [44]) as compared to the ones in this research.

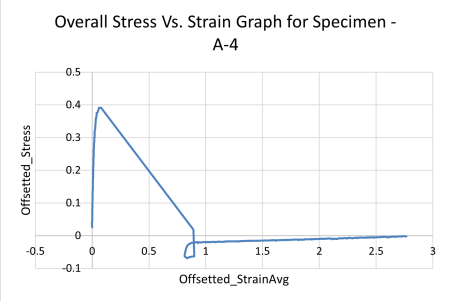

Figure 5.6: Stress-Strain Curve for Fixed-Rotational boundary conditions with no bumps

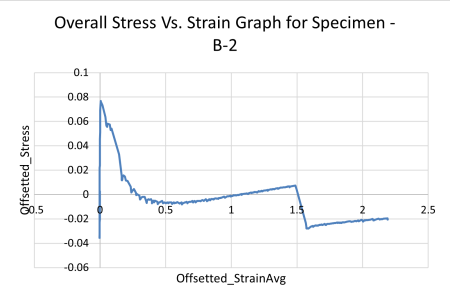

Figure 5.7: Stress-Strain Curve for Fixed-Fixed boundary conditions showcasing bumps in the softening curve

Table 5.2: Boundary conditions of Specimens during the inter-layer bond test-based on softening curves

Specimen Type		**Boundary Conditions of the Specimens**	
Preparation method		**Fixed-Fixed (Based on - bumps in softening curve)**	**Fixed-Rotational (Base on - no bumps in softening curve)**
Mould-Casting Based		A-3	A-1, A-2 and A-4
		B-2 and B-3	B-1 and B-4
		C-1	C-2, C-3 and C-4
Caulk-gun Based	Time-gap		
	5-mins	5-A-4	5-A-1, 5-A-2 and 5-A-3
		5-B-3	5-B-1, 5-B-2 and 5-B-4
		5-C-3	5-C-1, 5-C-2 and 5-C-4
	10-mins	10-A-1 and 10-A-3	10-A-2 and 10-A-4
		10-B-3 and 10-B-4	10-B-1 and 10-B-2
		10-C-4	10-C-1, 10-C-2 and 10-C-3
	20-mins	20-A-3	20-A-1, 20-A-2 and 20-A-4
		20-B-3 and 20-B-4	20-B-1 and 20-B-2
		20-C-1 and 20-C-3	20-C-2 and 20-C-4

5.3.2. Effect of specimen dimensions

As observed in the literature of Hordijk [34], the shorter dimensional prismatic specimen exhibits a higher rotational stiffness as illustrated in Figure 2.21 and 2.24 leading to reduced non-uniform cracking and making them less susceptible to tension-bending failure. Though the influence of specimens of different dimensions hasn't been studied in detail in the research herein, however, given the longer dimensions of the tested specimens (i.e. 80(L) x 30(W) x 48(H) mm^3) it can be confirmed that it is an important factor influencing the test results. Especially, when the tension-bending failure occurring in the specimens has been confirmed in Figures 5.4 and 5.5. Since the choice of the length of the specimen was based on the length over which the groove was spread which was about 80 mm as can be seen from Figure 4.1, it was inevitable to avoid the use of longer dimensional specimen for testing and its effects thereof.

Another aspect that is notable in the stress-strain curve for all the specimens is that the deformation capacity of the specimens is less which can be observed from the steep ascending curve. This is on the similar lines as identified in the research of Hordijk [34] suggesting that the snap-back behaviour is a function of the specimen length as seen in Figure 2.25. In the case of the research herein the specimen length is that of the specimen thickness which is used for strain calculations and is small as compared to the length dimensions. It is also important to note that owing to the shape of the specimen, the glue is

non-uniformly spread between the specimen and the plates which makes it harder to estimate the glue thickness. Also, even if approximations were considered to estimate the glue thickness, including it in the calculation of the specimen thickness does not alter the aspect ratio (ratio of thickness to length) of the specimen considerably and therefore, glue thickness is not considered in the specimen thickness as seen in Figure 4.11.

5.3.3. Effect of notching and symmetry of test specimen

In a uniaxial tensile test, if the samples allow for notching it is preferred that the location of the crack is predetermined by introducing a notch in the specimen. This helps in opening the crack at the notch during the test and this opening of the notch can be further used as a feedback signal in a CLC-based testing regime to ensure uniform crack distribution and hence, facilitate stable tensile tests [56]. Another similar approach that has been known to provide a stable response is that of adopting a dog-bone-shaped specimen in which the specimen has a smaller cross-section over the centre part. In case the specimens cannot be notched it is hard to define the location of the crack apriori. Owing to the complex osteomorphic topology of the inter-layer, it was nearly impossible to create a notch in the specimen used for testing in the research herein. Even though the specimens were un-notched and no sophisticated feedback signal alteration for the test was done, the debonding of the inter-layer was always the failure criteria of the specimens during the test which can be confirmed from the Appendix C. The research of Zhou [36], confirms that the rotation caused by the asymmetrical shape of a specimen has a similar effect on the test results as that of the rotation due to load eccentricity [36] [32]. The asymmetry of the specimens under test setup could be associated with the osteomorphic topology of the specimen this required grinding and chipping of the extruded layer. This was done to achieve a flat surface to ensure uniform glueing and increase the contact surface between the specimen and loading plates. The grinding of specimens influenced the test results in terms of causing non-uniform debonding as the load transfer from the extruded layer was non-uniform. Furthermore, the cutting and grinding of the specimens caused excess chipping of one extruded layer as compared to the other which added to further asymmetries in the specimen. This possibly resulted in uneven load transfer in the specimen causing non-uniform debonding as well which could be well observed in most of the caulk-gun based-specimens as uneven nozzle-induced extrusion of layers may have aggravated these problems, for example, in Specimen TG20-B-3 and TG5-B-3 as seen in Figure 5.8 and 5.9 below.

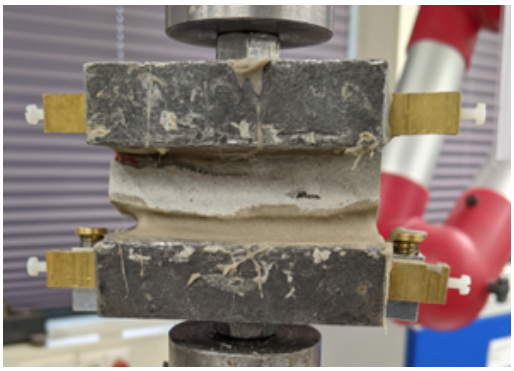

Figure 5.8: Specimen TG20-B-3 after failure: The thickness of the upper layer is less as compared to bottom extruded layer

Figure 5.9: Specimen TG5-B-3 after failure: The thickness of the bottom layer is less as compared to upper extruded layer

5.3.4. Effect of under-filling in the inter-layer

Almost all of the specimens exhibited under-filling and the major effects attributed to it, like that of the formation of air voids which is further said to cause a reduction of effective density and potentially affect the durability of the printed sample. The mould-casted specimens were prepared by pressing layer-

over-layer and then compacted overnight by placing a heavy weight on top in order to ensure effective layer intermixing which aided in achieving a uniform inter-layer bond. In the instance of pressing layers against each other, there is a possibility of air entrapment between them resulting in the formation of air voids. The under-filling related air voids formed in the mould-casted specimens in the research herein are similar to the one observed in the research of Le *et al.* [19]. Although no intricate studies on the void structure were performed in the research herein, the marked similarities can be observed from the images of the debonded inter-layers concluded, as seen in Figures 5.10 and 5.11.

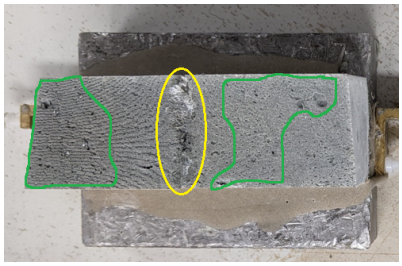

Figure 5.10: Inter-layer surface of Casted Specimen B-2 after failure with clustered voids (depicted by green regions) and mould-induced discontinuity (depicted by yellow)

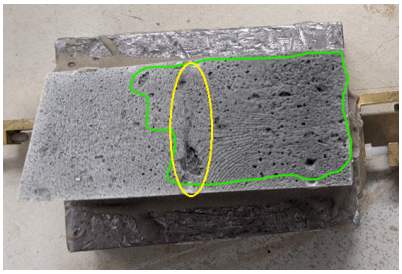

Figure 5.11: Inter-layer surface of Casted Specimen C-2 after failure with clustered voids (depicted by green regions) and mould-induced discontinuity (depicted by yellow)

The debonded inter-layer of caulk-gun-based specimens on undergoing tests also showed effects of under-filling as seen in mould-casted specimens which were worse than the one's observed in the latter. The layers of caulk-gun based-specimens were extruded through a nozzle. The speed and height of extrusion were attempted to maintain constant as much as possible by using the setup as shown in Figure 4.7. Therefore, even though the height of extrusion from the nozzle point of view was kept constant with the help of setup, it was variable owing to the other end i.e. the osteomorphic topology on which the extruded layer rested after extrusion. This meant that the extrusion height was shallow at peaks and deeper at grooves and resulting in a variable extrusion height. This along with a combination of grooving may have possibly resulted in the second extruded layer causing ineffective shape retention in the deeper grooves which led to the issue of under-filling when extruding over the deeper grooves of the topology as observed in Figure 5.12. This can be further confirmed through the conclusions obtained in the research of Buswell *et al.* [1], which suggested that for a given material formulation and nozzle geometry the filament is unable to follow the radius of the curve during a change of direction of the tool-path and causes under-filling as observed in the Figure 5.12. The change of direction could be correlated to the variable extrusion height in the research herein. The effects of under-filling observed in the caulk-gun based-specimens become more relevant and clear when referred to Figure 2.9 and 2.10 [25]. This variable extrusion height causes ineffective shape retention in the deeper grooves resulting in under-filling and is a major cause of cold joints formation due to lack of inter-layer mixing which was predicted in the research of Nerella *et al.* [27] which can further be confirmed by comparing the Figure 2.13, 5.12 and 5.13.

Figure 5.12: Extruded second layer on the first layer (Regions highlighted with red show defects in the specimens related to non-uniform contact between layers and non-uniform layer thickness induced due to the caulk gun extrusion process)

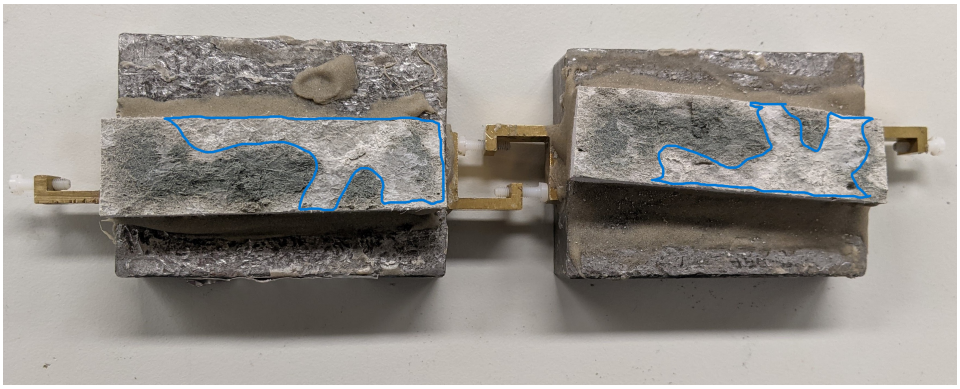

Figure 5.13: Inter-layer surface after failure for Specimen TG10-A-1 with visible under-filling effects like lack of inter-layer mixing (regions marked in blue)

5.3.5. Effect of roughness in inter-layer

The mould-casted specimens have a minor discontinuity in the inter-layer as illustrated in Figures 5.10 and 5.14. This is a result of the discontinuity in the mould used to cast these specimens. At first instance, it might seem like it could act as a weak plane and create a preferential path for debonding but as observed in Figure 5.10 since they are spread throughout the cross-section of the specimen and the fact that these specimens were compacted well enough to avoid large defects (like cold joints) suggests that good contact between successive layers exists within this mould-induced discontinuity. Hence, their effect on the inter-layer bond test results is considered to be negligible.

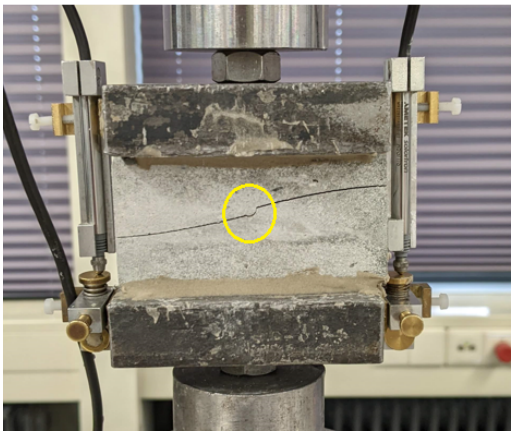

Figure 5.14: Mould-induced discontinuity (Specimen A-2) in the inter-layer (encircled yellow) when specimen is in the test setup

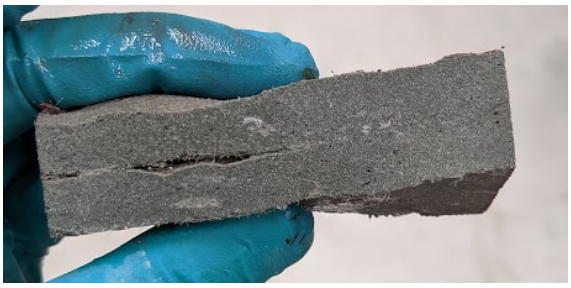

Figure 5.15: Cold joint formation in the inter-layer of saw-cut caulk-gun based-specimen

On the other hand, the roughness of the inter-layer in the caulk-gun-based specimens is not alike and has a considerable influence on the test results. The nozzle extruded layer had an imperfection in terms of having non-uniform layer thickness which led to an imperfect alignment of successive layers and hence, non-uniform contact as spotted in Figure 5.12. The speed of the extrusion is a major factor influencing the roughness in the inter-layer as suggested in the research of Putten *et al.* [6].

The research infers that the speed of the extrusion and surface roughness has an inverse relation and owing to which a lower speed of extrusion results in more roughness in the inter-layer and hence, reduced bond strength. In the research herein, the speed of the caulk gun was attempted to be kept constant as much as possible, however, since, it was manually operated the accuracy could not be maintained throughout. Also, given the variation in height, the speed had to be varied to ensure that the layer was extruded completely from the point of view of retaining the shape of the curve. Apart from this, the under-filling induced defects like cold joints resulted in non-uniform contact in the inter-layer as observed from Figure 5.13 and 5.15. These large defects result in reduced contact surface area between successive layers and eventually result in weak bonding as observed in Figure 5.15. For this purpose, the image analysis summarizer tool used herein serves as an effective and convenient bond quantification tool to analyse the quality of the bond from the fractured inter-layer of the specimen. It is important to note that the Image summarizer tool is not an essential requirement from the perspective of analysis but is preferred in-order to get a better insight into the bond test results. The results of the same are discussed extensively later. Since the specimens are un-notched, the roughness of the inter-layer is a major deciding factor (besides under-filling) towards the onset of debonding and hence, contributes majorly to non-uniform debonding during the test progress.

5.3.6. Effect of non-uniform glueing

Given the shape of the specimens as observed from Figure 4.10 it was difficult to ensure uniform glue distribution between the specimen and the loading plates. Even after the presence of non-uniform glue distribution between the specimen and loading plate, a glue-line failure was never encountered in any of the tested specimens as can be observed from Appendix C. Moreover, no failure in terms of crack initiation in the specimen was observed at the interface of glue and the specimens. This suggests that the glue was strong enough to transfer the load from the loading plate to the specimen to cause the failure through debonding of the inter-layer. However, owing to the non-uniform glue thickness there is a possibility of uneven load transfer from the glue to the specimen and eventually, this could have aggravated the problem of load eccentricities, but since, the glue was intact in all the tests and the failure occurred in the inter-layer it was impractical to execute a detailed study to analyse the same. Therefore, it is assumed that the glue distribution has no effect on the test results.

The under-filling and roughness-related effects encountered in mould-casted and caulk-gun based-specimens in the form of air voids and cold joints respectively lead to the reduced contact surface between the layers and hence, are considered to have an impact on the true mechanical properties of the specimens. In the inter-layer bond tests, these defects may lead to uneven stress distribution as the test progresses causing load eccentricities in the test and further non-uniform debonding of the specimens. It is hard to differentiate and identify the effect of under-filling and roughness in the specimens from their respective stress-strain curves, given that there are other factors like boundary conditions, notching, dimensions and symmetry of the specimens already influencing these results. While the research herein is not extensive in those aspects it provides an important insight into the approach in which specimen preparation and test setup can influence the reliability of test results.

5.4. Characteristics of stress-strain curve

5.4.1. Post-peak unloading-reloading

On examining the overall stress-strain curve for a uni-axial tensile test of a specimen an unloading-reloading cycle is observed in the post-peak curve as seen in Figure 5.16 which according to Hordijk [34] is common in uni-axial tensile tests on concrete and is a result of mismatch of closing of crack-surfaces in unloading stage resulting in propagation of existing micro-cracks in the reloading stage.

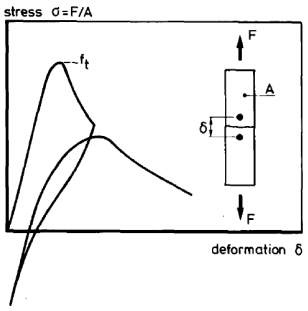

Figure 5.16: Post-peak cyclic tensile behaviour observed in stress-strain curve [34]

In the case of the research herein, similar behaviour was observed in the post-peak curve however, it's not as excessive as showcased in the research of Hordijk [34]. This unloading-reloading loop visible in Figure 5.17 is possibly due to the uneven closing of the de-bonded surfaces and the reloading stage is a result of debonding of small bonded regions. The part of the post-peak curve in terms of Specimen A-2 encircled in red in Figure 5.17 is indicative of this phenomenon and is not of interest in the analysis as all the test data after data point-3 is classified as unstable test part. The dotted red line after data point 3 indicates the point of the second snap-back occurring in the specimen after which the unloading-reloading cycle is said to occur in the green curve. Since this cycle occurs in the unstable test parts and a majority of debonding has already occurred in the specimen, it is not an important aspect but understanding this phenomenon is nevertheless important for future studies. Similar, behaviour can also be spotted in Specimen A-1 but is intense and noticeable as compared to the one in Specimen A-2 in Figure 5.18.

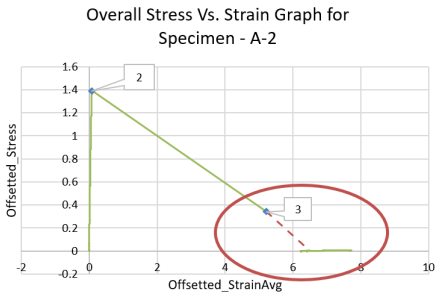

Figure 5.17: Post-peak cyclic tensile behaviour observed in the stress-strain curve of Specimen A-2

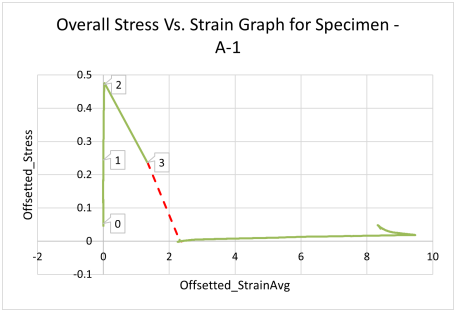

Figure 5.18: Post-peak cyclic tensile behaviour observed in the stress-strain curve of Specimen A-1

5.4.2. Influence of displacement-rate

For most of the specimens in this research, a sharp peak is encountered in the stress-strain curve which is counter-intuitive to the one observed in the literature which showcases a smooth peak for similar SHCC-based specimens as observed in Figure 2.31 [44]. This can be attributed to the choice of a faster displacement rate (0.1 µm/s) at which the deformation-controlled tests were performed. This can also be confirmed from the conclusions in the research of Cadoni *et al.* [57] wherein direct tensile tests were performed on concrete specimens with different strain rates. The results exhibited strain rate sensitivity consisting of a non-linear increase of the mechanical properties of concrete with an increase in strain rate as seen in Figure 5.19. The displacement rate for the test in the research herein was decided on the basis of tensile inter-layer bond tests performed on dummy planar specimens of 80 mm length, the purpose of which was to identify the maximum load required for such lengthy specimens to de-bond and estimate the time required to perform the test on each specimen. Based on the results of these tests and from the perspective of cutting down the time to perform tests on each specimen, it was

decided to adopt a faster displacement rate of 0.1 µm/s. There is a possibility of increased strength characteristics achieved in the obtained results due to this phenomenon, which, hasn't been verified in the research herein and may require attention while interpreting the results.

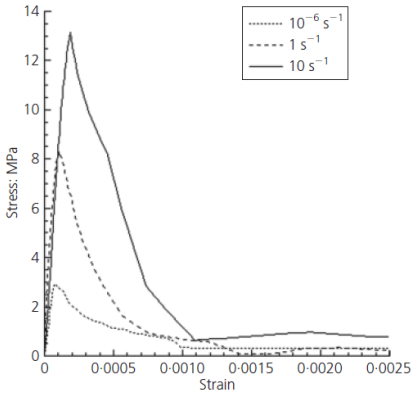

Figure 5.19: Strain rate sensitivity observed in stress-strain curves for different strain rates [57]

Owing to a lack of modification to the bonding tests apart from the issues pertaining to the boundary conditions, notching, symmetry and under-filling observed in the test specimens the non-uniform debonding led to load eccentricities which continued to persist and impaired the stability of the tests. These have been identified herewith and serve the purpose of explaining the reliability of the obtained test results and their assessment hereon in this research.

5.5. Overview on Bond Tests for Mould Casting based-specimens

Within all the mould-casted specimens, Specimen A-2 has the highest bond strength. At first instance, on the basis of the discussions in section 5.1 it seems like the Specimen A-2 is undergoing uniform debonding of the inter-layer. Given that the contact between the successive layers is uniform with an exception of a few air voids, the uniform debonding is justified. However, on keen observation of the softening part of the stress-strain curve for the specimen it can be confirmed that there is no counter-acting moment being generated and its effects like that of bumps are non-existent, as explained in the section 5.1, it is, therefore, evident that boundary conditions of the test specimen were fixed-rotating. This is an exceptional case which illustrates that pure tension failure does not always mean that the results are not influenced by the boundary conditions and given previous research [57] [32] it can be said that the high bond strength exhibited by this specimen is not a true property of the material under consideration which can further be confirmed by comparison of softening curve for SHCC-based specimens from the research of Chaves Figueiredo *et al.* [44] as seen in Figure 2.29.

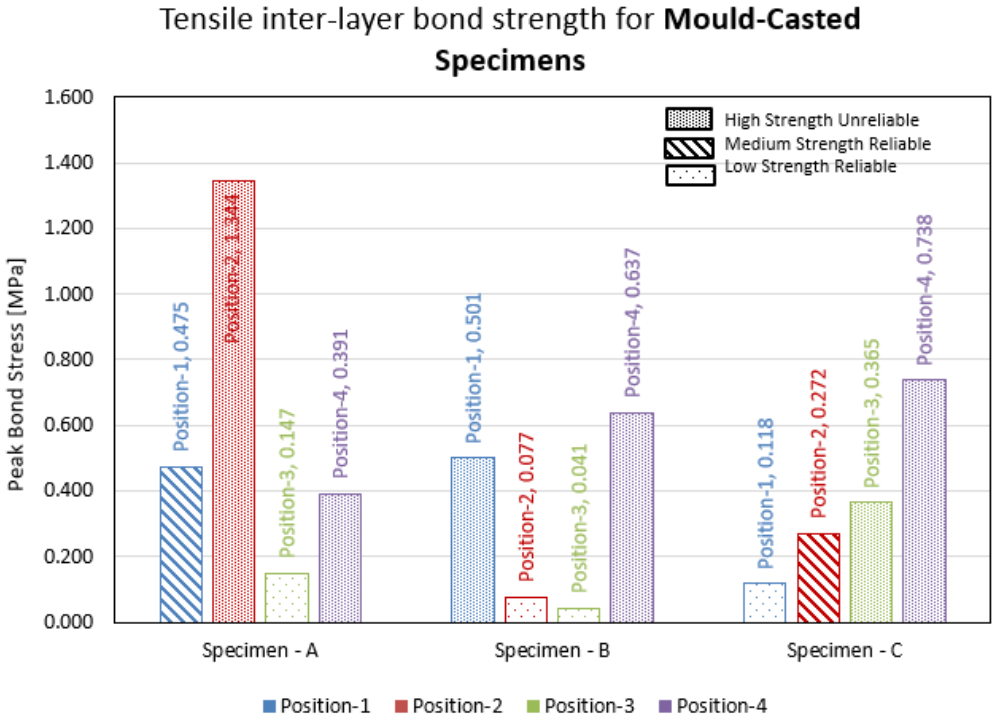

Figure 5.20: Tensile inter-layer bond strength results for Mould-Casted Specimens (refer Appendix E)

Therefore, it can be inferred that there is a possibility that some level of non-uniform debonding in the specimen existed during the test which was hidden due to the rotational boundary conditions balancing them out and eventually leading to erroneous results showcasing centric load application. Specimen A-4, B-1, B-4, C-3 and C-4 exhibit similar behaviour with an exception of slight non-uniform debonding as it approaches the peak and thereafter. The snap-back behaviour could be a possible reason for the load eccentricities post-peak. Since there is no data point recorded between the peak and the end of the unloading region suggesting that the test setup was not fast enough to overcome the sudden stress drop. All these specimens form a 'high strength unreliable' group and are expected to have erroneous test results which make them unreliable to consider for drawing further conclusions.

Contrary to the behaviour observed in the group of 'high strength unreliable' group of specimens, the rotational boundary conditions seem to have failed to balance out the non-uniform debonding occurring in Specimen A-1 and C-2 (as confirmed from Figure 5.4) and hence, the load eccentricities continue to persist which might have led to a less error-prone data as seen in Figure 5.5 but the reliability of

these results is still questionable. These specimens are thus, grouped as 'medium strength reliable' specimens.

Specimen A-3 has a softening curve with bumps which is suggestive of the test specimen having fixed-fixed boundaries. The softening curve further confirms this as it resembles the one obtained in previous research Chaves Figueiredo *et al.* [44] which should suggest that the test results are reliable. It does, however, exhibit tension-bending failure throughout the test duration which can be confirmed from Figure E.77 and E.78. The clustered voids as observed in Figure D.69 could have resulted in the non-uniform contact surface between successive layers and serves as a good explanation for the non-uniform debonding, apart from the other influencing factors such as the effect of notching and specimen dimension.

The softening curve of Specimen B-3 and B-2 follow similar trends as exhibited by Specimen A-3. In terms of Specimen B-3, though the specimen has fixed-fixed boundary conditions it undergoes uniform debonding until the peak, post which the debonded regions start closing in an uneven manner and further pull-out results in non-uniform debonding of the smaller bonded regions. This is a similar phenomenon as explained in the research of Hordijk [34], who states that such behaviour is common in direct tensile tests and leads to an unloading-reloading cycle in softening curve as illustrated in Figure 5.16. This unloading-reloading cycle can be spotted at data point-3 and on examination of strain at this point shows the initiation of non-uniform debonding as can be confirmed from Figure B.334. The test part after data point-3 is usually considered unstable as discussed in subsection 5.4.1 but since debonding can be seen taking place in major proportion in this region it has been accounted for in the analysis. Specimen C-1 also exhibits similar behaviour.

In the hindsight from the analysis of the inter-layer bond test results for Specimens A-3, B-2, B-3 and C-1 it can be inferred that they represent a 'low strength reliable' group. It is important to understand that these specimens had fixed-fixed boundary conditions and their softening curves show a strong resemblance to the one obtained by the previous researchers for SHCC-based specimens. Hence, the possibility of the results being error-prone is less and they can be said to exhibit the true material property. Clustered voids attributed to the under-filling related phenomenon in the inter-layer may have been the major cause of the lack of contact between the successive layers resulting in a weaker bonded region and hence, facilitating uneven pull-out of the inter-layer. The test results of this group of specimens can therefore be considered to be reliable.

5.6. Overview on Bond Tests for Caulk-Gun based-specimens

Apart from retrieving the groove size parameter as adopted in mould-casted specimens, additionally, a study of surface moisture characterisation over time-gaps of 5-, 10- and 20-minutes was also performed on the caulk-gun-based specimens. The results of the same are provided in Figure 5.21 alongside the bond test results.

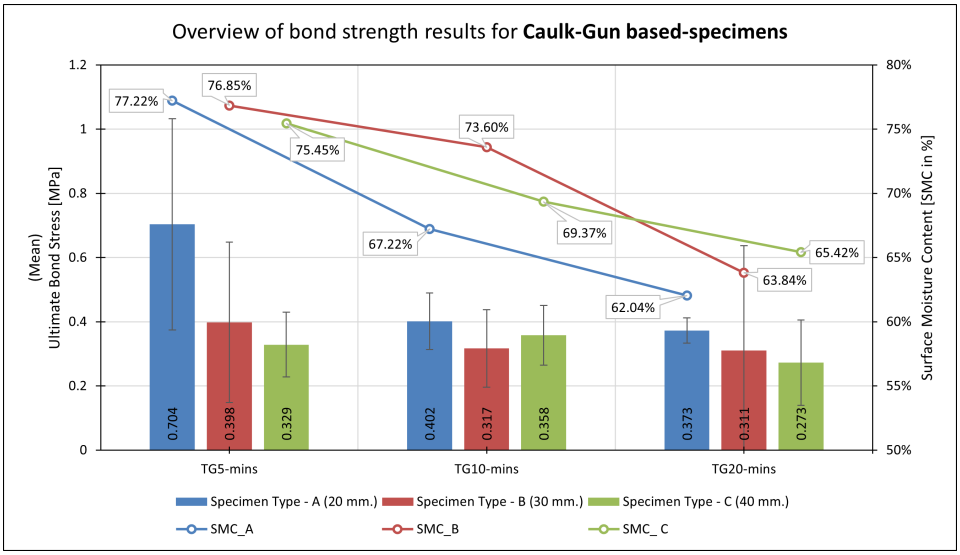

Figure 5.21: Plot of SMC Measurements against Bond Strength of different Time-gaps (TG's) based -**Caulk-gun specimens**

As observed in the research of Wang *et al.* [49] over a period of time the moisture evaporates from the surface of the layer which is then replaced by the moisture migrating from inside of the layer to the surface. This creates a moisture gradient over the height of the layer. On similar lines, it was hypothesised at the start of this research that the moisture would migrate from the crests to the grooves over time owing to the topology of the layer. As observed in Figure 5.21, since, there are fewer deviations in the Surface Moisture Content (SMC) values with respect to the time-gaps adopted, it poses difficulty in predicting the aforementioned hypothesis. Furthermore, the method and equipment used herewith to measure the SMC is not accurate and hence, pose numerous practical difficulties. One of the major issues in recording SMC data is that the equipment pins need to be pierced into the sample up to a certain depth in its fresh state which is a tedious task. Secondly, given the number of data points, it is hard to achieve the same accuracy in repetitions. It is important to note here that though the equipment comes pre-calibrated from the manufacturer the verification of the same hasn't been performed and it has solely been chosen for measurement based upon its industry applications and similar equipment chosen in previous research [55]. This might need attention in upcoming research.

Though the deviation in the data is less, from Figure 5.21, it can be confirmed that for a given specimen type the SMC values tend to decrease as time-gaps increase, which is as predicted by Van Der Putten *et al.* [48]. However, close observation of the results confirms that this trend in decrease is more or less similar over all three specimens. The decrease in SMC values for Specimen A and B is from 100% (at 0-minutes) to approx. 63% (refer Appendix F) and in the case of Specimen C, this decrease is slightly less and is limited to approx. 66% (refer Table 5.3). The room conditions were constant throughout. Also, the extrusion parameter like that height and speed were attempted to be kept constant throughout the process but some deviations could be expected as the height was non-constant owing to the osteomorphic topology and manual operation of the caulk-gun speed was variable. Since these deviations were not on a major scale and in-order to simplify the result analysis, the extrusion parameters are considered to have a negligible effect on the surface moisture content. Therefore, the slight less decrease in moisture for specimen type C could be attributed to its deeper groove size which might have led to more moisture retention in the layer.

As per the research of Sanjayan *et al.* [8] the trend in the surface moisture content over the time-gaps influences the adhesion between the layers. Accordingly, for longer time-gaps owing to the loss of moisture from the surface the adhesion between the layer is reduced. A similar trend, though not clearly distinguishable is encountered in the caulk-gun based specimens as can be observed from Figure 5.21. As can be confirmed from the Figure 5.21 specimens the time-gap of 5-minutes tend to have the highest average bond strength of approximately 0.48MPa followed by specimens of 10-minutes and 20-minute time-gap with an average bond strength of 0.36 and 0.32MPa respectively.

Given the previous research and the bond test results, at first instant, this trend seems logical. However, similar to the discussions in the mould-casted specimens, the detailed analysis of the bond test results (refer Appendix - B), reveals a major issue identified which is that of the reliability of the bond test results which interferes with the aforementioned logic. The caulk-gun specimens are not only influenced by the adopted time-gaps but also by the groove-sizing. The trend usually shows that Specimen A is the highest contributor to the average bond strength with Specimen C being the lowest which is also the case in mould-casted specimens. The trend seems a bit off in terms of specimens with time-gap of 10-minutes wherein Specimen B is the lowest contributor to the average. Since the specimens were extruded using a caulk-gun nozzle, the issues of under-filling and/or roughness due to variable height, speed and grooving are more predominant in these. The roughness of the inter-layer due to the formation of cold joints and due to poor quality of nozzle extrusion are major contributors to errors during the test. Therefore, in-order to understand how the specimens perform against each other in terms of strength, owing to the groove sizes and time-gaps, it is important to identify the reliability of the test results first based on the discussions provided in section 5.3.

Firstly, the specimens are identified for non-uniform and uniform debonding, the results of which can be correlated to the surface moisture content measurements and image analysis data thereafter. Secondly, based on the behaviour of the softening curve for each tested specimen the specimen boundary conditions are identified. The specimen with softening curves showing no bumps are considered to have fixed-rotational boundary conditions and the ones with bumps are considered to have fixed-fixed (as per the discussion provided in sub-section 5.3.1). The specimen with fixed-fixed boundary conditions are said to exhibit the true nature of material property [32] [36] and hence, are considered reliable. Owing to the above considerations and as can be confirmed from Table 5.2, only approximately 36% of the total tested specimens are reliable. The discussions on the reliability of the specimens is similar to the one provided in section 5.5 for the mould-casted specimens. Therefore, only the reliable specimens i.e. specimens with fixed-fixed boundary conditions and having a softening curve characteristically similar to the one obtained for SHCC-based specimens in the literature as highlighted in Table 5.2 and 5.3 and Figure 5.22 are only discussed in detail herewith in terms of surface moisture content and image analysis.

Table 5.3: Specimens with reliable test results

Specimen			**Strong Bonding [in %]**	**Bond Strength [MPa]**	**SMC [in %]**
Time-gap	**Type**	**Position**			
5-minutes	A	4	48.53%	0.333	78.52%
	B	3	47.40%	0.038	81.48%
	C	3	54.85%	0.211	77.14%
10-minutes	A	1	47.45%	0.273	67.20%
		3	50.88%	0.360	62.96%
	B	4	58.73%	0.321	71.11%
		3	50.27%	0.399	72.06%
	C	4	45.93%	0.249	59.79%
20-minutes	A	3	47.51%	0.319	62.22%
	B	3	45.42%	0.055	65.29%
		4	45.54%	0.005	69.84%
	C	1	42.92%	0.181	61.38%
		3	48.93%	0.182	68.57%

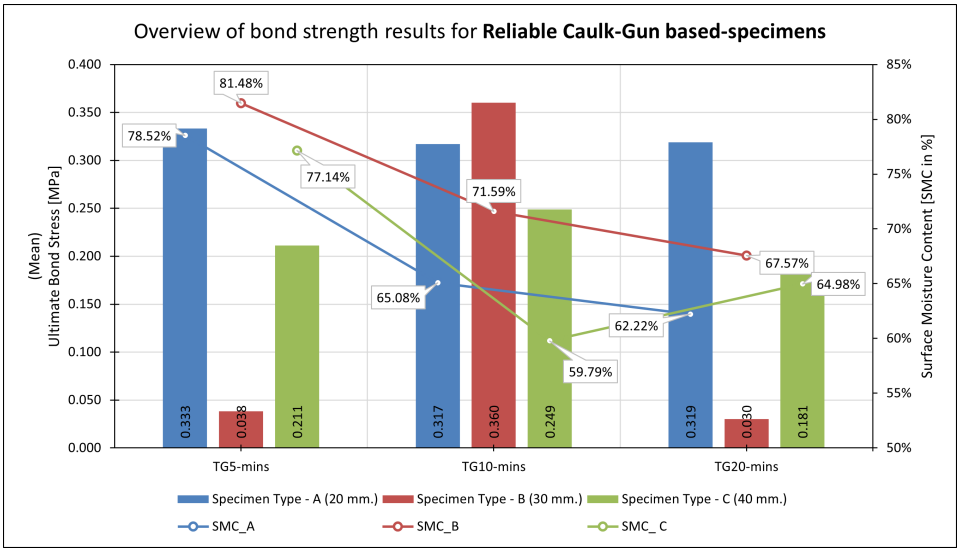

Figure 5.22: Plot of SMC Measurements against Bond Strength of different Time-gaps (TG's) based - **Caulk-gun specimens (Reliable)**

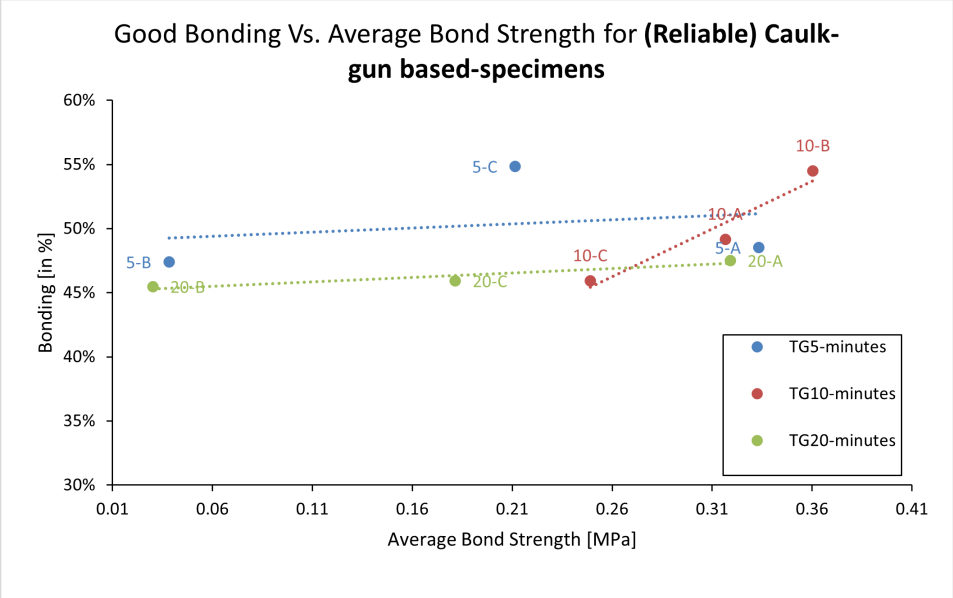

Figure 5.23: Plot of Bonding acquired from Image analysis Vs. Average Bond Strength for (reliable) caulk-gun specimens

One of the major observations from the test results is that the specimens of a time-gap of 20-minutes and 5-minutes seem to have similar behaviour. Though the SMC measurements for these groups differ and are on the similar lines as that suggested in previous research [49] [6] [8] the same cannot be said about inter-layer bond strength. The inter-layer bond strength for the specimens of these groups are in the similar range and they seem to perform poorly as compared to specimens with a time-gap of 10-minutes which is counter-intuitive to the conclusions observed in previous research wherein it suggests that longer time-gaps specimen should exhibit lower strength and vice versa. Since the aspect of boundary conditions is not interfering with the test results as explained before it can easily be ruled out. Therefore, the only factors responsible for this trend could be the issues of asymmetry of the specimens, under-filling and surface roughness which result in non-uniform bonding in the inter-layer and are further analysed in-depth hereon.

From Figure 5.22 it can be confirmed that the specimen type-B performs poorly in bond tests for time

gaps of 5- and 20-minutes. Specimens of group TG20-B have an average bond strength of 0.030MPa which when correlated to the image analysis results as observed in Figure 5.24 and 5.23 confirms that the bonding observed in these specimens is one of the lowest which is approx. 45%. Apart from non-uniform bonding, Specimen TG20-B-3 also has issues with regards to asymmetry induced due to cutting and grinding as explained in subsection 5.3.3 which might have influenced the non-uniform debonding during test progress, as seen in Figure E.45. Specimen TG20-B-4 undergoes uniform debonding throughout the test progress as observed in Figure E.47, however, given the image analysis result it can be confirmed that the bonding in the successive layers is low which might have led to an instantaneous debonding and hence, non-uniform debonding is non-existential in the test progress even though the fractured inter-layer surface suggests that non-uniform bond prevailed in the specimen. Specimen TG5-B-3 shows a similar trend as that observed in Specimen TG20-B-3 and also seems to have issues of asymmetry as seen in Figure 5.24a apart from the lack of strong bonding in the inter-layer. Specimen TG10-B-3 and TG10-B-4 have a strong bonding of about approx. 55% which is more than observed in any other caulk-gun-based specimen and hence, serves as a better explanation of the good bond strength exhibited by these specimens.

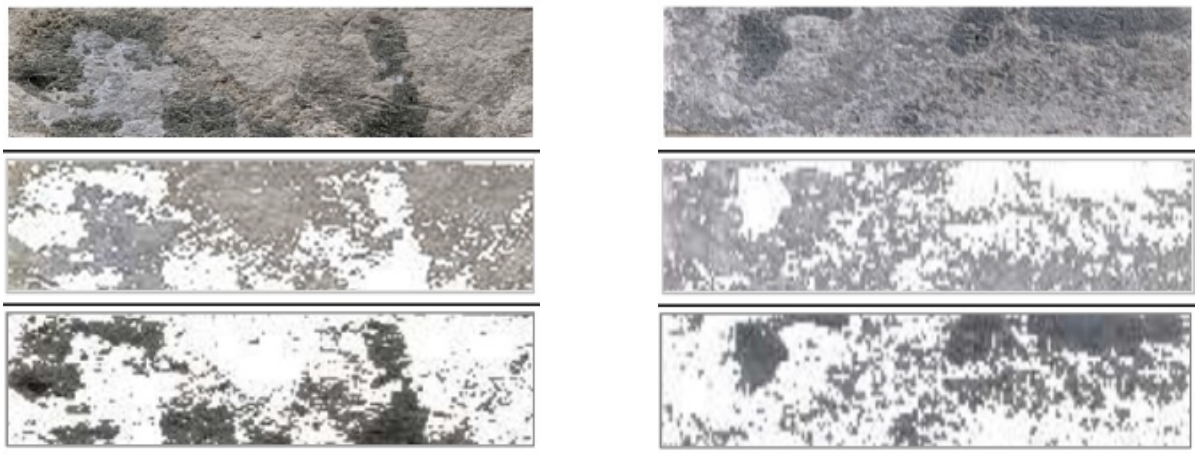

(a) Image analysis result for (Left) Specimen 20-B-3 (Right) Specimen 20-B-4

Figure 5.24: Image analysis results performed on fractured inter-layer surface: (Top) Original Image (Middle) Threshold image representing weak bond (Bottom) Threshold image representing good bond

Specimen type-C and A show good consistency in terms of the inter-layer bond strength results. Specimens TG5-C-3, TG20-C-1 and TG20-C-3 form the next lowest bond strength group. All the specimens seem to show similar behaviour on examining the test progress data, with slight non-uniform debonding initiated from the start of the test (as seen in Figure E.53, E.65 and E.69). The major factor influencing the results of Specimen TG20-C-1 and TG20-C-3 is that of non-uniform bonding which can be confirmed from the image analysis results. Though the bonding in the Specimen TG5-C-3 was strong approx. 54%, it clearly had the issue of asymmetry due to the thickness of the bottom layer being less, which possibly influenced the bond test results to large extent, which can be confirmed from Figure 5.25

Figure 5.25: Failure of Specimen TG5-C-3 influenced by asymmetry (bottom layer)

The specimen type-A shows consistent and better bond strengths in all the time-gaps as observed from Figure 5.22 and from its scatter in Figure 5.23. Though the specimens exhibit good and consistent bond strength the non-uniform debonding does exist mildly from the start of the test and intensifies post-peak, as can be confirmed from test progress data in Appendix-E. This is suggestive of the existence of under-filling and roughness-induced non-uniform bonding between successive layers which can be further confirmed by the image analysis results. Although the effects of under-filling and roughness persist, the asymmetry-related effects in the test setup are limited, except for in the case of TG5-A-4 which are considerable. The effect of specimen dimensions as discussed in subsection 5.3.2 could have been another factor responsible for the non-uniform debonding. Thus, it can be confirmed that specimen type-A is a good representation of the strength characteristics of these caulk-gun-based curved specimens.

5.7. Overview on Bond Tests for Reliable Specimens

In terms of caulk-gun-based specimens, there is no direct relationship that can be observed between bond strength and surface moisture content as obtained in the previous research [6], [48]. This might possibly be due to the fact that an additional groove sizing parameter interferes the results. From the Figures, 5.21 and 5.22, the groove sizing and surface moisture content relationship is inconclusive as well. Given that surface moisture content, data shows no appropriate trend in terms of groove sizing and bond strength parameters it is termed inconclusive and hence, for this purpose for further comparative analysis between caulk-gun and mould-casted based-specimens this parameter is not taken into consideration anymore. Owing to this, the results of the tests that have been considered reliable as per the discussions in previous sections are provided in Figure 5.26.

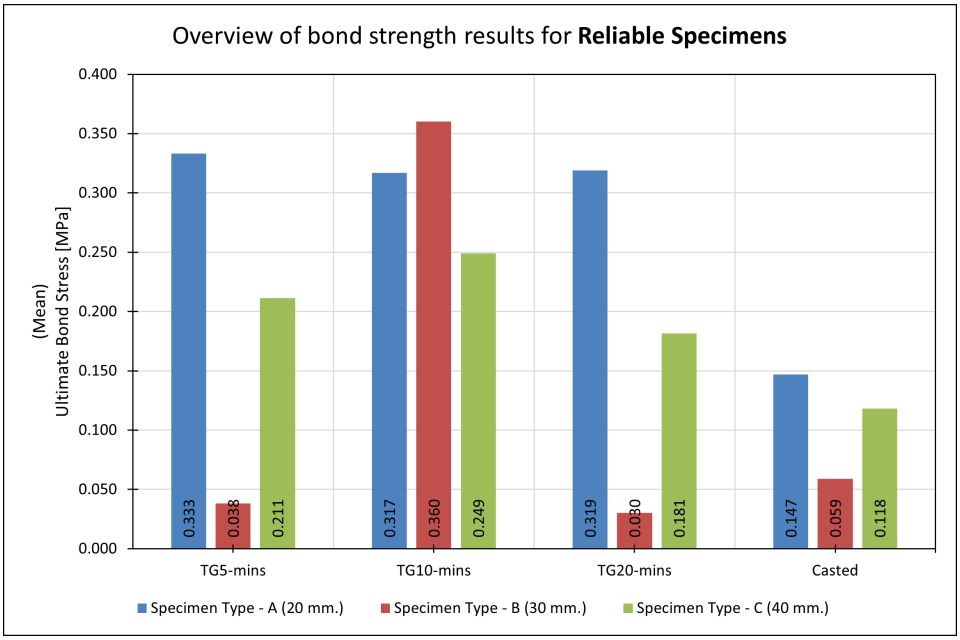

Figure 5.26: Overall comparison of bond strength results for samples with reliable test results

As observed from Figure 5.26, the mould-casted specimens perform poorly in bond strength tests as compared to the caulk-gun specimens. Since specimens of type-A and C perform consistently overall, the comparison of these between caulk-gun and mould-casted specimens suggests that the former exhibits 44 to 54% more tensile bond strength as compared to the latter. Although no studies in terms of the void structure have been performed herewith, the visual examination of the inter-layer suggests that the under-filling attributed effects like clustered voids in the interface of mould-casted specimens (as observed in the Figure 5.27) have an adverse effect on bond strength which is on the similar lines as that observed in various previous research literature's [19] [21] [22]. The phenomenon of the formation of voids in these specimens is explained in subsection 5.3.4, these clustered voids possibly caused reduced effective contact area and may have led to the formation of weaker joint planes within the interface [21] [19]. Based on this phenomenon and observing Figure 5.27 helps to confirm that the number of voids on the inter-layer surface of Specimen B is higher, which is suggestive of the weaker bond strengths exhibited by these specimens. From the image analysis result, it can be confirmed that bonding was also a major issue with caulk-gun based-specimen of type-B (as observed in Figure 5.24). Hence, the results for both specimens i.e. caulk-gun and mould-casted are in agreement over the order in which strength characteristics differ in terms of specimen types i.e. specimen type A and C perform consistently better than B (in that order - except for time-gap of 10-minutes).

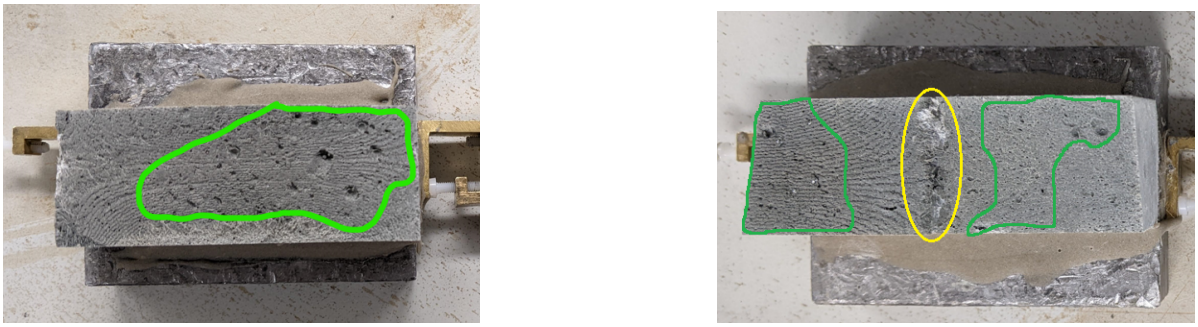

(a) Fractured inter-layer surface for (Left) Specimen A-3 (Right) Specimen B-2

(b) Fractured inter-layer surface for (Left) Specimen B-3 (Right) Specimen C-1

Figure 5.27: Fractured (bottom) inter-layer surface of mould casted specimen: exhibiting (green regions) clustered voids in the interface (yellow regions) mould induced-discontinuity (red regions) showing fibre dispersion in the layer

The variation in the speed of extrusion could be a good explanation for the trend observed in bond strengths of caulk-gun specimens as suggested in the previous research [6]. Owing to the shallower groove dimensions in Specimen type-A the variation in extrusion height was less which led to faster extrusion speed because the extruded layer from the nozzle could rest and retain the shape of curved topology underneath conveniently. The same wasn't the case in terms of Specimen type-B and C. Previous literature studies identified an inverse relationship between the speed of extrusion and the surface roughness which meant that the extruded layer in Specimen type-A was comparatively smoother than Specimen type-B and C and hence, was able to avoid defects and establish good contact between successive layers which can be confirmed from the image analysis results displayed in Figure 5.23. Specimen type-B of 5- and 20-minutes had issues with the asymmetry of the specimen in the test setup hence, it's hard to confirm this 'surface roughness'-related phenomenon there. However, if Specimen type-B of 10-minutes is to be analysed, it's suggestive of a good combination achieved between extrusion parameters and grooving leading to better contact in the inter-layer and therefore, enhanced bond strength. Specimen type-C exhibits the same phenomenon and is more reliable since, as compared to type-B the problems of asymmetry were not as major in these. Though it is hard to quantify and perform a comparative analysis of the specimen results based on this phenomenon, it provides a good perspective and insight for future research.

6

Conclusion and Recommendations

The research conducted as a part of this thesis aimed to resolve the issue of weak inter-layer bonding between layers of extrusion-based 3D printable concrete structures. The research question identified for the same is given below:

What is the effect on the inter-layer bond when the prevalent planar geometry of SHCC-based extruded layers is modified to one inspired by osteomorphic blocks in extrusion-based 3D concrete printing?

Two methods were used for sample preparation namely mould casting and caulk-gun extrusion and the samples derived from these methods were further tested for inter-layer bond strength. The specimens acquired from the aforementioned methods had various issues apart from the several drawbacks of the test setup, which led to the data achieved by performing inter-layer bond tests on the specimens being error-prone. This made the process of analysing the effect of implementing such a shape in the inter-layer complicated.

The intent of this chapter is to provide a detailed conclusion for each method and then provide a generalised conclusion. Furthermore the focus of the chapter shifts towards providing appropriate recommendations for future research on the topic.

6.1. Detailed Conclusions

6.1.1. Mould-casting method

The mould-casting-based specimens were produced with an intention of solely focusing on the aspect of grooving and with the exclusion of printing parameters. These specimens had issues of under-filling attributed to clustered voids which were caused due to the air entrapment during the casting process. Most of the mould-casted specimens endured non-uniform debonding for this reason under the test progress. The shape of the softening curve was a major deciding factor in establishing the boundary conditions of the specimen under the test setup. The fixed-rotational boundaries of the specimen led to load eccentricities during test progress which intensified the problems of non-uniform debonding in these specimens. Hence, it was imperative to first identify the reliability of the test results for each specimen. In doing so it was found that only one-third of the total tested specimens had fixed-fixed boundaries and their results could be deemed reliable. On those lines, Specimen type-A exhibited the highest bond strength followed by Specimen type-C and B (in that order). In terms of tensile inter-layer bond strength, Specimen type-A with a bond strength of 0.147MPa performed approximately 19% better

than that of type-C and about 60% better than that of type-B which exhibits an average bond strength of 0.118MPa and 0.060MPa respectively. The reduced adhesion due to voids present in the inter-layer is the main reason for the huge difference in the bond strength values. It can thus be concluded that a deeper grooving in the topology does not always lead to mechanical interlocking owing to the under-filling attributed voids in the inter-layer, specimen and hence, improvement of the inter-layer bond in extrusion-based 3D printed concrete. Owing to the specimen defects and test setup, the sample size used to arrive at this conclusion is not big enough. However, a comparison of the results obtained in terms of mould-casting specimens, with the literature shows good agreement with similar studies performed in the past and hence, results gain some level of credibility.

6.1.2. Caulk-gun extrusion method

The caulk-gun based-specimens retained groove sizing parameters from the mould-casting method besides the inclusion of other parameters like surface moisture migration and time-gaps. These specimens exhibited issues of non-uniform debonding during test progress as encountered in mould-casted specimens. Asymmetry of the specimen and non-uniform contact in the inter-layer due to under-filling attributed cold joints resulting from grooving and surface roughness of the extruded layer caused by variable extrusion parameters affected the adhesion of the inter-layer and hence, are said to have majorly influenced the debonding behaviour during test progress. Apart from these issues, the primary issue of boundary conditions of the specimen under test setup was also eminent in caulk-gun based-specimens. Therefore, in order to get rid of erroneous test data the softening curve was analysed first and specimens with fixed-fixed boundary conditions were identified which were then used for further detailed analysis.

Given that the deviations in the measured surface moisture are very minor, it is complicated to conclude if there is any surface moisture migration occurring within the extruded layers. However, as can be concluded from the results the surface moisture content on extruded layer decreases with an increase in time. As per previous research, owing to loss of moisture, a longer time gap should have resulted in decreased adhesion and hence, reduced bonding. This phenomenon is observed in caulk-gun-based specimens when the results are considered in entirety. However, the trend fails to prevail when the results are narrowed down based on their reliability. Accordingly, specimens of time-gap 5-minutes should have exhibited the highest bond strength followed by those of 10- and 20-minutes. However, on narrowing down the results based on their reliability, this trend does not exist and a random trend can be observed wherein specimens of time-gap 10-minutes with an average bond strength of 0.310MPa are performing 40% better than those of 5- and 20-minutes with an average bond strength of 0.194MPa and 0.180MPa respectively. The main reason identified for the poor performance of specimens with time-gaps 5-minutes is that they have asymmetry due to excessive grinding and chipping of one extruded layer more than the other. This might have caused uneven stress transfer from the loading plates to the inter-layer and this, in combination with non-uniform bonding between the inter-layer might have led to inaccurate test results.

Furthermore, in terms of the groove sizing parameter, Specimen Type-A and type-C perform consistently over the 3 time-gaps with an average bond strength of 0.320MPa and 0.210MPa respectively. On the other hand, Specimen type-B shows an unusual trend, performing poorly in time-gaps of 5- and 20-minutes with bond strength averaging at 0.034MPa which is 90% less than that exhibited by time-gap of 10-minutes which shows an average bond strength of 0.360MPa. As discussed earlier, in terms of time-gaps of 5- and 20-minutes, Specimen type-B had problems of asymmetry and weak bonding in the inter-layer which suggests some level of inaccuracy in the test data whereas the strong performance in time-gap of 10-minutes is attributed to the uniform bonding in the inter-layer which can be confirmed from the image analysis results. However, given the trend observed in the mould-casting-based specimens which were solely based on groove size parameters, the trend for time-gap of 10-minutes in caulk-gun-based specimens seems abnormal. One explanation for this could be that the speed and height of extrusion influence the surface roughness of the extruded layers and since they were variable during the sample preparation, they may have led to an inconsistent surface roughness of the specimens which resulted in an unconventional trend in bonding test results.

6.2. General Conclusions

The research herein, emphasises various important issues faced in terms of sample preparation and testing of the specimens. The mould-casted and caulk-gun based-specimens had under-filling attributed defects like clustered voids and cold joints respectively. Apart from that, the inclusion of extrusion parameters in caulk-gun-based specimens led to surface roughness which added to the issue of cold joint formation. The testing regime was mainly influenced by boundary conditions in combination with specimen dimensions and asymmetry (especially in terms of caulk-gun based-specimens). The displacement rate and absence of notching in the specimen are other factors that could have added to inaccuracies in the obtained test results.

After acknowledging the inaccuracies in the sample preparation and testing regime one of the important outcomes to draw from reliable test results is that deeper grooving does not always lead to enhanced mechanical interlocking in extrusion-based 3D-printed concrete. Factors like under-filling due to grooving and surface roughness induced by extrusion parameters interfere immensely in proving the same. The second important outcome to highlight is that the inverse relationship between time-gap and bond strength observed in various previous research may not hold true when combined with grooving. The same can be said about the direct relationship between surface moisture content and bond strength which is hard to predict as the groove sizing parameter and the defects associated with it interfere with doing so.

Although there is an ample amount of potential in trying to improve the inter-layer bond in extrusion-based 3D printable concrete by adopting the topological interlocking phenomenon, there is a long way to go before it can be completely implemented and its potential can be harnessed by the construction industry. Based on the outcomes, it can be said that it is imperative to devise a rigorous and accurate regime to prepare and test the specimens before even going on to prove and conclude the hypothesis stated initially. However, the research herein manages to provide crucial insights to help improve and build a strong basis for similar future research.

6.3. Recommendations

The research conducted herein is conceptual and is a first step towards implementing this approach in 3D concrete printing. It focuses extensively on the aspects of finding the appropriate combination between groove size and time-gap in-order to ensure that the topological interlocking is as effective as possible. A more comprehensive research can be planned in-order to explore the advantages of adopting topological interlocking phenomenon in 3D concrete printing, keeping the below pointers in perspective:

- As the specimen topology has a tendency to affect the results, the reliability of the tests highlighted in this research is a major aspect that needs attention in future research as well. Adopting sophisticated modified CLC-based testing could help avoid reliability issues to a large extent.
- Another aspect could be to adopt a smaller scaled-down version of the topology and saw prismatic specimens which are said to have higher rotational stiffness and would provide stable debonding and hence, could impart more accuracy in test results.
- Since notching of the specimens is hard to achieve due to the curved topology it is recommended to use small LVDT's or increase the number of LVDT's and adopt a modified control loop as suggested in the research of Li, Kulkarni, and Shah [35] which will help minimise the snap-back behaviour and would further help in reducing the chances of encountering unstable test progress.
- Adopting a slower displacement rate and estimation of the same with the help of dummy specimens prior to the commencement of the testing regime can help reduce the inaccuracy of the test results.
- The inter-layer bond test setup needs to be modified for the topology-based specimens by replacing flat plates with plates having a curved surface this will not only help in reducing the efforts of

grinding and cutting the specimens (facilitating uniform glue distribution between the plate and the specimen) but it will also help prevent non-uniform stress distribution and further help in avoiding inaccuracies induced in test results due to asymmetry of the specimens.

- The variable extrusion parameters influence the surface roughness and are also related to the under-filling attributed effects like cold joint formation. It is recommended to keep uniform height throughout and constant speed which can be achieved by using a scale model robotic arm attached to a nozzle which should provide good printing without the inclusion of cold joints.
- A dynamic nozzle can be devised which can help perfectly extrude the osteomorphic block-inspired shape as tried in this research initially. This is expected to help reduce problems like nozzle extrusion-induced roughness in the inter-layer and cold-joint formation.
- The quality of the bond can be characterised using sophisticated micro-structural analysis techniques instead of Image analysis which will prove to be more accurate.
- A study can be carried out on a micro-scale level to explore and confirm the benefits of fibre bridging in the fracture surface in combination with the topological interlocking phenomenon.
- Sophisticated equipment which provides accurate readings can be used to measure surface moisture migration in further research. Calibration of the device is an essential aspect that should not be overlooked as well.
- The inter-layer bond strength of the topology-based extruded specimens needs to be compared to that of planar shape-based extruded layers in-order to understand the effectiveness of using the topology phenomenon.
- The changes in room conditions can be experimented with and monitored with in-order to study surface moisture migration in this topology.

Bibliography

[1] R. A. Buswell, W. L. De Silva, S. Z. Jones, and J. Dirrenberger, "3d printing using concrete extrusion: A roadmap for research," *Cement and Concrete Research*, vol. 112, pp. 37–49, 2018.

[2] T. T. Le, S. A. Austin, S. Lim, R. A. Buswell, A. G. Gibb, and T. Thorpe, "Mix design and fresh properties for high-performance printing concrete," *Materials and structures*, vol. 45, no. 8, pp. 1221–1232, 2012.

[3] V. C. Li, F. P. Bos, K. Yu, W. McGee, T. Y. Ng, S. C. Figueiredo, K. Nefs, V. Mechtcherine, V. N. Nerella, J. Pan, *et al.*, "On the emergence of 3d printable engineered, strain hardening cementitious composites (ecc/shcc)," *Cement and Concrete Research*, vol. 132, p. 106 038, 2020.

[4] S. C. Figueiredo, C. R. Rodríguez, Z. Y. Ahmed, D. H. Bos, Y. Xu, T. M. Salet, O. Çopuroğlu, E. Schlangen, and F. P. Bos, "An approach to develop printable strain hardening cementitious composites," *Materials & Design*, vol. 169, p. 107 651, 2019.

[5] A. van Overmeir, "Designing an interlayer reinforcement solution for printable strain-hardening cement-based composites.: Practical research on various bond improvement concepts," 2020.

[6] J. Putten, G. D. Schutter, and K. V. Tittelboom, "The effect of print parameters on the (micro) structure of 3d printed cementitious materials," in *RILEM International Conference on Concrete and Digital Fabrication*, Springer, 2018, pp. 234–244.

[7] M. Lukovic, H. Schlangen, G. Ye, and B. Savija, "Impact of surface roughness on the debonding mechanism in concrete repairs," in *FraMCoS-8: Proceedings of the 8th International Conference on Fracture Mechanics of Concrete and Concrete Structures, Toledo, Spain, 10-14 March, 2013*, Citeseer, 2013.

[8] J. G. Sanjayan, B. Nematollahi, M. Xia, and T. Marchment, "Effect of surface moisture on interlayer strength of 3d printed concrete," *Construction and Building Materials*, vol. 172, pp. 468–475, 2018.

[9] T. Marchment, J. Sanjayan, and M. Xia, "Method of enhancing interlayer bond strength in construction scale 3d printing with mortar by effective bond area amplification," *Materials & Design*, vol. 169, p. 107 684, 2019.

[10] Y. He, X. Zhang, R. Hooton, and X. Zhang, "Effects of interface roughness and interface adhesion on new-to-old concrete bonding," *Construction and Building Materials*, vol. 151, pp. 582–590, 2017.

[11] Y. Estrin, A. V. Dyskin, and E. Pasternak, "Topological interlocking as a material design concept," *Materials Science and Engineering: C*, vol. 31, no. 6, pp. 1189–1194, 2011.

[12] Ł. Sadowski, *Adhesion in Layered Cement Composites*. Springer, 2019.

[13] A. Molotnikov, Y. Estrin, A. Dyskin, E. Pasternak, and A. Kanel-Belov, "Percolation mechanism of failure of a planar assembly of interlocked osteomorphic elements," *Engineering fracture mechanics*, vol. 74, no. 8, pp. 1222–1232, 2007.

[14] F. Bos, R. Wolfs, Z. Ahmed, and T. Salet, "Additive manufacturing of concrete in construction: Potentials and challenges of 3d concrete printing," *Virtual and physical prototyping*, vol. 11, no. 3, pp. 209–225, 2016.

[15] S. C. Paul, G. P. van Zijl, M. J. Tan, and I. Gibson, "A review of 3d concrete printing systems and materials properties: Current status and future research prospects," *Rapid Prototyping Journal*, 2018.

[16] G. H. A. Ting, T. K. N. Quah, J. H. Lim, Y. W. D. Tay, and M. J. Tan, "Extrudable region parametrical study of 3d printable concrete using recycled glass concrete," *Journal of Building Engineering*, vol. 50, p. 104 091, 2022.

[17] S. Muthukrishnan, S. Ramakrishnan, and J. Sanjayan, “Technologies for improving buildability in 3d concrete printing,” *Cement and Concrete Composites*, vol. 122, p. 104 144, 2021.

[18] B. Panda, S. C. Paul, N. A. N. Mohamed, Y. W. D. Tay, and M. J. Tan, “Measurement of tensile bond strength of 3d printed geopolymer mortar,” *Measurement*, vol. 113, pp. 108–116, 2018.

[19] T. T. Le, S. A. Austin, S. Lim, R. A. Buswell, R. Law, A. G. Gibb, and T. Thorpe, “Hardened properties of high-performance printing concrete,” *Cement and Concrete Research*, vol. 42, no. 3, pp. 558–566, 2012.

[20] B. Panda, S. C. Paul, L. J. Hui, Y. W. D. Tay, and M. J. Tan, “Additive manufacturing of geopolymer for sustainable built environment,” *Journal of cleaner production*, vol. 167, pp. 281–288, 2017.

[21] A. Rahul, M. Santhanam, H. Meena, and Z. Ghani, “Mechanical characterization of 3d printable concrete,” *Construction and Building Materials*, vol. 227, p. 116 710, 2019.

[22] C. Liu, R. Zhang, H. Liu, C. He, Y. Wang, Y. Wu, S. Liu, L. Song, and F. Zuo, “Analysis of the mechanical performance and damage mechanism for 3d printed concrete based on pore structure,” *Construction and Building Materials*, vol. 314, p. 125 572, 2022.

[23] B. Zareiyan and B. Khoshnevis, “Interlayer adhesion and strength of structures in contour crafting-effects of aggregate size, extrusion rate, and layer thickness,” *Automation in Construction*, vol. 81, pp. 112–121, 2017.

[24] ——, “Effects of interlocking on interlayer adhesion and strength of structures in 3d printing of concrete,” *Automation in Construction*, vol. 83, pp. 212–221, 2017.

[25] M. Bi, L. Xia, P. Tran, Z. Li, Q. Wan, L. Wang, W. Shen, G. Ma, and Y. M. Xie, “Continuous contour-zigzag hybrid toolpath for large format additive manufacturing,” *Additive Manufacturing*, vol. 55, p. 102 822, 2022.

[26] M. R. Shahmirzadi, A. Gholampour, A. Kashani, and T. D. Ngo, “Shrinkage behavior of cementitious 3d printing materials: Effect of temperature and relative humidity,” *Cement and Concrete Composites*, vol. 124, p. 104 238, 2021.

[27] V. N. Nerella, S. Hempel, and V. Mechtcherine, “Micro-and macroscopic investigations on the interface between layers of 3d-printed cementitious elements,” in *Proceedings of the International Conference on Advances in Construction Materials and Systems, Chennai, India*, vol. 3, 2017, p. 8.

[28] T. Wangler, E. Lloret, L. Reiter, N. Hack, F. Gramazio, M. Kohler, M. Bernhard, B. Dillenburger, J. Buchli, N. Roussel, *et al.*, “Digital concrete: Opportunities and challenges,” *RILEM Technical Letters*, vol. 1, pp. 67–75, 2016.

[29] J. Van Der Putten, G. De Schutter, and K. Van Tittelboom, “Surface modification as a technique to improve inter-layer bonding strength in 3d printed cementitious materials,” *RILEM Technical Letters*, vol. 4, pp. 33–38, 2019.

[30] J. Ye, C. Cui, J. Yu, K. Yu, and J. Xiao, “Fresh and anisotropic-mechanical properties of 3d printable ultra-high ductile concrete with crumb rubber,” *Composites Part B: Engineering*, vol. 211, p. 108 639, 2021.

[31] M. Ishtiyaque and M. Shaikh, “A review on study of fracture properties of concrete reinforced with mixed/hybrid fibers,”

[32] J. Van Mier and M. Van Vliet, “Uniaxial tension test for the determination of fracture parameters of concrete: State of the art,” *Engineering Fracture Mechanics*, vol. 69, no. 2, pp. 235–247, 2002.

[33] R. Gettu, B. Mobasher, S. Carmona, and D. C. Jansen, “Testing of concrete under closed-loop control,” *Advanced Cement Based Materials*, vol. 3, no. 2, pp. 54–71, 1996.

[34] D. A. Hordijk, “Local approach to fatigue of concrete.,” 1993.

[35] Z. Li, S. Kulkarni, and S. Shah, “New test method for obtaining softening response of unnotched concrete specimen under uniaxial tension,” *Experimental Mechanics*, vol. 33, no. 3, pp. 181–188, 1993.

[36] F. P. Zhou, “Some aspects of tensile fracture behaviour and structural response of cementitious materials,” 1988.

[37] S. Cattaneo and G. Rosati, “Effect of different boundary conditions in direct tensile tests: Experimental results,” *Magazine of Concrete Research*, vol. 51, no. 5, pp. 365–374, 1999.

[38] J. Van Mier, “Micromechanical analysis and experimental verification of boundary rotation effects in uniaxial tension tests on concrete,” *Mechanics of Brittle Disordered Materials, Concrete, Rock and Ceramics*, pp. 406–420, 1995.

[39] F. Wittmann and G. Van Zijl, “Durability of shcc conclusions,” 2006.

[40] M. B. Weimann and V. C. Li, “Hygral behavior of engineered cementitious composites (ecc)/vergleich der hygrischen eigenschaften von ecc mit beton,” *Restoration of Buildings and Monuments*, vol. 9, no. 5, pp. 513–534, 2003.

[41] B. Panda, S. C. Paul, and M. J. Tan, “Anisotropic mechanical performance of 3d printed fiber reinforced sustainable construction material,” *Materials Letters*, vol. 209, pp. 146–149, 2017.

[42] B. Nematollahi, M. Xia, J. Sanjayan, and P. Vijay, “Effect of type of fiber on inter-layer bond and flexural strengths of extrusion-based 3d printed geopolymer,” in *Materials science forum*, Trans Tech Publ, vol. 939, 2018, pp. 155–162.

[43] H. Ogura, V. N. Nerella, and V. Mechtcherine, “Developing and testing of strain-hardening cement-based composites (shcc) in the context of 3d-printing,” *Materials*, vol. 11, no. 8, p. 1375, 2018.

[44] S. Chaves Figueiredo, C. Romero Rodríguez, Z. Y Ahmed, D. H. Bos, Y. Xu, T. M. Salet, O. Çopuroğlu, E. Schlangen, and F. P. Bos, “Mechanical behavior of printed strain hardening cementitious composites,” *Materials*, vol. 13, no. 10, p. 2253, 2020.

[45] A. Hamilton, Y. Xu, M. E. Kartal, N. Gadegaard, and D. M. Mulvihill, “Enhancing strength and toughness of adhesive joints via micro-structured mechanical interlocking,” *International Journal of Adhesion and Adhesives*, vol. 105, p. 102 775, 2021.

[46] A. R. Javan, H. Seifi, X. Lin, and Y. M. Xie, “Mechanical behaviour of composite structures made of topologically interlocking concrete bricks with soft interfaces,” *Materials & Design*, vol. 186, p. 108 347, 2020.

[47] H. T. D. Yong, “Utilisation of topologically-interlocking osteomorphic blocks for multi-purpose civil construction,” 2011.

[48] J. Van Der Putten, M. Deprez, V. Cnudde, G. De Schutter, and K. Van Tittelboom, “Microstructural characterization of 3d printed cementitious materials,” *Materials*, vol. 12, no. 18, p. 2993, 2019.

[49] X.-Y. Wang and K.-B. Park, “Analysis of the compressive strength development of concrete considering the interactions between hydration and drying,” *Cement and concrete research*, vol. 102, pp. 1–15, 2017.

[50] W. Tian and N. Han, “Pore characteristics (> 0.1 mm) of non-air entrained concrete destroyed by freeze-thaw cycles based on ct scanning and 3d printing,” *Cold Regions Science and Technology*, vol. 151, pp. 314–322, 2018.

[51] J. Valença, D. Dias-da-Costa, E. Júlio, H. Araújo, and H. Costa, “Automatic crack monitoring using photogrammetry and image processing,” *Measurement*, vol. 46, no. 1, pp. 433–441, 2013.

[52] D. Miriello and G. M. Crisci, “Image analysis and flatbed scanners. a visual procedure in order to study the macro-porosity of the archaeological and historical mortars,” *Journal of cultural heritage*, vol. 7, no. 3, pp. 186–192, 2006.

[53] K. W. Peterson, R. A. Swartz, L. L. Sutter, and T. J. Van Dam, “Hardened concrete air void analysis with a flatbed scanner,” *Transportation Research Record*, vol. 1775, no. 1, pp. 36–43, 2001.

[54] K. Nefs, A. L. van Overmeir, T. A. Salet, A. S. Suiker, B. Šavija, E. Schlangen, and F. Bos, “Consistency of mechanical properties of 3d printed strain hardening cementitious composites within one printing system,” in *RILEM International Conference on Concrete and Digital Fabrication*, Springer, 2022, pp. 145–151.

[55] T. Pan, Y. Jiang, H. He, Y. Wang, and K. Yin, “Effect of structural build-up on interlayer bond strength of 3d printed cement mortars,” *Materials*, vol. 14, no. 2, p. 236, 2021.

[56] V. Gopalaratnam and S. P. Shah, “Softening response of plain concrete in direct tension,” in *Journal Proceedings*, vol. 82, 1985, pp. 310–323.

[57] E. Cadoni, G. Solomos, and C. Albertini, “Concrete behaviour in direct tension tests at high strain rates,” *Magazine of Concrete Research*, vol. 65, no. 11, pp. 660–672, 2013.

A

Appendix-A

A.1. Designing and Testing a Dynamic Nozzle

This was the first step in exploring the possibilities to extrude a layer which was inspired from the osteomorphic block shape of consisting of variable thickness in a single layer as seen in Figure A.2. It was practically impossible to extrude concrete in such layers with the use of conventional (down-flow) nozzle. Owing to which changes were suggested so as to implement a modified (dynamic) nozzle setup as seen in Figure A.6. The proposed modifications to the nozzle did produce acceptable results as seen in Figure A.7 but were not enough to proceed further in the sense that the specimens required to carry further testing were printable. Hence, looking at the time required for fine tuning the details with the modified nozzle it was decided to explore other options namely trying with the conventional nozzle with base blocks set on the print bed for extruding the proposed layer from the perspective of ease in execution.

Hereon, owing to the dependencies and avoiding laborious 3D printing sessions the research was simplified by proposing the concrete extrusion to be done with conventional (down-flow) nozzle on the base layer (as seen in Figure A.1). The shape of the extruded layer was sinusoidal with a constant thickness. The entire specimen would finally look as the one on right in Figure A.2.

A.1.1. Nozzle Design

At the start of the research, one of the major problem encountered was that of extruding the topology. It was first decided that the base layer would be printed with the Poly-Lactic Acid (PLA) material based 3D printing. After which the concrete would be extruded over the base layer using the 3D concrete printing setup as shown in Figure A.1

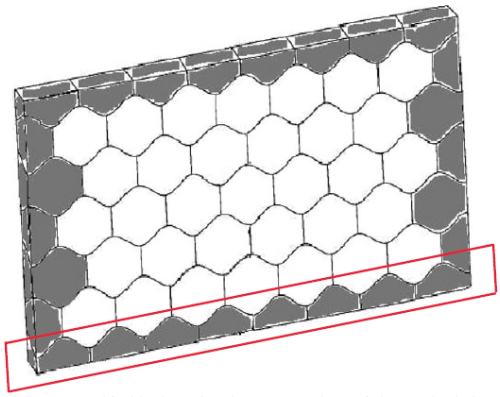

Figure A.1: Printing of base layer with PLA based 3D printing

The concrete was expected to take the shape of the base layer underneath. But as shown in Figure A.2 the layer extrusion as proposed in this research was practically impossible to print with conventional (down-flow) nozzle. Using a conventional (down-flow) nozzle one would have ended up with the specimen as shown in the right of Figure A.2 which has a deviation in interlocking at inter-layers. To avoid this, modifications at the nozzle level were proposed and carried out which would make possible to extrude the specimen as shown in the left of Figure A.2. A nozzle with moving walls was devised which would ensure that shape of the extruded layers would be reminiscent of osteomorphic topology as shown in left of Figure A.2.

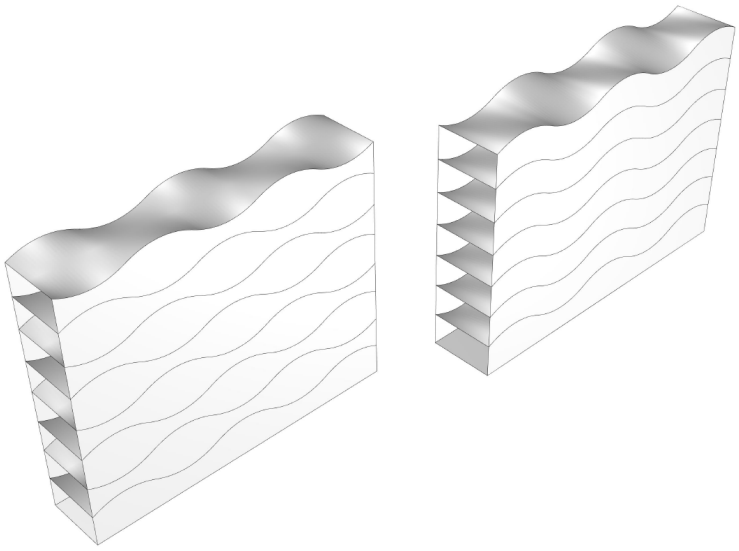

Figure A.2: 3D concrete printing renders (as modelled and visualised in RHINO) (left) the expected topology for research (right) extruded topology with a conventional nozzle nozzle

A.1.2. Conventional Nozzle

The conventional (down-flow) nozzle is as shown in Figure A.3. At present the standard dimensions (with regards to 3D concrete printer available at TU Delft's Stevin Lab) of extruded concrete layer by this nozzle is 40 x 14mm. The geometrical dimensions of the conventional (down-flow) nozzle are as shown in Figure A.4 which was implemented in the research at a later stage to extrude the specimen as shown in the right of Figure A.2.

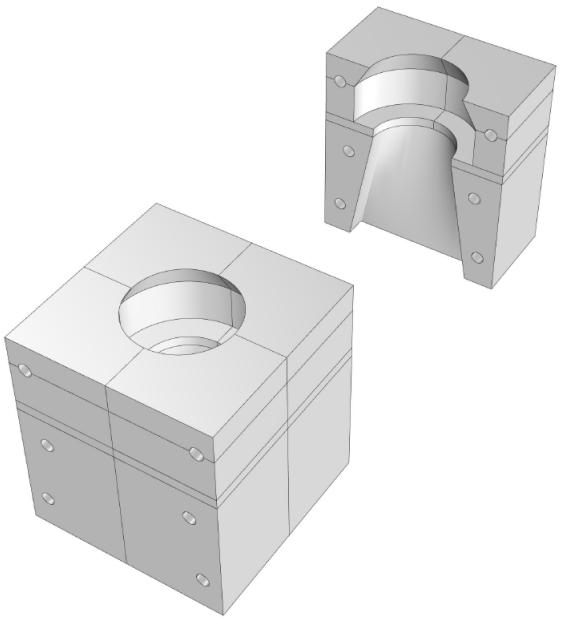

Figure A.3: Conventional (down-flow) Nozzle used for 3D concrete printing renders (as modelled and visualised in RHINO) (Left) Perspective View (Right) Sectional View

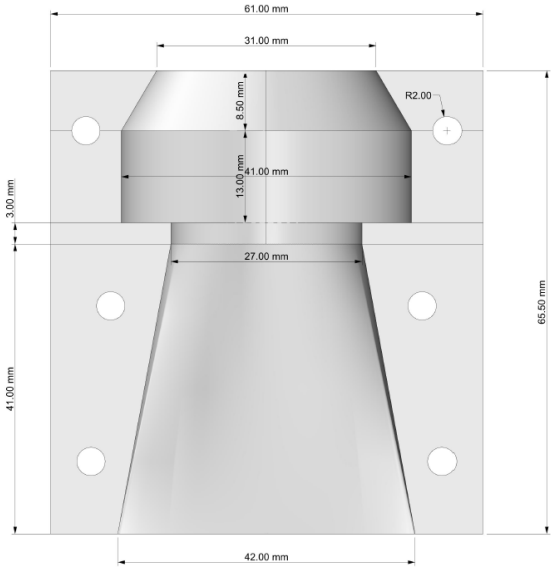

Figure A.4: Conventional Nozzle dimensions used for 3D concrete printing

A.1.3. Modified Nozzle

Due to the limitations of conventional (down-flow) nozzle of not being able to extrude an osteomorphic block shaped layer (as seen in left of the Figure A.2) the modified (down-flow) nozzle was designed which is as shown in the Figure A.5. This nozzle consists of the conventional (down-flow) nozzle (with slightly bigger opening of 40 x 20mm) mounted over a setup consisting of 2 walls (placed symmetrically opposite to each other) and slider-crank arrangement powered by NEMA 17 stepper motors which are controlled by Arduino UNO microchip running on a 12V battery pack.

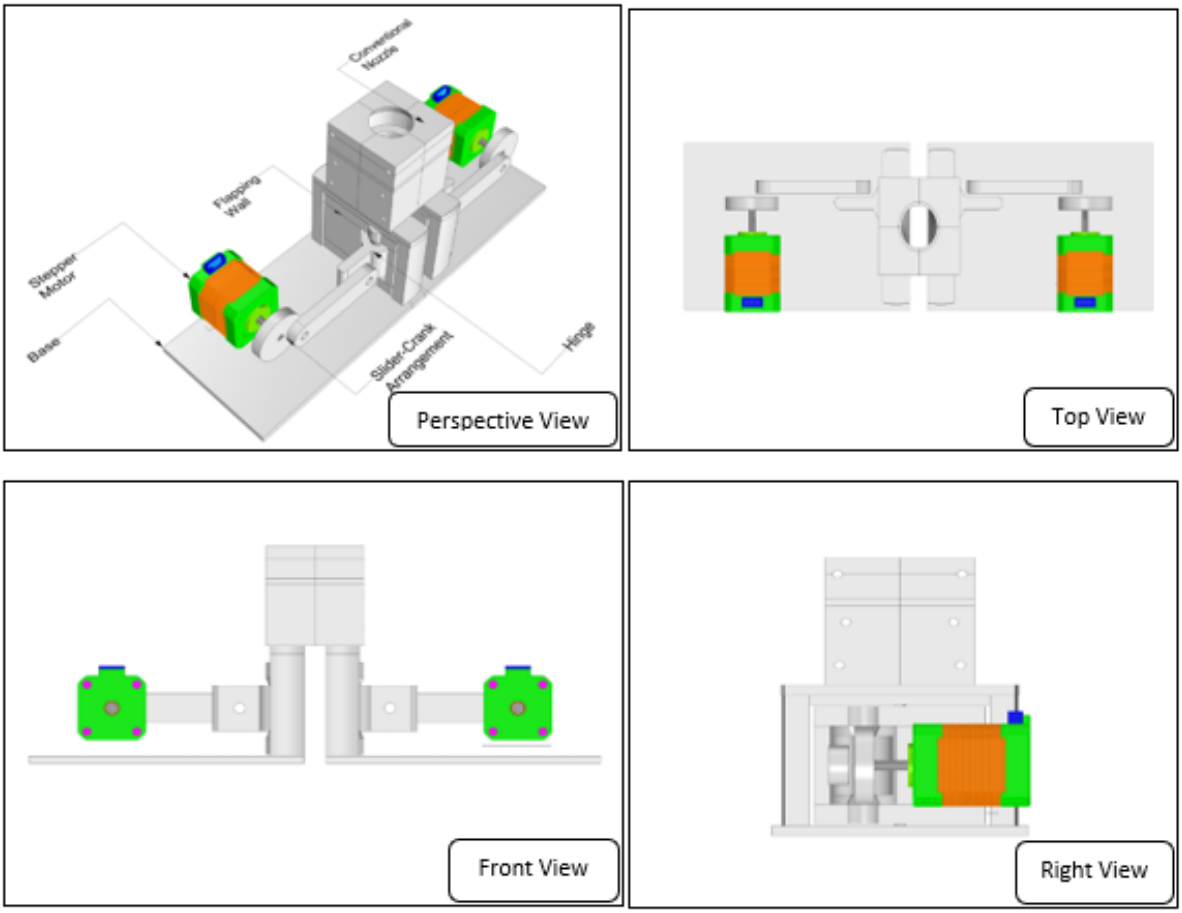

Figure A.5: Modified Nozzle Design with flapping walls used for 3D concrete printing (3D model from RHINO)

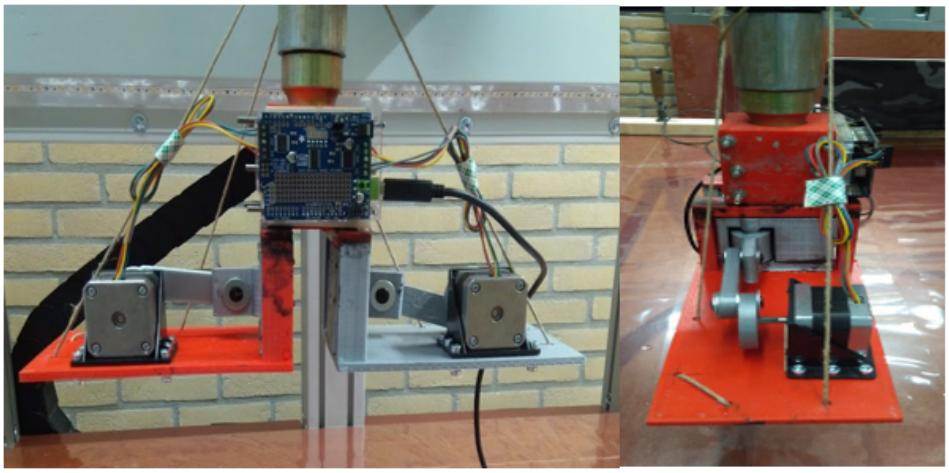

Figure A.6: Modified Nozzle Setup used for extrusion-based 3D concrete printing

The entire nozzle setup for the same can be seen in Figure A.6 The modified (down-flow) nozzle was dynamic in the sense that the walls (operated with crank and slider arrangement) placed underneath the conventional (down-flow) nozzle were able to move on a central pivot point and form a position which could shape the layer being extruded in such a way that resulting extruded layer on the print bed would be similar to that of an osteomorphic block pattern (Figure 2.40).

Figure A.7: Modified Nozzle Specimen printed by using extrusion-based 3D concrete printing (Zoomed in: Resulting osteomorphic block-based shape of extruded layer)

The resulting extruded specimen can be seen in the Figure A.7. The walls were programmed to move in a ±14.26 ° angle about the pivot point with the help of slider-crank arrangement which was operated by stepper motors. The code to run the stepper motors was written in C++ programming language which can be found in the Annex A.1.4 herewith. A specific angle was chosen with an aim to extrude the layer of specific size which was in correlation to the speed of the stepper motor (controlled by the parameters in the code which was uploaded on Arduino UNO microchip). The dynamic action of the nozzle was kept in sync with the G-CODE (Annex A.1.5) of the robot.

A.1.4. Code to be uploaded on Arduino UNO for synchronous run of stepper motors

```
// Shows how to run three Steppers at once with varying speeds

// Requires the Adafruit_Motorshield v2 library
// https://github.com/adafruit/Adafruit_Motor_Shield_V2_Library
// And AccelStepper with AFMotor support
// https://github.com/adafruit/AccelStepper

// This tutorial is for Adafruit Motorshield v2 only!
// Will not work with v1 shields

#include <Wire.h>
#include <AccelStepper.h>
#include <Adafruit_MotorShield.h>

// Adafruit_MotorShield AFMSbot(0x61);
// Rightmost jumper closed Adafruit_MotorShield AFMStop(0x60);
// Default address, no jumpers

// Connect two steppers with 200 steps per revolution (1.8 degree)
// to the top shield
Adafruit_StepperMotor *myStepper1 = AFMStop.getStepper(200, 1);
Adafruit_StepperMotor *myStepper2 = AFMStop.getStepper(200, 2);

// Connect one stepper with 200 steps per revolution (1.8 degree)
// to the bottom shield
// Adafruit_StepperMotor *myStepper3 = AFMSbot.getStepper(200, 2);

// You can change these to DOUBLE or INTERLEAVE or MICROSTEP!
// wrappers for the first motor!
void forwardstep1() {
  myStepper1->onestep(FORWARD, DOUBLE);
}
void backwardstep1() {
  myStepper1->onestep(BACKWARD, DOUBLE);
}

// wrappers for the second motor!
void forwardstep2() {
  myStepper2->onestep(FORWARD, DOUBLE);
}
void backwardstep2() {
  myStepper2->onestep(BACKWARD, DOUBLE);
}

// wrappers for the third motor!
// void forwardstep3() {
//   myStepper3->onestep(FORWARD, INTERLEAVE);
// }
// void backwardstep3() {
//   myStepper3->onestep(BACKWARD, INTERLEAVE);
// }

// Now we'll wrap the 3 steppers in an AccelStepper object
```

```
AccelStepper stepper1(forwardstep1, backwardstep1);
AccelStepper stepper2(forwardstep2, backwardstep2);
// AccelStepper stepper3(forwardstep3, backwardstep3);

void setup()
{
  // AFMSbot.begin(); // Start the bottom shield
  AFMStop.begin(); // Start the top shield

  stepper1.setMaxSpeed(200.0);
  stepper1.setAcceleration(100.0);
  stepper1.moveTo(50000);

  stepper2.setMaxSpeed(200.0);
  stepper2.setAcceleration(100.0);
  stepper2.moveTo(50000);

  // stepper3.setMaxSpeed(300.0);
  // stepper3.setAcceleration(100.0);
  // stepper3.moveTo(1000000);
}
void loop()
{
   //  Change direction at the limits
   //  if (stepper1.distanceToGo() == 0)
   //  stepper1.moveTo(-stepper1.currentPosition());

   //  if (stepper2.distanceToGo() == 0)
   // stepper2.moveTo(-stepper2.currentPosition());

  //    if (stepper3.distanceToGo() == 0)
  // stepper3.moveTo(-stepper3.currentPosition());

    stepper1.run();
    stepper2.run();
 // stepper3.run();
}
```

A.1.5. G-Code for Modified Nozzle based Printing

```
G-Code for Modified Nozzle based Printing
//Feed Rate
//F[#101] = 2400

F[#101] G1 X-20  Y40
F[#101] G1 Z25
F[#101] G1 X-980 Y40
F[#101] G1 X-980 Y140
F[#101] G1 X-20  Y140
G4 P20
```

B

Appendix-B

B.1. Detailed analysis of Bond test results

B.1.1. Caulk-gun Specimens

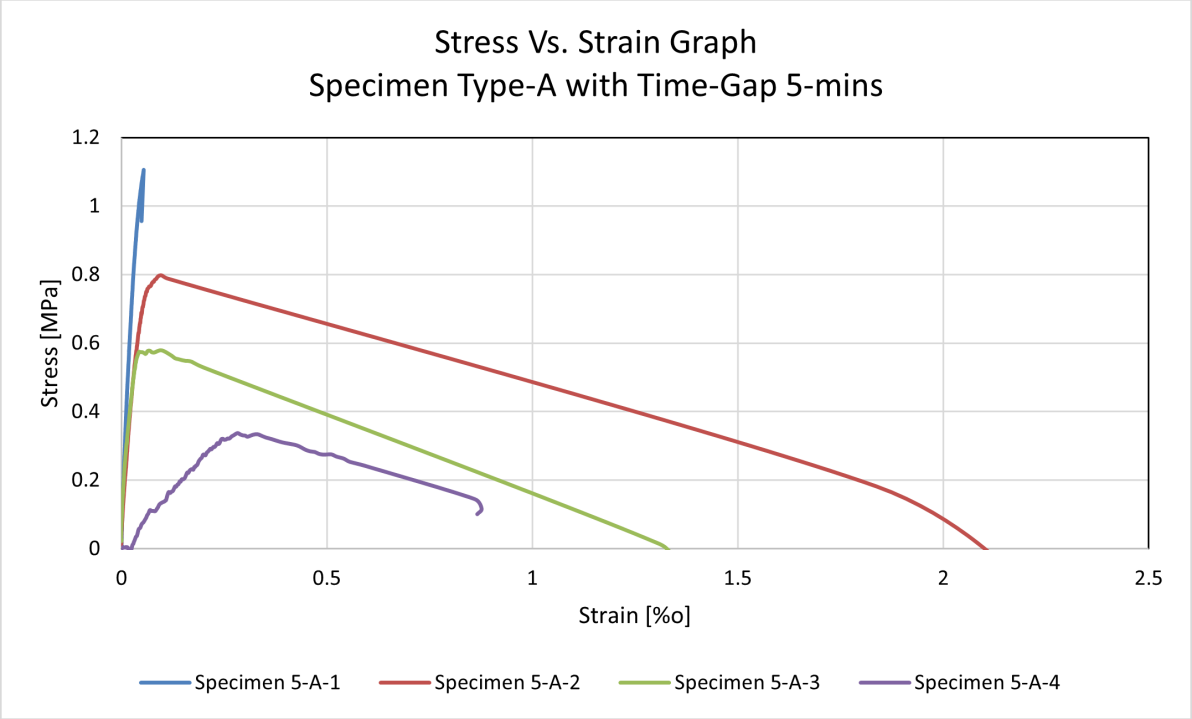

Figure B.1: Stress vs. Strain curve for Specimen TG5-A

Specimen TG5-A-1

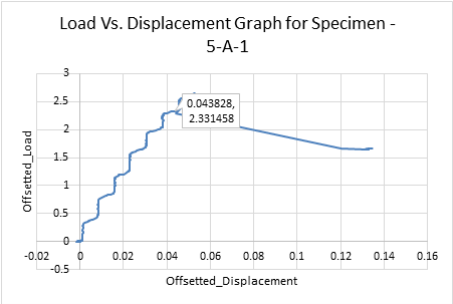

Figure B.2: Overall Load Vs. Displacement curve for Specimen TG5-A-1

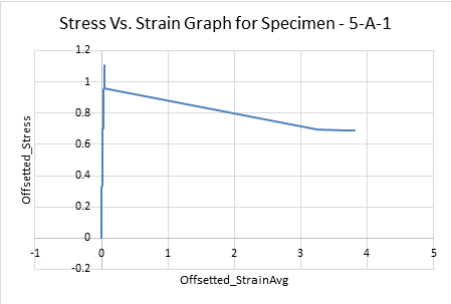

Figure B.3: Overall Stress Vs. Strain Graph for Specimen TG5-A-1

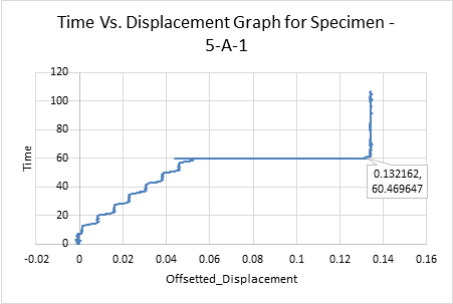

Figure B.4: Overall Time Vs. Displacement graph for Specimen TG5-A-1

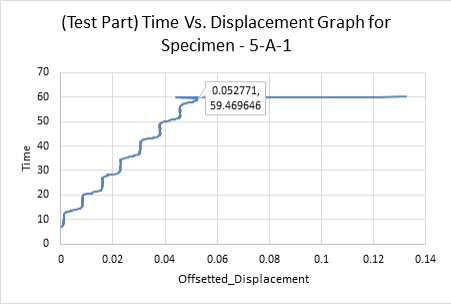

Figure B.5: First sampling Time Vs. Displacement graph for Specimen TG5-A-1

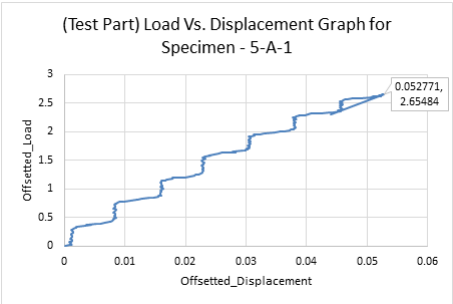

Figure B.6: Sampling Load Vs. Displacement graph for Specimen TG5-A-1

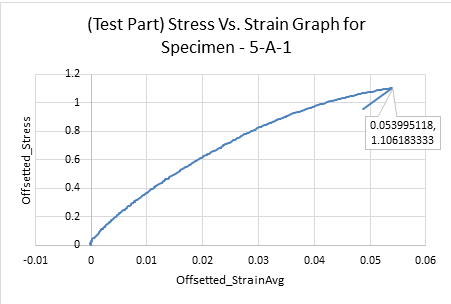

Figure B.7: Stress Vs. Strain Graph for the sampled data for the Specimen TG5-A-1

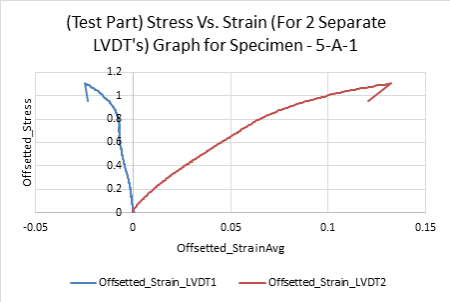

Figure B.8: Comparison graph of Stress Vs. Strain for 2 LVDT's for Specimen TG5-A-1

Specimen TG5-A-2

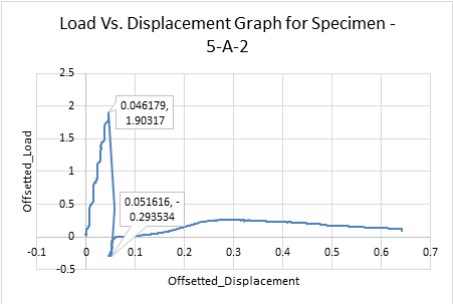

Figure B.9: Overall Load Vs. Displacement curve for Specimen TG5-A-2

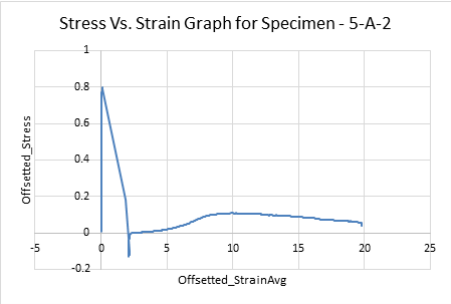

Figure B.10: Overall Stress Vs. Strain Graph for Specimen TG5-A-2

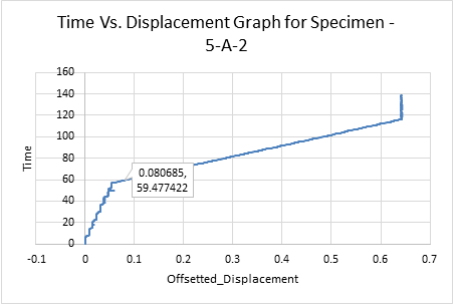

Figure B.11: Overall Time Vs. Displacement graph for Specimen TG5-A-2

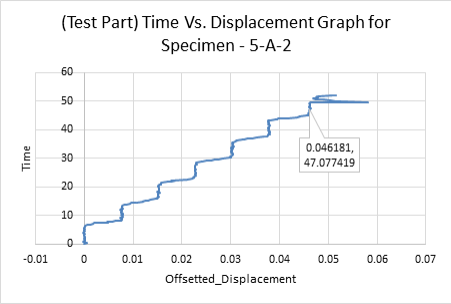

Figure B.12: First sampling Time Vs. Displacement graph for Specimen TG5-A-2

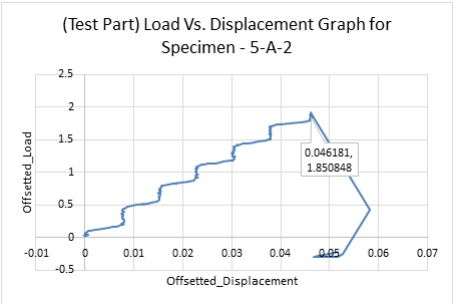

Figure B.13: Sampled Load Vs. Displacement graph for Specimen TG5-A-2

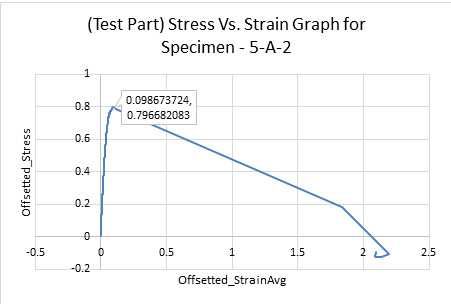

Figure B.14: Stress Vs. Strain Graph for the (third) sampled data for the Specimen TG5-A-2

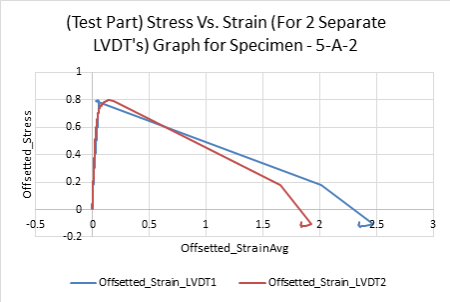

Figure B.15: Comparison graph of Stress Vs. Strain for 2 LVDT's for Specimen TG5-A-2

Specimen TG5-A-3

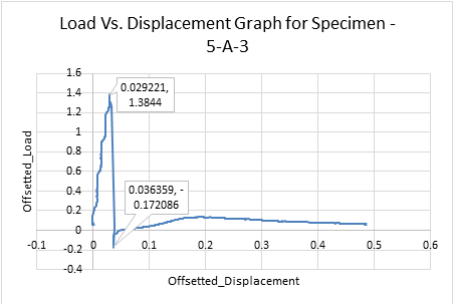

Figure B.16: Overall Load Vs. Displacement curve for Specimen TG5-A-3

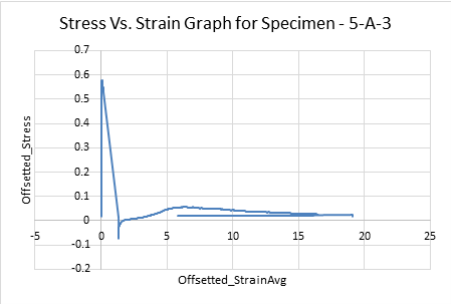

Figure B.17: Overall Stress Vs. Strain Graph for Specimen TG5-A-3

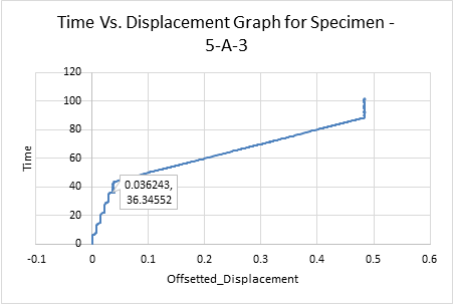

Figure B.18: Overall Time Vs. Displacement graph for Specimen TG5-A-3

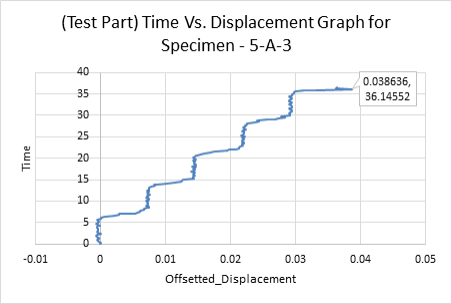

Figure B.19: First sampling Time Vs. Displacement graph for Specimen TG5-A-3

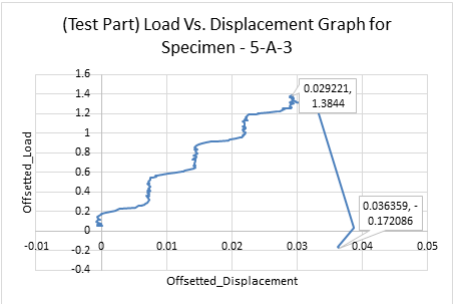

Figure B.20: Sampled Load Vs. Displacement graph for Specimen TG5-A-3

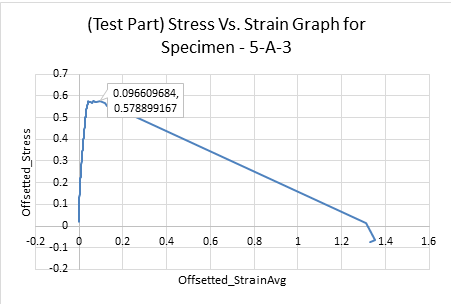

Figure B.21: Stress Vs. Strain Graph for the (third) sampled data for the Specimen TG5-A-3

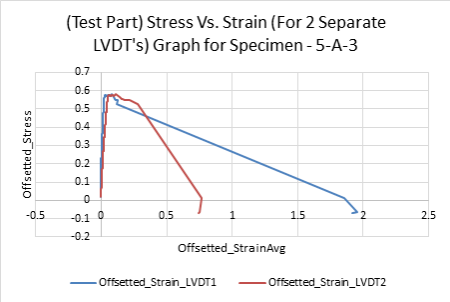

Figure B.22: Comparison graph of Stress Vs. Strain for 2 LVDT's for Specimen TG5-A-3

Specimen TG5-A-4

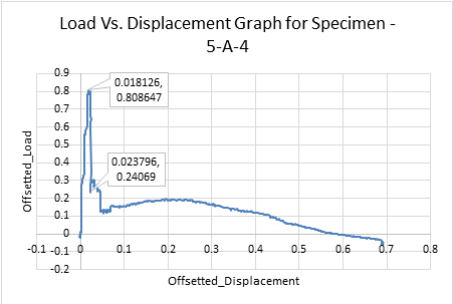

Figure B.23: Overall Load Vs. Displacement curve for Specimen TG5-A-4

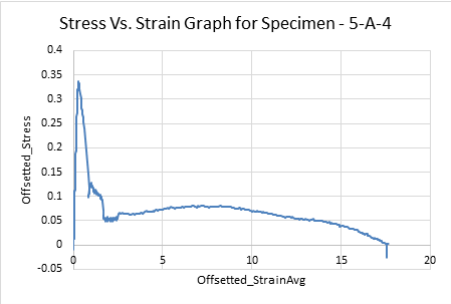

Figure B.24: Overall Stress Vs. Strain Graph for Specimen TG5-A-4

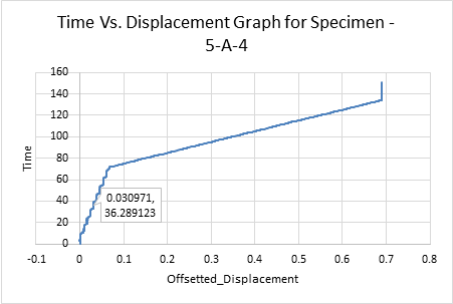

Figure B.25: Overall Time Vs. Displacement graph for Specimen TG5-A-4

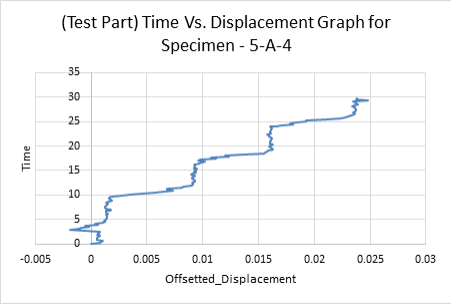

Figure B.26: First sampling Time Vs. Displacement graph for Specimen TG5-A-4

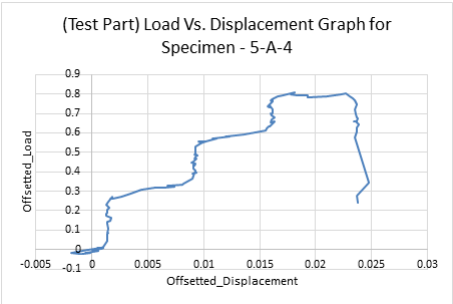

Figure B.27: Sampled Load Vs. Displacement graph for Specimen TG5-A-4

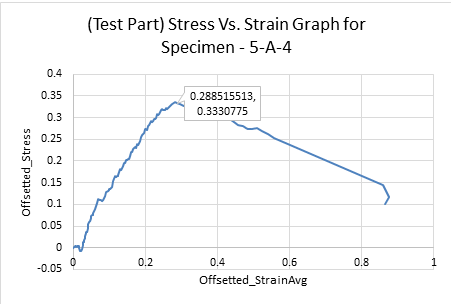

Figure B.28: Stress Vs. Strain Graph for the (third) sampled data for the Specimen TG5-A-4

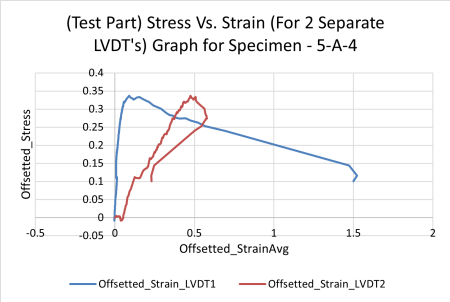

Figure B.29: Comparison graph of Stress Vs. Strain for 2 LVDT's for Specimen TG5-A-4

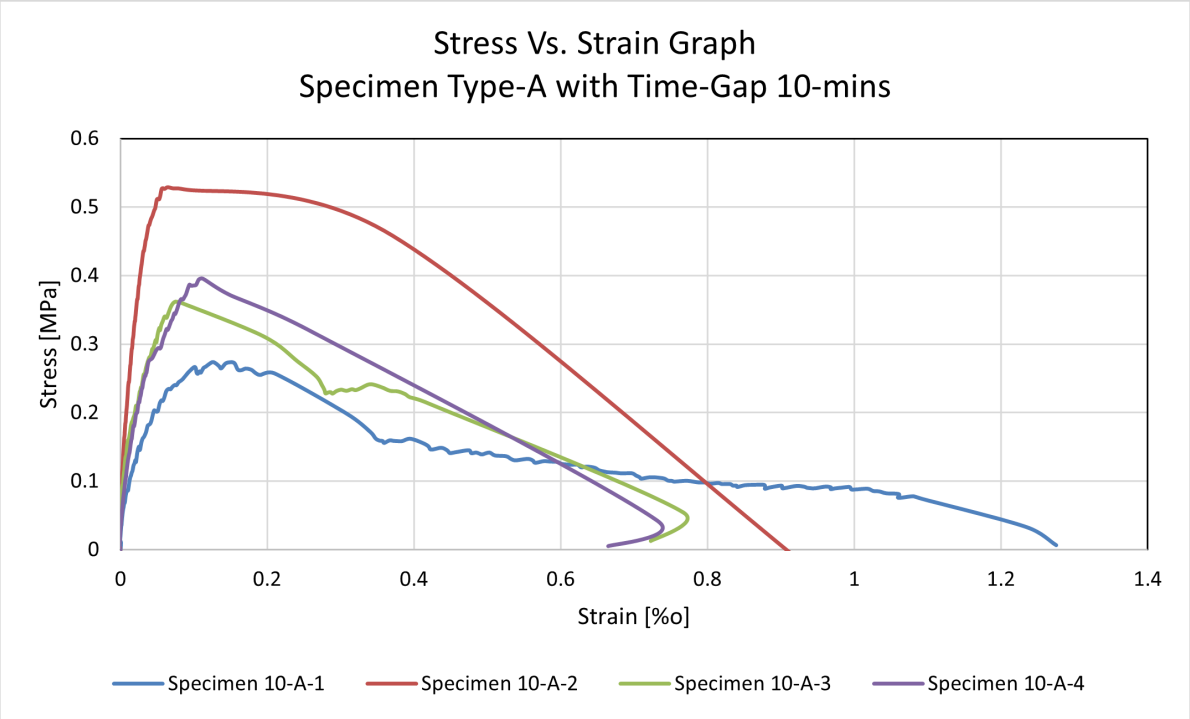

Figure B.30: Stress vs. Strain curve for Specimen TG10-A

Specimen TG10-A-1

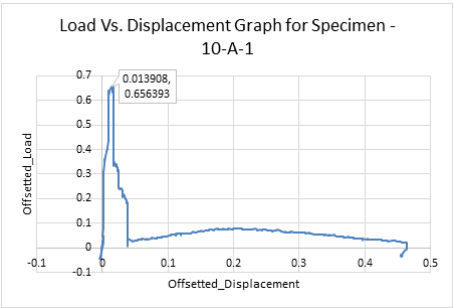

Figure B.31: Overall Load Vs. Displacement curve for Specimen TG10-A-1

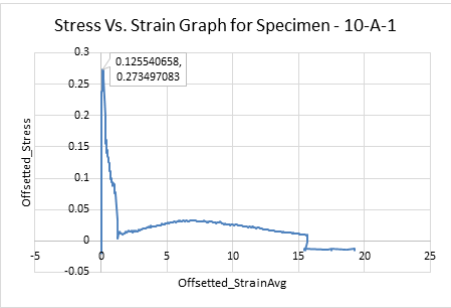

Figure B.32: Overall Stress Vs. Strain Graph for Specimen TG10-A-1

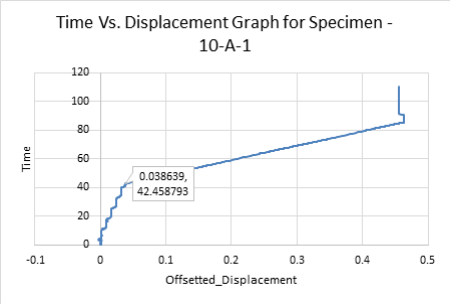

Figure B.33: Overall Time Vs. Displacement graph for Specimen TG10-A-1

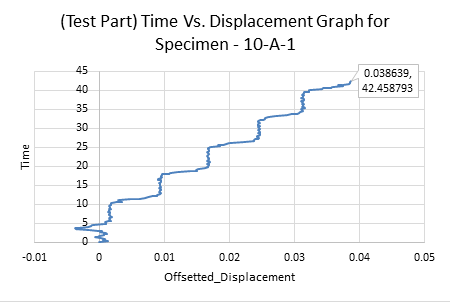

Figure B.34: First sampling Time Vs. Displacement graph for Specimen TG10-A-1

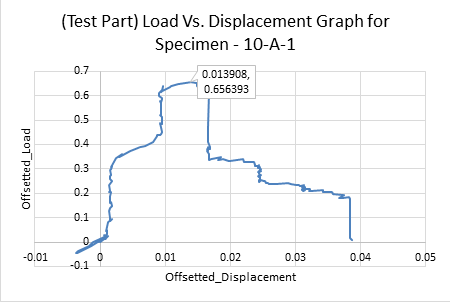

Figure B.35: Sampled Load Vs. Displacement graph for Specimen TG10-A-1

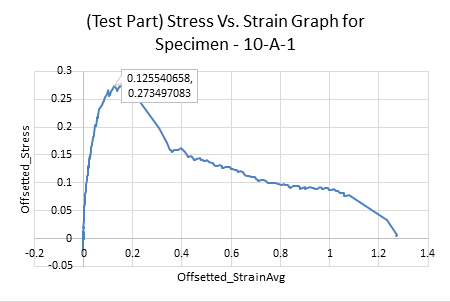

Figure B.36: Stress Vs. Strain Graph for the (third) sampled data for the Specimen TG10-A-1

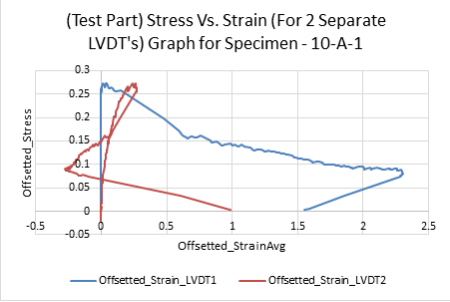

Figure B.37: Comparison graph of Stress Vs. Strain for 2 LVDT's for Specimen TG10-A-1

Specimen TG10-A-2

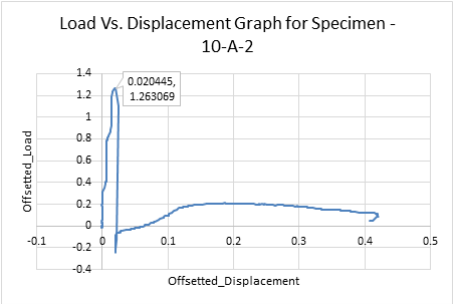

Figure B.38: Overall Load Vs. Displacement curve for Specimen TG10-A-2

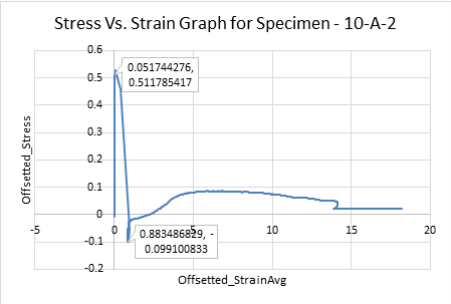

Figure B.39: Overall Stress Vs. Strain Graph for Specimen TG10-A-2

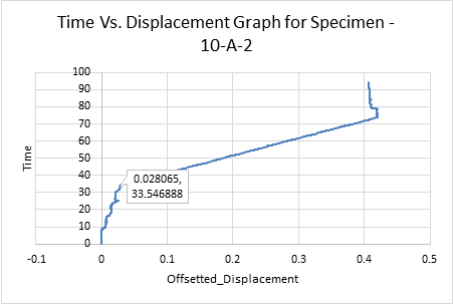

Figure B.40: Overall Time Vs. Displacement graph for Specimen TG10-A-2

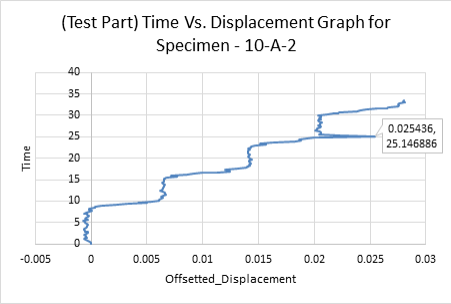

Figure B.41: First sampling Time Vs. Displacement graph for Specimen TG10-A-2

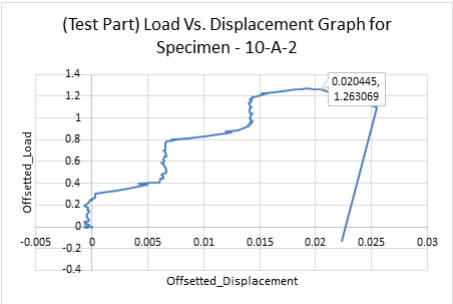

Figure B.42: Sampled Load Vs. Displacement graph for Specimen TG10-A-2

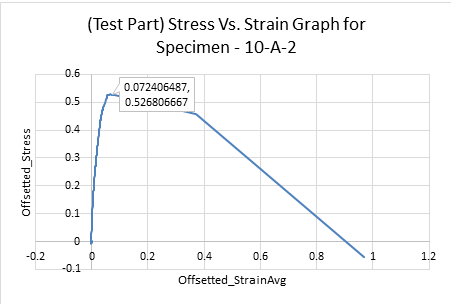

Figure B.43: Stress Vs. Strain Graph for the (third) sampled data for the Specimen TG10-A-2

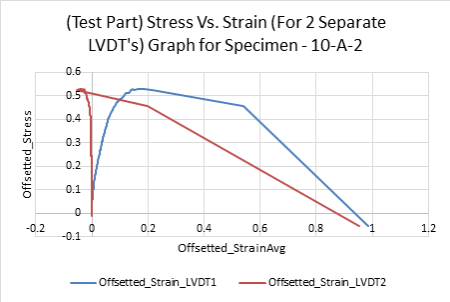

Figure B.44: Comparison graph of Stress Vs. Strain for 2 LVDT's for Specimen TG10-A-2

Specimen TG10-A-3

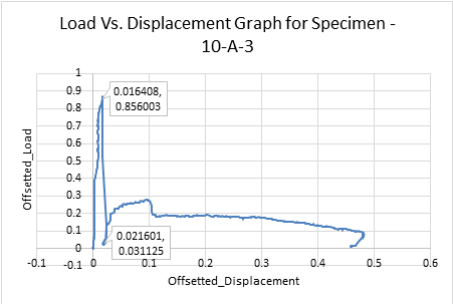

Figure B.45: Overall Load Vs. Displacement curve for Specimen TG10-A-3

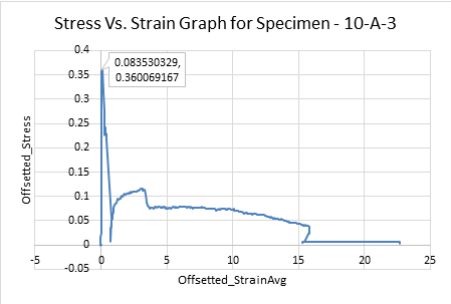

Figure B.46: Overall Stress Vs. Strain Graph for Specimen TG10-A-3

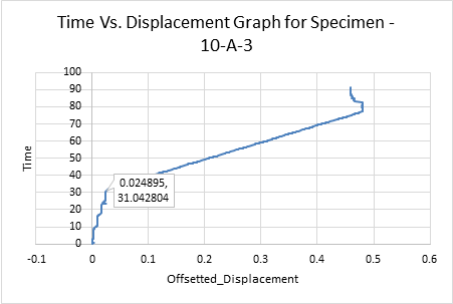

Figure B.47: Overall Time Vs. Displacement graph for Specimen TG10-A-3

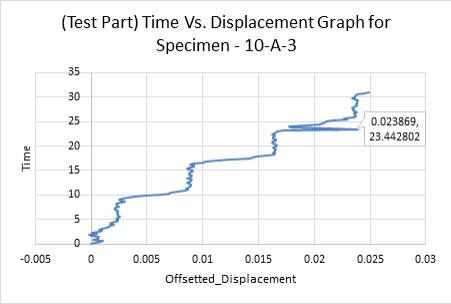

Figure B.48: First sampling Time Vs. Displacement graph for Specimen TG10-A-3

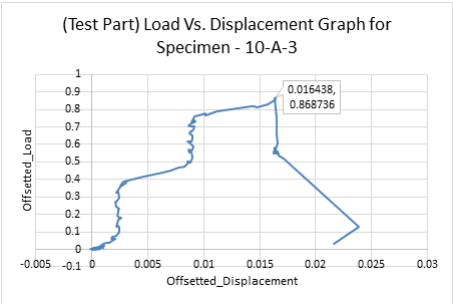

Figure B.49: Sampled Load Vs. Displacement graph for Specimen TG10-A-3

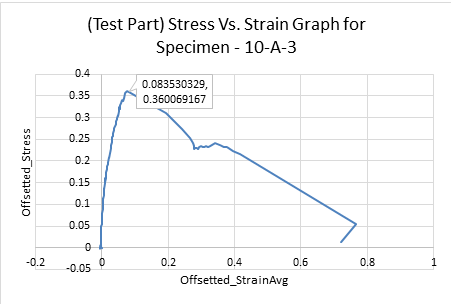

Figure B.50: Stress Vs. Strain Graph for the (third) sampled data for the Specimen TG10-A-3

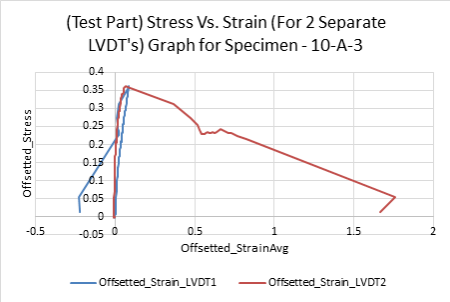

Figure B.51: Comparison graph of Stress Vs. Strain for 2 LVDT's for Specimen TG10-A-3

Specimen TG10-A-4

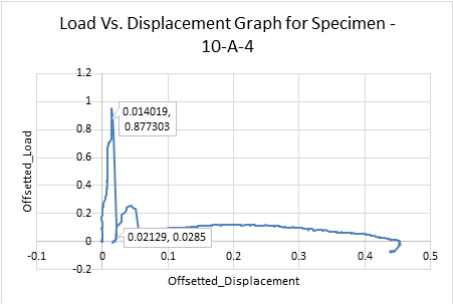

Figure B.52: Overall Load Vs. Displacement curve for Specimen TG10-A-4

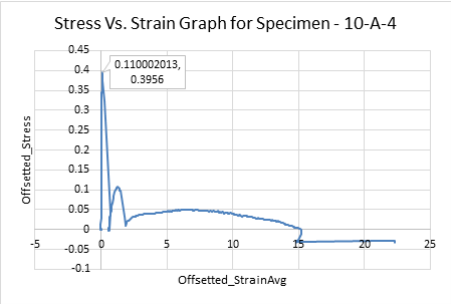

Figure B.53: Overall Stress Vs. Strain Graph for Specimen TG10-A-4

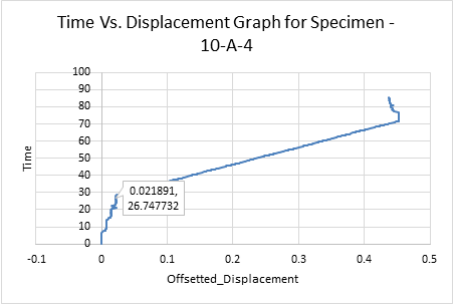

Figure B.54: Overall Time Vs. Displacement graph for Specimen TG10-A-4

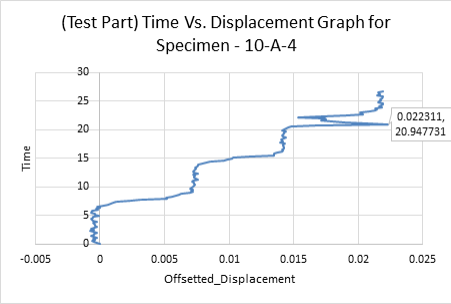

Figure B.55: First sampling Time Vs. Displacement graph for Specimen TG10-A-4

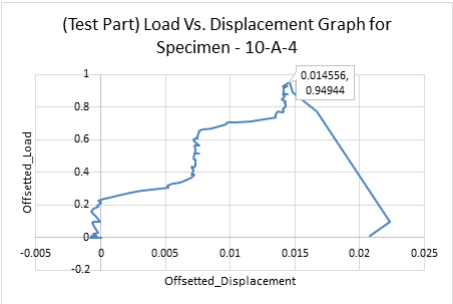

Figure B.56: Sampled Load Vs. Displacement graph for Specimen TG10-A-4

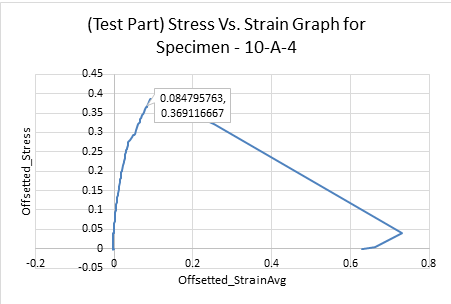

Figure B.57: Stress Vs. Strain Graph for the (third) sampled data for the Specimen TG10-A-4

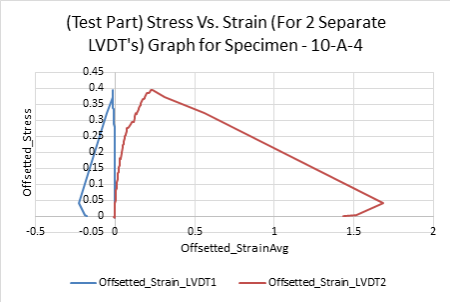

Figure B.58: Comparison graph of Stress Vs. Strain for 2 LVDT's for Specimen TG10-A-4

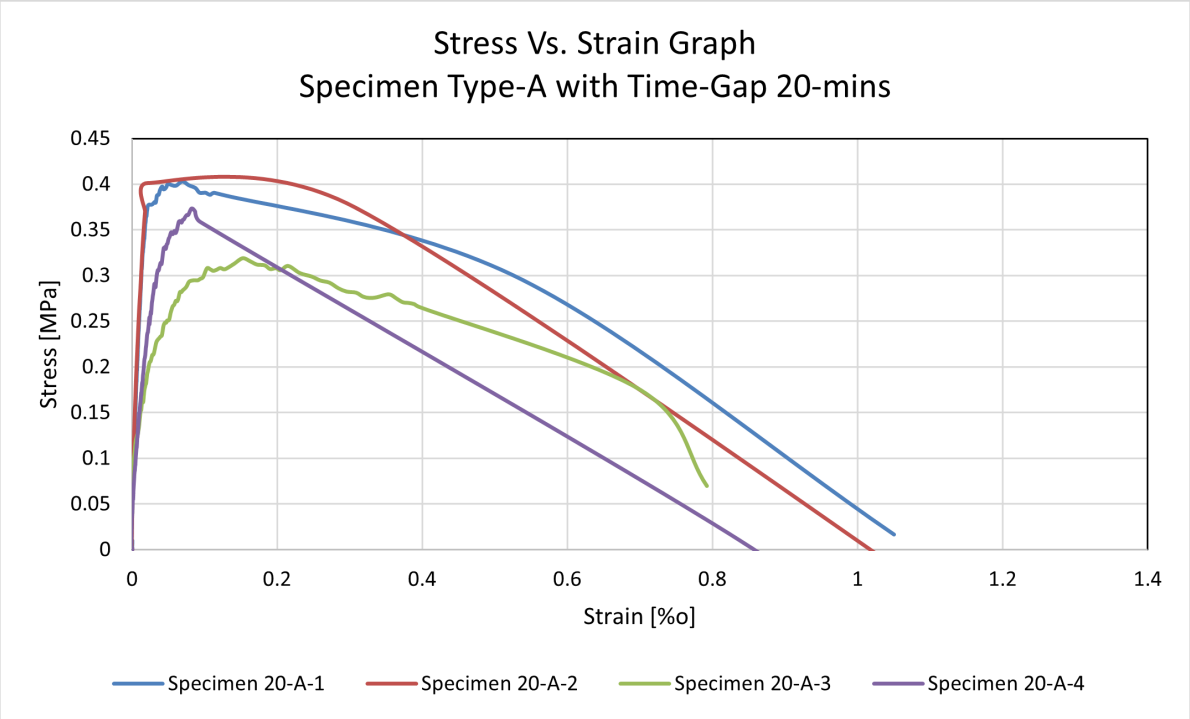

Figure B.59: Stress vs. Strain curve for Specimen TG20-A

Specimen TG20-A-1

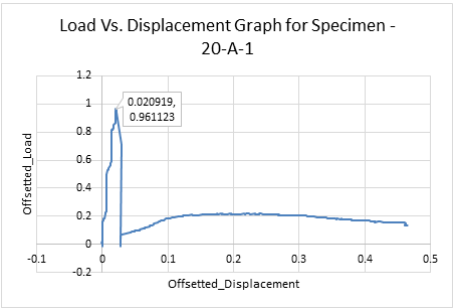

Figure B.60: Overall Load Vs. Displacement curve for Specimen TG20-A-1

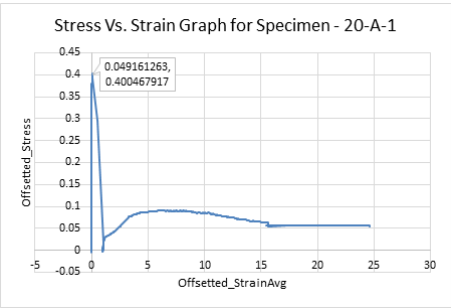

Figure B.61: Overall Stress Vs. Strain Graph for Specimen TG20-A-1

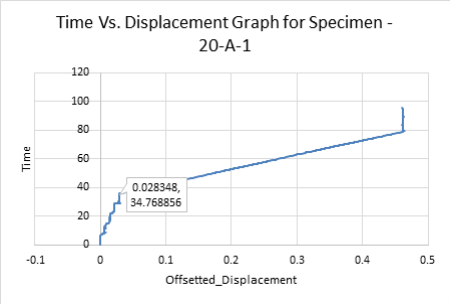

Figure B.62: Overall Time Vs. Displacement graph for Specimen TG20-A-1

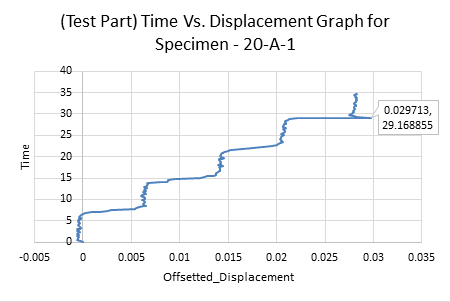

Figure B.63: First sampling Time Vs. Displacement graph for Specimen TG20-A-1

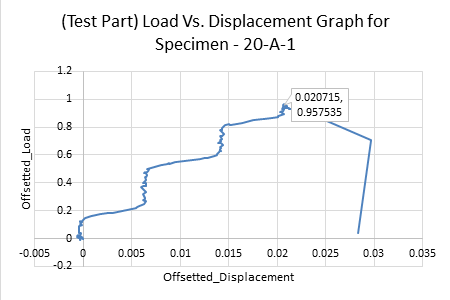

Figure B.64: Sampled Load Vs. Displacement graph for Specimen TG20-A-1

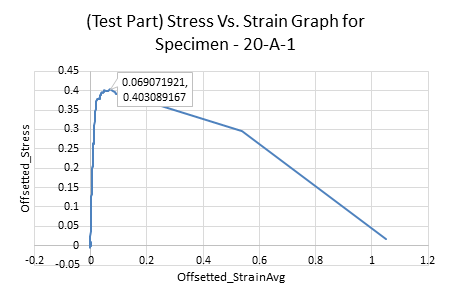

Figure B.65: Stress Vs. Strain Graph for the (third) sampled data for the Specimen TG20-A-1

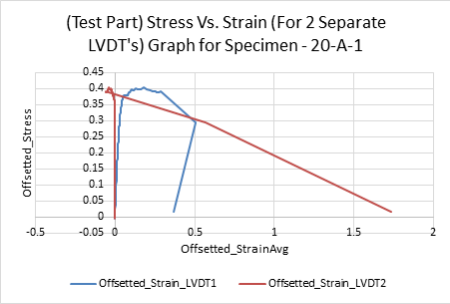

Figure B.66: Comparison graph of Stress Vs. Strain for 2 LVDT's for Specimen TG20-A-1

Specimen TG20-A-2

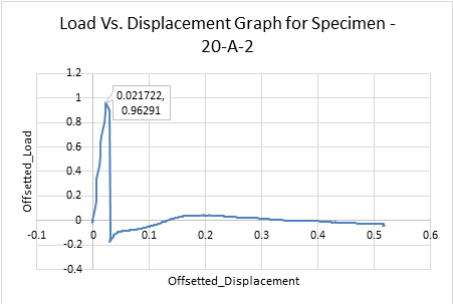

Figure B.67: Overall Load Vs. Displacement curve for Specimen TG20-A-2

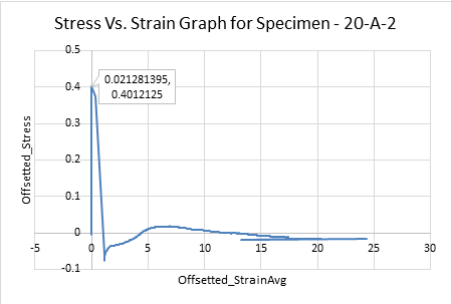

Figure B.68: Overall Stress Vs. Strain Graph for Specimen TG20-A-2

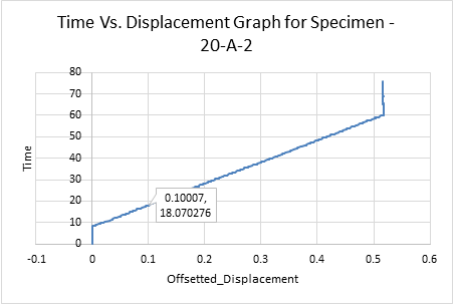

Figure B.69: Overall Time Vs. Displacement graph for Specimen TG20-A-2

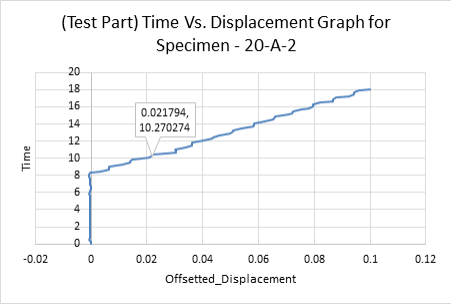

Figure B.70: First sampling Time Vs. Displacement graph for Specimen TG20-A-2

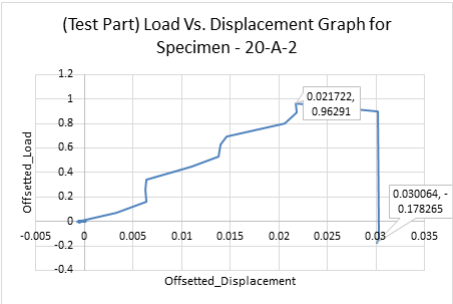

Figure B.71: Sampled Load Vs. Displacement graph for Specimen TG20-A-2

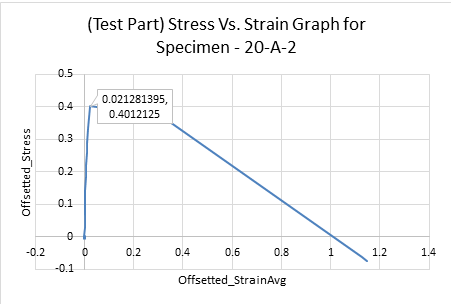

Figure B.72: Stress Vs. Strain Graph for the (third) sampled data for the Specimen TG20-A-2

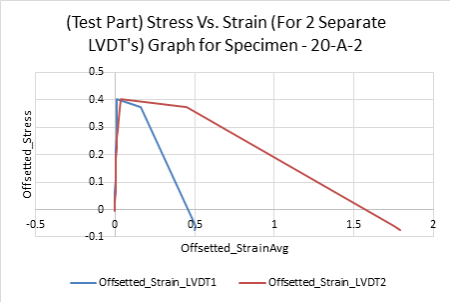

Figure B.73: Comparison graph of Stress Vs. Strain for 2 LVDT's for Specimen TG20-A-2

Specimen TG20-A-3

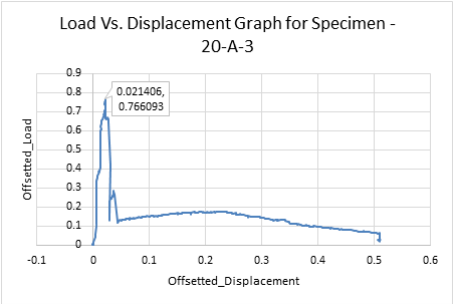

Figure B.74: Overall Load Vs. Displacement curve for Specimen TG20-A-3

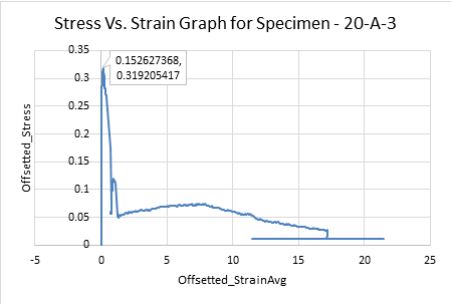

Figure B.75: Overall Stress Vs. Strain Graph for Specimen TG20-A-3

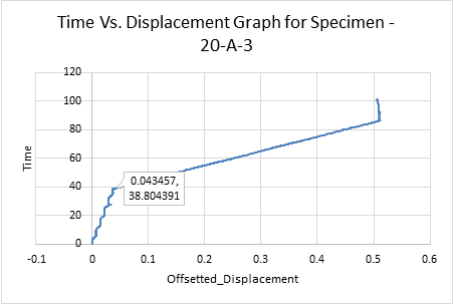

Figure B.76: Overall Time Vs. Displacement graph for Specimen TG20-A-3

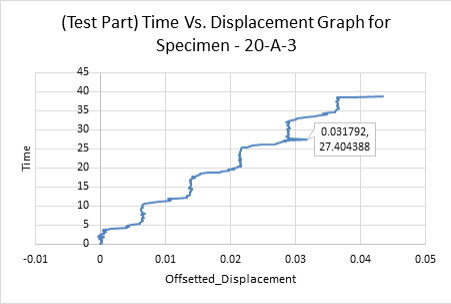

Figure B.77: First sampling Time Vs. Displacement graph for Specimen TG20-A-3

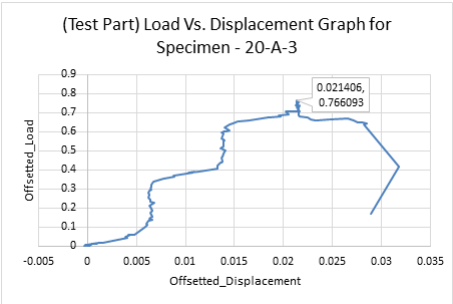

Figure B.78: Sampled Load Vs. Displacement graph for Specimen TG20-A-3

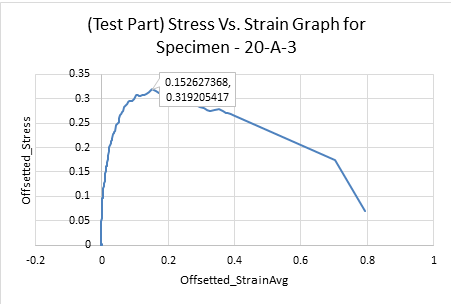

Figure B.79: Stress Vs. Strain Graph for the (third) sampled data for the Specimen TG20-A-3

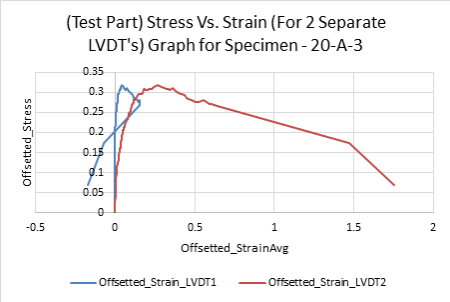

Figure B.80: Comparison graph of Stress Vs. Strain for 2 LVDT's for Specimen TG20-A-3

Specimen TG20-A-4

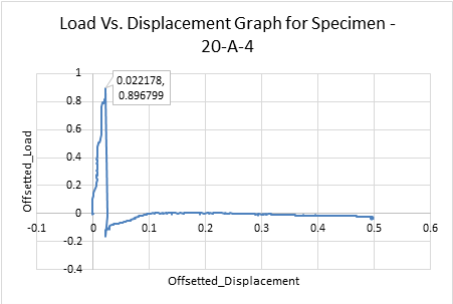

Figure B.81: Overall Load Vs. Displacement curve for Specimen TG20-A-4

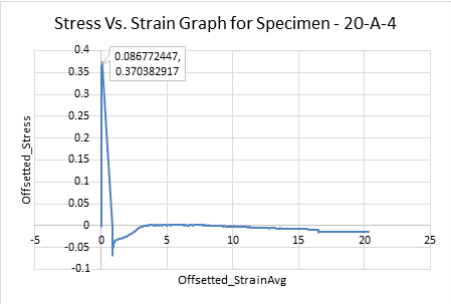

Figure B.82: Overall Stress Vs. Strain Graph for Specimen TG20-A-4

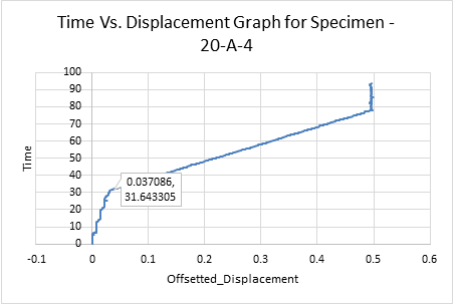

Figure B.83: Overall Time Vs. Displacement graph for Specimen TG20-A-4

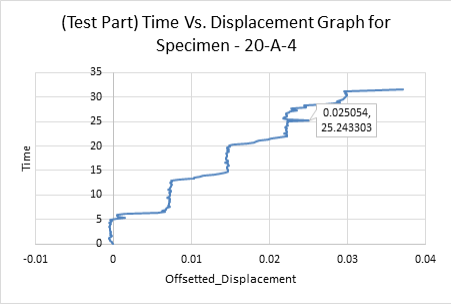

Figure B.84: First sampling Time Vs. Displacement graph for Specimen TG20-A-4

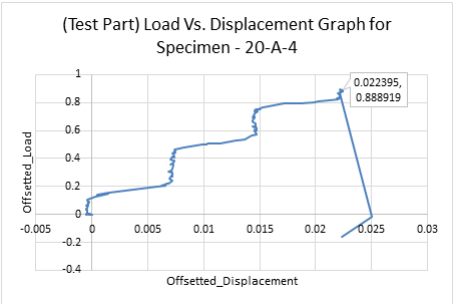

Figure B.85: Sampled Load Vs. Displacement graph for Specimen TG20-A-4

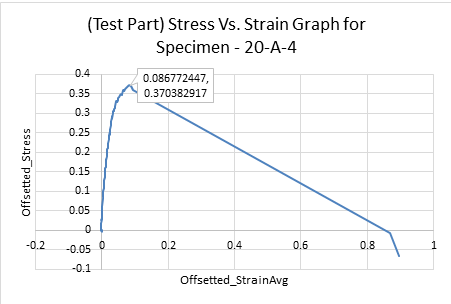

Figure B.86: Stress Vs. Strain Graph for the (third) sampled data for the Specimen TG20-A-4

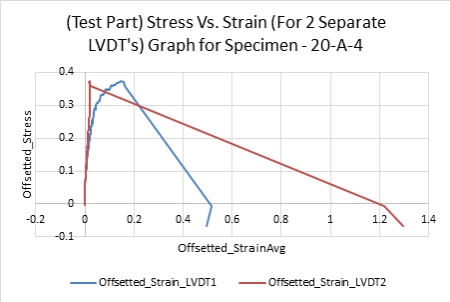

Figure B.87: Comparison graph of Stress Vs. Strain for 2 LVDT's for Specimen TG20-A-4

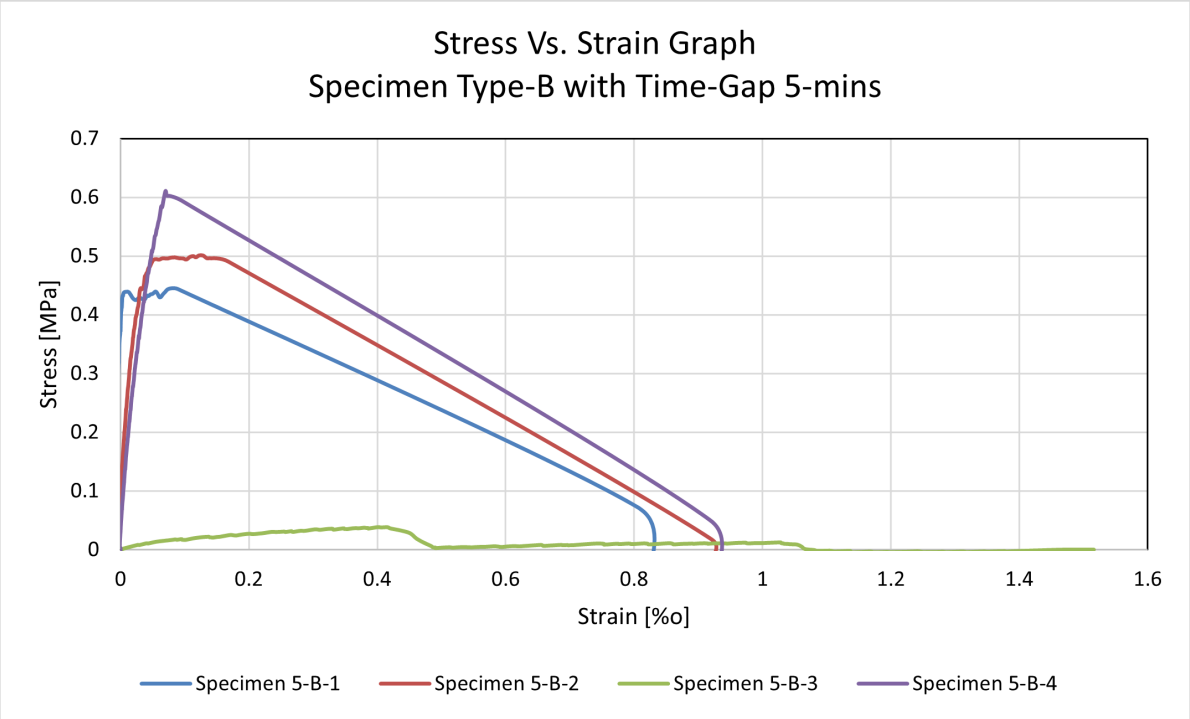

Figure B.88: Stress vs. Strain curve for Specimen TG5-B

Specimen TG5-B-1

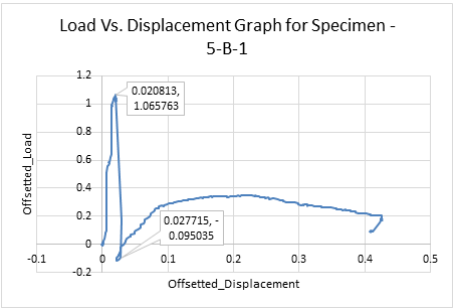

Figure B.89: Overall Load Vs. Displacement curve for Specimen TG5-B-1

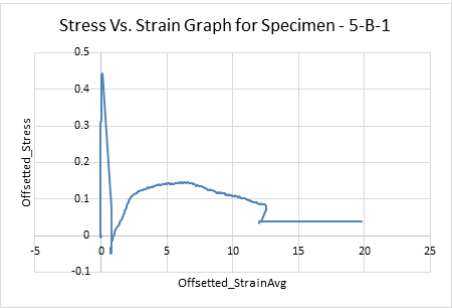

Figure B.90: Overall Stress Vs. Strain Graph for Specimen TG5-B-1

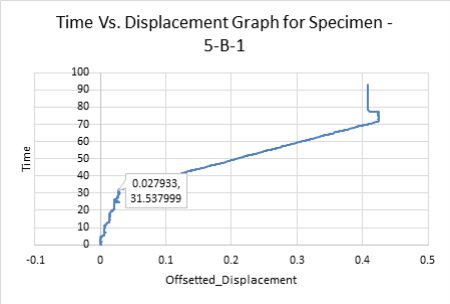

Figure B.91: Overall Time Vs. Displacement graph for Specimen TG5-B-1

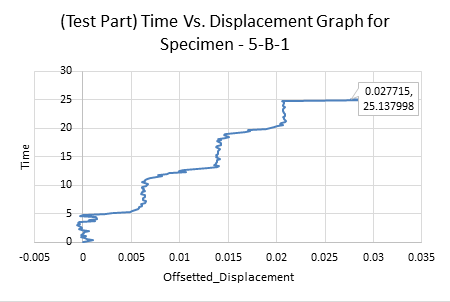

Figure B.92: First sampling Time Vs. Displacement graph for Specimen TG5-B-1

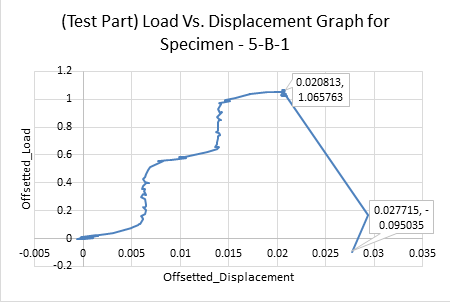

Figure B.93: Sampled Load Vs. Displacement graph for Specimen TG5-B-1

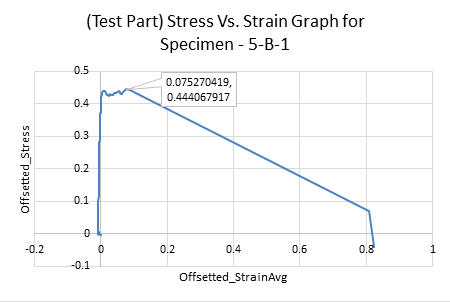

Figure B.94: Stress Vs. Strain Graph for the (third) sampled data for the Specimen TG5-B-1

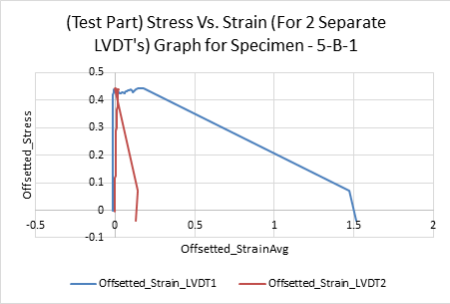

Figure B.95: Comparison graph of Stress Vs. Strain for 2 LVDT's for Specimen TG5-B-1

Specimen TG5-B-2

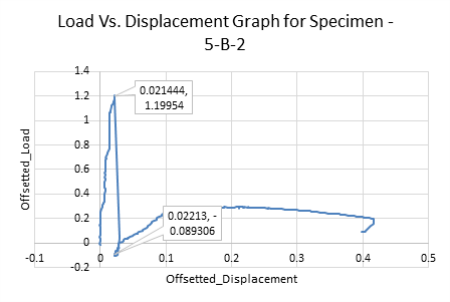

Figure B.96: Overall Load Vs. Displacement curve for Specimen TG5-B-2

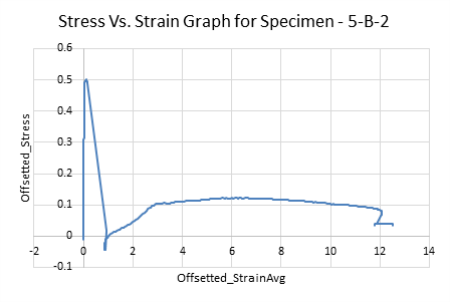

Figure B.97: Overall Stress Vs. Strain Graph for Specimen TG5-B-2

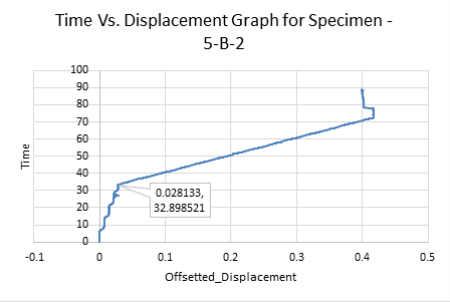

Figure B.98: Overall Time Vs. Displacement graph for Specimen TG5-B-2

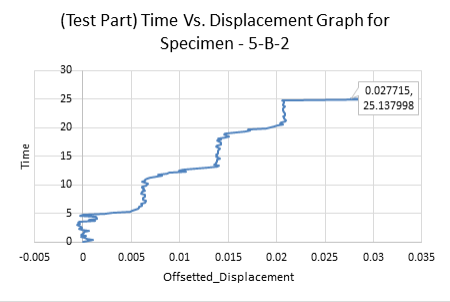

Figure B.99: First sampling Time Vs. Displacement graph for Specimen TG5-B-2

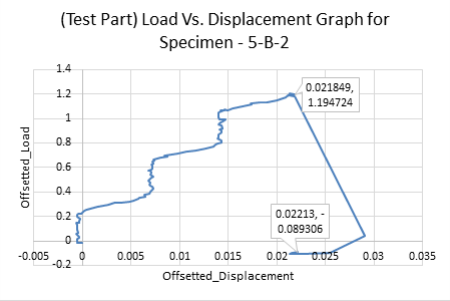

Figure B.100: Sampled Load Vs. Displacement graph for Specimen TG5-B-2

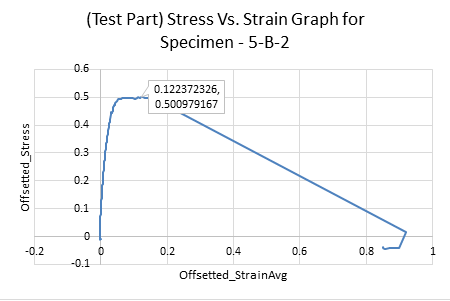

Figure B.101: Stress Vs. Strain Graph for the (third) sampled data for the Specimen TG5-B-2

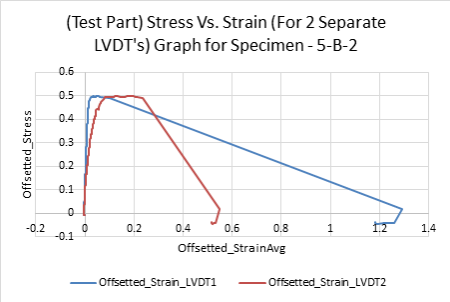

Figure B.102: Comparison graph of Stress Vs. Strain for 2 LVDT's for Specimen TG5-B-2

Specimen TG5-B-3

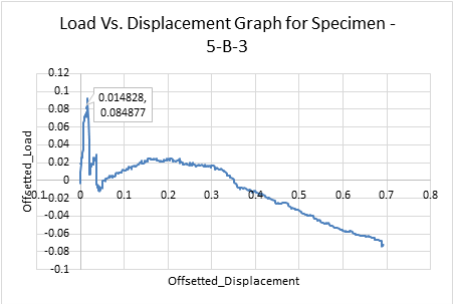

Figure B.103: Overall Load Vs. Displacement curve for Specimen TG5-B-3

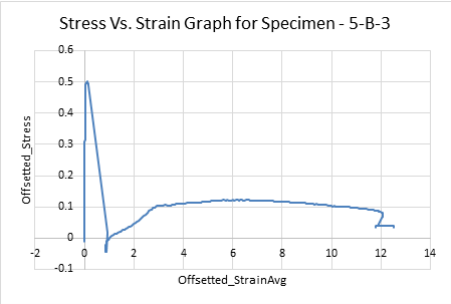

Figure B.104: Overall Stress Vs. Strain Graph for Specimen TG5-B-3

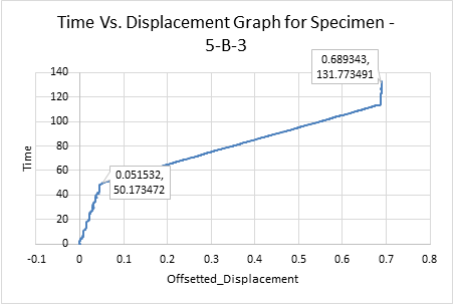

Figure B.105: Overall Time Vs. Displacement graph for Specimen TG5-B-3

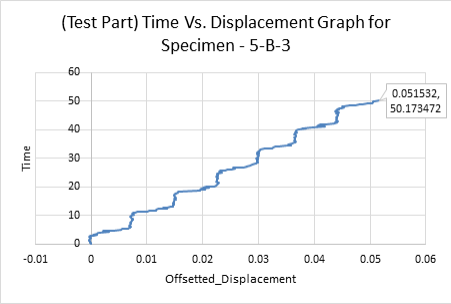

Figure B.106: First sampling Time Vs. Displacement graph for Specimen TG5-B-3

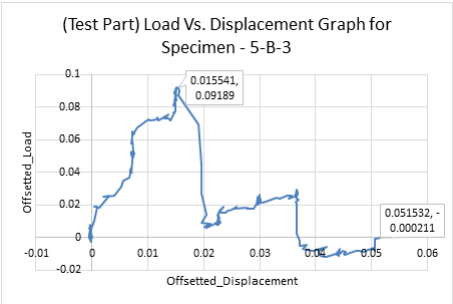

Figure B.107: Sampled Load Vs. Displacement graph for Specimen TG5-B-3

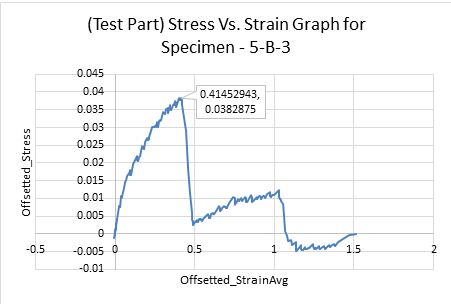

Figure B.108: Stress Vs. Strain Graph for the (third) sampled data for the Specimen TG5-B-3

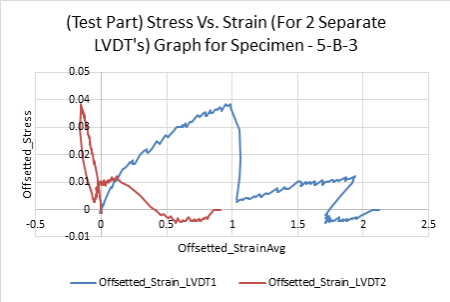

Figure B.109: Comparison graph of Stress Vs. Strain for 2 LVDT's for Specimen TG5-B-3

Specimen TG5-B-4

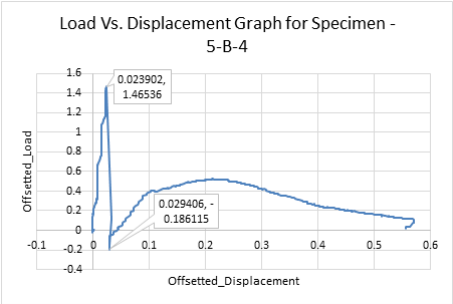

Figure B.110: Overall Load Vs. Displacement curve for Specimen TG5-B-4

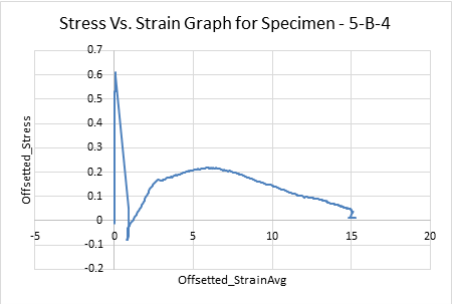

Figure B.111: Overall Stress Vs. Strain Graph for Specimen TG5-B-4

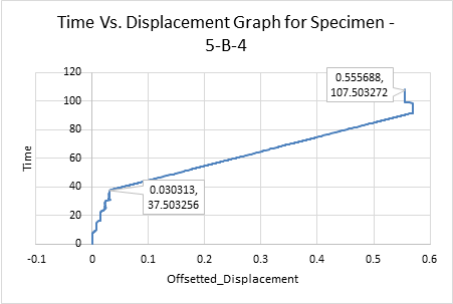

Figure B.112: Overall Time Vs. Displacement graph for Specimen TG5-B-4

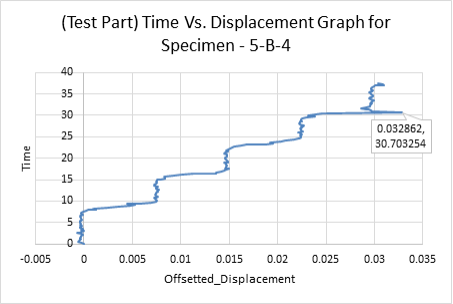

Figure B.113: First sampling Time Vs. Displacement graph for Specimen TG5-B-4

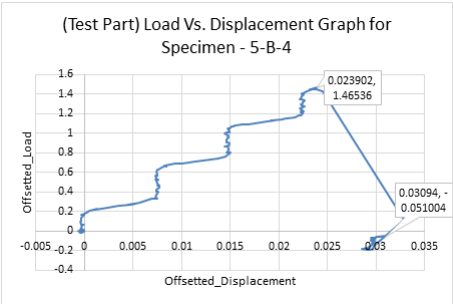

Figure B.114: Sampled Load Vs. Displacement graph for Specimen TG5-B-4

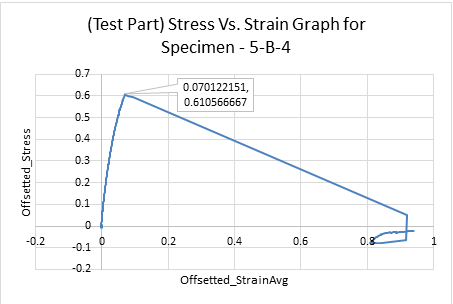

Figure B.115: Stress Vs. Strain Graph for the (third) sampled data for the Specimen TG5-B-4

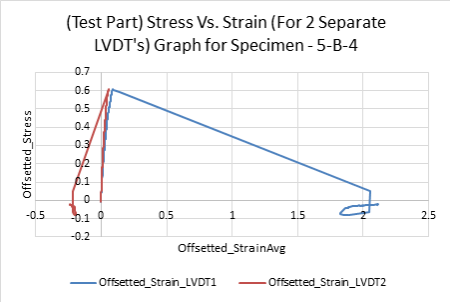

Figure B.116: Comparison graph of Stress Vs. Strain for 2 LVDT's for Specimen TG5-B-4

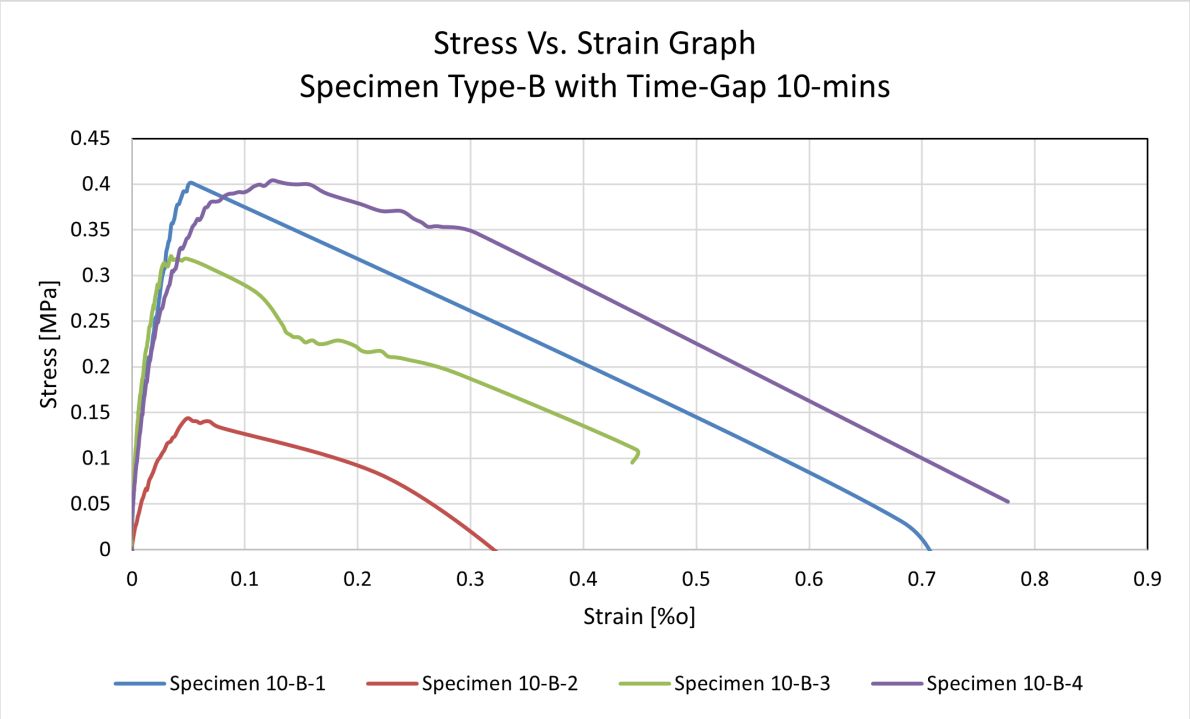

Figure B.117: Stress vs. Strain curve for Specimen TG10-B

Specimen TG10-B-1

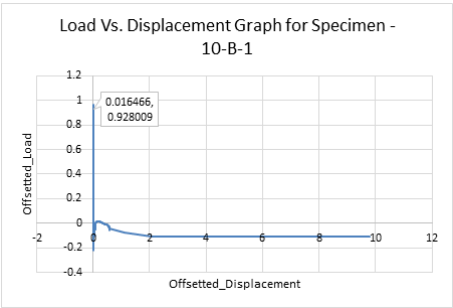

Figure B.118: Overall Load Vs. Displacement curve for Specimen TG10-B-1

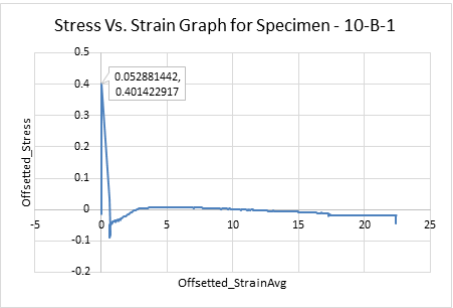

Figure B.119: Overall Stress Vs. Strain Graph for Specimen TG10-B-1

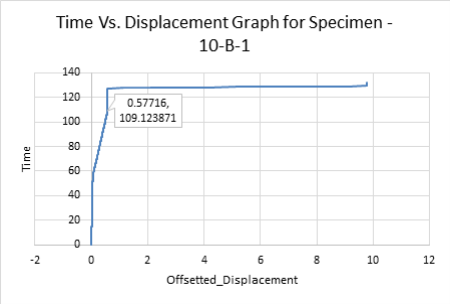

Figure B.120: Overall Time Vs. Displacement graph for Specimen TG10-B-1

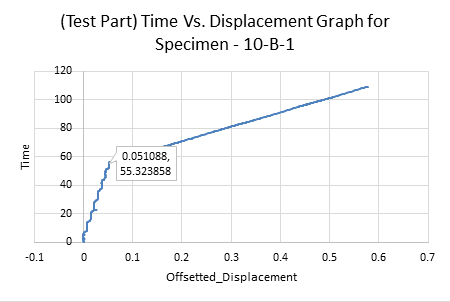

Figure B.121: First sampling Time Vs. Displacement graph for Specimen TG10-B-1

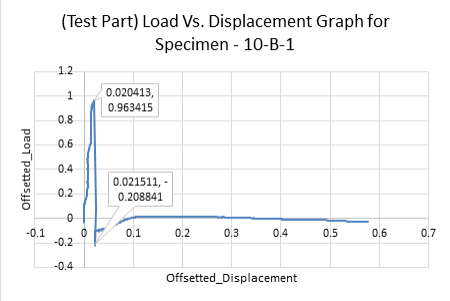

Figure B.122: Sampled Load Vs. Displacement graph for Specimen TG10-B-1

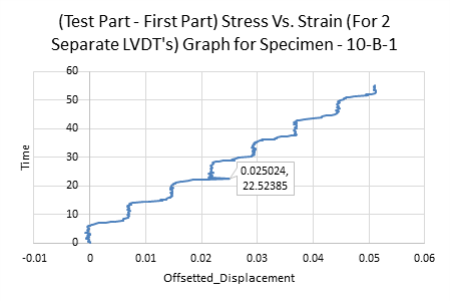

Figure B.123: Stress Vs. Strain Graph for the sampled data for the Specimen TG10-B-1

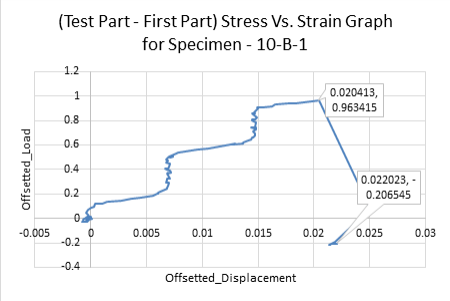

Figure B.124: Sampled Load Vs. Displacement graph for Specimen TG10-B-1

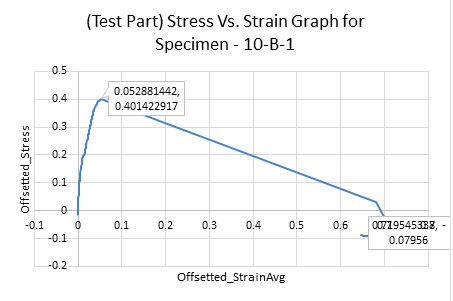

Figure B.125: Stress Vs. Strain Graph for the (second) sampled data for the Specimen TG10-B-1

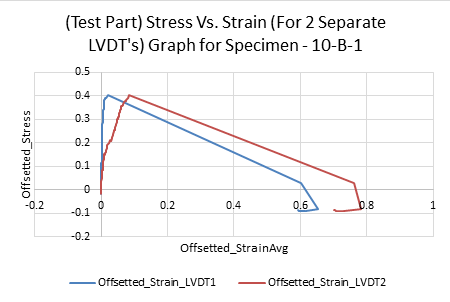

Figure B.126: Comparison graph of Stress Vs. Strain for 2 LVDT's for Specimen TG10-B-1

Specimen TG10-B-2

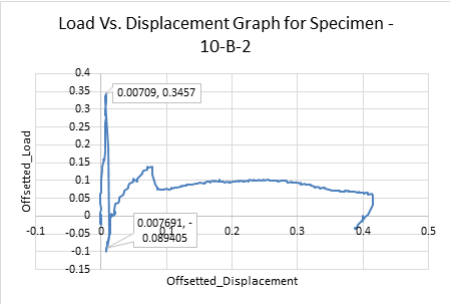

Figure B.127: Overall Load Vs. Displacement curve for Specimen TG10-B-2

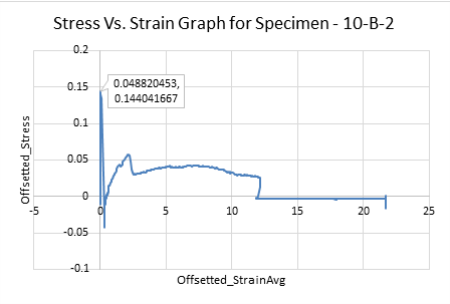

Figure B.128: Overall Stress Vs. Strain Graph for Specimen TG10-B-2

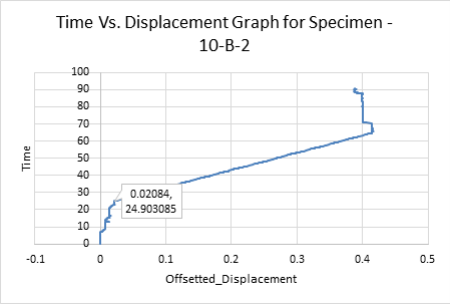

Figure B.129: Overall Time Vs. Displacement graph for Specimen TG10-B-2

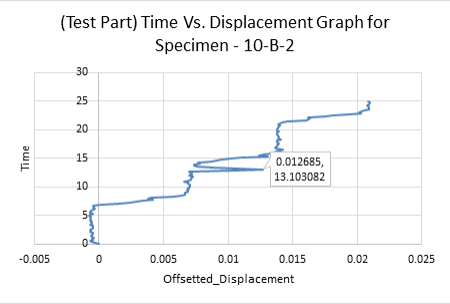

Figure B.130: First sampling Time Vs. Displacement graph for Specimen TG10-B-2

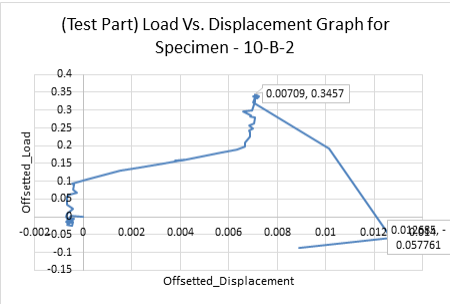

Figure B.131: Sampled Load Vs. Displacement graph for Specimen TG10-B-2

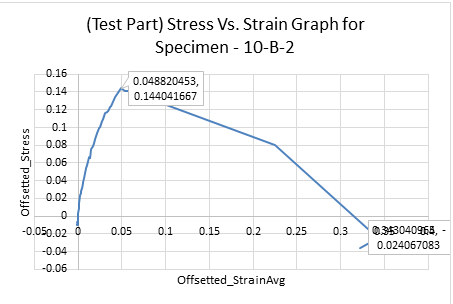

Figure B.132: Stress Vs. Strain Graph for the sampled data for Specimen TG10-B-2

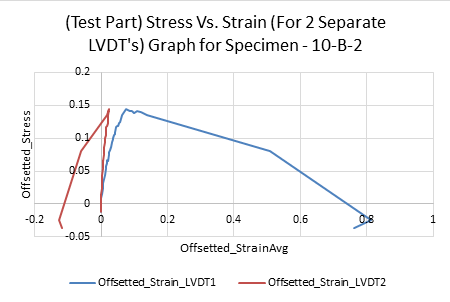

Figure B.133: Comparison graph of Stress Vs. Strain for 2 LVDT's for Specimen TG10-B-2

Specimen TG10-B-3

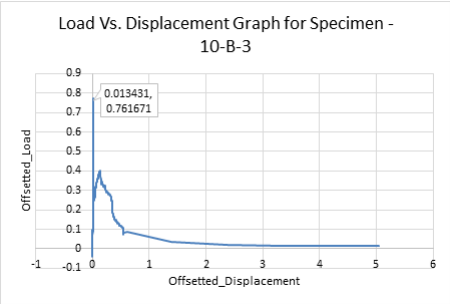

Figure B.134: Overall Load Vs. Displacement curve for Specimen TG10-B-3

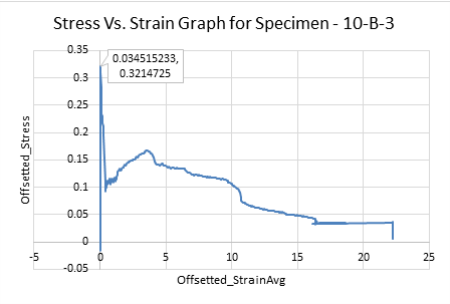

Figure B.135: Overall Stress Vs. Strain Graph for Specimen TG10-B-3

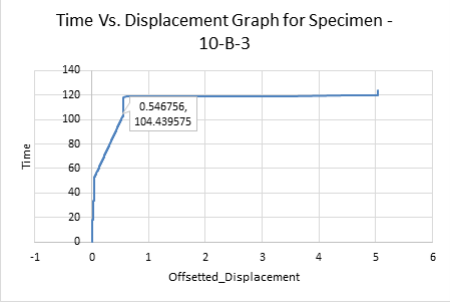

Figure B.136: Overall Time Vs. Displacement graph for Specimen TG10-B-3

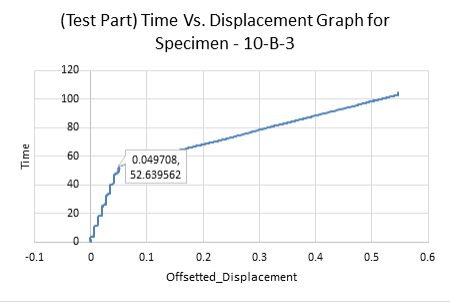

Figure B.137: First sampling Time Vs. Displacement graph for Specimen TG10-B-3

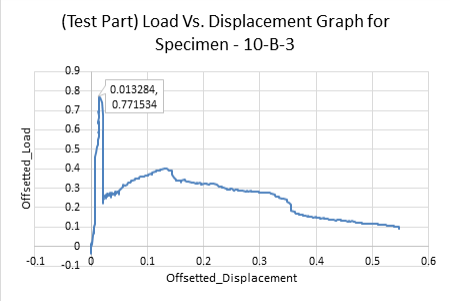

Figure B.138: Sampled Load Vs. Displacement graph for Specimen TG10-B-3

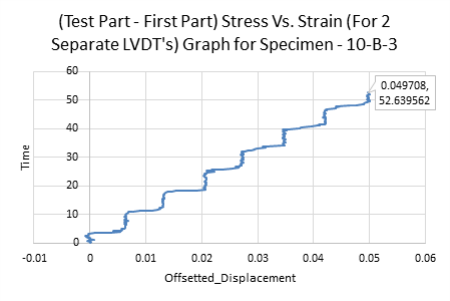

Figure B.139: Stress Vs. Strain Graph for the sampled data for the Specimen TG10-B-3

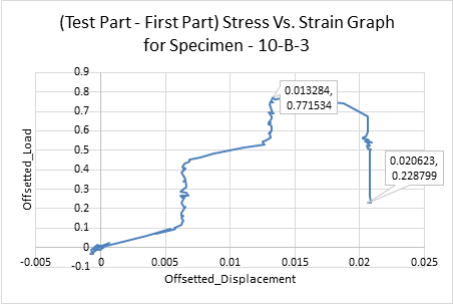

Figure B.140: Sampled Load Vs. Displacement graph for Specimen TG10-B-3

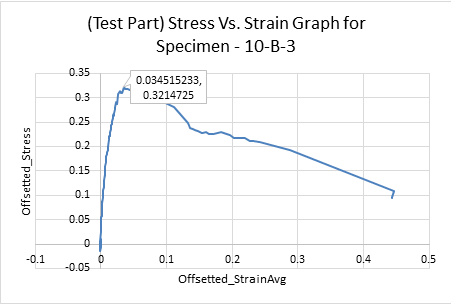

Figure B.141: Stress Vs. Strain Graph for the (second) sampled data for the Specimen TG10-B-3

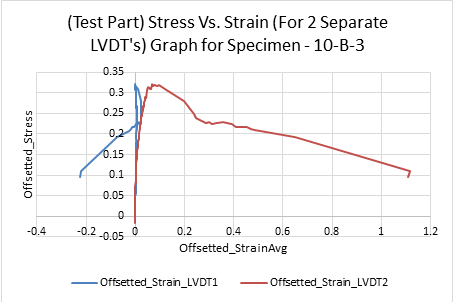

Figure B.142: Comparison graph of Stress Vs. Strain for 2 LVDT's for Specimen TG10-B-3

Specimen TG10-B-4

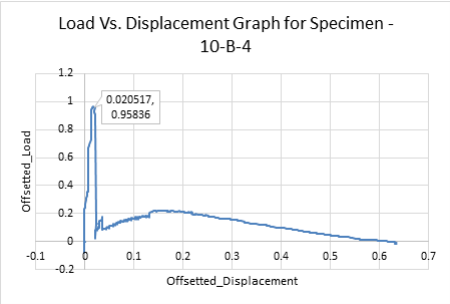

Figure B.143: Overall Load Vs. Displacement curve for Specimen TG10-B-4

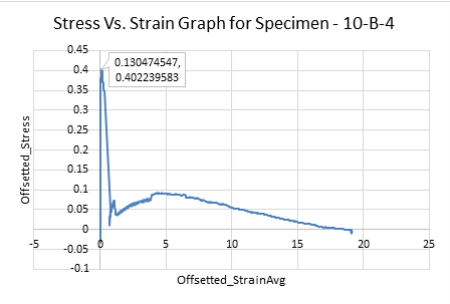

Figure B.144: Overall Stress Vs. Strain Graph for Specimen TG10-B-4

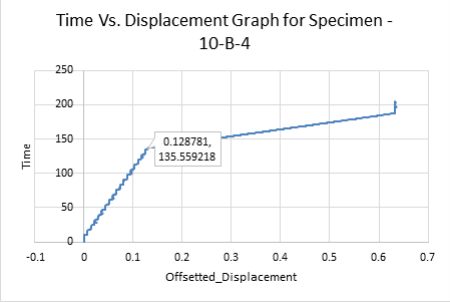

Figure B.145: Overall Time Vs. Displacement graph for Specimen TG10-B-4

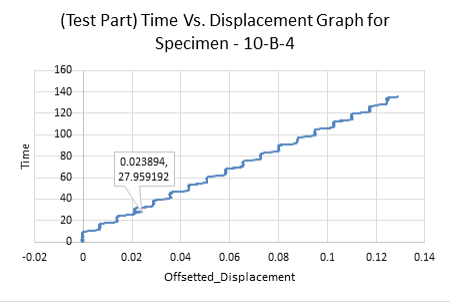

Figure B.146: First sampling Time Vs. Displacement graph for Specimen TG10-B-4

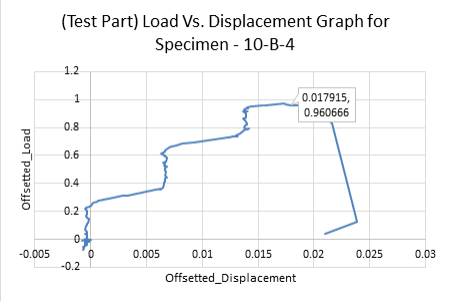

Figure B.147: Sampled Load Vs. Displacement graph for Specimen TG10-B-4

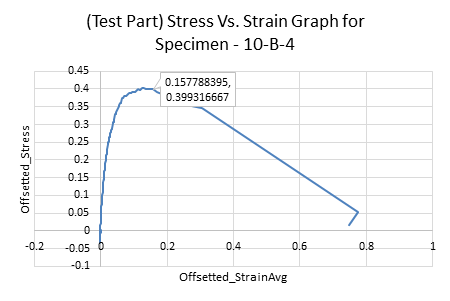

Figure B.148: Stress Vs. Strain Graph for the sampled data for Specimen TG10-B-4

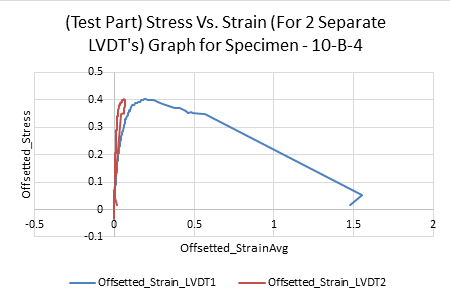

Figure B.149: Comparison graph of Stress Vs. Strain for 2 LVDT's for Specimen TG10-B-4

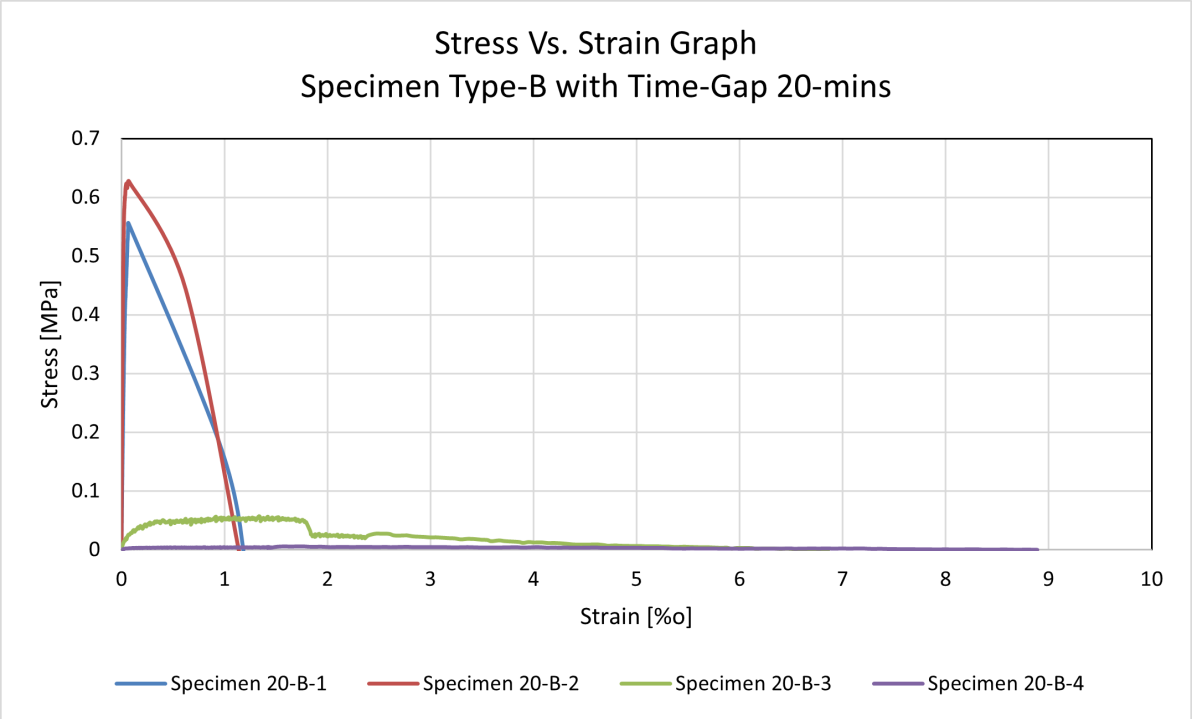

Figure B.150: Stress vs. Strain curve for Specimen TG20-B

Specimen TG20-B-1

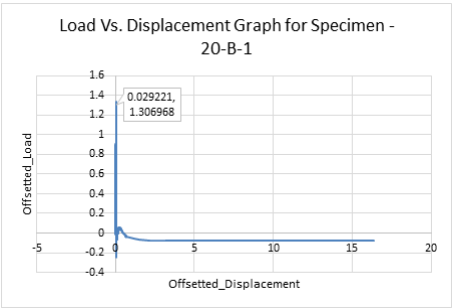

Figure B.151: Overall Load Vs. Displacement curve for Specimen TG20-B-1

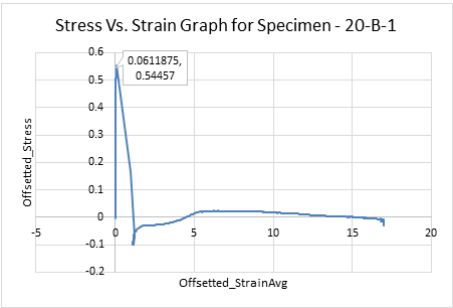

Figure B.152: Overall Stress Vs. Strain Graph for Specimen TG20-B-1

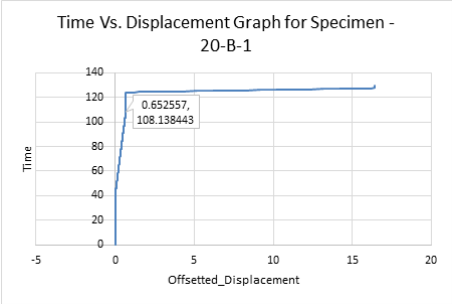

Figure B.153: Overall Time Vs. Displacement graph for Specimen TG20-B-1

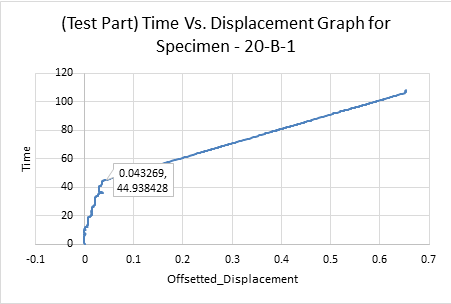

Figure B.154: First sampling Time Vs. Displacement graph for Specimen TG20-B-1

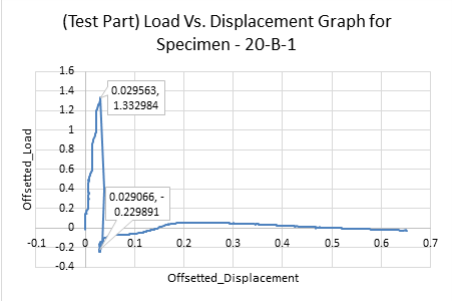

Figure B.155: Sampled Load Vs. Displacement graph for Specimen TG20-B-1

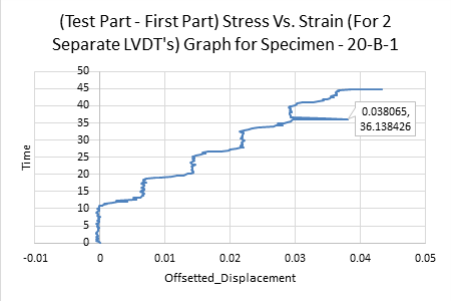

Figure B.156: Stress Vs. Strain Graph for the sampled data for the Specimen TG20-B-1

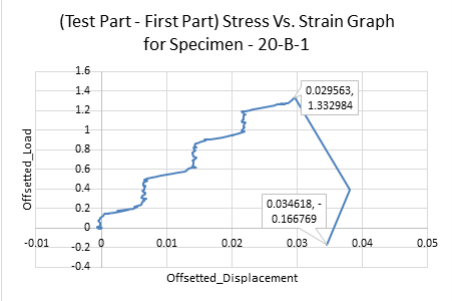

Figure B.157: Sampled Load Vs. Displacement graph for Specimen TG20-B-1

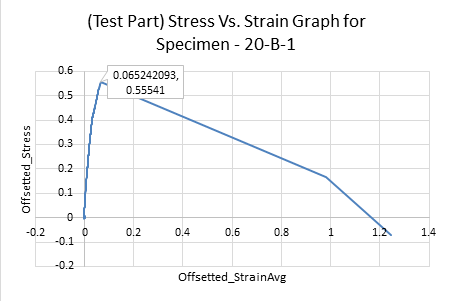

Figure B.158: Stress Vs. Strain Graph for the (second) sampled data for the Specimen TG20-B-1

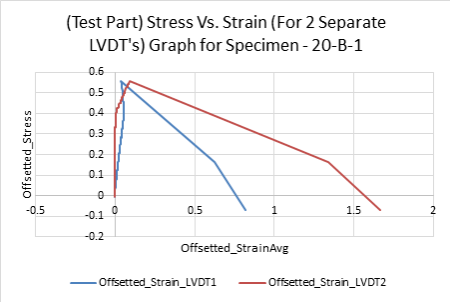

Figure B.159: Comparison graph of Stress Vs. Strain for 2 LVDT's for Specimen TG20-B-1

Specimen TG20-B-2

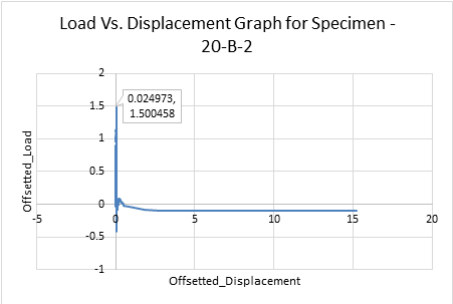

Figure B.160: Overall Load Vs. Displacement curve for Specimen TG20-B-2

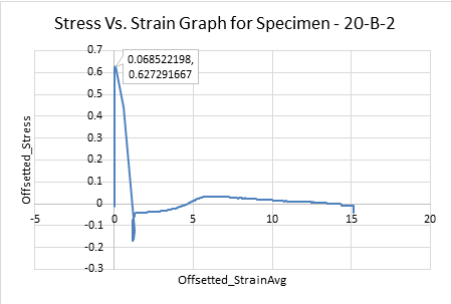

Figure B.161: Overall Stress Vs. Strain Graph for Specimen TG20-B-2

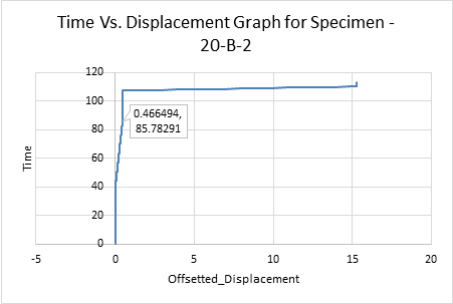

Figure B.162: Overall Time Vs. Displacement graph for Specimen TG20-B-2

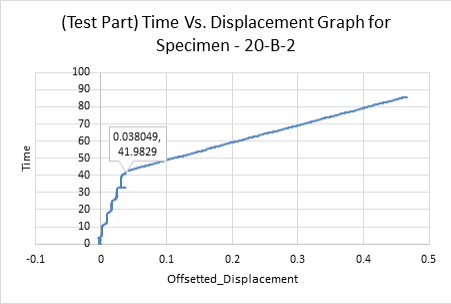

Figure B.163: First sampling Time Vs. Displacement graph for Specimen TG20-B-2

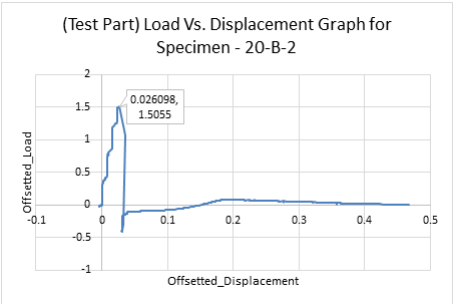

Figure B.164: Sampled Load Vs. Displacement graph for Specimen TG20-B-2

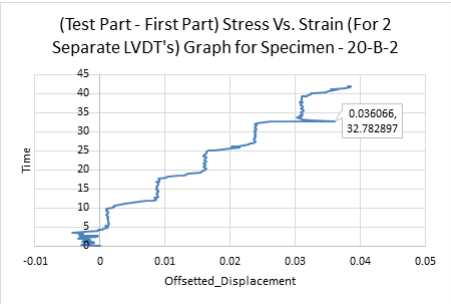

Figure B.165: Stress Vs. Strain Graph for the sampled data for the Specimen TG20-B-2

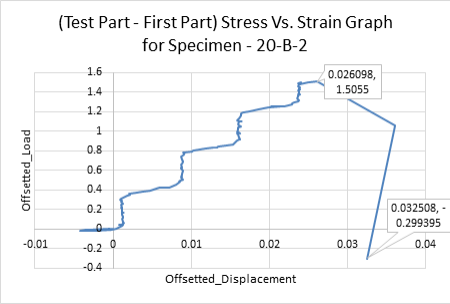

Figure B.166: Sampled Load Vs. Displacement graph for Specimen TG20-B-2

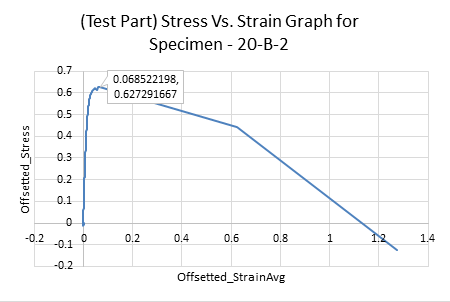

Figure B.167: Stress Vs. Strain Graph for the (second) sampled data for the Specimen TG20-B-2

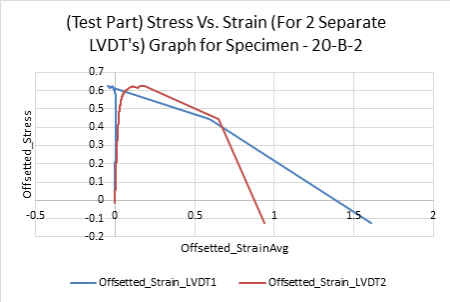

Figure B.168: Comparison graph of Stress Vs. Strain for 2 LVDT's for Specimen TG20-B-2

Specimen TG20-B-3

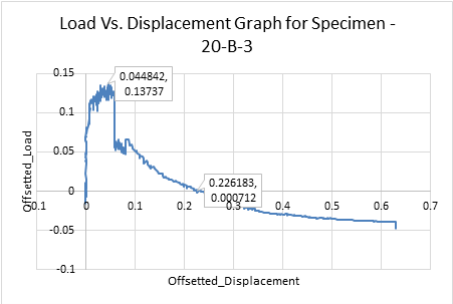

Figure B.169: Overall Load Vs. Displacement curve for Specimen TG20-B-3

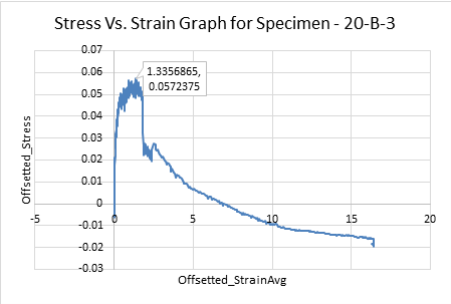

Figure B.170: Overall Stress Vs. Strain Graph for Specimen TG20-B-3

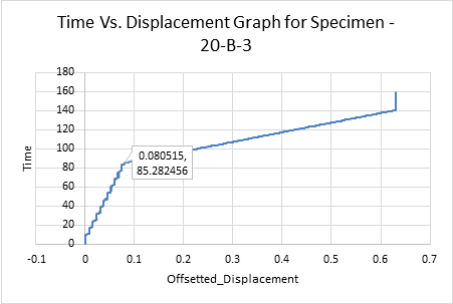

Figure B.171: Overall Time Vs. Displacement graph for Specimen TG20-B-3

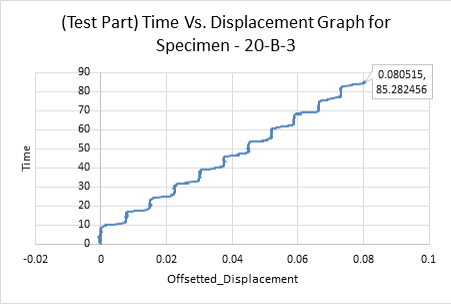

Figure B.172: First sampling Time Vs. Displacement graph for Specimen TG20-B-3

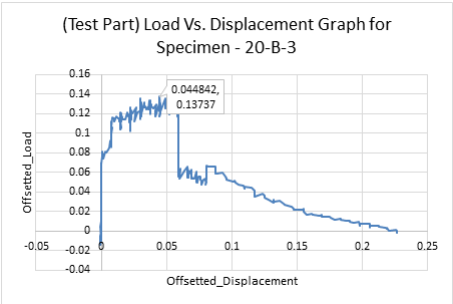

Figure B.173: Sampled Load Vs. Displacement graph for Specimen TG20-B-3

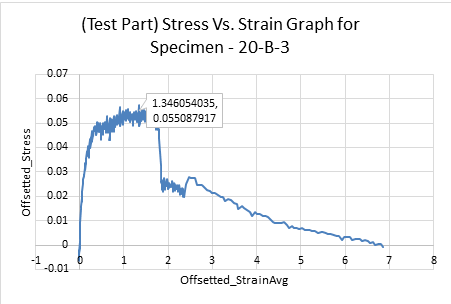

Figure B.174: Stress Vs. Strain Graph for the sampled data for Specimen TG20-B-3

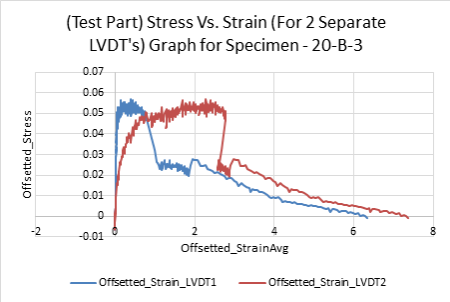

Figure B.175: Comparison graph of Stress Vs. Strain for 2 LVDT's for Specimen TG20-B-3

Specimen TG20-B-4

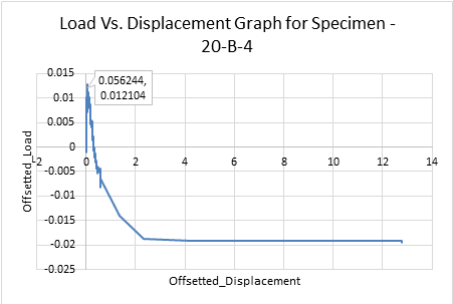

Figure B.176: Overall Load Vs. Displacement curve for Specimen TG20-B-4

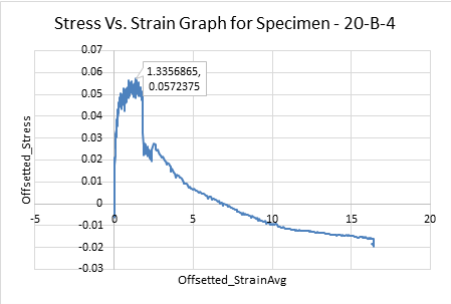

Figure B.177: Overall Stress Vs. Strain Graph for Specimen TG20-B-4

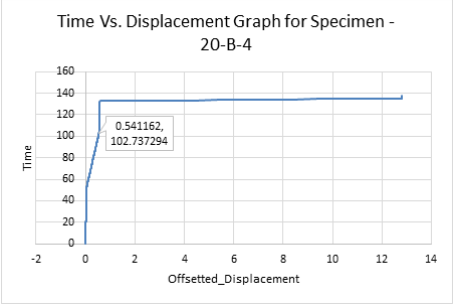

Figure B.178: Overall Time Vs. Displacement graph for Specimen TG20-B-4

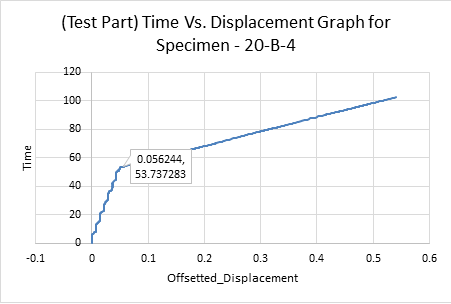

Figure B.179: First sampling Time Vs. Displacement graph for Specimen TG20-B-4

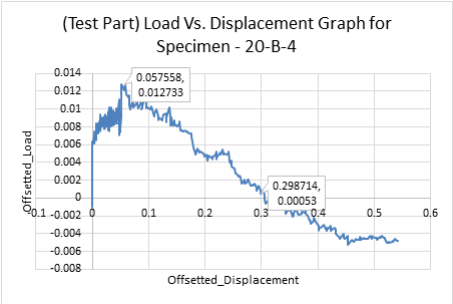

Figure B.180: Sampled Load Vs. Displacement graph for Specimen TG20-B-4

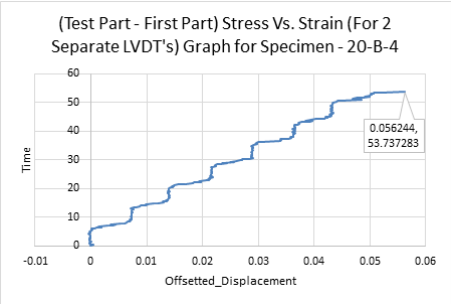

Figure B.181: Stress Vs. Strain Graph for the sampled data for the Specimen TG20-B-4

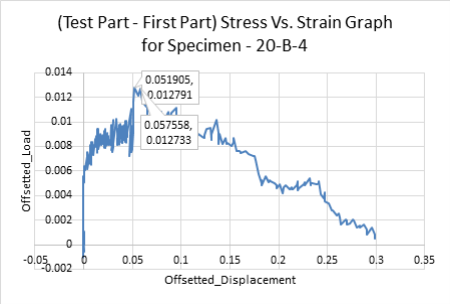

Figure B.182: Sampled Load Vs. Displacement graph for Specimen TG20-B-4

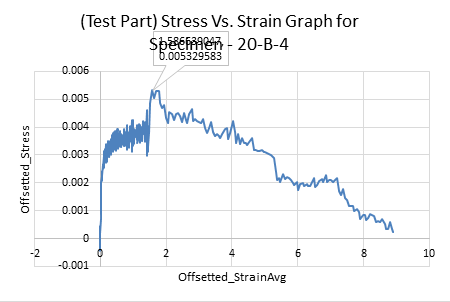

Figure B.183: Stress Vs. Strain Graph for the (second) sampled data for the Specimen TG20-B-4

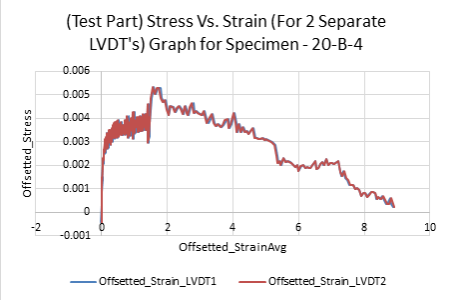

Figure B.184: Comparison graph of Stress Vs. Strain for 2 LVDT's for Specimen TG20-B-4

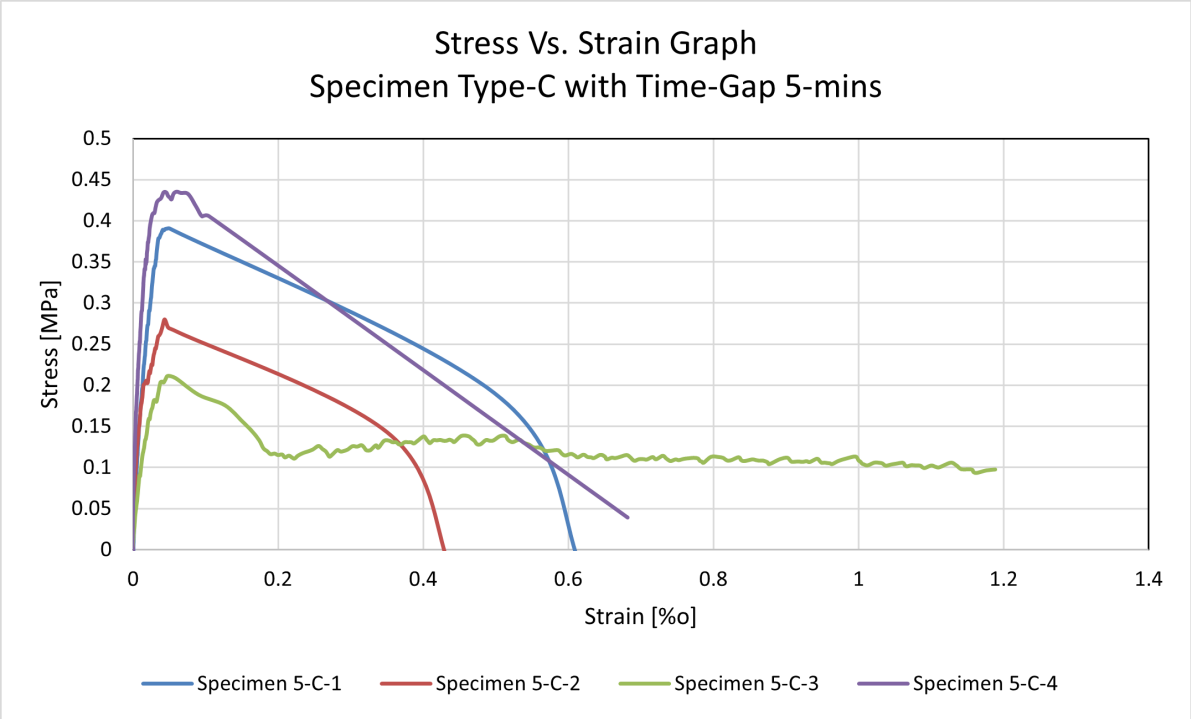

Figure B.185: Stress vs. Strain curve for Specimen TG5-C

Specimen TG5-C-1

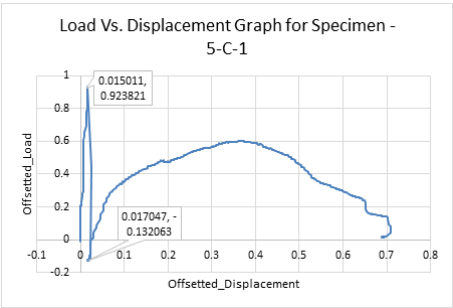

Figure B.186: Overall Load Vs. Displacement curve for Specimen TG5-C-1

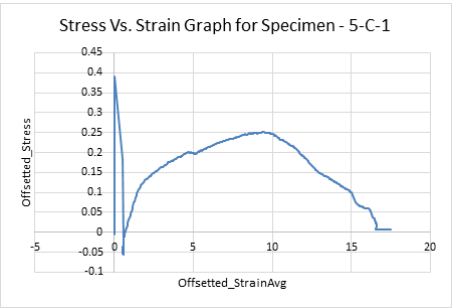

Figure B.187: Overall Stress Vs. Strain Graph for Specimen TG5-C-1

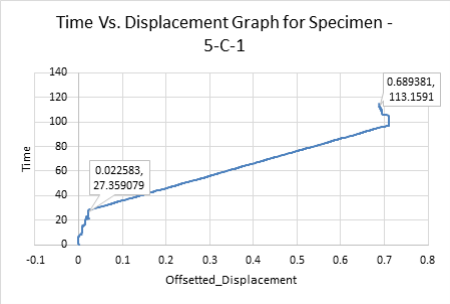

Figure B.188: Overall Time Vs. Displacement graph for Specimen TG5-C-1

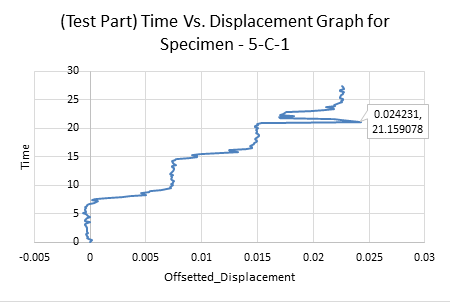

Figure B.189: First sampling Time Vs. Displacement graph for Specimen TG5-C-1

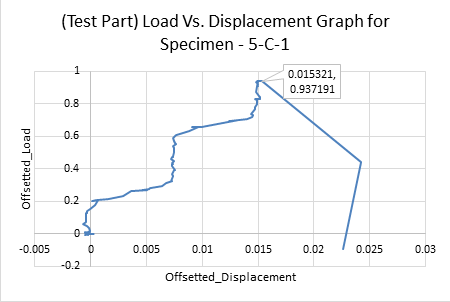

Figure B.190: Sampled Load Vs. Displacement graph for Specimen TG5-C-1

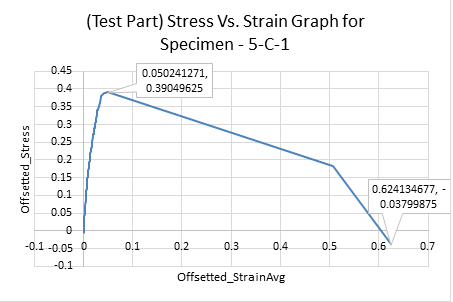

Figure B.191: Stress Vs. Strain Graph for the sampled data for Specimen TG5-C-1

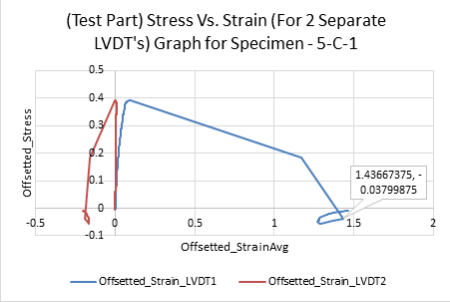

Figure B.192: Comparison graph of Stress Vs. Strain for 2 LVDT's for Specimen TG5-C-1

Specimen TG5-C-2

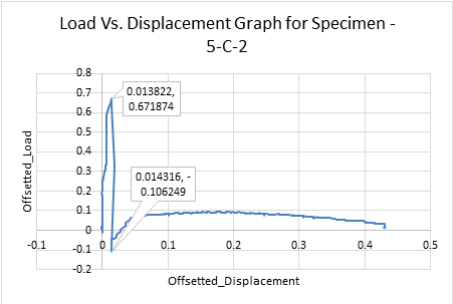

Figure B.193: Overall Load Vs. Displacement curve for Specimen TG5-C-2

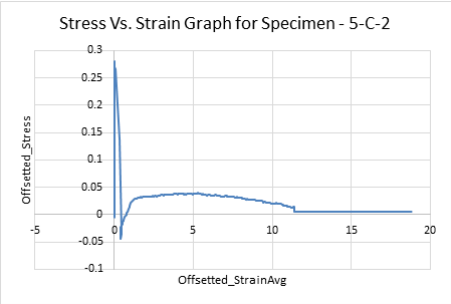

Figure B.194: Overall Stress Vs. Strain Graph for Specimen TG5-C-2

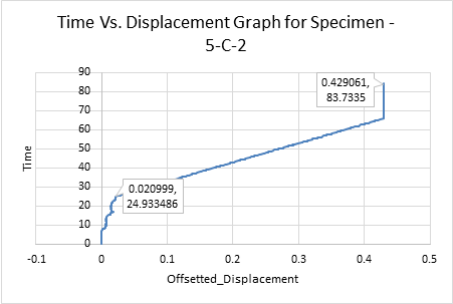

Figure B.195: Overall Time Vs. Displacement graph for Specimen TG5-C-2

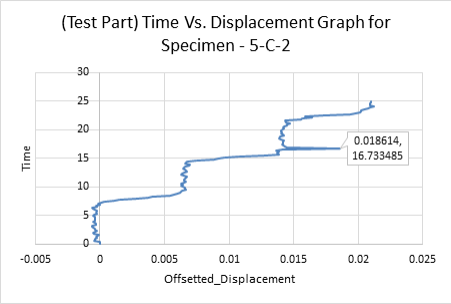

Figure B.196: First sampling Time Vs. Displacement graph for Specimen TG5-C-2

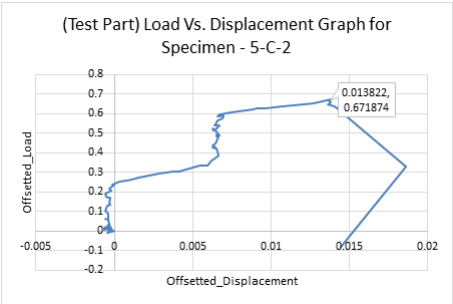

Figure B.197: Sampled Load Vs. Displacement graph for Specimen TG5-C-2

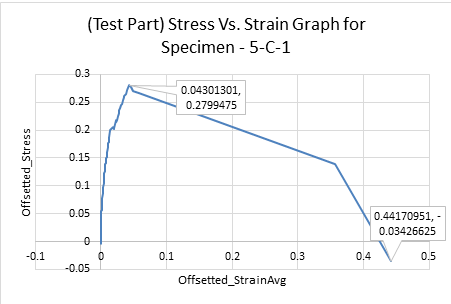

Figure B.198: Stress Vs. Strain Graph for the sampled data for Specimen TG5-C-2

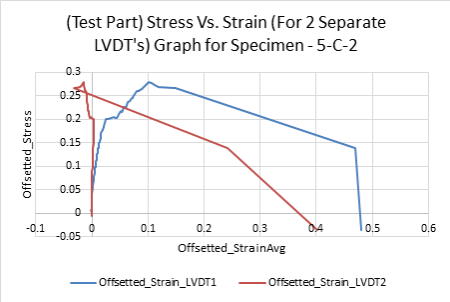

Figure B.199: Comparison graph of Stress Vs. Strain for 2 LVDT's for Specimen TG5-C-2

Specimen TG5-C-3

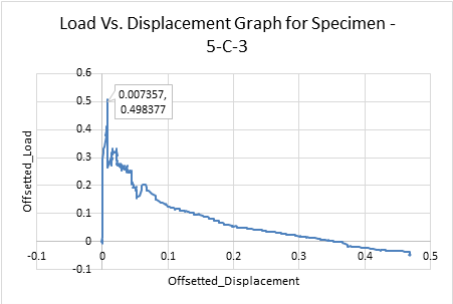

Figure B.200: Overall Load Vs. Displacement curve for Specimen TG5-C-3

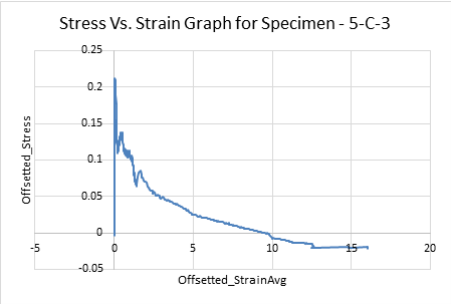

Figure B.201: Overall Stress Vs. Strain Graph for Specimen TG5-C-3

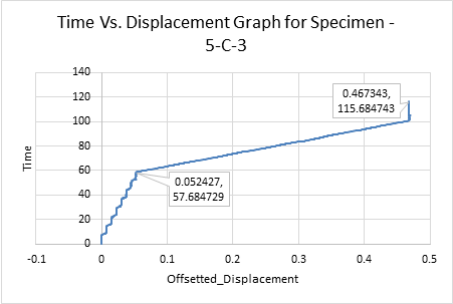

Figure B.202: Overall Time Vs. Displacement graph for Specimen TG5-C-3

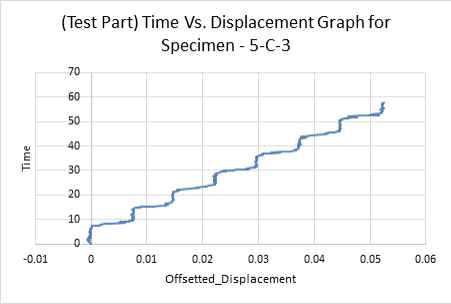

Figure B.203: First sampling Time Vs. Displacement graph for Specimen TG5-C-3

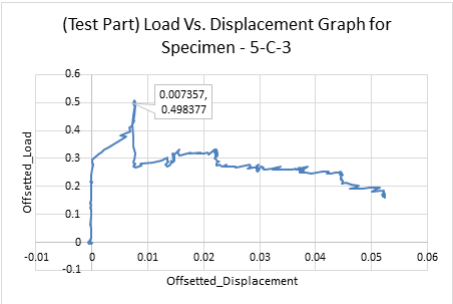

Figure B.204: Sampled Load Vs. Displacement graph for Specimen TG5-C-3

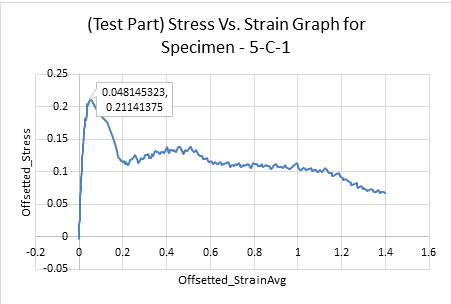

Figure B.205: Stress Vs. Strain Graph for the sampled data for Specimen TG5-C-3

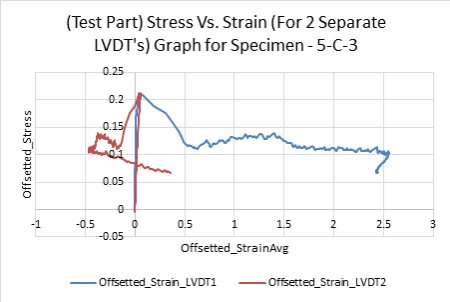

Figure B.206: Comparison graph of Stress Vs. Strain for 2 LVDT's for Specimen TG5-C-3

Specimen TG5-C-4

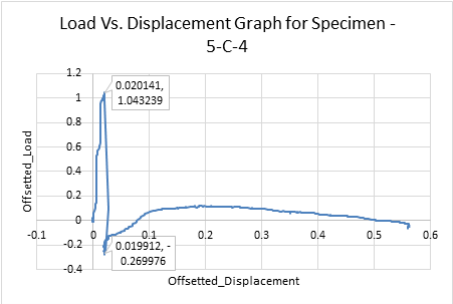

Figure B.207: Overall Load Vs. Displacement curve for Specimen TG5-C-4

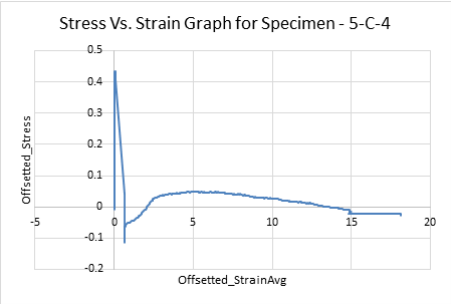

Figure B.208: Overall Stress Vs. Strain Graph for Specimen TG5-C-4

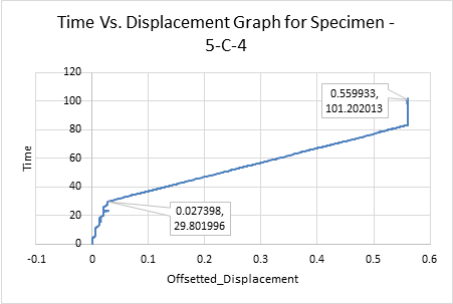

Figure B.209: Overall Time Vs. Displacement graph for Specimen TG5-C-4

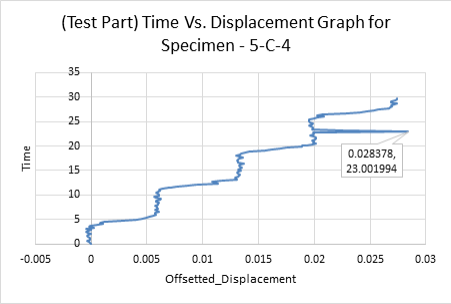

Figure B.210: First sampling Time Vs. Displacement graph for Specimen TG5-C-4

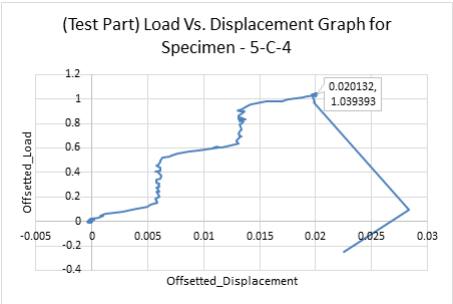

Figure B.211: Sampled Load Vs. Displacement graph for Specimen TG5-C-4

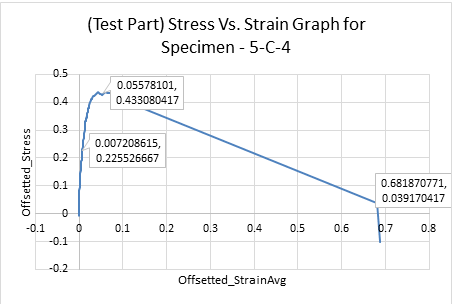

Figure B.212: Stress Vs. Strain Graph for the sampled data for Specimen TG5-C-4

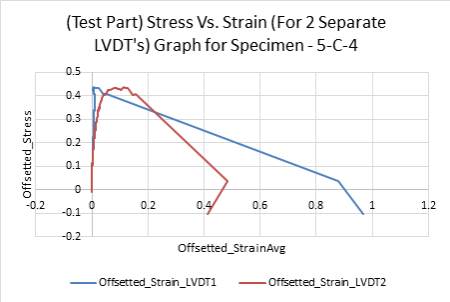

Figure B.213: Comparison graph of Stress Vs. Strain for 2 LVDT's for Specimen TG5-C-4

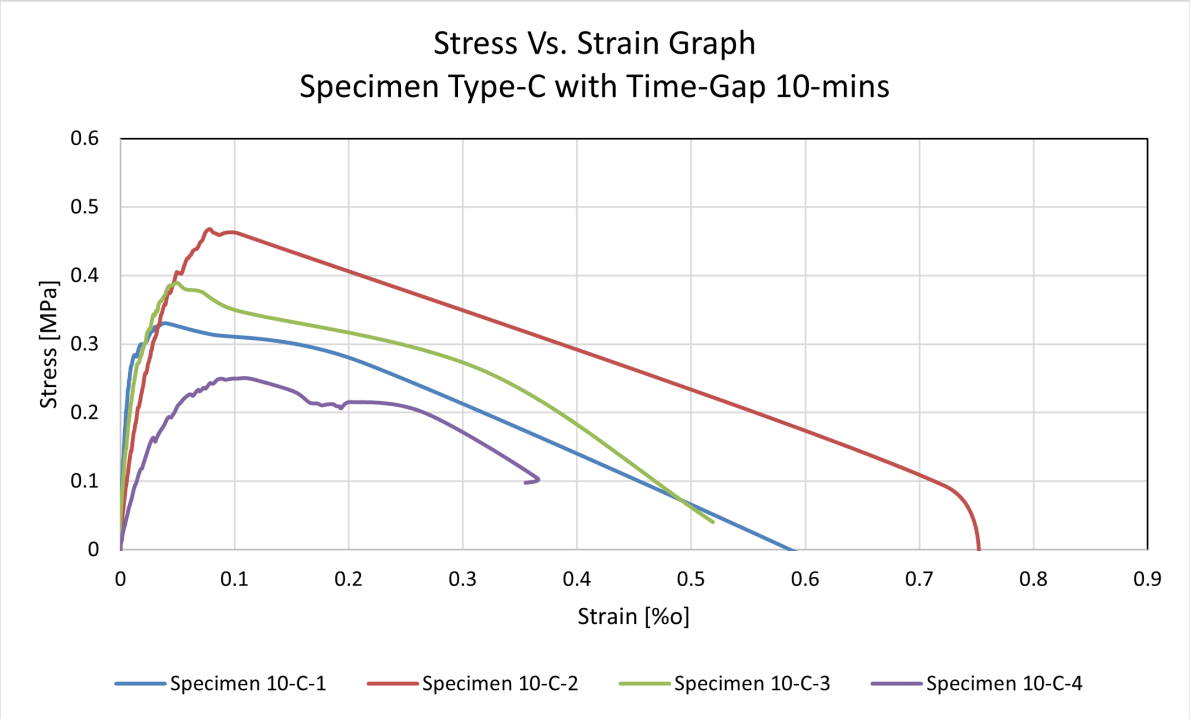

Figure B.214: Stress vs. Strain curve for Specimen TG10-C

Specimen TG10-C-1

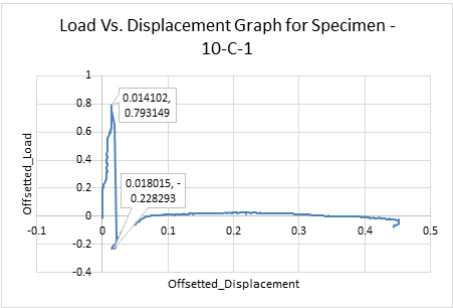

Figure B.215: Overall Load Vs. Displacement curve for Specimen TG10-C-1

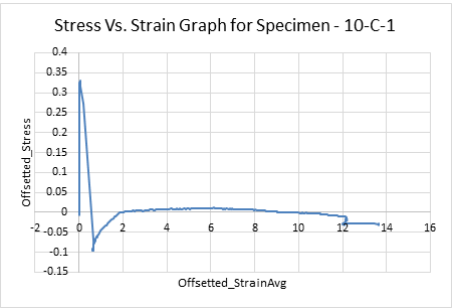

Figure B.216: Overall Stress Vs. Strain Graph for Specimen TG10-C-1

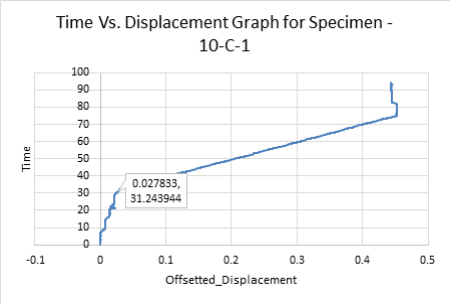

Figure B.217: Overall Time Vs. Displacement graph for Specimen TG10-C-1

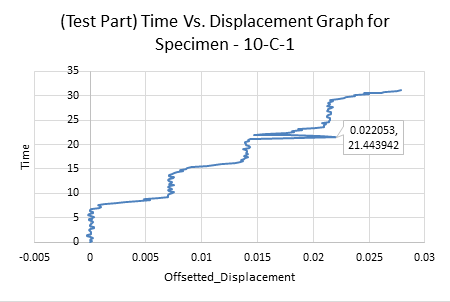

Figure B.218: First sampling Time Vs. Displacement graph for Specimen TG10-C-1

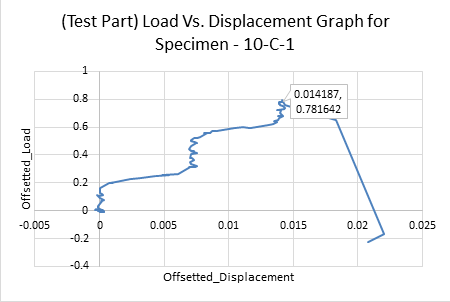

Figure B.219: Sampled Load Vs. Displacement graph for Specimen TG10-C-1

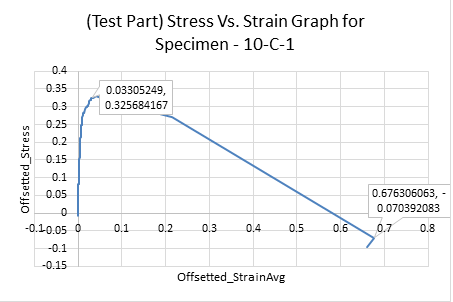

Figure B.220: Stress Vs. Strain Graph for the sampled data for Specimen TG10-C-1

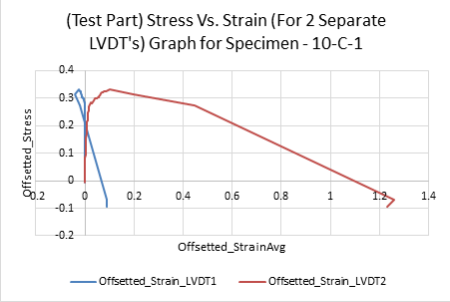

Figure B.221: Comparison graph of Stress Vs. Strain for 2 LVDT's for Specimen TG10-C-1

Specimen TG10-C-2

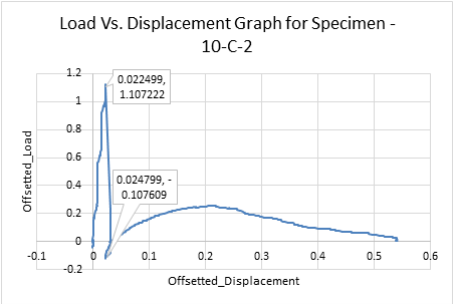

Figure B.222: Overall Load Vs. Displacement curve for Specimen TG10-C-2

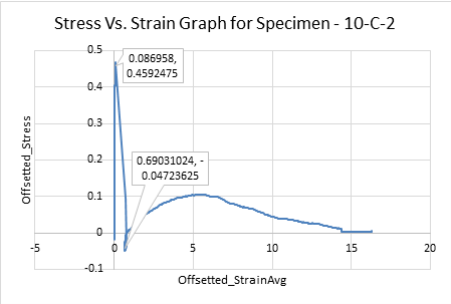

Figure B.223: Overall Stress Vs. Strain Graph for Specimen TG10-C-2

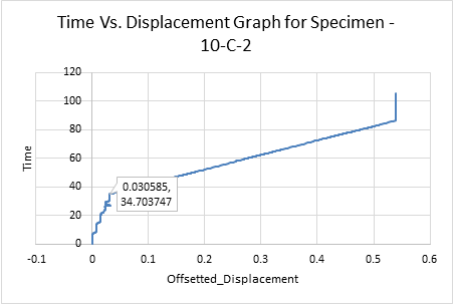

Figure B.224: Overall Time Vs. Displacement graph for Specimen TG10-C-2

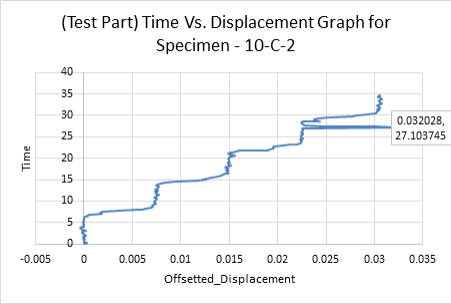

Figure B.225: First sampling Time Vs. Displacement graph for Specimen TG10-C-2

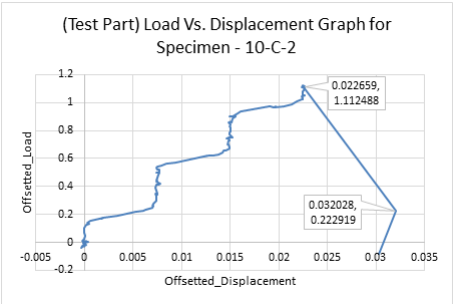

Figure B.226: Sampled Load Vs. Displacement graph for Specimen TG10-C-2

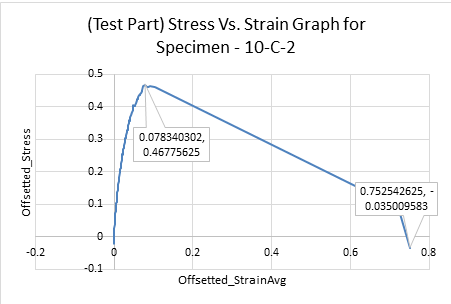

Figure B.227: Stress Vs. Strain Graph for the sampled data for Specimen TG10-C-2

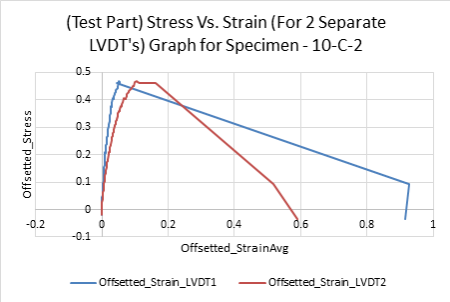

Figure B.228: Comparison graph of Stress Vs. Strain for 2 LVDT's for Specimen TG10-C-2

Specimen TG10-C-3

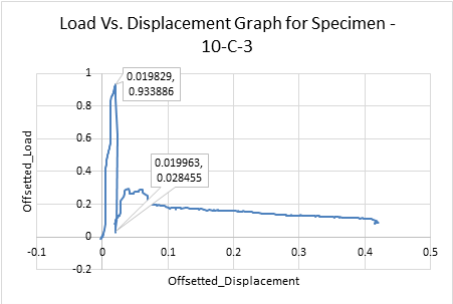

Figure B.229: Overall Load Vs. Displacement curve for Specimen TG10-C-3

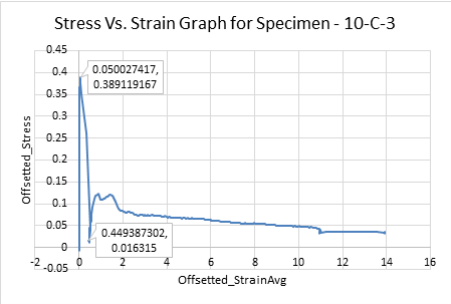

Figure B.230: Overall Stress Vs. Strain Graph for Specimen TG10-C-3

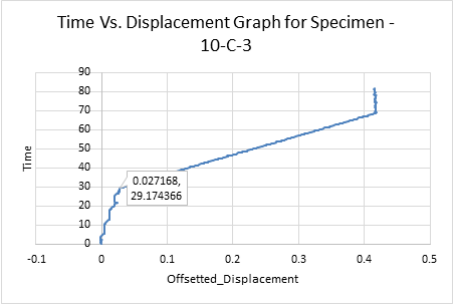

Figure B.231: Overall Time Vs. Displacement graph for Specimen TG10-C-3

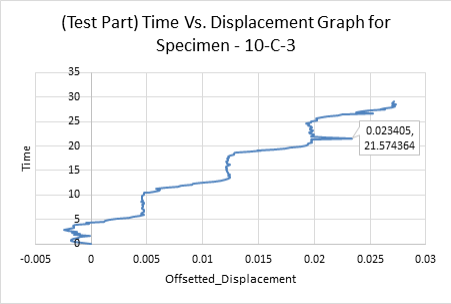

Figure B.232: First sampling Time Vs. Displacement graph for Specimen TG10-C-3

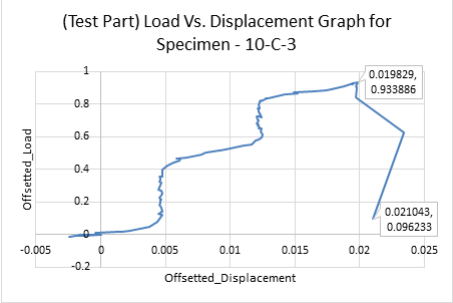

Figure B.233: Sampled Load Vs. Displacement graph for Specimen TG10-C-3

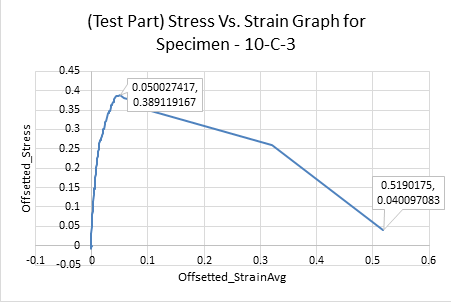

Figure B.234: Stress Vs. Strain Graph for the sampled data for Specimen TG10-C-3

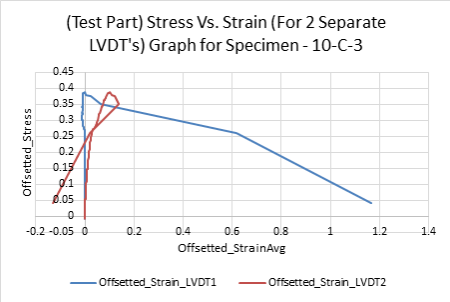

Figure B.235: Comparison graph of Stress Vs. Strain for 2 LVDT's for Specimen TG10-C-3

Specimen TG10-C-4

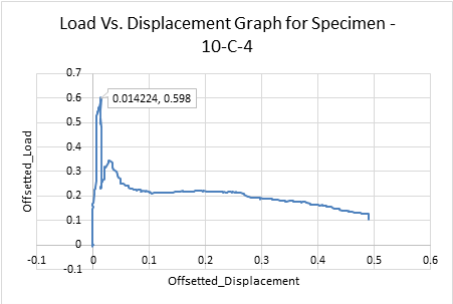

Figure B.236: Overall Load Vs. Displacement curve for Specimen TG10-C-4

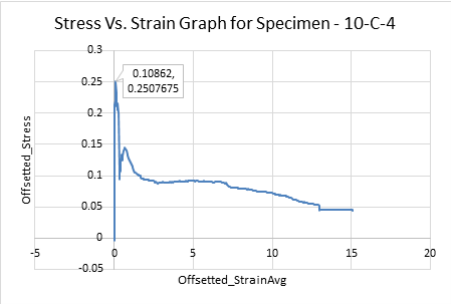

Figure B.237: Overall Stress Vs. Strain Graph for Specimen TG10-C-4

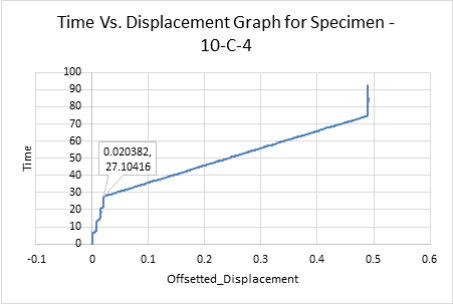

Figure B.238: Overall Time Vs. Displacement graph for Specimen TG10-C-4

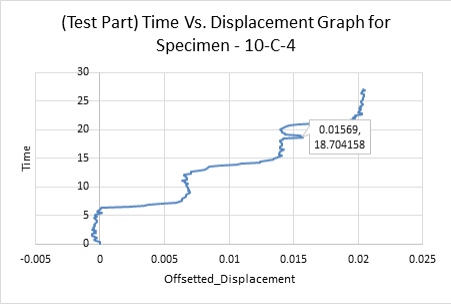

Figure B.239: First sampling Time Vs. Displacement graph for Specimen TG10-C-4

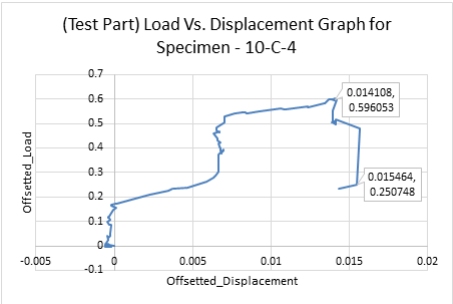

Figure B.240: Sampled Load Vs. Displacement graph for Specimen TG10-C-4

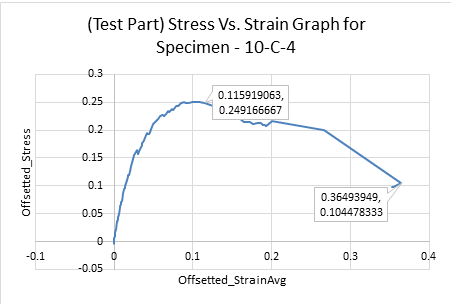

Figure B.241: Stress Vs. Strain Graph for the sampled data for Specimen TG10-C-4

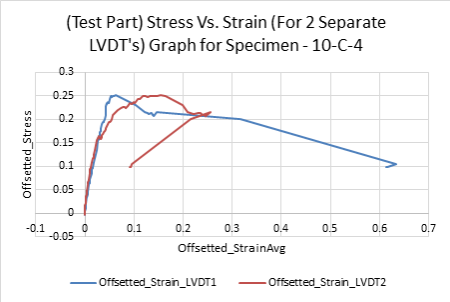

Figure B.242: Comparison graph of Stress Vs. Strain for 2 LVDT's for Specimen TG10-C-4

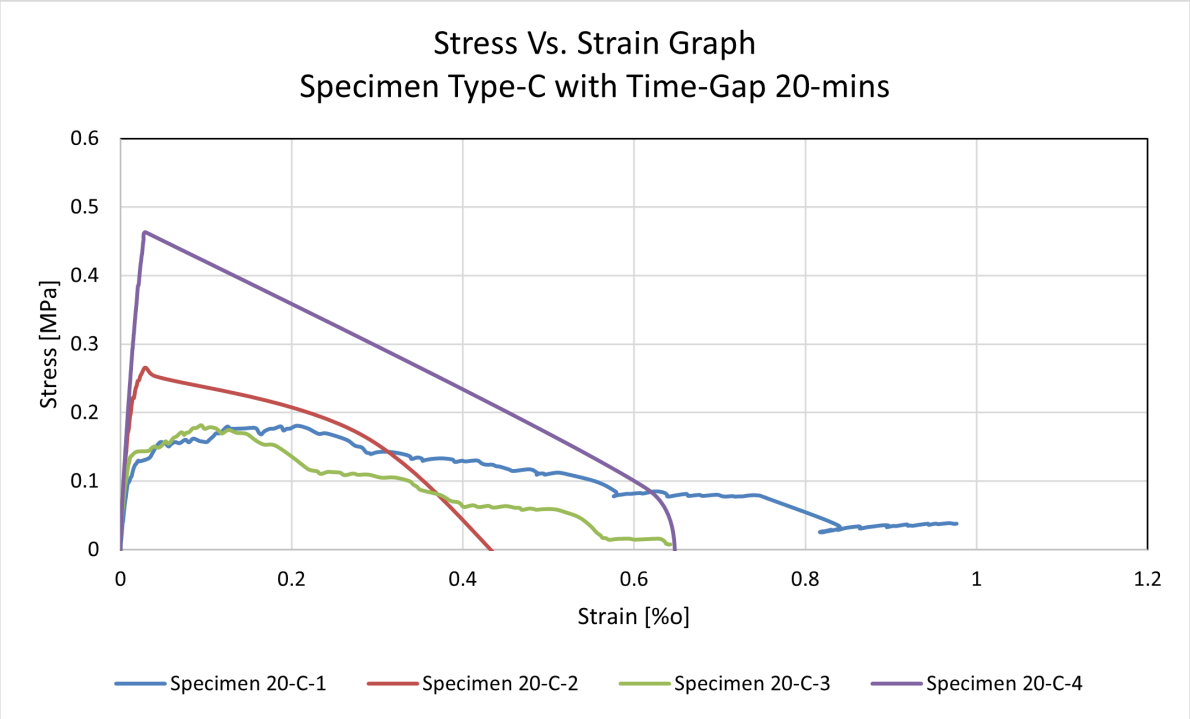

Figure B.243: Stress vs. Strain curve for Specimen TG20-C

Specimen TG20-C-1

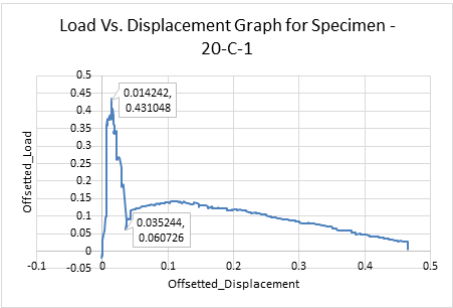

Figure B.244: Overall Load Vs. Displacement curve for Specimen TG20-C-1

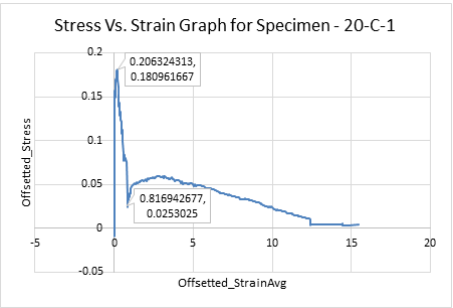

Figure B.245: Overall Stress Vs. Strain Graph for Specimen TG20-C-1

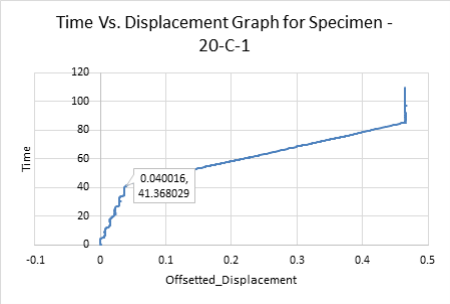

Figure B.246: Overall Time Vs. Displacement graph for Specimen TG20-C-1

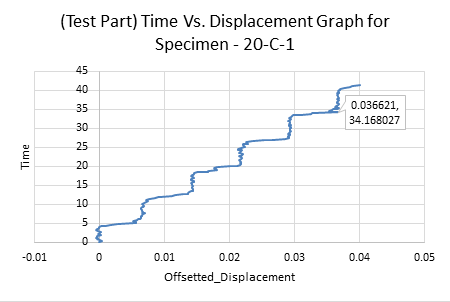

Figure B.247: First sampling Time Vs. Displacement graph for Specimen TG20-C-1

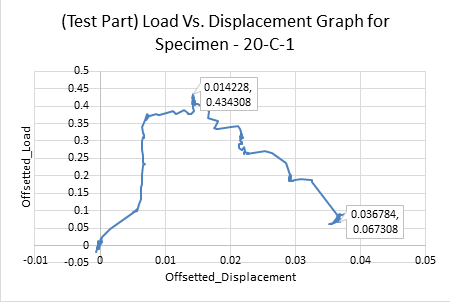

Figure B.248: Sampled Load Vs. Displacement graph for Specimen TG20-C-1

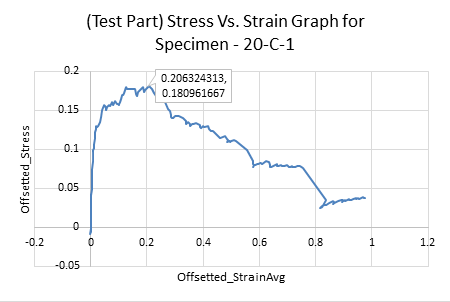

Figure B.249: Stress Vs. Strain Graph for the sampled data for Specimen TG20-C-1

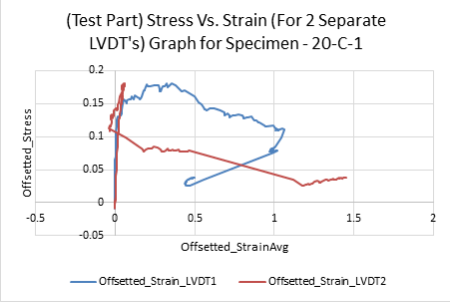

Figure B.250: Comparison graph of Stress Vs. Strain for 2 LVDT's for Specimen TG20-C-1

Specimen TG20-C-2

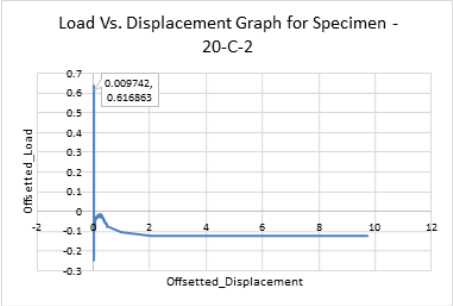

Figure B.251: Overall Load Vs. Displacement curve for Specimen TG20-C-2

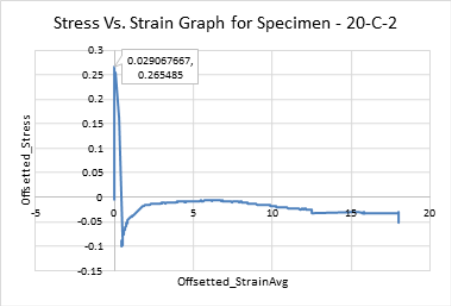

Figure B.252: Overall Stress Vs. Strain Graph for Specimen TG20-C-2

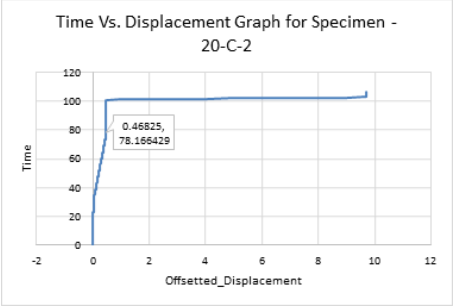

Figure B.253: Overall Time Vs. Displacement graph for Specimen TG20-C-2

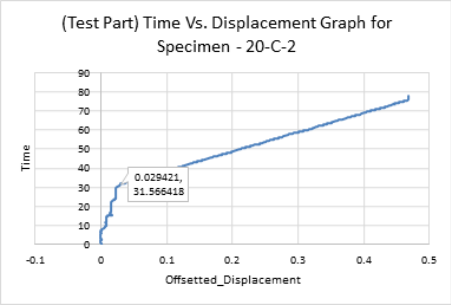

Figure B.254: First sampling Time Vs. Displacement graph for Specimen TG20-C-2

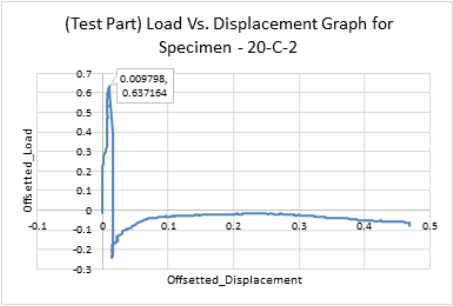

Figure B.255: Sampled Load Vs. Displacement graph for Specimen TG20-C-2

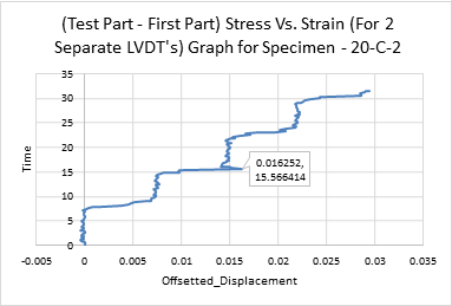

Figure B.256: Stress Vs. Strain Graph for the sampled data for the Specimen TG20-C-2

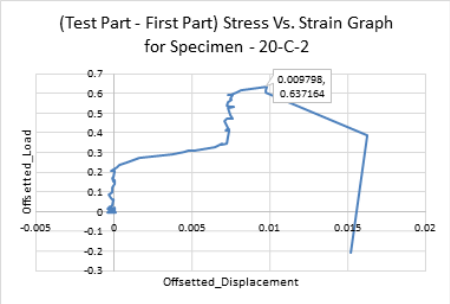

Figure B.257: Sampled Load Vs. Displacement graph for Specimen TG20-C-2

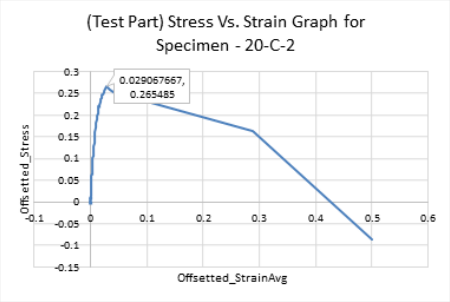

Figure B.258: Stress Vs. Strain Graph for the (second) sampled data for the Specimen TG20-C-2

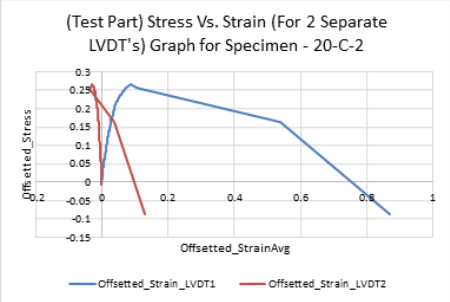

Figure B.259: Comparison graph of Stress Vs. Strain for 2 LVDT's for Specimen TG20-C-2

Specimen TG20-C-3

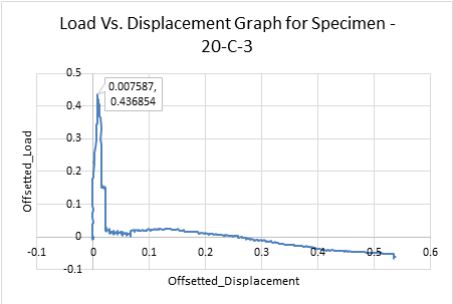

Figure B.260: Overall Load Vs. Displacement curve for Specimen TG20-C-3

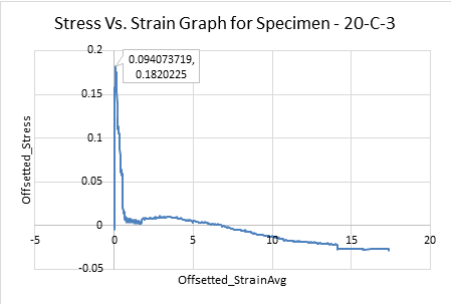

Figure B.261: Overall Stress Vs. Strain Graph for Specimen TG20-C-3

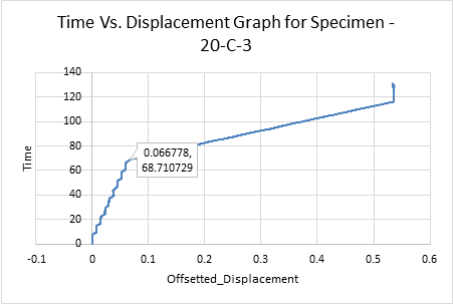

Figure B.262: Overall Time Vs. Displacement graph for Specimen TG20-C-3

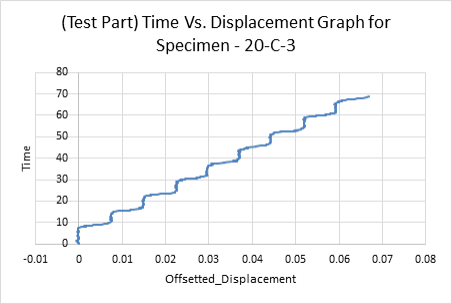

Figure B.263: First sampling Time Vs. Displacement graph for Specimen TG20-C-3

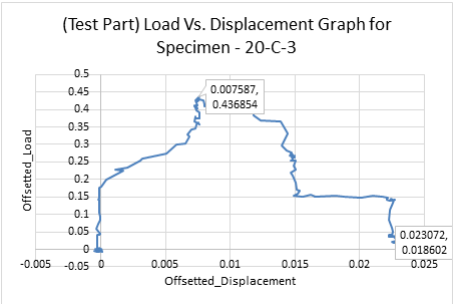

Figure B.264: Sampled Load Vs. Displacement graph for Specimen TG20-C-3

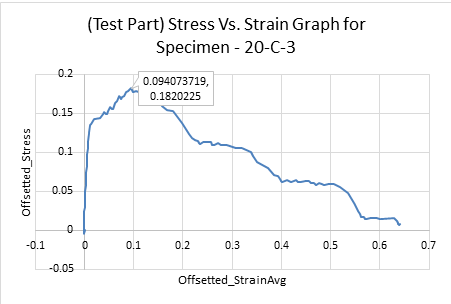

Figure B.265: Stress Vs. Strain Graph for the sampled data for Specimen TG20-C-3

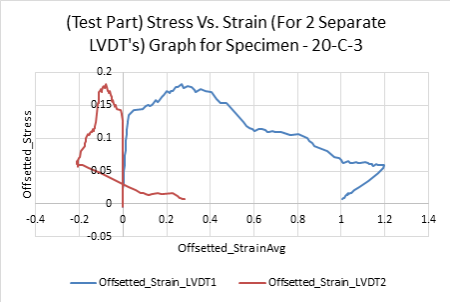

Figure B.266: Comparison graph of Stress Vs. Strain for 2 LVDT's for Specimen TG20-C-3

Specimen TG20-C-4

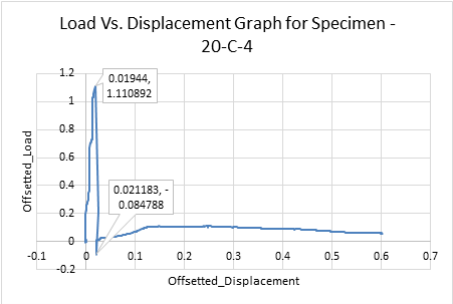

Figure B.267: Overall Load Vs. Displacement curve for Specimen TG20-C-4

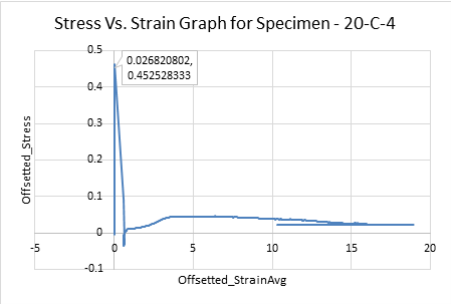

Figure B.268: Overall Stress Vs. Strain Graph for Specimen TG20-C-4

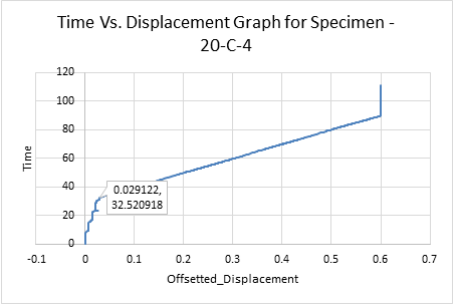

Figure B.269: Overall Time Vs. Displacement graph for Specimen TG20-C-4

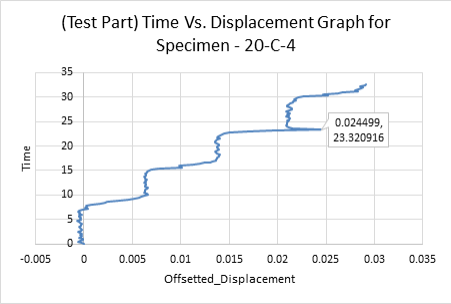

Figure B.270: First sampling Time Vs. Displacement graph for Specimen TG20-C-4

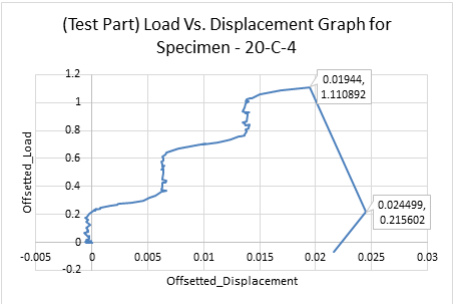

Figure B.271: Sampled Load Vs. Displacement graph for Specimen TG20-C-4

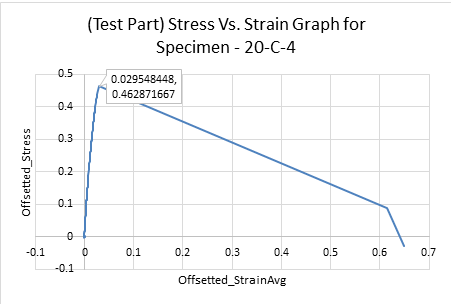

Figure B.272: Stress Vs. Strain Graph for the sampled data for Specimen TG20-C-4

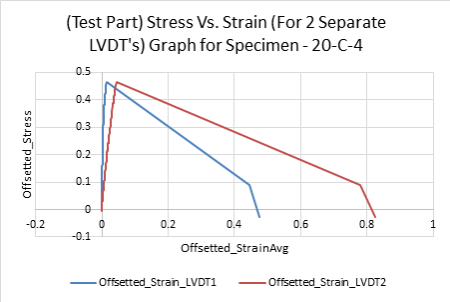

Figure B.273: Comparison graph of Stress Vs. Strain for 2 LVDT's for Specimen TG20-C-4

B.1.2. Casting based Specimens

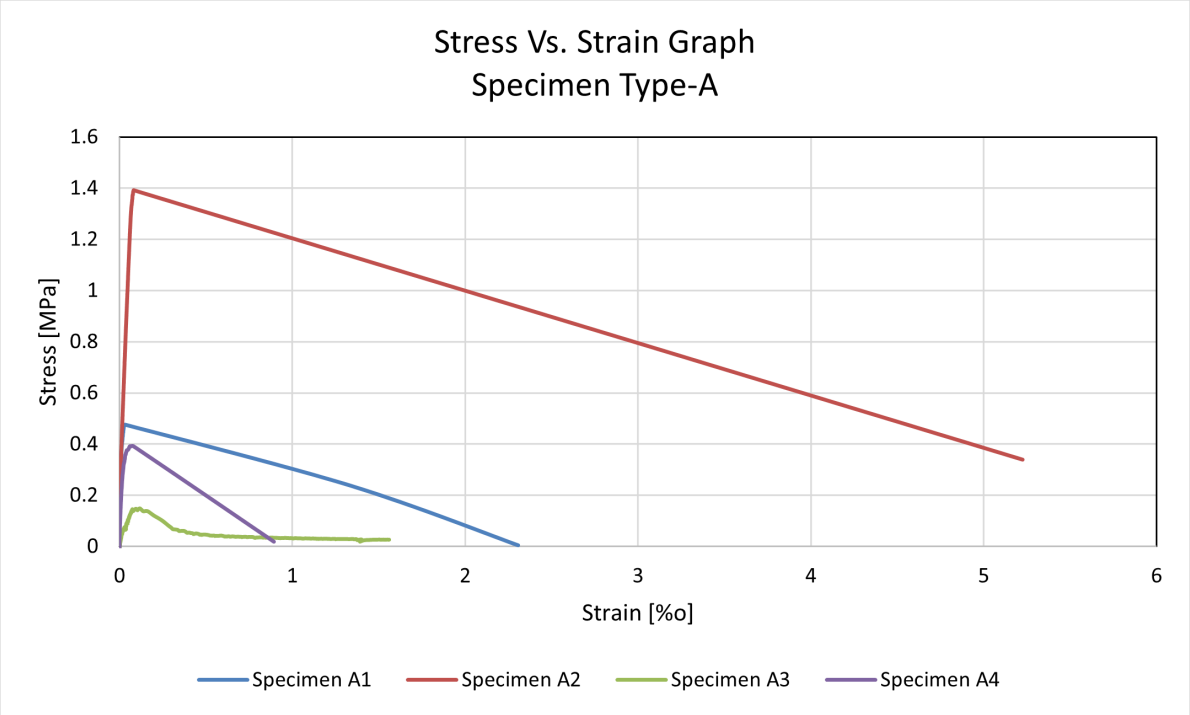

Figure B.274: Stress vs. Strain curve for Casted Specimen Type-A

Specimen A-1

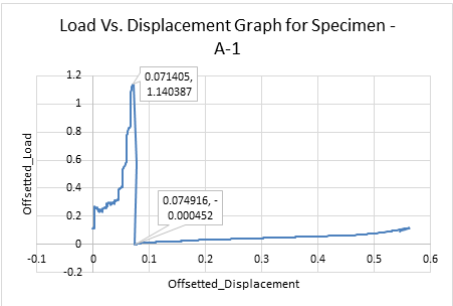

Figure B.275: Overall Load Vs. Displacement curve for Specimen A-1

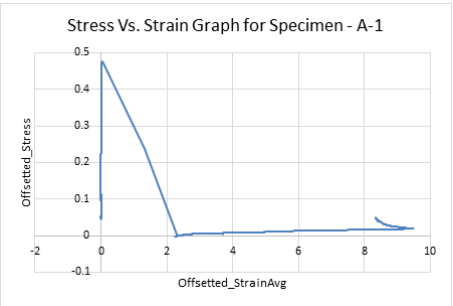

Figure B.276: Overall Stress Vs. Strain Graph for Specimen A-1

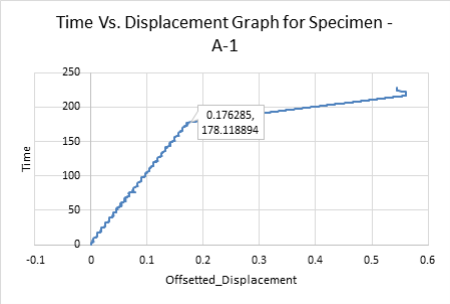

Figure B.277: Overall Time Vs. Displacement graph for Specimen A-1

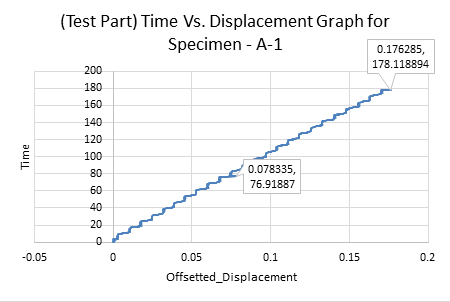

Figure B.278: First sampling Time Vs. Displacement graph for Specimen A-1

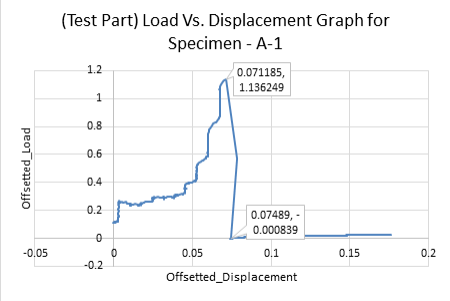

Figure B.279: First sampling Load Vs. Displacement graph for Specimen A-1

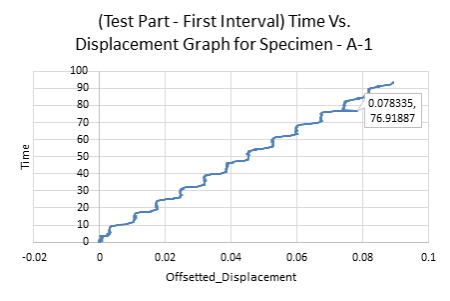

Figure B.280: Second sampling Time Vs. Displacement graph for Specimen A-1

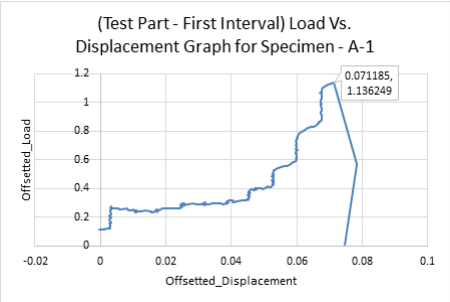

Figure B.281: Second sampling Load Vs. Displacement graph for Specimen A-1

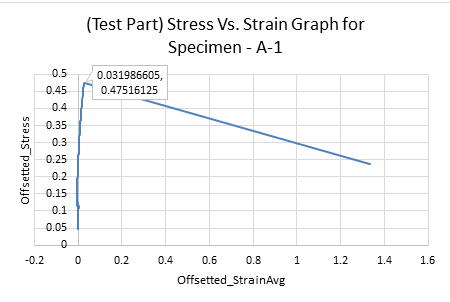

Figure B.282: Stress Vs. Strain Graph for the (second) sampled data for the Specimen A-1

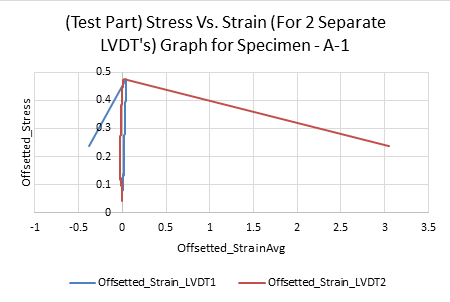

Figure B.283: Comparison graph of Stress Vs. Strain for 2 LVDT's for Specimen A-1

Specimen A-2

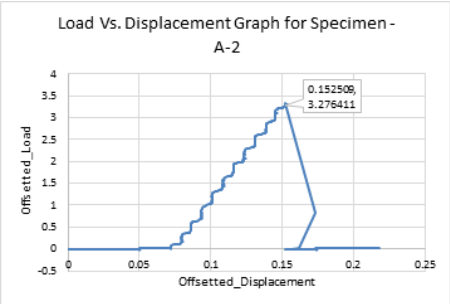

Figure B.284: Overall Load Vs. Displacement curve for Specimen A-2

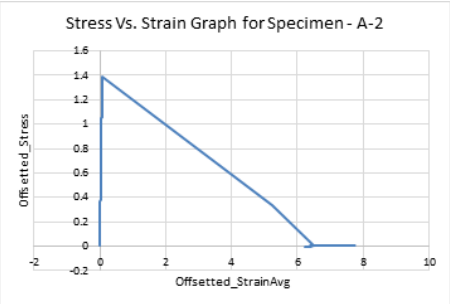

Figure B.285: Overall Stress Vs. Strain Graph for Specimen A-2

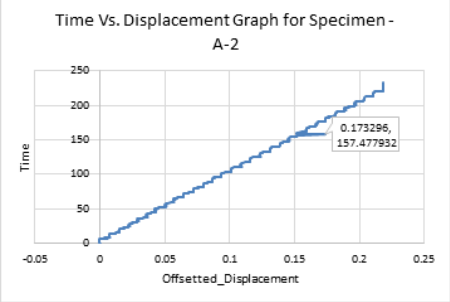

Figure B.286: Overall Time Vs. Displacement graph for Specimen A-2

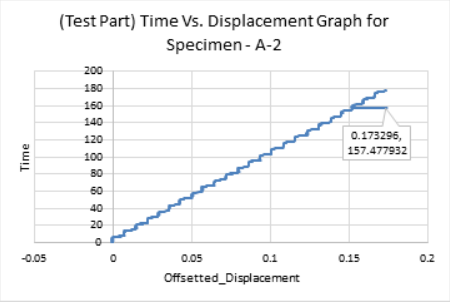

Figure B.287: First sampling Time Vs. Displacement graph for Specimen A-2

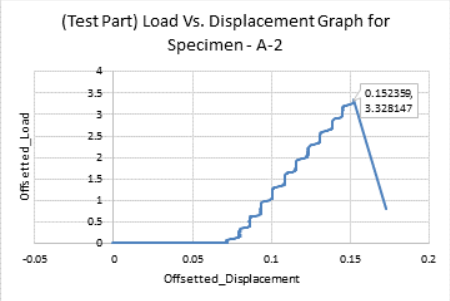

Figure B.288: Sampled Load Vs. Displacement graph for Specimen A-2

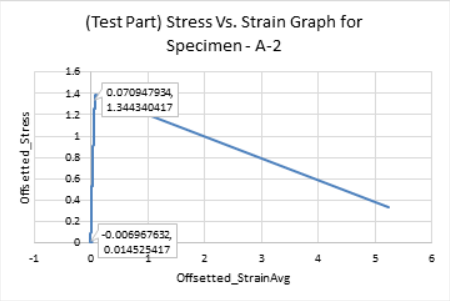

Figure B.289: Stress Vs. Strain Graph for the sampled data for Specimen A-2

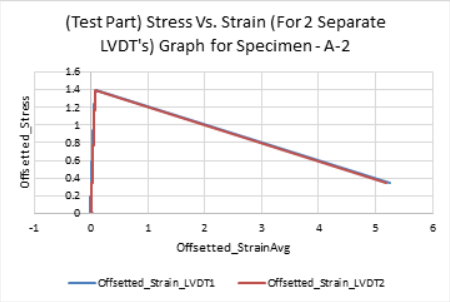

Figure B.290: Comparison graph of Stress Vs. Strain for 2 LVDT's for Specimen A-2

Specimen A-3

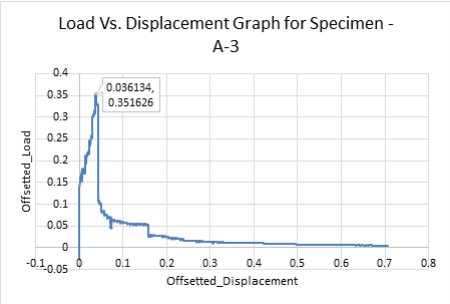

Figure B.291: Overall Load Vs. Displacement curve for Specimen A-3

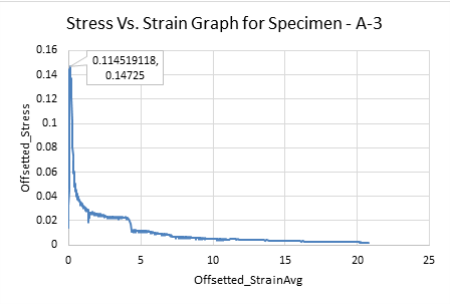

Figure B.292: Overall Stress Vs. Strain Graph for Specimen A-3

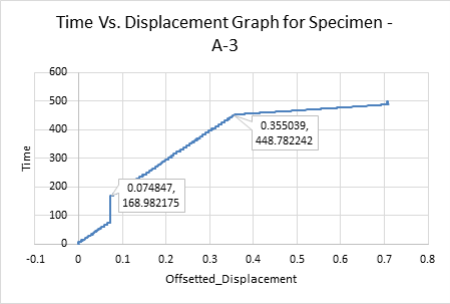

Figure B.293: Overall Time Vs. Displacement graph for Specimen A-3

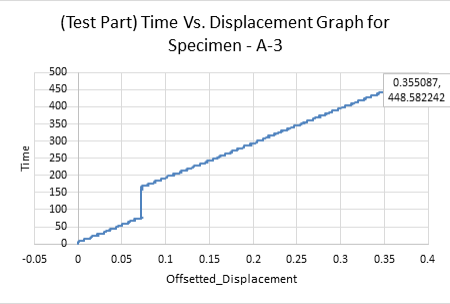

Figure B.294: First sampling Time Vs. Displacement graph for Specimen A-3

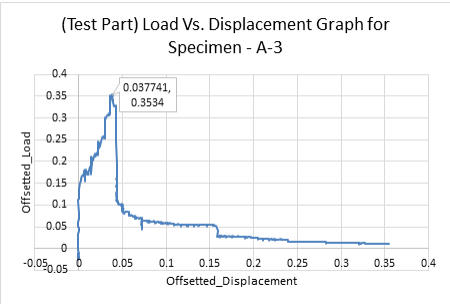

Figure B.295: First sampling Load Vs. Displacement graph for Specimen A-3

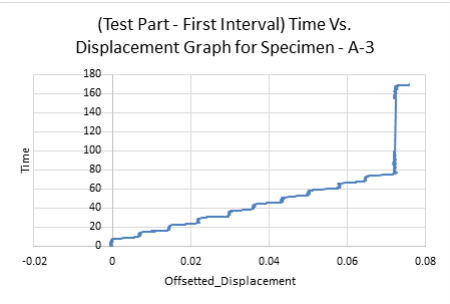

Figure B.296: Second sampling Time Vs. Displacement graph for Specimen A-3

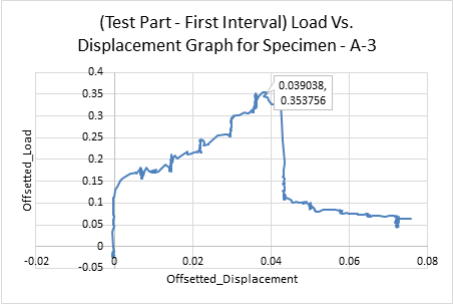

Figure B.297: Second sampling Load Vs. Displacement graph for Specimen A-3

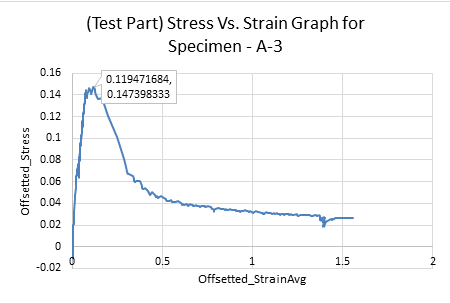

Figure B.298: Stress Vs. Strain Graph for the (second) sampled data for the Specimen A-3

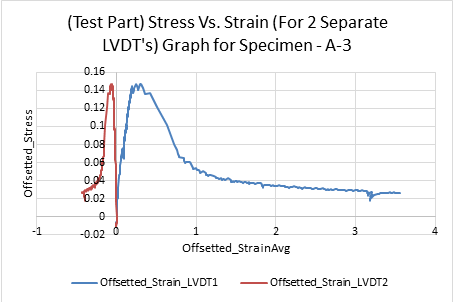

Figure B.299: Comparison graph of Stress Vs. Strain for 2 LVDT's for Specimen A-3

Specimen A-4

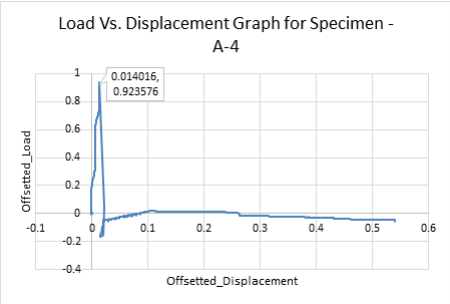

Figure B.300: Overall Load Vs. Displacement curve for Specimen A-4

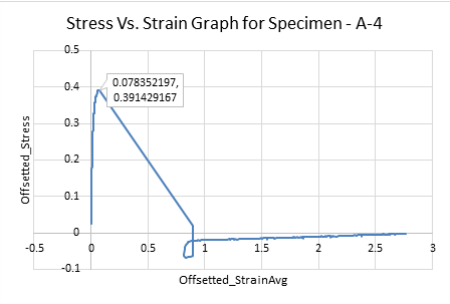

Figure B.301: Overall Stress Vs. Strain Graph for Specimen A-4

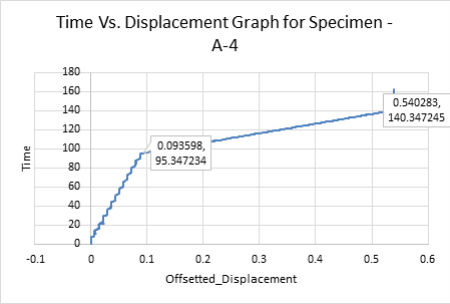

Figure B.302: Overall Time Vs. Displacement graph for Specimen A-4

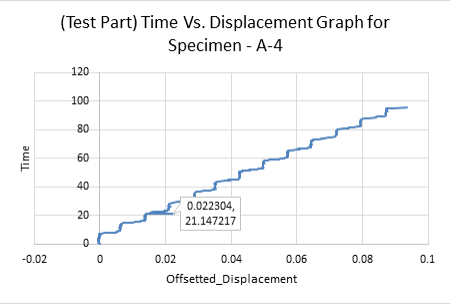

Figure B.303: First sampling Time Vs. Displacement graph for Specimen A-4

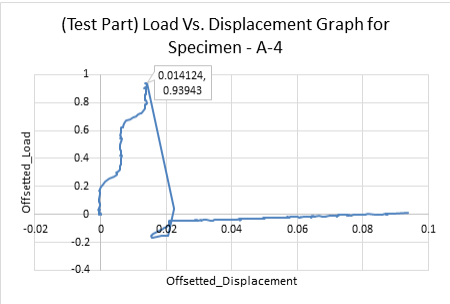

Figure B.304: First sampling Load Vs. Displacement graph for Specimen A-4

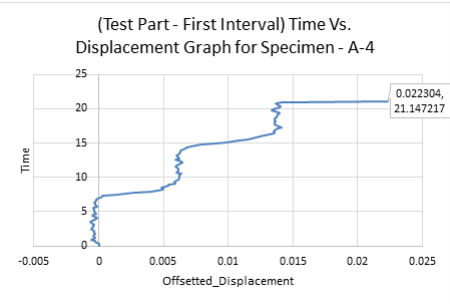

Figure B.305: Second sampling Time Vs. Displacement graph for Specimen A-4

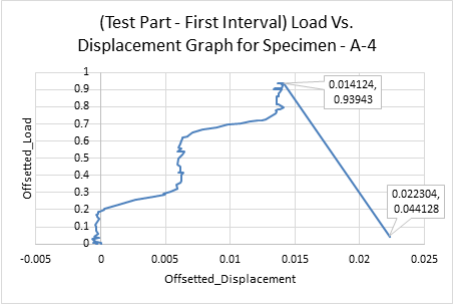

Figure B.306: Second sampling Load Vs. Displacement graph for Specimen A-4

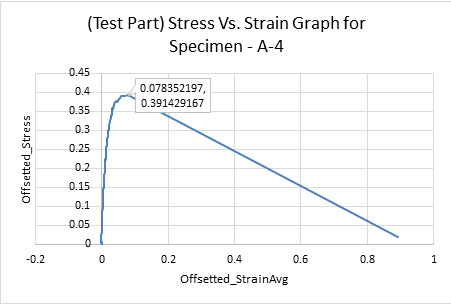

Figure B.307: Stress Vs. Strain Graph for the (second) sampled data for the Specimen A-4

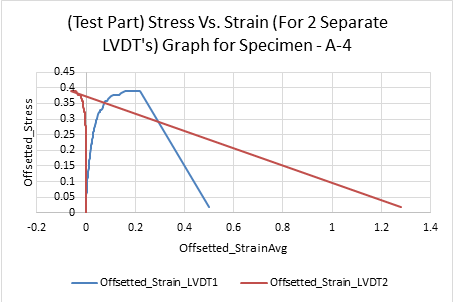

Figure B.308: Comparison graph of Stress Vs. Strain for 2 LVDT's for Specimen A-4

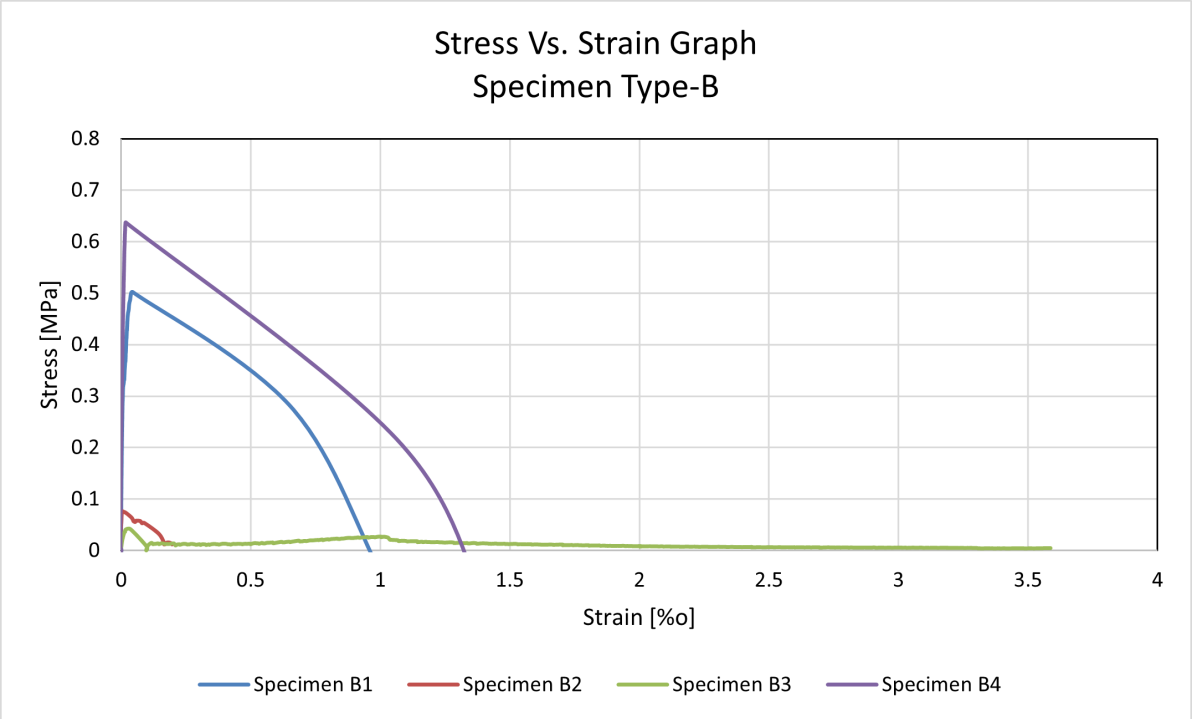

Figure B.309: Stress vs. Strain curve for Casted Specimen Type-B

Specimen B-1

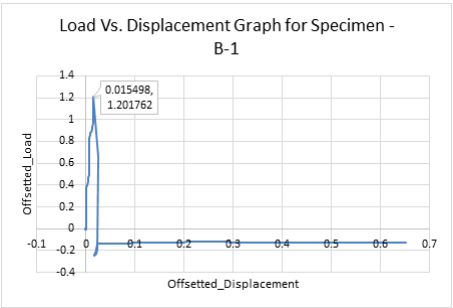

Figure B.310: Overall Load Vs. Displacement curve for Specimen B-1

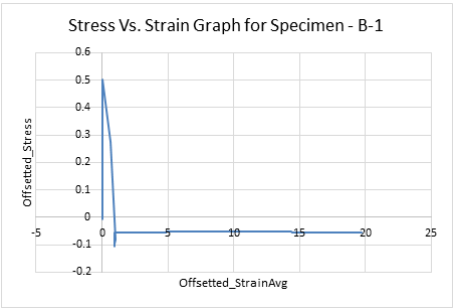

Figure B.311: Overall Stress Vs. Strain Graph for Specimen B-1

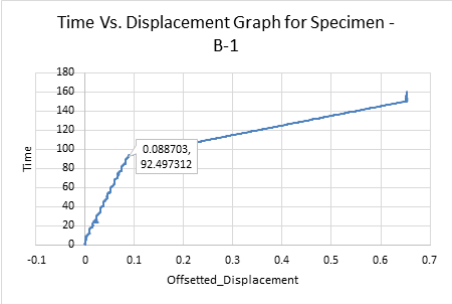

Figure B.312: Overall Time Vs. Displacement graph for Specimen B-1

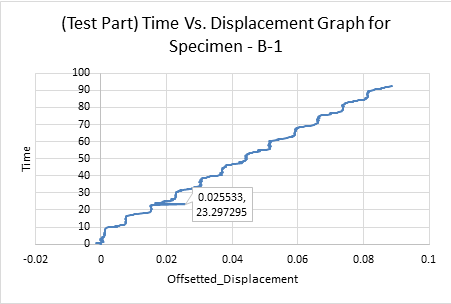

Figure B.313: First sampling Time Vs. Displacement graph for Specimen B-1

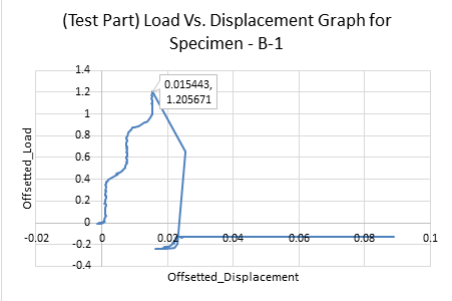

Figure B.314: First sampling Load Vs. Displacement graph for Specimen B-1

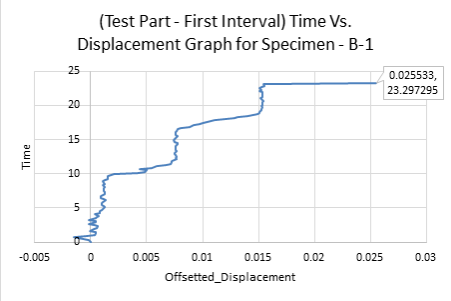

Figure B.315: Second sampling Time Vs. Displacement graph for Specimen B-1

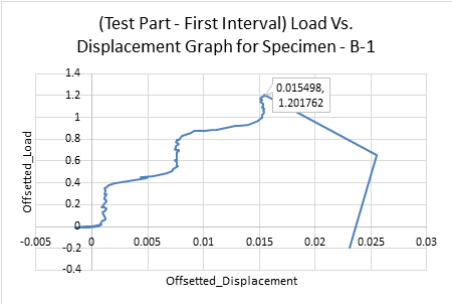

Figure B.316: Second sampling Load Vs. Displacement graph for Specimen B-1

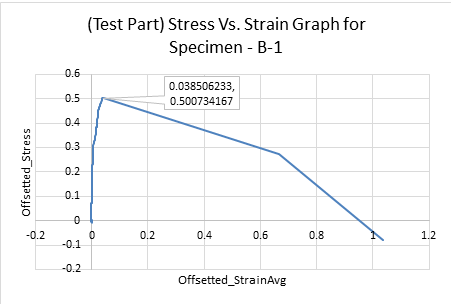

Figure B.317: Stress Vs. Strain Graph for the (second) sampled data for the Specimen B-1

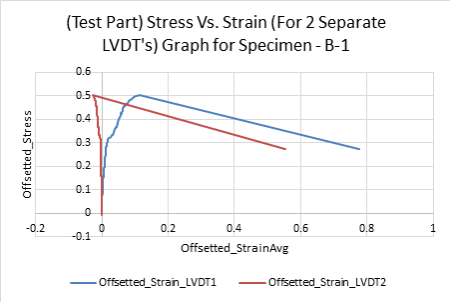

Figure B.318: Comparison graph of Stress Vs. Strain for 2 LVDT's for Specimen B-1

Specimen B-2

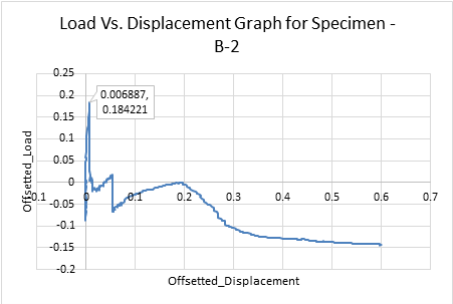

Figure B.319: Overall Load Vs. Displacement curve for Specimen B-2

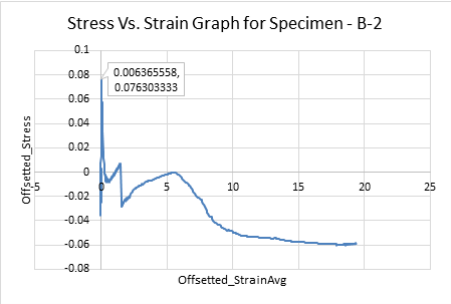

Figure B.320: Overall Stress Vs. Strain Graph for Specimen B-2

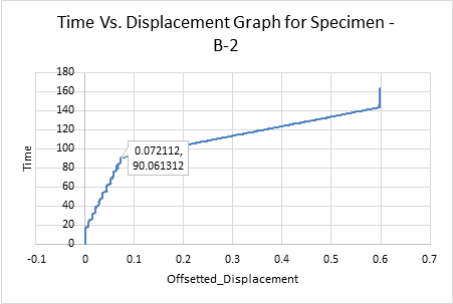

Figure B.321: Overall Time Vs. Displacement graph for Specimen B-2

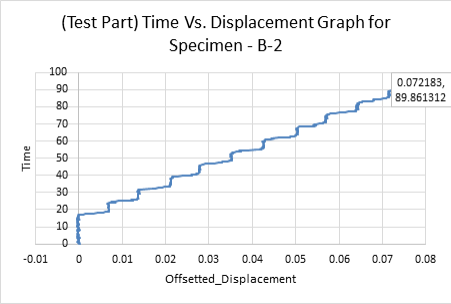

Figure B.322: First sampling Time Vs. Displacement graph for Specimen B-2

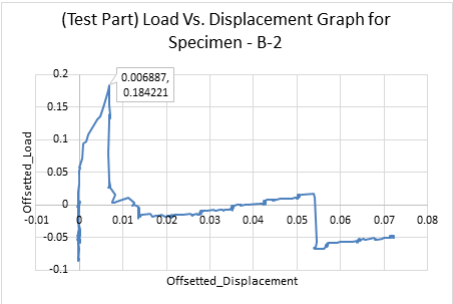

Figure B.323: Sampled Load Vs. Displacement graph for Specimen B-2

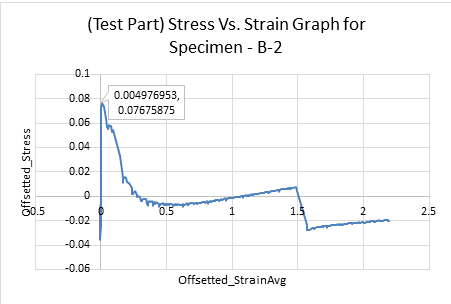

Figure B.324: Stress Vs. Strain Graph for the sampled data for Specimen B-2

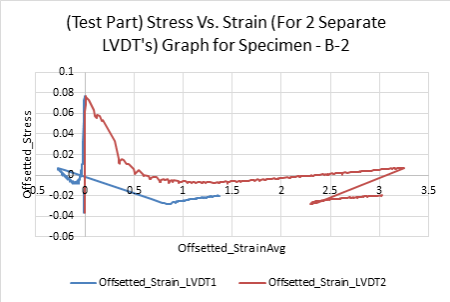

Figure B.325: Comparison graph of Stress Vs. Strain for 2 LVDT's for Specimen B-2

Specimen B-3

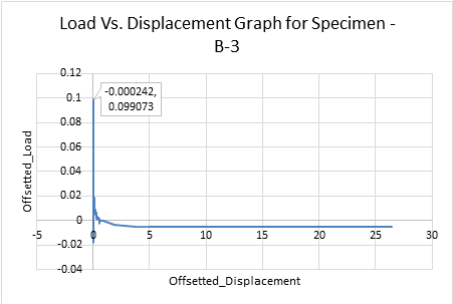

Figure B.326: Overall Load Vs. Displacement curve for Specimen B-3

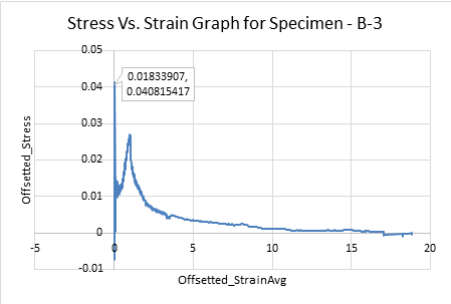

Figure B.327: Overall Stress Vs. Strain Graph for Specimen B-3

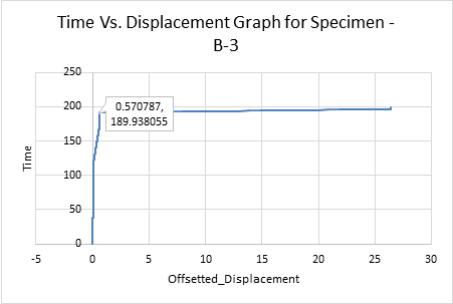

Figure B.328: Overall Time Vs. Displacement graph for Specimen B-3

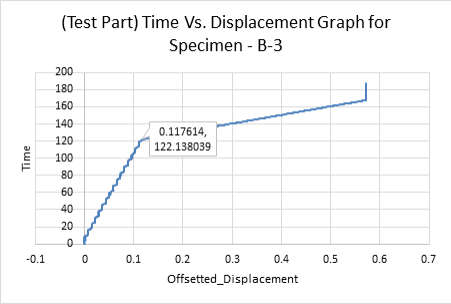

Figure B.329: First sampling Time Vs. Displacement graph for Specimen B-3

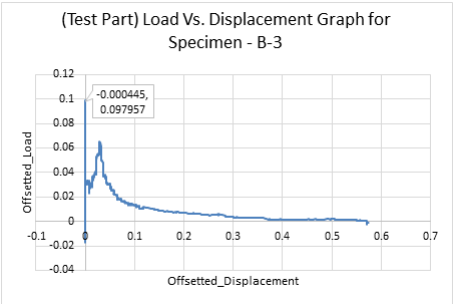

Figure B.330: First sampling Load Vs. Displacement graph for Specimen B-3

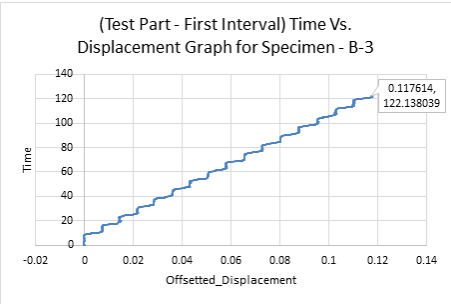

Figure B.331: Second sampling Time Vs. Displacement graph for Specimen B-3

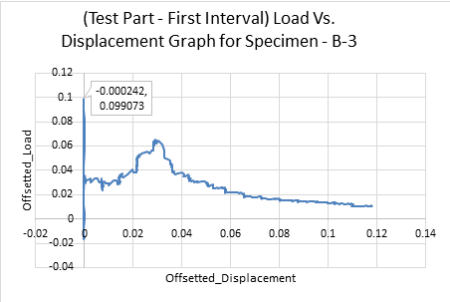

Figure B.332: Second sampling Load Vs. Displacement graph for Specimen B-3

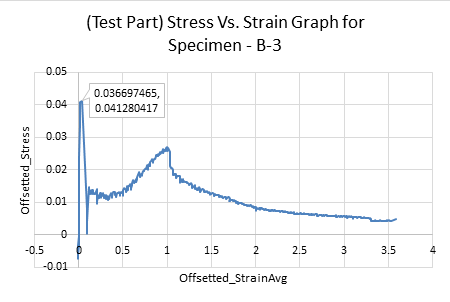

Figure B.333: Stress Vs. Strain Graph for the (second) sampled data for the Specimen B-3

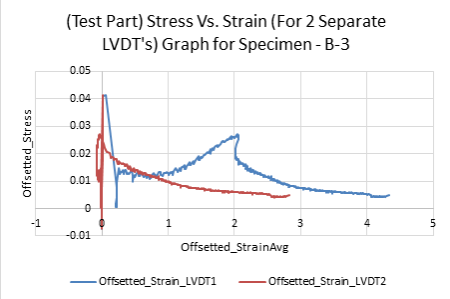

Figure B.334: Comparison graph of Stress Vs. Strain for 2 LVDT's for Specimen B-3

Specimen B-4

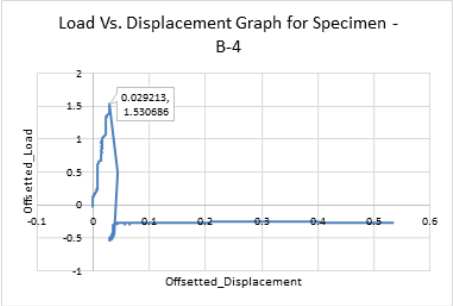

Figure B.335: Overall Load Vs. Displacement curve for Specimen B-4

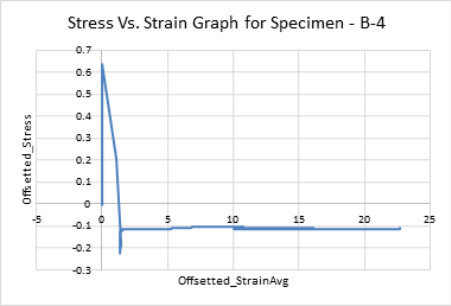

Figure B.336: Overall Stress Vs. Strain Graph for Specimen B-4

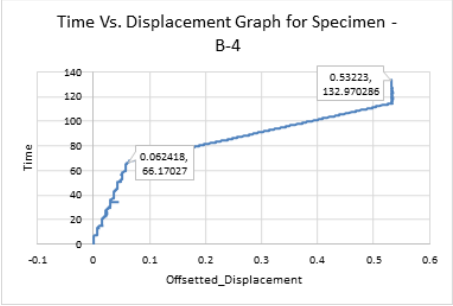

Figure B.337: Overall Time Vs. Displacement graph for Specimen B-4

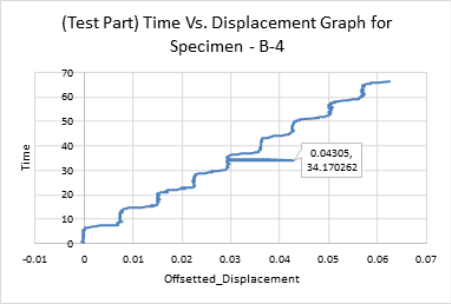

Figure B.338: First sampling Time Vs. Displacement graph for Specimen B-4

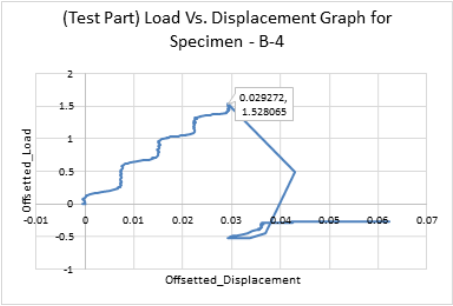

Figure B.339: First sampling Load Vs. Displacement graph for Specimen B-4

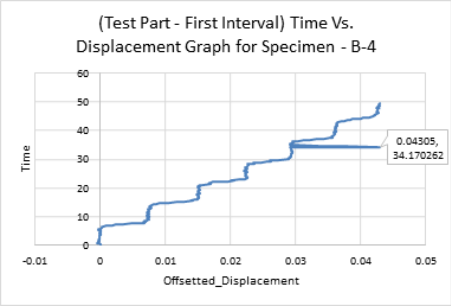

Figure B.340: Second sampling Time Vs. Displacement graph for Specimen B-4

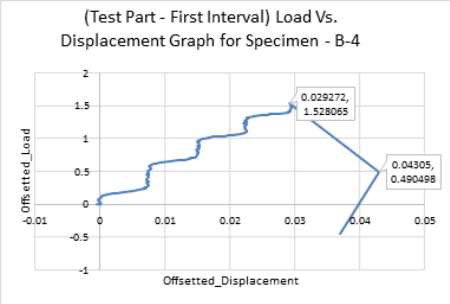

Figure B.341: Second sampling Load Vs. Displacement graph for Specimen B-4

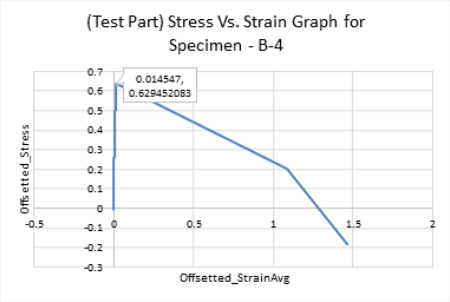

Figure B.342: Stress Vs. Strain Graph for the (second) sampled data for the Specimen B-4

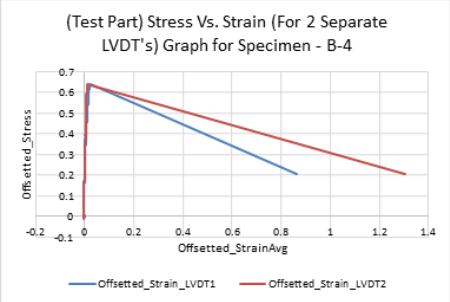

Figure B.343: Comparison graph of Stress Vs. Strain for 2 LVDT's for Specimen B-4

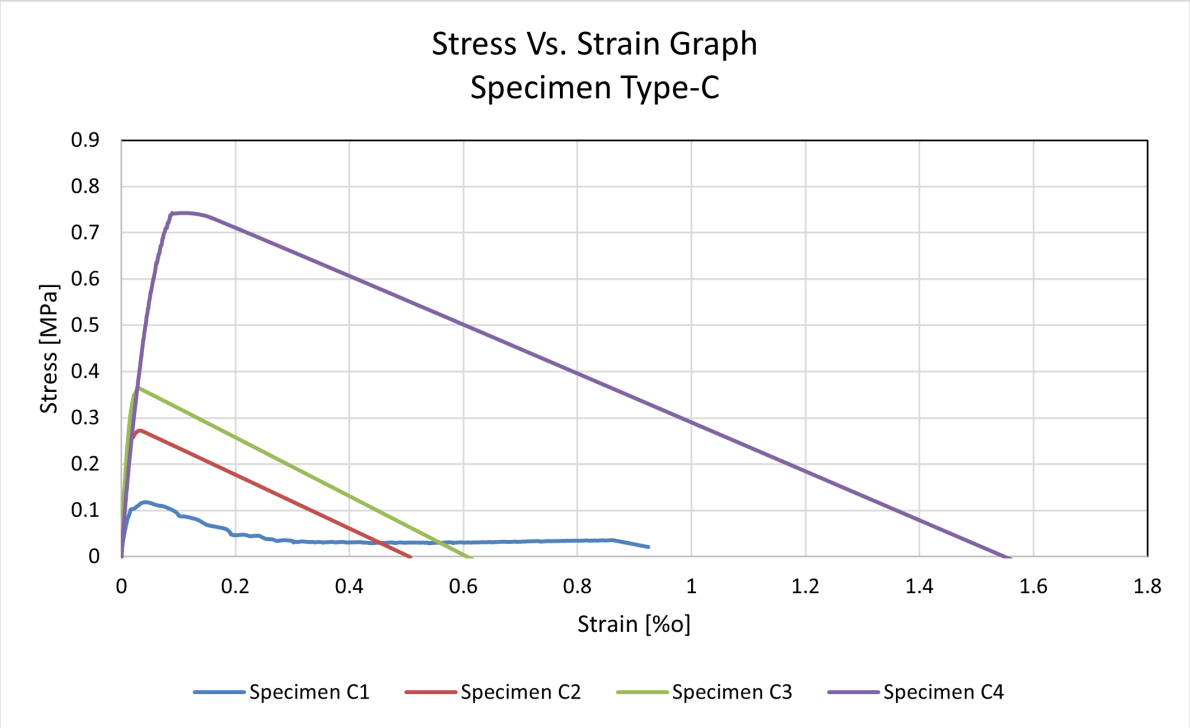

Figure B.344: Stress vs. Strain curve for Casted Specimen Type-C

Specimen C-1

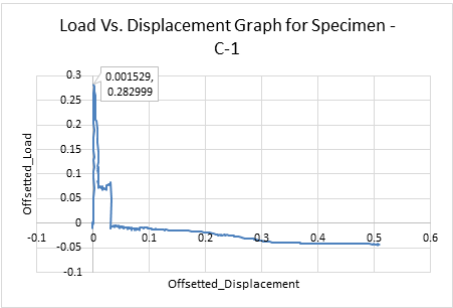

Figure B.345: Overall Load Vs. Displacement curve for Specimen C-1

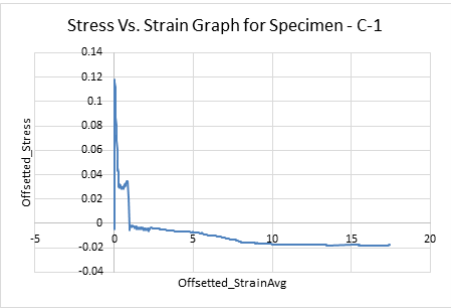

Figure B.346: Overall Stress Vs. Strain Graph for Specimen C-1

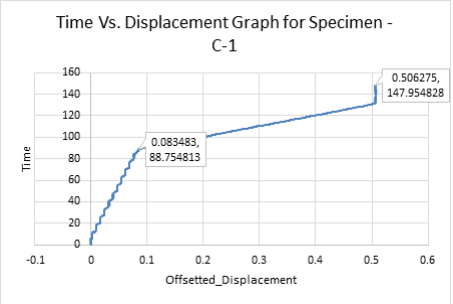

Figure B.347: Overall Time Vs. Displacement graph for Specimen C-1

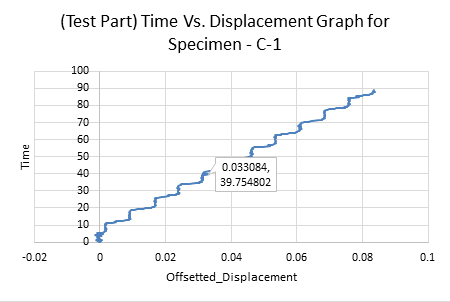

Figure B.348: First sampling Time Vs. Displacement graph for Specimen C-1

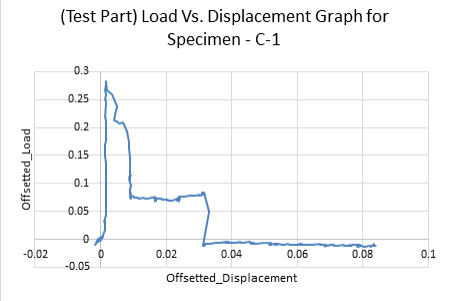

Figure B.349: First sampling Load Vs. Displacement graph for Specimen C-1

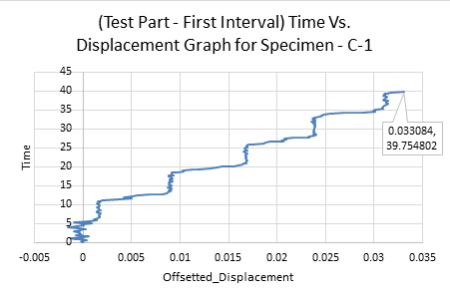

Figure B.350: Second sampling Time Vs. Displacement graph for Specimen C-1

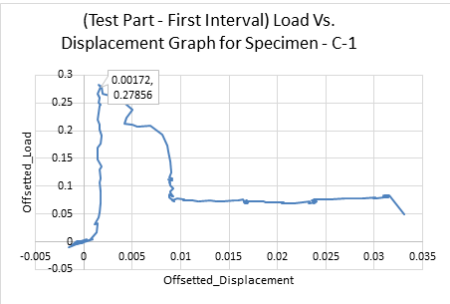

Figure B.351: Second sampling Load Vs. Displacement graph for Specimen C-1

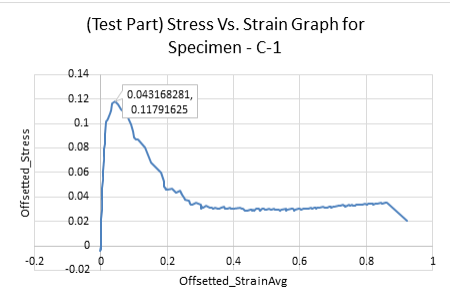

Figure B.352: Stress Vs. Strain Graph for the (second) sampled data for the Specimen C-1

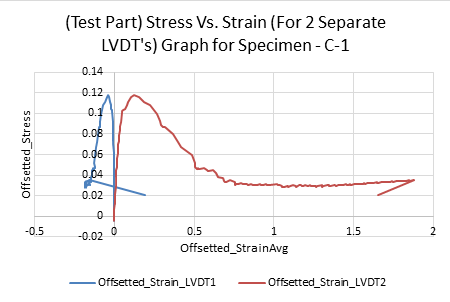

Figure B.353: Comparison graph of Stress Vs. Strain for 2 LVDT's for Specimen C-1

Specimen C-2

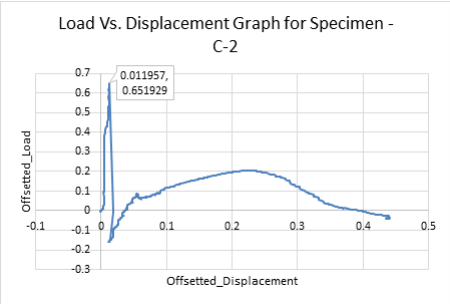

Figure B.354: Overall Load Vs. Displacement curve for Specimen C-2

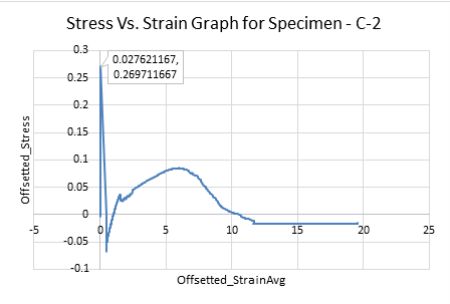

Figure B.355: Overall Stress Vs. Strain Graph for Specimen C-2

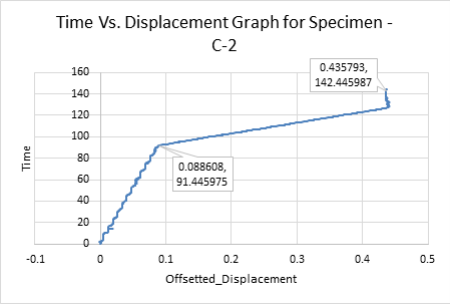

Figure B.356: Overall Time Vs. Displacement graph for Specimen C-2

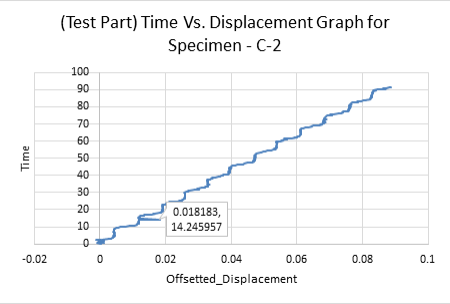

Figure B.357: First sampling Time Vs. Displacement graph for Specimen C-2

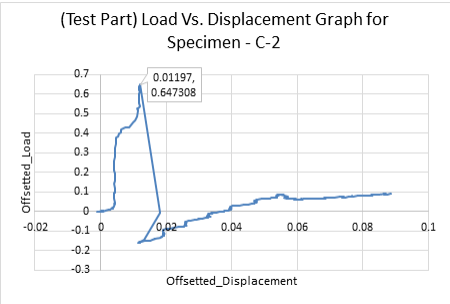

Figure B.358: First sampling Load Vs. Displacement graph for Specimen C-2

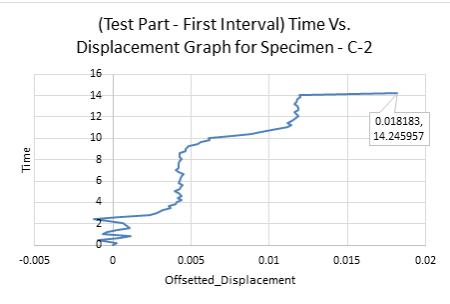

Figure B.359: Second sampling Time Vs. Displacement graph for Specimen C-2

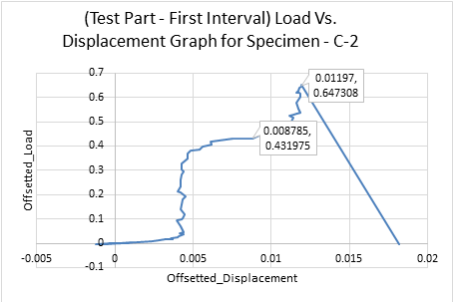

Figure B.360: Second sampling Load Vs. Displacement graph for Specimen C-2

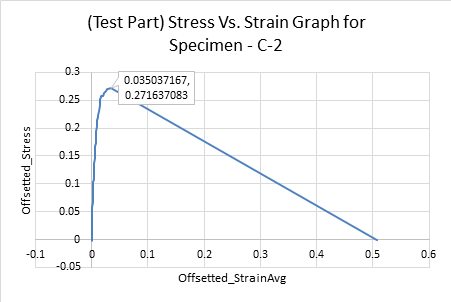

Figure B.361: Stress Vs. Strain Graph for the (second) sampled data for the Specimen C-2

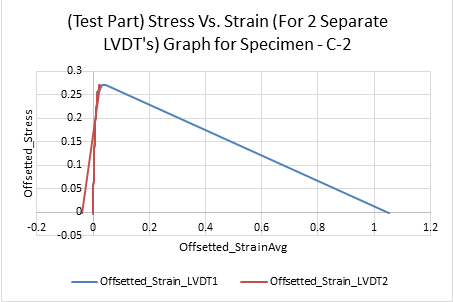

Figure B.362: Comparison graph of Stress Vs. Strain for 2 LVDT's for Specimen C-2

Specimen C-3

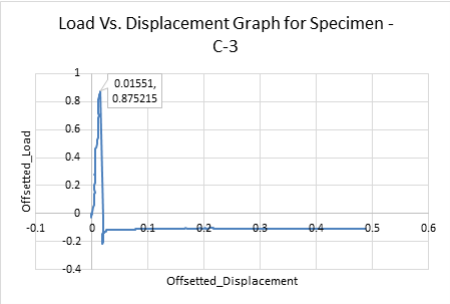

Figure B.363: Overall Load Vs. Displacement curve for Specimen C-3

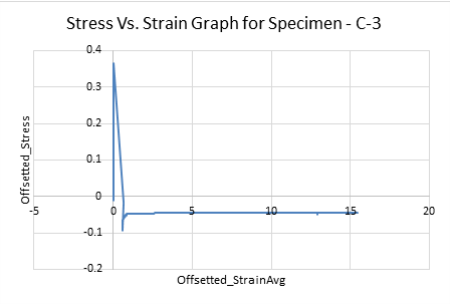

Figure B.364: Overall Stress Vs. Strain Graph for Specimen C-3

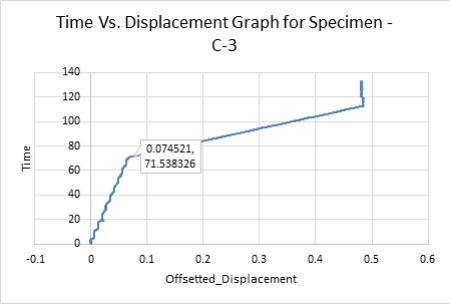

Figure B.365: Overall Time Vs. Displacement graph for Specimen C-3

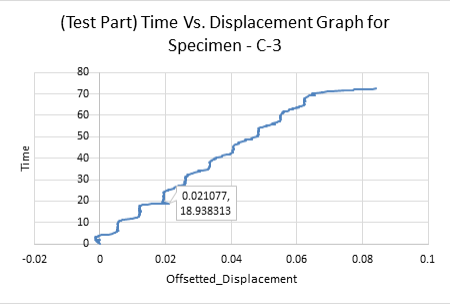

Figure B.366: First sampling Time Vs. Displacement graph for Specimen C-3

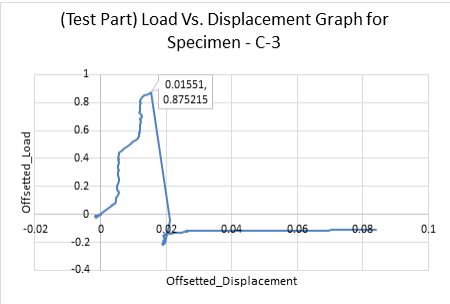

Figure B.367: First sampling Load Vs. Displacement graph for Specimen C-3

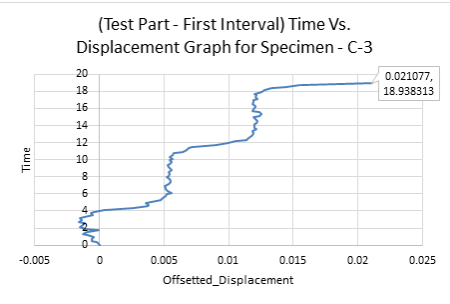

Figure B.368: Second sampling Time Vs. Displacement graph for Specimen C-3

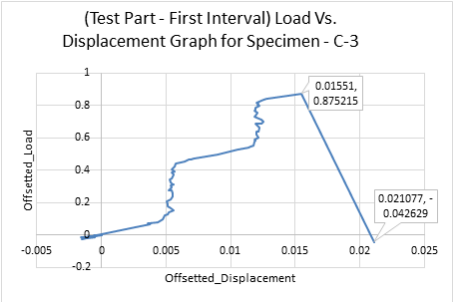

Figure B.369: Second sampling Load Vs. Displacement graph for Specimen C-3

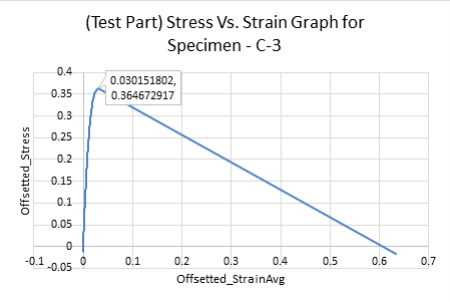

Figure B.370: Stress Vs. Strain Graph for the (second) sampled data for the Specimen C-3

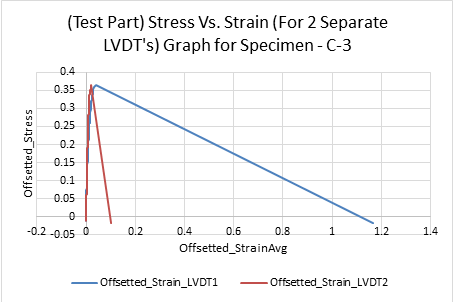

Figure B.371: Comparison graph of Stress Vs. Strain for 2 LVDT's for Specimen C-3

Specimen C-4

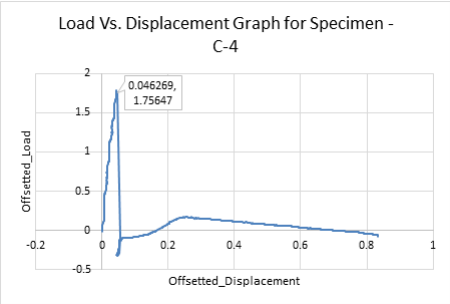

Figure B.372: Overall Load Vs. Displacement curve for Specimen C-4

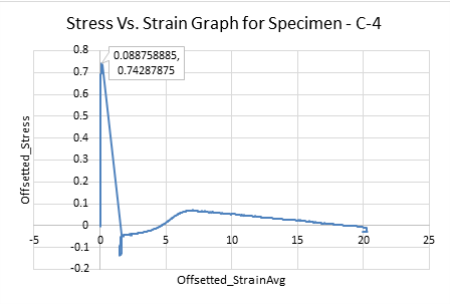

Figure B.373: Overall Stress Vs. Strain Graph for Specimen C-4

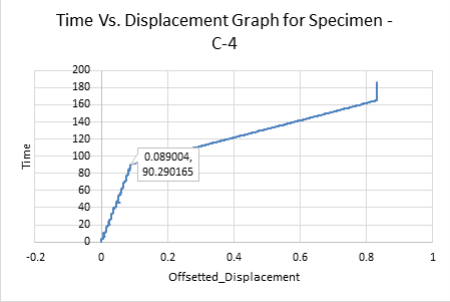

Figure B.374: Overall Time Vs. Displacement graph for Specimen C-4

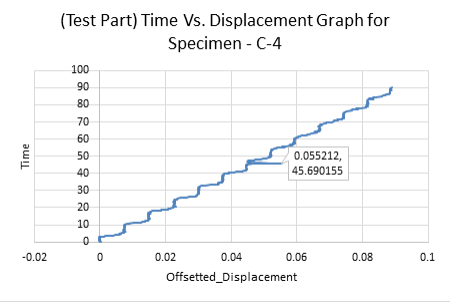

Figure B.375: First sampling Time Vs. Displacement graph for Specimen C-4

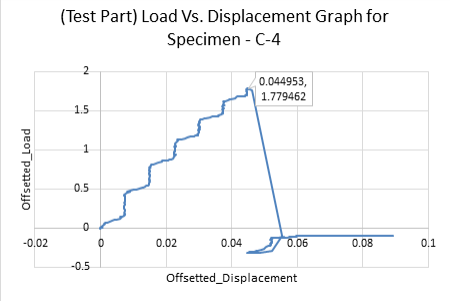

Figure B.376: First sampling Load Vs. Displacement graph for Specimen C-4

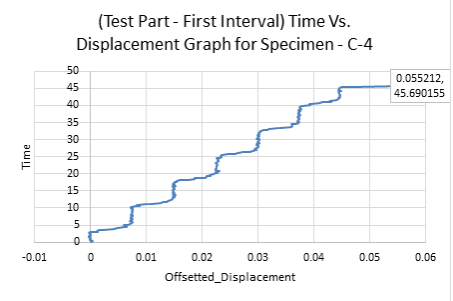

Figure B.377: Second sampling Time Vs. Displacement graph for Specimen C-4

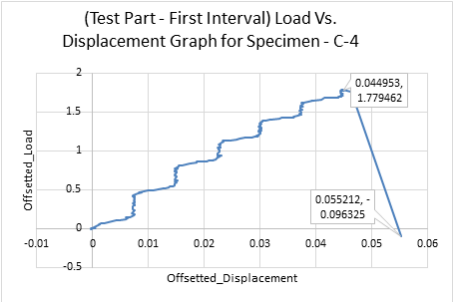

Figure B.378: Second sampling Load Vs. Displacement graph for Specimen C-4

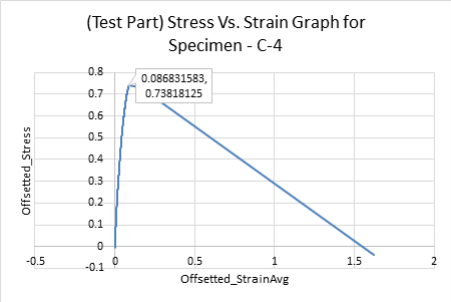

Figure B.379: Stress Vs. Strain Graph for the (second) sampled data for the Specimen C-4

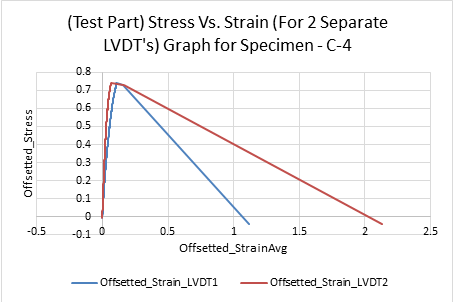

Figure B.380: Comparison graph of Stress Vs. Strain for 2 LVDT's for Specimen C-4

C

Appendix-C

C.1. Images of failed specimens post Inter-layer Bond Test

C.1.1. Failed specimens from Caulk-gun extrusion

Specimen Type-A

***Missing Images of Specimen: TG5-A-1*

Figure C.1: Specimen TG5-A-2 after failure

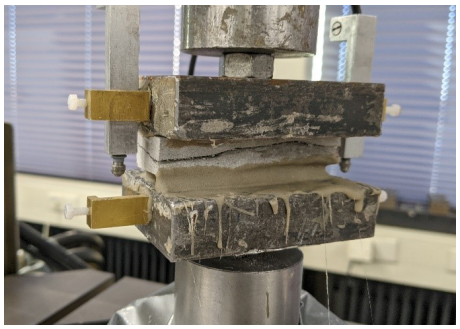

Figure C.2: Specimen TG5-A-3 after failure

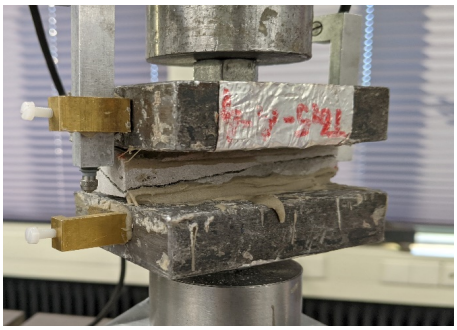

Figure C.3: Specimen TG5-A-4 after failure

Figure C.4: Specimen TG10-A-3 after failure

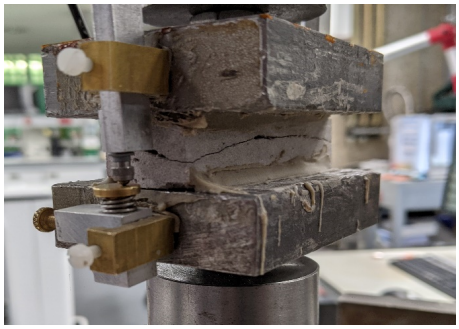

Figure C.5: Specimen TG10-A-2 after failure

Figure C.6: Specimen TG10-A-3 after failure

Figure C.7: Specimen TG10-A-4 after failure

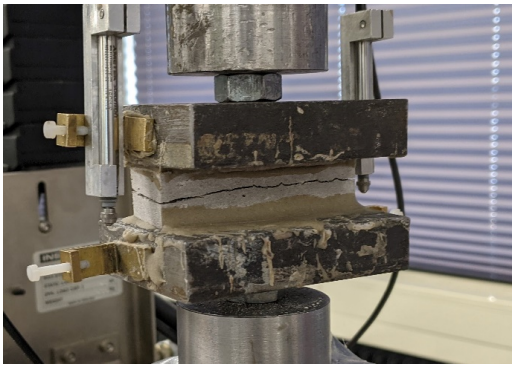

Figure C.8: Specimen TG20-A-1 after failure

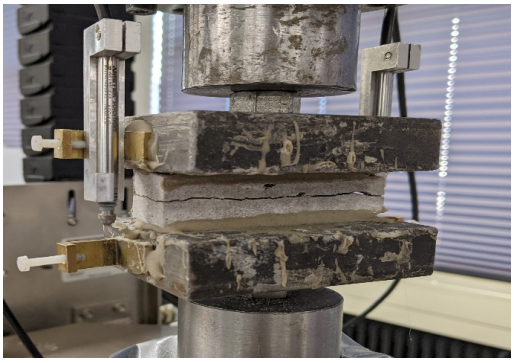

Figure C.9: Specimen TG20-A-2 after failure

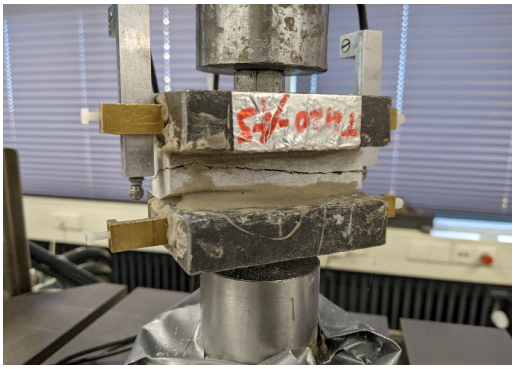

Figure C.10: Specimen TG20-A-3 after failure

Figure C.11: Specimen TG20-A-4 after failure

Specimen Type-B

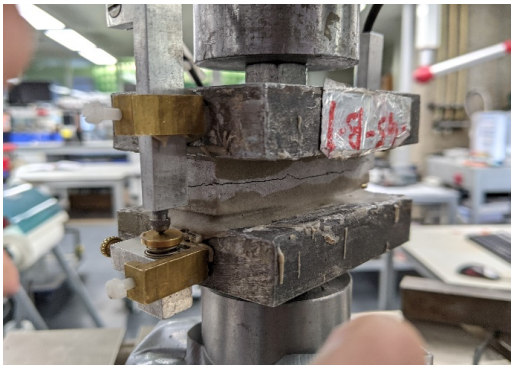

Figure C.12: Specimen TG5-B-1 after failure

Figure C.13: Specimen TG5-B-2 after failure

Figure C.14: Specimen TG5-B-3 after failure

Figure C.15: Specimen TG5-B-4 after failure

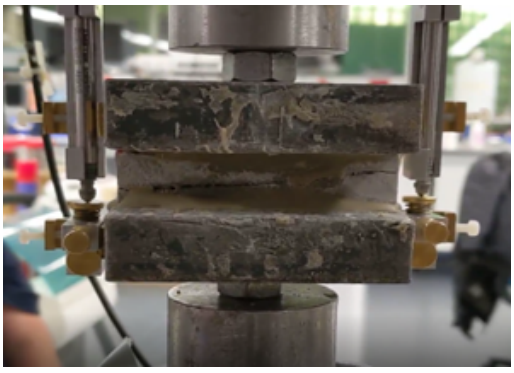

Figure C.16: Specimen TG10-B-1 after failure

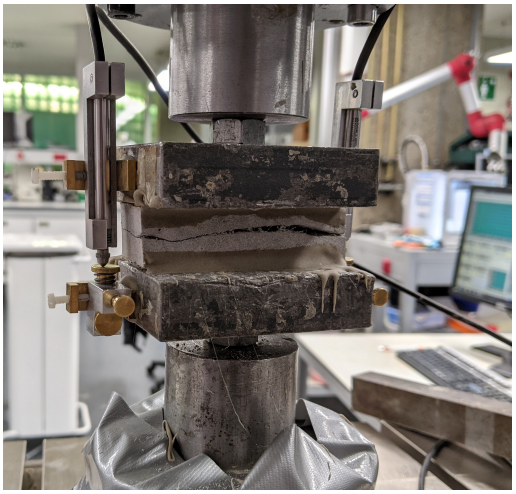

Figure C.17: Specimen TG10-B-2 after failure

Figure C.18: Specimen TG10-B-3 after failure

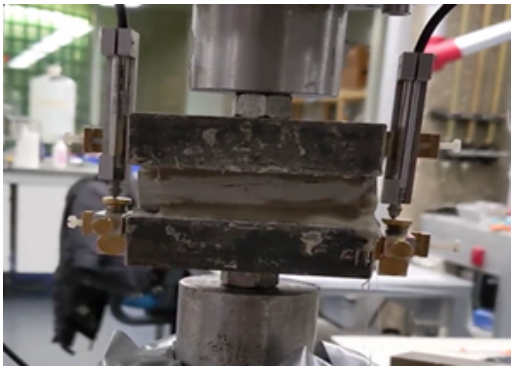

Figure C.19: Specimen TG10-B-4 after failure

Figure C.20: Specimen TG20-B-1 after failure

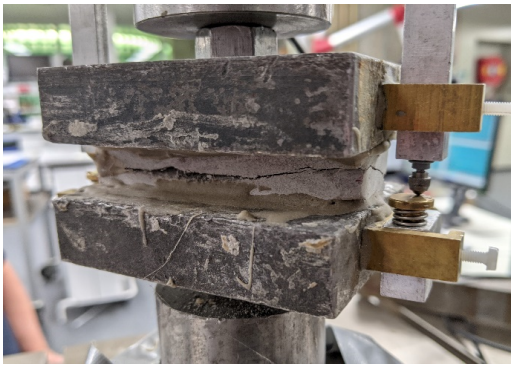

Figure C.21: Specimen TG20-B-2 after failure

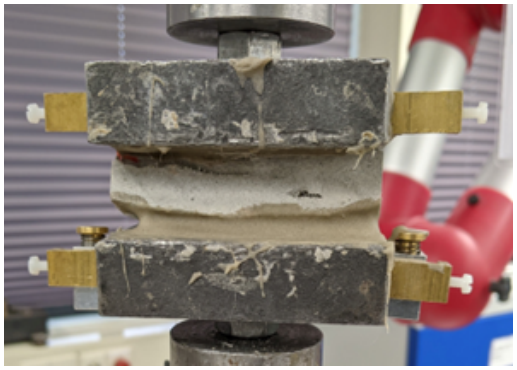

Figure C.22: Specimen TG20-B-3 after failure

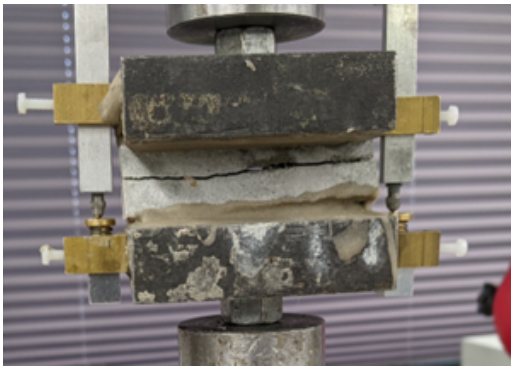

Figure C.23: Specimen TG20-B-4 after failure

Specimen Type-C

***Missing Images of Specimen: TG10-C-1, TG10-C-4 and TG20-C-3*

Figure C.24: Specimen TG5-C-1 after failure

Figure C.25: Specimen TG5-C-2 after failure

Figure C.26: Specimen TG5-C-3 after failure

Figure C.27: Specimen TG5-C-4 after failure

Figure C.28: Specimen TG10-C-2 after failure

Figure C.29: Specimen TG10-C-3 after failure

Figure C.30: Specimen TG20-C-1 after failure

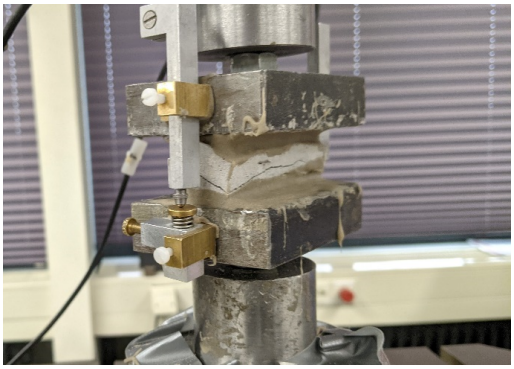

Figure C.31: Specimen TG20-C-2 after failure

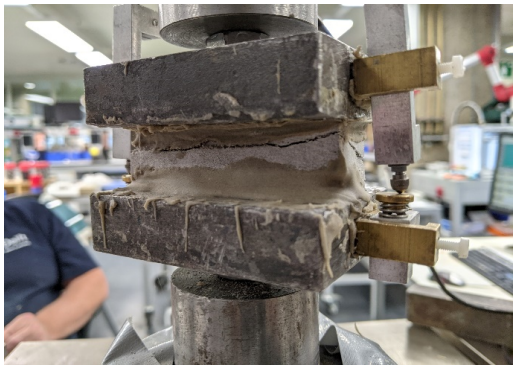

Figure C.32: Specimen TG20-C-4 after failure

C.1.2. Failed specimens from Casting method

Casted Specimen Type-A

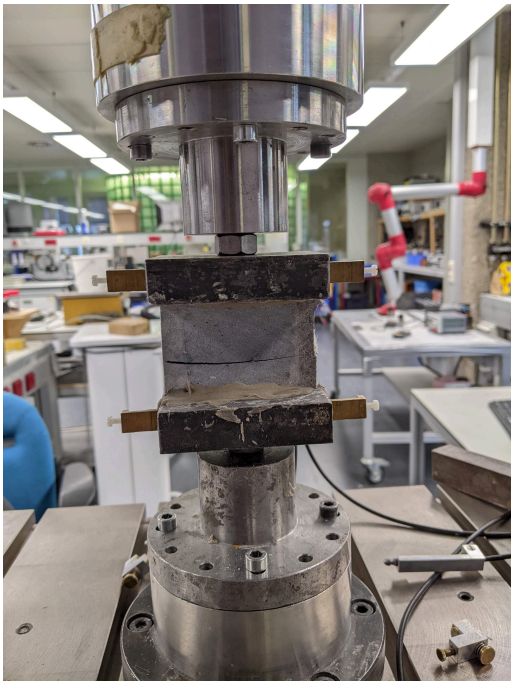

Figure C.33: Casted Specimen A-1 after failure

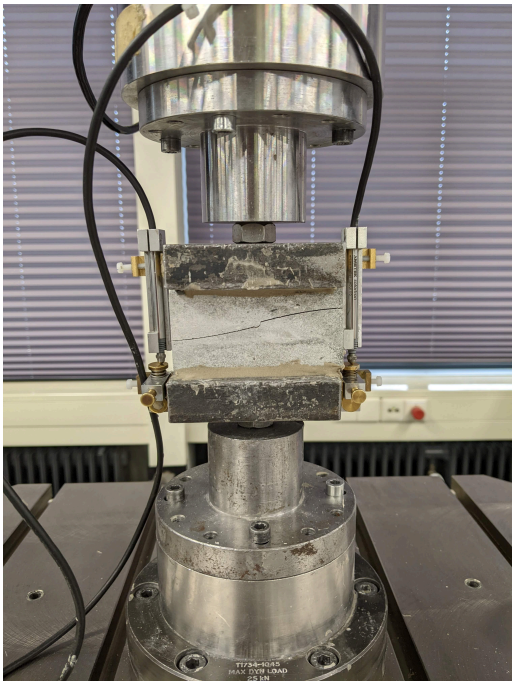

Figure C.34: Casted Specimen A-2 after failure

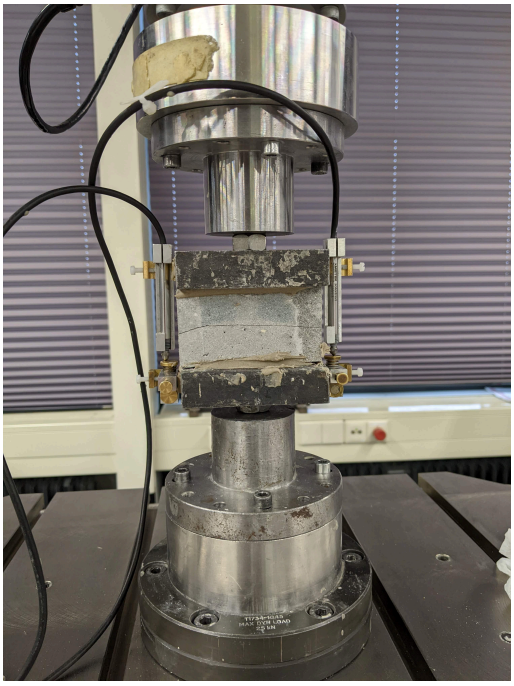

Figure C.35: Casted Specimen A-3 after failure

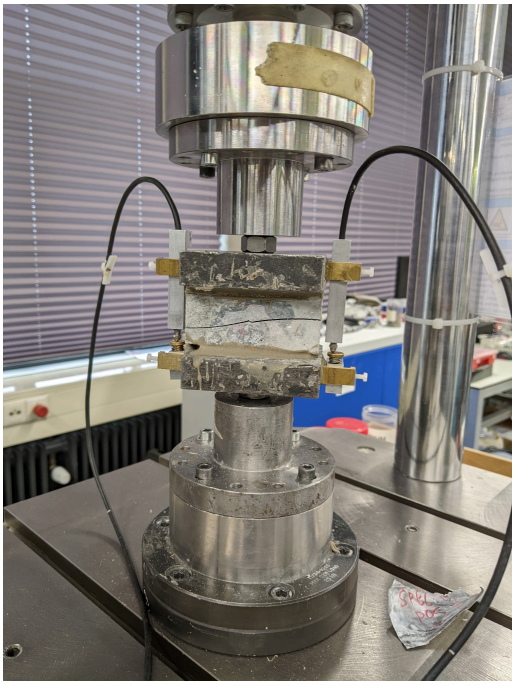

Figure C.36: Casted Specimen A-4 after failure

Casted Specimen Type-B

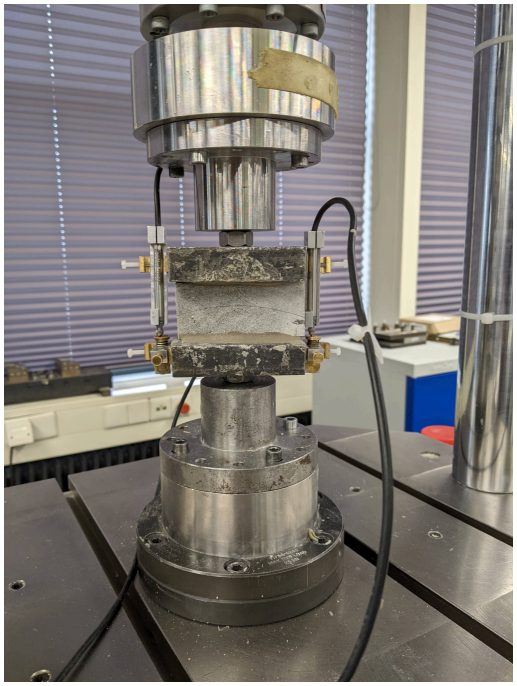

Figure C.37: Casted Specimen B-1 after failure

Figure C.38: Casted Specimen B-2 after failure

Figure C.39: Casted Specimen B-3 after failure

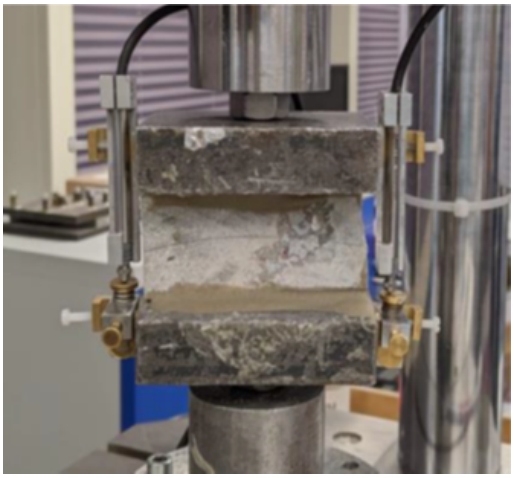

Figure C.40: Casted Specimen B-4 after failure

Casted Specimen Type-C

Figure C.41: Casted Specimen C-1 after failure

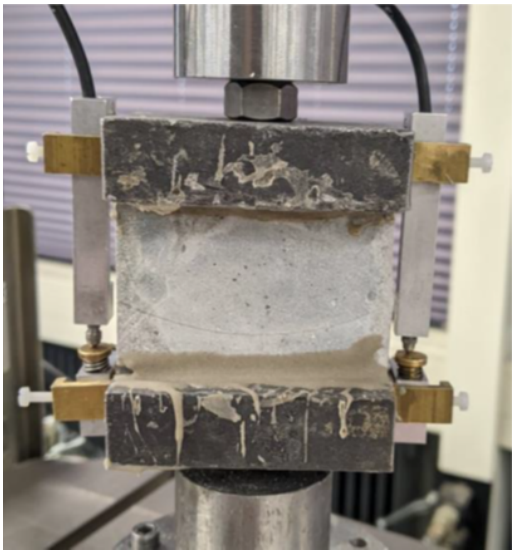

Figure C.42: Casted Specimen C-2 after failure

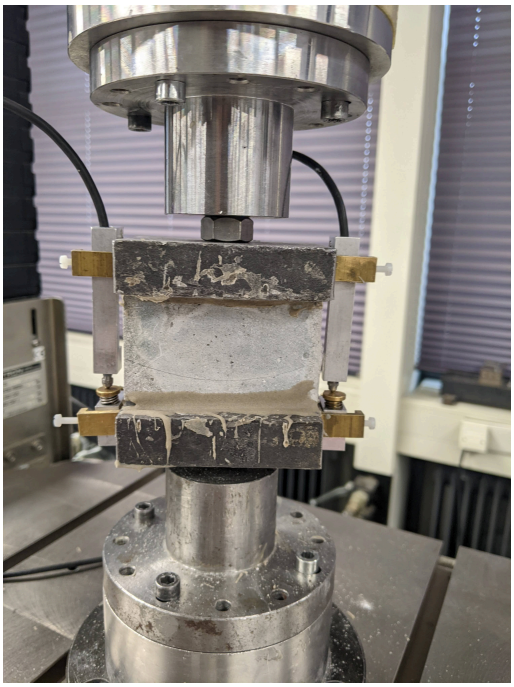

Figure C.43: Casted Specimen C-3 after failure

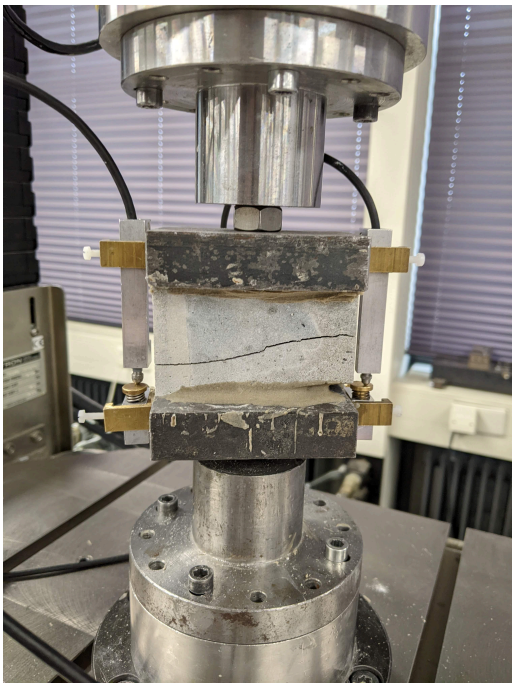

Figure C.44: Casted Specimen C-4 after failure

D

Appendix-D

D.1. Images analysis of Inter-layer surface of failed specimens

D.1.1. Specimen Type-A

***Missing Images of Specimen: TG5-A-1*

Summary of Image Analysis for Specimen TG5-A-2

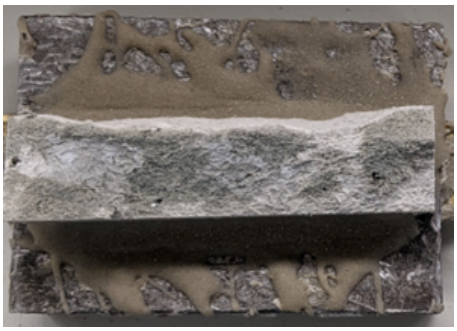

Figure D.1: Bottom debonded part of Specimen TG5-A-2

Figure D.2: Top debonded part of Specimen TG5-A-2

Table D.1: Summary of Image analysis result for specimen TG5-A-2

Contact Type	Colour Cluster	Results of Image analysis		Contact (%)		Average Contact (in %)
		Bottom Debonded Layer	Top Debonded Layer	Bottom Debonded Layer	Top Debonded Layer	
						
Poor				44,50%	41,68%	**43,09%**
Good				55,75%	58,32%	**57,04%**

Detailed report - Bottom debonded part of Specimen TG5-A-2

IMAGE COLOR SUMMARIZER

RGB, HSV, LCH & Lab image color statistics and clustering—simple and easy

HOME ANALYZE EXAMPLES API DOWNLOAD FAQ NEWS

IMAGE COLOR SUMMARY

THE IMAGE IN WORDS

aluminium blast cloudy dark double dove gauntlet grey light masala medium quarter quick rakaia silver stack stonehenge tarmac traffic

COLOR CLUSTERS

Colors in the image were clustered into 2 groups (k-means). The average color of the colors for each cluster is shown. The name is the closest named color and its distance is shown using ΔE. The tags are the set of words formed by all named neighbours within ΔE ≤ 5. The list of words above is the set of all unique words in this set of words.

Cluster colors, sized by number of pixels:

cluster	pixels	name	HEX	RGB	HSV	LCH	Lab	tags
	52.46%	169,165,165 double rakaia ΔE=0.8	#A9A4A2	169 164 162	18 4 66	68 2 51	68 1 2	medium light dark cloudy double quarter quick rakaia silver stonehenge grey
	47.54%	113,110,107 blast grey ΔE=0.6	#73706D	115 112 109	28 5 45	47 2 71	47 1 2	aluminium blast double dove gauntlet masala quarter stack tarmac traffic grey

IMAGE CLUSTER PARTITIONS

Pixels of the image assigned to each cluster. The border is the color of the cluster as calculated by the average value of its pixels.

RGB HISTOGRAM

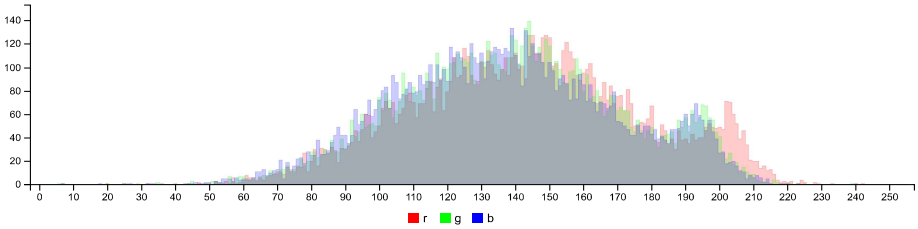

HSV HISTOGRAMS

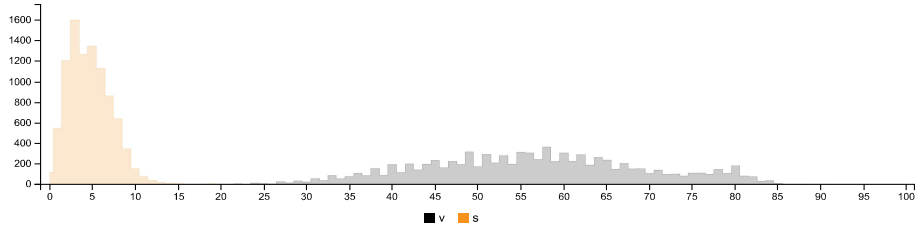

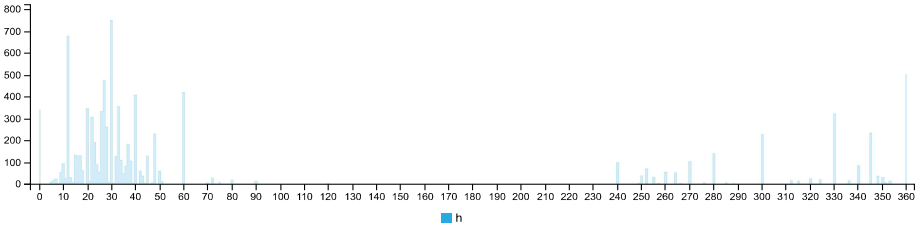

LCH HISTOGRAMS

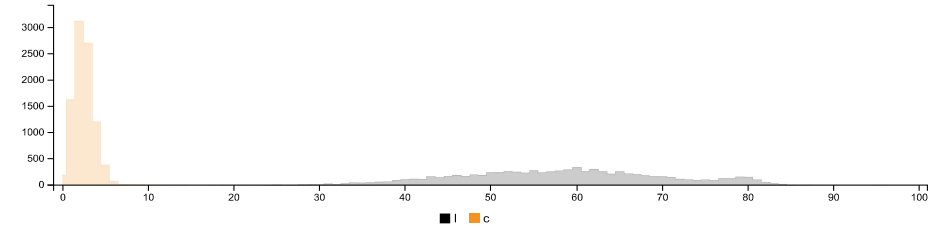

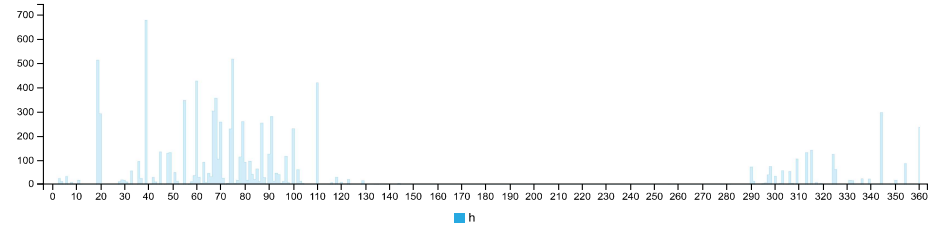

LAB HISTOGRAMS

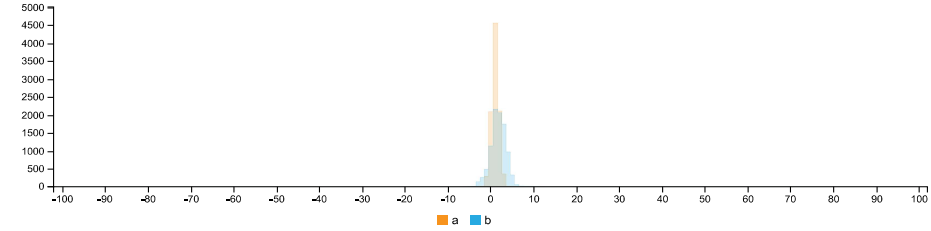

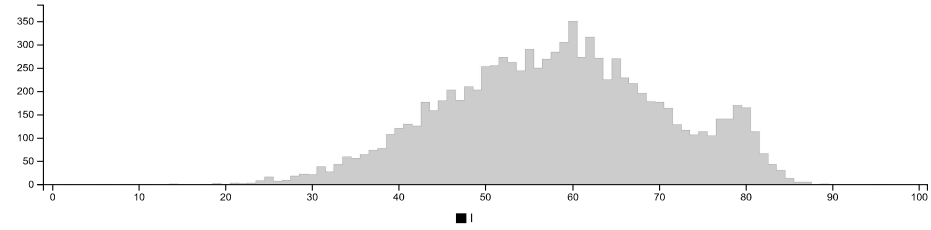

COLOR SPACE AND CHANNEL STATISTICS

	avg	med	min	max
RGB:R	144	144	7	242
RGB:G	140	139	6	239
RGB:B	137	136	7	240
HSV:H	15 1.00	32	0	360
HSV:S	5	4	0	32
HSV:V	56	56	3	95
LCH:L	58	58	2	95
LCH:C	3	2	0	12
LCH:H	51 1.00	75	2	360
LAB:L	58	58	2	95
LAB:A	1	1	-2	4
LAB:B	2	2	-6	12

Detailed report - Top debonded part of Specimen TG5-A-2

IMAGE COLOR SUMMARIZER

RGB, HSV, LCH & Lab image color statistics and clustering—simple and easy

HOME ANALYZE EXAMPLES API DOWNLOAD FAQ NEWS

IMAGE COLOR SUMMARY

THE IMAGE IN WORDS

ajay aluminium bombay chicago concord concrete delta detroit dove eighth fantail friar grey half industrial mist mountain nobel sidewinder silver tapa triple

COLOR CLUSTERS

Colors in the image were clustered into 2 groups (k-means). The average color of the colors for each cluster is shown. The name is the closest named color and its distance is shown using ΔE. The tags are the set of words formed by all named neighbours within ΔE ≤ 5. The list of words above is the set of all unique words in this set of words.

Cluster colors, sized by number of pixels:

cluster	pixels	name	HEX	RGB	HSV	LCH	Lab	tags
	53.90%	183,177,177 nobel ΔE=1.4	#B5AFAD	181 175 173	19 5 71	72 3 54	72 2 2	ajay bombay concrete eighth fantail half mist mountain nobel sidewinder triple grey
	46.10%	123,120,116 tapa ΔE=0.9	#7C7874	124 120 116	29 6 49	51 3 74	51 1 2	aluminium chicago concord delta detroit dove friar half industrial silver tapa triple grey

IMAGE CLUSTER PARTITIONS

Pixels of the image assigned to each cluster. The border is the color of the cluster as calculated by the average value of its pixels.

RGB HISTOGRAM

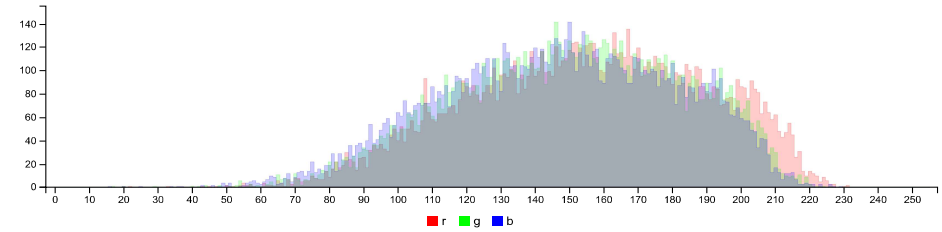

HSV HISTOGRAMS

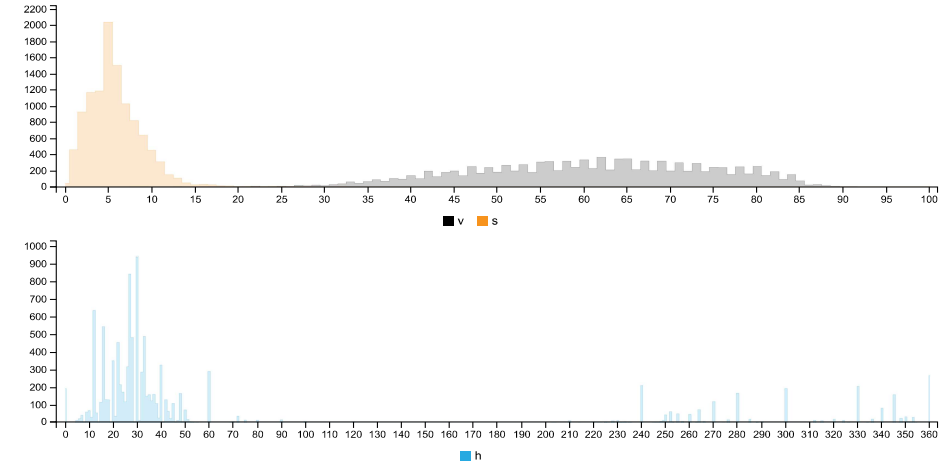

LCH HISTOGRAMS

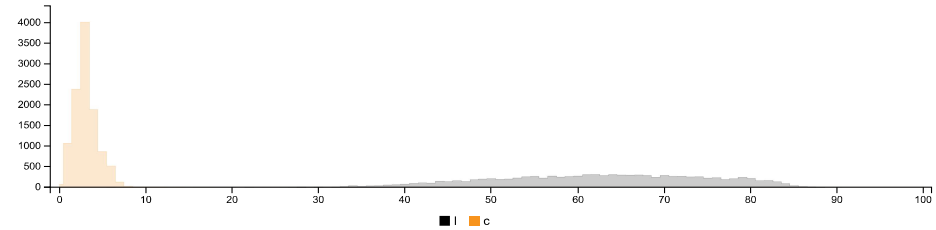

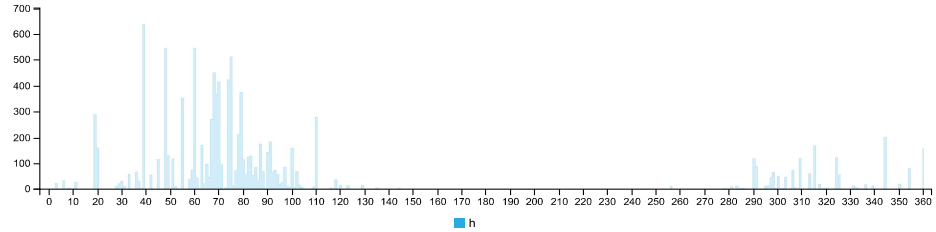

LAB HISTOGRAMS

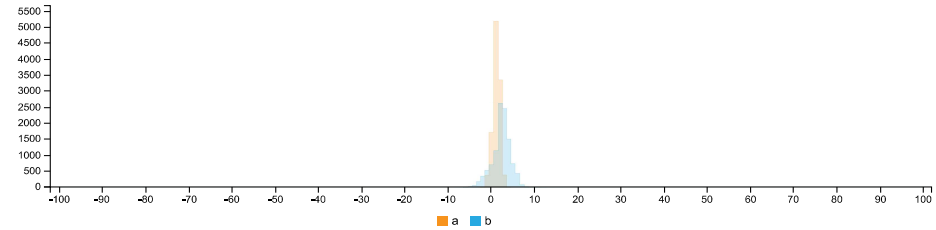

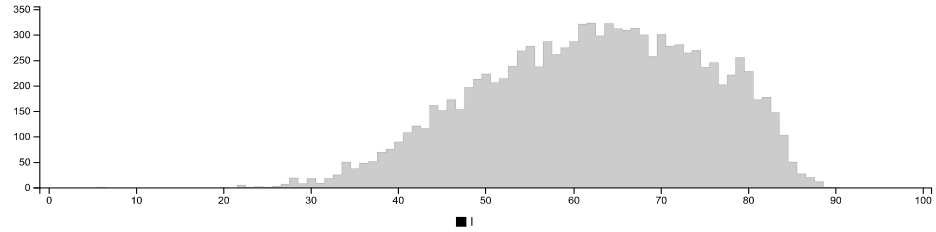

COLOR SPACE AND CHANNEL STATISTICS

	avg	med	min	max
RGB:R	155	156	20	231
RGB:G	150	151	17	226
RGB:B	147	148	16	229
HSV:H	18 1.00	30	0	360
HSV:S	6	5	0	32
HSV:V	61	62	8	91
LCH:L	62	63	6	90
LCH:C	3	3	0	17
LCH:H	56 1.00	74	2	360
LAB:L	62	63	6	90
LAB:A	1	1	-2	4
LAB:B	2	2	-8	16

Summary of Image Analysis for Specimen TG5-A-3

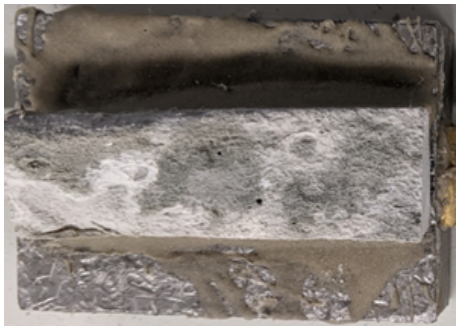

Figure D.3: Bottom debonded part of Specimen TG5-A-3

Figure D.4: Top debonded part of Specimen TG5-A-3

Table D.2: Summary of Image analysis result for specimen TG5-A-3

Contact Type	Colour Cluster	Results of Image analysis		Contact (%)		Average Contact (in %)
		Bottom Debonded Layer	Top Debonded Layer	Bottom Debonded Layer	Top Debonded Layer	
		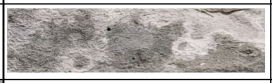				
Poor				45,80%	49,64%	**47,72%**
Good				54,20%	50,36%	**52,28%**

Detailed report - Bottom debonded part of Specimen TG5-A-3

IMAGE COLOR SUMMARIZER

RGB, HSV, LCH & Lab image color statistics and clustering—simple and easy

HOME ANALYZE EXAMPLES API DOWNLOAD FAQ NEWS

IMAGE COLOR SUMMARY

THE IMAGE IN WORDS

battleship cotton dover eighth friar grey imagine jumbo masala natural old pale pink quarter rakaia rust schooner seashell seed silver slate steel stonehenge swan tide white

COLOR CLUSTERS

Colors in the image were clustered into 2 groups (k-means). The average color of the colors for each cluster is shown. The name is the closest named color and its distance is shown using ΔE. The tags are the set of words formed by all named neighbours within ΔE ≤ 5. The list of words above is the set of all unique words in this set of words.

Cluster colors, sized by number of pixels:

cluster	pixels	name	HEX	RGB	HSV	LCH	Lab	tags
	54.20%	139,134,130 seashell ΔE=0.7	#89847F	137 132 127	27 7 54	55 3 70	55 1 3	battleship eighth friar jumbo masala natural old schooner seashell silver steel grey
	45.80%	195,190,187 pale slate ΔE=1.7	#C0B9B6	192 185 182	19 6 75	76 3 52	76 2 3	pale slate cotton dover eighth imagine quarter rakaia rust seed silver stonehenge swan tide pink white

IMAGE CLUSTER PARTITIONS

Pixels of the image assigned to each cluster. The border is the color of the cluster as calculated by the average value of its pixels.

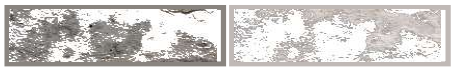

RGB HISTOGRAM

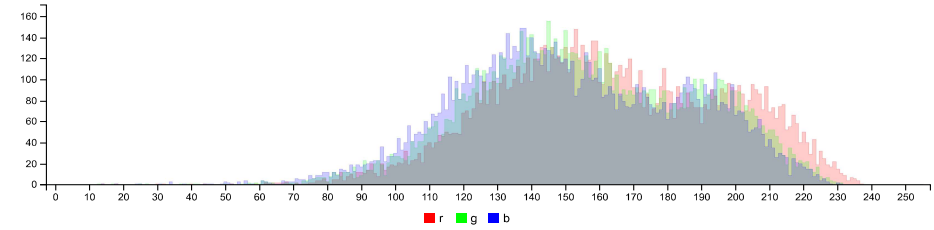

HSV HISTOGRAMS

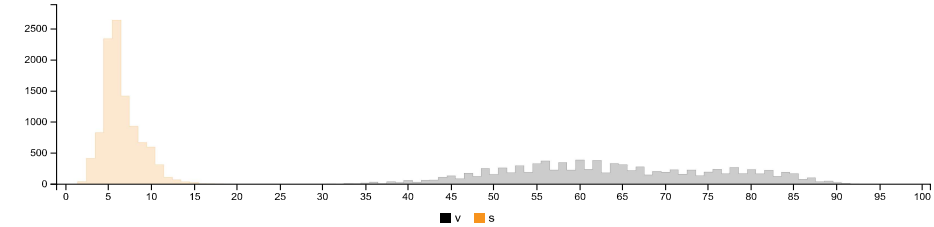

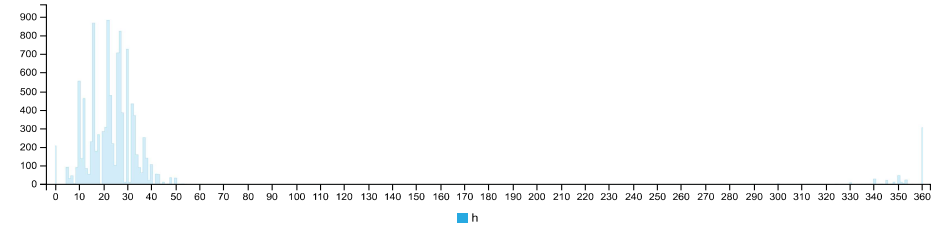

LCH HISTOGRAMS

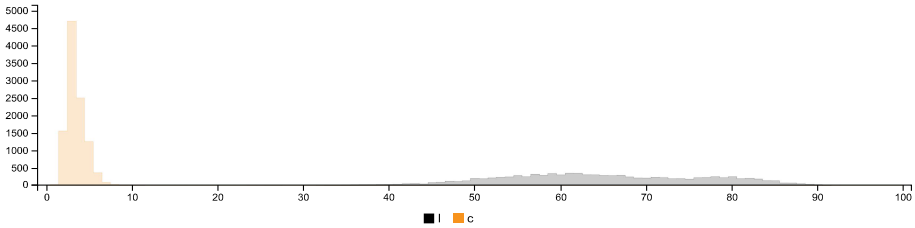

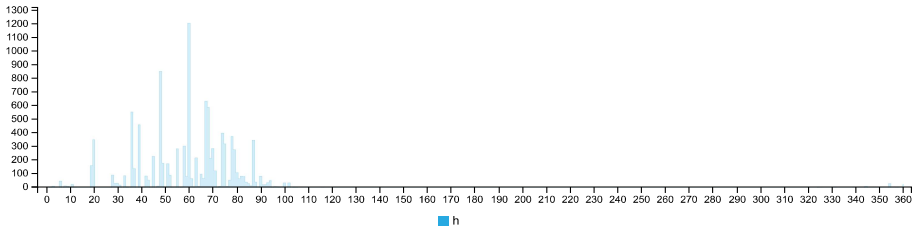

LAB HISTOGRAMS

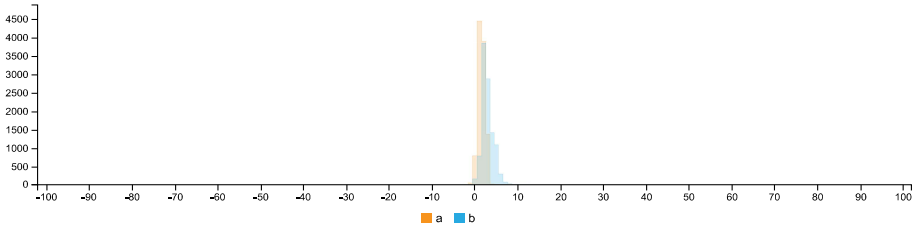

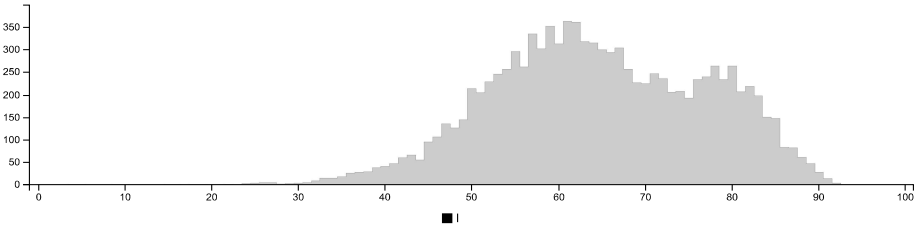

COLOR SPACE AND CHANNEL STATISTICS

	avg	med	min	max
RGB:R	163	160	14	237
RGB:G	156	154	13	231
RGB:B	152	150	14	231
HSV:H	21 1.00	24	0	360
HSV:S	7	6	1	45
HSV:V	64	63	5	93
LCH:L	65	64	4	92
LCH:C	4	3	1	13
LCH:H	58 1.00	60	2	360
LAB:L	65	64	4	92
LAB:A	2	2	-2	7
LAB:B	3	3	-3	12

Detailed report - Top debonded part of Specimen TG5-A-3

IMAGE COLOR SUMMARIZER

RGB, HSV, LCH & Lab image color statistics and clustering—simple and easy

HOME ANALYZE EXAMPLES API DOWNLOAD FAQ NEWS

IMAGE COLOR SUMMARY

THE IMAGE IN WORDS

atmosphere chicago cloudy concord dark detroit double dove friar grey half industrial light lining medium quarter quick rakaia silver stonehenge tapa

COLOR CLUSTERS

Colors in the image were clustered into 2 groups (k-means). The average color of the colors for each cluster is shown. The name is the closest named color and its distance is shown using ΔE. The tags are the set of words formed by all named neighbours within ΔE ≤ 5. The list of words above is the set of all unique words in this set of words.

Cluster colors, sized by number of pixels:

cluster	pixels	name	HEX	RGB	HSV	LCH	Lab	tags
	50.36%	123,120,116 tapa ΔE=1.4	#807B76	128 123 118	31 8 50	52 4 76	52 1 3	chicago concord detroit dove friar half industrial lining silver stonehenge tapa grey
	49.64%	169,165,165 double rakaia ΔE=1.5	#ACA6A3	172 166 163	24 6 67	69 3 63	69 1 3	medium light dark atmosphere cloudy double quarter quick rakaia silver stonehenge grey

IMAGE CLUSTER PARTITIONS

Pixels of the image assigned to each cluster. The border is the color of the cluster as calculated by the average value of its pixels.

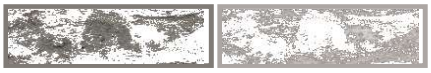

RGB HISTOGRAM

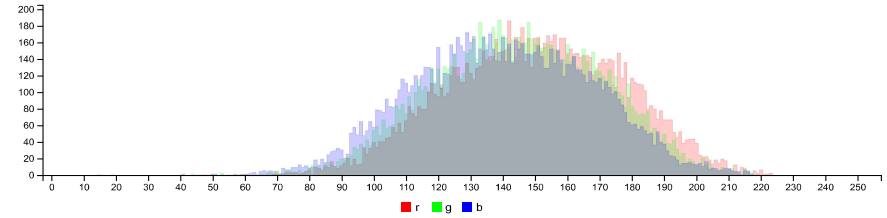

HSV HISTOGRAMS

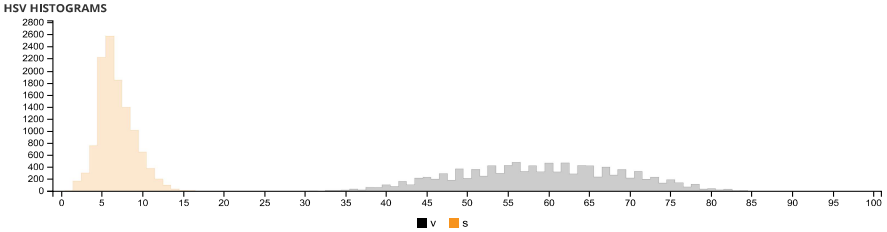

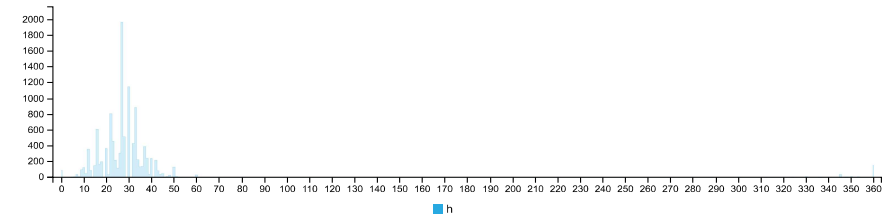

LCH HISTOGRAMS

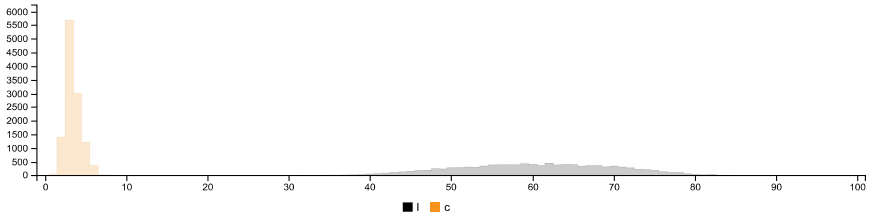

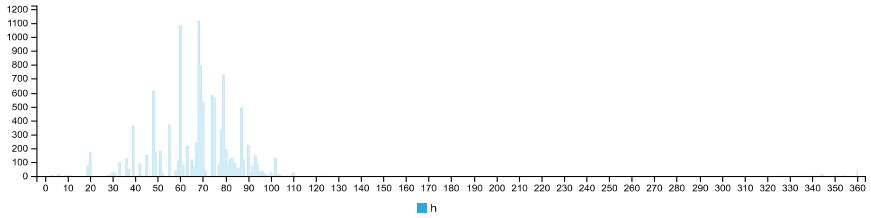

LAB HISTOGRAMS

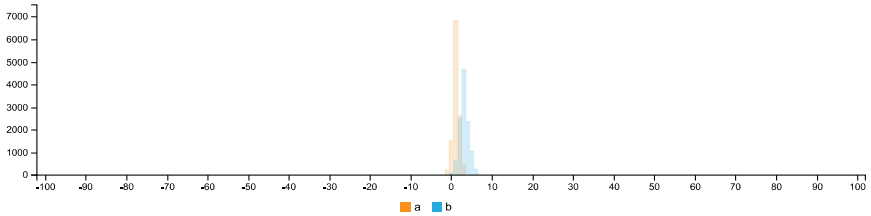

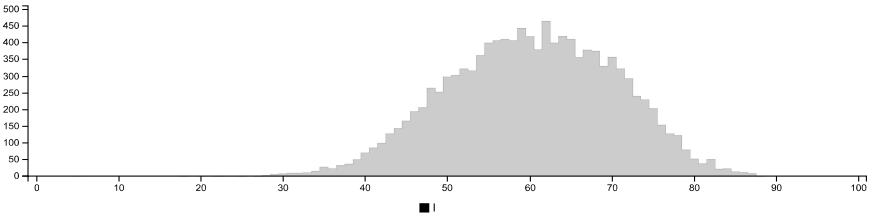

COLOR SPACE AND CHANNEL STATISTICS

	avg	med	min	max
RGB:R	150	151	19	223
RGB:G	145	145	15	222
RGB:B	140	140	15	219
HSV:H	26 1.00	27	0	360
HSV:S	7	6	1	21
HSV:V	59	59	7	87
LCH:L	60	60	5	88
LCH:C	3	3	0	9
LCH:H	66 1.00	69	2	360
LAB:L	60	60	5	88
LAB:A	1	1	-2	4
LAB:B	3	3	-2	8

Summary of Image Analysis for Specimen TG5-A-4

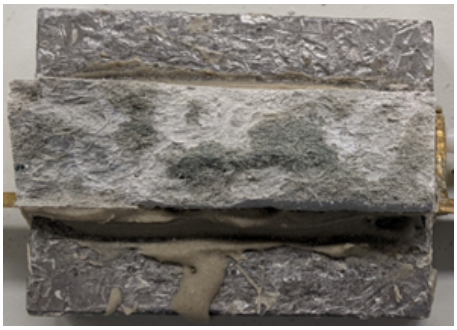

Figure D.5: Bottom debonded part of Specimen TG5-A-4

Figure D.6: Top debonded part of Specimen TG5-A-4

Table D.3: Summary of Image analysis result for specimen TG5-A-4

Contact Type	Colour Cluster	Results of Image analysis		Contact (%)		Average Contact (in %)
		Bottom Debonded Layer	Top Debonded Layer	Bottom Debonded Layer	Top Debonded Layer	
						
Poor				49,64%	53,30%	**51,47%**
Good				50,36%	46,70%	**48,53%**

Detailed report - Bottom debonded part of Specimen TG5-A-4

IMAGE COLOR SUMMARIZER

RGB, HSV, LCH & Lab image color statistics and clustering—simple and easy

HOME ANALYZE EXAMPLES API DOWNLOAD FAQ NEWS

IMAGE COLOR SUMMARY

THE IMAGE IN WORDS

blast chicane cloudy dawn delta double dust flint gauntlet grey ironside kensington mist mountain quarter rakaia schooner stack star stonehenge tapa traffic transmission triple viaduct

COLOR CLUSTERS

Colors in the image were clustered into 2 groups (k-means). The average color of the colors for each cluster is shown. The name is the closest named color and its distance is shown using ΔE. The tags are the set of words formed by all named neighbours within ΔE ≤ 5. The list of words above is the set of all unique words in this set of words.

Cluster colors, sized by number of pixels:

cluster	pixels	name	HEX	RGB	HSV	LCH	Lab	tags
	50.36%	108,109,104 traffic ΔE=1.2	#6D6B65	109 107 101	41 7 43	45 3 91	45 0 3	blast chicane double flint gauntlet ironside schooner stack tapa traffic triple grey
	49.64%	160,159,156 mountain mist ΔE=1.4	#A39F9A	163 159 154	32 6 64	66 3 79	66 1 3	cloudy dawn delta dust kensington mist mountain quarter rakaia star stonehenge transmission triple viaduct grey

IMAGE CLUSTER PARTITIONS

Pixels of the image assigned to each cluster. The border is the color of the cluster as calculated by the average value of its pixels.

RGB HISTOGRAM

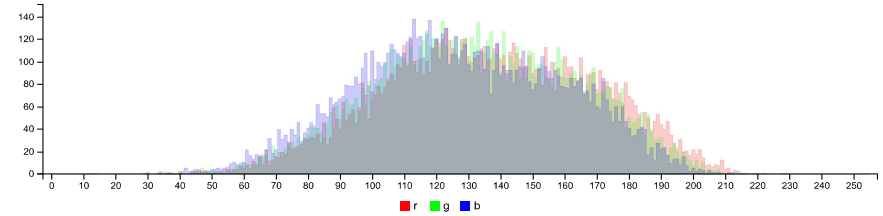

HSV HISTOGRAMS

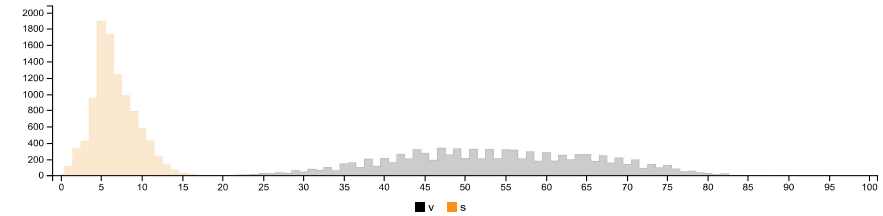

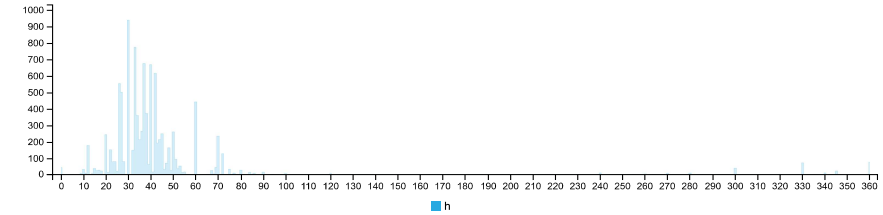

LCH HISTOGRAMS

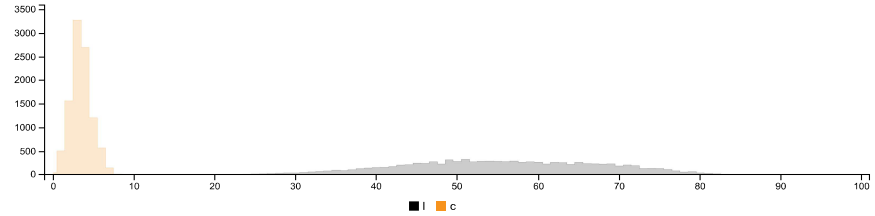

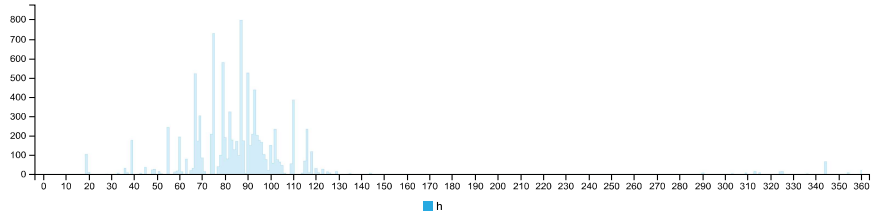

LAB HISTOGRAMS

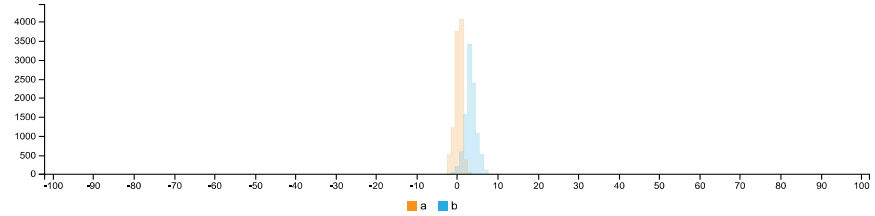

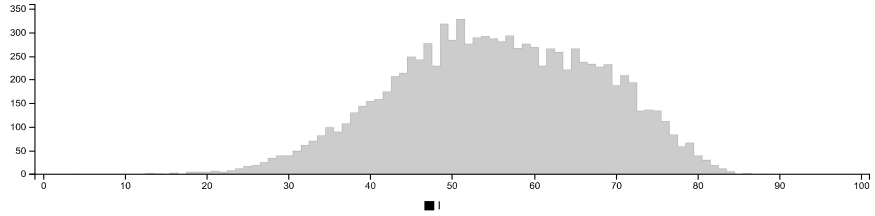

COLOR SPACE AND CHANNEL STATISTICS

	avg	med	min	max
RGB:R	136	136	14	228
RGB:G	133	132	13	221
RGB:B	128	126	12	216
HSV:H	36 1.00	37	0	360
HSV:S	7	6	0	44
HSV:V	53	53	5	89
LCH:L	55	55	4	88
LCH:C	3	3	0	21
LCH:H	82 1.00	86	3	360
LAB:L	55	55	4	88
LAB:A	0	0	-3	4
LAB:B	3	3	-4	21

Detailed report - Top debonded part of Specimen TG5-A-4

IMAGE COLOR SUMMARIZER

RGB, HSV, LCH & Lab image color statistics and clustering—simple and easy

HOME ANALYZE EXAMPLES API DOWNLOAD FAQ NEWS

IMAGE COLOR SUMMARY

THE IMAGE IN WORDS

archive blast chicane delta double dust fern flint friar gauntlet grey half imagine ironside masala mist mountain quarter rakaia sandstone schooner silver star tapa taupe traffic triple

COLOR CLUSTERS

Colors in the image were clustered into 2 groups (k-means). The average color of the colors for each cluster is shown. The name is the closest named color and its distance is shown using ΔE. The tags are the set of words formed by all named neighbours within ΔE ≤ 5. The list of words above is the set of all unique words in this set of words.

Cluster colors, sized by number of pixels:

cluster	pixels	name	HEX	RGB	HSV	LCH	Lab	tags
	53.30%	161,154,152 triple rakaia ΔE=1.8	#9E9994	158 153 148	31 6 62	64 3 76	64 1 3	archive delta dust fern friar half imagine mist mountain quarter rakaia sandstone silver star taupe triple grey
	46.70%	114,105,98 double schooner ΔE=1.9	#6E6A64	110 106 100	37 8 43	45 4 86	45 0 4	blast chicane double flint gauntlet half ironside masala schooner tapa traffic grey

IMAGE CLUSTER PARTITIONS

Pixels of the image assigned to each cluster. The border is the color of the cluster as calculated by the average value of its pixels.

RGB HISTOGRAM

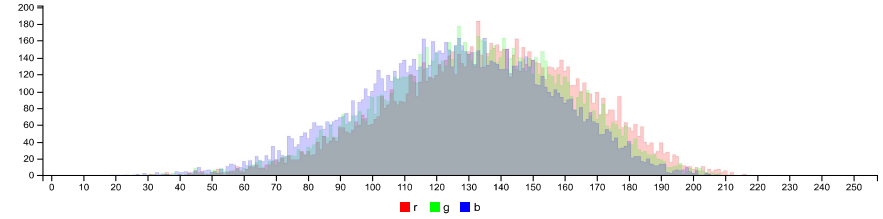

HSV HISTOGRAMS

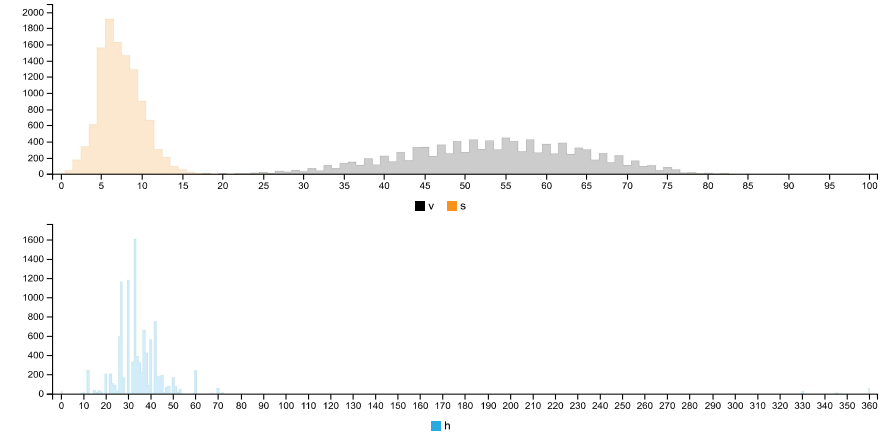

LCH HISTOGRAMS

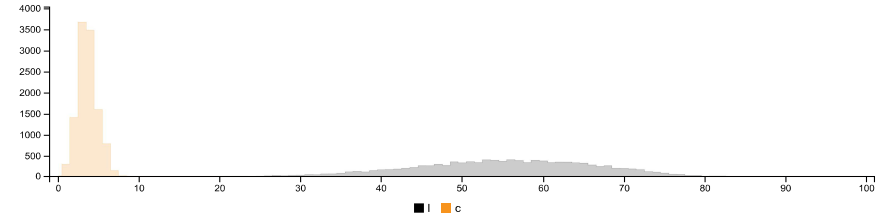

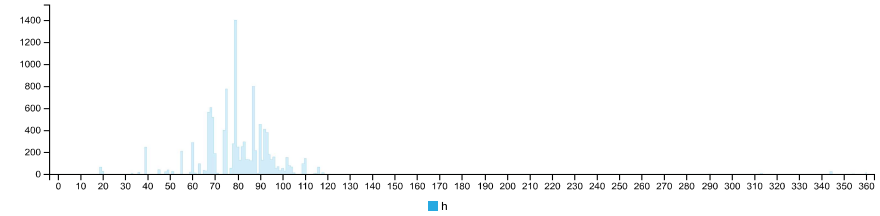

LAB HISTOGRAMS

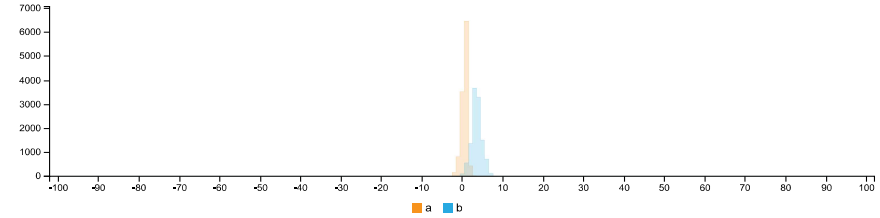

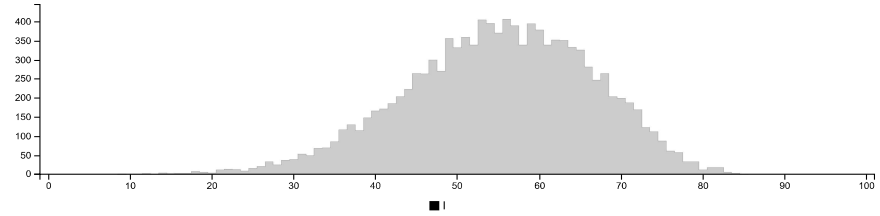

COLOR SPACE AND CHANNEL STATISTICS

	avg	med	min	max
RGB:R	136	137	27	216
RGB:G	132	132	24	211
RGB:B	126	127	19	208
HSV:H	33 1.00	33	0	360
HSV:S	7	7	0	37
HSV:V	53	54	11	85
LCH:L	55	56	9	85
LCH:C	4	4	0	8
LCH:H	78 1.00	79	3	360
LAB:L	55	56	9	85
LAB:A	1	1	-3	4
LAB:B	4	3	-3	8

Summary of Image Analysis for Specimen TG10-A-1

Figure D.7: Bottom debonded part of Specimen TG10-A-1

Figure D.8: Top debonded part of Specimen TG10-A-1

Table D.4: Summary of Image analysis result for specimen TG10-A-1

Contact Type	Colour Cluster	Results of Image analysis		Contact (%)		Average Contact (in %)
		Bottom Debonded Layer	Top Debonded Layer	Bottom Debonded Layer	Top Debonded Layer	
						
Poor				54,66%	55,63%	**55,15%**
Good				45,34%	44.37.%	**45,34%**

Detailed report - Bottom debonded part of Specimen TG10-A-1

IMAGE COLOR SUMMARIZER

RGB, HSV, LCH & Lab image color statistics and clustering—simple and easy

HOME ANALYZE EXAMPLES API DOWNLOAD FAQ NEWS

IMAGE COLOR SUMMARY

THE IMAGE IN WORDS

bombay concord concrete delta detroit fantail friar grey gunsmoke half industrial lining medium mist mountain nobel rakaia silver tapa triple

COLOR CLUSTERS

Colors in the image were clustered into 2 groups (k-means). The average color of the colors for each cluster is shown. The name is the closest named color and its distance is shown using ΔE. The tags are the set of words formed by all named neighbours within ΔE ≤ 5. The list of words above is the set of all unique words in this set of words.

Cluster colors, sized by number of pixels:

cluster	pixels	name	HEX	RGB	HSV	LCH	Lab	tags
	53.08%	183,180,176 half mountain mist ΔE=1.0	#B5B1AE	181 177 174	25 4 71	72 2 65	72 1 2	bombay concrete fantail half mist mountain nobel rakaia triple grey
	46.92%	128,126,121 friar grey ΔE=0.9	#7E7D78	126 125 120	51 4 49	52 3 103	52 -1 3	medium concord delta detroit friar gunsmoke industrial lining silver tapa triple grey

IMAGE CLUSTER PARTITIONS

Pixels of the image assigned to each cluster. The border is the color of the cluster as calculated by the average value of its pixels.

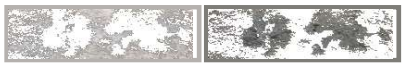

RGB HISTOGRAM

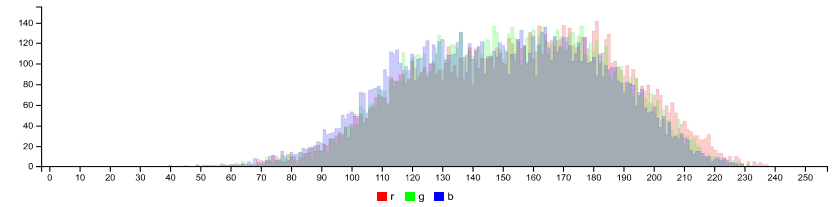

HSV HISTOGRAMS

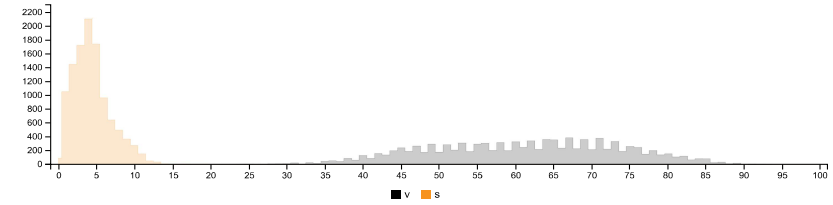

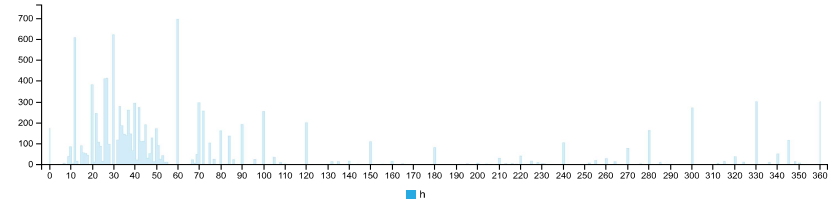

LCH HISTOGRAMS

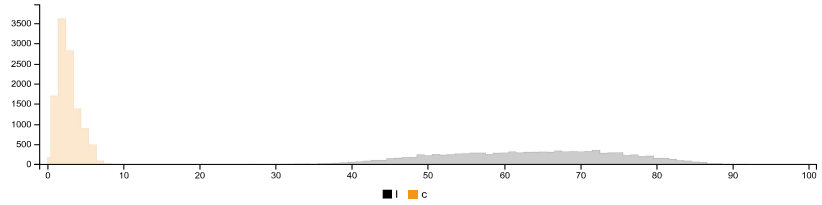

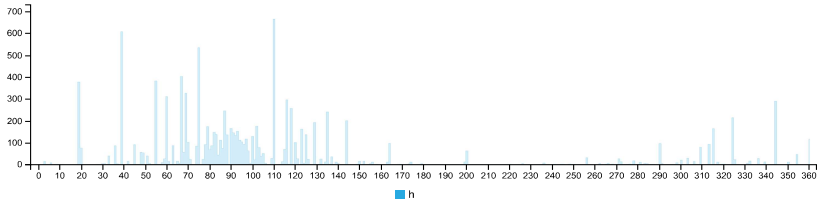

LAB HISTOGRAMS

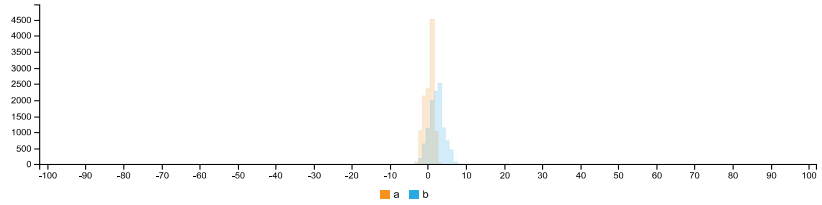

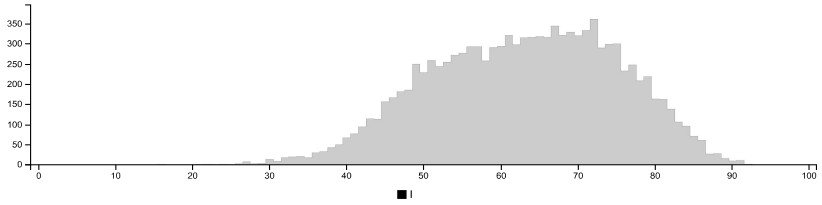

COLOR SPACE AND CHANNEL STATISTICS

	avg	med	min	max
RGB:R	155	157	40	237
RGB:G	153	153	40	231
RGB:B	149	150	40	231
HSV:H	34 1.00	43	0	360
HSV:S	4	4	0	19
HSV:V	61	62	16	93
LCH:L	63	64	16	92
LCH:C	3	3	0	11
LCH:H	77 1.00	92	3	360
LAB:L	63	64	16	92
LAB:A	0	0	-4	4
LAB:B	2	2	-6	11

Detailed report - Top debonded part of Specimen TG10-A-1

IMAGE COLOR SUMMARIZER

RGB, HSV, LCH & Lab image color statistics and clustering—simple and easy

HOME ANALYZE EXAMPLES API DOWNLOAD FAQ NEWS

IMAGE COLOR SUMMARY

THE IMAGE IN WORDS

aluminium atmosphere blast bombay chalice double fantail grey half masala mist mountain nobel quarter rakaia silver sonic stack tarmac traffic

COLOR CLUSTERS

Colors in the image were clustered into 2 groups (k-means). The average color of the colors for each cluster is shown. The name is the closest named color and its distance is shown using ΔE. The tags are the set of words formed by all named neighbours within ΔE ≤ 5. The list of words above is the set of all unique words in this set of words.

Cluster colors, sized by number of pixels:

cluster	pixels	name	HEX	RGB	HSV	LCH	Lab	tags
	52.01%	174,174,173 bombay ΔE=1.7	#B1ACA9	177 172 169	26 4 69	71 2 68	71 1 2	atmosphere bombay chalice double fantail half mist mountain nobel rakaia silver grey
	47.99%	116,115,111 quarter masala ΔE=0.5	#72716E	114 113 110	52 4 45	48 2 104	48 -1 2	aluminium blast double masala quarter silver sonic stack tarmac traffic grey

IMAGE CLUSTER PARTITIONS

Pixels of the image assigned to each cluster. The border is the color of the cluster as calculated by the average value of its pixels.

RGB HISTOGRAM

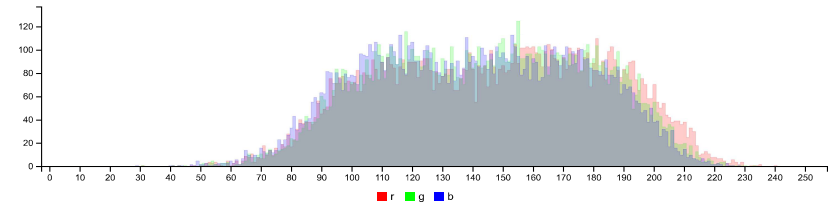

HSV HISTOGRAMS

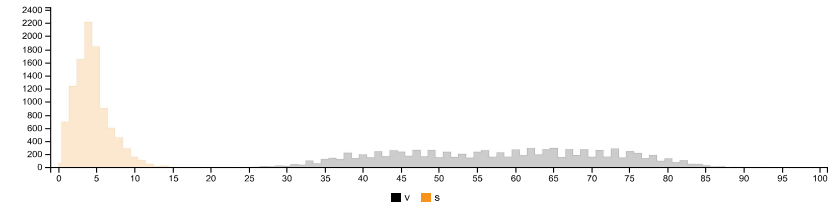

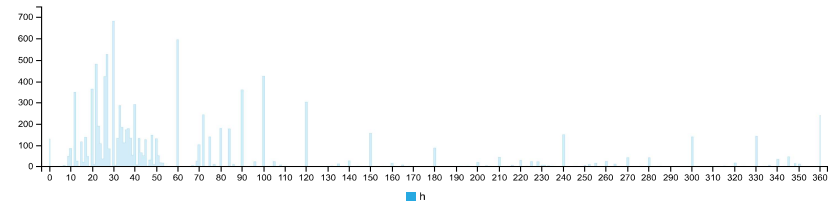

LCH HISTOGRAMS

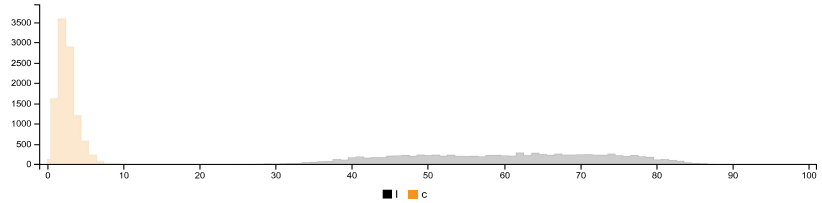

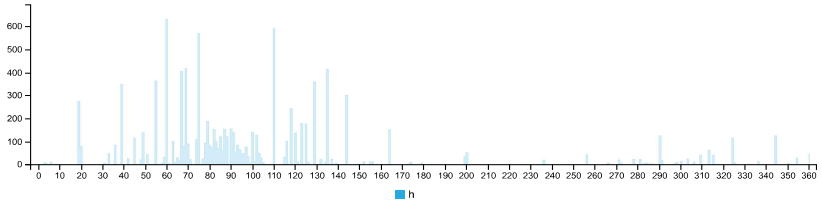

LAB HISTOGRAMS

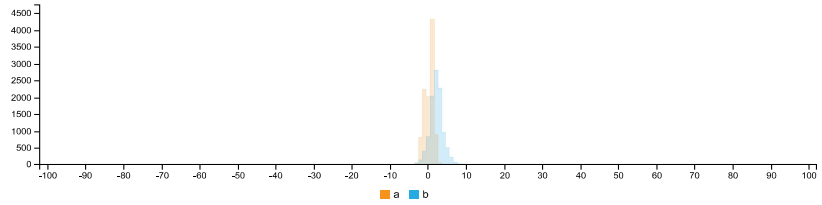

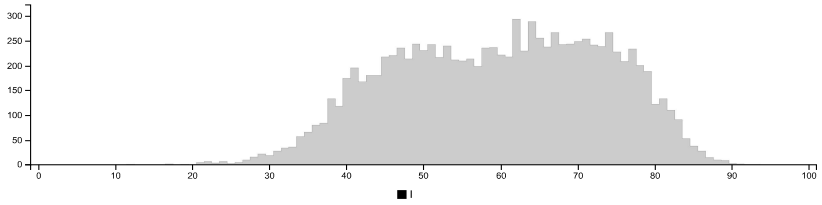

COLOR SPACE AND CHANNEL STATISTICS

	avg	med	min	max
RGB:R	147	149	31	240
RGB:G	144	145	31	233
RGB:B	141	141	29	228
HSV:H	40 1.00	40	0	360
HSV:S	5	4	0	48
HSV:V	58	58	12	94
LCH:L	60	60	12	93
LCH:C	3	2	0	17
LCH:H	82 1.00	87	3	360
LAB:L	60	60	12	93
LAB:A	0	1	-4	11
LAB:B	2	2	-6	13

Summary of Image Analysis for Specimen TG10-A-2

Figure D.9: Bottom debonded part of Specimen TG10-A-2

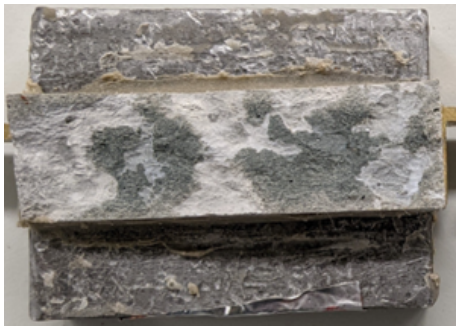

Figure D.10: Top debonded part of Specimen TG10-A-2

Table D.5: Summary of Image analysis result for specimen TG10-A-2

Contact Type	Colour Cluster	Results of Image analysis		Contact (%)		Average Contact (in %)
		Bottom Debonded Layer	Top Debonded Layer	Bottom Debonded Layer	Top Debonded Layer	
						
Poor				53,08%	52,01%	**52,55%**
Good				46,92%	47,99%	**47,46%**

Detailed report - Bottom debonded part of Specimen TG10-A-2

IMAGE COLOR SUMMARIZER

RGB, HSV, LCH & Lab image color statistics and clustering—simple and easy

HOME ANALYZE EXAMPLES API DOWNLOAD FAQ NEWS

IMAGE COLOR SUMMARY

THE IMAGE IN WORDS

bombay concord concrete delta detroit fantail friar grey gunsmoke half industrial lining medium mist mountain nobel rakaia silver tapa triple

COLOR CLUSTERS

Colors in the image were clustered into 2 groups (k-means). The average color of the colors for each cluster is shown. The name is the closest named color and its distance is shown using ΔE. The tags are the set of words formed by all named neighbours within ΔE ≤ 5. The list of words above is the set of all unique words in this set of words.

Cluster colors, sized by number of pixels:

cluster	pixels	name	HEX	RGB	HSV	LCH	Lab	tags
	53.08%	183,180,176 half mountain mist ΔE=1.0	#B5B1AE	181 177 174	25 4 71	72 2 65	72 1 2	bombay concrete fantail half mist mountain nobel rakaia triple grey
	46.92%	128,126,121 friar grey ΔE=0.9	#7E7D78	126 125 120	51 4 49	52 3 103	52 -1 3	medium concord delta detroit friar gunsmoke industrial lining silver tapa triple grey

IMAGE CLUSTER PARTITIONS

Pixels of the image assigned to each cluster. The border is the color of the cluster as calculated by the average value of its pixels.

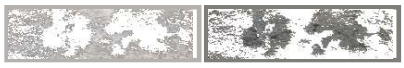

RGB HISTOGRAM

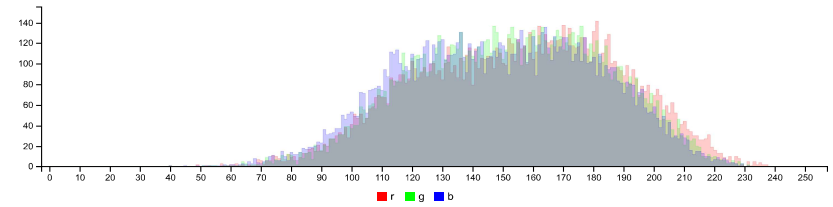

HSV HISTOGRAMS

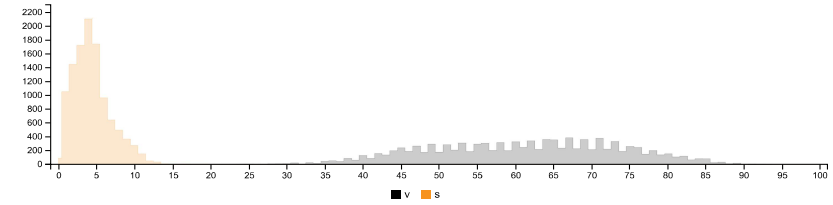

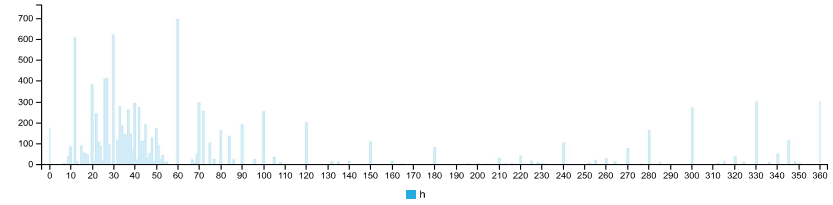

LCH HISTOGRAMS

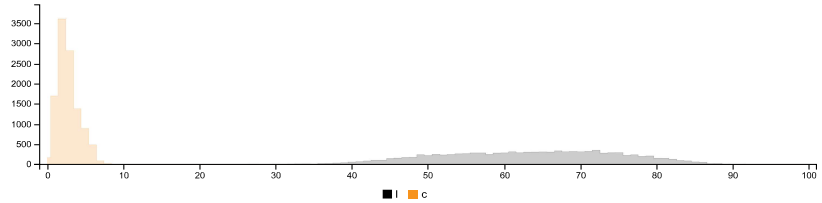

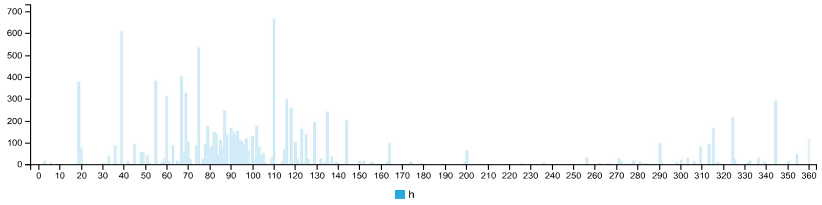

LAB HISTOGRAMS

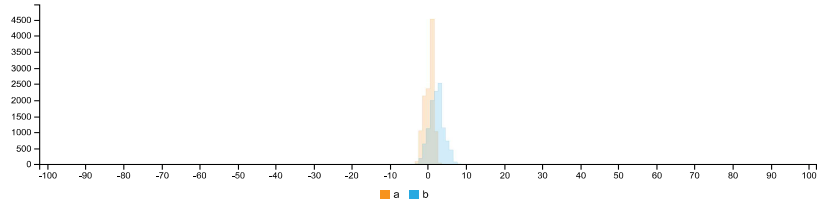

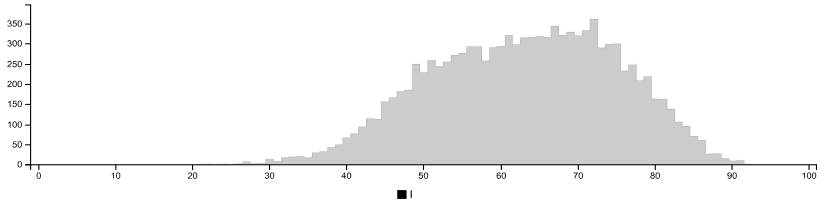

COLOR SPACE AND CHANNEL STATISTICS

	avg	med	min	max
RGB:R	155	157	40	237
RGB:G	153	153	40	231
RGB:B	149	150	40	231
HSV:H	34 1.00	43	0	360
HSV:S	4	4	0	19
HSV:V	61	62	16	93
LCH:L	63	64	16	92
LCH:C	3	3	0	11
LCH:H	77 1.00	92	3	360
LAB:L	63	64	16	92
LAB:A	0	0	-4	4
LAB:B	2	2	-6	11

Detailed report - Top debonded part of Specimen TG10-A-2

IMAGE COLOR SUMMARIZER

RGB, HSV, LCH & Lab image color statistics and clustering—simple and easy

HOME ANALYZE EXAMPLES API DOWNLOAD FAQ NEWS

IMAGE COLOR SUMMARY

THE IMAGE IN WORDS

aluminium atmosphere blast bombay chalice double fantail grey half masala mist mountain nobel quarter rakaia silver sonic stack tarmac traffic

COLOR CLUSTERS

Colors in the image were clustered into 2 groups (k-means). The average color of the colors for each cluster is shown. The name is the closest named color and its distance is shown using ΔE. The tags are the set of words formed by all named neighbours within ΔE ≤ 5. The list of words above is the set of all unique words in this set of words.

Cluster colors, sized by number of pixels:

cluster	pixels	name	HEX	RGB	HSV	LCH	Lab	tags
	52.01%	174,174,173 bombay ΔE=1.7	#B1ACA9	177 172 169	26 4 69	71 2 68	71 1 2	atmosphere bombay chalice double fantail half mist mountain nobel rakaia silver grey
	47.99%	116,115,111 quarter masala ΔE=0.5	#72716E	114 113 110	52 4 45	48 2 104	48 -1 2	aluminium blast double masala quarter silver sonic stack tarmac traffic grey

IMAGE CLUSTER PARTITIONS

Pixels of the image assigned to each cluster. The border is the color of the cluster as calculated by the average value of its pixels.

RGB HISTOGRAM

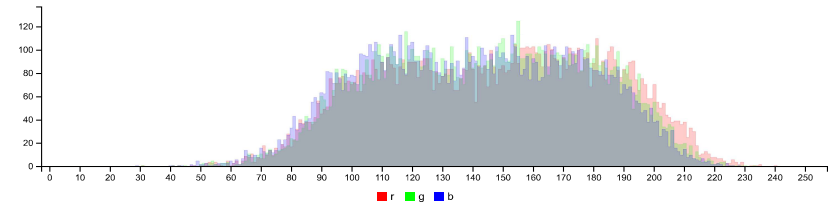

HSV HISTOGRAMS

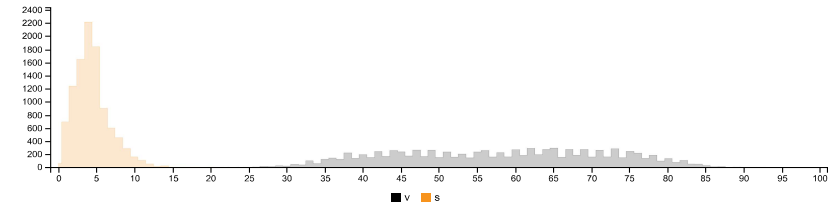

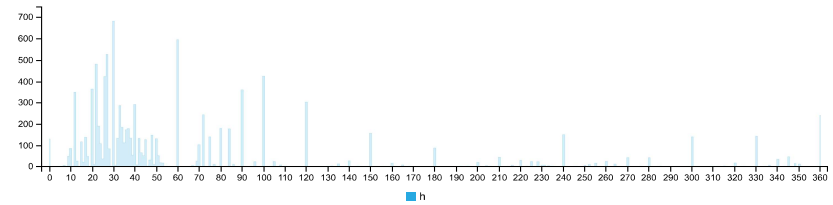

LCH HISTOGRAMS

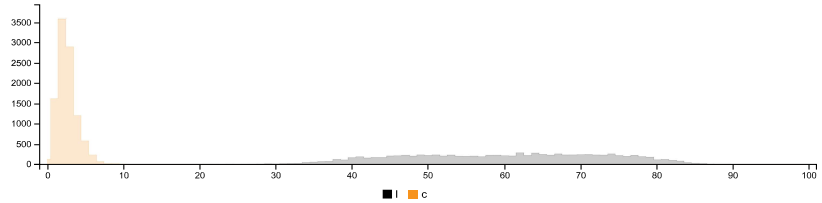

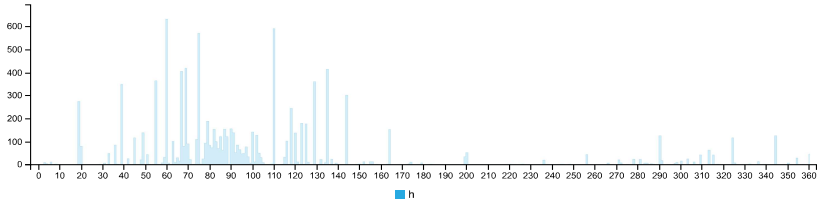

LAB HISTOGRAMS

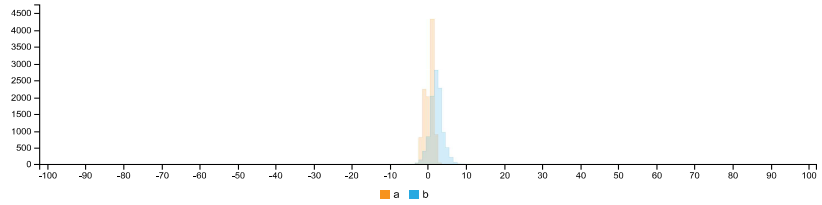

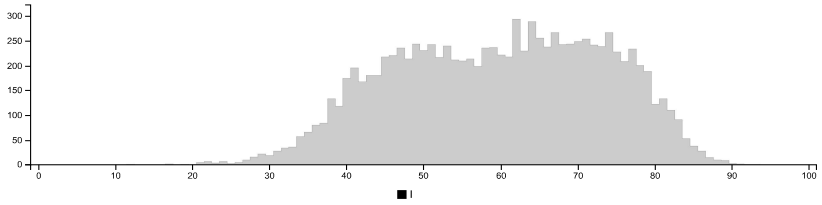

COLOR SPACE AND CHANNEL STATISTICS

	avg	med	min	max
RGB:R	147	149	31	240
RGB:G	144	145	31	233
RGB:B	141	141	29	228
HSV:H	40 1.00	40	0	360
HSV:S	5	4	0	48
HSV:V	58	58	12	94
LCH:L	60	60	12	93
LCH:C	3	2	0	17
LCH:H	82 1.00	87	3	360
LAB:L	60	60	12	93
LAB:A	0	1	-4	11
LAB:B	2	2	-6	13

Summary of Image Analysis for Specimen TG10-A-3

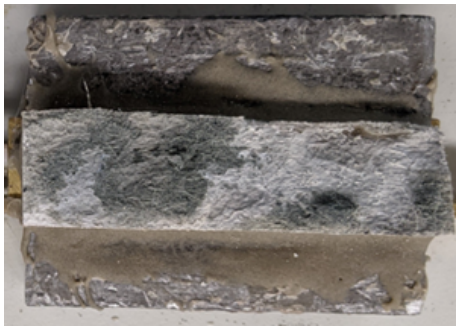

Figure D.11: Bottom debonded part of Specimen TG10-A-3

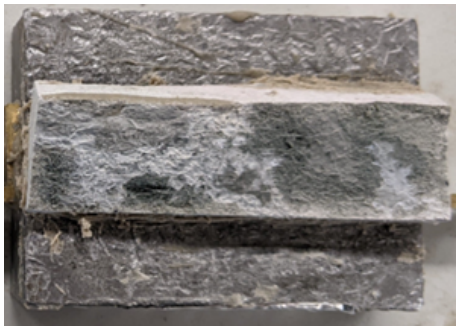

Figure D.12: Top debonded part of Specimen TG10-A-3

Table D.6: Summary of Image analysis result for specimen TG10-A-3

Contact Type	Colour Cluster	Results of Image analysis		Contact (%)		Average Contact (in %)
		Bottom Debonded Layer	Top Debonded Layer	Bottom Debonded Layer	Top Debonded Layer	
						
Poor				51,53%	46,71%	**49,12%**
Good			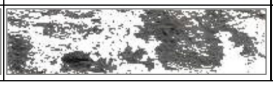	48,47%	53,29%	**50,88%**

Detailed report - Bottom debonded part of Specimen TG10-A-3

IMAGE COLOR SUMMARIZER

RGB, HSV, LCH & Lab image color statistics and clustering—simple and easy

HOME ANALYZE EXAMPLES API DOWNLOAD FAQ NEWS

IMAGE COLOR SUMMARY

THE IMAGE IN WORDS

alley chicago double dust grey lady metal mist mountain rakaia shady spanish storm tinpan triple trojan white

COLOR CLUSTERS

Colors in the image were clustered into 2 groups (k-means). The average color of the colors for each cluster is shown. The name is the closest named color and its distance is shown using ΔE. The tags are the set of words formed by all named neighbours within ΔE ≤ 5. The list of words above is the set of all unique words in this set of words.

Cluster colors, sized by number of pixels:

cluster	pixels	name	HEX	RGB	HSV	LCH	Lab	tags
	51.53%	150,150,150 grey ΔE=1.3	#999695	153 150 149	4 2 60	62 1 26	62 1 1	lady metal mist mountain rakaia shady spanish triple grey white
	48.47%	94,94,94 grey ΔE=0.7	#5F5F5E	95 95 94	39 2 37	40 1 89	40 0 1	alley chicago double dust storm tinpan trojan grey

IMAGE CLUSTER PARTITIONS

Pixels of the image assigned to each cluster. The border is the color of the cluster as calculated by the average value of its pixels.

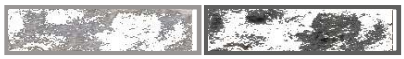

RGB HISTOGRAM

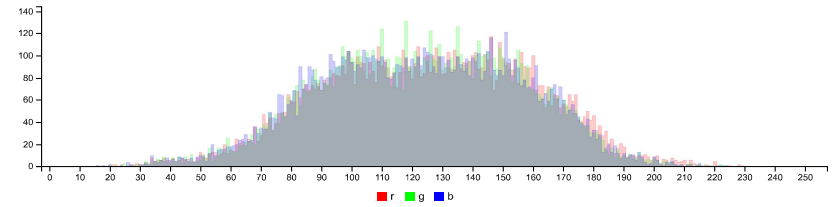

HSV HISTOGRAMS

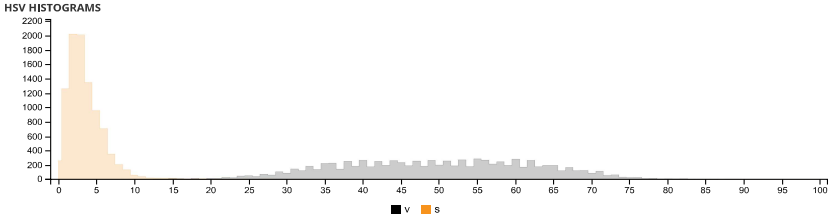

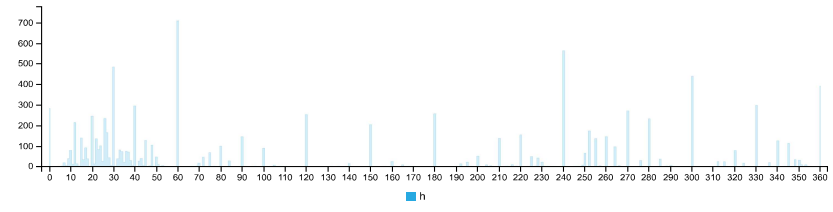

LCH HISTOGRAMS

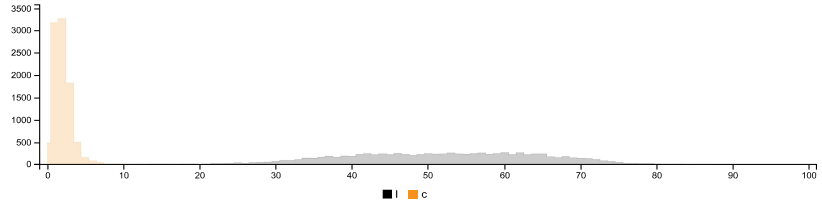

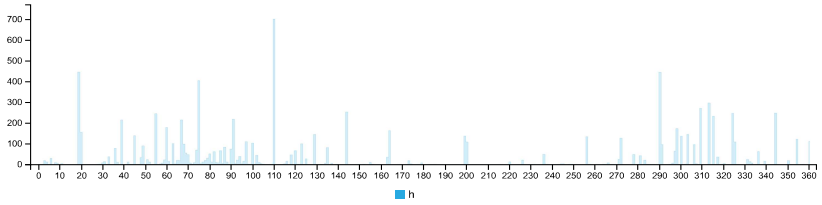

LAB HISTOGRAMS

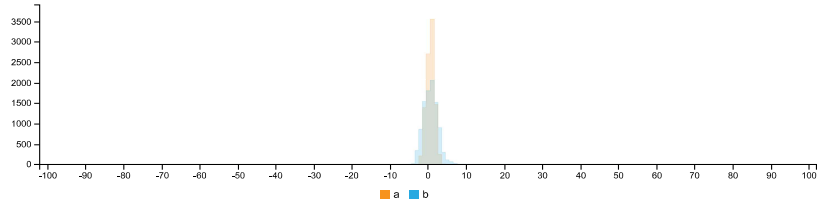

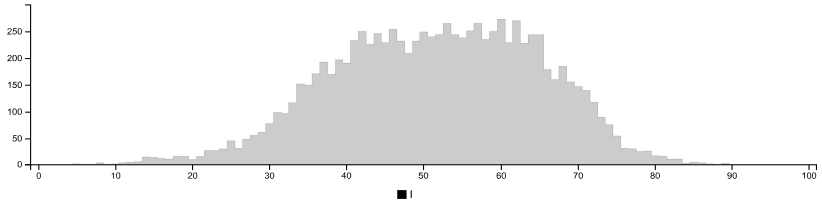

COLOR SPACE AND CHANNEL STATISTICS

	avg	med	min	max
RGB:R	125	126	16	229
RGB:G	123	124	16	223
RGB:B	123	123	16	224
HSV:H	4 0.00	100	0	360
HSV:S	4	3	0	53
HSV:V	49	50	6	90
LCH:L	52	52	5	89
LCH:C	2	2	0	21
LCH:H	36 0.00	118	0	360
LAB:L	52	52	5	89
LAB:A	1	1	-4	5
LAB:B	1	1	-7	20

Detailed report - Top debonded part of Specimen TG10-A-3

IMAGE COLOR SUMMARIZER

RGB, HSV, LCH & Lab image color statistics and clustering—simple and easy

HOME ANALYZE EXAMPLES API DOWNLOAD FAQ NEWS

IMAGE COLOR SUMMARY

THE IMAGE IN WORDS

chicane dim dimgray double dust granite grey ironside lady metal mist mountain quarter rakaia shady sidewinder spanish storm triple trojan white

COLOR CLUSTERS

Colors in the image were clustered into 2 groups (k-means). The average color of the colors for each cluster is shown. The name is the closest named color and its distance is shown using ΔE. The tags are the set of words formed by all named neighbours within ΔE ≤ 5. The list of words above is the set of all unique words in this set of words.

Cluster colors, sized by number of pixels:

cluster	pixels	name	HEX	RGB	HSV	LCH	Lab	tags
	53.29%	100,100,99 storm dust ΔE=0.4	#646362	100 99 98	42 2 39	42 1 93	42 0 1	chicane dim dimgray double dust granite ironside storm trojan grey
	46.71%	152,152,152 spanish grey ΔE=1.3	#9A9798	154 151 152	354 1 60	63 1 11	63 1 0	lady metal mist mountain quarter rakaia shady sidewinder spanish triple grey white

IMAGE CLUSTER PARTITIONS

Pixels of the image assigned to each cluster. The border is the color of the cluster as calculated by the average value of its pixels.

RGB HISTOGRAM

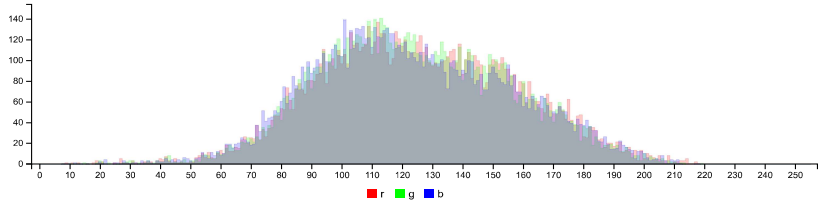

HSV HISTOGRAMS

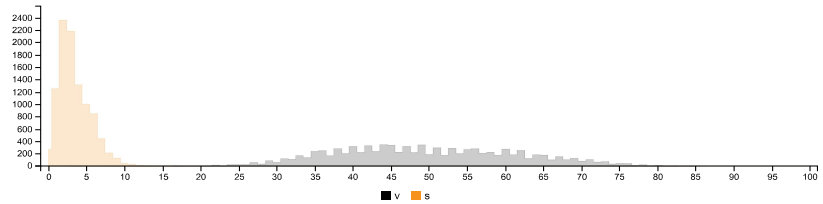

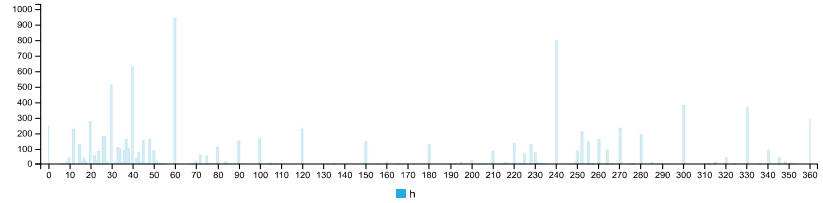

LCH HISTOGRAMS

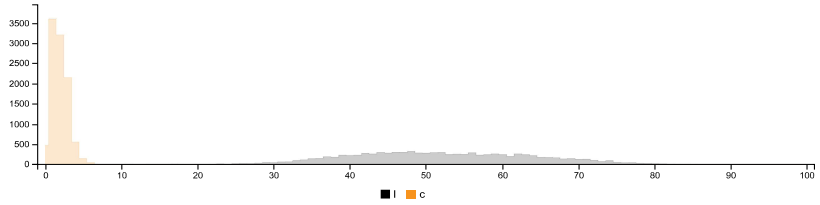

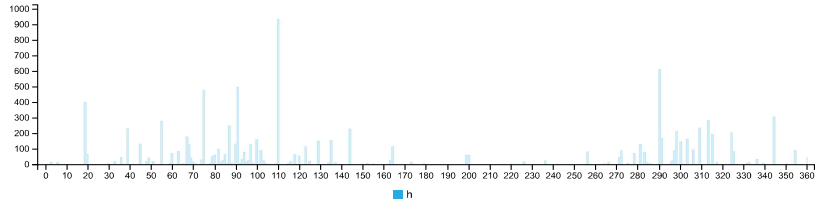

LAB HISTOGRAMS

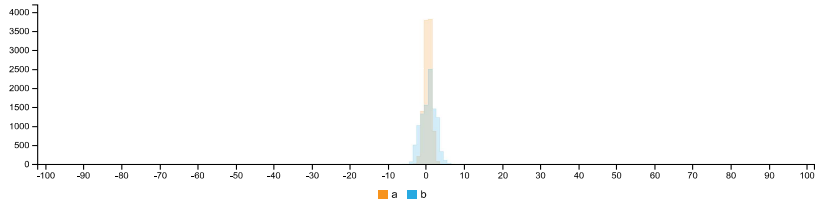

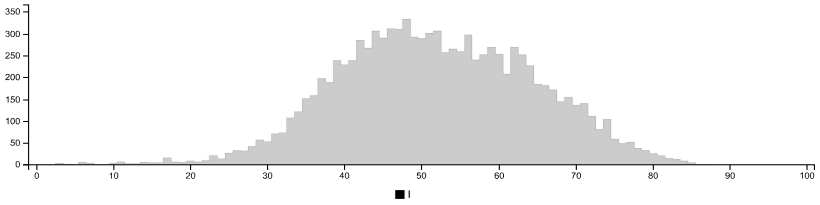

COLOR SPACE AND CHANNEL STATISTICS

	avg	med	min	max
RGB:R	125	124	8	218
RGB:G	124	122	8	219
RGB:B	123	121	8	218
HSV:H	12 0.00	75	0	360
HSV:S	4	3	0	19
HSV:V	50	49	3	86
LCH:L	52	51	2	87
LCH:C	2	2	0	9
LCH:H	48 0.00	110	3	360
LAB:L	52	51	2	87
LAB:A	0	0	-3	4
LAB:B	1	1	-6	9

Summary of Image Analysis for Specimen TG10-A-4

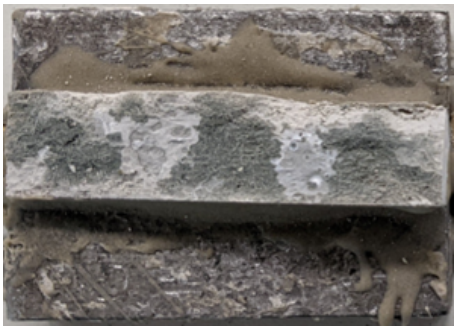

Figure D.13: Bottom debonded part of Specimen TG10-A-4

Figure D.14: Top debonded part of Specimen TG10-A-4

Table D.7: Summary of Image analysis result for specimen TG10-A-4

Contact Type	Colour Cluster	Results of Image analysis		Contact (%)		Average Contact (in %)
		Bottom Debonded Layer	Top Debonded Layer	Bottom Debonded Layer	Top Debonded Layer	
		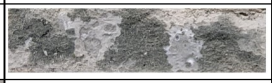				
Poor				48,79%	49,23%	**49,01%**
Good			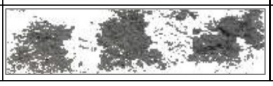	51,21%	50,77%	**50,99%**

Detailed report - Bottom debonded part of Specimen TG10-A-4

IMAGE COLOR SUMMARIZER

RGB, HSV, LCH & Lab image color statistics and clustering—simple and easy

HOME ANALYZE EXAMPLES API DOWNLOAD FAQ NEWS

IMAGE COLOR SUMMARY

THE IMAGE IN WORDS

atmosphere blast chalice cliff dark double dove face grey light masala medium quarter quick rakaia silver stack tarmac traffic

COLOR CLUSTERS

Colors in the image were clustered into 2 groups (k-means). The average color of the colors for each cluster is shown. The name is the closest named color and its distance is shown using ΔE. The tags are the set of words formed by all named neighbours within ΔE ≤ 5. The list of words above is the set of all unique words in this set of words.

Cluster colors, sized by number of pixels:

cluster	pixels	name	HEX	RGB	HSV	LCH	Lab	tags
	51.21%	111,113,110 double stack ΔE=1.0	#6E6E6B	110 110 107	61 2 43	46 2 111	46 -1 1	blast cliff double dove face masala quarter stack tarmac traffic grey
	48.79%	169,165,165 double rakaia ΔE=1.2	#ABA8A6	171 168 166	20 3 67	69 1 55	69 1 1	medium light dark atmosphere chalice double quick rakaia silver grey

IMAGE CLUSTER PARTITIONS

Pixels of the image assigned to each cluster. The border is the color of the cluster as calculated by the average value of its pixels.

RGB HISTOGRAM

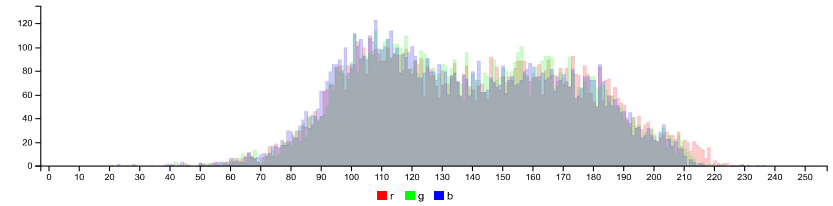

HSV HISTOGRAMS

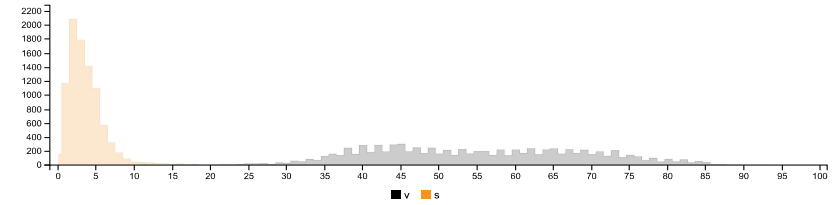

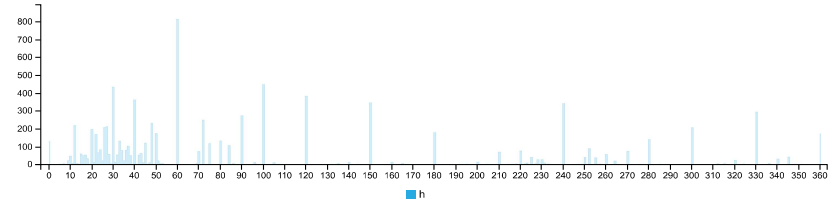

LCH HISTOGRAMS

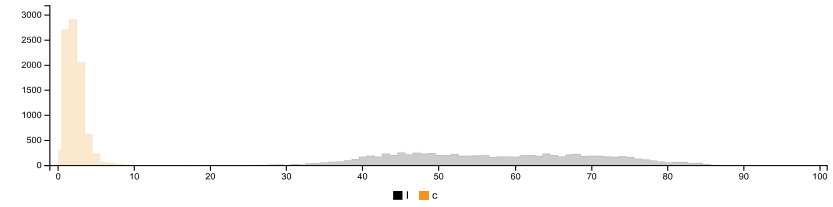

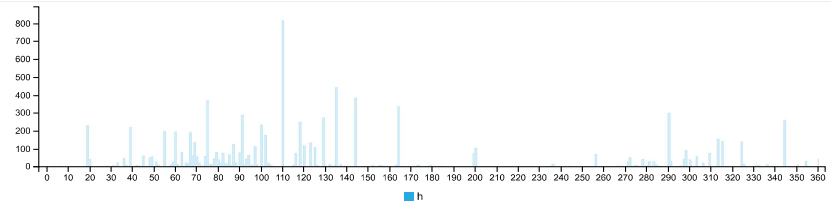

LAB HISTOGRAMS

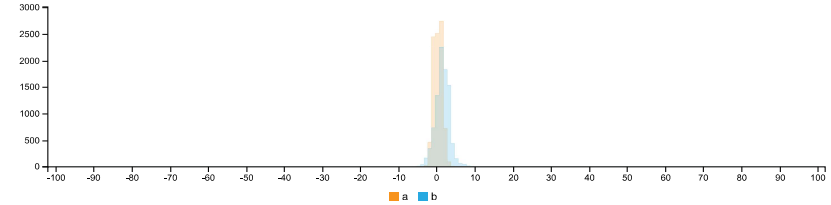

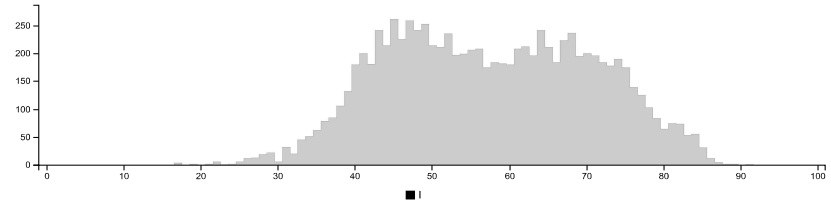

COLOR SPACE AND CHANNEL STATISTICS

	avg	med	min	max
RGB:R	140	138	21	229
RGB:G	138	136	21	229
RGB:B	136	133	23	236
HSV:H	44 0.00	60	0	360
HSV:S	4	3	0	39
HSV:V	55	54	9	93
LCH:L	57	57	7	91
LCH:C	2	2	0	11
LCH:H	87 0.00	110	3	360
LAB:L	57	57	7	91
LAB:A	0	0	-3	5
LAB:B	1	1	-7	11

Detailed report - Top debonded part of Specimen TG10-A-4

IMAGE COLOR SUMMARIZER

RGB, HSV, LCH & Lab image color statistics and clustering—simple and easy

HOME ANALYZE EXAMPLES API DOWNLOAD FAQ NEWS

IMAGE COLOR SUMMARY

THE IMAGE IN WORDS

atmosphere chicane dark dim dimgray dimgrey double granite grey ironside light medium quick rakaia silver traffic trojan

COLOR CLUSTERS

Colors in the image were clustered into 2 groups (k-means). The average color of the colors for each cluster is shown. The name is the closest named color and its distance is shown using ΔE. The tags are the set of words formed by all named neighbours within ΔE ≤ 5. The list of words above is the set of all unique words in this set of words.

Cluster colors, sized by number of pixels:

cluster	pixels	name	HEX	RGB	HSV	LCH	Lab	tags
	50.77%	104,103,101 chicane ΔE=1.2	#6A6A67	106 106 103	60 3 42	45 2 110	45 -1 2	chicane dim dimgray dimgrey double granite ironside traffic trojan grey
	49.23%	169,165,165 double rakaia ΔE=0.6	#A9A6A4	169 166 164	23 3 66	68 2 61	68 1 1	medium light dark atmosphere double quick rakaia silver grey

IMAGE CLUSTER PARTITIONS

Pixels of the image assigned to each cluster. The border is the color of the cluster as calculated by the average value of its pixels.

RGB HISTOGRAM

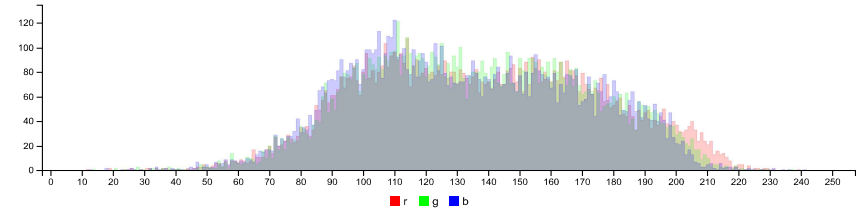

HSV HISTOGRAMS

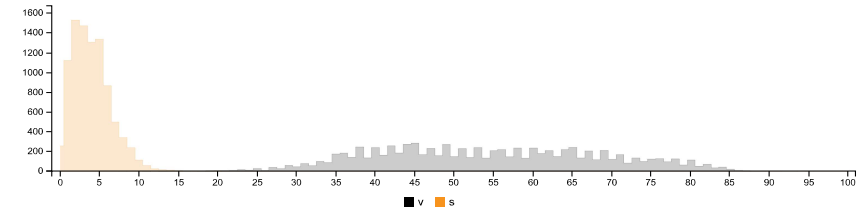

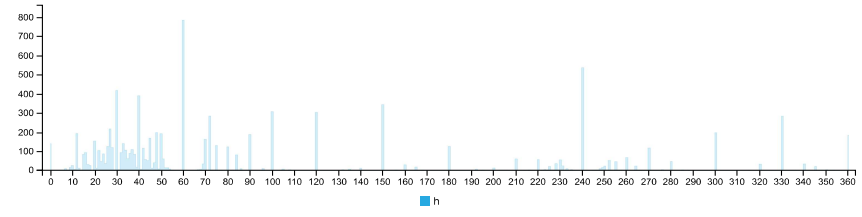

LCH HISTOGRAMS

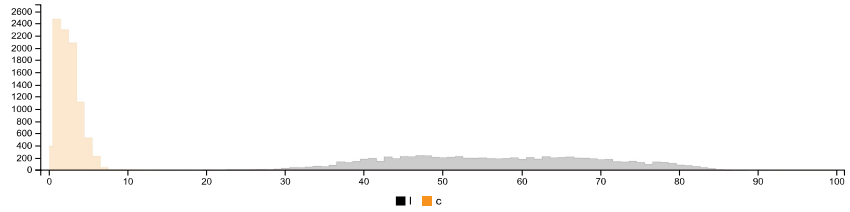

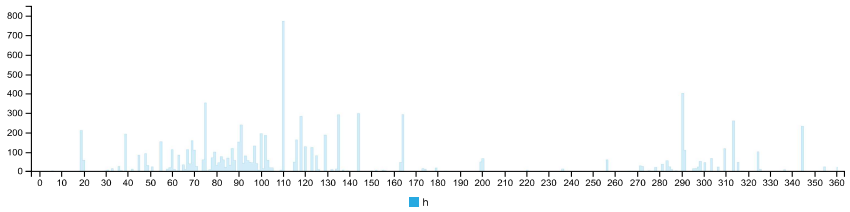

LAB HISTOGRAMS

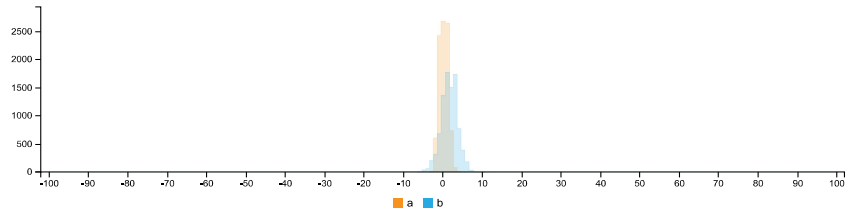

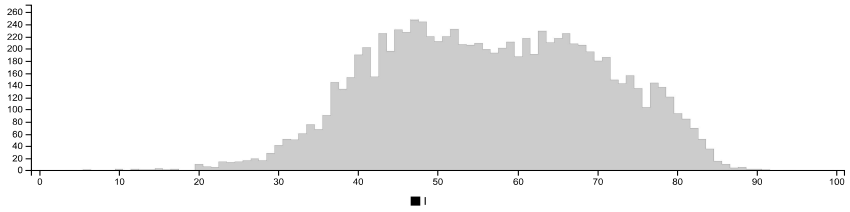

COLOR SPACE AND CHANNEL STATISTICS

	avg	med	min	max
RGB:R	137	136	12	239
RGB:G	136	135	14	237
RGB:B	133	131	13	241
HSV:H	42 0.00	60	0	360
HSV:S	4	4	0	22
HSV:V	54	53.5	5	95
LCH:L	56	56	4	94
LCH:C	2	2	0	13
LCH:H	86 0.00	110	2	360
LAB:L	56	56	4	94
LAB:A	0	0	-3	5
LAB:B	2	2	-8	12

Summary of Image Analysis for Specimen TG20-A-1

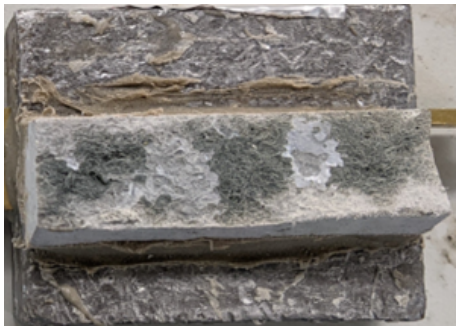

Figure D.15: Bottom debonded part of Specimen TG20-A-1

Figure D.16: Top debonded part of Specimen TG20-A-1

Table D.8: Summary of Image analysis result for specimen TG20-A-1

Contact Type	Colour Cluster	Results of Image analysis		Contact (%)		Average Contact (in %)
		Bottom Debonded Layer	Top Debonded Layer	Bottom Debonded Layer	Top Debonded Layer	
						
Poor				57,18%	56,84%	**57,01%**
Good				42,82%	43,16%	**42,99%**

Detailed report - Bottom debonded part of Specimen TG20-A-1

IMAGE COLOR SUMMARIZER

RGB, HSV, LCH & Lab image color statistics and clustering—simple and easy

HOME ANALYZE EXAMPLES API DOWNLOAD FAQ NEWS

IMAGE COLOR SUMMARY

THE IMAGE IN WORDS

aluminium boulder cloudy concord dark detroit double dove grey light masala medium nobel quarter quick rakaia silver sonic stonehenge tapa

COLOR CLUSTERS

Colors in the image were clustered into 2 groups (k-means). The average color of the colors for each cluster is shown. The name is the closest named color and its distance is shown using ΔE. The tags are the set of words formed by all named neighbours within ΔE ≤ 5. The list of words above is the set of all unique words in this set of words.

Cluster colors, sized by number of pixels:

cluster	pixels	name	HEX	RGB	HSV	LCH	Lab	tags
	57.18%	169,165,165 double rakaia ΔE=1.5	#ACA5A3	172 165 163	17 5 68	68 3 49	68 2 2	medium light dark cloudy double nobel quarter quick rakaia silver stonehenge grey
	42.82%	120,119,116 detroit ΔE=1.4	#7B7673	123 118 115	26 7 48	50 3 66	50 1 3	aluminium boulder concord detroit dove masala quarter silver sonic tapa grey

IMAGE CLUSTER PARTITIONS

Pixels of the image assigned to each cluster. The border is the color of the cluster as calculated by the average value of its pixels.

RGB HISTOGRAM

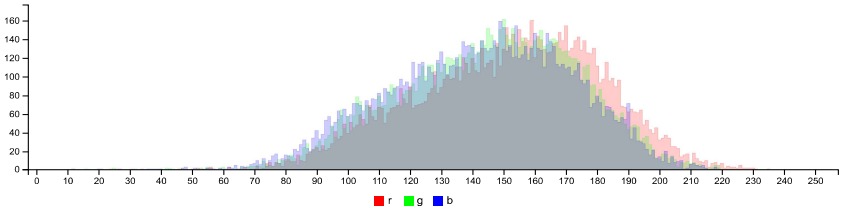

HSV HISTOGRAMS

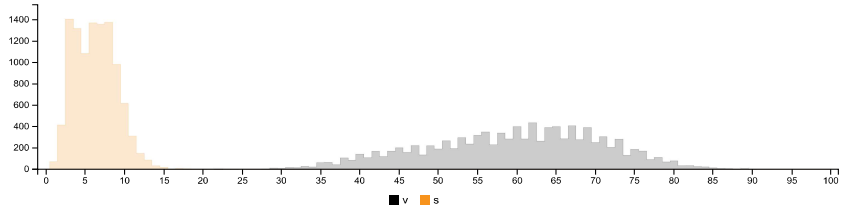

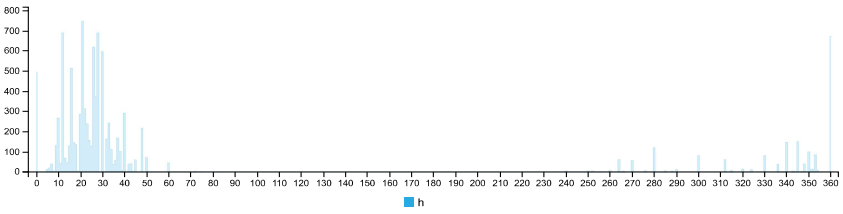

LCH HISTOGRAMS

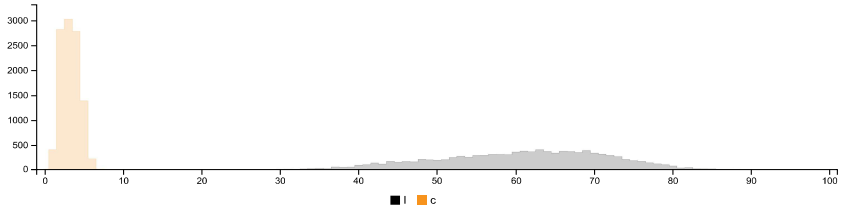

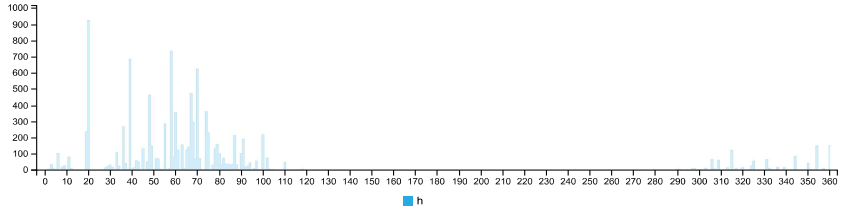

LAB HISTOGRAMS

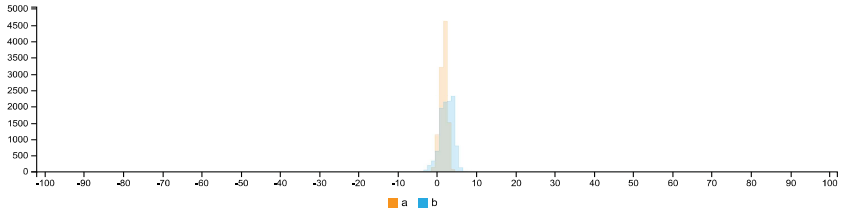

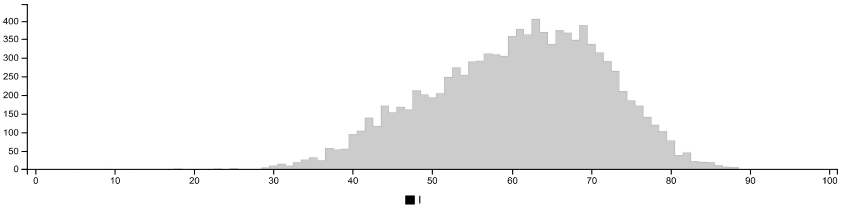

COLOR SPACE AND CHANNEL STATISTICS

	avg	med	min	max
RGB:R	151	154	24	235
RGB:G	145	147	16	223
RGB:B	142	144	12	219
HSV:H	16 1.00	27	0	360
HSV:S	6	6	0	50
HSV:V	59	60	9	92
LCH:L	61	62	5	90
LCH:C	3	3	0	8
LCH:H	50 1.00	61	2	360
LAB:L	61	62	5	90
LAB:A	2	2	-2	4
LAB:B	2	3	-5	8

Detailed report - Top debonded part of Specimen TG20-A-1

IMAGE COLOR SUMMARIZER

RGB, HSV, LCH & Lab image color statistics and clustering—simple and easy

HOME ANALYZE EXAMPLES API DOWNLOAD FAQ NEWS

IMAGE COLOR SUMMARY

THE IMAGE IN WORDS

chicane dim dimgray dimgrey double fern granite grey ironside metal mist mountain rakaia silver spanish traffic triple trojan white

COLOR CLUSTERS

Colors in the image were clustered into 2 groups (k-means). The average color of the colors for each cluster is shown. The name is the closest named color and its distance is shown using ΔE. The tags are the set of words formed by all named neighbours within ΔE ≤ 5. The list of words above is the set of all unique words in this set of words.

Cluster colors, sized by number of pixels:

cluster	pixels	name	HEX	RGB	HSV	LCH	Lab	tags
	56.84%	161,154,152 triple rakaia ΔE=1.9	#9A9694	154 150 148	19 4 60	62 2 54	62 1 2	fern metal mist mountain rakaia silver spanish triple grey white
	43.16%	104,103,101 chicane ΔE=1.1	#6B6966	107 105 102	31 5 42	44 2 77	44 0 2	chicane dim dimgray dimgrey double granite ironside traffic trojan grey

IMAGE CLUSTER PARTITIONS

Pixels of the image assigned to each cluster. The border is the color of the cluster as calculated by the average value of its pixels.

RGB HISTOGRAM

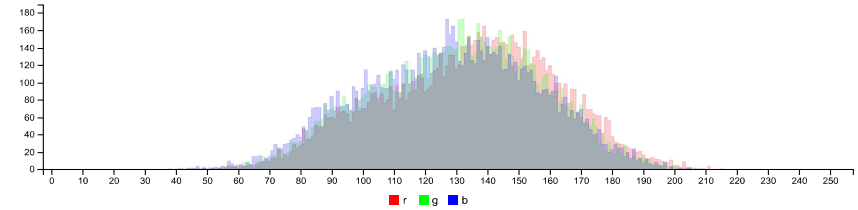

HSV HISTOGRAMS

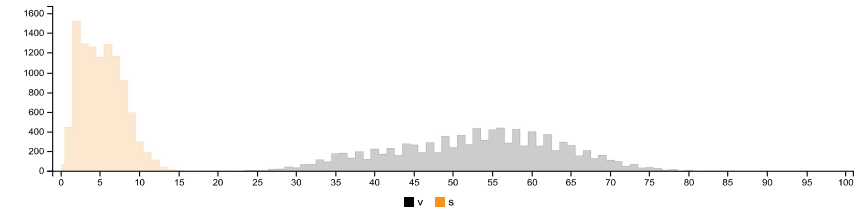

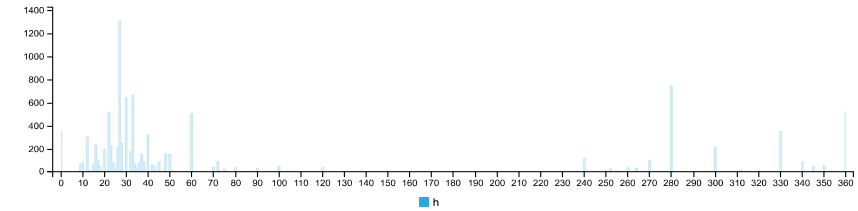

LCH HISTOGRAMS

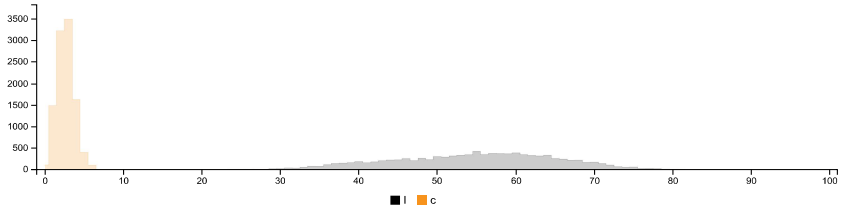

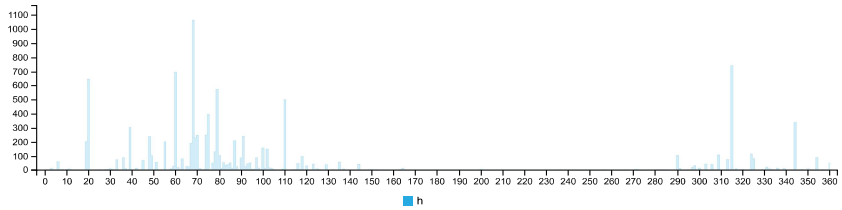

LAB HISTOGRAMS

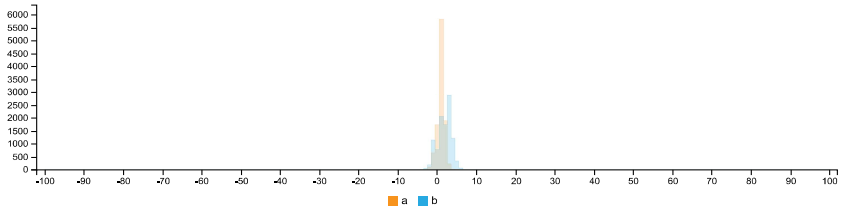

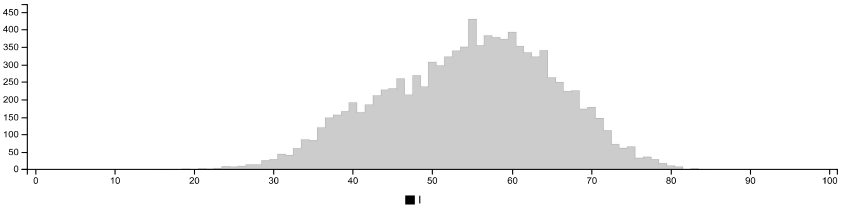

COLOR SPACE AND CHANNEL STATISTICS

	avg	med	min	max
RGB:R	134	136	41	215
RGB:G	130	132	40	209
RGB:B	128	129	38	209
HSV:H	16 1.00	33	0	360
HSV:S	5	5	0	19
HSV:V	53	54	16	84
LCH:L	55	55	16	84
LCH:C	3	3	0	7
LCH:H	55 1.00	75	2	360
LAB:L	55	55	16	84
LAB:A	1	1	-3	7
LAB:B	2	2	-4	7

Summary of Image Analysis for Specimen TG20-A-2

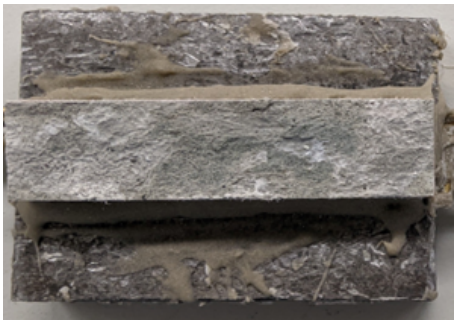

Figure D.17: Bottom debonded part of Specimen TG20-A-2

Figure D.18: Top debonded part of Specimen TG20-A-2

Table D.9: Summary of Image analysis result for specimen TG20-A-2

Contact Type	Colour Cluster	Results of Image analysis		Contact (%)		Average Contact (in %)
		Bottom Debonded Layer	Top Debonded Layer	Bottom Debonded Layer	Top Debonded Layer	
						
Poor				50,11%	49,82%	**49,97%**
Good				49,89%	50,18%	**50,04%**

Detailed report - Bottom debonded part of Specimen TG20-A-2

IMAGE COLOR SUMMARIZER

RGB, HSV, LCH & Lab image color statistics and clustering—simple and easy

HOME ANALYZE EXAMPLES API DOWNLOAD FAQ NEWS

IMAGE COLOR SUMMARY

THE IMAGE IN WORDS

aluminium chicago concord delta detroit dove dust friar grey half imagine industrial kensington masala mist mountain quarter rakaia silver star tapa transmission triple

COLOR CLUSTERS

Colors in the image were clustered into 2 groups (k-means). The average color of the colors for each cluster is shown. The name is the closest named color and its distance is shown using ΔE. The tags are the set of words formed by all named neighbours within ΔE ≤ 5. The list of words above is the set of all unique words in this set of words.

Cluster colors, sized by number of pixels:

cluster	pixels	name	HEX	RGB	HSV	LCH	Lab	tags
	50.11%	160,159,156 mountain mist ΔE=0.9	#A19D99	161 157 153	28 5 63	65 3 72	65 1 3	delta dust imagine kensington mist mountain rakaia star transmission triple grey
	49.89%	123,120,116 tapa ΔE=1.1	#7B7773	123 119 115	33 6 48	50 3 80	50 0 3	aluminium chicago concord detroit dove friar half industrial masala quarter silver tapa grey

IMAGE CLUSTER PARTITIONS

Pixels of the image assigned to each cluster. The border is the color of the cluster as calculated by the average value of its pixels.

RGB HISTOGRAM

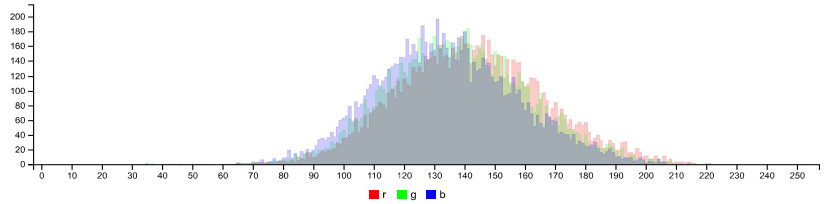

HSV HISTOGRAMS

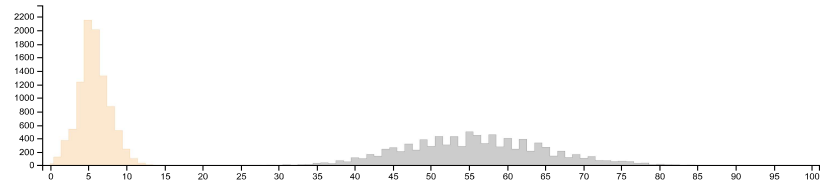

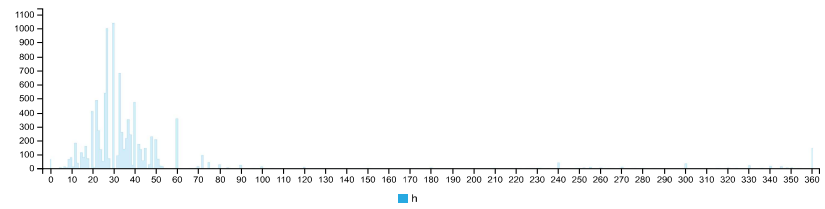

LCH HISTOGRAMS

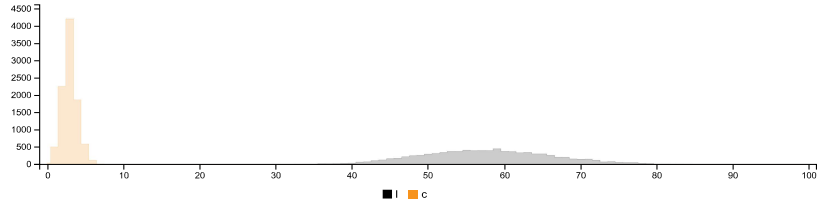

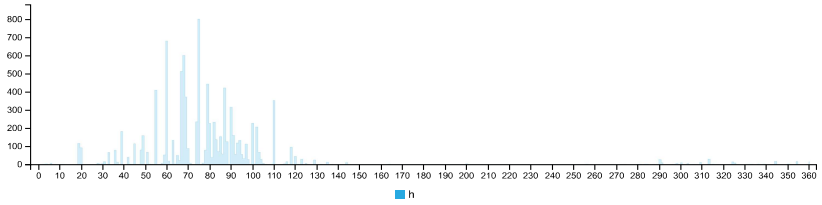

LAB HISTOGRAMS

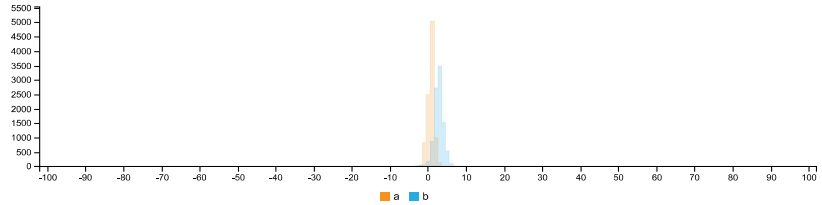

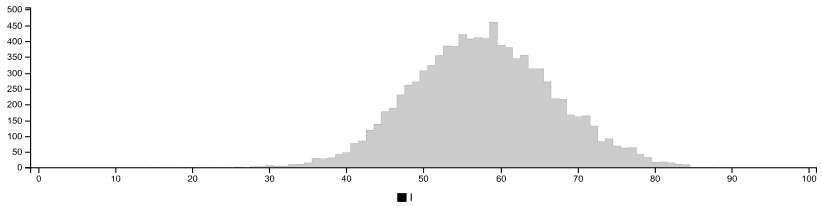

COLOR SPACE AND CHANNEL STATISTICS

	avg	med	min	max
RGB:R	142	142	42	221
RGB:G	138	138	37	216
RGB:B	134	133	35	214
HSV:H	30 1.00	30	0	360
HSV:S	6	6	0	19
HSV:V	56	56	16	87
LCH:L	58	58	15	87
LCH:C	3	3	0	8
LCH:H	73 1.00	75	2	360
LAB:L	58	58	15	87
LAB:A	1	1	-3	5
LAB:B	3	3	-5	8

Detailed report - Top debonded part of Specimen TG20-A-2

IMAGE COLOR SUMMARIZER

RGB, HSV, LCH & Lab image color statistics and clustering—simple and easy

HOME ANALYZE EXAMPLES API DOWNLOAD FAQ NEWS

IMAGE COLOR SUMMARY

THE IMAGE IN WORDS

battleship concrete eighth fantail foggy grey half jumbo masala mist mountain natural nobel old rakaia schooner seashell silver steel stonehenge suva tapa tide triple

COLOR CLUSTERS

Colors in the image were clustered into 2 groups (k-means). The average color of the colors for each cluster is shown. The name is the closest named color and its distance is shown using ΔE. The tags are the set of words formed by all named neighbours within ΔE ≤ 5. The list of words above is the set of all unique words in this set of words.

Cluster colors, sized by number of pixels:

cluster	pixels	name	HEX	RGB	HSV	LCH	Lab	tags
	50.18%	139,134,130 seashell ΔE=0.5	#898581	137 133 129	35 6 54	56 3 83	56 0 3	battleship eighth jumbo masala natural old schooner seashell silver steel suva grey
	49.82%	183,180,176 half mountain mist ΔE=1.3	#B8B3AF	184 179 175	26 5 72	73 3 68	73 1 3	concrete eighth fantail foggy half mist mountain nobel rakaia stonehenge tapa tide triple grey

IMAGE CLUSTER PARTITIONS

Pixels of the image assigned to each cluster. The border is the color of the cluster as calculated by the average value of its pixels.

RGB HISTOGRAM

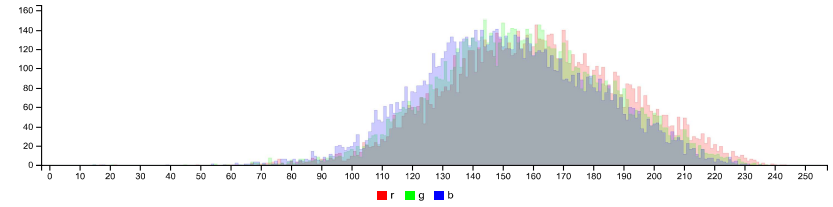

HSV HISTOGRAMS

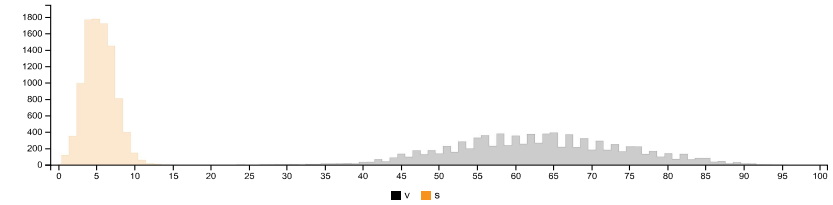

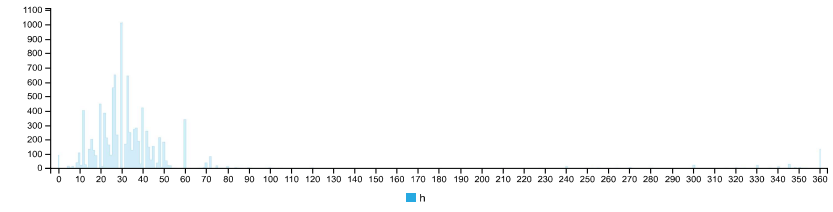

LCH HISTOGRAMS

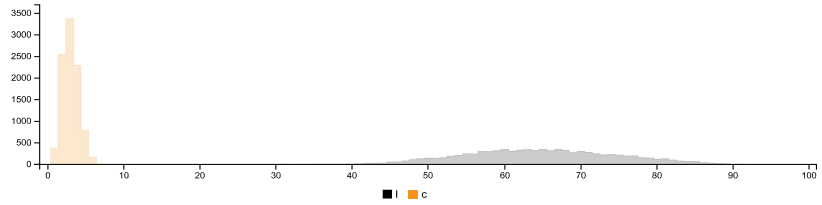

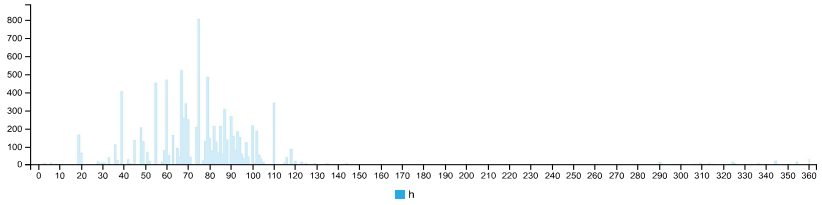

LAB HISTOGRAMS

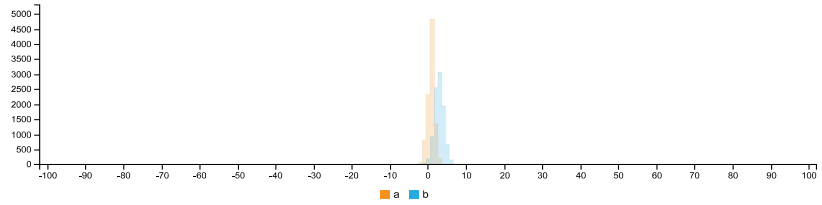

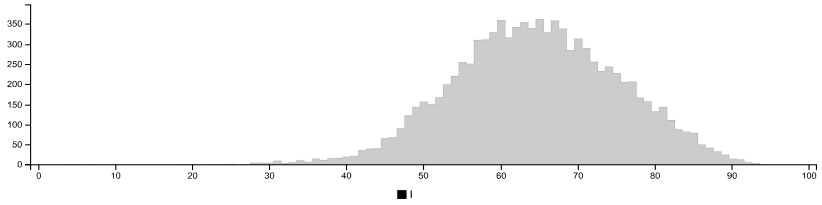

COLOR SPACE AND CHANNEL STATISTICS

	avg	med	min	max
RGB:R	160	160	17	243
RGB:G	156	156	15	237
RGB:B	152	151	15	235
HSV:H	30 1.00	30	0	360
HSV:S	5	5	0	20
HSV:V	63	63	7	95
LCH:L	64	64	4	94
LCH:C	3	3	0	7
LCH:H	72 1.00	75	2	360
LAB:L	64	64	4	94
LAB:A	1	1	-3	4
LAB:B	3	3	-4	7

Summary of Image Analysis for Specimen TG20-A-3

Figure D.19: Bottom debonded part of Specimen TG20-A-3

Figure D.20: Top debonded part of Specimen TG20-A-3

Table D.10: Summary of Image analysis result for specimen TG20-A-3

Contact Type	Colour Cluster	Results of Image analysis		Contact (%)		Average Contact (in %)
		Bottom Debonded Layer	Top Debonded Layer	Bottom Debonded Layer	Top Debonded Layer	
		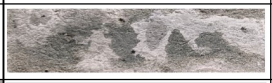				
Poor				51,95%	53,02%	**52,49%**
Good				48,03%	46,98%	**47,51%**

Detailed report - Bottom debonded part of Specimen TG20-A-3

IMAGE COLOR SUMMARIZER

RGB, HSV, LCH & Lab image color statistics and clustering—simple and easy

HOME ANALYZE EXAMPLES API DOWNLOAD FAQ NEWS

IMAGE COLOR SUMMARY

THE IMAGE IN WORDS

bombay concord concrete detroit dove eighth fantail felix friar grey half industrial lining medium milestone mist mountain nobel pink rakaia silver swan tapa triple

COLOR CLUSTERS

Colors in the image were clustered into 2 groups (k-means). The average color of the colors for each cluster is shown. The name is the closest named color and its distance is shown using ΔE. The tags are the set of words formed by all named neighbours within ΔE ≤ 5. The list of words above is the set of all unique words in this set of words.

Cluster colors, sized by number of pixels:

cluster	pixels	name	HEX	RGB	HSV	LCH	Lab	tags
	51.95%	183,177,177 nobel ΔE=1.2	#B9B1AF	185 177 175	12 5 73	73 3 40	73 2 2	bombay concrete fantail half milestone mist mountain nobel rakaia swan triple grey pink
	48.05%	123,120,116 tapa ΔE=1.5	#807B77	128 123 119	28 7 50	52 3 71	52 1 3	medium concord detroit dove eighth felix friar industrial lining silver tapa grey

IMAGE CLUSTER PARTITIONS

Pixels of the image assigned to each cluster. The border is the color of the cluster as calculated by the average value of its pixels.

RGB HISTOGRAM

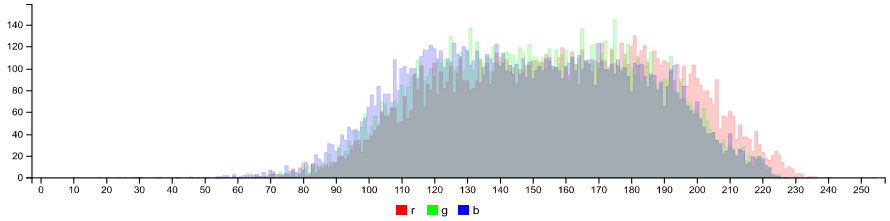

HSV HISTOGRAMS

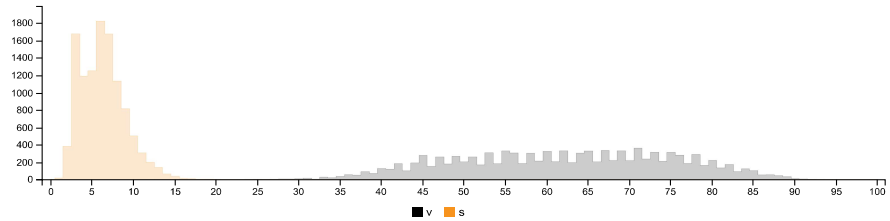

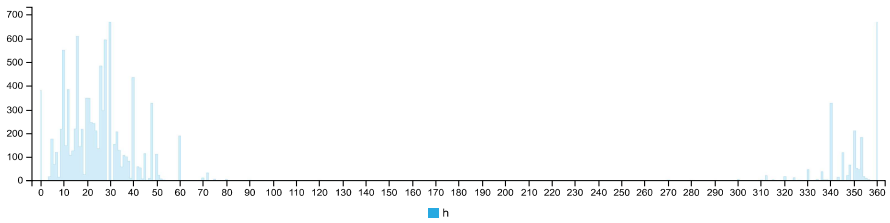

LCH HISTOGRAMS

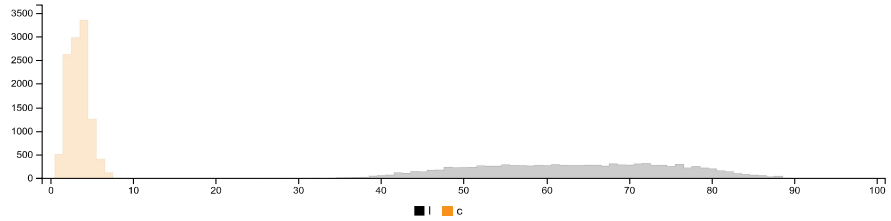

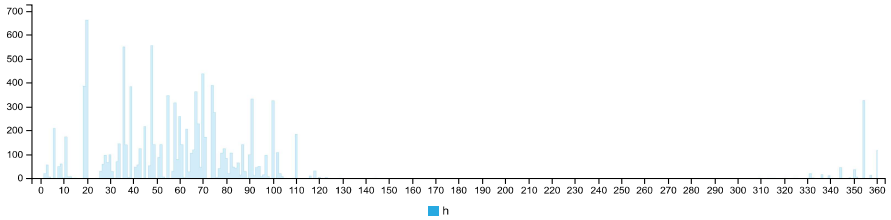

LAB HISTOGRAMS

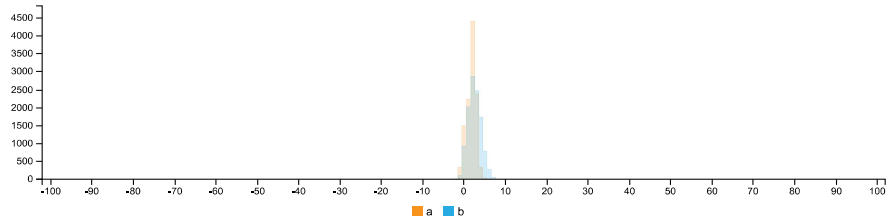

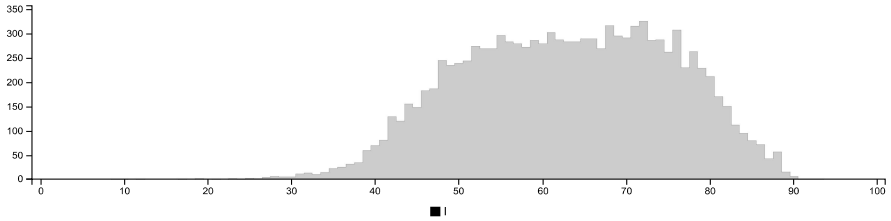

COLOR SPACE AND CHANNEL STATISTICS

	avg	med	min	max
RGB:R	158	159	29	240
RGB:G	152	152	26	233
RGB:B	149	148	18	234
HSV:H	18 1.00	27	0	360
HSV:S	6	6	0	40
HSV:V	62	62	12	94
LCH:L	63	63	9	93
LCH:C	3	3	0	8
LCH:H	52 1.00	60	2	360
LAB:L	63	63	9	93
LAB:A	2	2	−2	6
LAB:B	2	2	−2	8

Detailed report - Top debonded part of Specimen TG20-A-3

IMAGE COLOR SUMMARIZER

RGB, HSV, LCH & Lab image color statistics and clustering—simple and easy

HOME ANALYZE EXAMPLES API DOWNLOAD FAQ NEWS

IMAGE COLOR SUMMARY

THE IMAGE IN WORDS

aluminium blast cloudy double gauntlet gravel grey ironside masala mist mountain nobel quarter quick rakaia schooner silver stack stonehenge tarmac traffic viaduct

COLOR CLUSTERS

Colors in the image were clustered into 2 groups (k-means). The average color of the colors for each cluster is shown. The name is the closest named color and its distance is shown using ΔE. The tags are the set of words formed by all named neighbours within ΔE ≤ 5. The list of words above is the set of all unique words in this set of words.

Cluster colors, sized by number of pixels:

cluster	pixels	name	HEX	RGB	HSV	LCH	Lab	tags
	53.02%	169,165,165 double rakaia ΔE=1.8	#A8A29F	168 162 159	21 6 66	67 3 58	67 2 2	cloudy double mist mountain nobel quarter quick rakaia silver stonehenge viaduct grey
	46.98%	113,111,105 gauntlet ΔE=1.2	#706D68	112 109 104	34 7 44	46 3 81	46 0 3	aluminium blast double gauntlet gravel ironside masala quarter schooner stack tarmac traffic grey

IMAGE CLUSTER PARTITIONS

Pixels of the image assigned to each cluster. The border is the color of the cluster as calculated by the average value of its pixels.

RGB HISTOGRAM

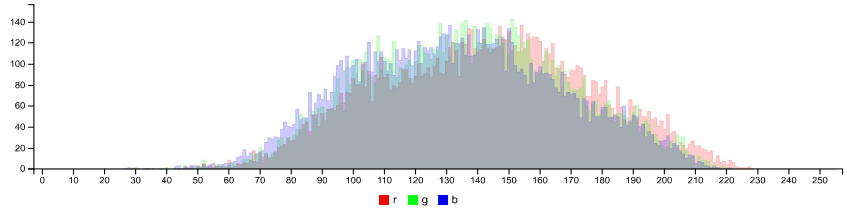

HSV HISTOGRAMS

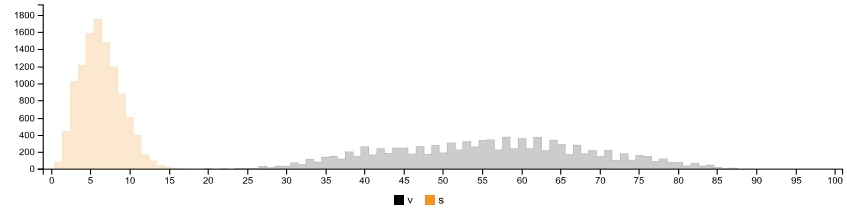

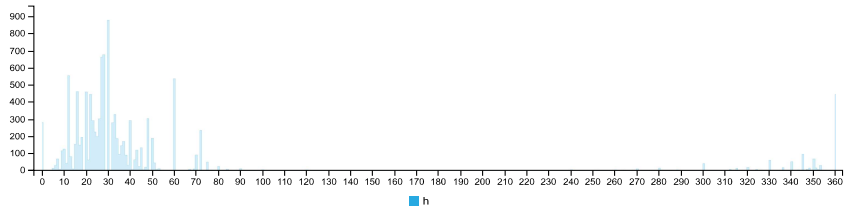

LCH HISTOGRAMS

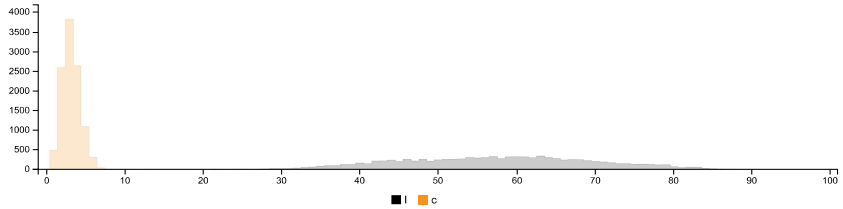

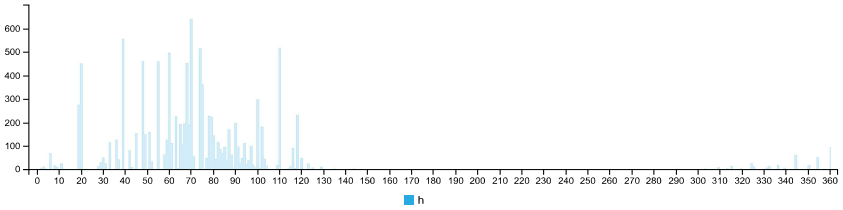

LAB HISTOGRAMS

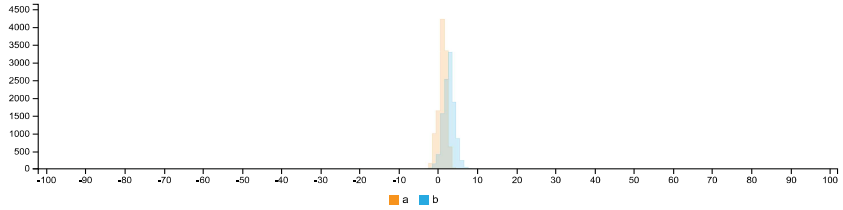

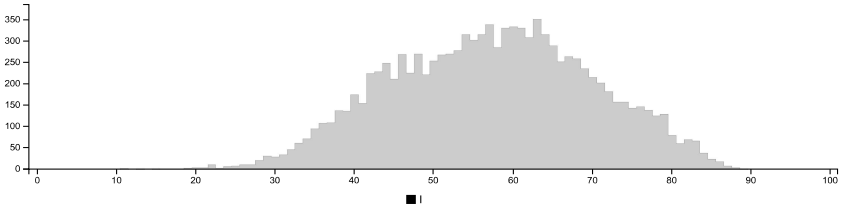

COLOR SPACE AND CHANNEL STATISTICS

	avg	med	min	max
RGB:R	142	143	30	228
RGB:G	137	137	29	222
RGB:B	133	133	26	221
HSV:H	26 1.00	28	0	360
HSV:S	6	6	0	30
HSV:V	56	56	12	89
LCH:L	57	57	11	89
LCH:C	3	3	0	8
LCH:H	65 1.00	69	2	360
LAB:L	57	57	11	89
LAB:A	1	1	-3	5
LAB:B	3	3	-3	8

Summary of Image Analysis for Specimen TG20-A-4

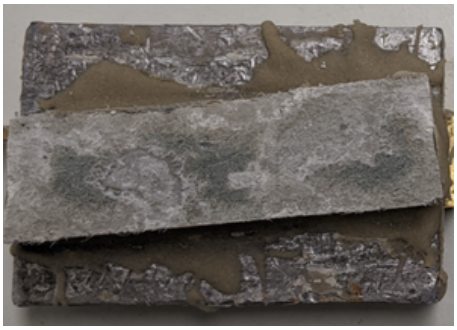

Figure D.21: Bottom debonded part of Specimen TG20-A-4

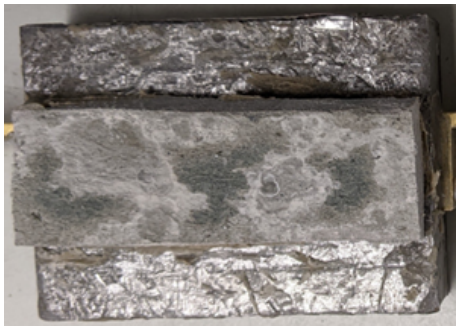

Figure D.22: Top debonded part of Specimen TG20-A-4

Table D.11: Summary of Image analysis result for specimen TG20-A-4

Contact Type	Colour Cluster	Results of Image analysis		Contact (%)		Average Contact (in %)
		Bottom Debonded Layer	Top Debonded Layer	Bottom Debonded Layer	Top Debonded Layer	
						
Poor				57,88%	55,12%	**56,50%**
Good				42,12%	44,88%	**43,50%**

Detailed report - Bottom debonded part of Specimen TG20-A-4

IMAGE COLOR SUMMARIZER

RGB, HSV, LCH & Lab image color statistics and clustering—simple and easy

HOME ANALYZE EXAMPLES API DOWNLOAD FAQ NEWS

IMAGE COLOR SUMMARY

THE IMAGE IN WORDS

alley chicago concord dark detroit dust eighth felix friar grey half hurricane industrial ironside lining masala medium olivish silver storm tapa tinpan

COLOR CLUSTERS

Colors in the image were clustered into 2 groups (k-means). The average color of the colors for each cluster is shown. The name is the closest named color and its distance is shown using ΔE. The tags are the set of words formed by all named neighbours within ΔE ≤ 5. The list of words above is the set of all unique words in this set of words.

Cluster colors, sized by number of pixels:

cluster	pixels	name	HEX	RGB	HSV	LCH	Lab	tags
	57.88%	128,126,121 friar grey ΔE=1.2	#827D79	130 125 121	26 6 51	53 3 67	53 1 3	medium concord detroit eighth felix friar hurricane industrial lining silver tapa grey
	42.12%	93,92,88 chicago ΔE=1.9	#635F5B	99 95 91	32 8 39	41 3 78	41 1 3	dark alley chicago dust half ironside masala olivish storm tinpan grey

IMAGE CLUSTER PARTITIONS

Pixels of the image assigned to each cluster. The border is the color of the cluster as calculated by the average value of its pixels.

RGB HISTOGRAM

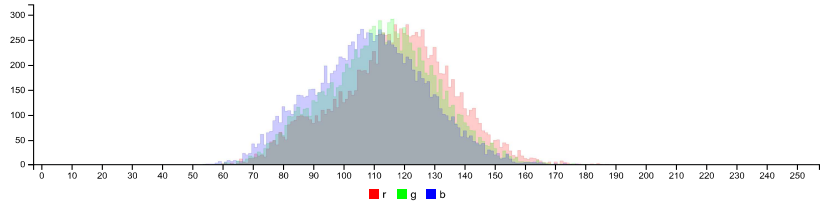

HSV HISTOGRAMS

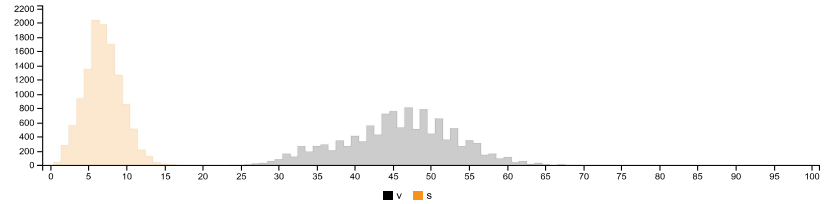

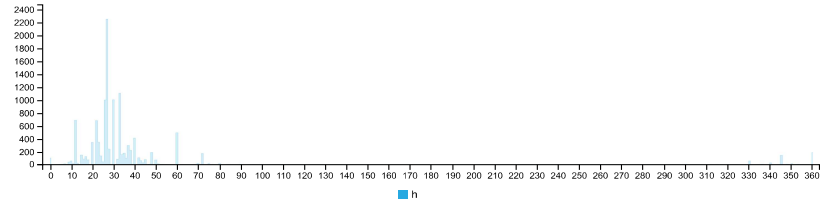

LCH HISTOGRAMS

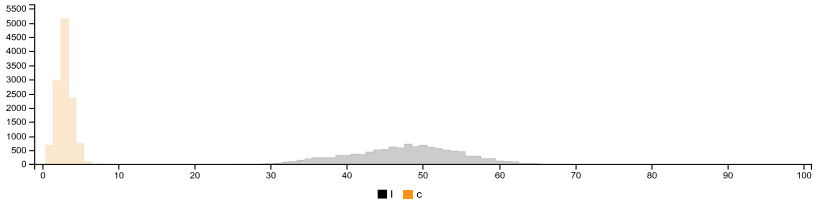

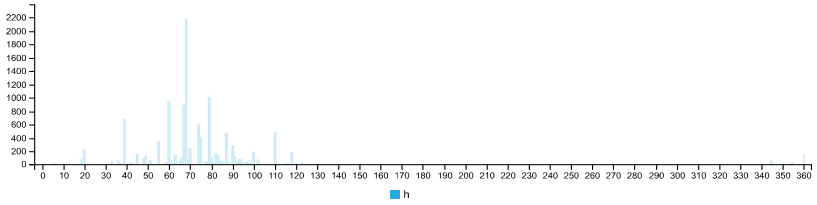

LAB HISTOGRAMS

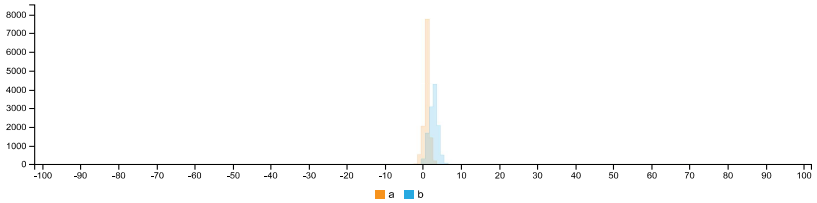

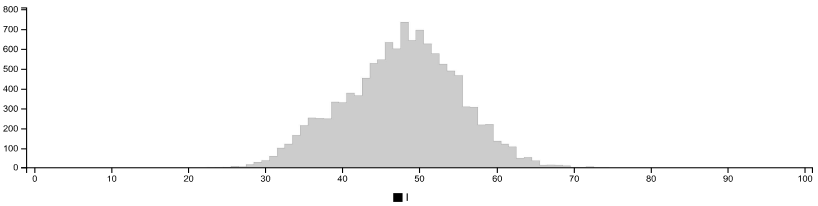

COLOR SPACE AND CHANNEL STATISTICS

	avg	med	min	max
RGB:R	117	118	55	187
RGB:G	112	113	54	180
RGB:B	109	109	51	178
HSV:H	28 1.00	27	0	360
HSV:S	7	7	0	29
HSV:V	46	46	22	73
LCH:L	48	48	23	74
LCH:C	3	3	0	11
LCH:H	69 1.00	68	3	360
LAB:L	48	48	23	74
LAB:A	1	1	-2	4
LAB:B	3	3	-3	11

IMAGE COLOR SUMMARIZER

RGB, HSV, LCH & Lab image color statistics and clustering—simple and easy

HOME ANALYZE EXAMPLES API DOWNLOAD FAQ NEWS

IMAGE COLOR SUMMARY

THE IMAGE IN WORDS

aluminium archive blast double fern friar gauntlet gravel grey half imagine ironside masala quarter rakaia schooner silver spanish stack stonehenge tarmac traffic triple

COLOR CLUSTERS

Colors in the image were clustered into 2 groups (k-means). The average color of the colors for each cluster is shown. The name is the closest named color and its distance is shown using ΔE. The tags are the set of words formed by all named neighbours within ΔE ≤ 5. The list of words above is the set of all unique words in this set of words.

Cluster colors, sized by number of pixels:

cluster	pixels	name	HEX	RGB	HSV	LCH	Lab	tags
	55.12%	153,147,140 silver fern ΔE=1.6	#9A9591	154 149 145	25 6 60	62 3 65	62 1 3	archive fern friar half imagine rakaia silver spanish stonehenge triple grey
	44.88%	113,111,105 gauntlet ΔE=0.9	#726E69	114 110 105	34 8 45	47 3 81	47 0 3	aluminium blast double gauntlet gravel ironside masala quarter schooner stack tarmac traffic grey

IMAGE CLUSTER PARTITIONS

Pixels of the image assigned to each cluster. The border is the color of the cluster as calculated by the average value of its pixels.

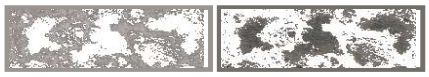

RGB HISTOGRAM

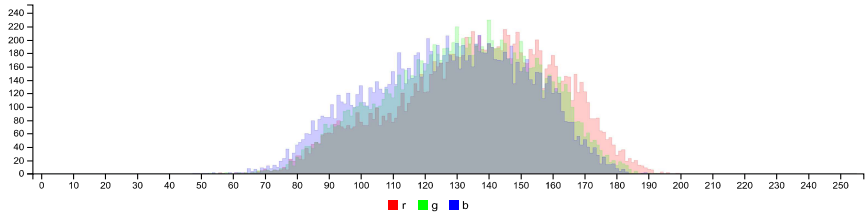

HSV HISTOGRAMS

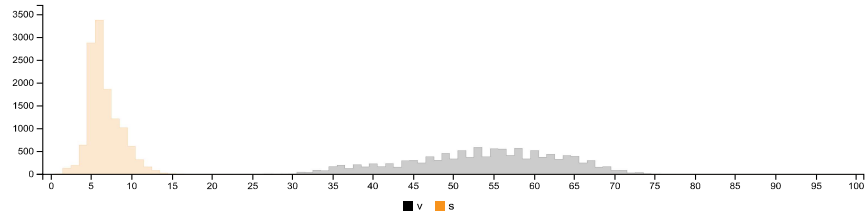

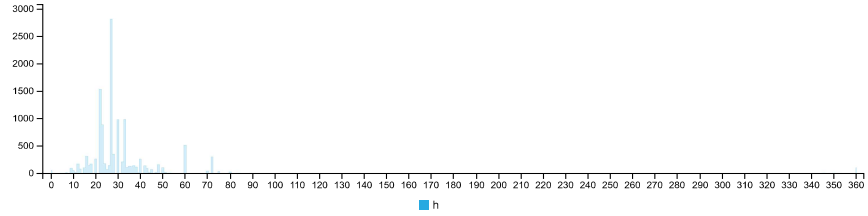

LCH HISTOGRAMS

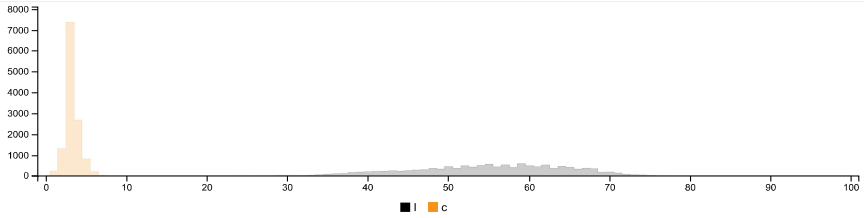

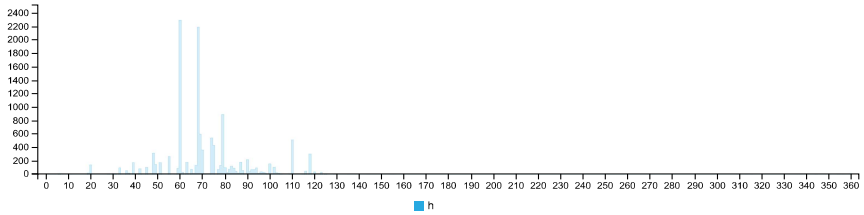

LAB HISTOGRAMS

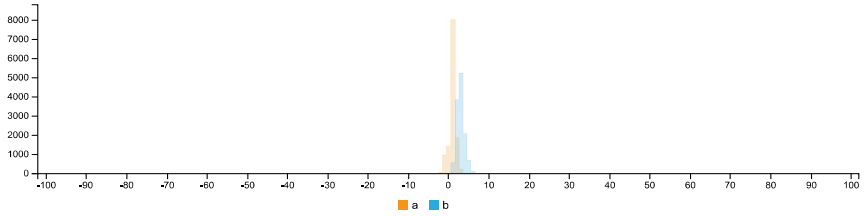

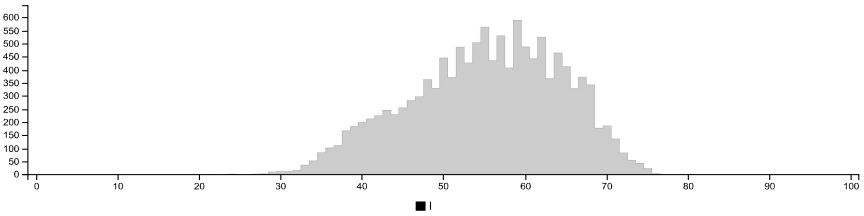

COLOR SPACE AND CHANNEL STATISTICS

	avg	med	min	max
RGB:R	136	138	54	199
RGB:G	131	133	53	192
RGB:B	127	128	48	189
HSV:H	29 1.00	27	0	360
HSV:S	7	6	0	24
HSV:V	53	54	21	78
LCH:L	55	56	22	78
LCH:C	3	3	0	8
LCH:H	71 1.00	68	2	360
LAB:L	55	56	22	78
LAB:A	1	1	-3	4
LAB:B	3	3	-2	8

D.1.2. Specimen Type-B

Summary of Image Analysis for Specimen TG5-B-1

Figure D.23: Bottom debonded part of Specimen TG5-B-1

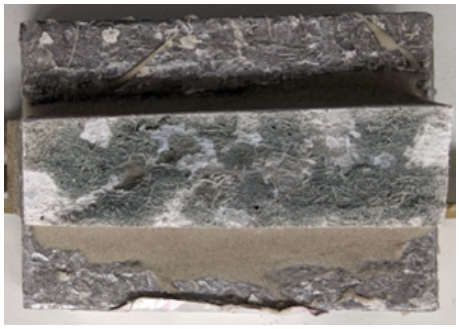

Figure D.24: Top debonded part of Specimen TG5-B-1

Table D.12: Summary of Image analysis result for specimen TG5-B-1

Contact Type	Colour Cluster	Results of Image analysis		Contact (%)		Average Contact (in %)
		Bottom Debonded Layer	Top Debonded Layer	Bottom Debonded Layer	Top Debonded Layer	
		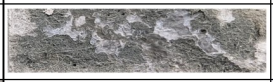				
Poor				38,40%	32,54%	**35,47%**
Good				61,60%	67,46%	**64,53%**

Detailed report - Bottom debonded part of Specimen TG5-B-1

IMAGE COLOR SUMMARIZER

RGB, HSV, LCH & Lab image color statistics and clustering—simple and easy

HOME ANALYZE EXAMPLES API DOWNLOAD FAQ NEWS

IMAGE COLOR SUMMARY

THE IMAGE IN WORDS

atmosphere blast cloudy dawn delta double flint foggy friar gauntlet gravel grey ironside lattitude quarter rakaia stack stonehenge swordfish tapa traffic triple

COLOR CLUSTERS

Colors in the image were clustered into 2 groups (k-means). The average color of the colors for each cluster is shown. The name is the closest named color and its distance is shown using ΔE. The tags are the set of words formed by all named neighbours within ΔE ≤ 5. The list of words above is the set of all unique words in this set of words.

Cluster colors, sized by number of pixels:

cluster	pixels	name	HEX	RGB	HSV	LCH	Lab	tags
	55.75%	108,109,104 traffic ΔE=0.7	#6D6C66	109 108 102	53 6 43	46 3 104	46 -1 3	blast double flint gauntlet gravel ironside lattitude quarter stack tapa traffic triple grey
	44.25%	172,165,159 cloudy ΔE=1.1	#A8A49F	168 164 159	32 5 66	68 3 79	68 1 3	atmosphere cloudy dawn delta double foggy friar quarter rakaia stonehenge swordfish tapa grey

IMAGE CLUSTER PARTITIONS

Pixels of the image assigned to each cluster. The border is the color of the cluster as calculated by the average value of its pixels.

RGB HISTOGRAM

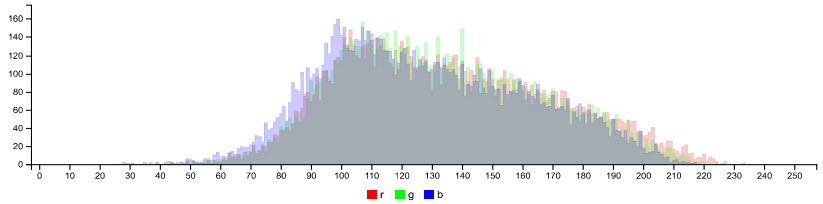

HSV HISTOGRAMS

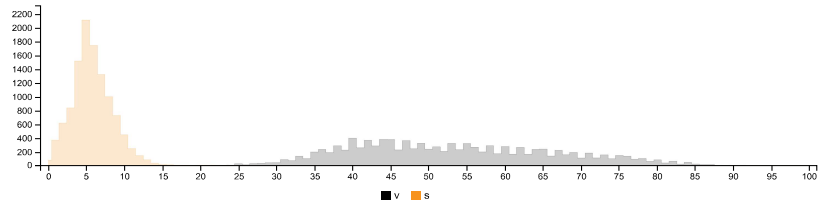

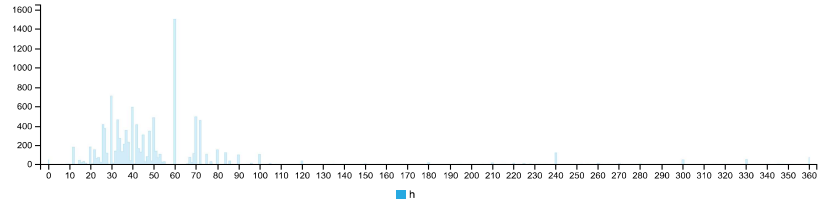

LCH HISTOGRAMS

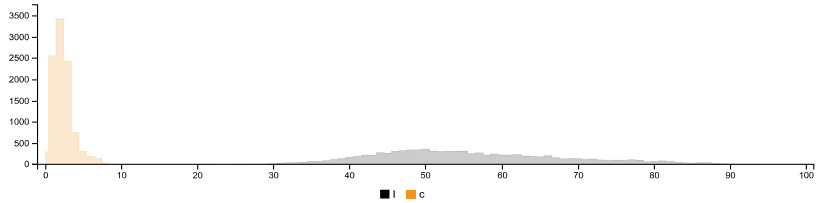

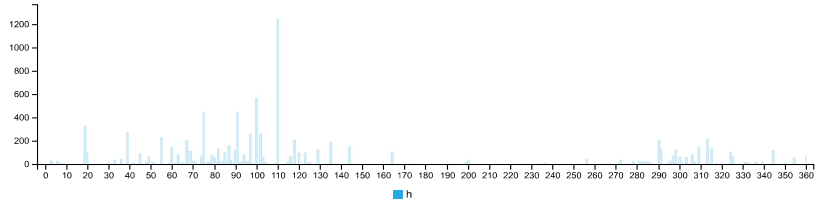

LAB HISTOGRAMS

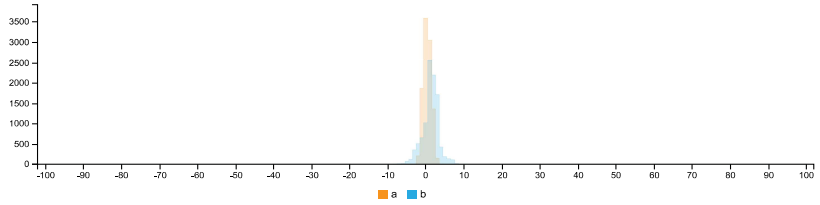

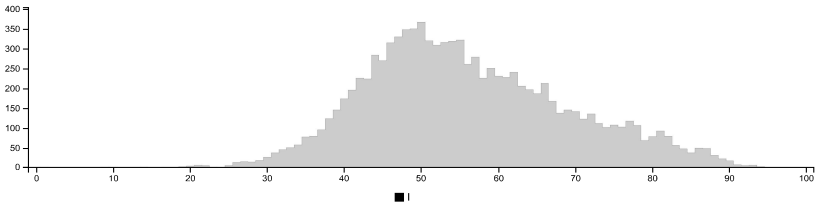

COLOR SPACE AND CHANNEL STATISTICS

	avg	med	min	max
RGB:R	136	131	4	242
RGB:G	135	129	4	238
RGB:B	133	127	4	237
HSV:H	30 1.00	52	0	360
HSV:S	4	4	0	22
HSV:V	54	51	2	95
LCH:L	56	54	1	94
LCH:C	2	2	0	10
LCH:H	73 1.00	102	3	360
LAB:L	56	54	1	94
LAB:A	0	0	-3	4
LAB:B	1	1	-8	10

Detailed report - Top debonded part of Specimen TG5-B-1

IMAGE COLOR SUMMARIZER

RGB, HSV, LCH & Lab image color statistics and clustering—simple and easy

HOME ANALYZE EXAMPLES API DOWNLOAD FAQ NEWS

IMAGE COLOR SUMMARY

THE IMAGE IN WORDS

chicane delta double dust granite grey half ironside kensington masala mist mountain rakaia stack star storm traffic transmission triple trojan

COLOR CLUSTERS

Colors in the image were clustered into 2 groups (k-means). The average color of the colors for each cluster is shown. The name is the closest named color and its distance is shown using ΔE. The tags are the set of words formed by all named neighbours within ΔE ≤ 5. The list of words above is the set of all unique words in this set of words.

Cluster colors, sized by number of pixels:

cluster	pixels	name	HEX	RGB	HSV	LCH	Lab	tags
	58.32%	103,102,98 ironside grey ΔE=1.5	#696863	105 104 99	51 6 41	44 3 103	44 -1 3	chicane double dust granite half ironside masala stack storm traffic triple trojan grey
	41.68%	160,159,156 mountain mist ΔE=0.9	#A29F9B	162 159 155	32 4 63	65 2 78	65 0 2	delta double dust kensington mist mountain rakaia star transmission triple grey

IMAGE CLUSTER PARTITIONS

Pixels of the image assigned to each cluster. The border is the color of the cluster as calculated by the average value of its pixels.

RGB HISTOGRAM

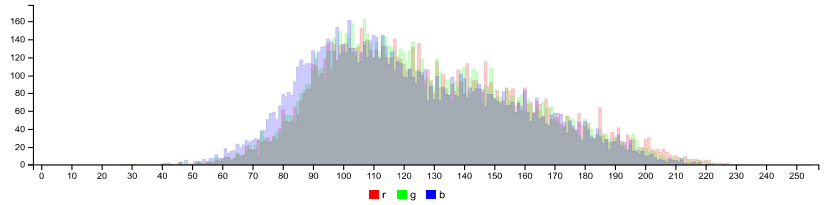

HSV HISTOGRAMS

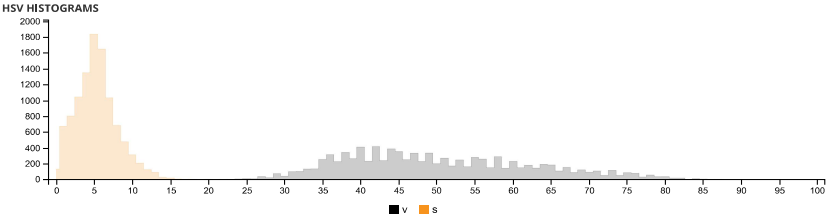

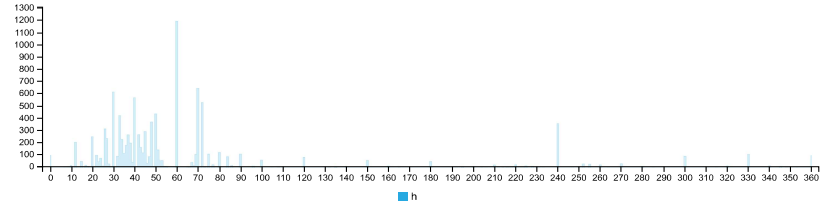

LCH HISTOGRAMS

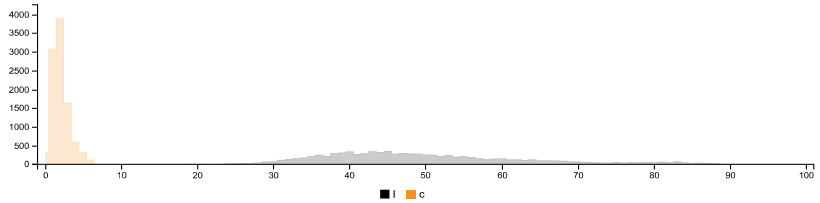

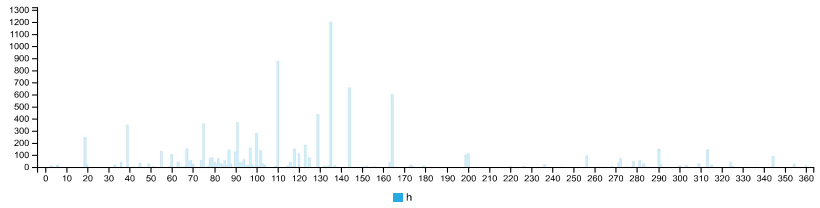

LAB HISTOGRAMS

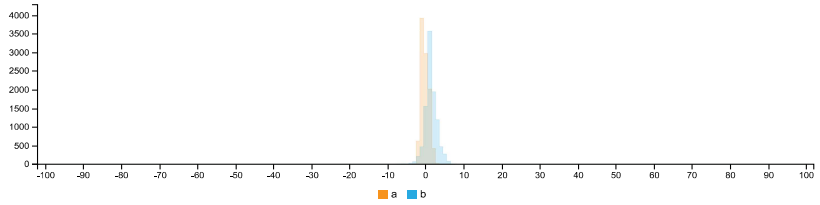

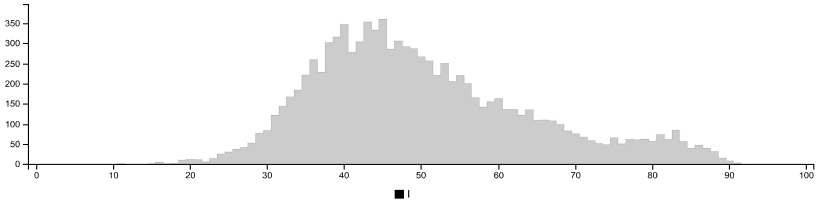

COLOR SPACE AND CHANNEL STATISTICS

	avg	med	min	max
RGB:R	121	113	4	239
RGB:G	121	113	4	232
RGB:B	118	110	3	232
HSV:H	66 1.00	75	0	360
HSV:S	4	3	0	25
HSV:V	48	45	2	94
LCH:L	50	48	1	93
LCH:C	2	2	0	11
LCH:H	107 1.00	118	2	360
LAB:L	50	48	1	93
LAB:A	-0	0	-3	4
LAB:B	1	1	-9	10

Summary of Image Analysis for Specimen TG5-B-2

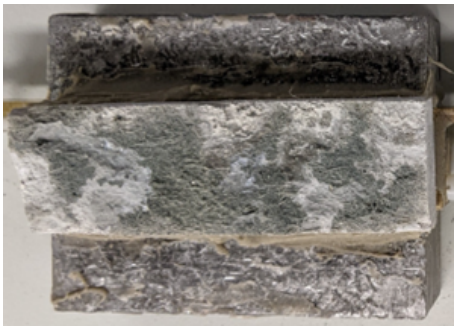

Figure D.25: Bottom debonded part of Specimen TG5-B-2

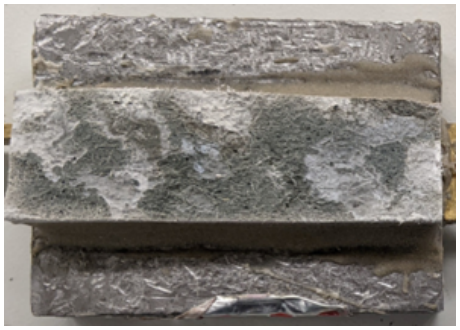

Figure D.26: Top debonded part of Specimen TG5-B-2

Table D.13: Summary of Image analysis result for specimen TG5-B-2

Contact Type	Colour Cluster	Results of Image analysis		Contact (%)		Average Contact (in %)
		Bottom Debonded Layer	Top Debonded Layer	Bottom Debonded Layer	Top Debonded Layer	
		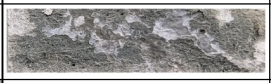				
Poor				44,25%	41,68%	**44,25%**
Good				55,75%	58,32%	**55,75%**

Detailed report - Bottom debonded part of Specimen TG5-B-2

IMAGE COLOR SUMMARIZER

RGB, HSV, LCH & Lab image color statistics and clustering—simple and easy

HOME ANALYZE EXAMPLES API DOWNLOAD FAQ NEWS

IMAGE COLOR SUMMARY

THE IMAGE IN WORDS

atmosphere blast cloudy dawn delta double flint foggy friar gauntlet gravel grey ironside lattitude quarter rakaia stack stonehenge swordfish tapa traffic triple

COLOR CLUSTERS

Colors in the image were clustered into 2 groups (k-means). The average color of the colors for each cluster is shown. The name is the closest named color and its distance is shown using ΔE. The tags are the set of words formed by all named neighbours within ΔE ≤ 5. The list of words above is the set of all unique words in this set of words.

Cluster colors, sized by number of pixels:

cluster	pixels	name	HEX	RGB	HSV	LCH	Lab	tags
	55.75%	108,109,104 traffic ΔE=0.7	#6D6C66	109 108 102	53 6 43	46 3 104	46 -1 3	blast double flint gauntlet gravel ironside lattitude quarter stack tapa traffic triple grey
	44.25%	172,165,159 cloudy ΔE=1.1	#A8A49F	168 164 159	32 5 66	68 3 79	68 1 3	atmosphere cloudy dawn delta double foggy friar quarter rakaia stonehenge swordfish tapa grey

IMAGE CLUSTER PARTITIONS

Pixels of the image assigned to each cluster. The border is the color of the cluster as calculated by the average value of its pixels.

RGB HISTOGRAM

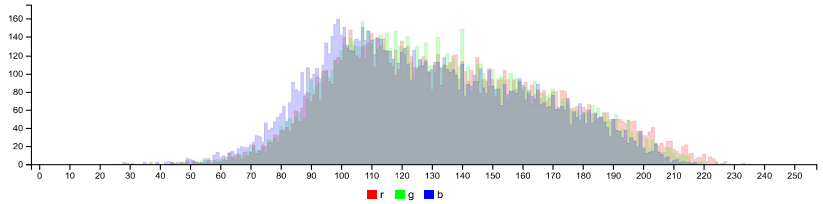

HSV HISTOGRAMS

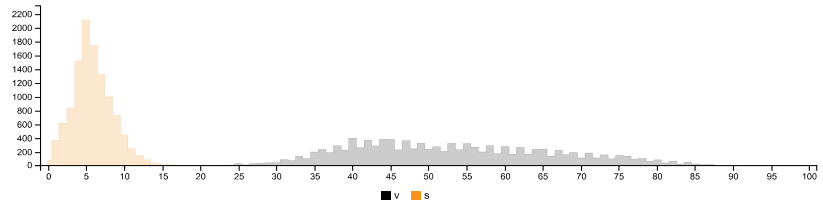

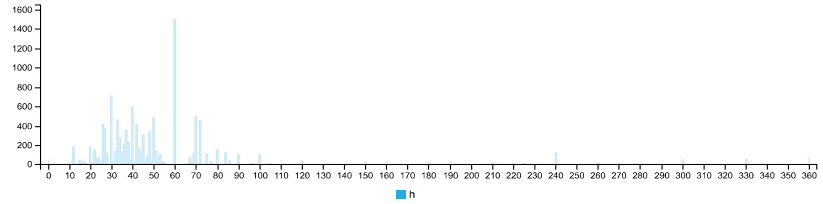

LCH HISTOGRAMS

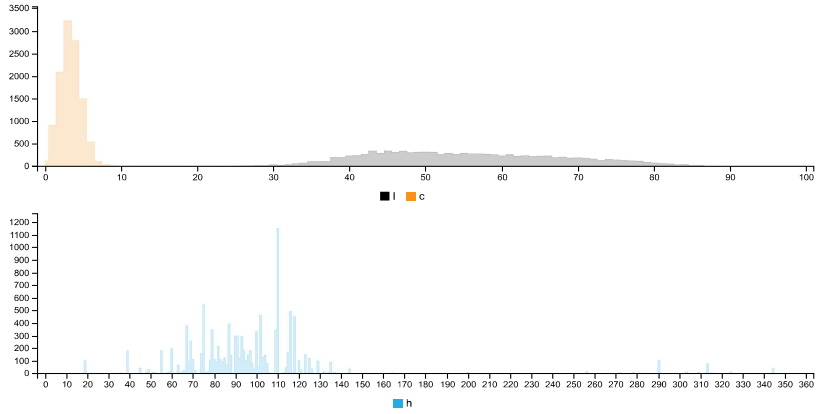

LAB HISTOGRAMS

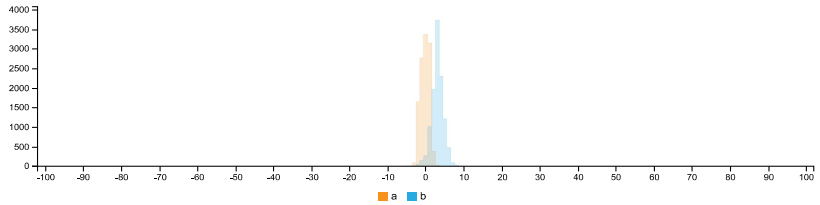

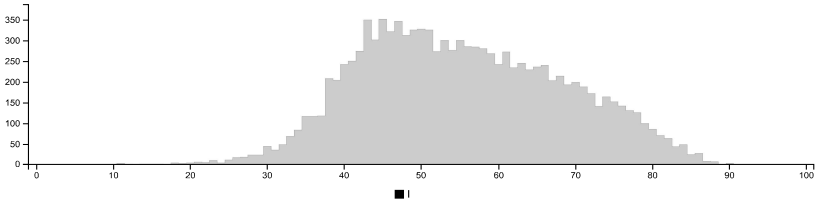

COLOR SPACE AND CHANNEL STATISTICS

	avg	med	min	max
RGB:R	135	132	29	235
RGB:G	133	130	29	226
RGB:B	128	124	25	218
HSV:H	45 1.00	44	0	360
HSV:S	6	6	0	25
HSV:V	53	52	11	92
LCH:L	55	54	11	90
LCH:C	3	3	0	15
LCH:H	91 1.00	95	3	360
LAB:L	55	54	11	90
LAB:A	-0	0	-4	3
LAB:B	3	3	-6	15

IMAGE COLOR SUMMARIZER

RGB, HSV, LCH & Lab image color statistics and clustering—simple and easy

HOME ANALYZE EXAMPLES API DOWNLOAD FAQ NEWS

IMAGE COLOR SUMMARY

THE IMAGE IN WORDS

chicane delta double dust granite grey half ironside kensington masala mist mountain rakaia stack star storm traffic transmission triple trojan

COLOR CLUSTERS

Colors in the image were clustered into 2 groups (k-means). The average color of the colors for each cluster is shown. The name is the closest named color and its distance is shown using ΔE. The tags are the set of words formed by all named neighbours within ΔE ≤ 5. The list of words above is the set of all unique words in this set of words.

Cluster colors, sized by number of pixels:

cluster	pixels	name	HEX	RGB	HSV	LCH	Lab	tags
	58.32%	103,102,98 ironside grey ΔE=1.5	#696863	105 104 99	51 6 41	44 3 103	44 -1 3	chicane double dust granite half ironside masala stack storm traffic triple trojan grey
	41.68%	160,159,156 mountain mist ΔE=0.9	#A29F9B	162 159 155	32 4 63	65 2 78	65 0 2	delta double dust kensington mist mountain rakaia star transmission triple grey

IMAGE CLUSTER PARTITIONS

Pixels of the image assigned to each cluster. The border is the color of the cluster as calculated by the average value of its pixels.

RGB HISTOGRAM

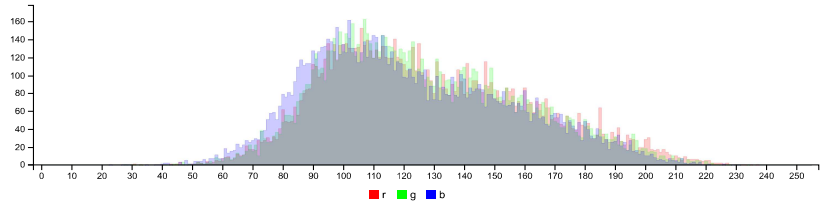

HSV HISTOGRAMS

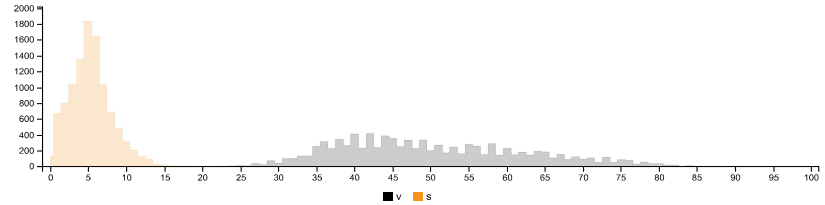

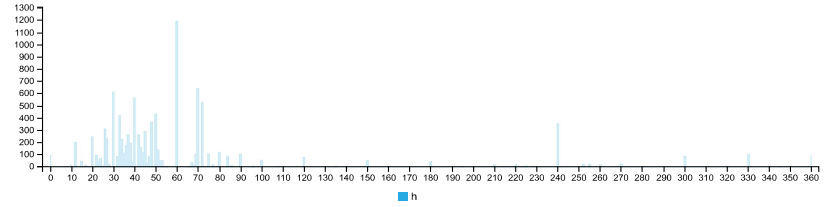

LCH HISTOGRAMS

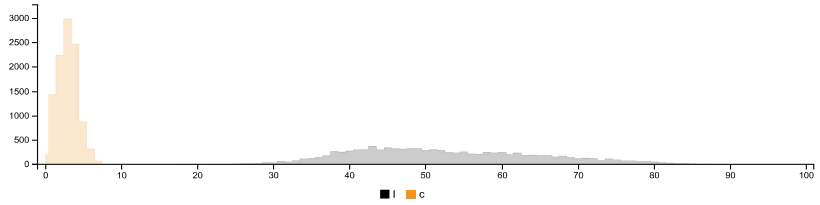

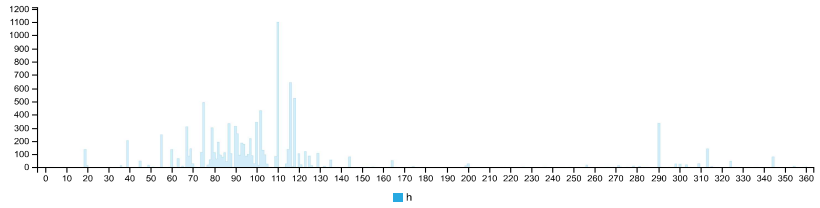

LAB HISTOGRAMS

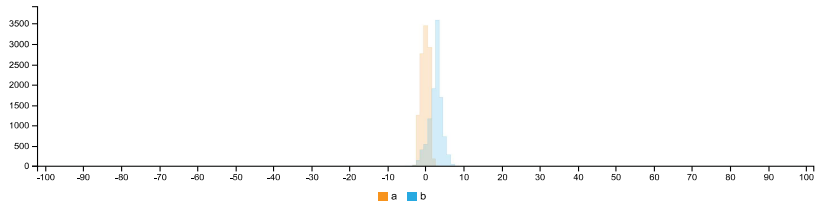

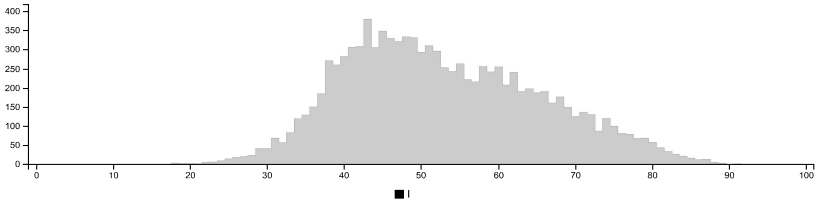

COLOR SPACE AND CHANNEL STATISTICS

	avg	med	min	max
RGB:R	129	124	30	237
RGB:G	127	122	28	234
RGB:B	122	117	23	231
HSV:H	44 1.00	48	0	360
HSV:S	5	5	0	26
HSV:V	51	49	12	93
LCH:L	53	51	10	93
LCH:C	3	3	0	11
LCH:H	91 1.00	99	3	360
LAB:L	53	51	10	93
LAB:A	-0	0	-3	4
LAB:B	3	3	-7	11

Summary of Image Analysis for Specimen TG5-B-3

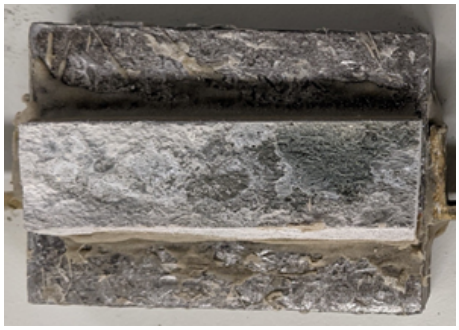

Figure D.27: Bottom debonded part of Specimen TG5-B-3

Figure D.28: Top debonded part of Specimen TG5-B-3

Table D.14: Summary of Image analysis result for specimen TG5-B-3

Contact Type	Colour Cluster	Results of Image analysis		Contact (%)		Average Contact (in %)
		Bottom Debonded Layer	Top Debonded Layer	Bottom Debonded Layer	Top Debonded Layer	
						
Poor				52,02%	53,19%	**52,61%**
Good				47,98%	46,81%	**47,40%**

Detailed report - Bottom debonded part of Specimen TG5-B-3

IMAGE COLOR SUMMARIZER

RGB, HSV, LCH & Lab image color statistics and clustering—simple and easy

HOME ANALYZE EXAMPLES API DOWNLOAD FAQ NEWS

IMAGE COLOR SUMMARY

THE IMAGE IN WORDS

atmosphere chicane cloudy dark double dust granite grey half ironside light masala quarter quick rakaia silver stack stonehenge storm triple trojan

COLOR CLUSTERS

Colors in the image were clustered into 2 groups (k-means). The average color of the colors for each cluster is shown. The name is the closest named color and its distance is shown using ΔE. The tags are the set of words formed by all named neighbours within ΔE ≤ 5. The list of words above is the set of all unique words in this set of words.

Cluster colors, sized by number of pixels:

cluster	pixels	name	HEX	RGB	HSV	LCH	Lab	tags
	52.02%	169,165,165 double rakaia ΔE=1.1	#A8A4A1	168 164 161	25 4 66	68 2 64	68 1 2	light dark atmosphere cloudy double quarter quick rakaia silver stonehenge grey
	47.98%	103,102,98 ironside grey ΔE=0.6	#676561	103 101 97	39 5 40	43 2 89	43 0 2	chicane double dust granite half ironside masala stack storm triple trojan grey

IMAGE CLUSTER PARTITIONS

Pixels of the image assigned to each cluster. The border is the color of the cluster as calculated by the average value of its pixels.

RGB HISTOGRAM

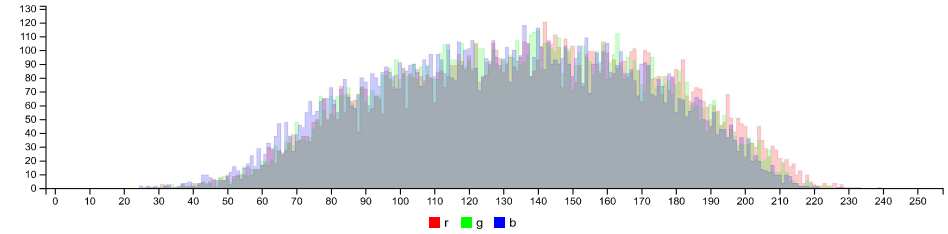

HSV HISTOGRAMS

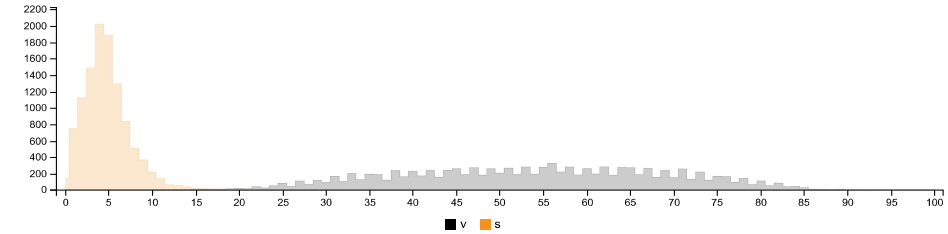

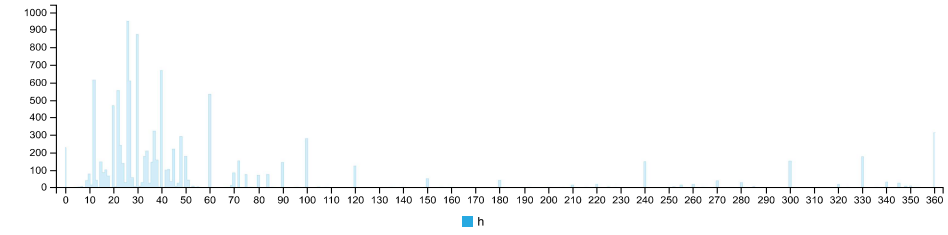

LCH HISTOGRAMS

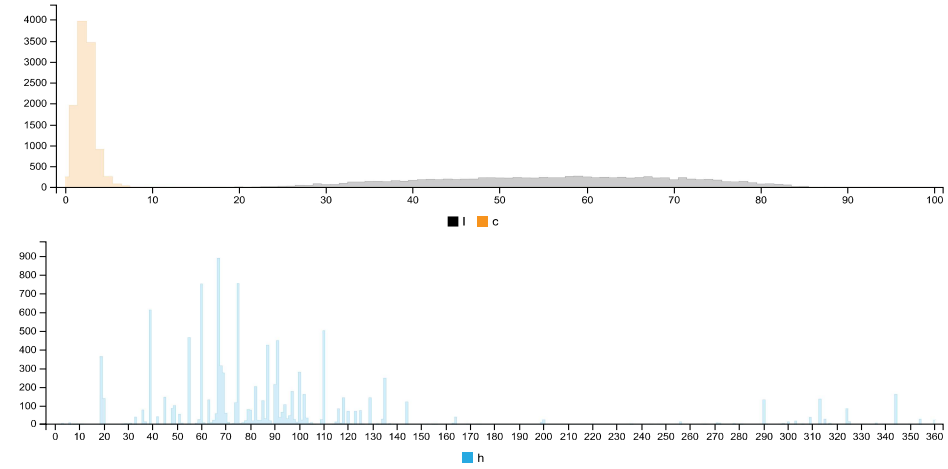

LAB HISTOGRAMS

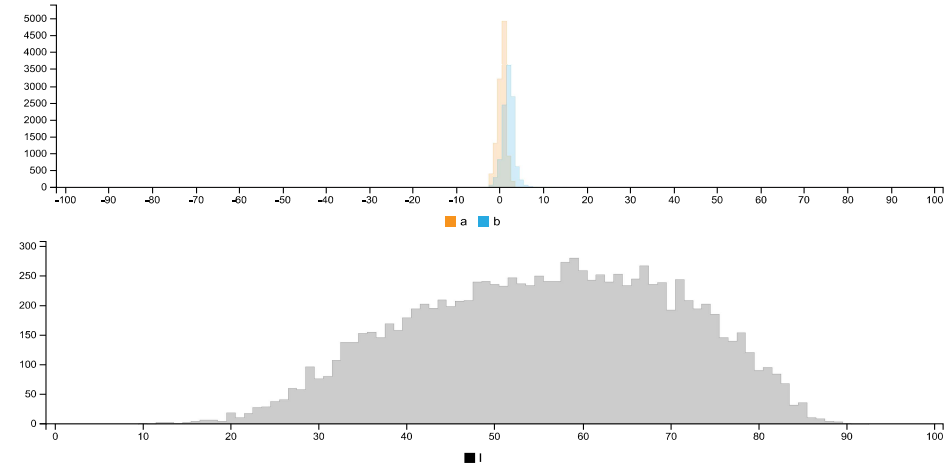

COLOR SPACE AND CHANNEL STATISTICS

	avg	med	min	max
RGB:R	137	138	27	239
RGB:G	134	135	28	231
RGB:B	131	132	25	228
HSV:H	31 1.00	33	0	360
HSV:S	5	4	0	35
HSV:V	54	54	11	94
LCH:L	56	56	10	92
LCH:C	2	2	0	15
LCH:H	72 1.00	75	2	360
LAB:L	56	56	10	92
LAB:A	0	1	-3	5
LAB:B	2	2	-3	14

Detailed report - Top debonded part of Specimen TG5-B-3

IMAGE COLOR SUMMARIZER

RGB, HSV, LCH & Lab image color statistics and clustering—simple and easy

HOME ANALYZE EXAMPLES API DOWNLOAD FAQ NEWS

IMAGE COLOR SUMMARY

THE IMAGE IN WORDS

alley chicago dark double dust grey kensington mist mountain olivish rakaia star storm tinpan torque transmission triple

COLOR CLUSTERS

Colors in the image were clustered into 2 groups (k-means). The average color of the colors for each cluster is shown. The name is the closest named color and its distance is shown using ΔE. The tags are the set of words formed by all named neighbours within ΔE ≤ 5. The list of words above is the set of all unique words in this set of words.

Cluster colors, sized by number of pixels:

cluster	pixels	name	HEX	RGB	HSV	LCH	Lab	tags
	53.19%	160,159,156 mountain mist ΔE=0.6	#A19F9C	161 159 156	35 3 63	66 2 83	66 0 2	double dust kensington mist mountain rakaia star transmission triple grey
	46.81%	92,91,89 tinpan alley ΔE=0.6	#5E5D5B	94 93 91	45 3 37	40 2 97	40 0 2	dark alley chicago dust olivish storm tinpan torque grey

IMAGE CLUSTER PARTITIONS

Pixels of the image assigned to each cluster. The border is the color of the cluster as calculated by the average value of its pixels.

RGB HISTOGRAM

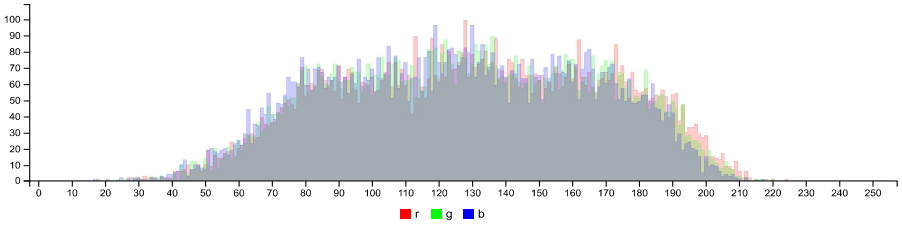

HSV HISTOGRAMS

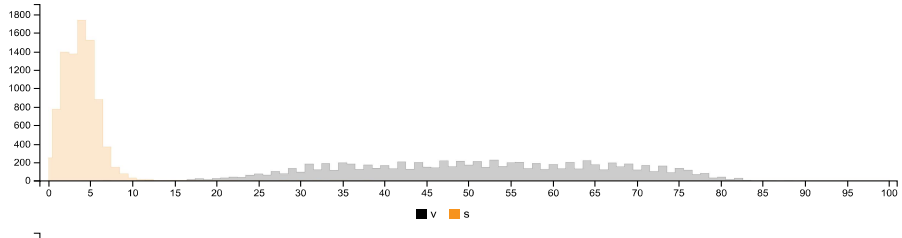

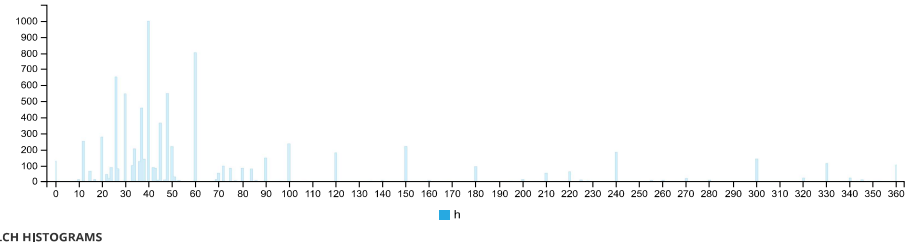

LCH HISTOGRAMS

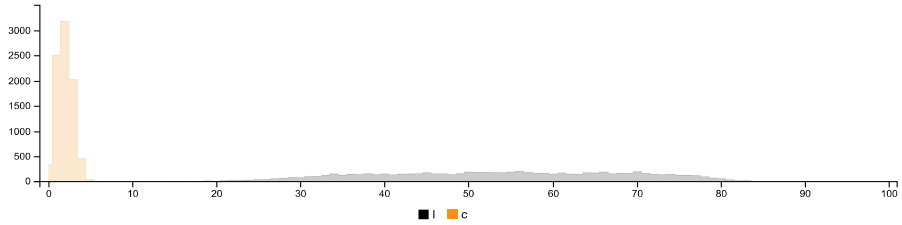

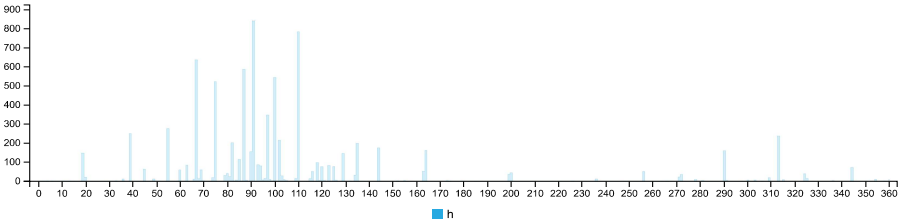

LAB HISTOGRAMS

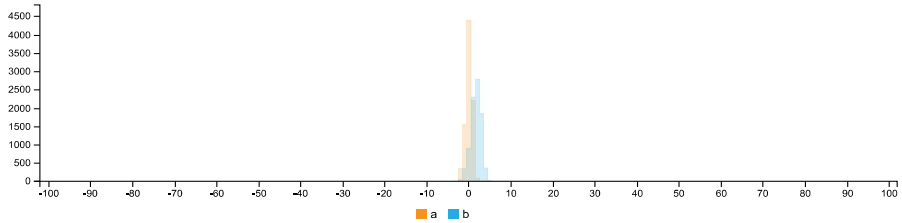

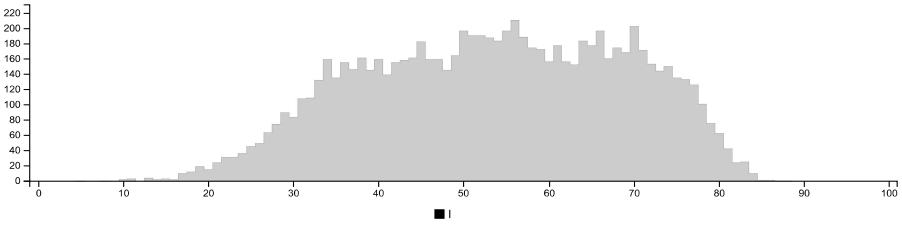

COLOR SPACE AND CHANNEL STATISTICS

	avg	med	min	max
RGB:R	130	130	18	224
RGB:G	129	129	18	220
RGB:B	126	126	17	217
HSV:H	42 1.00	42	0	360
HSV:S	4	4	0	38
HSV:V	51	51	7	88
LCH:L	53	54	5	88
LCH:C	2	2	0	16
LCH:H	88 1.00	92	1	360
LAB:L	53	54	5	88
LAB:A	0	0	-4	14
LAB:B	2	2	-3	16

Summary of Image Analysis for Specimen TG5-B-4

Figure D.29: Bottom debonded part of Specimen TG5-B-4

Figure D.30: Top debonded part of Specimen TG5-B-4

Table D.15: Summary of Image analysis result for specimen TG5-B-4

Contact Type	Colour Cluster	Results of Image analysis		Contact (%)		Average Contact (in %)
		Bottom Debonded Layer	Top Debonded Layer	Bottom Debonded Layer	Top Debonded Layer	
						
Poor				53,65%	53,76%	**53,71%**
Good				46,35%	46,24%	**46,30%**

Detailed report - Bottom debonded part of Specimen TG5-B-4

IMAGE COLOR SUMMARIZER

RGB, HSV, LCH & Lab image color statistics and clustering—simple and easy

HOME ANALYZE EXAMPLES API DOWNLOAD FAQ NEWS

IMAGE COLOR SUMMARY

THE IMAGE IN WORDS

battleship brownish davy davy's dim grey jumbo lining old reddish ricochet silver steel torque trolley tundora web wireless

COLOR CLUSTERS

Colors in the image were clustered into 2 groups (k-means). The average color of the colors for each cluster is shown. The name is the closest named color and its distance is shown using ΔE. The tags are the set of words formed by all named neighbours within ΔE ≤ 5. The list of words above is the set of all unique words in this set of words.

Cluster colors, sized by number of pixels:

cluster	pixels	name	HEX	RGB	HSV	LCH	Lab	tags
	53.65%	132,132,130 battleship grey ΔE=1.0	#858280	133 130 128	24 4 52	55 2 63	55 1 2	battleship jumbo lining old ricochet silver steel trolley web grey
	46.35%	90,87,85 torque ΔE=0.9	#585654	88 86 84	34 5 34	37 2 82	37 0 2	brownish davy davy's dim reddish torque tundora wireless grey

IMAGE CLUSTER PARTITIONS

Pixels of the image assigned to each cluster. The border is the color of the cluster as calculated by the average value of its pixels.

RGB HISTOGRAM

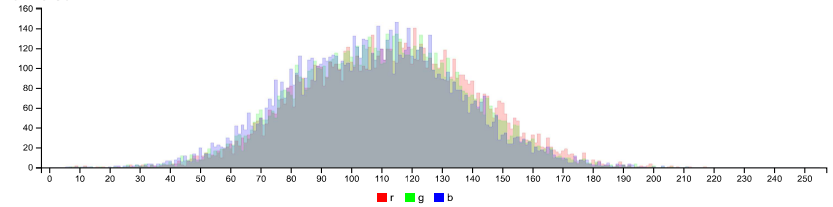

HSV HISTOGRAMS

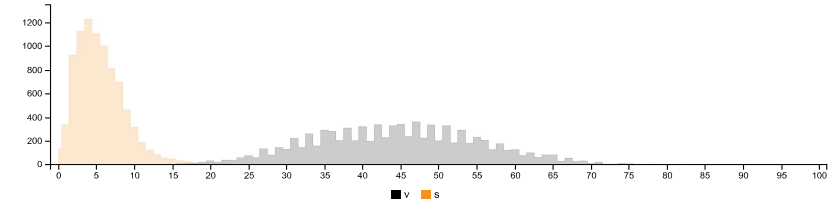

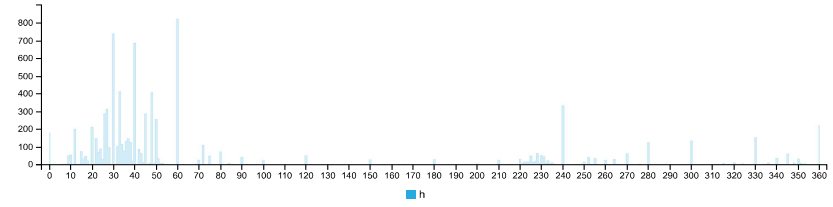

LCH HISTOGRAMS

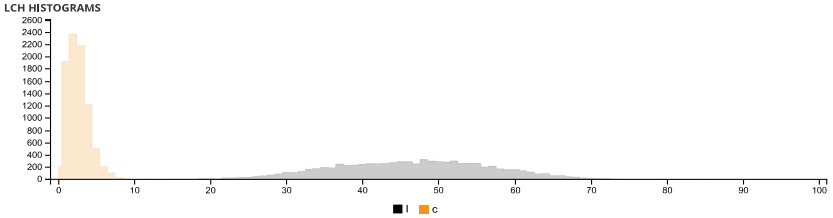

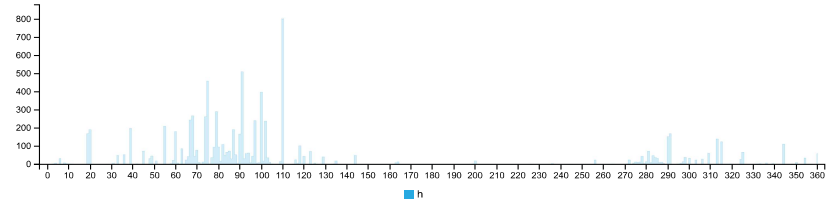

LAB HISTOGRAMS

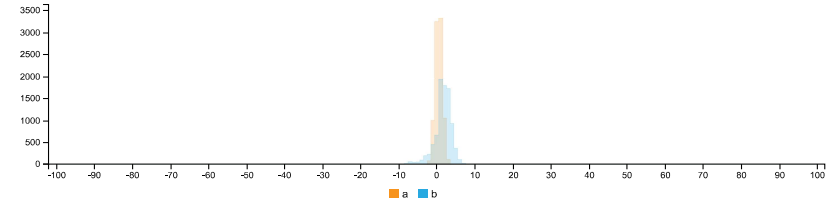

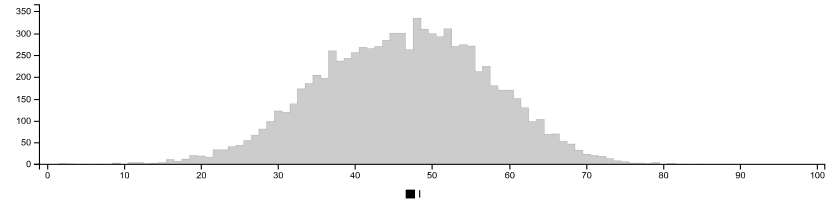

COLOR SPACE AND CHANNEL STATISTICS

	avg	med	min	max
RGB:R	112	112	8	217
RGB:G	110	110	7	211
RGB:B	108	108	6	211
HSV:H	28 1.00	40	0	360
HSV:S	6	5	0	27
HSV:V	44	44	3	85
LCH:L	46	47	2	85
LCH:C	3	2	0	11
LCH:H	71 1.00	91	3	360
LAB:L	46	47	2	85
LAB:A	1	1	-3	4
LAB:B	2	2	-10	8

Detailed report - Top debonded part of Specimen TG5-B-4

IMAGE COLOR SUMMARIZER

RGB, HSV, LCH & Lab image color statistics and clustering—simple and easy

HOME ANALYZE EXAMPLES API DOWNLOAD FAQ NEWS

IMAGE COLOR SUMMARY

THE IMAGE IN WORDS

battleship blast concord delta double dune electric friar grey ironsand jumbo natural old quarter schooner seashell ship silver steel streak thunder wireless

COLOR CLUSTERS

Colors in the image were clustered into 2 groups (k-means). The average color of the colors for each cluster is shown. The name is the closest named color and its distance is shown using ΔE. The tags are the set of words formed by all named neighbours within ΔE ≤ 5. The list of words above is the set of all unique words in this set of words.

Cluster colors, sized by number of pixels:

cluster	pixels	name	HEX	RGB	HSV	LCH	Lab	tags
	53.76%	85,83,80 wireless ΔE=0.9	#51514E	81 81 78	48 4 32	34 2 100	34 0 2	blast dune electric ironsand quarter ship silver streak thunder wireless grey
	46.24%	139,134,130 seashell ΔE=1.4	#86837F	134 131 127	35 5 52	55 3 84	55 0 3	battleship concord delta double friar jumbo natural old schooner seashell silver steel grey

IMAGE CLUSTER PARTITIONS

Pixels of the image assigned to each cluster. The border is the color of the cluster as calculated by the average value of its pixels.

RGB HISTOGRAM

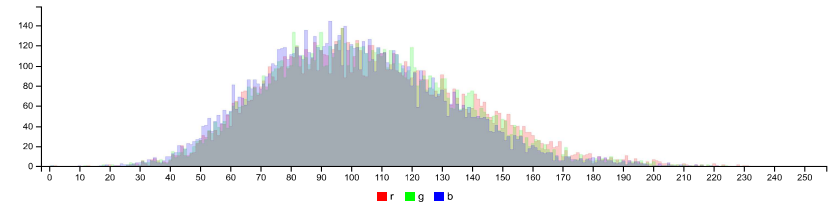

HSV HISTOGRAMS

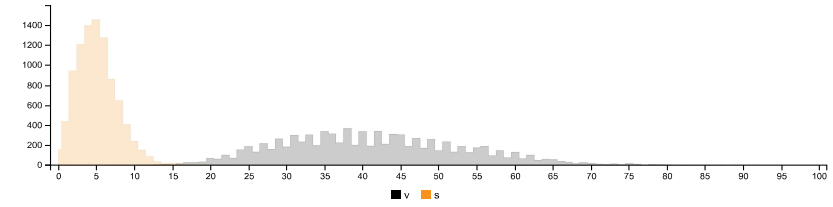

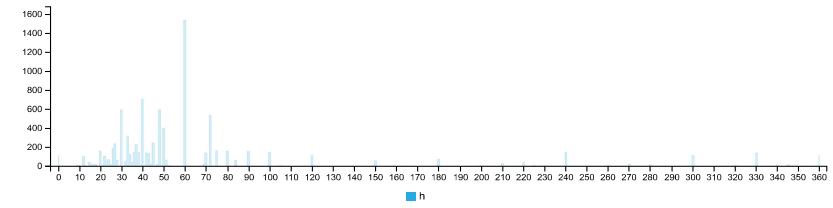

LCH HISTOGRAMS

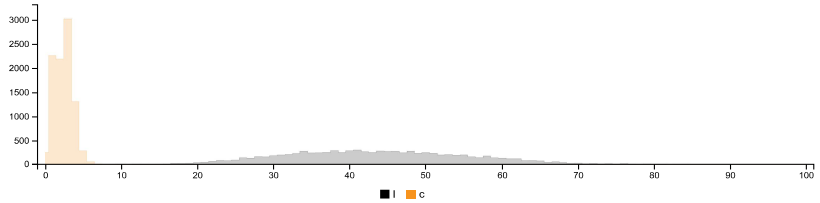

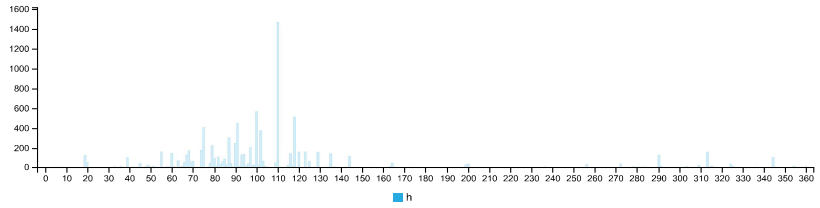

LAB HISTOGRAMS

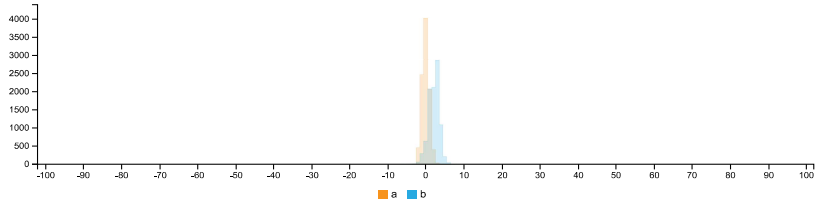

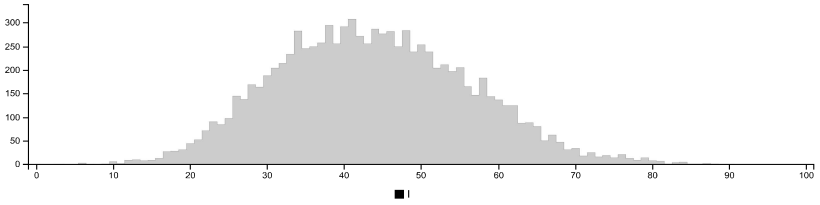

COLOR SPACE AND CHANNEL STATISTICS

	avg	med	min	max
RGB:R	106	103	2	231
RGB:G	104	102	1	224
RGB:B	101	99	1	221
HSV:H	45 1.00	48	0	360
HSV:S	5	5	0	50
HSV:V	42	40	1	91
LCH:L	44	43	0	90
LCH:C	2	2	0	7
LCH:H	92 1.00	100	0	360
LAB:L	44	43	0	90
LAB:A	-0	0	-4	4
LAB:B	2	2	-5	7

Summary of Image Analysis for Specimen TG10-B-1

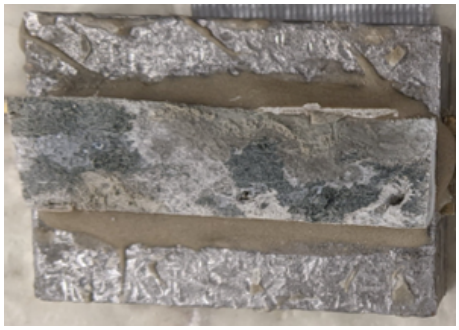

Figure D.31: Bottom debonded part of Specimen TG10-B-1

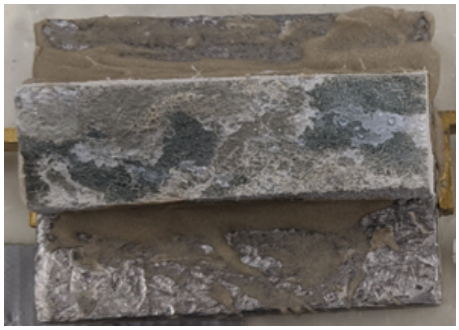

Figure D.32: Top debonded part of Specimen TG10-B-1

Table D.16: Summary of Image analysis result for specimen TG10-B-1

Contact Type	Colour Cluster	Results of Image analysis		Contact (%)		Average Contact (in %)
		Bottom Debonded Layer	Top Debonded Layer	Bottom Debonded Layer	Top Debonded Layer	
			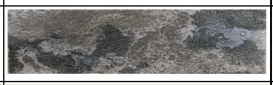			
Poor				44,44%	45,61%	**45,03%**
Good				55,55%	54,39%	**54,97%**

Detailed report - Bottom debonded part of Specimen TG10-B-1

IMAGE COLOR SUMMARIZER

RGB, HSV, LCH & Lab image color statistics and clustering—simple and easy

HOME ANALYZE EXAMPLES API DOWNLOAD FAQ NEWS

IMAGE COLOR SUMMARY

THE IMAGE IN WORDS

alley chicane double dust fern gannet gauntlet grey half ironside silver storm tinpan trojan

COLOR CLUSTERS

Colors in the image were clustered into 2 groups (k-means). The average color of the colors for each cluster is shown. The name is the closest named color and its distance is shown using ΔE. The tags are the set of words formed by all named neighbours within ΔE ≤ 5. The list of words above is the set of all unique words in this set of words.

Cluster colors, sized by number of pixels:

cluster	pixels	name	HEX	RGB	HSV	LCH	Lab	tags
	55.56%	100,100,99 storm dust ΔE=0.5	#636260	99 98 96	43 4 39	42 2 95	42 0 2	alley chicane double dust ironside storm tinpan trojan grey
	44.44%	149,145,140 grey ΔE=1.1	#93908D	147 144 141	26 4 58	60 2 68	60 1 2	fern gannet gauntlet half silver grey

IMAGE CLUSTER PARTITIONS

Pixels of the image assigned to each cluster. The border is the color of the cluster as calculated by the average value of its pixels.

RGB HISTOGRAM

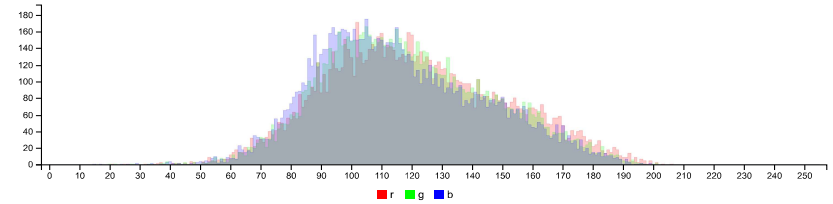

HSV HISTOGRAMS

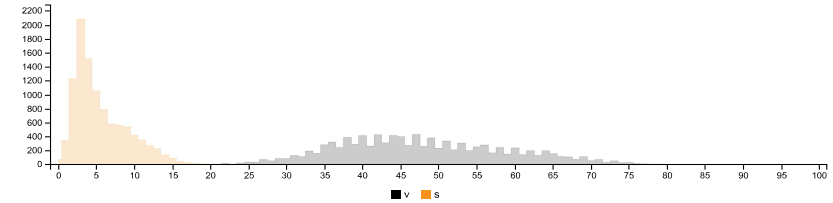

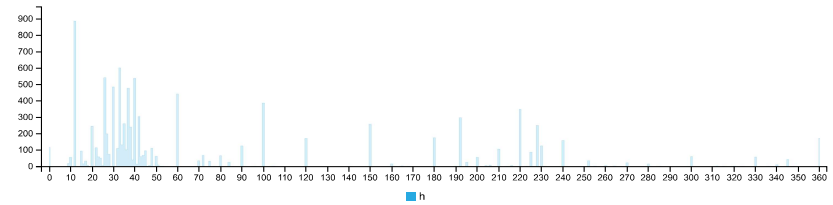

LCH HISTOGRAMS

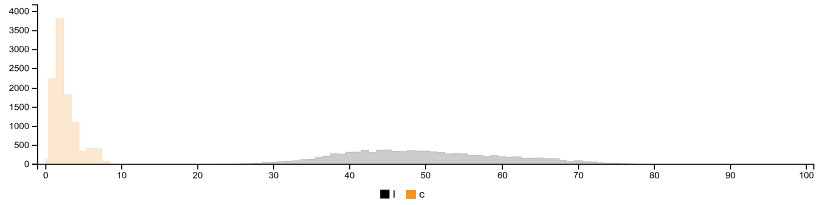

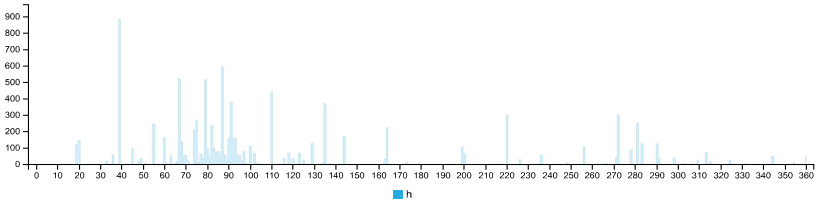

LAB HISTOGRAMS

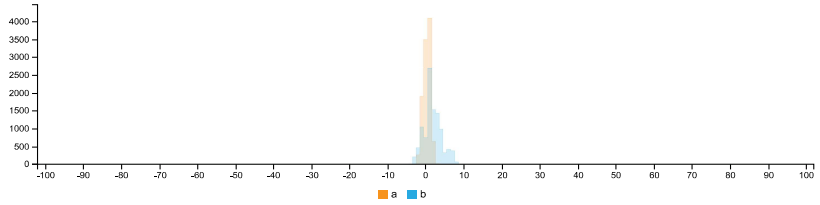

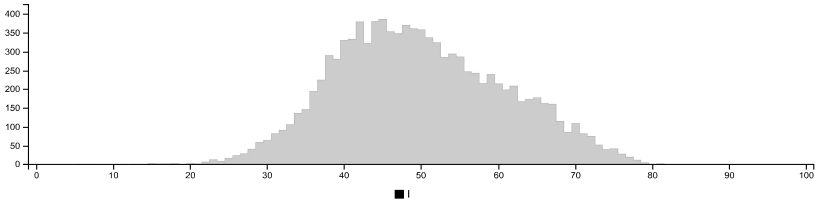

COLOR SPACE AND CHANNEL STATISTICS

	avg	med	min	max
RGB:R	121	119	21	206
RGB:G	119	116	20	201
RGB:B	116	112	15	199
HSV:H	38 1.00	40	0	360
HSV:S	6	4	0	32
HSV:V	48	47	8	81
LCH:L	50	49	6	81
LCH:C	3	2	0	10
LCH:H	80 1.00	88	3	360
LAB:L	50	49	6	81
LAB:A	0	0	-3	3
LAB:B	2	1	-7	10

Detailed report - Top debonded part of Specimen TG10-B-1

IMAGE COLOR SUMMARIZER

RGB, HSV, LCH & Lab image color statistics and clustering—simple and easy

HOME ANALYZE EXAMPLES API DOWNLOAD FAQ NEWS

IMAGE COLOR SUMMARY

THE IMAGE IN WORDS

baltic battleship davy davy's dim grey half landscape lining medium old ricochet sea silver torque trolley tundora web

COLOR CLUSTERS

Colors in the image were clustered into 2 groups (k-means). The average color of the colors for each cluster is shown. The name is the closest named color and its distance is shown using ΔE. The tags are the set of words formed by all named neighbours within ΔE ≤ 5. The list of words above is the set of all unique words in this set of words.

Cluster colors, sized by number of pixels:

cluster	pixels	name	HEX	RGB	HSV	LCH	Lab	tags
	54.39%	87,87,87 grey ΔE=0.8	#575655	87 86 85	43 3 34	37 1 94	37 0 1	baltic davy davy's dim half landscape sea torque tundora grey
	45.61%	132,132,130 battleship grey ΔE=1.0	#83817F	131 129 127	23 3 52	54 1 61	54 1 1	medium battleship lining old ricochet silver trolley web grey

IMAGE CLUSTER PARTITIONS

Pixels of the image assigned to each cluster. The border is the color of the cluster as calculated by the average value of its pixels.

RGB HISTOGRAM

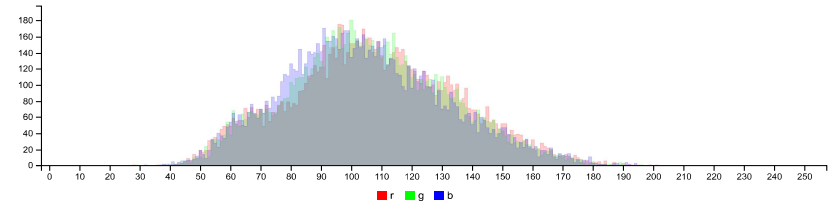

HSV HISTOGRAMS

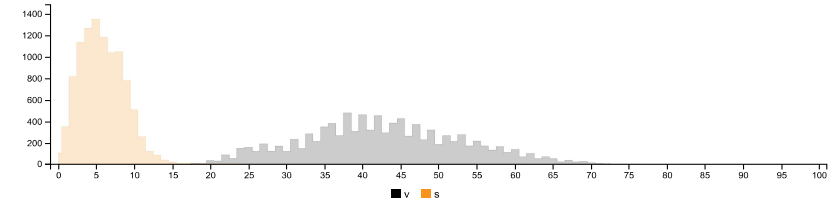

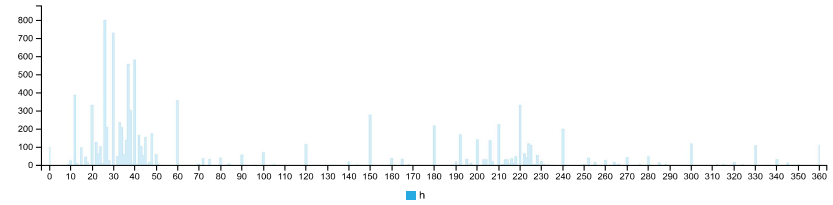

LCH HISTOGRAMS

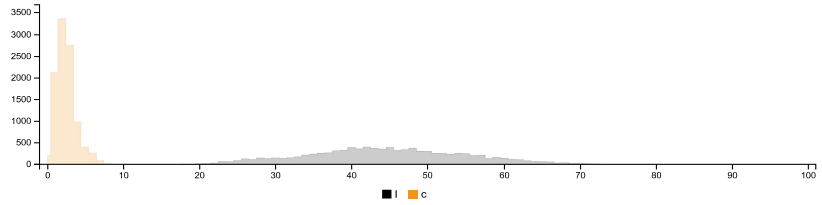

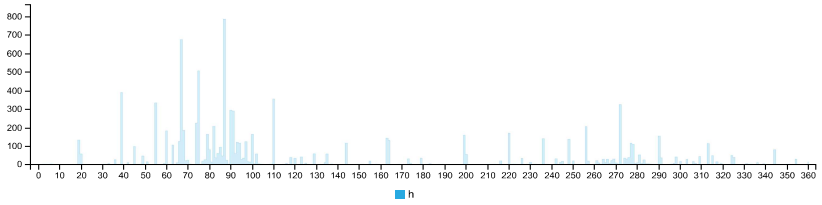

LAB HISTOGRAMS

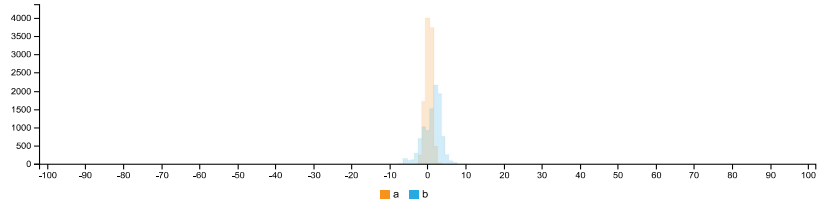

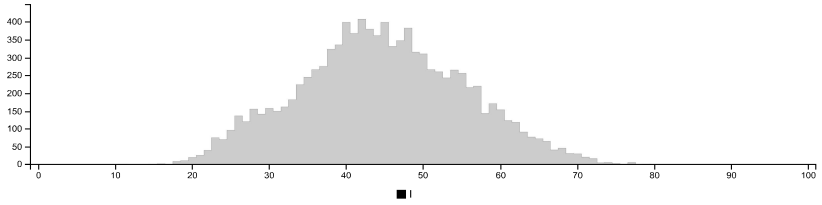

COLOR SPACE AND CHANNEL STATISTICS

	avg	med	min	max
RGB:R	107	106	28	201
RGB:G	106	105	29	196
RGB:B	104	102	32	194
HSV:H	34 0.00	40	0	360
HSV:S	6	6	0	27
HSV:V	43	42	13	79
LCH:L	45	44	11	79
LCH:C	3	2	0	11
LCH:H	77 0.00	91	3	360
LAB:L	45	44	11	79
LAB:A	0	0	-4	3
LAB:B	1	2	-8	11

Summary of Image Analysis for Specimen TG10-B-2

Figure D.33: Bottom debonded part of Specimen TG10-B-2

Figure D.34: Top debonded part of Specimen TG10-B-2

Table D.17: Summary of Image analysis result for specimen TG10-B-2

Contact Type	Colour Cluster	Results of Image analysis		Contact (%)		Average Contact (in %)
		Bottom Debonded Layer	Top Debonded Layer	Bottom Debonded Layer	Top Debonded Layer	
						
Poor				52,47%	65,72%	**59,10%**
Good				47,53%	34,28%	**40,91%**

Detailed report - Bottom debonded part of Specimen TG10-B-2

IMAGE COLOR SUMMARIZER

RGB, HSV, LCH & Lab image color statistics and clustering—simple and easy

HOME ANALYZE EXAMPLES API DOWNLOAD FAQ NEWS

IMAGE COLOR SUMMARY

THE IMAGE IN WORDS

archive blast chicane dim dimgray dust fern friar gauntlet granite grey half imagine ironside mist mountain quarter rakaia sandstone silver star tarmac taupe traffic triple viaduct

COLOR CLUSTERS

Colors in the image were clustered into 2 groups (k-means). The average color of the colors for each cluster is shown. The name is the closest named color and its distance is shown using ΔE. The tags are the set of words formed by all named neighbours within ΔE ≤ 5. The list of words above is the set of all unique words in this set of words.

Cluster colors, sized by number of pixels:

cluster	pixels	name	HEX	RGB	HSV	LCH	Lab	tags
	52.47%	161,154,152 triple rakaia ΔE=1.6	#9F9994	159 153 148	26 6 62	64 3 67	64 1 3	archive dust fern friar half imagine mist mountain quarter rakaia sandstone silver star taupe triple viaduct grey
	47.53%	108,109,104 traffic ΔE=1.8	#6D6A66	109 106 102	31 7 43	45 3 77	45 1 3	blast chicane dim dimgray gauntlet granite ironside tarmac traffic grey

IMAGE CLUSTER PARTITIONS

Pixels of the image assigned to each cluster. The border is the color of the cluster as calculated by the average value of its pixels.

RGB HISTOGRAM

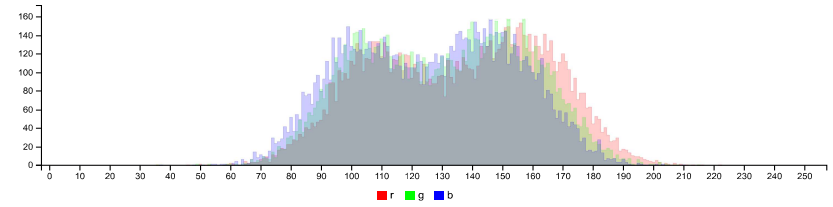

HSV HISTOGRAMS

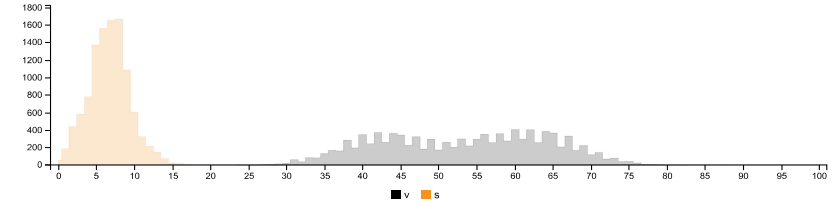

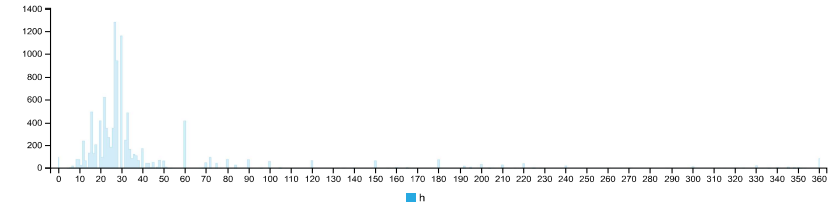

LCH HISTOGRAMS

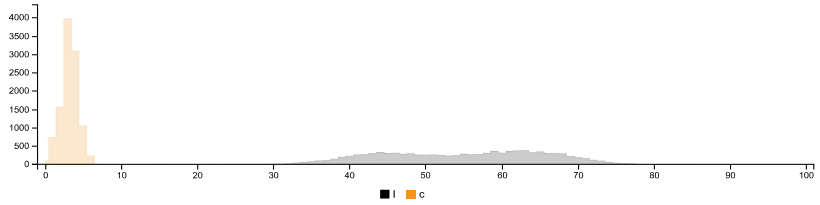

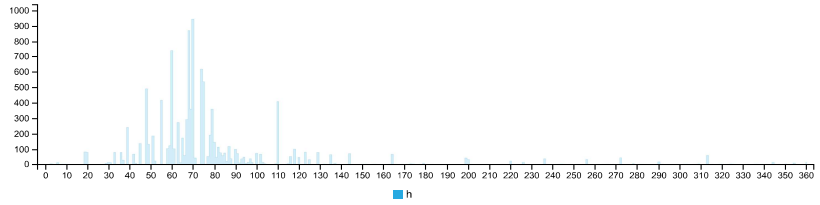

LAB HISTOGRAMS

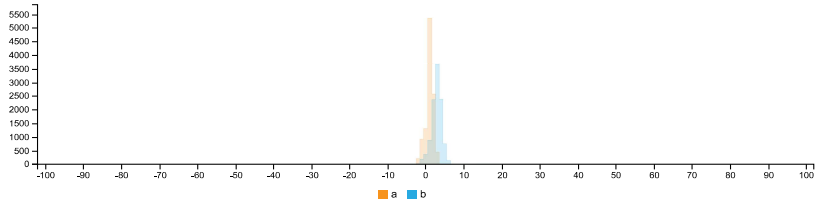

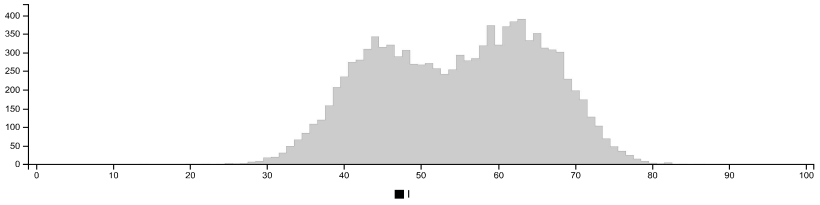

COLOR SPACE AND CHANNEL STATISTICS

	avg	med	min	max
RGB:R	135	137	36	222
RGB:G	131	132	36	215
RGB:B	126	128	37	210
HSV:H	30 1.00	28	0	360
HSV:S	7	7	0	27
HSV:V	53	54	15	87
LCH:L	55	55	14	86
LCH:C	3	3	0	18
LCH:H	70 1.00	70	3	360
LAB:L	55	55	14	86
LAB:A	1	1	-3	5
LAB:B	3	3	-4	18

Detailed report - Top debonded part of Specimen TG10-B-2

IMAGE COLOR SUMMARIZER

RGB, HSV, LCH & Lab image color statistics and clustering—simple and easy

HOME ANALYZE EXAMPLES API DOWNLOAD FAQ NEWS

IMAGE COLOR SUMMARY

THE IMAGE IN WORDS

alley archive chicago dust fern friar grey half imagine ironside mist mountain rakaia silver spanish storm tinpan triple

COLOR CLUSTERS

Colors in the image were clustered into 2 groups (k-means). The average color of the colors for each cluster is shown. The name is the closest named color and its distance is shown using ΔE. The tags are the set of words formed by all named neighbours within ΔE ≤ 5. The list of words above is the set of all unique words in this set of words.

Cluster colors, sized by number of pixels:

cluster	pixels	name	HEX	RGB	HSV	LCH	Lab	tags
	65.72%	153,147,140 silver fern ΔE=1.9	#9B9692	155 150 146	24 6 61	62 3 64	62 1 3	archive fern friar half imagine mist mountain rakaia silver spanish triple grey
	34.28%	94,94,94 grey ΔE=1.5	#615F5D	97 95 93	39 4 38	41 2 89	41 0 2	alley chicago dust ironside storm tinpan grey

IMAGE CLUSTER PARTITIONS

Pixels of the image assigned to each cluster. The border is the color of the cluster as calculated by the average value of its pixels.

RGB HISTOGRAM

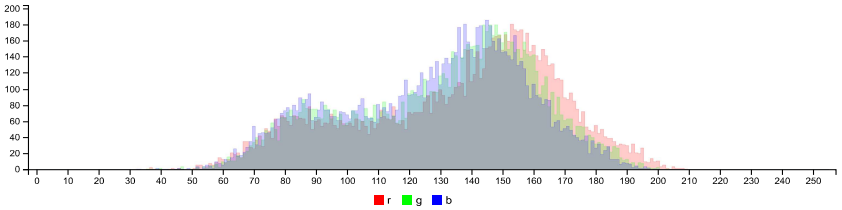

HSV HISTOGRAMS

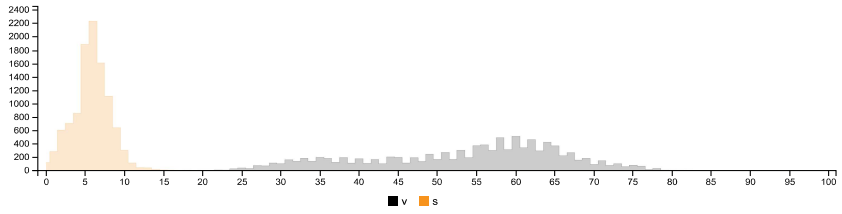

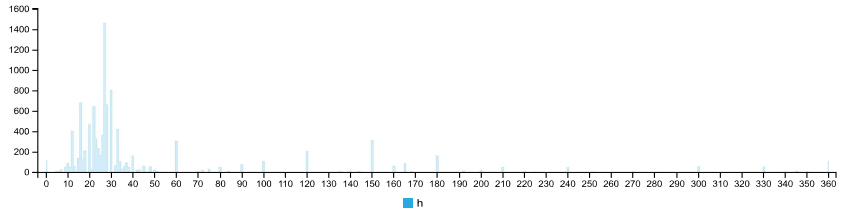

LCH HISTOGRAMS

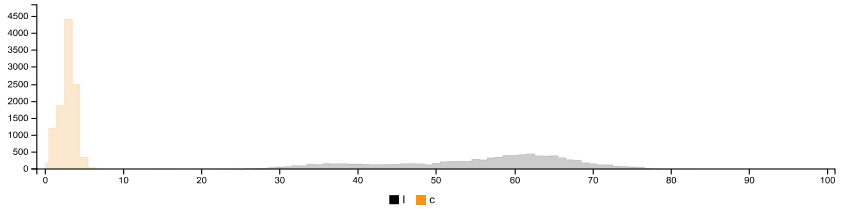

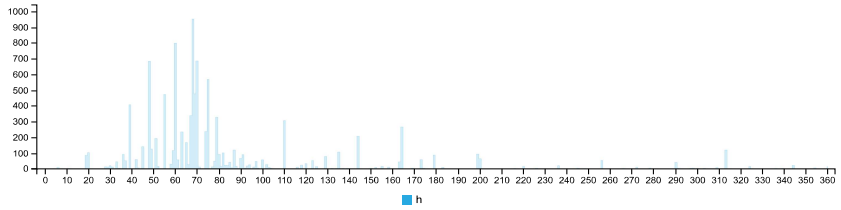

LAB HISTOGRAMS

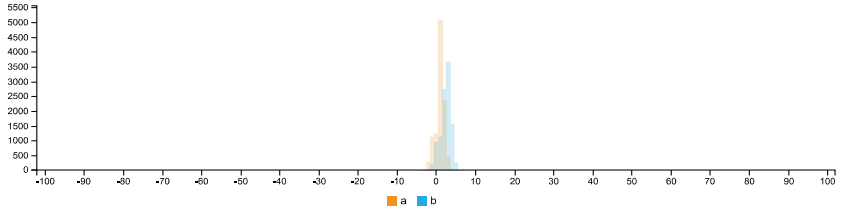

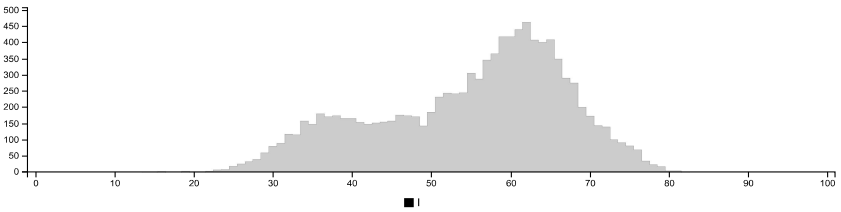

COLOR SPACE AND CHANNEL STATISTICS

	avg	med	min	max
RGB:R	135	143	36	209
RGB:G	131	137	36	203
RGB:B	128	133	33	200
HSV:H	30 1.00	27	0	360
HSV:S	6	6	0	18
HSV:V	53	56	14	82
LCH:L	55	58	14	82
LCH:C	3	3	0	7
LCH:H	70 1.00	68	2	360
LAB:L	55	58	14	82
LAB:A	1	1	-4	4
LAB:B	2	3	-4	7

Summary of Image Analysis for Specimen TG10-B-3

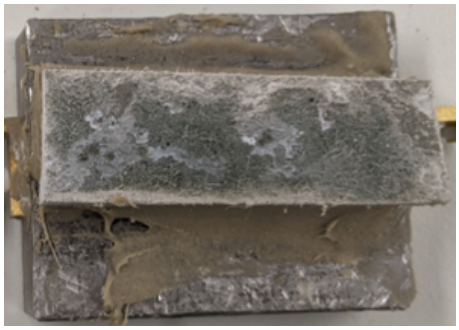

Figure D.35: Bottom debonded part of Specimen TG10-B-3

Figure D.36: Top debonded part of Specimen TG10-B-3

Table D.18: Summary of Image analysis result for specimen TG10-B-3

Contact Type	Colour Cluster	Results of Image analysis		Contact (%)		Average Contact (in %)
		Bottom Debonded Layer	Top Debonded Layer	Bottom Debonded Layer	Top Debonded Layer	
			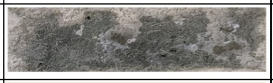			
Poor				58,03%	59,43%	**58,73%**
Good				41,98%	40,57%	**41,28%**

Detailed report - Bottom debonded part of Specimen TG10-B-3

IMAGE COLOR SUMMARIZER

RGB, HSV, LCH & Lab image color statistics and clustering—simple and easy

HOME ANALYZE EXAMPLES API DOWNLOAD FAQ NEWS

IMAGE COLOR SUMMARY

THE IMAGE IN WORDS

alley ash chicago condor dark dust eighth gauntlet gravel grey half jumbo masala natural oilskin olivish schooner seashell silver smokey steel storm suva tinpan torque

COLOR CLUSTERS

Colors in the image were clustered into 2 groups (k-means). The average color of the colors for each cluster is shown. The name is the closest named color and its distance is shown using ΔE. The tags are the set of words formed by all named neighbours within ΔE ≤ 5. The list of words above is the set of all unique words in this set of words.

Cluster colors, sized by number of pixels:

cluster	pixels	name	HEX	RGB	HSV	LCH	Lab	tags
	58.03%	93,92,88 chicago ΔE=1.2	#5E5C57	94 92 87	49 7 37	39 3 101	39 -1 3	dark alley ash chicago condor dust gravel half olivish smokey storm tinpan torque grey
	41.98%	139,134,130 seashell1 ΔE=0.7	#8C8782	140 135 130	30 7 55	56 3 75	56 1 3	eighth gauntlet gravel half jumbo masala natural oilskin schooner seashell silver steel suva grey

IMAGE CLUSTER PARTITIONS

Pixels of the image assigned to each cluster. The border is the color of the cluster as calculated by the average value of its pixels.

RGB HISTOGRAM

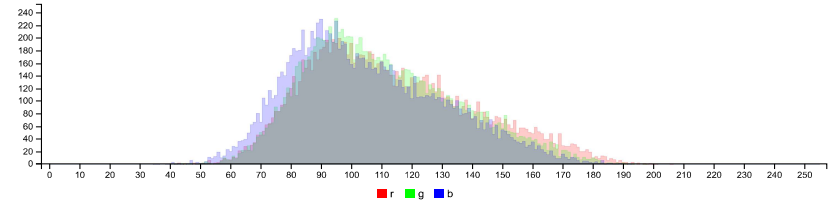

HSV HISTOGRAMS

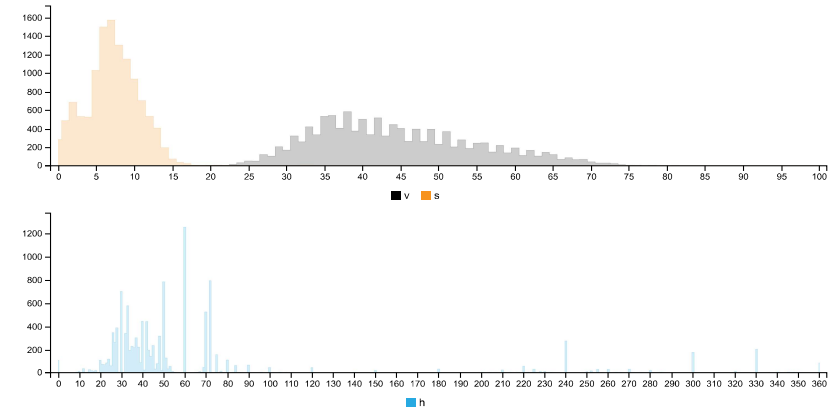

LCH HISTOGRAMS

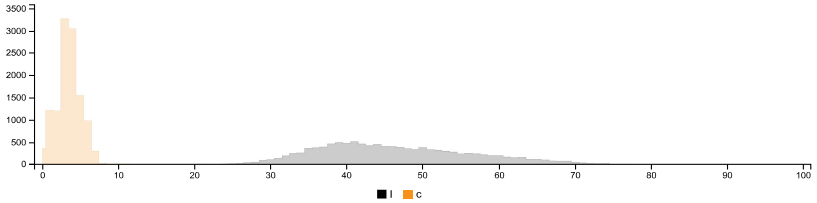

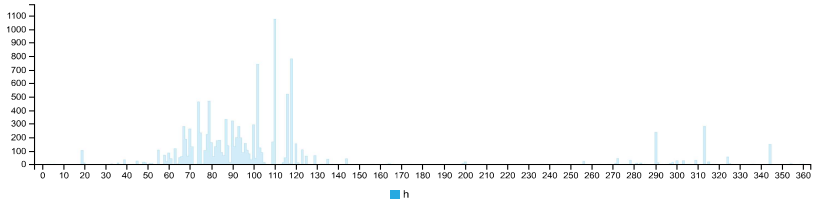

LAB HISTOGRAMS

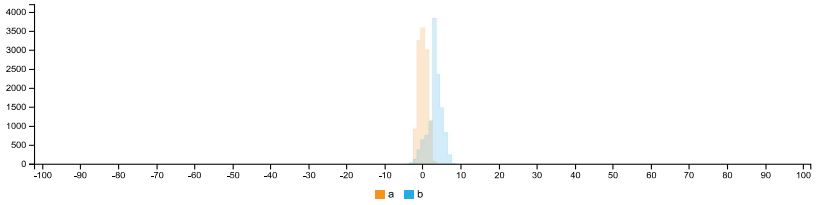

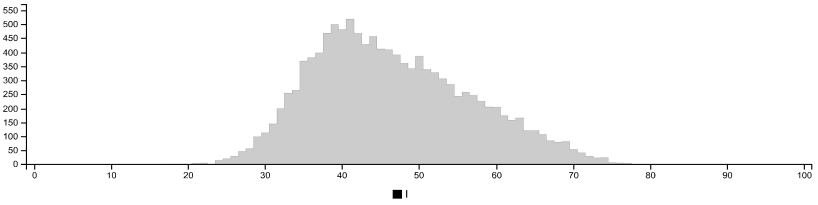

COLOR SPACE AND CHANNEL STATISTICS

	avg	med	min	max
RGB:R	113	109	42	206
RGB:G	110	107	42	197
RGB:B	105	102	35	192
HSV:H	42 1.00	45	0	360
HSV:S	7	7	0	34
HSV:V	44	43	17	81
LCH:L	46	45	17	80
LCH:C	4	3	0	17
LCH:H	88 1.00	96	3	360
LAB:L	46	45	17	80
LAB:A	0	0	-3	4
LAB:B	3	3	-6	17

Detailed report - Top debonded part of Specimen TG10-B-3

IMAGE COLOR SUMMARIZER

RGB, HSV, LCH & Lab image color statistics and clustering—simple and easy

HOME ANALYZE EXAMPLES API DOWNLOAD FAQ NEWS

IMAGE COLOR SUMMARY

THE IMAGE IN WORDS

aquashield archive chicago condor double dust fern friar gannet gravel grey half ironside masala quarter sandstone silver stack stonehenge storm tapa triple trojan

COLOR CLUSTERS

Colors in the image were clustered into 2 groups (k-means). The average color of the colors for each cluster is shown. The name is the closest named color and its distance is shown using ΔE. The tags are the set of words formed by all named neighbours within ΔE ≤ 5. The list of words above is the set of all unique words in this set of words.

Cluster colors, sized by number of pixels:

cluster	pixels	name	HEX	RGB	HSV	LCH	Lab	tags
	59.43%	101,100,95 storm dust ΔE=1.0	#61615C	97 97 92	54 5 38	41 3 105	41 -1 3	chicago condor double dust gravel half ironside masala stack storm triple trojan grey
	40.57%	153,147,140 silver fern ΔE=0.7	#97928D	151 146 141	29 7 59	61 4 74	61 1 3	aquashield archive fern friar gannet half quarter sandstone silver stonehenge tapa grey

IMAGE CLUSTER PARTITIONS

Pixels of the image assigned to each cluster. The border is the color of the cluster as calculated by the average value of its pixels.

RGB HISTOGRAM

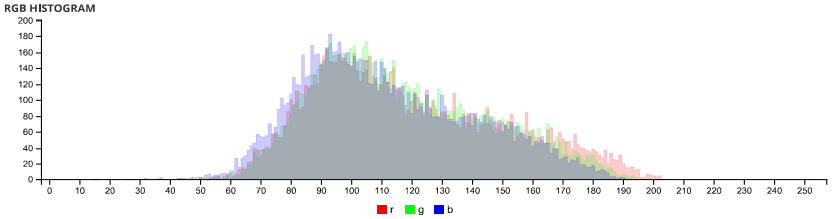

HSV HISTOGRAMS

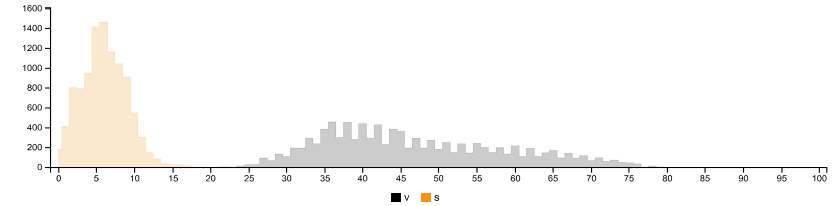

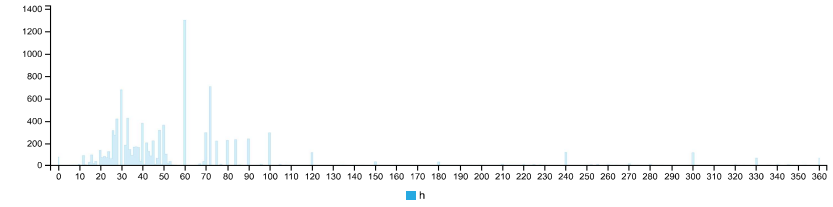

LCH HISTOGRAMS

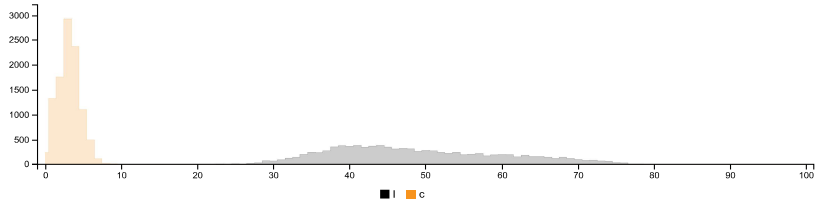

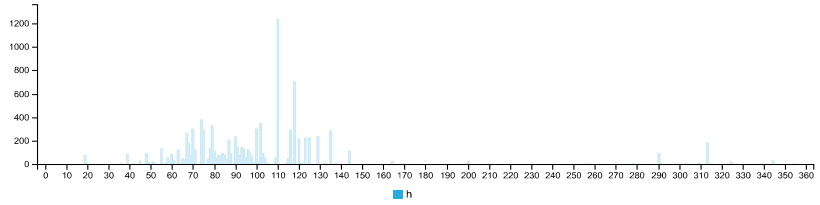

LAB HISTOGRAMS

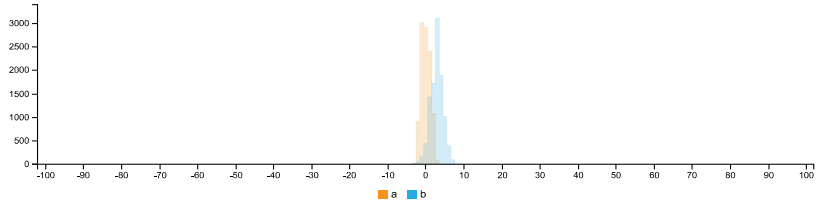

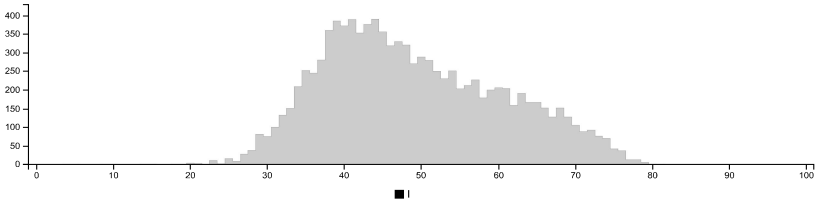

COLOR SPACE AND CHANNEL STATISTICS

	avg	med	min	max
RGB:R	119	113	15	207
RGB:G	117	112	15	201
RGB:B	112	108	15	203
HSV:H	47 1.00	48	0	360
HSV:S	6	6	0	23
HSV:V	47	45	6	81
LCH:L	49	47	4	81
LCH:C	3	3	0	14
LCH:H	93 1.00	100	11	360
LAB:L	49	47	4	81
LAB:A	-0	0	-4	4
LAB:B	3	3	-5	14

Summary of Image Analysis for Specimen TG10-B-4

Figure D.37: Bottom debonded part of Specimen TG10-B-4

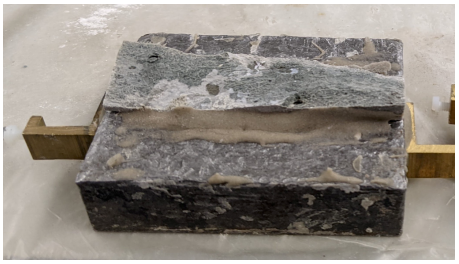

Figure D.38: Top debonded part of Specimen TG10-B-4

Table D.19: Summary of Image analysis result for specimen TG10-B-4

Contact Type	Colour Cluster	Results of Image analysis		Contact (%)		Average Contact (in %)
		Bottom Debonded Layer	Top Debonded Layer	Bottom Debonded Layer	Top Debonded Layer	
						
Poor			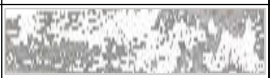	51,21%	50,67%	**50,94%**
Good				48,79%	49,33%	**49,06%**

Detailed report - Bottom debonded part of Specimen TG10-B-4

IMAGE COLOR SUMMARIZER

RGB, HSV, LCH & Lab image color statistics and clustering—simple and easy

HOME ANALYZE EXAMPLES API DOWNLOAD FAQ NEWS

IMAGE COLOR SUMMARY

THE IMAGE IN WORDS

atmosphere blast chalice cliff dark double dove face grey light masala medium quarter quick rakaia silver stack tarmac traffic

COLOR CLUSTERS

Colors in the image were clustered into 2 groups (k-means). The average color of the colors for each cluster is shown. The name is the closest named color and its distance is shown using ΔE. The tags are the set of words formed by all named neighbours within ΔE ≤ 5. The list of words above is the set of all unique words in this set of words.

Cluster colors, sized by number of pixels:

cluster	pixels	name	HEX	RGB	HSV	LCH	Lab	tags
	51.21%	111,113,110 double stack ΔE=1.0	#6E6E6B	110 110 107	61 2 43	46 2 111	46 -1 1	blast cliff double dove face masala quarter stack tarmac traffic grey
	48.79%	169,165,165 double rakaia ΔE=1.2	#ABA8A6	171 168 166	20 3 67	69 1 55	69 1 1	medium light dark atmosphere chalice double quick rakaia silver grey

IMAGE CLUSTER PARTITIONS

Pixels of the image assigned to each cluster. The border is the color of the cluster as calculated by the average value of its pixels.

RGB HISTOGRAM

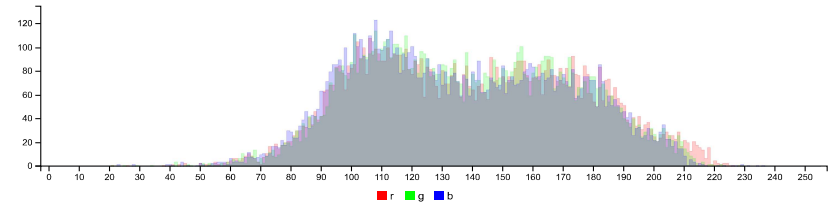

HSV HISTOGRAMS

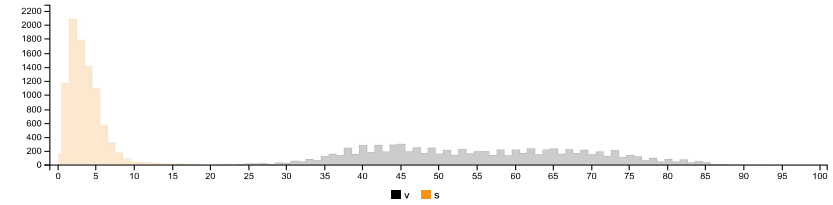

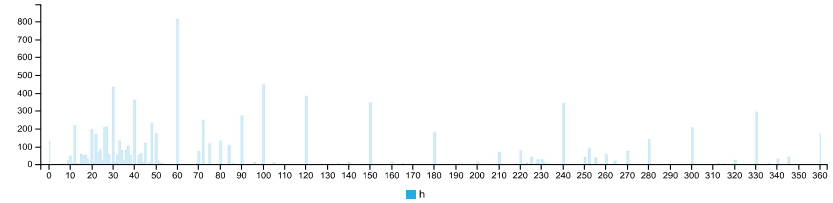

LCH HISTOGRAMS

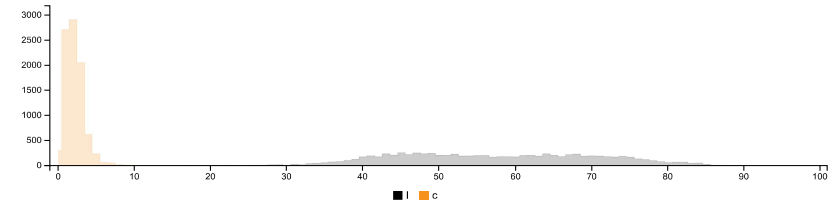

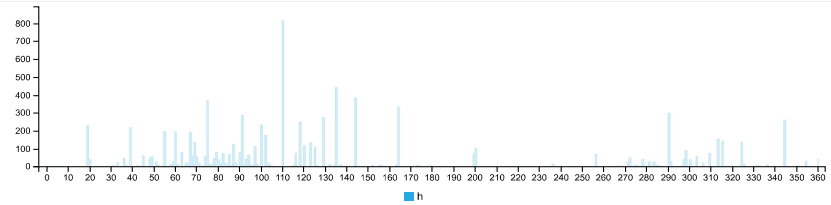

LAB HISTOGRAMS

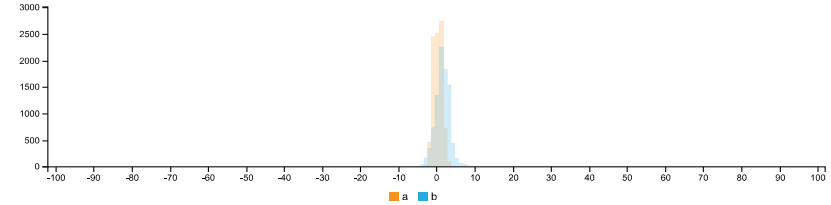

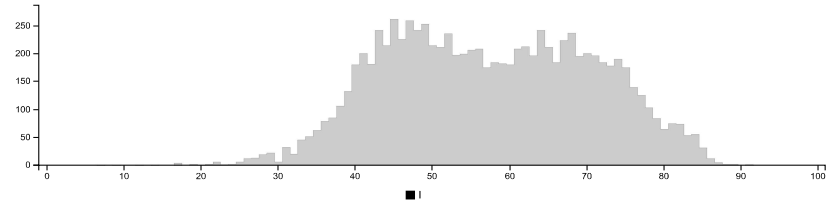

COLOR SPACE AND CHANNEL STATISTICS

	avg	med	min	max
RGB:R	140	138	21	229
RGB:G	138	136	21	229
RGB:B	136	133	23	236
HSV:H	44 0.00	60	0	360
HSV:S	4	3	0	39
HSV:V	55	54	9	93
LCH:L	57	57	7	91
LCH:C	2	2	0	11
LCH:H	87 0.00	110	3	360
LAB:L	57	57	7	91
LAB:A	0	0	-3	5
LAB:B	1	1	-7	11

Detailed report - Top debonded part of Specimen TG10-B-4

IMAGE COLOR SUMMARIZER

RGB, HSV, LCH & Lab image color statistics and clustering—simple and easy

HOME ANALYZE EXAMPLES API DOWNLOAD FAQ NEWS

IMAGE COLOR SUMMARY

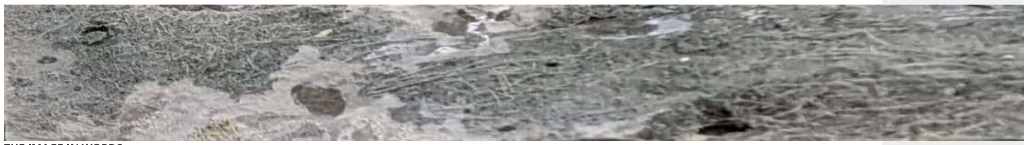

THE IMAGE IN WORDS

aluminium boulder detroit dove dust grey half kensington masala mist mountain quarter spanish stack star tapa transmission trojan

COLOR CLUSTERS

Colors in the image were clustered into 2 groups (k-means). The average color of the colors for each cluster is shown. The name is the closest named color and its distance is shown using ΔE. The tags are the set of words formed by all named neighbours within ΔE ≤ 5. The list of words above is the set of all unique words in this set of words.

Cluster colors, sized by number of pixels:

cluster	pixels	name	HEX	RGB	HSV	LCH	Lab	tags
	50.67%	160,159,156 mountain mist ΔE=0.8	#9F9E9C	159 158 156	35 2 62	65 1 83	65 0 1	dust half kensington mist mountain spanish stack star transmission grey
	49.33%	120,119,116 detroit ΔE=0.3	#787774	120 119 116	48 3 47	50 2 100	50 0 2	aluminium boulder detroit dove masala quarter tapa trojan grey

IMAGE CLUSTER PARTITIONS

Pixels of the image assigned to each cluster. The border is the color of the cluster as calculated by the average value of its pixels.

RGB HISTOGRAM

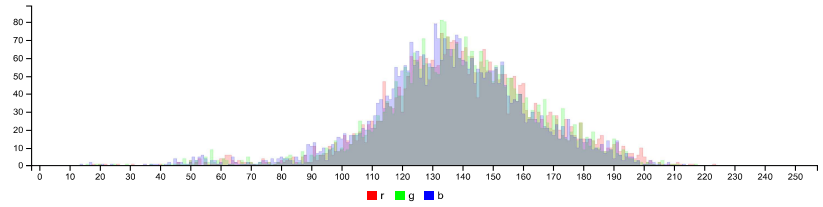

HSV HISTOGRAMS

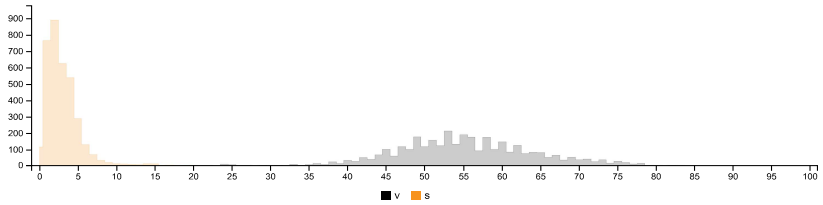

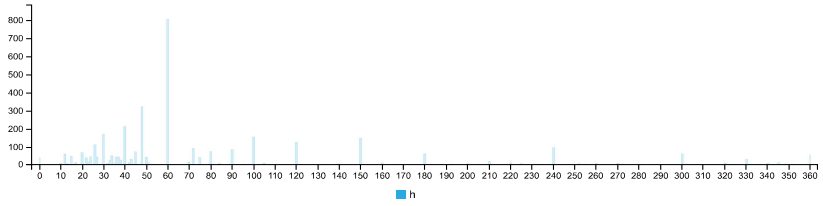

LCH HISTOGRAMS

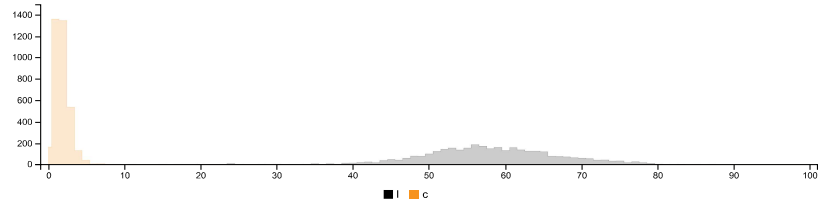

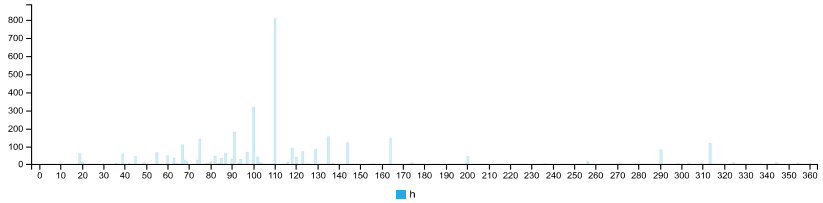

LAB HISTOGRAMS

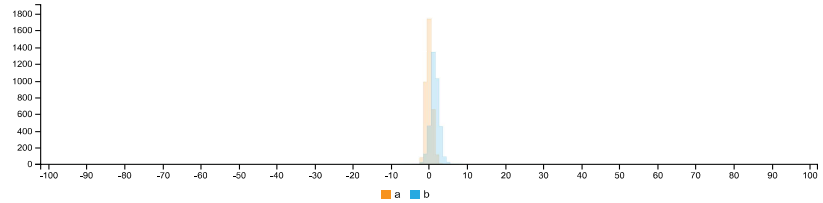

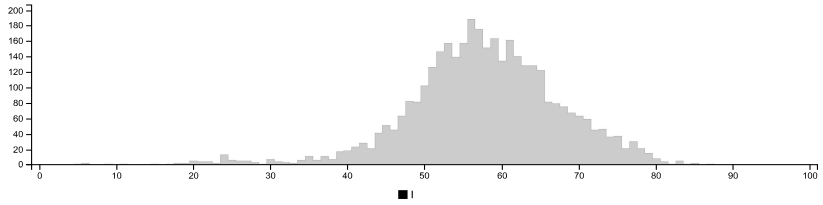

COLOR SPACE AND CHANNEL STATISTICS

	avg	med	min	max
RGB:R	140	139	18	223
RGB:G	139	139	16	217
RGB:B	136	136	14	213
HSV:H	52 1.00	60	0	360
HSV:S	3	3	0	23
HSV:V	55	55	7	87
LCH:L	58	58	5	87
LCH:C	2	2	0	8
LCH:H	98 1.00	110	3	360
LAB:L	58	58	5	87
LAB:A	-0	0	-3	5
LAB:B	1	1	-7	8

Summary of Image Analysis for Specimen TG20-B-1

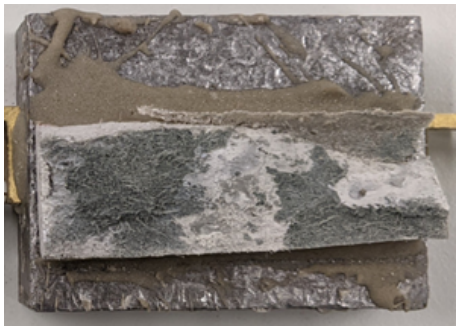

Figure D.39: Bottom debonded part of Specimen TG20-B-1

Figure D.40: Top debonded part of Specimen TG20-B-1

Table D.20: Summary of Image analysis result for specimen TG20-B-1

Contact Type	Colour Cluster	Results of Image analysis		Contact (%)		Average Contact (in %)
		Bottom Debonded Layer	Top Debonded Layer	Bottom Debonded Layer	Top Debonded Layer	
						
Poor				38,88%	40,16%	**38,88%**
Good				61,12%	59,84%	**61,12%**

Detailed report - Bottom debonded part of Specimen TG20-B-1

IMAGE COLOR SUMMARIZER

RGB, HSV, LCH & Lab image color statistics and clustering—simple and easy

HOME ANALYZE EXAMPLES API DOWNLOAD FAQ NEWS

IMAGE COLOR SUMMARY

THE IMAGE IN WORDS

alley chicago cloudy dawn delta double dust friar grey half ironside masala mist mountain nobel quarter rakaia stonehenge storm tinpan triple trojan viaduct

COLOR CLUSTERS

Colors in the image were clustered into 2 groups (k-means). The average color of the colors for each cluster is shown. The name is the closest named color and its distance is shown using ΔE. The tags are the set of words formed by all named neighbours within ΔE ≤ 5. The list of words above is the set of all unique words in this set of words.

Cluster colors, sized by number of pixels:

cluster	pixels	name	HEX	RGB	HSV	LCH	Lab	tags
	61.12%	101,100,95 storm dust ΔE=1.6	#62605C	98 96 92	39 6 38	41 2 89	41 0 2	alley chicago double dust half ironside masala storm tinpan trojan grey
	38.88%	172,165,159 cloudy ΔE=1.6	#A8A29E	168 162 158	21 6 66	67 3 58	67 2 3	cloudy dawn delta double friar mist mountain nobel quarter rakaia stonehenge triple viaduct grey

IMAGE CLUSTER PARTITIONS

Pixels of the image assigned to each cluster. The border is the color of the cluster as calculated by the average value of its pixels.

RGB HISTOGRAM

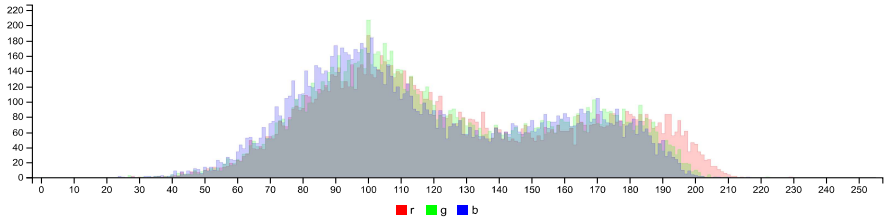

HSV HISTOGRAMS

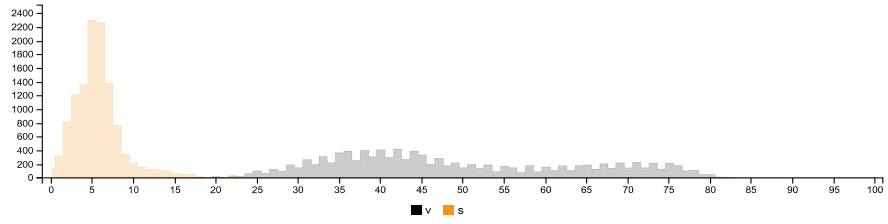

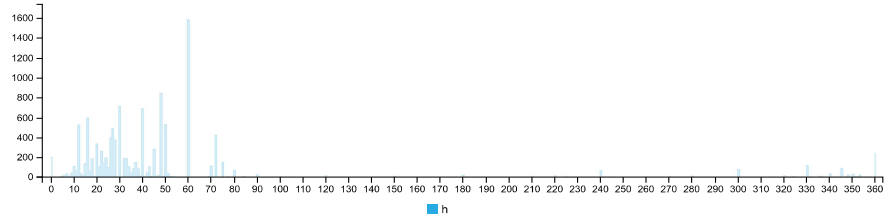

LCH HISTOGRAMS

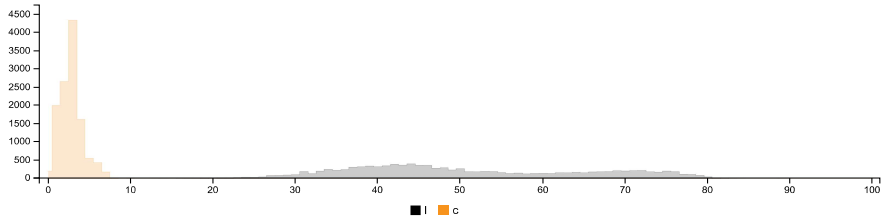

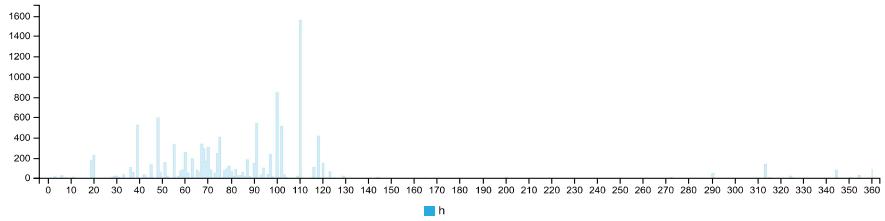

LAB HISTOGRAMS

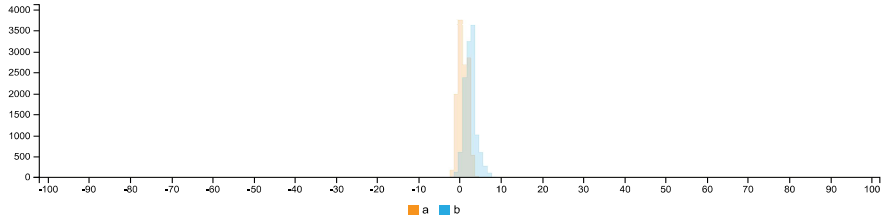

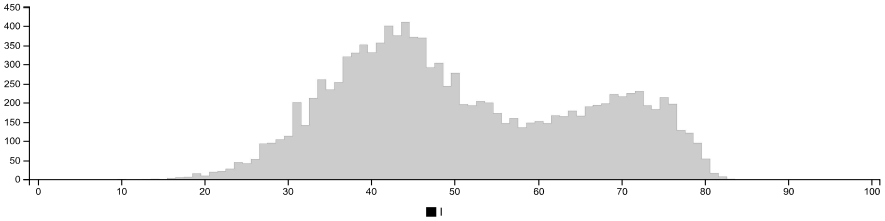

COLOR SPACE AND CHANNEL STATISTICS

	avg	med	min	max
RGB:R	125	116	28	229
RGB:G	122	113	27	222
RGB:B	118	109	24	216
HSV:H	34 1.00	38	0	360
HSV:S	6	5	0	30
HSV:V	49	45	11	90
LCH:L	51	48	10	89
LCH:C	3	3	0	9
LCH:H	76 1.00	82	2	360
LAB:L	51	48	10	89
LAB:A	1	1	-3	5
LAB:B	2	2	-4	8

Detailed report - Top debonded part of Specimen TG20-B-1

IMAGE COLOR SUMMARIZER

RGB, HSV, LCH & Lab image color statistics and clustering—simple and easy

HOME ANALYZE EXAMPLES API DOWNLOAD FAQ NEWS

IMAGE COLOR SUMMARY

THE IMAGE IN WORDS

alley chicago dark gravel grey half imagine lady mist mountain olivish rakaia reddish shady spanish tinpan tonto torque triple

COLOR CLUSTERS

Colors in the image were clustered into 2 groups (k-means). The average color of the colors for each cluster is shown. The name is the closest named color and its distance is shown using ΔE. The tags are the set of words formed by all named neighbours within ΔE ≤ 5. The list of words above is the set of all unique words in this set of words.

Cluster colors, sized by number of pixels:

cluster	pixels	name	HEX	RGB	HSV	LCH	Lab	tags
	59.84%	93,92,88 chicago ΔE=0.2	#5E5C59	94 92 89	36 5 37	39 2 85	39 0 2	dark alley chicago gravel half olivish tinpan torque grey
	40.16%	161,154,152 triple rakaia ΔE=0.4	#9F9997	159 153 151	16 5 62	64 2 47	64 2 2	imagine lady mist mountain rakaia reddish shady spanish tonto triple grey

IMAGE CLUSTER PARTITIONS

Pixels of the image assigned to each cluster. The border is the color of the cluster as calculated by the average value of its pixels.

RGB HISTOGRAM

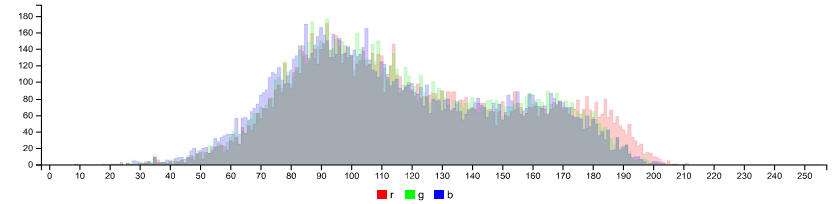

HSV HISTOGRAMS

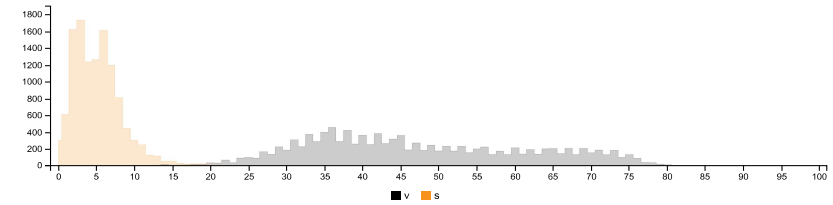

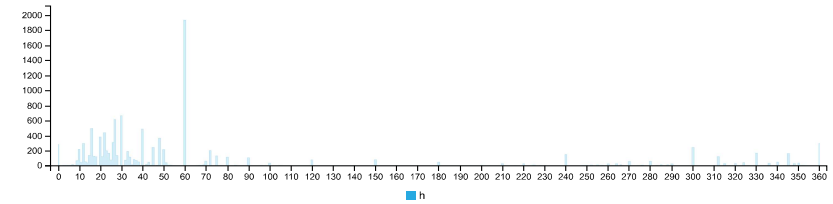

LCH HISTOGRAMS

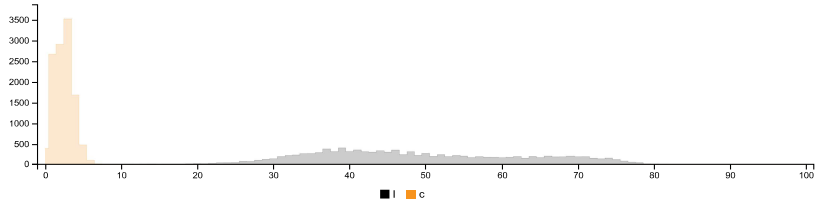

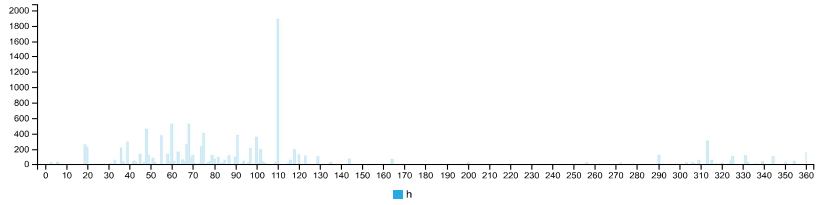

LAB HISTOGRAMS

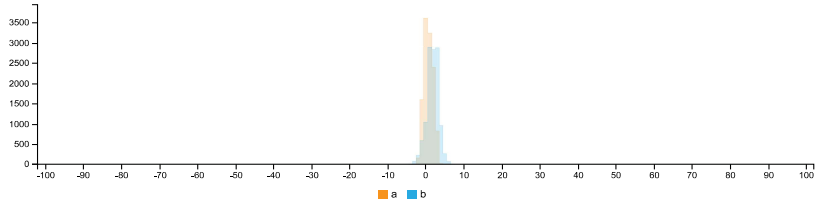

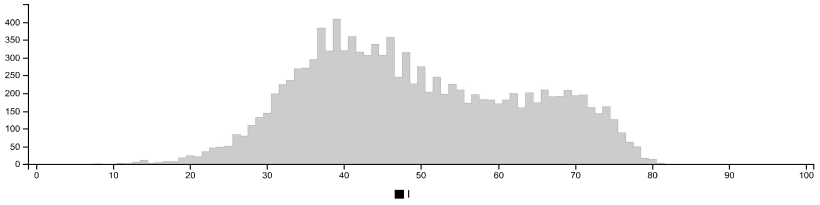

COLOR SPACE AND CHANNEL STATISTICS

	avg	med	min	max
RGB:R	120	114	9	211
RGB:G	117	111	9	207
RGB:B	114	108	9	207
HSV:H	29 1.00	40	0	360
HSV:S	5	5	0	22
HSV:V	47	45	4	83
LCH:L	49	47	2	83
LCH:C	2	2	0	9
LCH:H	69 1.00	87	3	360
LAB:L	49	47	2	83
LAB:A	1	1	-3	9
LAB:B	2	2	-4	7

Summary of Image Analysis for Specimen TG20-B-2

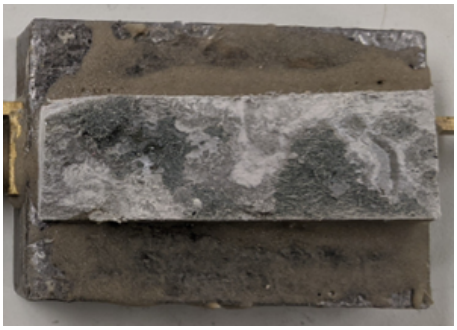

Figure D.41: Bottom debonded part of Specimen TG20-B-2

Figure D.42: Top debonded part of Specimen TG20-B-2

Table D.21: Summary of Image analysis result for specimen TG20-B-2

Contact Type	Colour Cluster	Results of Image analysis		Contact (%)		Average Contact (in %)
		Bottom Debonded Layer	Top Debonded Layer	Bottom Debonded Layer	Top Debonded Layer	
						
Poor				51,99%	44,39%	**48,19%**
Good				48,01%	55,61%	**51,81%**

Detailed report - Bottom debonded part of Specimen TG20-B-2

IMAGE COLOR SUMMARIZER

RGB, HSV, LCH & Lab image color statistics and clustering—simple and easy

HOME ANALYZE EXAMPLES API DOWNLOAD FAQ NEWS

IMAGE COLOR SUMMARY

THE IMAGE IN WORDS

blast brownish dark dim dune eighth electric fuscous gauntlet grey half jumbo masala natural olivish reddish schooner seashell silver snow steel suva torque tundora wireless

COLOR CLUSTERS

Colors in the image were clustered into 2 groups (k-means). The average color of the colors for each cluster is shown. The name is the closest named color and its distance is shown using ΔE. The tags are the set of words formed by all named neighbours within ΔE ≤ 5. The list of words above is the set of all unique words in this set of words.

Cluster colors, sized by number of pixels:

cluster	pixels	name	HEX	RGB	HSV	LCH	Lab	tags
	51.99%	139,134,130 seashell ΔE=1.6	#8E8986	142 137 134	24 6 56	57 3 64	57 1 2	eighth gauntlet half jumbo masala natural schooner seashell silver snow steel suva grey
	48.01%	88,84,82 tundora ΔE=1.2	#575551	87 85 81	37 6 34	36 2 86	36 0 2	dark blast brownish dim dune electric fuscous olivish reddish torque tundora wireless grey

IMAGE CLUSTER PARTITIONS

Pixels of the image assigned to each cluster. The border is the color of the cluster as calculated by the average value of its pixels.

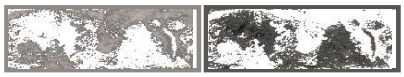

RGB HISTOGRAM

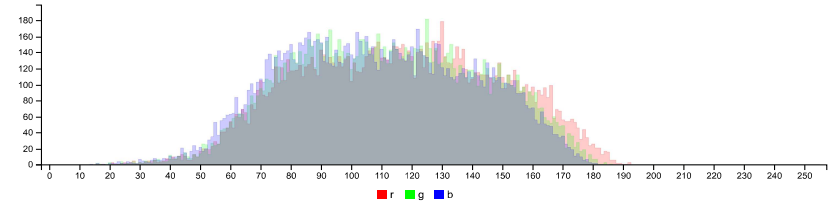

HSV HISTOGRAMS

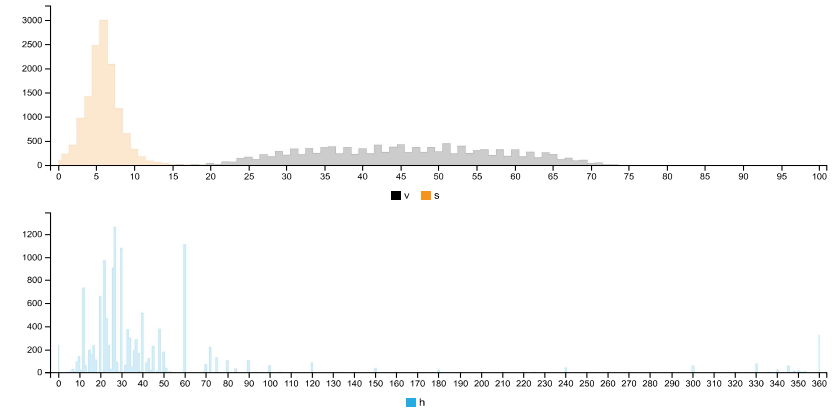

LCH HISTOGRAMS

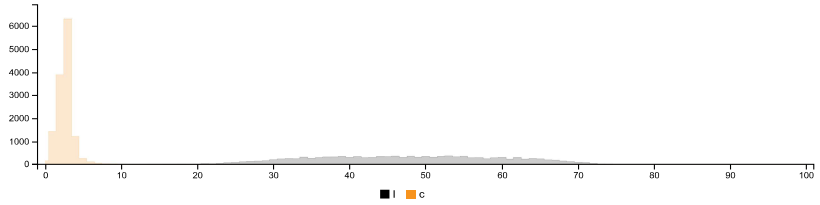

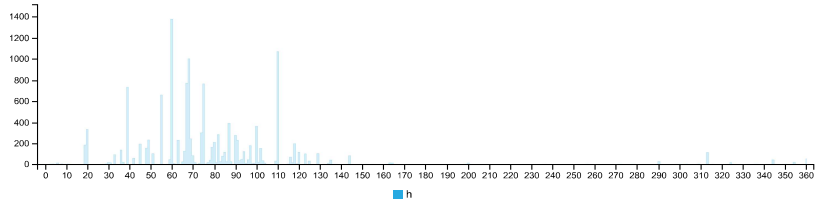

LAB HISTOGRAMS

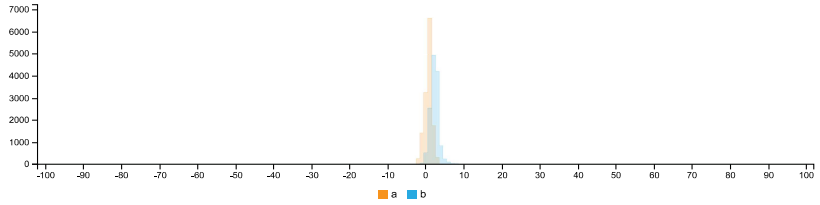

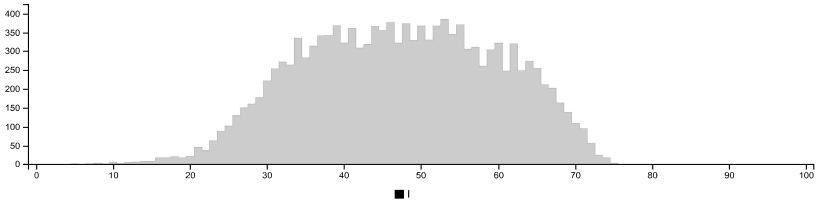

COLOR SPACE AND CHANNEL STATISTICS

	avg	med	min	max
RGB:R	116	116	16	192
RGB:G	112	111	16	186
RGB:B	109	108	14	181
HSV:H	31 1.00	30	0	360
HSV:S	6	6	0	32
HSV:V	45	45	6	75
LCH:L	47	47	5	76
LCH:C	3	3	0	11
LCH:H	71 1.00	69	0	360
LAB:L	47	47	5	76
LAB:A	1	1	-3	7
LAB:B	2	2	-3	11

Detailed report - Top debonded part of Specimen TG20-B-2

IMAGE COLOR SUMMARIZER

RGB, HSV, LCH & Lab image color statistics and clustering—simple and easy

HOME ANALYZE EXAMPLES API DOWNLOAD FAQ NEWS

IMAGE COLOR SUMMARY

THE IMAGE IN WORDS

alley chicago condor dark eighth gauntlet gravel grey half jumbo masala natural olivish seashell silver steel tinpan torque

COLOR CLUSTERS

Colors in the image were clustered into 2 groups (k-means). The average color of the colors for each cluster is shown. The name is the closest named color and its distance is shown using ΔE. The tags are the set of words formed by all named neighbours within ΔE ≤ 5. The list of words above is the set of all unique words in this set of words.

Cluster colors, sized by number of pixels:

cluster	pixels	name	HEX	RGB	HSV	LCH	Lab	tags
	55.61%	93,92,88 chicago ΔE=0.6	#5D5C58	93 92 88	46 6 37	39 3 98	39 0 3	dark alley chicago condor gravel half olivish tinpan torque grey
	44.39%	139,138,136 half gauntlet ΔE=1.6	#8E8B87	142 139 135	32 5 56	58 3 78	58 1 3	eighth gauntlet gravel half jumbo masala natural seashell silver steel grey

IMAGE CLUSTER PARTITIONS

Pixels of the image assigned to each cluster. The border is the color of the cluster as calculated by the average value of its pixels.

RGB HISTOGRAM

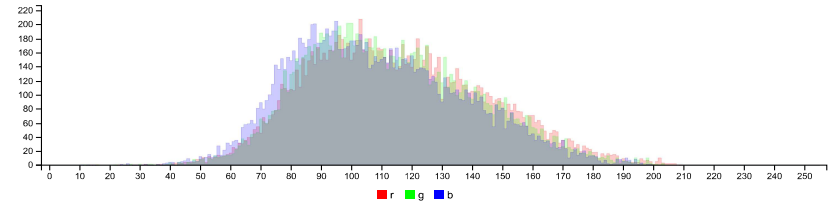

HSV HISTOGRAMS

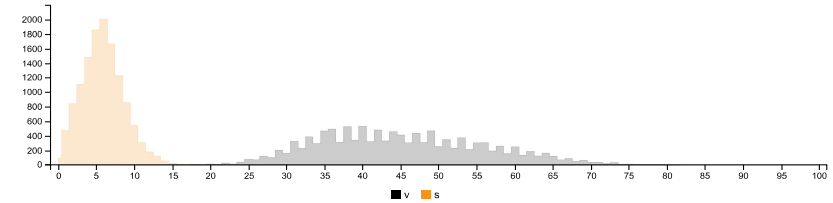

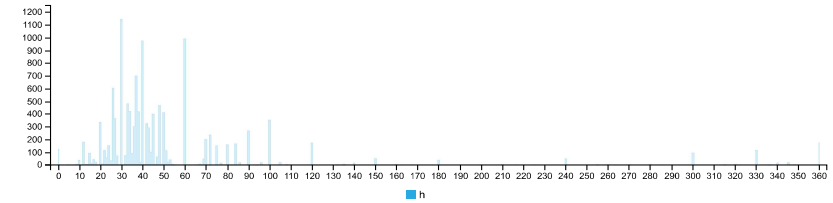

LCH HISTOGRAMS

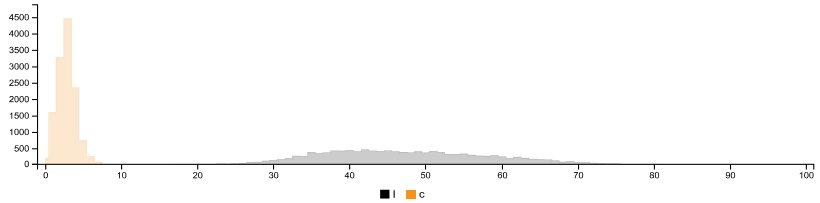

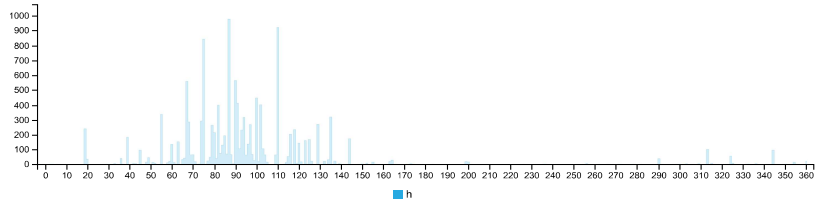

LAB HISTOGRAMS

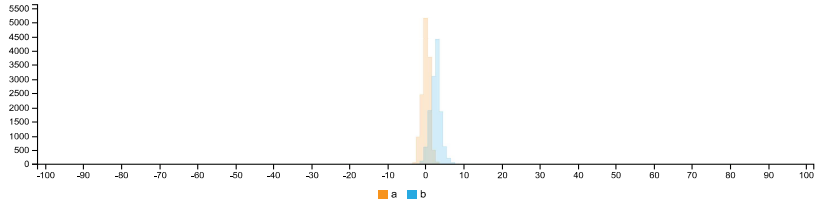

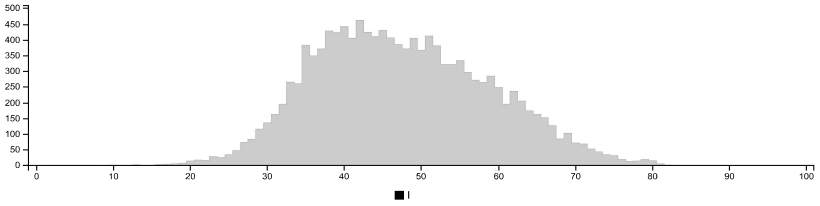

COLOR SPACE AND CHANNEL STATISTICS

	avg	med	min	max
RGB:R	115	113	13	209
RGB:G	113	110	12	203
RGB:B	109	105	11	199
HSV:H	42 1.00	40	0	360
HSV:S	6	6	0	28
HSV:V	45	44	5	82
LCH:L	47	47	3	82
LCH:C	3	3	0	12
LCH:H	88 1.00	90	3	360
LAB:L	47	47	3	82
LAB:A	0	0	-4	4
LAB:B	3	3	-3	12

Summary of Image Analysis for Specimen TG20-B-3

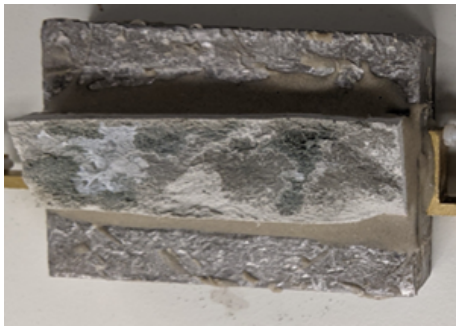

Figure D.43: Bottom debonded part of Specimen TG20-B-3

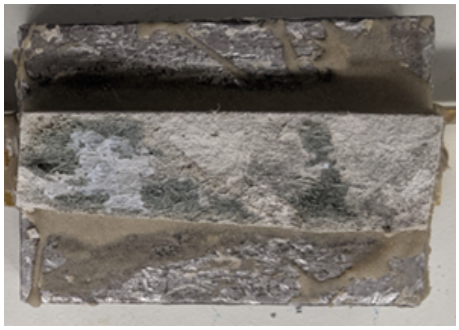

Figure D.44: Top debonded part of Specimen TG20-B-3

Table D.22: Summary of Image analysis result for specimen TG20-B-3

Contact Type	Colour Cluster	Results of Image analysis		Contact (%)		Average Contact (in %)
		Bottom Debonded Layer	Top Debonded Layer	Bottom Debonded Layer	Top Debonded Layer	
						
Poor				64,04%	45,13%	**54,59%**
Good				35,96%	54,87%	**45,42%**

Detailed report - Bottom debonded part of Specimen TG20-B-3

IMAGE COLOR SUMMARIZER

RGB, HSV, LCH & Lab image color statistics and clustering—simple and easy

HOME ANALYZE EXAMPLES API DOWNLOAD FAQ NEWS

IMAGE COLOR SUMMARY

THE IMAGE IN WORDS

archive chicane double dust fern friar grey half ironside masala mist mountain rakaia silver spanish stack star storm triple trojan

COLOR CLUSTERS

Colors in the image were clustered into 2 groups (k-means). The average color of the colors for each cluster is shown. The name is the closest named color and its distance is shown using ΔE. The tags are the set of words formed by all named neighbours within ΔE ≤ 5. The list of words above is the set of all unique words in this set of words.

Cluster colors, sized by number of pixels:

cluster	pixels	name	HEX	RGB	HSV	LCH	Lab	tags
	64.04%	161,154,152 triple rakaia ΔE=1.9	#9B9793	155 151 147	28 5 61	63 3 71	63 1 3	archive dust fern friar half mist mountain rakaia silver spanish star triple grey
	35.96%	101,100,95 storm dust ΔE=0.9	#66645F	102 100 95	42 6 40	42 3 93	42 0 3	chicane double dust half ironside masala stack storm triple trojan grey

IMAGE CLUSTER PARTITIONS

Pixels of the image assigned to each cluster. The border is the color of the cluster as calculated by the average value of its pixels.

RGB HISTOGRAM

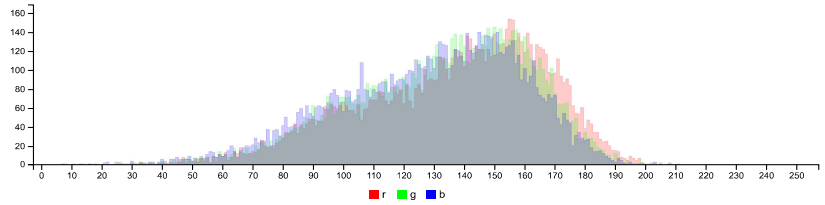

HSV HISTOGRAMS

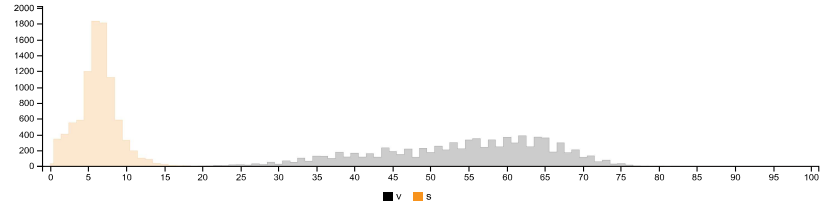

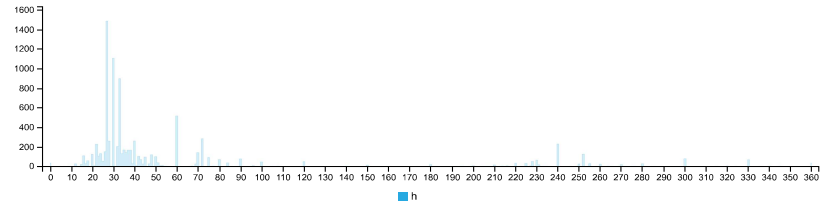

LCH HISTOGRAMS

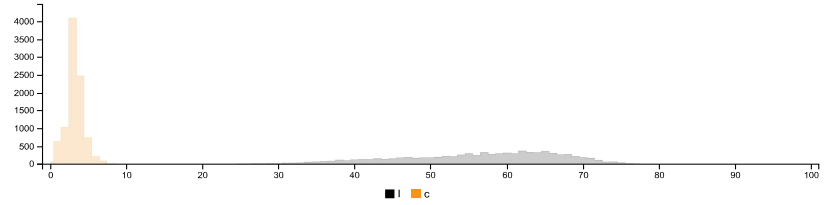

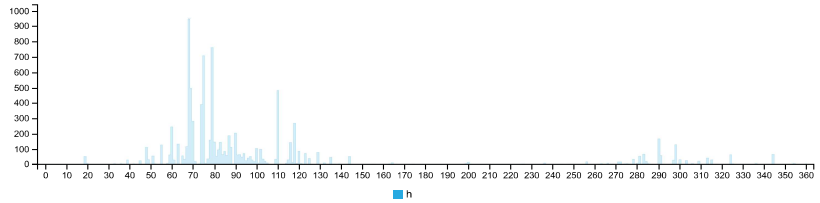

LAB HISTOGRAMS

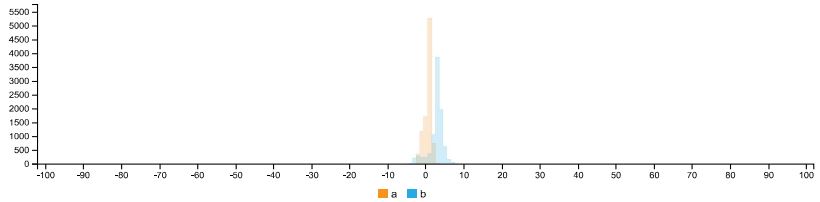

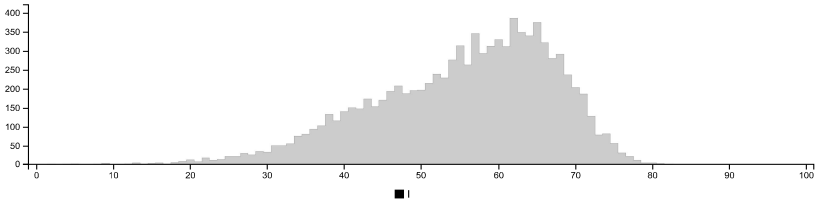

COLOR SPACE AND CHANNEL STATISTICS

	avg	med	min	max
RGB:R	136	141	8	211
RGB:G	133	137	8	201
RGB:B	129	132	7	208
HSV:H	33 1.00	33	0	360
HSV:S	6	6	0	30
HSV:V	54	56	3	83
LCH:L	55	57	2	82
LCH:C	3	3	0	9
LCH:H	77 1.00	79	6	360
LAB:L	55	57	2	82
LAB:A	1	1	-3	4
LAB:B	3	3	-7	9

Detailed report - Top debonded part of Specimen TG20-B-3

IMAGE COLOR SUMMARIZER

RGB, HSV, LCH & Lab image color statistics and clustering—simple and easy

HOME ANALYZE EXAMPLES API DOWNLOAD FAQ NEWS

IMAGE COLOR SUMMARY

THE IMAGE IN WORDS

archive chicago condor dark dust fern friar gravel grey half ironside masala olivish quarter rakaia sandstone silver stack stonehenge storm taupe triple

COLOR CLUSTERS

Colors in the image were clustered into 2 groups (k-means). The average color of the colors for each cluster is shown. The name is the closest named color and its distance is shown using ΔE. The tags are the set of words formed by all named neighbours within ΔE ≤ 5. The list of words above is the set of all unique words in this set of words.

Cluster colors, sized by number of pixels:

cluster	pixels	name	HEX	RGB	HSV	LCH	Lab	tags
	54.87%	101,100,95 storm dust ΔE=1.2	#63615B	99 97 91	41 8 39	41 3 92	41 0 3	dark chicago condor dust gravel half ironside masala olivish stack storm triple grey
	45.13%	153,147,140 silver fern ΔE=1.3	#999590	153 149 144	32 5 60	62 3 78	62 1 3	archive fern friar half quarter rakaia sandstone silver stonehenge taupe triple grey

IMAGE CLUSTER PARTITIONS

Pixels of the image assigned to each cluster. The border is the color of the cluster as calculated by the average value of its pixels.

RGB HISTOGRAM

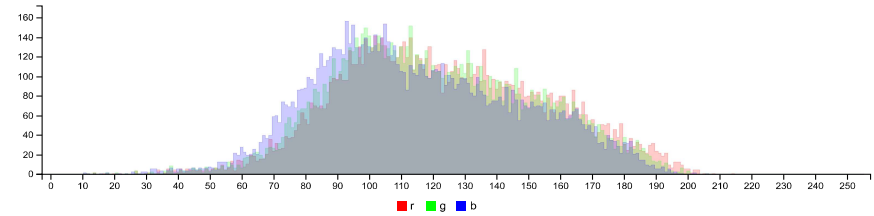

HSV HISTOGRAMS

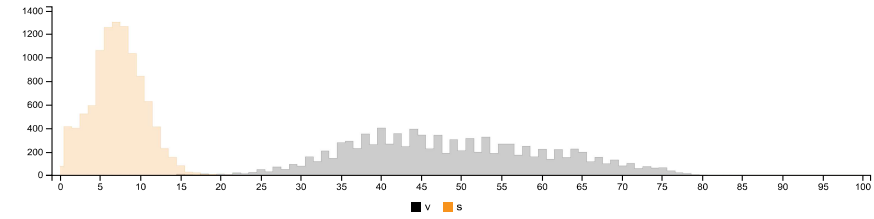

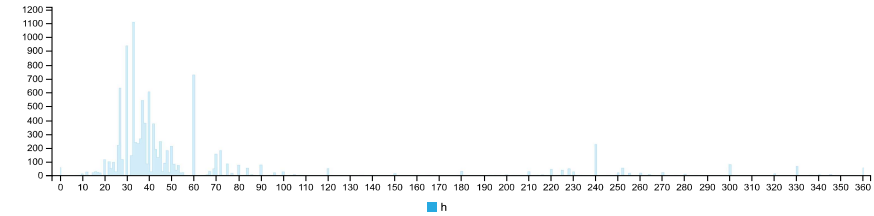

LCH HISTOGRAMS

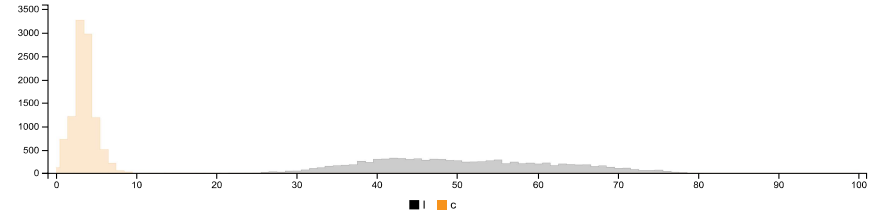

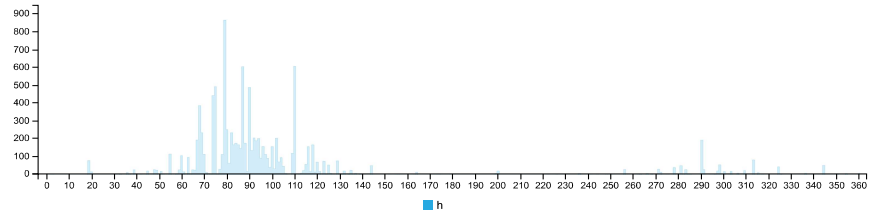

LAB HISTOGRAMS

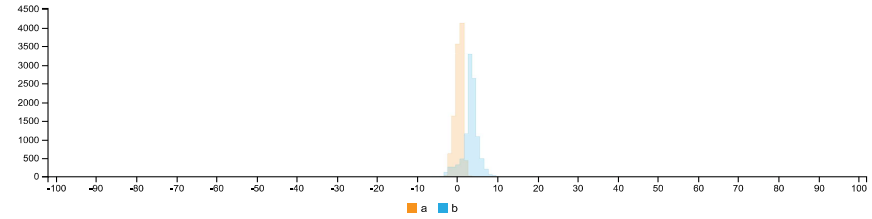

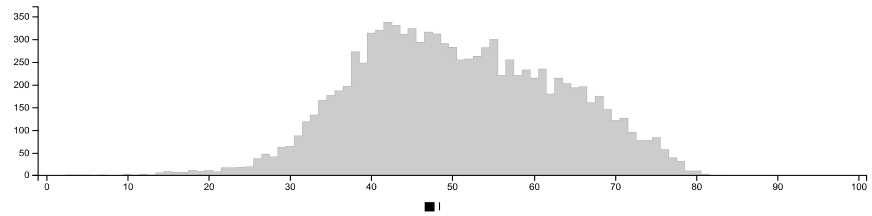

COLOR SPACE AND CHANNEL STATISTICS

	avg	med	min	max
RGB:R	123	121	11	214
RGB:G	120	118	11	206
RGB:B	116	112	11	206
HSV:H	38 1.00	38	0	360
HSV:S	7	7	0	22
HSV:V	49	47	4	84
LCH:L	50	50	3	83
LCH:C	4	3	0	10
LCH:H	84 1.00	87	3	360
LAB:L	50	50	3	83
LAB:A	0	0	-3	3
LAB:B	3	3	-6	10

Summary of Image Analysis for Specimen TG20-B-4

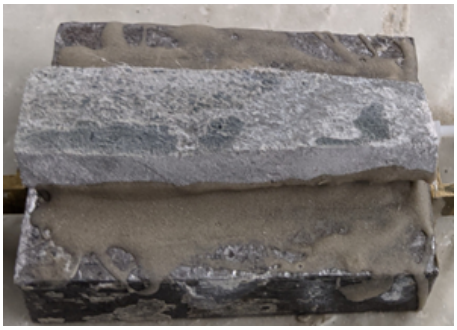

Figure D.45: Bottom debonded part of Specimen TG20-B-4

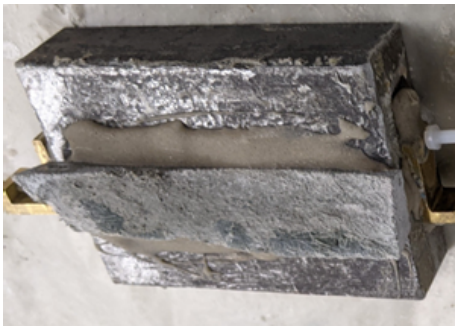

Figure D.46: Top debonded part of Specimen TG20-B-4

Table D.23: Summary of Image analysis result for specimen TG20-B-4

Contact Type	Colour Cluster	Results of Image analysis		Contact (%)		Average Contact (in %)
		Bottom Debonded Layer	Top Debonded Layer	Bottom Debonded Layer	Top Debonded Layer	
						
Poor				56,54%	55,63%	**56,09%**
Good				43,46%	44,37%	**43,92%**

Detailed report - Bottom debonded part of Specimen TG20-B-4

IMAGE COLOR SUMMARIZER

RGB, HSV, LCH & Lab image color statistics and clustering—simple and easy

HOME ANALYZE EXAMPLES API DOWNLOAD FAQ NEWS

IMAGE COLOR SUMMARY

THE IMAGE IN WORDS

blast double dove grey lady masala metal quarter rakaia shady silver sonic spanish stack surrender tarmac triple white

COLOR CLUSTERS

Colors in the image were clustered into 2 groups (k-means). The average color of the colors for each cluster is shown. The name is the closest named color and its distance is shown using ΔE. The tags are the set of words formed by all named neighbours within ΔE ≤ 5. The list of words above is the set of all unique words in this set of words.

Cluster colors, sized by number of pixels:

cluster	pixels	name	HEX	RGB	HSV	LCH	Lab	tags
	56.54%	115,115,115 grey ΔE=0.7	#737271	115 114 113	9 1 45	48 0 34	48 0 0	blast double dove masala quarter silver sonic stack tarmac grey
	43.46%	152,152,152 spanish grey ΔE=0.8	#9A9898	154 152 152	351 1 60	63 1 7	63 1 0	lady metal rakaia shady spanish surrender triple grey white

IMAGE CLUSTER PARTITIONS

Pixels of the image assigned to each cluster. The border is the color of the cluster as calculated by the average value of its pixels.

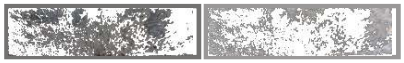

RGB HISTOGRAM

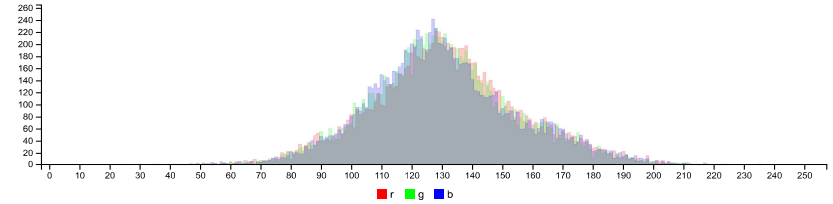

HSV HISTOGRAMS

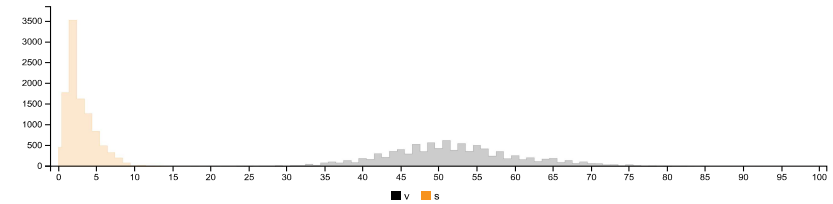

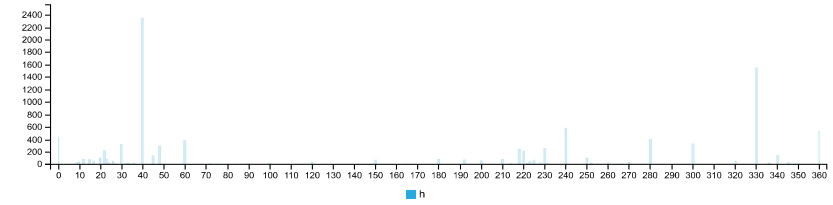

LCH HISTOGRAMS

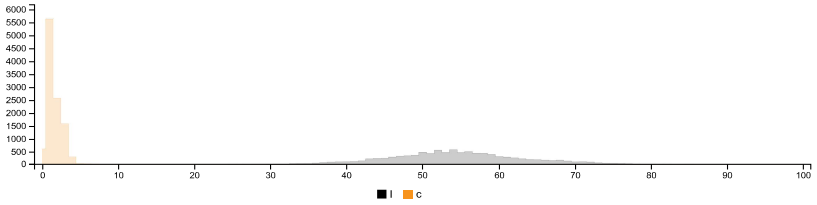

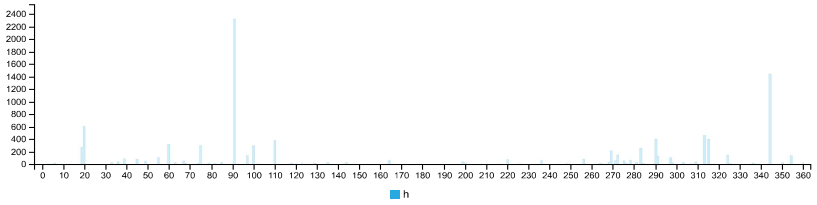

LAB HISTOGRAMS

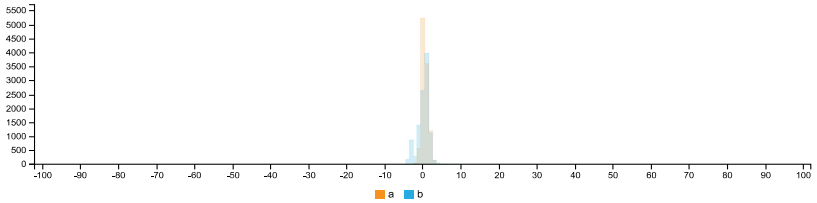

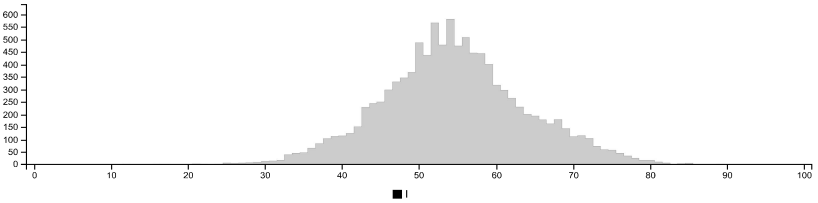

COLOR SPACE AND CHANNEL STATISTICS

	avg	med	min	max
RGB:R	132	131	35	235
RGB:G	130	129	30	220
RGB:B	130	128	25	218
HSV:H	357 0.00	190	0	360
HSV:S	3	2	0	29
HSV:V	52	51	14	92
LCH:L	54	54	12	89
LCH:C	2	1	0	10
LCH:H	22 0.00	110	3	360
LAB:L	54	54	12	89
LAB:A	1	0	-4	4
LAB:B	0	0	-6	9

Detailed report - Top debonded part of Specimen TG20-B-4

IMAGE COLOR SUMMARIZER

RGB, HSV, LCH & Lab image color statistics and clustering—simple and easy

HOME ANALYZE EXAMPLES API DOWNLOAD FAQ NEWS

IMAGE COLOR SUMMARY

THE IMAGE IN WORDS

aluminium boulder chateau cool eighth grey jumbo lady mid monsoon quarter raven shady sidewinder silver so storm tuna

COLOR CLUSTERS

Colors in the image were clustered into 2 groups (k-means). The average color of the colors for each cluster is shown. The name is the closest named color and its distance is shown using ΔE. The tags are the set of words formed by all named neighbours within ΔE ≤ 5. The list of words above is the set of all unique words in this set of words.

Cluster colors, sized by number of pixels:

cluster	pixels	name	HEX	RGB	HSV	LCH	Lab	tags
	55.63%	159,155,157 shady lady ΔE=2.0	#A09EA3	160 158 163	260 3 64	66 3 303	66 1 -2	aluminium chateau cool lady quarter shady sidewinder silver so grey
	44.37%	124,123,130 jumbo ΔE=1.9	#79797E	121 121 126	241 4 49	51 3 291	51 1 -3	boulder eighth jumbo mid monsoon raven storm tuna grey

IMAGE CLUSTER PARTITIONS

Pixels of the image assigned to each cluster. The border is the color of the cluster as calculated by the average value of its pixels.

RGB HISTOGRAM

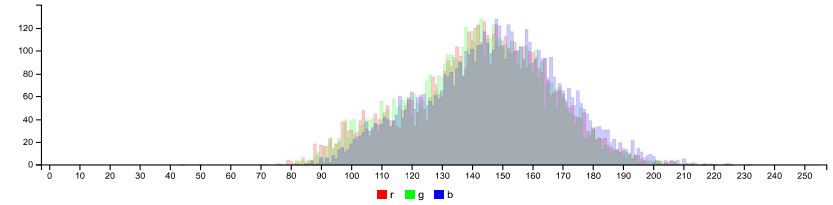

HSV HISTOGRAMS

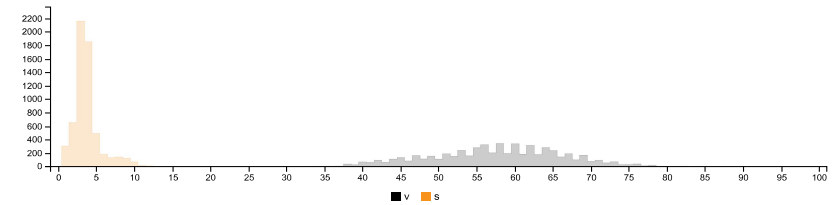

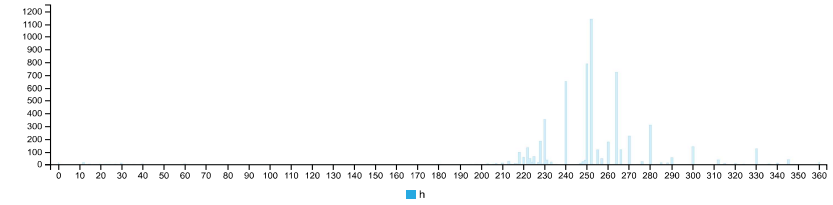

LCH HISTOGRAMS

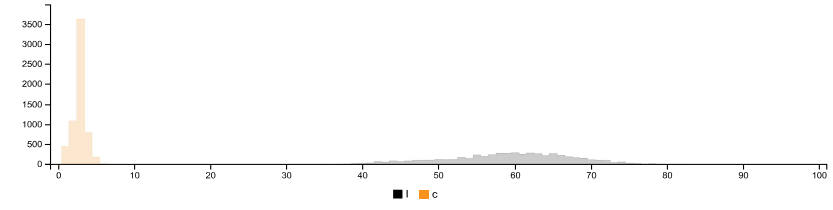

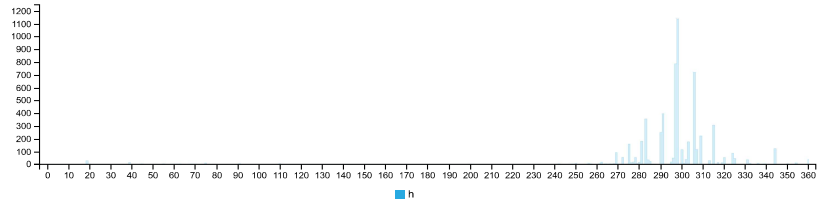

LAB HISTOGRAMS

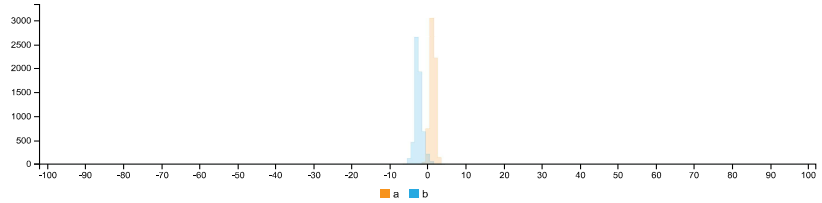

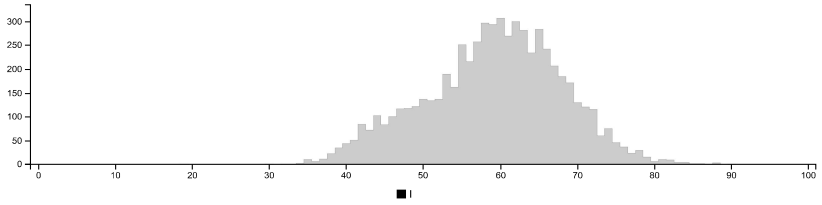

COLOR SPACE AND CHANNEL STATISTICS

	avg	med	min	max
RGB:R	143	144	44	231
RGB:G	142	143	45	226
RGB:B	147	148	50	232
HSV:H	255 1.00	252	0	360
HSV:S	4	3	0	13
HSV:V	58	58	20	91
LCH:L	59	60	19	90
LCH:C	3	3	0	7
LCH:H	300 1.00	298	3	360
LAB:L	59	60	19	90
LAB:A	1	1	-2	3
LAB:B	-2	-3	-6	4

D.1.3. Specimen Type-C

***Analysis for Specimen TG5-C-4 and TG10-C-1 missing as the inter-layer surface images after the test were not captured*

Summary of Image Analysis for Specimen TG5-C-1

Figure D.47: Bottom debonded part of Specimen TG5-C-1

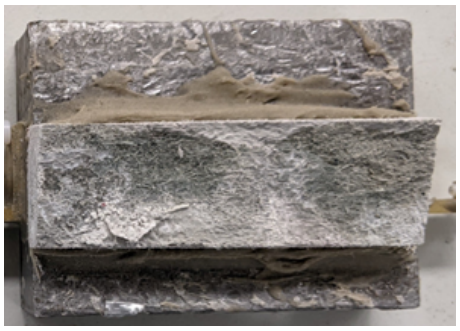

Figure D.48: Top debonded part of Specimen TG5-C-1

Table D.24: Summary of Image analysis result for specimen TG5-C-1

Contact Type	Colour Cluster	Results of Image analysis		Contact (%)		Average Contact (in %)
		Bottom Debonded Layer	Top Debonded Layer	Bottom Debonded Layer	Top Debonded Layer	
			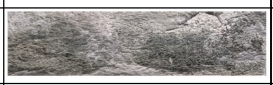			
Poor				51,38%	51,87%	**51,63%**
Good				48,62%	48,93%	**48,78%**

Detailed report - Bottom debonded part of Specimen TG5-C-1

IMAGE COLOR SUMMARIZER

RGB, HSV, LCH & Lab image color statistics and clustering—simple and easy

HOME ANALYZE EXAMPLES API DOWNLOAD FAQ NEWS

IMAGE COLOR SUMMARY

THE IMAGE IN WORDS

chicane cliff dim dimgray dimgrey double dove dust face granite grey mist mountain rakaia star transmission triple

COLOR CLUSTERS

Colors in the image were clustered into 2 groups (k-means). The average color of the colors for each cluster is shown. The name is the closest named color and its distance is shown using ΔE. The tags are the set of words formed by all named neighbours within ΔE ≤ 5. The list of words above is the set of all unique words in this set of words.

Cluster colors, sized by number of pixels:

cluster	pixels	name	HEX	RGB	HSV	LCH	Lab	tags
	51.38%	161,161,161 grey ΔE=1.6	#A39F9E	163 159 158	17 3 64	66 2 49	66 1 1	double dust mist mountain rakaia star transmission triple grey
	48.62%	104,103,101 chicane ΔE=0.9	#6B6A68	107 106 104	42 3 42	45 1 94	45 0 1	chicane cliff dim dimgray dimgrey dove face granite grey

IMAGE CLUSTER PARTITIONS

Pixels of the image assigned to each cluster. The border is the color of the cluster as calculated by the average value of its pixels.

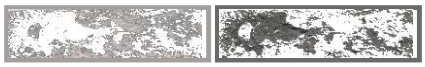

RGB HISTOGRAM

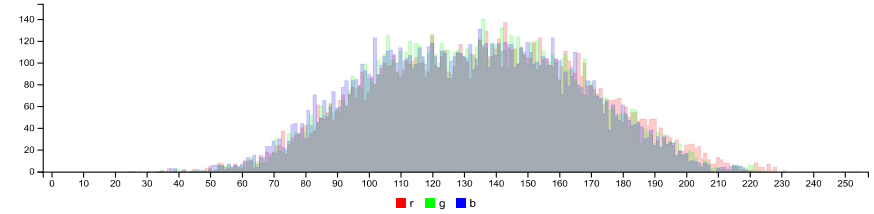

HSV HISTOGRAMS

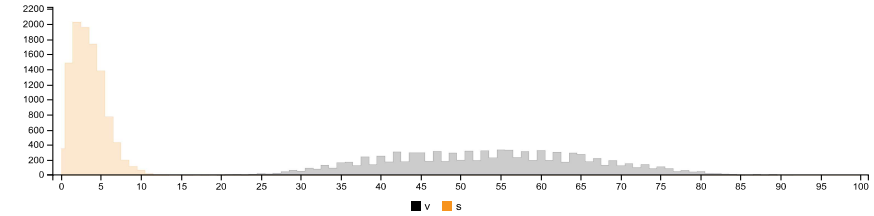

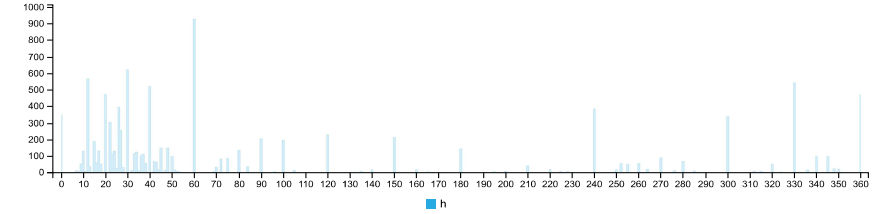

LCH HISTOGRAMS

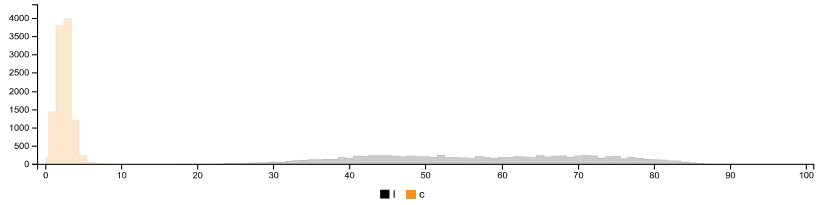

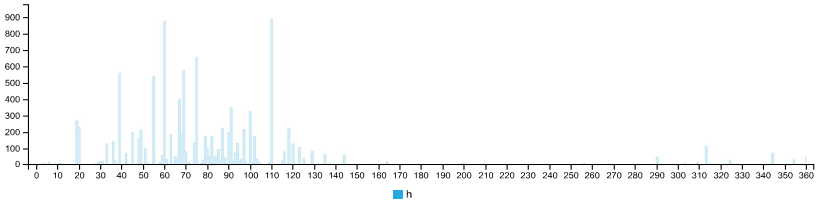

LAB HISTOGRAMS

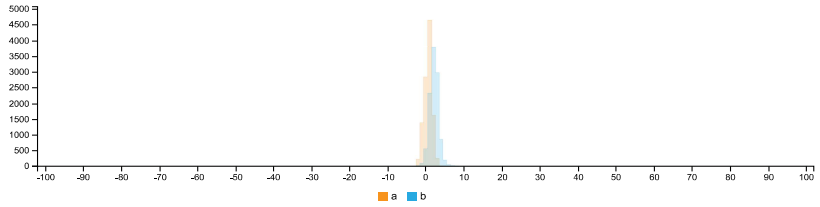

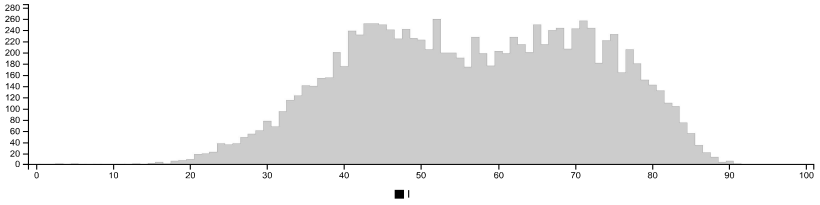

COLOR SPACE AND CHANNEL STATISTICS

	avg	med	min	max
RGB:R	140	139	5	233
RGB:G	136	136	5	229
RGB:B	133	133	4	226
HSV:H	31 1.00	30	0	360
HSV:S	5	5	0	36
HSV:V	55	55	2	91
LCH:L	57	57	1	91
LCH:C	3	3	0	9
LCH:H	71 1.00	75	3	360
LAB:L	57	57	1	91
LAB:A	1	1	-3	4
LAB:B	2	2	-3	8

Detailed report - Top debonded part of Specimen TG5-C-1

IMAGE COLOR SUMMARIZER

RGB, HSV, LCH & Lab image color statistics and clustering—simple and easy

HOME ANALYZE EXAMPLES API DOWNLOAD FAQ NEWS

IMAGE COLOR SUMMARY

THE IMAGE IN WORDS

chicane delta dim dimgray dimgrey double dust granite grey ironside kensington mist mountain rakaia star storm transmission triple trojan

COLOR CLUSTERS

Colors in the image were clustered into 2 groups (k-means). The average color of the colors for each cluster is shown. The name is the closest named color and its distance is shown using ΔE. The tags are the set of words formed by all named neighbours within ΔE ≤ 5. The list of words above is the set of all unique words in this set of words.

Cluster colors, sized by number of pixels:

cluster	pixels	name	HEX	RGB	HSV	LCH	Lab	tags
	51.07%	160,159,156 mountain mist ΔE=1.2	#A3A09D	163 160 157	27 4 64	66 2 70	66 1 2	delta double dust kensington mist mountain rakaia star transmission triple grey
	48.93%	103,102,98 ironside grey ΔE=0.8	#676664	103 102 100	46 3 40	43 2 98	43 0 2	chicane dim dimgray dimgrey double dust granite ironside storm trojan grey

IMAGE CLUSTER PARTITIONS

Pixels of the image assigned to each cluster. The border is the color of the cluster as calculated by the average value of its pixels.

RGB HISTOGRAM

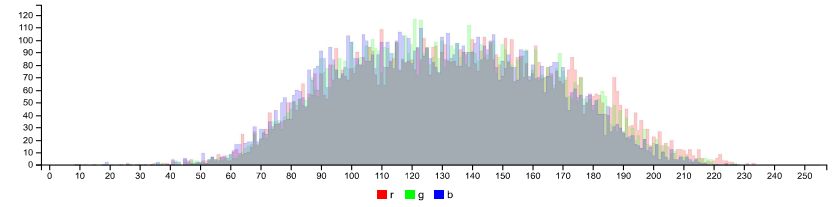

HSV HISTOGRAMS

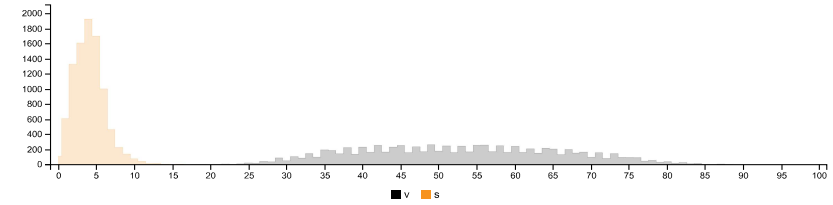

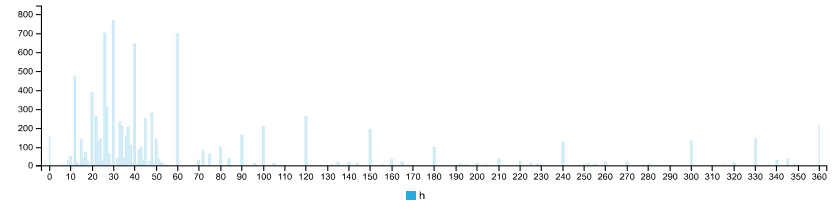

LCH HISTOGRAMS

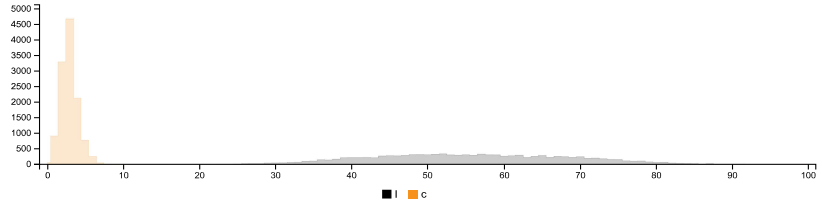

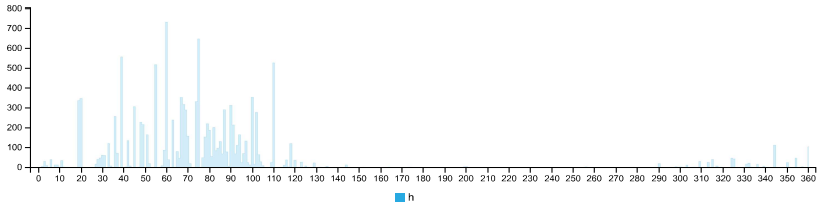

LAB HISTOGRAMS

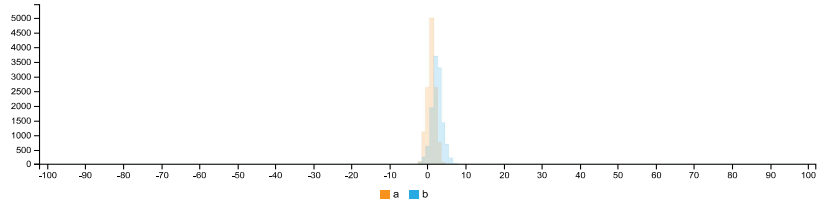

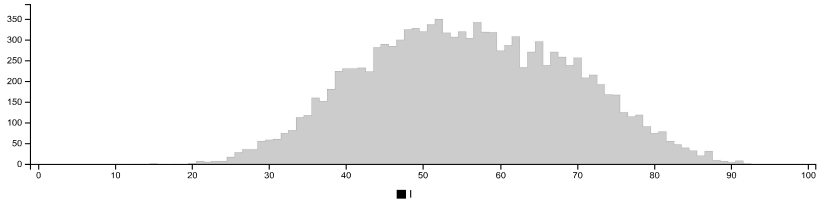

COLOR SPACE AND CHANNEL STATISTICS

	avg	med	min	max
RGB:R	138	136	28	237
RGB:G	134	132	28	231
RGB:B	130	128	27	229
HSV:H	25 1.00	30	0	360
HSV:S	6	6	0	31
HSV:V	54	53	11	93
LCH:L	56	55	10	92
LCH:C	3	3	0	16
LCH:H	65 1.00	71	2	360
LAB:L	56	55	10	92
LAB:A	1	1	-3	16
LAB:B	2	2	-3	9

Summary of Image Analysis for Specimen TG5-C-2

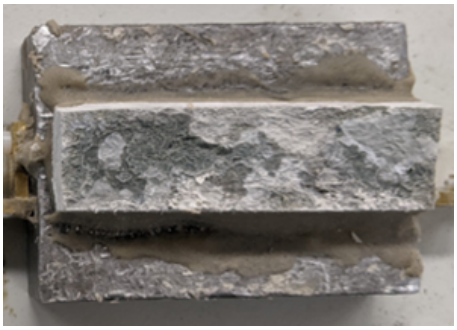

Figure D.49: Bottom debonded part of Specimen TG5-C-2

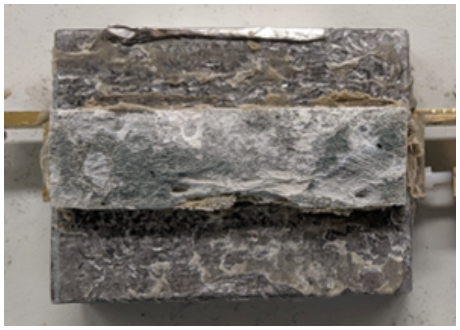

Figure D.50: Top debonded part of Specimen TG5-C-2

Table D.25: Summary of Image analysis result for specimen TG5-C-2

Contact Type	Colour Cluster	Results of Image analysis		Contact (%)		Average Contact (in %)
		Bottom Debonded Layer	Top Debonded Layer	Bottom Debonded Layer	Top Debonded Layer	
						
Poor				51,38%	51,07%	**51,23%**
Good				48,62%	48,93%	**48,78%**

Detailed report - Bottom debonded part of Specimen TG5-C-2

IMAGE COLOR SUMMARIZER

RGB, HSV, LCH & Lab image color statistics and clustering—simple and easy

HOME ANALYZE EXAMPLES API DOWNLOAD FAQ NEWS

IMAGE COLOR SUMMARY

THE IMAGE IN WORDS

chicane cliff dim dimgray dimgrey double dove dust face granite grey mist mountain rakaia star transmission triple

COLOR CLUSTERS

Colors in the image were clustered into 2 groups (k-means). The average color of the colors for each cluster is shown. The name is the closest named color and its distance is shown using ΔE. The tags are the set of words formed by all named neighbours within ΔE ≤ 5. The list of words above is the set of all unique words in this set of words.

Cluster colors, sized by number of pixels:

cluster	pixels	name	HEX	RGB	HSV	LCH	Lab	tags
	51.38%	161,161,161 grey ΔE=1.6	#A39F9E	163 159 158	17 3 64	66 2 49	66 1 1	double dust mist mountain rakaia star transmission triple grey
	48.62%	104,103,101 chicane ΔE=0.9	#6B6A68	107 106 104	42 3 42	45 1 94	45 0 1	chicane cliff dim dimgray dimgrey dove face granite grey

IMAGE CLUSTER PARTITIONS

Pixels of the image assigned to each cluster. The border is the color of the cluster as calculated by the average value of its pixels.

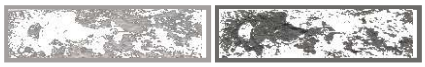

RGB HISTOGRAM

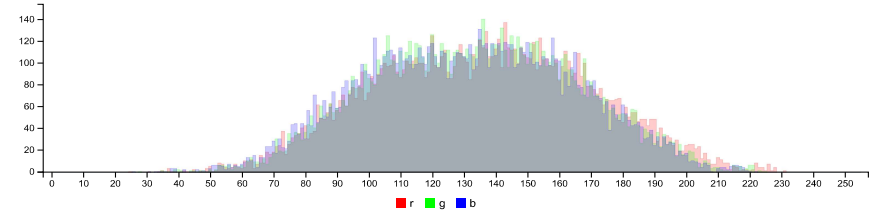

HSV HISTOGRAMS

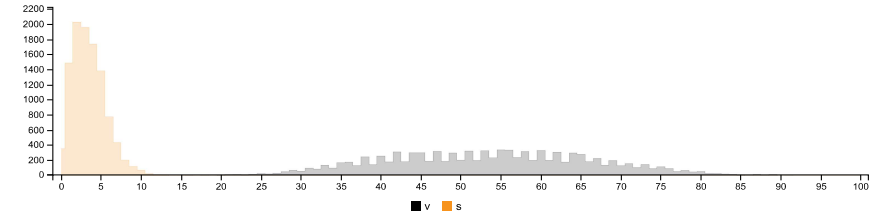

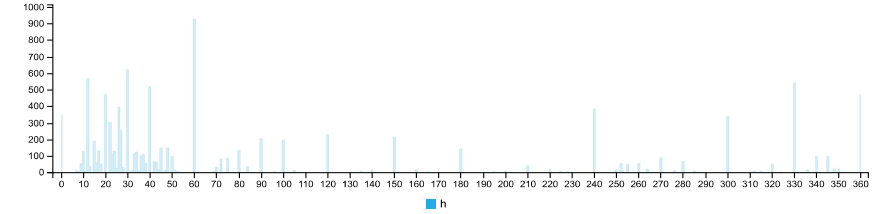

LCH HISTOGRAMS

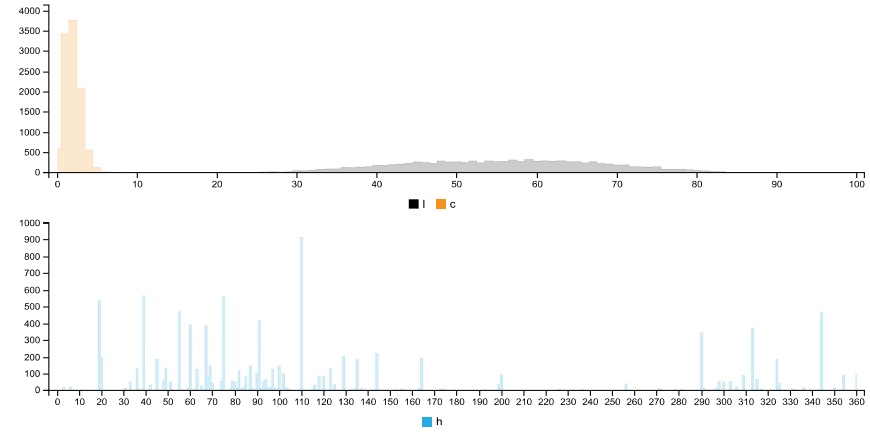

LAB HISTOGRAMS

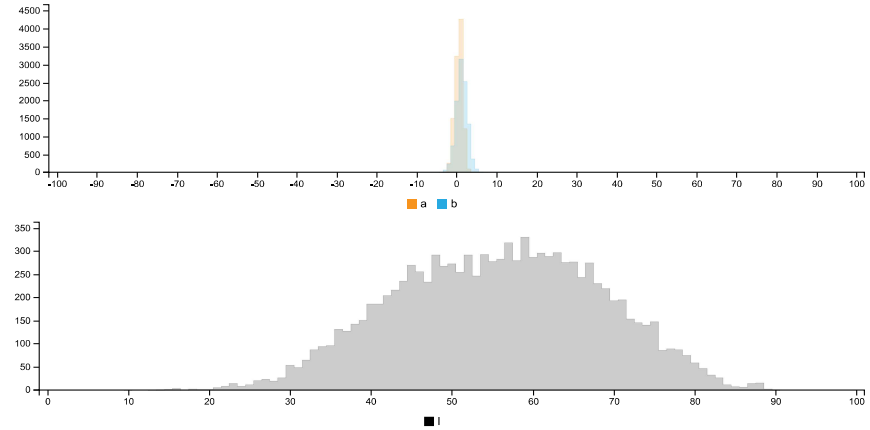

COLOR SPACE AND CHANNEL STATISTICS

	avg	med	min	max
RGB:R	136	136	25	231
RGB:G	134	134	28	225
RGB:B	132	132	26	222
HSV:H	24 1.00	45	0	360
HSV:S	4	3	0	20
HSV:V	53	54	11	91
LCH:L	56	56	10	90
LCH:C	2	2	0	8
LCH:H	62 1.00	91	3	360
LAB:L	56	56	10	90
LAB:A	0	1	-3	4
LAB:B	1	1	-6	8

Detailed report - Top debonded part of Specimen TG5-C-2

IMAGE COLOR SUMMARIZER

RGB, HSV, LCH & Lab image color statistics and clustering—simple and easy

HOME ANALYZE EXAMPLES API DOWNLOAD FAQ NEWS

IMAGE COLOR SUMMARY

THE IMAGE IN WORDS

chicane delta dim dimgray dimgrey double dust granite grey ironside kensington mist mountain rakaia star storm transmission triple trojan

COLOR CLUSTERS

Colors in the image were clustered into 2 groups (k-means). The average color of the colors for each cluster is shown. The name is the closest named color and its distance is shown using ΔE. The tags are the set of words formed by all named neighbours within ΔE ≤ 5. The list of words above is the set of all unique words in this set of words.

Cluster colors, sized by number of pixels:

cluster	pixels	name	HEX	RGB	HSV	LCH	Lab	tags
	51.07%	160,159,156 mountain mist ΔE=1.2	#A3A09D	163 160 157	27 4 64	66 2 70	66 1 2	delta double dust kensington mist mountain rakaia star transmission triple grey
	48.93%	103,102,98 ironside grey ΔE=0.8	#676664	103 102 100	46 3 40	43 2 98	43 0 2	chicane dim dimgray dimgrey double dust granite ironside storm trojan grey

IMAGE CLUSTER PARTITIONS

Pixels of the image assigned to each cluster. The border is the color of the cluster as calculated by the average value of its pixels.

RGB HISTOGRAM

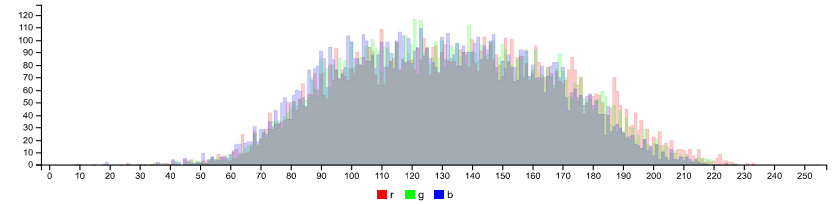

HSV HISTOGRAMS

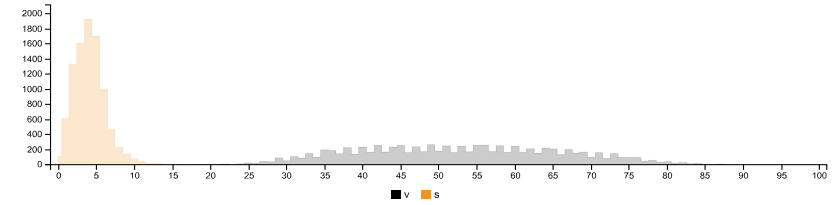

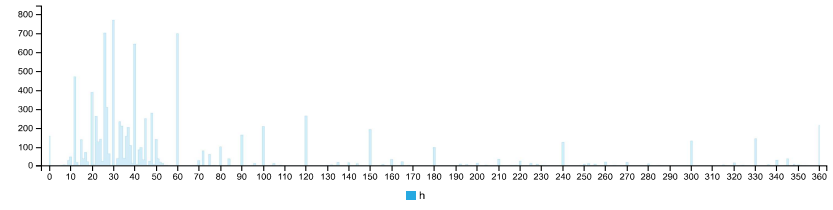

LCH HISTOGRAMS

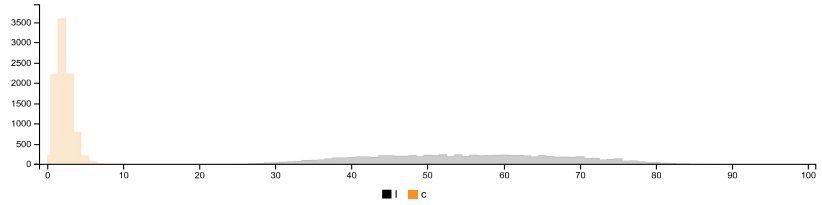

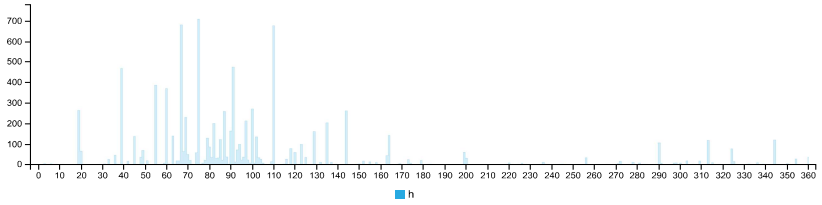

LAB HISTOGRAMS

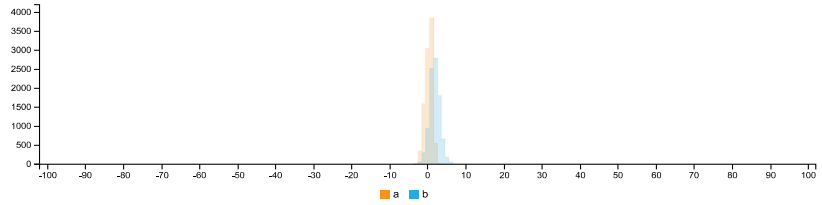

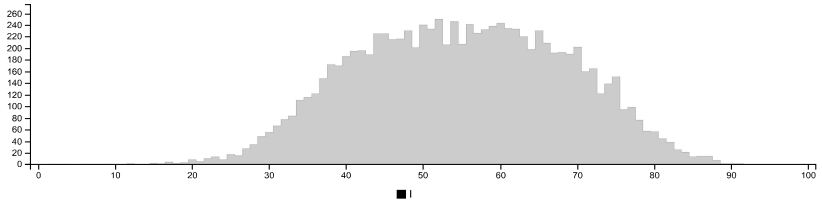

COLOR SPACE AND CHANNEL STATISTICS

	avg	med	min	max
RGB:R	134	134	9	233
RGB:G	132	131	9	227
RGB:B	129	129	9	227
HSV:H	37 1.00	38	0	360
HSV:S	4	4	0	46
HSV:V	53	53	4	91
LCH:L	55	55	2	91
LCH:C	2	2	0	11
LCH:H	80 1.00	87	3	360
LAB:L	55	55	2	91
LAB:A	0	0	-4	5
LAB:B	2	2	-4	11

Summary of Image Analysis for Specimen TG5-C-3

Figure D.51: Bottom debonded part of Specimen TG5-C-3

Figure D.52: Top debonded part of Specimen TG5-C-3

Table D.26: Summary of Image analysis result for specimen TG5-C-3

Contact Type	Colour Cluster	Results of Image analysis		Contact (%)		Average Contact (in %)
		Bottom Debonded Layer	Top Debonded Layer	Bottom Debonded Layer	Top Debonded Layer	
						
Poor				45,16%	45,15%	**45,16%**
Good				54,84%	54,85%	**54,85%**

Detailed report - Bottom debonded part of Specimen TG5-C-3

IMAGE COLOR SUMMARIZER

RGB, HSV, LCH & Lab image color statistics and clustering—simple and easy

HOME ANALYZE EXAMPLES API DOWNLOAD FAQ NEWS

IMAGE COLOR SUMMARY

THE IMAGE IN WORDS

alley chicago dark fern gannet gravel grey half metal mist mountain olivish silver spanish tinpan torque tundora white

COLOR CLUSTERS

Colors in the image were clustered into 2 groups (k-means). The average color of the colors for each cluster is shown. The name is the closest named color and its distance is shown using ΔE. The tags are the set of words formed by all named neighbours within ΔE ≤ 5. The list of words above is the set of all unique words in this set of words.

Cluster colors, sized by number of pixels:

cluster	pixels	name	HEX	RGB	HSV	LCH	Lab	tags
	54.85%	93,92,88 chicago ΔE=0.8	#5B5A57	91 90 87	45 4 36	38 2 96	38 0 2	dark alley chicago gravel half olivish tinpan torque tundora grey
	45.15%	149,145,140 grey ΔE=1.9	#979391	151 147 145	24 4 59	61 2 64	61 1 2	fern gannet metal mist mountain silver spanish grey white

IMAGE CLUSTER PARTITIONS

Pixels of the image assigned to each cluster. The border is the color of the cluster as calculated by the average value of its pixels.

RGB HISTOGRAM

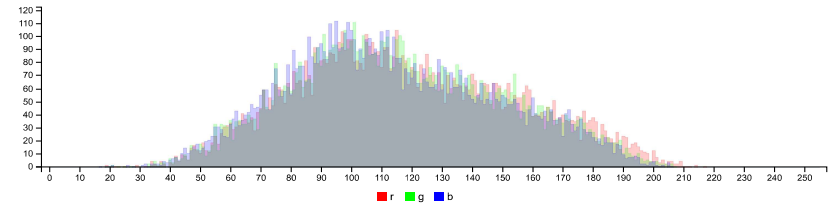

HSV HISTOGRAMS

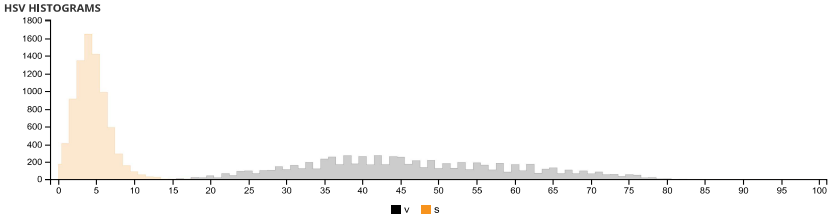

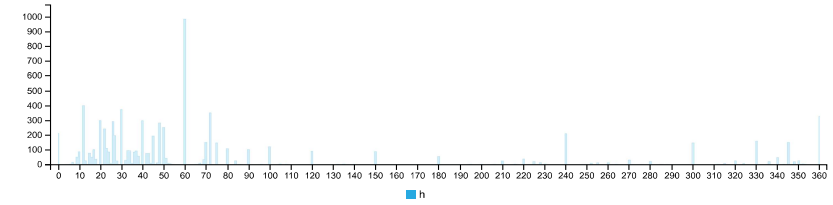

LCH HISTOGRAMS

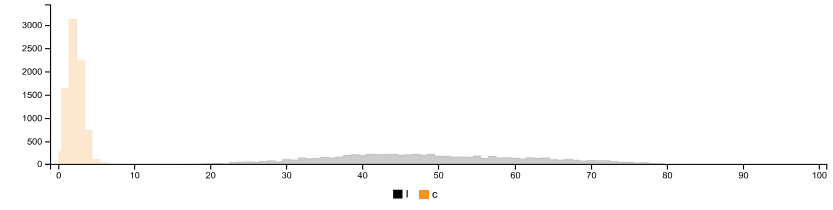

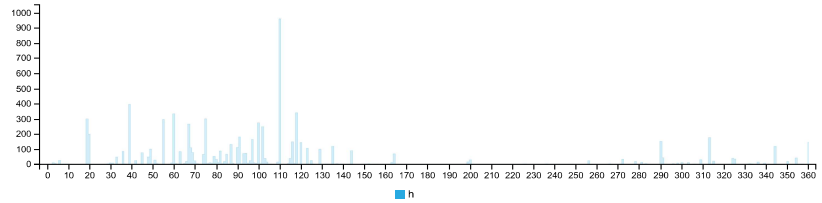

LAB HISTOGRAMS

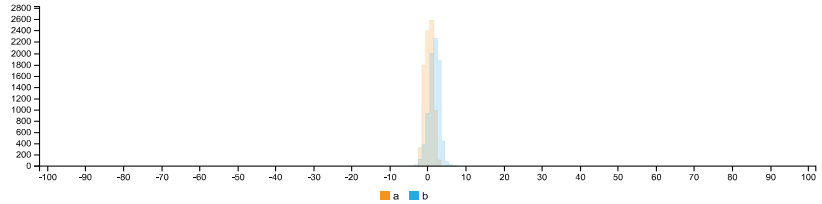

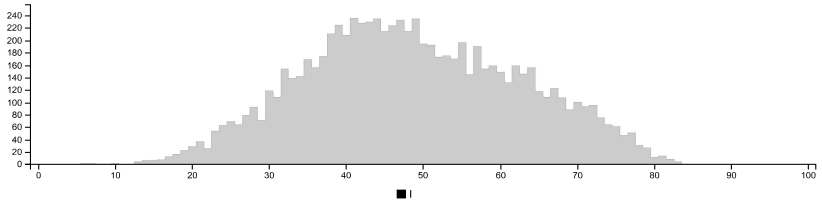

COLOR SPACE AND CHANNEL STATISTICS

	avg	med	min	max
RGB:R	118	115	19	217
RGB:G	116	113	19	207
RGB:B	114	110	17	206
HSV:H	34 1.00	48	0	360
HSV:S	4	4	0	22
HSV:V	47	45	7	85
LCH:L	49	48	6	84
LCH:C	2	2	0	7
LCH:H	75 1.00	97	0	360
LAB:L	49	48	6	84
LAB:A	0	0	-3	5
LAB:B	2	2	-5	7

Detailed report - Top debonded part of Specimen TG5-C-3

IMAGE COLOR SUMMARIZER

RGB, HSV, LCH & Lab image color statistics and clustering—simple and easy

HOME ANALYZE EXAMPLES API DOWNLOAD FAQ NEWS

IMAGE COLOR SUMMARY

THE IMAGE IN WORDS

chicane dim double dust granite grey ironside lady mist mountain rakaia shady spanish storm transmission triple trojan

COLOR CLUSTERS

Colors in the image were clustered into 2 groups (k-means). The average color of the colors for each cluster is shown. The name is the closest named color and its distance is shown using ΔE. The tags are the set of words formed by all named neighbours within ΔE ≤ 5. The list of words above is the set of all unique words in this set of words.

Cluster colors, sized by number of pixels:

cluster	pixels	name	HEX	RGB	HSV	LCH	Lab	tags
	54.84%	100,100,99 storm dust ΔE=0.6	#656361	101 99 97	36 4 40	42 1 86	42 0 1	chicane dim double dust granite ironside storm trojan grey
	45.16%	158,158,158 grey ΔE=1.6	#A29E9E	162 158 158	11 3 64	66 1 38	66 1 1	double lady mist mountain rakaia shady spanish transmission triple grey

IMAGE CLUSTER PARTITIONS

Pixels of the image assigned to each cluster. The border is the color of the cluster as calculated by the average value of its pixels.

RGB HISTOGRAM

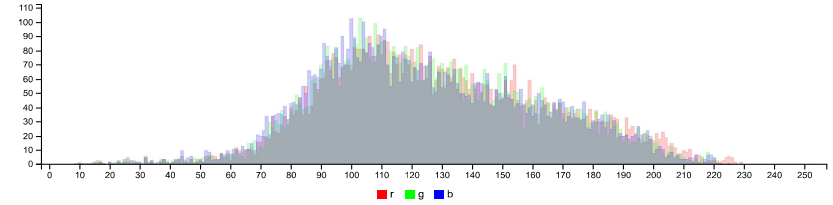

HSV HISTOGRAMS

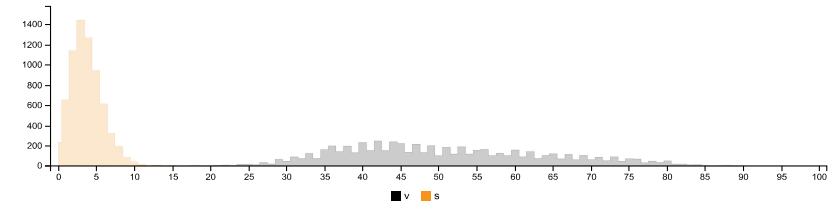

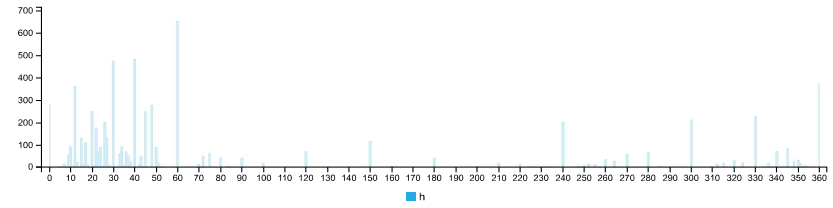

LCH HISTOGRAMS

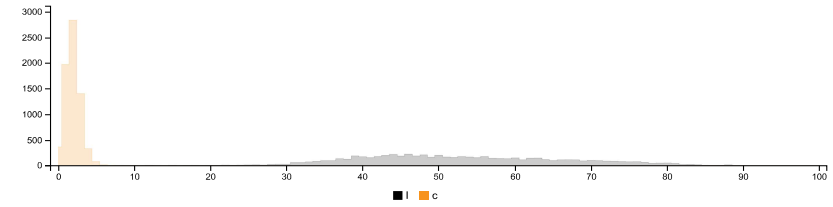

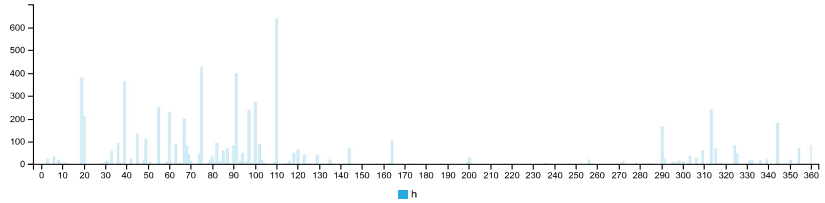

LAB HISTOGRAMS

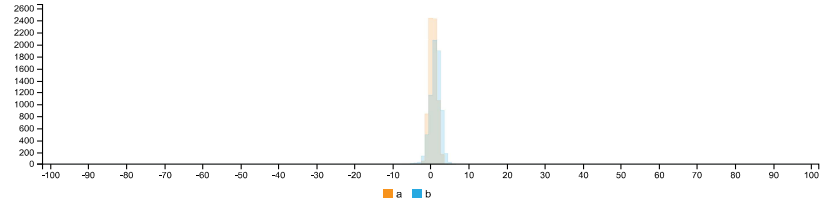

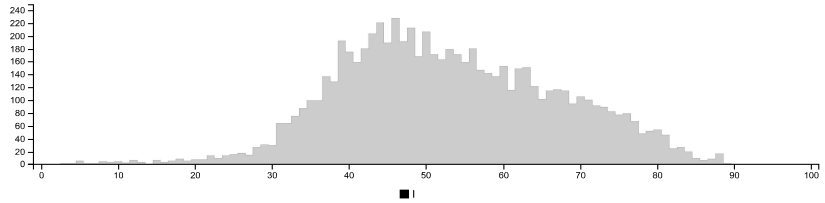

COLOR SPACE AND CHANNEL STATISTICS

	avg	med	min	max
RGB:R	129	124	10	229
RGB:G	126	122	10	223
RGB:B	125	120	9	225
HSV:H	21 1.00	45	0	360
HSV:S	4	4	0	27
HSV:V	51	49	4	90
LCH:L	53	52	3	89
LCH:C	2	2	0	8
LCH:H	59 1.00	91	0	360
LAB:L	53	52	3	89
LAB:A	1	1	-2	4
LAB:B	1	1	-7	7

Summary of Image Analysis for Specimen TG10-C-2

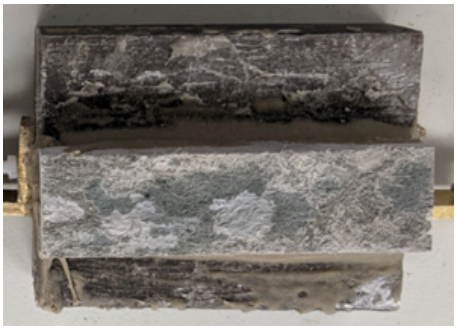

Figure D.53: Bottom debonded part of Specimen TG10-C-2

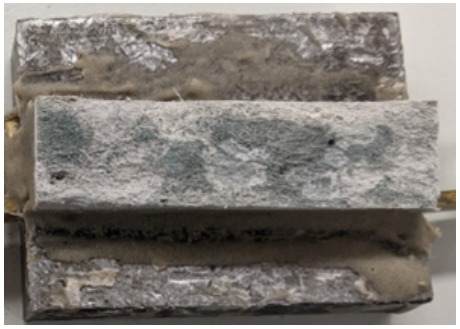

Figure D.54: Top debonded part of Specimen TG10-C-2

Table D.27: Summary of Image analysis result for specimen TG10-C-2

Contact Type	Colour Cluster	Results of Image analysis		Contact (%)		Average Contact (in %)
		Bottom Debonded Layer	Top Debonded Layer	Bottom Debonded Layer	Top Debonded Layer	
						
Poor				49,88%	51,88%	**50,88%**
Good				50,92%	48,12%	**49,52%**

Detailed report - Bottom debonded part of Specimen TG10-C-2

IMAGE COLOR SUMMARIZER

RGB, HSV, LCH & Lab image color statistics and clustering—simple and easy

HOME ANALYZE EXAMPLES API DOWNLOAD FAQ NEWS

IMAGE COLOR SUMMARY

THE IMAGE IN WORDS

aluminium blast delta detroit double dove dust grey imagine kensington masala mist mountain quarter rakaia silver sonic stack star tarmac transmission triple viaduct

COLOR CLUSTERS

Colors in the image were clustered into 2 groups (k-means). The average color of the colors for each cluster is shown. The name is the closest named color and its distance is shown using ΔE. The tags are the set of words formed by all named neighbours within ΔE ≤ 5. The list of words above is the set of all unique words in this set of words.

Cluster colors, sized by number of pixels:

cluster	pixels	name	HEX	RGB	HSV	LCH	Lab	tags
	50.92%	116,115,111 quarter masala ΔE=0.3	#73726F	115 114 111	41 4 45	48 2 91	48 0 2	aluminium blast detroit double dove masala quarter silver sonic stack tarmac grey
	49.08%	160,159,156 mountain mist ΔE=1.0	#A29E9A	162 158 154	29 5 63	65 3 73	65 1 2	delta dust imagine kensington mist mountain rakaia star transmission triple viaduct grey

IMAGE CLUSTER PARTITIONS

Pixels of the image assigned to each cluster. The border is the color of the cluster as calculated by the average value of its pixels.

RGB HISTOGRAM

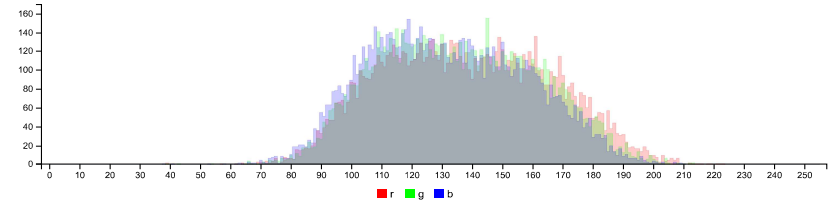

HSV HISTOGRAMS

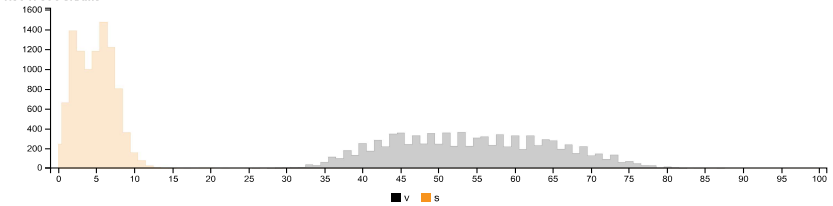

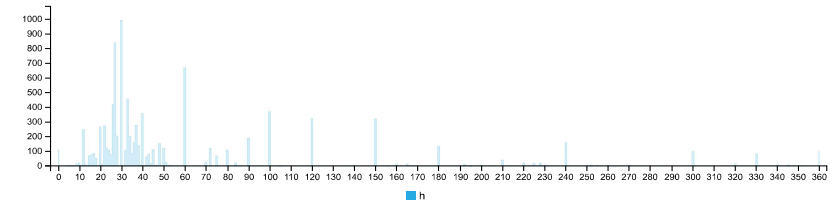

LCH HISTOGRAMS

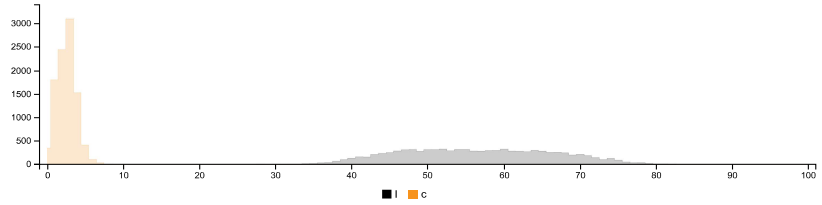

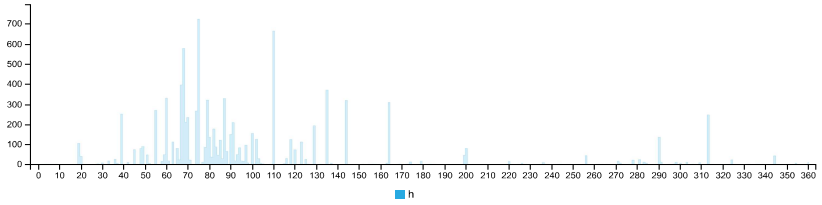

LAB HISTOGRAMS

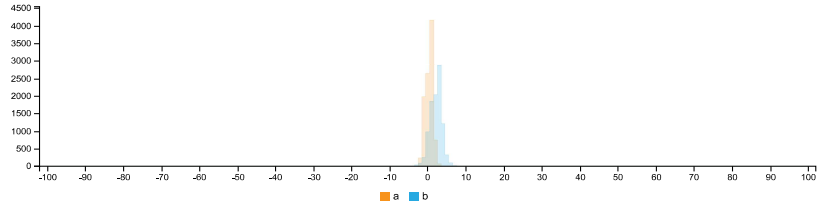

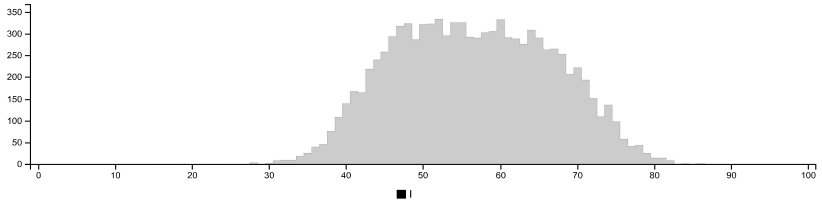

COLOR SPACE AND CHANNEL STATISTICS

	avg	med	min	max
RGB:R	138	137	39	223
RGB:G	135	134	39	213
RGB:B	132	131	38	210
HSV:H	40 1.00	35	0	360
HSV:S	5	5	0	20
HSV:V	54	54	15	87
LCH:L	56	56	16	86
LCH:C	3	3	0	14
LCH:H	84 1.00	82	4	360
LAB:L	56	56	16	86
LAB:A	0	1	-3	4
LAB:B	2	2	-6	14

Detailed report - Top debonded part of Specimen TG10-C-2

IMAGE COLOR SUMMARIZER

RGB, HSV, LCH & Lab image color statistics and clustering—simple and easy

HOME ANALYZE EXAMPLES API DOWNLOAD FAQ NEWS

IMAGE COLOR SUMMARY

THE IMAGE IN WORDS

aluminium atmosphere bombay boulder cloudy dark detroit double dove friar grey light masala medium quarter rakaia silver sonic stonehenge tapa trojan

COLOR CLUSTERS

Colors in the image were clustered into 2 groups (k-means). The average color of the colors for each cluster is shown. The name is the closest named color and its distance is shown using ΔE. The tags are the set of words formed by all named neighbours within ΔE ≤ 5. The list of words above is the set of all unique words in this set of words.

Cluster colors, sized by number of pixels:

cluster	pixels	name	HEX	RGB	HSV	LCH	Lab	tags
	51.88%	168,170,166 atmosphere ΔE=1.8	#ACA8A4	172 168 164	29 5 68	69 3 72	69 1 3	medium light dark atmosphere bombay cloudy double friar quarter rakaia stonehenge grey
	48.12%	120,119,116 detroit ΔE=0.8	#767673	118 118 115	53 2 46	49 1 104	49 0 1	aluminium boulder detroit dove masala quarter silver sonic tapa trojan grey

IMAGE CLUSTER PARTITIONS

Pixels of the image assigned to each cluster. The border is the color of the cluster as calculated by the average value of its pixels.

RGB HISTOGRAM

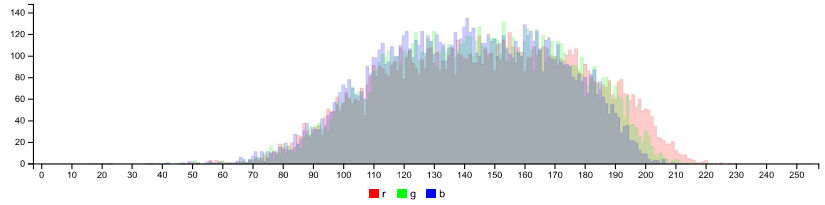

HSV HISTOGRAMS

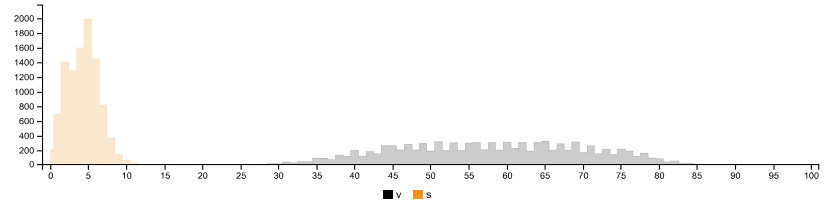

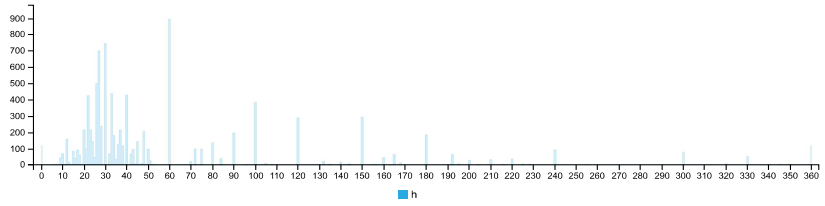

LCH HISTOGRAMS

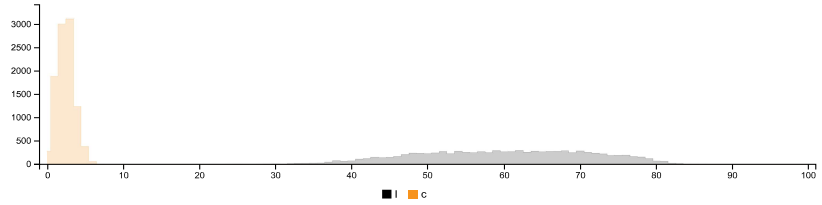

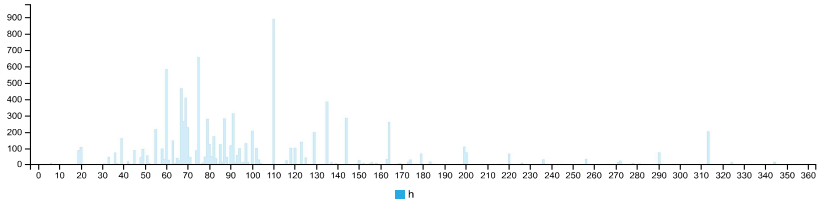

LAB HISTOGRAMS

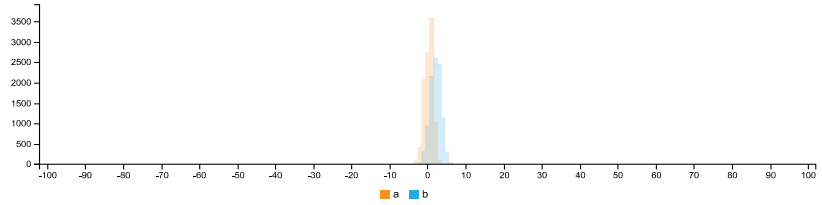

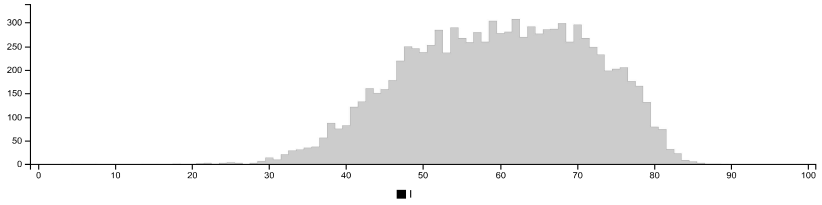

COLOR SPACE AND CHANNEL STATISTICS

	avg	med	min	max
RGB:R	146	147	16	230
RGB:G	144	145	17	221
RGB:B	141	141	18	214
HSV:H	44 1.00	37	0	360
HSV:S	4	4	0	24
HSV:V	58	58	8	90
LCH:L	60	60	5	89
LCH:C	2	2	0	9
LCH:H	87 1.00	85	3	360
LAB:L	60	60	5	89
LAB:A	0	0	-4	4
LAB:B	2	2	-3	9

Summary of Image Analysis for Specimen TG10-C-3

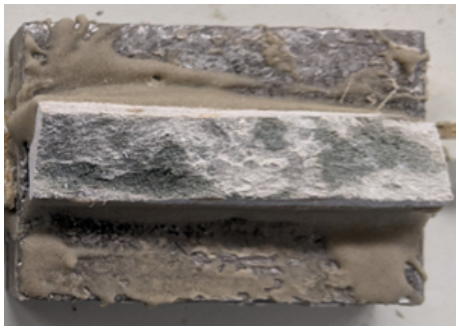

Figure D.55: Bottom debonded part of Specimen TG10-C-3

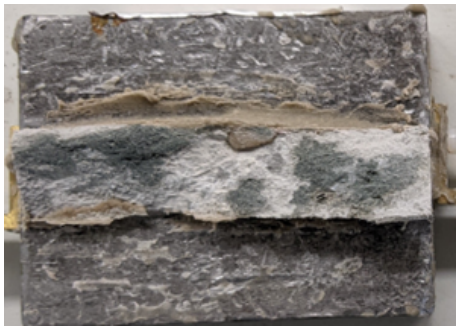

Figure D.56: Top debonded part of Specimen TG10-C-3

Table D.28: Summary of Image analysis result for specimen TG10-C-3

Contact Type	Colour Cluster	Results of Image analysis		Contact (%)		Average Contact (in %)
		Bottom Debonded Layer	Top Debonded Layer	Bottom Debonded Layer	Top Debonded Layer	
						
Poor				53,50%	47,58%	**50,54%**
Good				46,50%	52,42%	**49,46%**

Detailed report - Bottom debonded part of Specimen TG10-C-3

IMAGE COLOR SUMMARIZER

RGB, HSV, LCH & Lab image color statistics and clustering—simple and easy

HOME ANALYZE EXAMPLES API DOWNLOAD FAQ NEWS

IMAGE COLOR SUMMARY

THE IMAGE IN WORDS

atmosphere bombay chalice chicane dark dim dimgray dimgrey double dove flow granite grey light medium rakaia scarpa silver

COLOR CLUSTERS

Colors in the image were clustered into 2 groups (k-means). The average color of the colors for each cluster is shown. The name is the closest named color and its distance is shown using ΔE. The tags are the set of words formed by all named neighbours within ΔE ≤ 5. The list of words above is the set of all unique words in this set of words.

Cluster colors, sized by number of pixels:

cluster	pixels	name	HEX	RGB	HSV	LCH	Lab	tags
	53.50%	169,165,165 double rakaia ΔE=2.0	#AFA9A7	175 169 167	20 4 68	70 2 55	70 1 2	medium light dark atmosphere bombay chalice double rakaia silver grey
	46.50%	107,107,107 grey ΔE=1.0	#6C6A69	108 106 105	32 2 42	45 1 79	45 0 1	chicane dim dimgray dimgrey dove flow granite scarpa grey

IMAGE CLUSTER PARTITIONS

Pixels of the image assigned to each cluster. The border is the color of the cluster as calculated by the average value of its pixels.

RGB HISTOGRAM

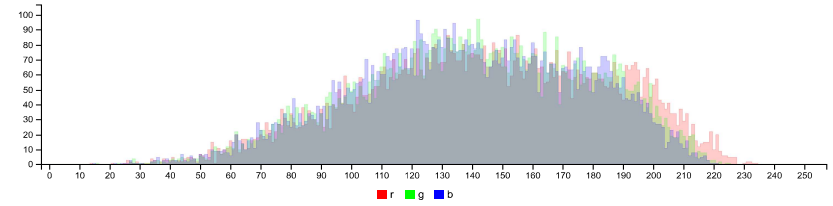

HSV HISTOGRAMS

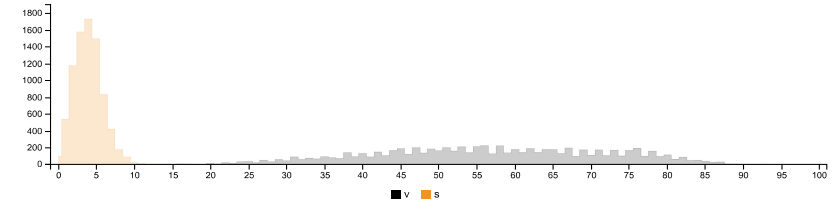

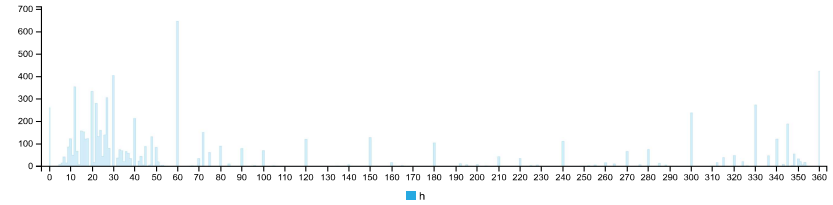

LCH HISTOGRAMS

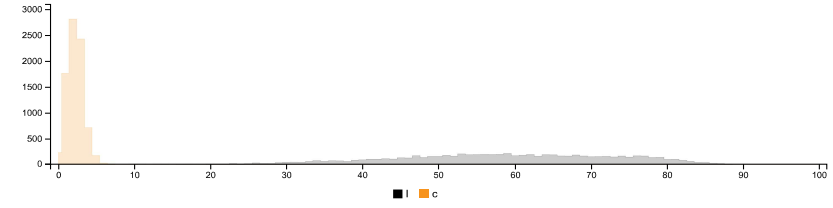

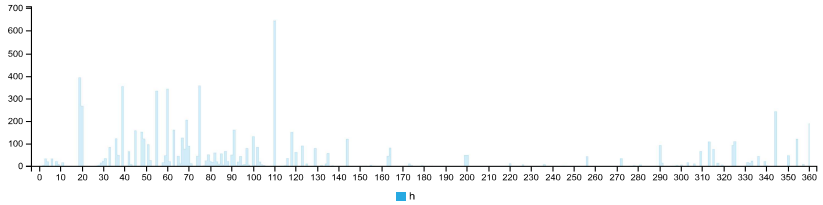

LAB HISTOGRAMS

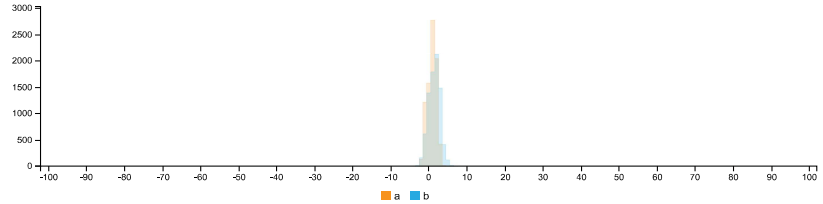

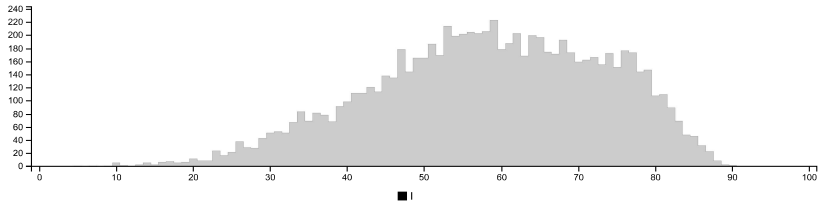

COLOR SPACE AND CHANNEL STATISTICS

	avg	med	min	max
RGB:R	144	144	14	234
RGB:G	140	141	16	225
RGB:B	139	139	15	221
HSV:H	21 1.00	40	0	360
HSV:S	4	4	0	13
HSV:V	56	56	6	92
LCH:L	58	59	5	90
LCH:C	2	2	0	7
LCH:H	56 1.00	78	2	360
LAB:L	58	59	5	90
LAB:A	1	1	-3	6
LAB:B	1	2	-4	7

Detailed report - Top debonded part of Specimen TG10-C-3

IMAGE COLOR SUMMARIZER

RGB, HSV, LCH & Lab image color statistics and clustering—simple and easy

HOME ANALYZE EXAMPLES API DOWNLOAD FAQ NEWS

IMAGE COLOR SUMMARY

THE IMAGE IN WORDS

atmosphere bombay chicane cloudy dark dim double dust granite grey ironside light medium quarter rakaia stonehenge storm trojan

COLOR CLUSTERS

Colors in the image were clustered into 2 groups (k-means). The average color of the colors for each cluster is shown. The name is the closest named color and its distance is shown using ΔE. The tags are the set of words formed by all named neighbours within ΔE ≤ 5. The list of words above is the set of all unique words in this set of words.

Cluster colors, sized by number of pixels:

cluster	pixels	name	HEX	RGB	HSV	LCH	Lab	tags
	52.42%	100,100,99 storm dust ΔE=0.5	#656462	101 100 98	43 3 39	42 1 95	42 0 1	chicane dim double dust granite ironside storm trojan grey
	47.58%	169,165,165 double rakaia ΔE=1.5	#ACA8A5	172 168 165	24 4 68	69 2 63	69 1 2	medium light dark atmosphere bombay cloudy double quarter rakaia stonehenge grey

IMAGE CLUSTER PARTITIONS

Pixels of the image assigned to each cluster. The border is the color of the cluster as calculated by the average value of its pixels.

RGB HISTOGRAM

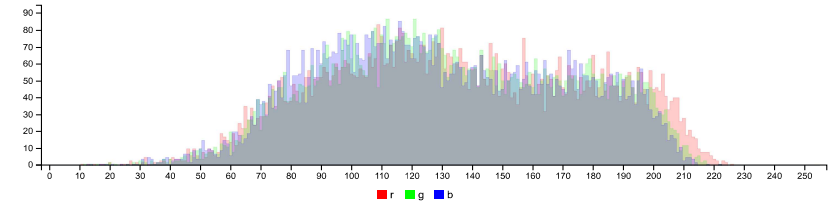

HSV HISTOGRAMS

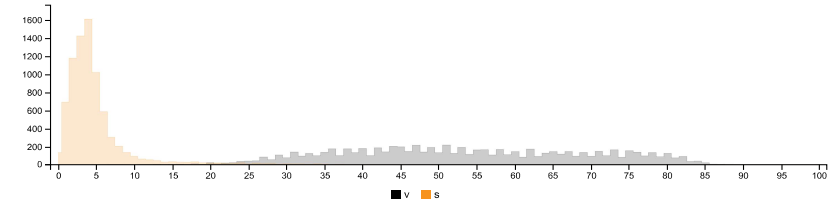

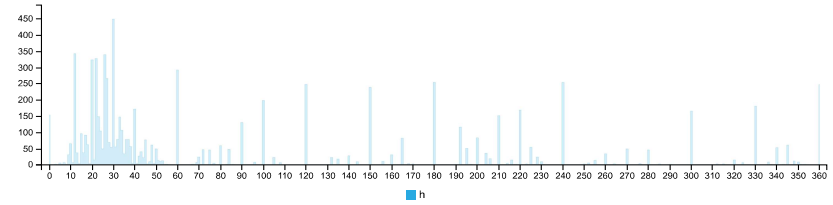

LCH HISTOGRAMS

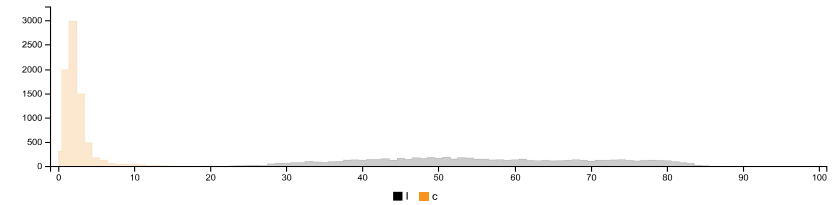

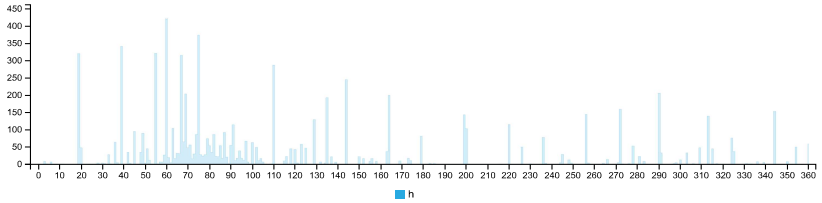

LAB HISTOGRAMS

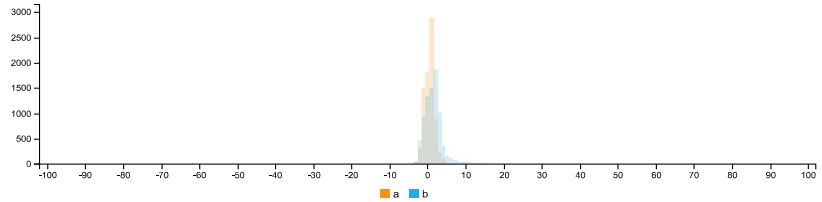

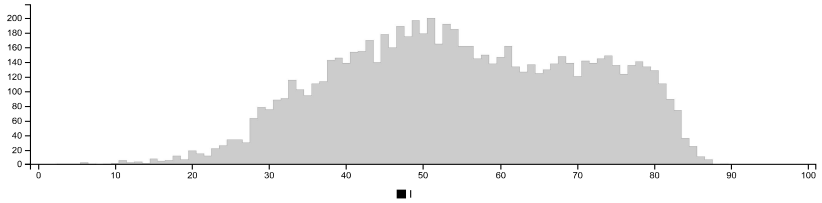

COLOR SPACE AND CHANNEL STATISTICS

	avg	med	min	max
RGB:R	135	133	11	226
RGB:G	133	129	12	222
RGB:B	130	126	13	222
HSV:H	34 0.00	45	0	360
HSV:S	5	4	0	41
HSV:V	53	52	5	89
LCH:L	55	54	3	89
LCH:C	3	2	0	17
LCH:H	73 0.00	90	0	360
LAB:L	55	54	3	89
LAB:A	0	1	-4	7
LAB:B	2	1	-5	17

Summary of Image Analysis for Specimen TG10-C-4

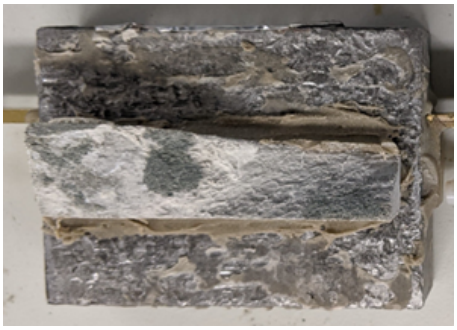

Figure D.57: Bottom debonded part of Specimen TG10-C-4

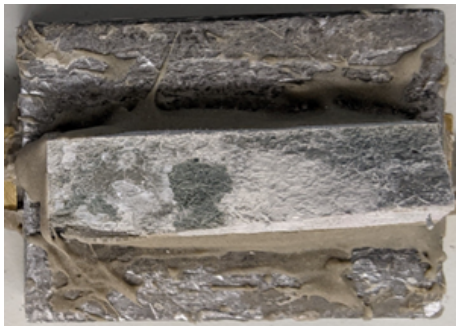

Figure D.58: Top debonded part of Specimen TG10-C-4

Table D.29: Summary of Image analysis result for specimen TG10-C-4

Contact Type	Colour Cluster	Results of Image analysis		Contact (%)		Average Contact (in %)
		Bottom Debonded Layer	Top Debonded Layer	Bottom Debonded Layer	Top Debonded Layer	
						
Poor				53,93%	54,22%	**54,08%**
Good				46,07%	45,78%	**45,93%**

Detailed report - Bottom debonded part of Specimen TG10-C-4

IMAGE COLOR SUMMARIZER

RGB, HSV, LCH & Lab image color statistics and clustering—simple and easy

HOME ANALYZE EXAMPLES API DOWNLOAD FAQ NEWS

IMAGE COLOR SUMMARY

THE IMAGE IN WORDS

chicane cloudy dim dimgray dimgrey double dust granite grey ironside mist mountain nobel quarter rakaia star stonehenge transmission triple trojan

COLOR CLUSTERS

Colors in the image were clustered into 2 groups (k-means). The average color of the colors for each cluster is shown. The name is the closest named color and its distance is shown using ΔE. The tags are the set of words formed by all named neighbours within ΔE ≤ 5. The list of words above is the set of all unique words in this set of words.

Cluster colors, sized by number of pixels:

cluster	pixels	name	HEX	RGB	HSV	LCH	Lab	tags
	53.93%	169,165,165 double rakaia ΔE=1.9	#A6A19E	166 161 158	27 5 65	67 3 70	67 1 2	cloudy double dust mist mountain nobel quarter rakaia star stonehenge transmission triple grey
	46.07%	104,103,101 chicane ΔE=0.9	#686865	104 104 101	43 3 41	44 1 94	44 0 1	chicane dim dimgray dimgrey double granite ironside trojan grey

IMAGE CLUSTER PARTITIONS

Pixels of the image assigned to each cluster. The border is the color of the cluster as calculated by the average value of its pixels.

RGB HISTOGRAM

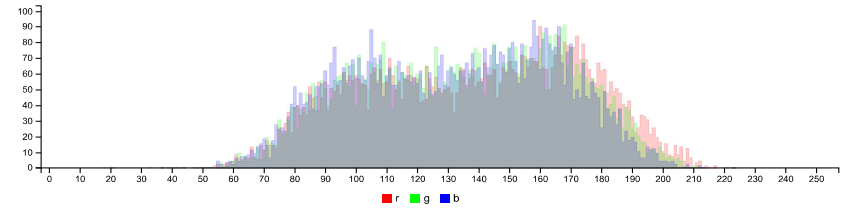

HSV HISTOGRAMS

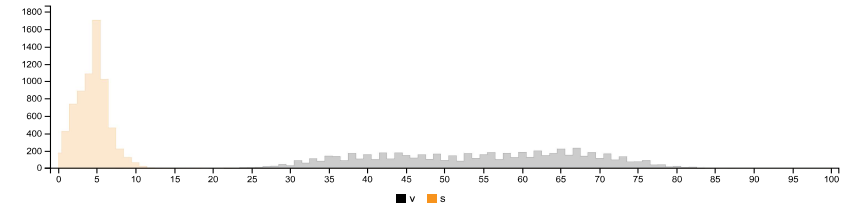

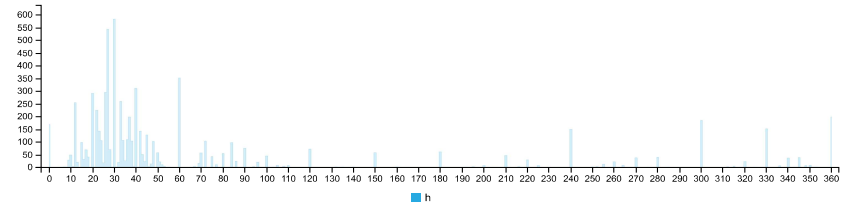

LCH HISTOGRAMS

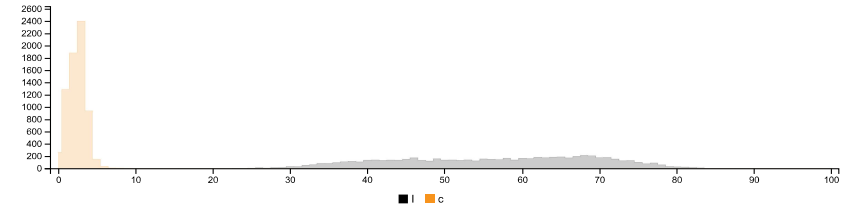

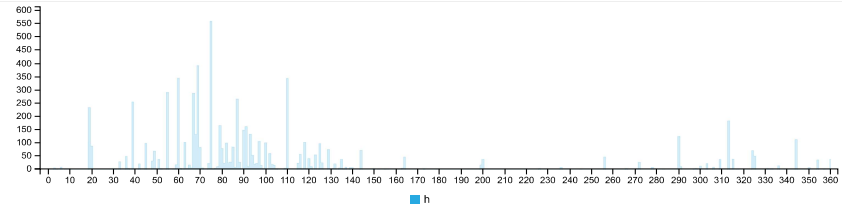

LAB HISTOGRAMS

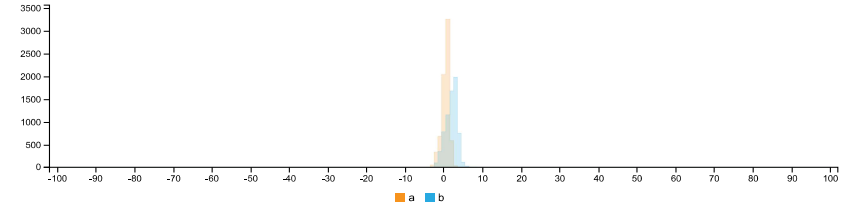

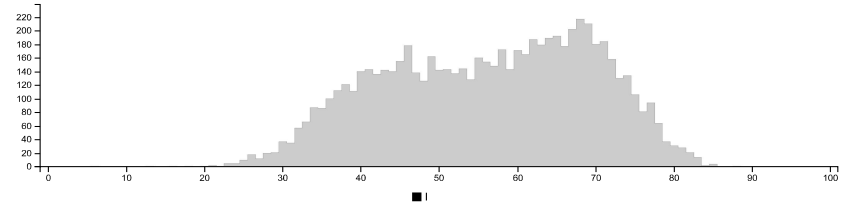

COLOR SPACE AND CHANNEL STATISTICS

	avg	med	min	max
RGB:R	138	140	20	223
RGB:G	135	137	18	221
RGB:B	132	134	21	223
HSV:H	29 1.00	36	0	360
HSV:S	4	5	0	22
HSV:V	54	55	8	87
LCH:L	56	57	6	88
LCH:C	2	3	0	9
LCH:H	70 1.00	81	0	360
LAB:L	56	57	6	88
LAB:A	0	1	-4	4
LAB:B	2	2	-3	9

IMAGE COLOR SUMMARIZER

RGB, HSV, LCH & Lab image color statistics and clustering—simple and easy

HOME ANALYZE EXAMPLES API DOWNLOAD FAQ NEWS

IMAGE COLOR SUMMARY

THE IMAGE IN WORDS

atmosphere blast bombay chalice chicane cliff double dove face fantail grey half mist mountain nobel quarter silver stack tarmac taupe traffic

COLOR CLUSTERS

Colors in the image were clustered into 2 groups (k-means). The average color of the colors for each cluster is shown. The name is the closest named color and its distance is shown using ΔE. The tags are the set of words formed by all named neighbours within ΔE ≤ 5. The list of words above is the set of all unique words in this set of words.

Cluster colors, sized by number of pixels:

cluster	pixels	name	HEX	RGB	HSV	LCH	Lab	tags
	54.22%	174,174,173 bombay ΔE=2.0	#B2ADA9	178 173 169	27 5 70	71 3 69	71 1 3	atmosphere bombay chalice fantail half mist mountain nobel quarter silver taupe grey
	45.78%	108,109,104 traffic ΔE=1.5	#6D6C69	109 108 105	38 3 43	45 1 89	45 0 1	blast chicane cliff double dove face stack tarmac traffic grey

IMAGE CLUSTER PARTITIONS

Pixels of the image assigned to each cluster. The border is the color of the cluster as calculated by the average value of its pixels.

RGB HISTOGRAM

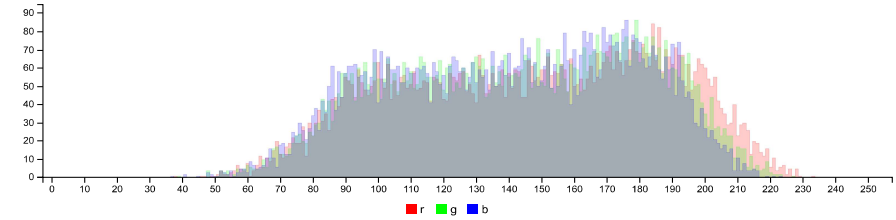

HSV HISTOGRAMS

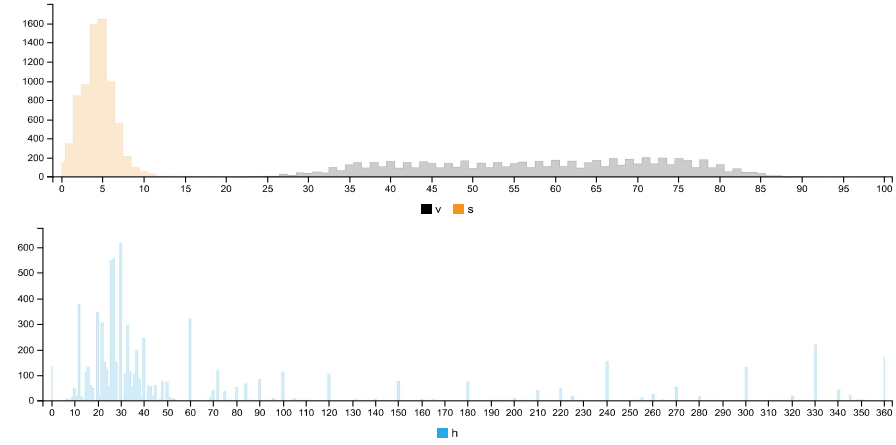

LCH HISTOGRAMS

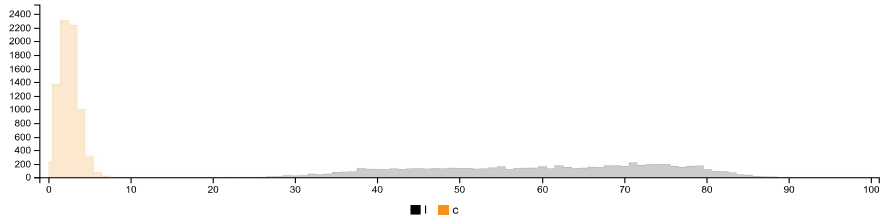

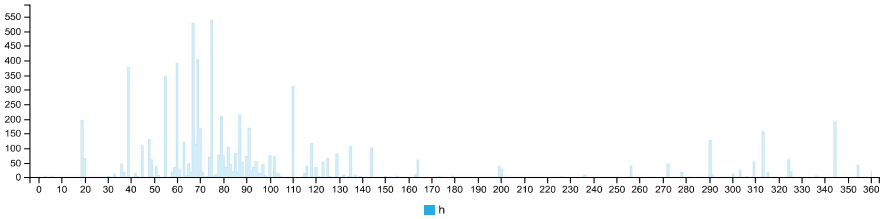

LAB HISTOGRAMS

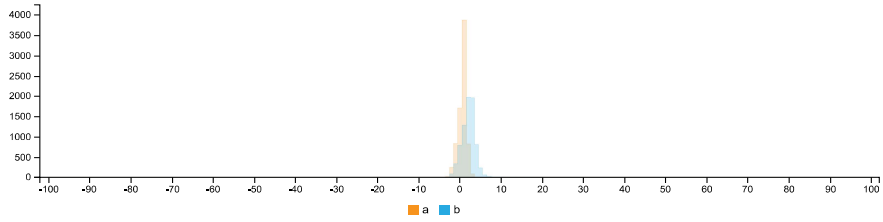

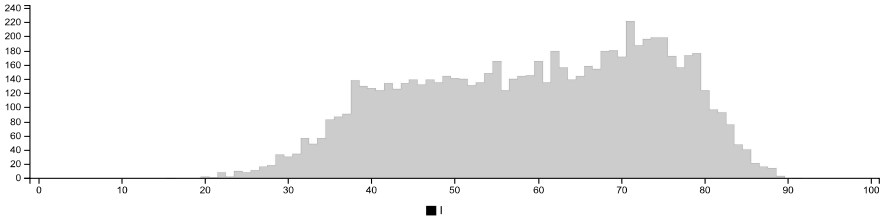

COLOR SPACE AND CHANNEL STATISTICS

	avg	med	min	max
RGB:R	147	149	38	233
RGB:G	143	146	39	227
RGB:B	140	142	37	223
HSV:H	28 1.00	30	0	360
HSV:S	5	4	0	36
HSV:V	58	58.5	16	91
LCH:L	59	61	16	91
LCH:C	3	2	0	17
LCH:H	68 1.00	75	3	360
LAB:L	59	61	16	91
LAB:A	1	1	-3	4
LAB:B	2	2	-3	17

Summary of Image Analysis for Specimen TG20-C-1

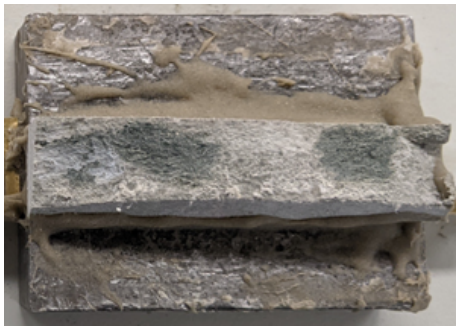

Figure D.59: Bottom debonded part of Specimen TG20-C-1

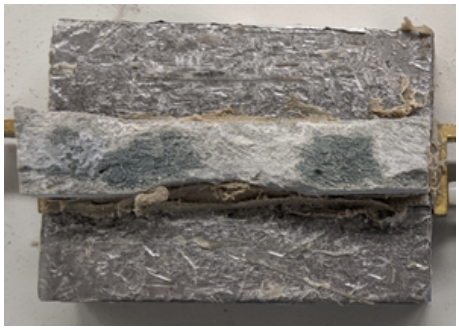

Figure D.60: Top debonded part of Specimen TG20-C-1

Table D.30: Summary of Image analysis result for specimen TG20-C-1

Contact Type	Colour Cluster	Results of Image analysis		Contact (%)		Average Contact (in %)
		Bottom Debonded Layer	Top Debonded Layer	Bottom Debonded Layer	Top Debonded Layer	
						
Poor				58,24%	55,93%	**57,09%**
Good				41,76%	44,07%	**42,92%**

Detailed report - Bottom debonded part of Specimen TG20-C-1

IMAGE COLOR SUMMARIZER

RGB, HSV, LCH & Lab image color statistics and clustering—simple and easy

HOME ANALYZE EXAMPLES API DOWNLOAD FAQ NEWS

IMAGE COLOR SUMMARY

THE IMAGE IN WORDS

blast cliff cloudy dawn delta double dove face foggy friar gauntlet grey lattitude masala quarter rakaia stack stonehenge swordfish tapa tarmac traffic viaduct

COLOR CLUSTERS

Colors in the image were clustered into 2 groups (k-means). The average color of the colors for each cluster is shown. The name is the closest named color and its distance is shown using ΔE. The tags are the set of words formed by all named neighbours within ΔE ≤ 5. The list of words above is the set of all unique words in this set of words.

Cluster colors, sized by number of pixels:

cluster	pixels	name	HEX	RGB	HSV	LCH	Lab	tags
	58.24%	172,165,159 cloudy ΔE=0.9	#A8A39D	168 163 157	31 6 66	67 4 77	67 1 4	cloudy dawn delta double foggy friar quarter rakaia stonehenge swordfish tapa viaduct grey
	41.76%	108,109,104 traffic ΔE=0.9	#6E6E6A	110 110 106	58 4 43	46 2 108	46 -1 2	blast cliff double dove face gauntlet lattitude masala quarter stack tarmac traffic grey

IMAGE CLUSTER PARTITIONS

Pixels of the image assigned to each cluster. The border is the color of the cluster as calculated by the average value of its pixels.

RGB HISTOGRAM

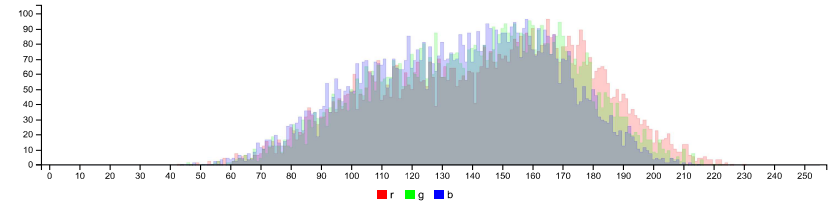

HSV HISTOGRAMS

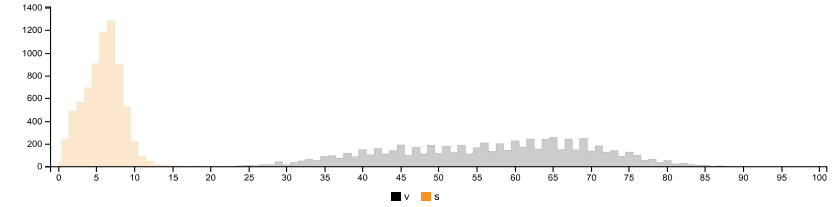

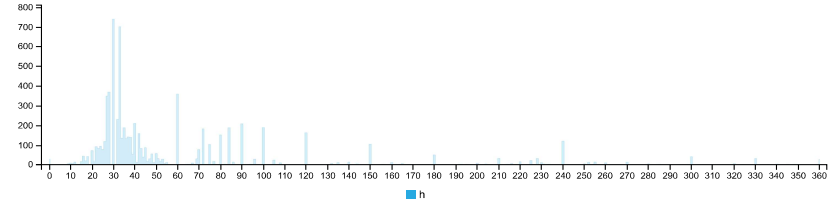

LCH HISTOGRAMS

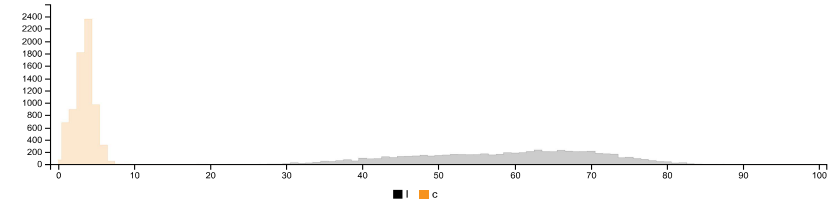

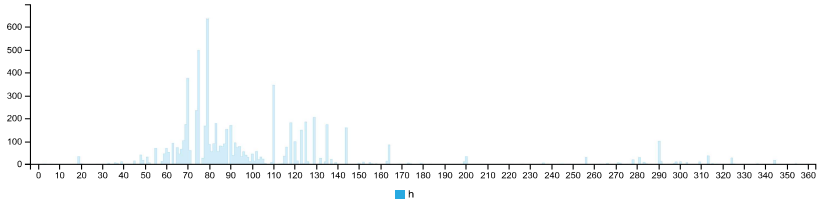

LAB HISTOGRAMS

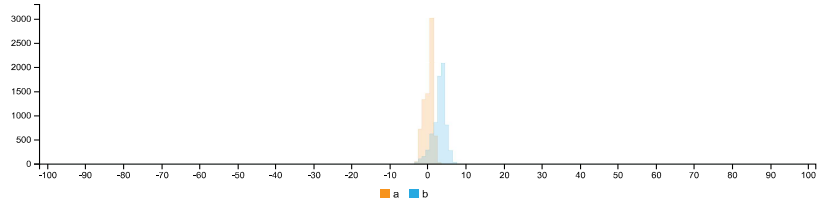

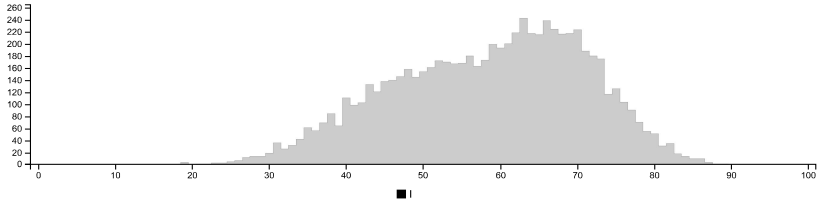

COLOR SPACE AND CHANNEL STATISTICS

	avg	med	min	max
RGB:R	144	148	43	230
RGB:G	141	144	44	222
RGB:B	136	138	44	215
HSV:H	45 1.00	37	0	360
HSV:S	6	6	0	18
HSV:V	57	58	18	90
LCH:L	58	60	19	89
LCH:C	3	4	0	10
LCH:H	89 1.00	85	3	360
LAB:L	58	60	19	89
LAB:A	0	1	-5	4
LAB:B	3	3	-4	10

Detailed report - Top debonded part of Specimen TG20-C-1

IMAGE COLOR SUMMARIZER

RGB, HSV, LCH & Lab image color statistics and clustering—simple and easy

HOME ANALYZE EXAMPLES API DOWNLOAD FAQ NEWS

IMAGE COLOR SUMMARY

THE IMAGE IN WORDS

atmosphere chicane cloudy dawn delta dim dimgray dimgrey double foggy friar granite grey ironside quarter rakaia stonehenge swordfish tapa trojan

COLOR CLUSTERS

Colors in the image were clustered into 2 groups (k-means). The average color of the colors for each cluster is shown. The name is the closest named color and its distance is shown using ΔE. The tags are the set of words formed by all named neighbours within ΔE ≤ 5. The list of words above is the set of all unique words in this set of words.

Cluster colors, sized by number of pixels:

cluster	pixels	name	HEX	RGB	HSV	LCH	Lab	tags
	55.93%	172,165,159 cloudy ΔE=1.4	#A7A49F	167 164 159	35 5 66	67 3 82	67 0 3	atmosphere cloudy dawn delta double foggy friar quarter rakaia stonehenge swordfish tapa grey
	44.07%	101,102,100 double trojan ΔE=0.8	#666866	102 104 102	119 2 41	44 2 144	44 -1 1	chicane dim dimgray dimgrey double granite ironside trojan grey

IMAGE CLUSTER PARTITIONS

Pixels of the image assigned to each cluster. The border is the color of the cluster as calculated by the average value of its pixels.

RGB HISTOGRAM

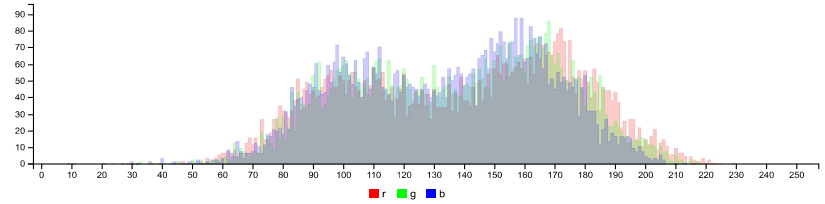

HSV HISTOGRAMS

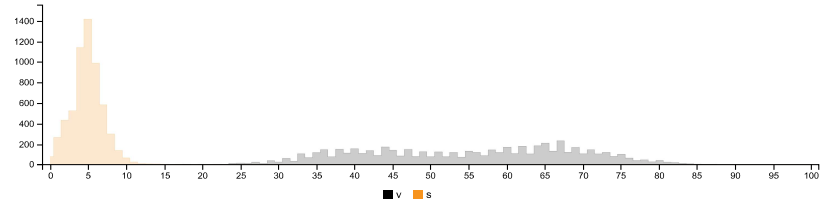

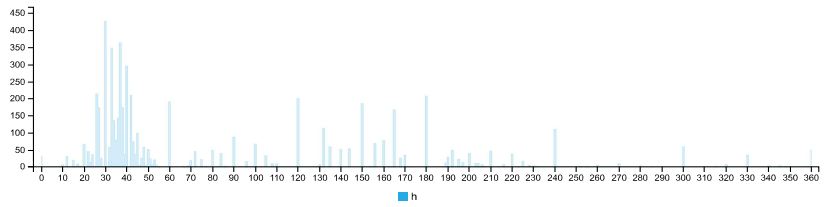

LCH HISTOGRAMS

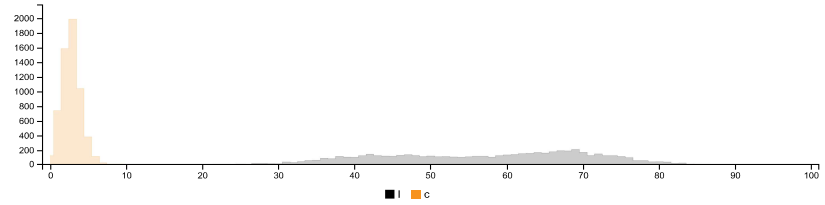

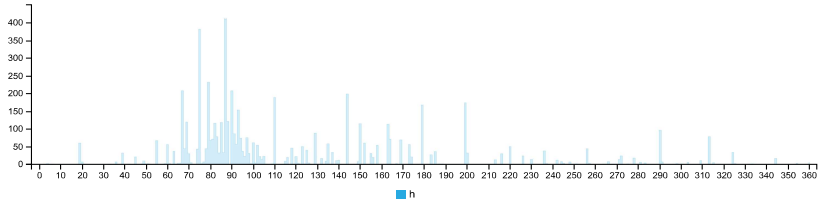

LAB HISTOGRAMS

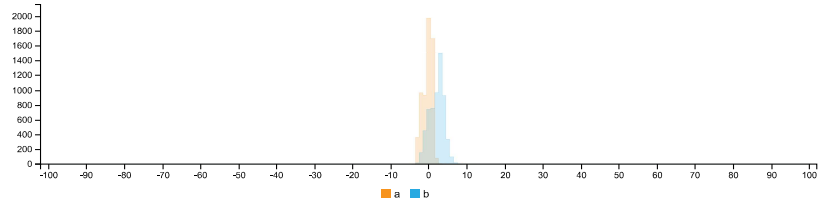

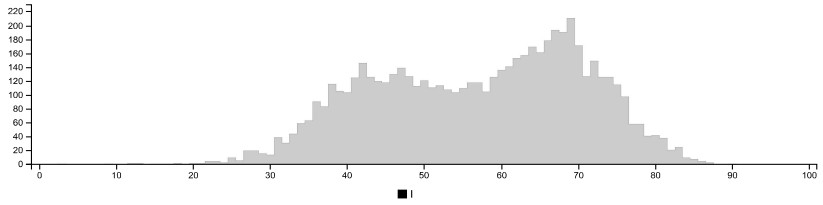

COLOR SPACE AND CHANNEL STATISTICS

	avg	med	min	max
RGB:R	138	143	9	229
RGB:G	137	141	10	225
RGB:B	134	137	11	216
HSV:H	59 1.00	43	0	360
HSV:S	5	5	0	34
HSV:V	55	56	4	90
LCH:L	57	59	3	90
LCH:C	3	3	0	12
LCH:H	104 1.00	93	3	360
LAB:L	57	59	3	90
LAB:A	-0	0	-4	4
LAB:B	2	2	-4	12

Summary of Image Analysis for Specimen TG20-C-2

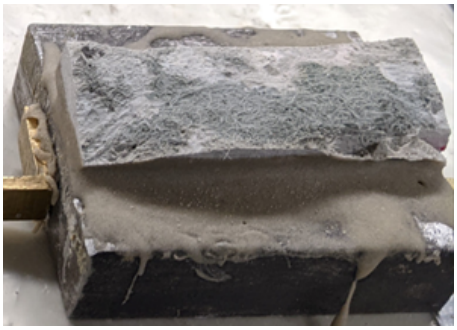

Figure D.61: Bottom debonded part of Specimen TG20-C-2

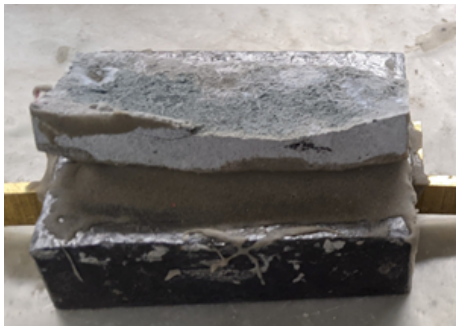

Figure D.62: Top debonded part of Specimen TG20-C-2

Table D.31: Summary of Image analysis result for specimen TG20-C-2

Contact Type	Colour Cluster	Results of Image analysis		Contact (%)		Average Contact (in %)
		Bottom Debonded Layer	Top Debonded Layer	Bottom Debonded Layer	Top Debonded Layer	
			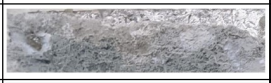			
Poor				50,71%	48,07%	**49,39%**
Good				49,29%	51,93%	**50,61%**

Detailed report - Bottom debonded part of Specimen TG20-C-2

IMAGE COLOR SUMMARIZER

RGB, HSV, LCH & Lab image color statistics and clustering—simple and easy

HOME ANALYZE EXAMPLES API DOWNLOAD FAQ NEWS

IMAGE COLOR SUMMARY

THE IMAGE IN WORDS

ajay bombay chalice eighth grey lining meridian metro nobel ricochet sidewinder silver sword trolley web

COLOR CLUSTERS

Colors in the image were clustered into 2 groups (k-means). The average color of the colors for each cluster is shown. The name is the closest named color and its distance is shown using ΔE. The tags are the set of words formed by all named neighbours within ΔE ≤ 5. The list of words above is the set of all unique words in this set of words.

Cluster colors, sized by number of pixels:

cluster	pixels	name	HEX	RGB	HSV	LCH	Lab	tags
	50.71%	173,173,173 grey ΔE=1.0	#B0AEAF	176 174 175	327 1 69	71 1 341	71 1 0	ajay bombay chalice eighth metro nobel sidewinder silver grey
	49.29%	128,130,132 sword ΔE=0.6	#808081	128 128 129	240 1 50	53 1 291	53 0 -1	lining meridian ricochet silver sword trolley web grey

IMAGE CLUSTER PARTITIONS

Pixels of the image assigned to each cluster. The border is the color of the cluster as calculated by the average value of its pixels.

RGB HISTOGRAM

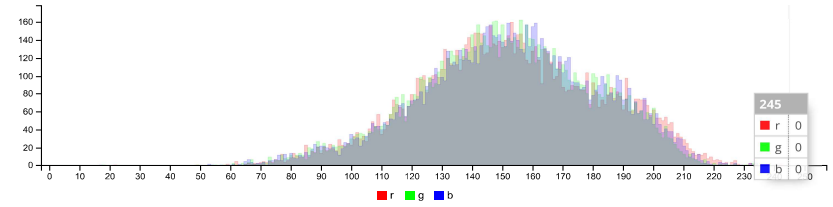

HSV HISTOGRAMS

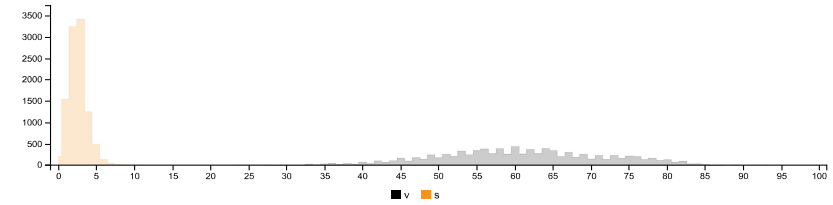

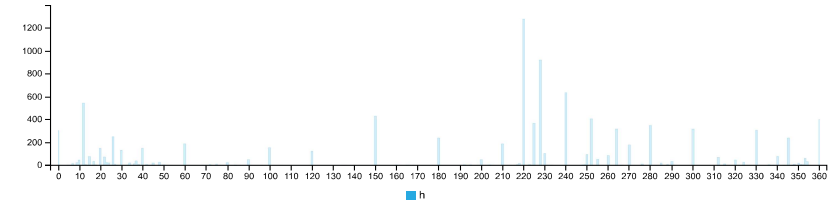

LCH HISTOGRAMS

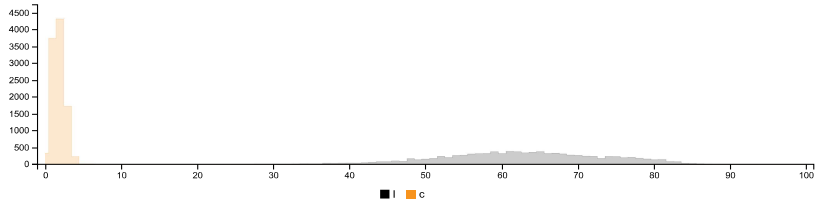

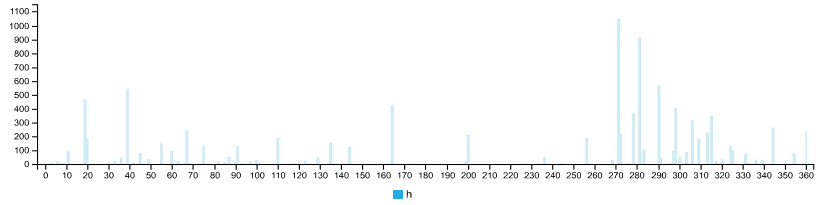

LAB HISTOGRAMS

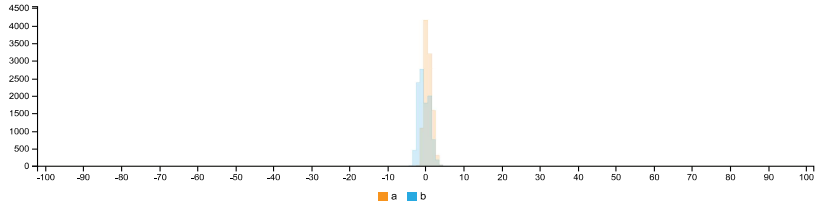

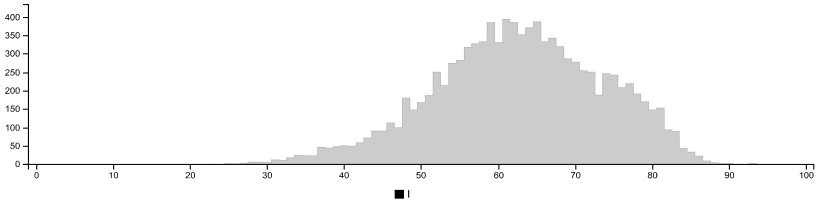

COLOR SPACE AND CHANNEL STATISTICS

	avg	med	min	max
RGB:R	153	152	22	242
RGB:G	151	152	18	234
RGB:B	153	153	17	234
HSV:H	274 0.00	225	0	360
HSV:S	3	3	0	23
HSV:V	61	60	9	95
LCH:L	63	63	6	93
LCH:C	2	2	0	6
LCH:H	316 0.00	271	2	360
LAB:L	63	63	6	93
LAB:A	1	0	-3	5
LAB:B	-0	-1	-5	6

Detailed report - Top debonded part of Specimen TG20-C-2

IMAGE COLOR SUMMARIZER

RGB, HSV, LCH & Lab image color statistics and clustering—simple and easy

HOME ANALYZE EXAMPLES API DOWNLOAD FAQ NEWS

IMAGE COLOR SUMMARY

THE IMAGE IN WORDS

aluminium chateau french gauntlet grey greywacke half lavender misty oslo rakaia ricochet snow surrender

COLOR CLUSTERS

Colors in the image were clustered into 2 groups (k-means). The average color of the colors for each cluster is shown. The name is the closest named color and its distance is shown using ΔE. The tags are the set of words formed by all named neighbours within ΔE ≤ 5. The list of words above is the set of all unique words in this set of words.

Cluster colors, sized by number of pixels:

cluster	pixels	name	HEX	RGB	HSV	LCH	Lab	tags
	51.93%	138,138,138 grey ΔE=1.8	#88898C	136 137 140	222 3 55	57 2 274	57 0 -2	aluminium gauntlet half oslo ricochet snow grey
	48.07%	182,181,185 misty lavender ΔE=0.6	#B8B7BB	184 183 187	260 2 73	74 2 303	74 1 -2	misty chateau french greywacke half rakaia surrender grey lavender

IMAGE CLUSTER PARTITIONS

Pixels of the image assigned to each cluster. The border is the color of the cluster as calculated by the average value of its pixels.

RGB HISTOGRAM

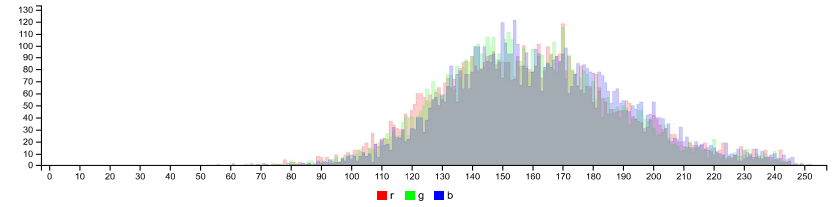

HSV HISTOGRAMS

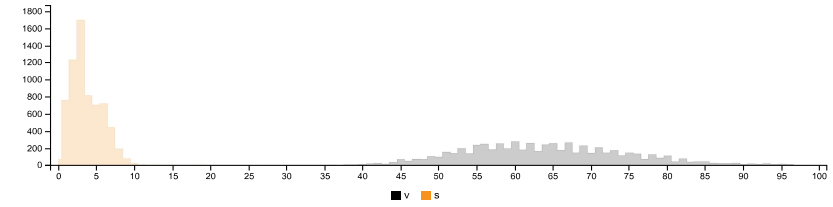

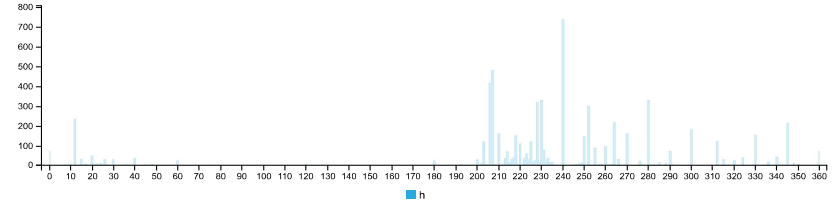

LCH HISTOGRAMS

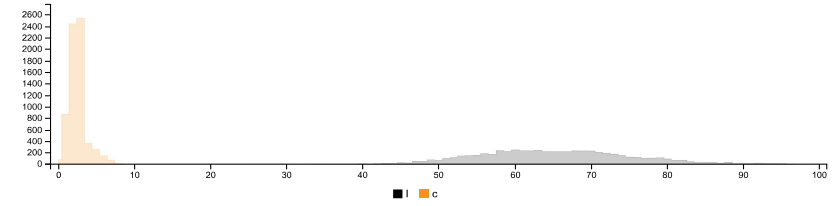

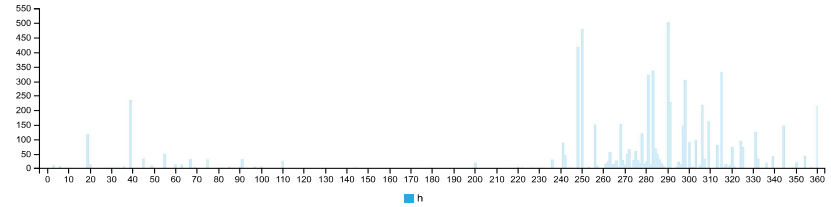

LAB HISTOGRAMS

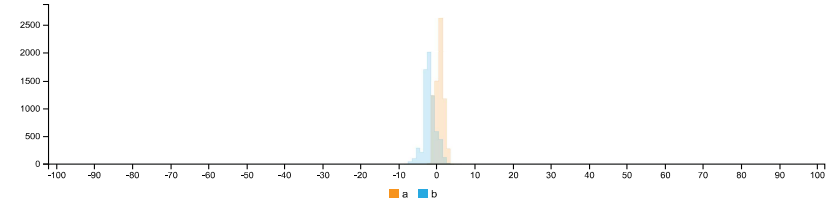

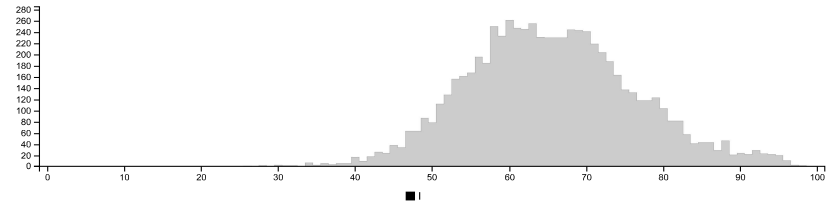

COLOR SPACE AND CHANNEL STATISTICS

	avg	med	min	max
RGB:R	159	158	56	251
RGB:G	159	157	61	249
RGB:B	163	161	69	252
HSV:H	251 1.00	231	0	360
HSV:S	4	3	0	19
HSV:V	64	64	27	99
LCH:L	65	65	26	98
LCH:C	3	3	0	9
LCH:H	296 1.00	283	3	360
LAB:L	65	65	26	98
LAB:A	1	1	-2	5
LAB:B	-2	-2	-9	6

Summary of Image Analysis for Specimen TG20-C-3

Figure D.63: Bottom debonded part of Specimen TG20-C-3

Figure D.64: Top debonded part of Specimen TG20-C-3

Table D.32: Summary of Image analysis result for specimen TG20-C-3

Contact Type	Colour Cluster	Results of Image analysis		Contact (%)		Average Contact (in %)
		Bottom Debonded Layer	Top Debonded Layer	Bottom Debonded Layer	Top Debonded Layer	
						
Poor				52,04%	50,06%	**51,05%**
Good				47,96%	49,90%	**48,93%**

Detailed report - Bottom debonded part of Specimen TG20-C-3

IMAGE COLOR SUMMARIZER

RGB, HSV, LCH & Lab image color statistics and clustering—simple and easy

HOME ANALYZE EXAMPLES API DOWNLOAD FAQ NEWS

IMAGE COLOR SUMMARY

THE IMAGE IN WORDS

alley chicago cloudy dawn delta double dust grey ironside kensington mist mountain quarter rakaia star stonehenge storm tinpan transmission triple trojan viaduct

COLOR CLUSTERS

Colors in the image were clustered into 2 groups (k-means). The average color of the colors for each cluster is shown. The name is the closest named color and its distance is shown using ΔE. The tags are the set of words formed by all named neighbours within ΔE ≤ 5. The list of words above is the set of all unique words in this set of words.

Cluster colors, sized by number of pixels:

cluster	pixels	name	HEX	RGB	HSV	LCH	Lab	tags
	52.04%	160,159,156 mountain mist ΔE=1.4	#A39F9A	163 159 154	31 6 64	66 3 77	66 1 3	cloudy dawn delta dust kensington mist mountain quarter rakaia star stonehenge transmission triple viaduct grey
	47.96%	100,100,99 storm dust ΔE=1.3	#61605E	97 96 94	44 3 38	41 1 95	41 0 1	alley chicago double dust ironside storm tinpan trojan grey

IMAGE CLUSTER PARTITIONS

Pixels of the image assigned to each cluster. The border is the color of the cluster as calculated by the average value of its pixels.

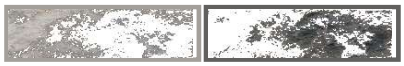

RGB HISTOGRAM

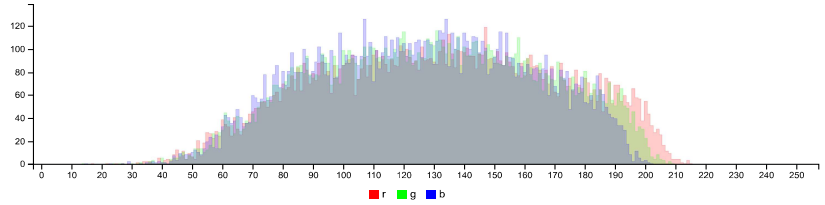

HSV HISTOGRAMS

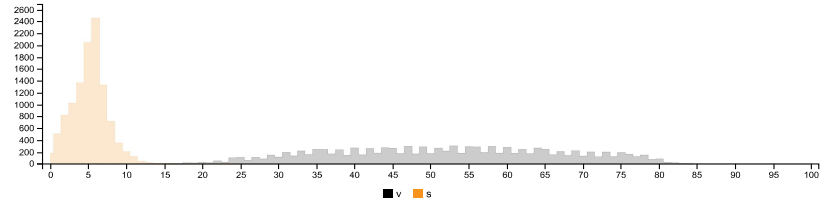

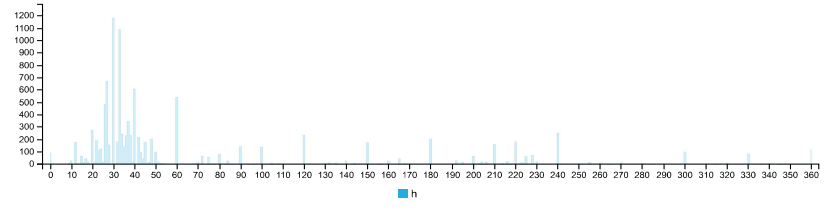

LCH HISTOGRAMS

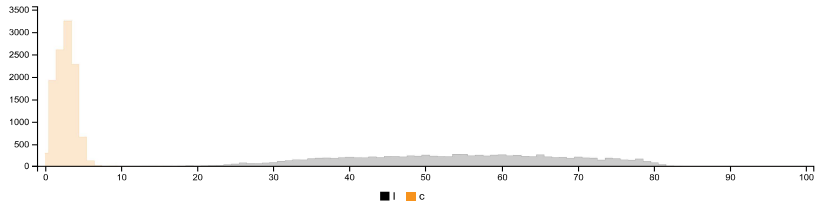

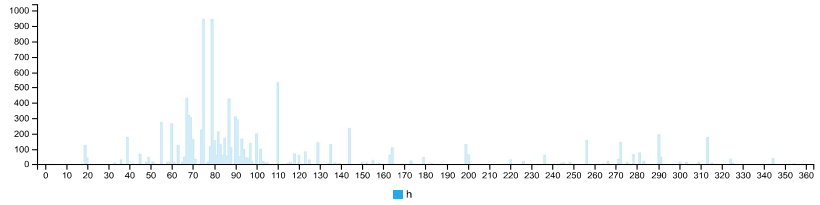

LAB HISTOGRAMS

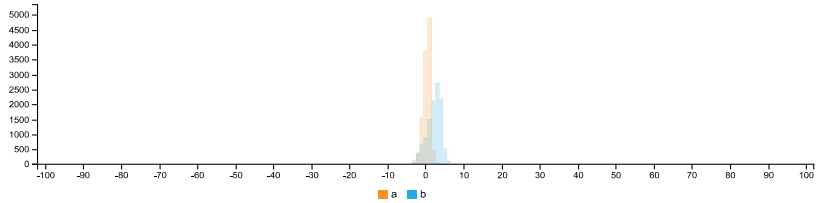

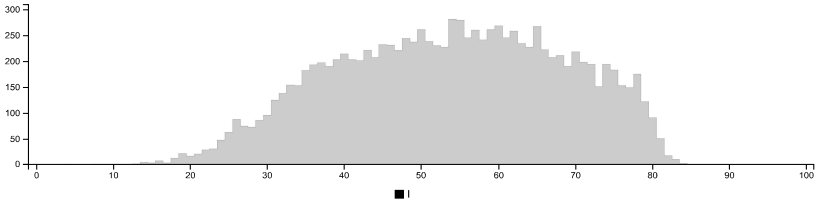

COLOR SPACE AND CHANNEL STATISTICS

	avg	med	min	max
RGB:R	131	132	17	215
RGB:G	129	129	14	209
RGB:B	125	126	15	202
HSV:H	38 1.00	36	0	360
HSV:S	5	5	0	25
HSV:V	52	52	7	84
LCH:L	54	54	4	84
LCH:C	3	3	0	16
LCH:H	83 1.00	85	4	360
LAB:L	54	54	4	84
LAB:A	0	0	-4	5
LAB:B	2	2	-5	15

Detailed report - Top debonded part of Specimen TG20-C-3

IMAGE COLOR SUMMARIZER

RGB, HSV, LCH & Lab image color statistics and clustering—simple and easy

HOME ANALYZE EXAMPLES API DOWNLOAD FAQ NEWS

IMAGE COLOR SUMMARY

THE IMAGE IN WORDS

chicane cloudy dawn delta dim dimgray dimgrey double dust friar granite grey ironside mist mountain quarter rakaia star stonehenge storm transmission trojan viaduct

COLOR CLUSTERS

Colors in the image were clustered into 2 groups (k-means). The average color of the colors for each cluster is shown. The name is the closest named color and its distance is shown using ΔE. The tags are the set of words formed by all named neighbours within ΔE ≤ 5. The list of words above is the set of all unique words in this set of words.

Cluster colors, sized by number of pixels:

cluster	pixels	name	HEX	RGB	HSV	LCH	Lab	tags
	50.06%	164,164,157 delta ΔE=1.9	#A5A19C	165 161 156	29 6 65	66 3 74	66 1 3	cloudy dawn delta double dust friar mist mountain quarter rakaia star stonehenge transmission viaduct grey
	49.94%	103,102,98 ironside grey ΔE=0.8	#666563	102 101 99	33 3 40	43 1 81	43 0 1	chicane dim dimgray dimgrey double dust granite ironside storm trojan grey

IMAGE CLUSTER PARTITIONS

Pixels of the image assigned to each cluster. The border is the color of the cluster as calculated by the average value of its pixels.

RGB HISTOGRAM

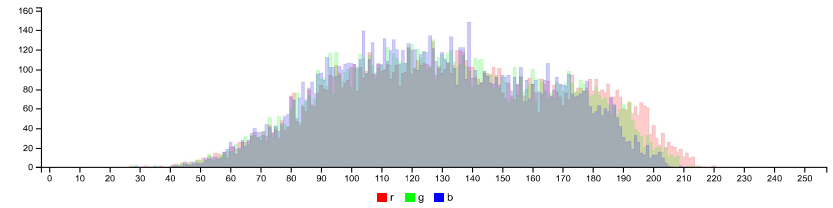

HSV HISTOGRAMS

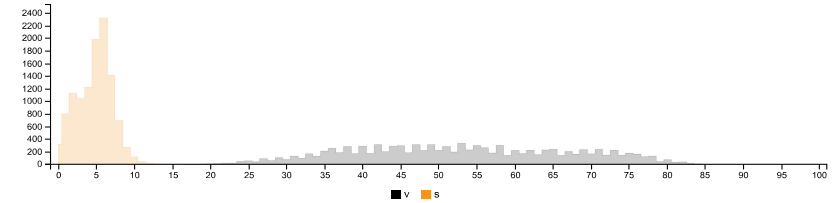

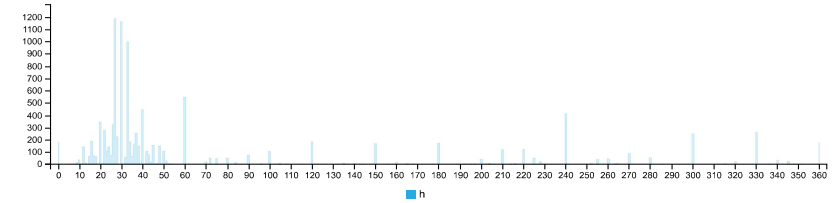

LCH HISTOGRAMS

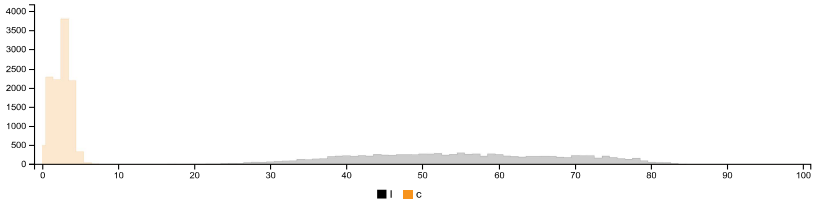

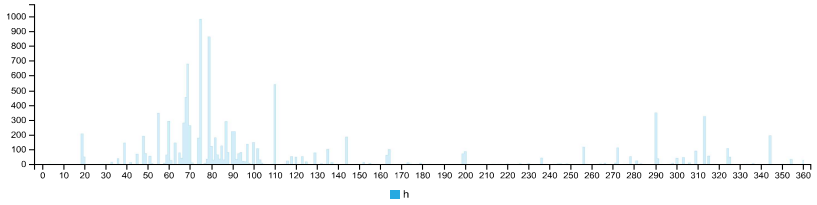

LAB HISTOGRAMS

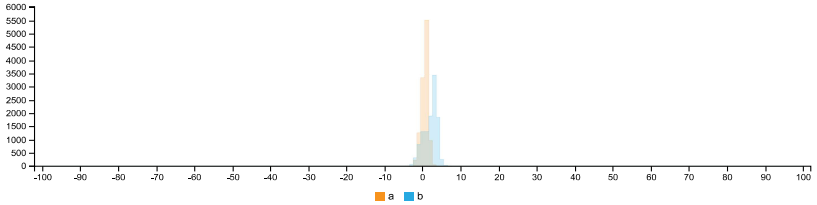

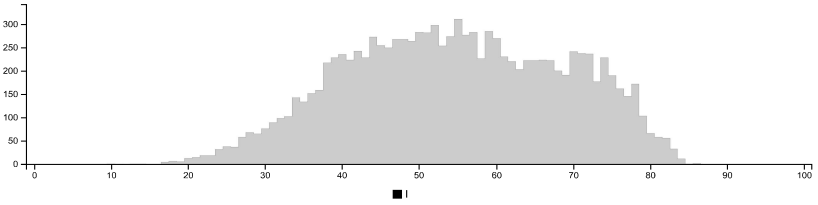

COLOR SPACE AND CHANNEL STATISTICS

	avg	med	min	max
RGB:R	134	133	27	220
RGB:G	131	130	28	215
RGB:B	128	127	29	211
HSV:H	29 1.00	33	0	360
HSV:S	5	5	0	15
HSV:V	53	52	11	86
LCH:L	55	55	10	86
LCH:C	3	3	0	7
LCH:H	71 1.00	79	4	360
LAB:L	55	55	10	86
LAB:A	1	1	-3	4
LAB:B	2	2	-4	7

Summary of Image Analysis for Specimen TG20-C-4

Figure D.65: Bottom debonded part of Specimen TG20-C-4

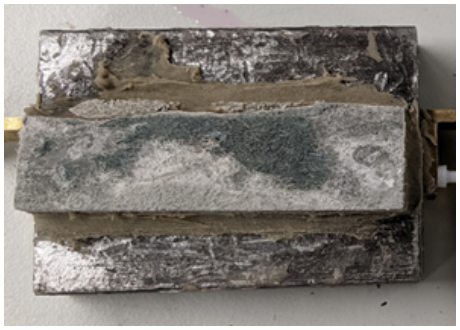

Figure D.66: Top debonded part of Specimen TG20-C-4

Table D.33: Summary of Image analysis result for specimen TG20-C-4

Contact Type	Colour Cluster	Results of Image analysis		Contact (%)		Average Contact (in %)
		Bottom Debonded Layer	Top Debonded Layer	Bottom Debonded Layer	Top Debonded Layer	
		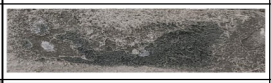				
Poor				52,75%	59,41%	**56,08%**
Good		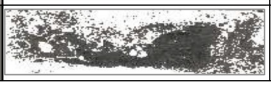		47,25%	40,59%	**43,92%**

IMAGE COLOR SUMMARIZER

RGB, HSV, LCH & Lab image color statistics and clustering—simple and easy

HOME ANALYZE EXAMPLES API DOWNLOAD FAQ NEWS

IMAGE COLOR SUMMARY

THE IMAGE IN WORDS

battleship blast brownish dark dim dune eighth electric friar fuscous grey jumbo masala natural old olivish reddish schooner seashell silver steel suva torque tundora wireless

COLOR CLUSTERS

Colors in the image were clustered into 2 groups (k-means). The average color of the colors for each cluster is shown. The name is the closest named color and its distance is shown using ΔE. The tags are the set of words formed by all named neighbours within ΔE ≤ 5. The list of words above is the set of all unique words in this set of words.

Cluster colors, sized by number of pixels:

cluster	pixels	name	HEX	RGB	HSV	LCH	Lab	tags
	52.75%	88,84,82 tundora ΔE=1.2	#575551	87 85 81	41 6 34	36 2 91	36 0 2	dark blast brownish dim dune electric fuscous olivish reddish torque tundora wireless grey
	47.25%	139,134,130 seashell1 ΔE=0.6	#898480	137 132 128	28 7 54	56 3 72	56 1 3	battleship eighth friar jumbo masala natural old schooner seashell silver steel suva grey

IMAGE CLUSTER PARTITIONS

Pixels of the image assigned to each cluster. The border is the color of the cluster as calculated by the average value of its pixels.

RGB HISTOGRAM

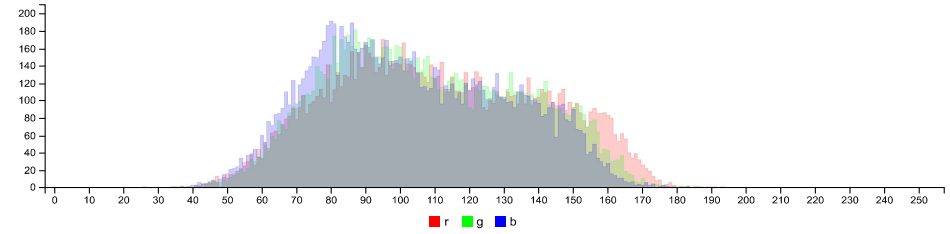

HSV HISTOGRAMS

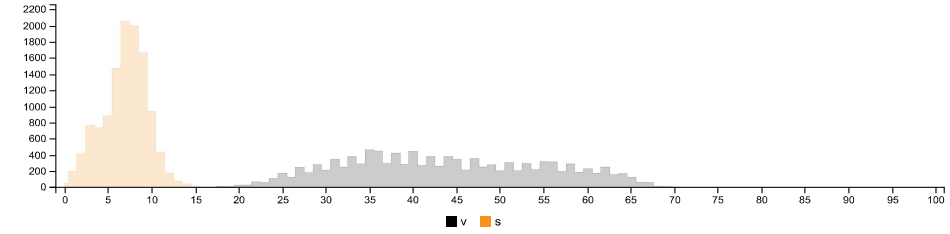

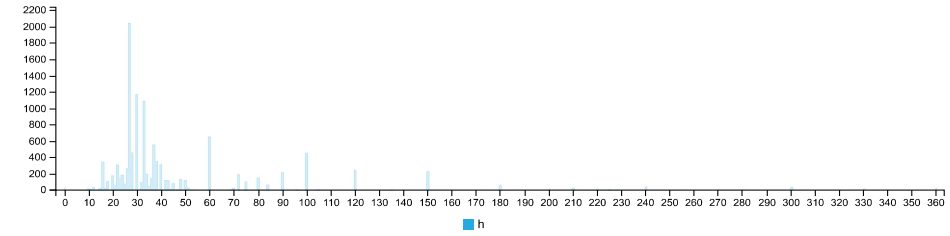

LCH HISTOGRAMS

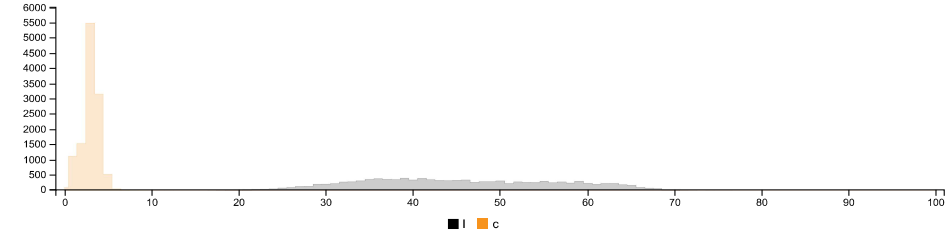

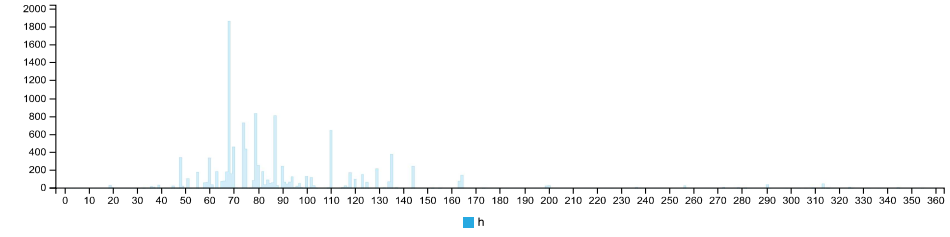

LAB HISTOGRAMS

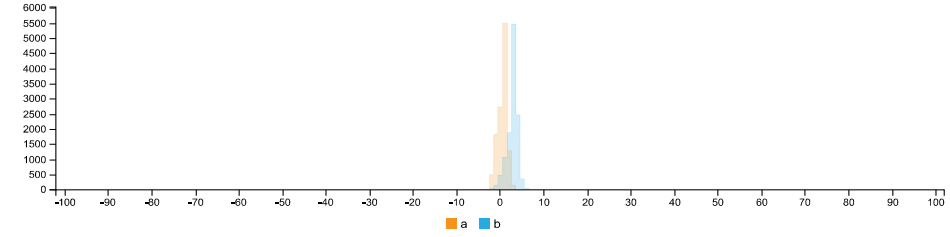

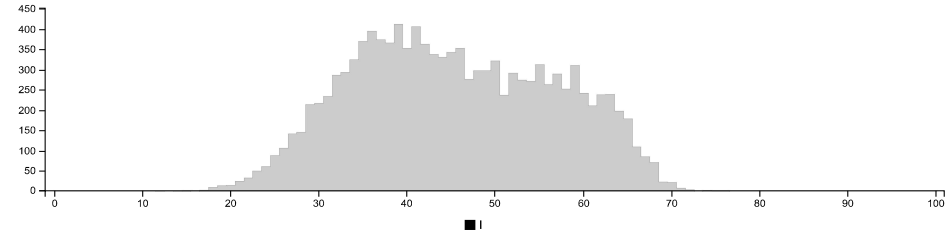

COLOR SPACE AND CHANNEL STATISTICS

	avg	med	min	max
RGB:R	111	109	35	193
RGB:G	108	105	30	185
RGB:B	103	100	26	186
HSV:H	40 1.00	33	0	360
HSV:S	7	7	0	26
HSV:V	44	43	14	76
LCH:L	45	45	12	76
LCH:C	3	3	0	9
LCH:H	83 1.00	79	3	360
LAB:L	45	45	12	76

IMAGE COLOR SUMMARIZER

RGB, HSV, LCH & Lab image color statistics and clustering—simple and easy

HOME ANALYZE EXAMPLES API DOWNLOAD FAQ NEWS

IMAGE COLOR SUMMARY

THE IMAGE IN WORDS

alley archive chicago condor dark fern friar gannet gravel grey half olivish silver stonehenge tinpan

COLOR CLUSTERS

Colors in the image were clustered into 2 groups (k-means). The average color of the colors for each cluster is shown. The name is the closest named color and its distance is shown using ΔE. The tags are the set of words formed by all named neighbours within ΔE ≤ 5. The list of words above is the set of all unique words in this set of words.

Cluster colors, sized by number of pixels:

cluster	pixels	name	HEX	RGB	HSV	LCH	Lab	tags
	59.41%	149,145,140 grey ΔE=1.2	#97938F	151 147 143	33 6 59	61 3 80	61 1 3	archive fern friar gannet half silver stonehenge grey
	40.59%	92,91,89 tinpan alley ΔE=1.6	#595B58	89 91 88	87 3 36	38 2 127	38 -1 1	dark alley chicago condor gravel half olivish tinpan grey

IMAGE CLUSTER PARTITIONS

Pixels of the image assigned to each cluster. The border is the color of the cluster as calculated by the average value of its pixels.

RGB HISTOGRAM

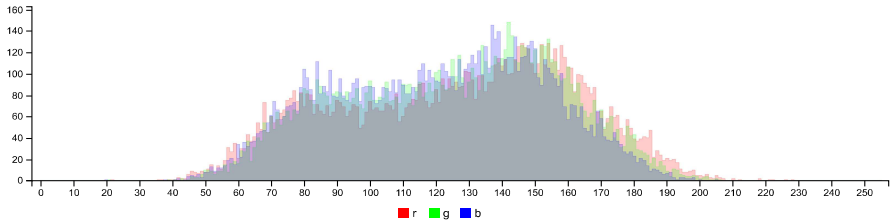

HSV HISTOGRAMS

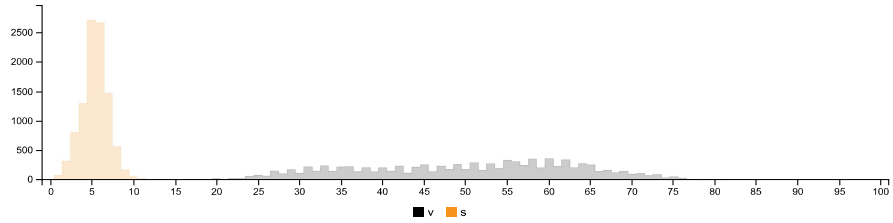

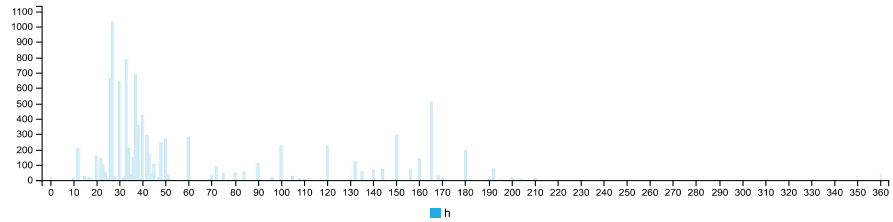

LCH HISTOGRAMS

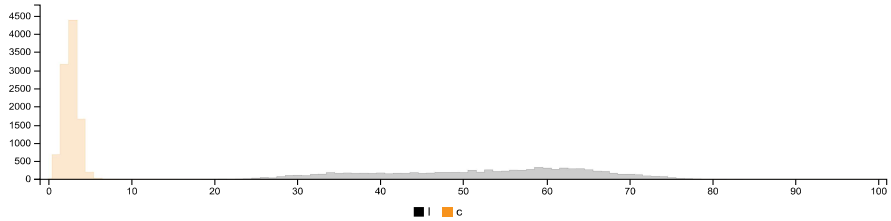

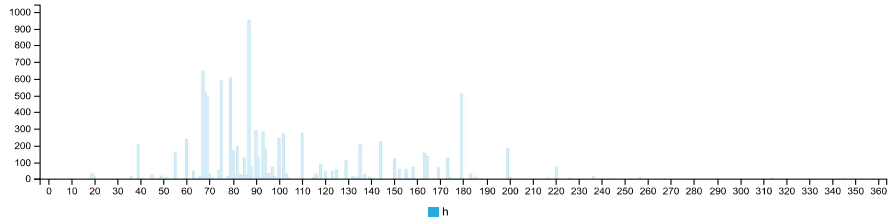

LAB HISTOGRAMS

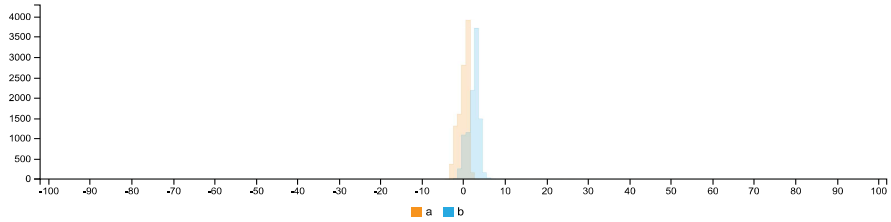

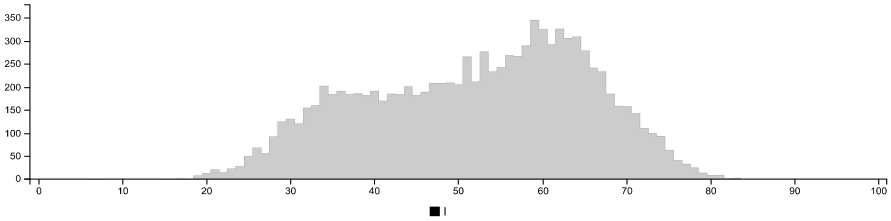

COLOR SPACE AND CHANNEL STATISTICS

	avg	med	min	max
RGB:R	126	131	22	228
RGB:G	125	127	21	206
RGB:B	121	123	20	205
HSV:H	51 1.00	38	0	360
HSV:S	6	5	0	35
HSV:V	50	51	9	89
LCH:L	52	54	7	83
LCH:C	3	3	0	31
LCH:H	96 1.00	87	6	360
LAB:L	52	54	7	83
LAB:A	-0	0	-4	5
LAB:B	2	3	-3	31

D.1.4. Inter-layer surface of Casting based - Failed Specimens

Figure D.67: Inter-layer surface of Casted Specimen A-1 after failure

Figure D.68: Inter-layer surface of Casted Specimen A-2 after failure

Figure D.69: Inter-layer surface of Casted Specimen A-3 after failure

Figure D.70: Inter-layer surface of Casted Specimen A-4 after failure

Figure D.71: Inter-layer surface of Casted Specimen B-2 after failure

Figure D.72: Inter-layer surface of Casted Specimen B-3 after failure

Figure D.73: Inter-layer surface of Casted Specimen B-4 after failure

Figure D.74: Inter-layer surface of Casted Specimen C-1 after failure

Figure D.75: Inter-layer surface of Casted Specimen C-2 after failure

Figure D.76: Inter-layer surface of Casted Specimen C-3 after failure

Figure D.77: Inter-layer surface of Casted Specimen C-4 after failure

E

Appendix-E

E.1. Failure Mechanism in tested Specimens

E.1.1. Failure Mechanism in Caulk-gun extrusion-based specimens

Specimen Type-A

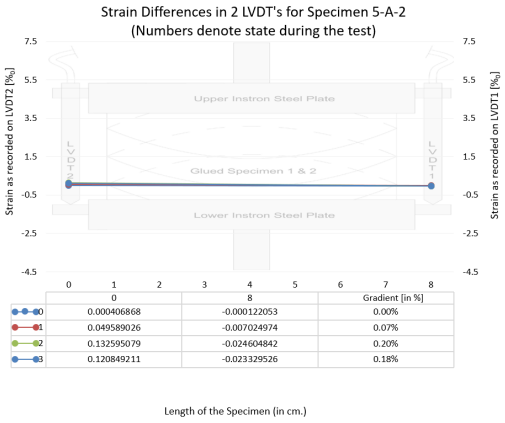

	0	8	Gradient [in %]
0	0.000406868	-0.000122053	0.00%
1	0.049589026	-0.007024974	0.07%
2	0.132595079	-0.024604842	0.20%
3	0.120849211	-0.023329526	0.18%

Figure E.1: Failure mechanism in Specimen TG5-A-1

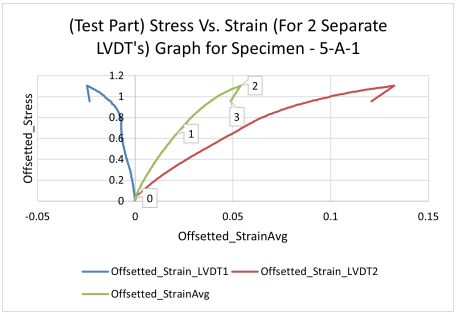

Figure E.2: Stress-strain curve for Specimen TG5-A-1

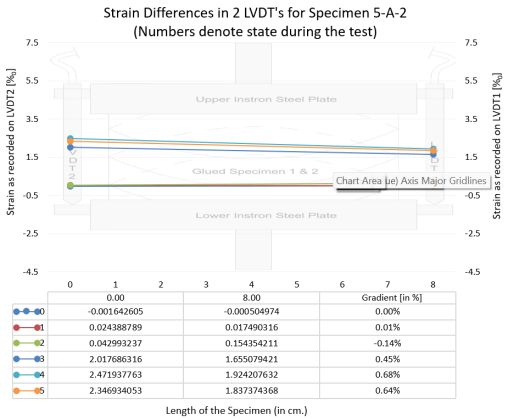

	0.00	8.00	Gradient [in %]
0	-0.001642605	-0.000504974	0.00%
1	0.024388789	0.017490316	0.01%
2	0.042993237	0.154354211	-0.14%
3	2.017686316	1.655079421	0.45%
4	2.471937763	1.924207632	0.68%
5	2.346934053	1.837374368	0.64%

Figure E.3: Failure mechanism in Specimen TG5-A-2

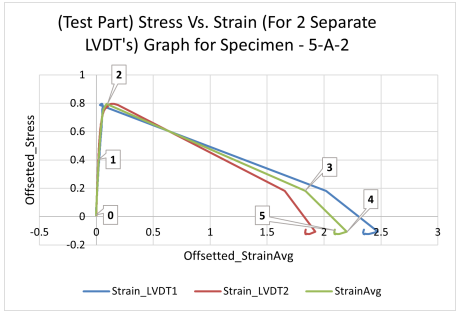

Figure E.4: Stress-strain curve for Specimen TG5-A-2

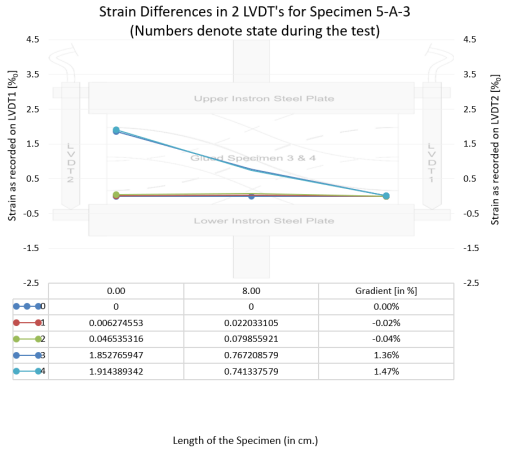

	0.00	8.00	Gradient [in %]
0	0	0	0.00%
1	0.006274553	0.022033105	-0.02%
2	0.046535316	0.079855921	-0.04%
3	1.852765947	0.767208579	1.36%
4	1.914389342	0.741337579	1.47%

Figure E.5: Failure mechanism in Specimen TG5-A-3

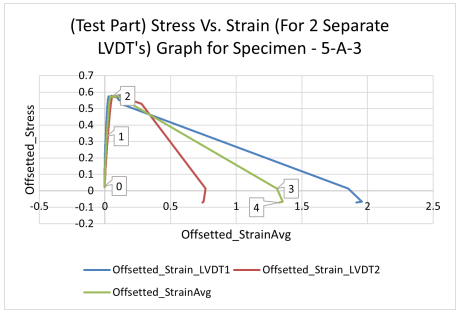

Figure E.6: Stress-strain curve for Specimen TG5-A-3

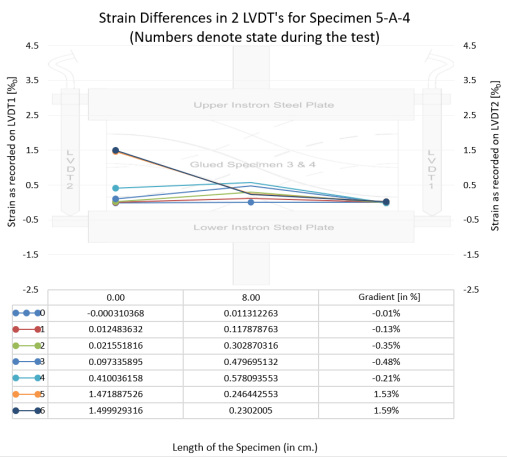

	0.00	8.00	Gradient [in %]
0	-0.000310368	0.011312263	-0.01%
1	0.012483632	0.117878763	-0.13%
2	0.021551816	0.302870316	-0.35%
3	0.097335895	0.479695132	-0.48%
4	0.410036158	0.578093553	-0.21%
5	1.471887526	0.246442553	1.53%
6	1.499929316	0.2302005	1.59%

Figure E.7: Failure mechanism in Specimen TG5-A-4

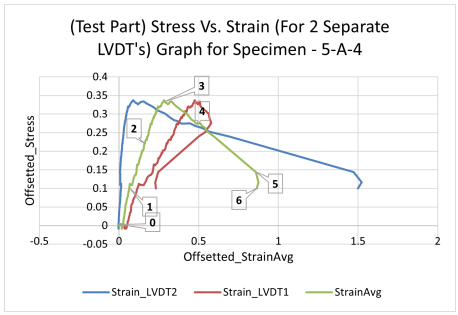

Figure E.8: Stress-strain curve for Specimen TG5-A-4

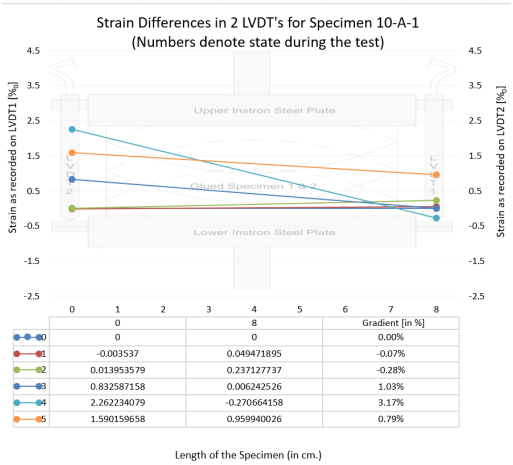

	0	8	Gradient [in %]
0	0	0	0.00%
1	-0.003537	0.049471895	-0.07%
2	0.013953579	0.237127737	-0.28%
3	0.832587158	0.006242526	1.03%
4	2.262234079	-0.270664158	3.17%
5	1.590159658	0.959940026	0.79%

Figure E.9: Failure mechanism in Specimen TG10-A-1

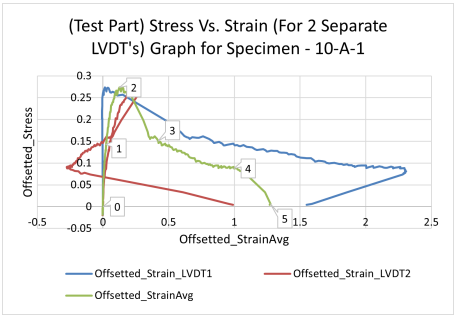

Figure E.10: Stress-strain curve for Specimen TG10-A-1

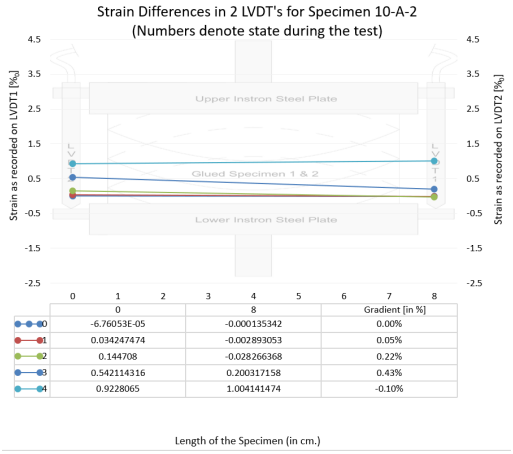

	0	8	Gradient [in %]
0	-6.76053E-05	-0.000135342	0.00%
1	0.034247474	-0.002893053	0.05%
2	0.144708	-0.028266368	0.22%
3	0.542114316	0.200317158	0.43%
4	0.9228065	1.004141474	-0.10%

Figure E.11: Failure mechanism in Specimen TG10-A-2

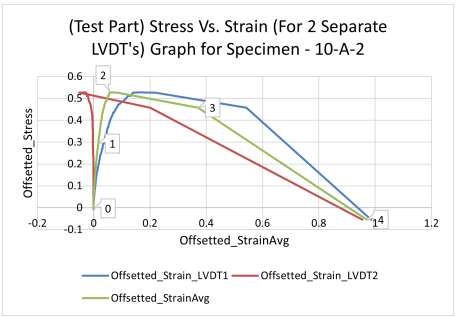

Figure E.12: Stress-strain curve for Specimen TG10-A-2

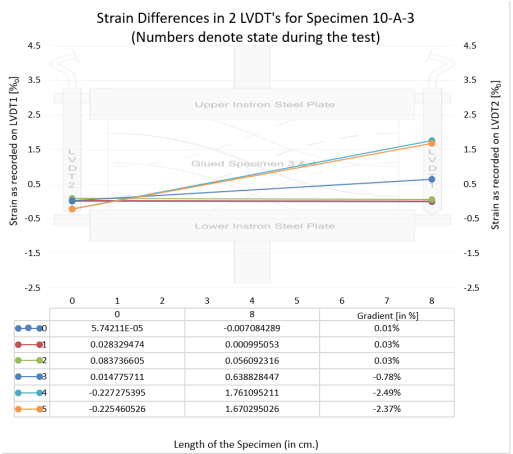

	0	8	Gradient [in %]
0	5.74211E-05	-0.007084289	0.01%
1	0.028329474	0.000995053	0.03%
2	0.083736605	0.056092316	0.03%
3	0.014775711	0.638828447	-0.78%
4	-0.227275395	1.761095211	-2.49%
5	-0.225460526	1.670295026	-2.37%

Figure E.13: Failure mechanism in Specimen TG10-A-3

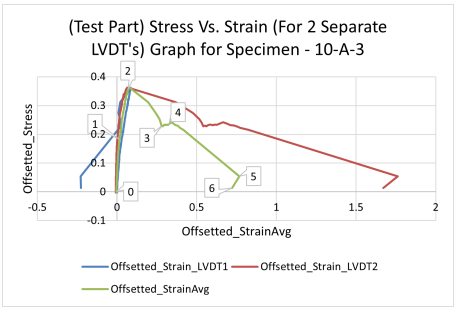

Figure E.14: Stress-strain curve for Specimen TG10-A-3

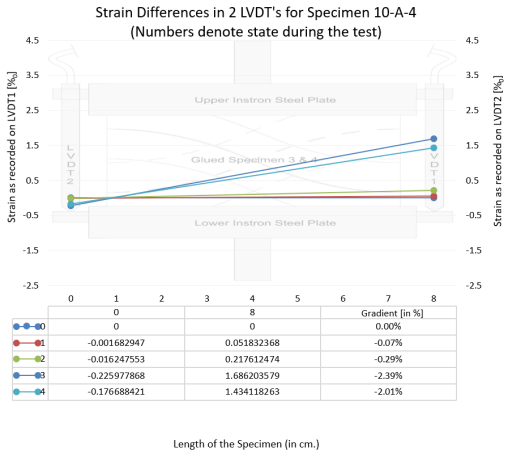

	0	8	Gradient [in %]
0	0	0	0.00%
1	-0.001682947	0.051832368	-0.07%
2	-0.016247553	0.217612474	-0.29%
3	-0.225977868	1.686203579	-2.39%
4	-0.176688421	1.434118263	-2.01%

Figure E.15: Failure mechanism in Specimen TG10-A-4

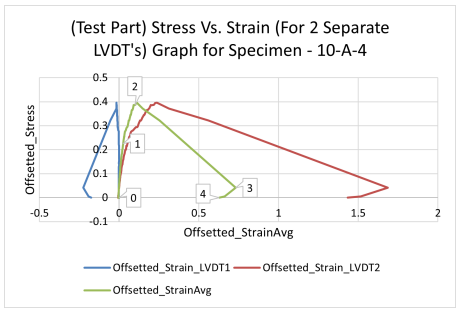

Figure E.16: Stress-strain curve for Specimen TG10-A-4

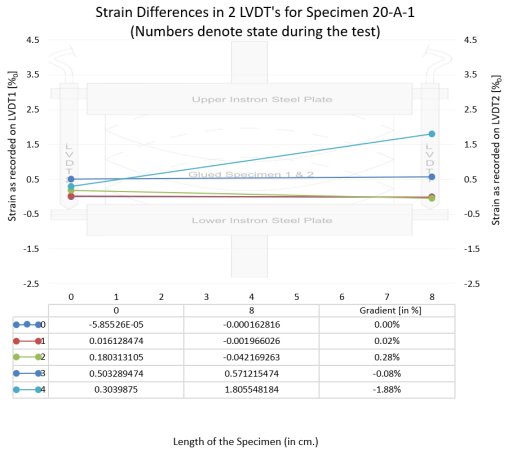

	0	8	Gradient [in %]
0	-5.85526E-05	-0.000162816	0.00%
1	0.016128474	-0.001966026	0.02%
2	0.180313105	-0.042169263	0.28%
3	0.503289474	0.571215474	-0.08%
4	0.3039875	1.805548184	-1.88%

Figure E.17: Failure mechanism in Specimen TG20-A-1

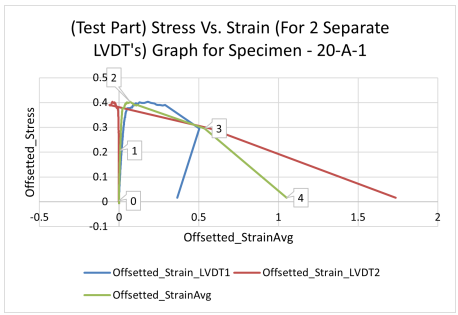

Figure E.18: Stress-strain curve for Specimen TG20-A-1

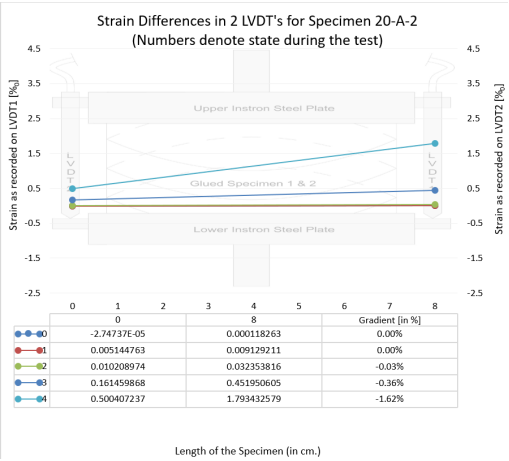

	0	8	Gradient [in %]
0	-2.74737E-05	0.000118263	0.00%
1	0.005144763	0.009129211	0.00%
2	0.010208974	0.032353816	-0.03%
3	0.161459868	0.451950605	-0.36%
4	0.500407237	1.793432579	-1.62%

Figure E.19: Failure mechanism in Specimen TG20-A-2

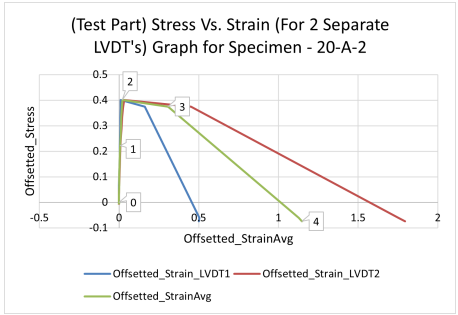

Figure E.20: Stress-strain curve for Specimen TG20-A-2

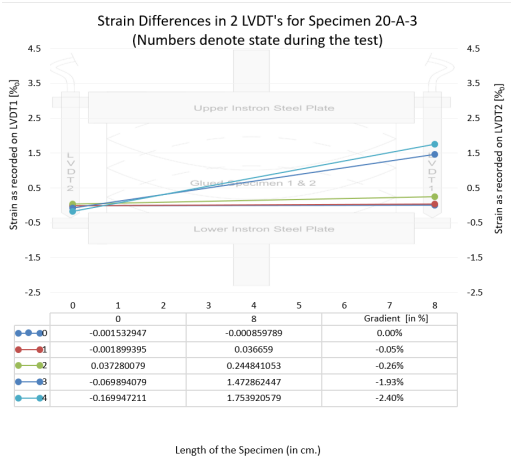

Figure E.21: Failure mechanism in Specimen TG20-A-3

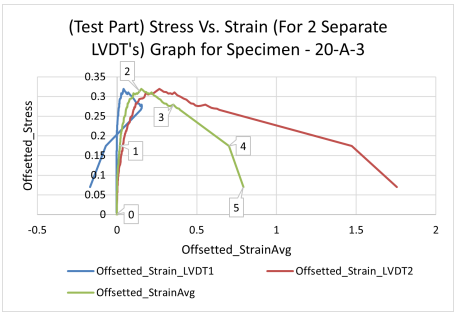

Figure E.22: Stress-strain curve for Specimen TG20-A-3

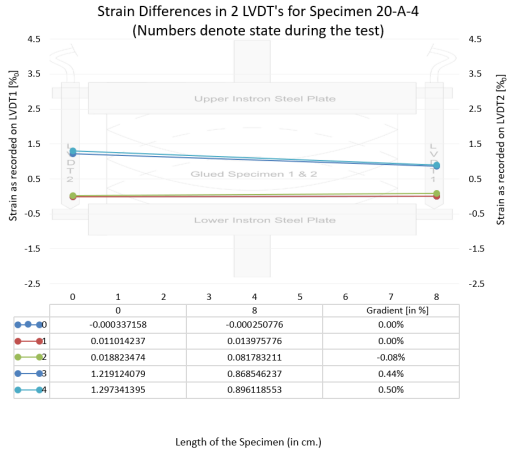

Figure E.23: Failure mechanism in Specimen TG20-A-4

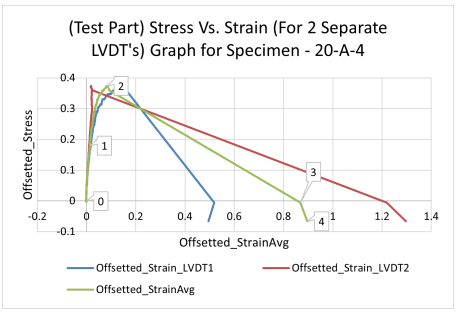

Figure E.24: Stress-strain curve for Specimen TG20-A-4

Specimen Type-B

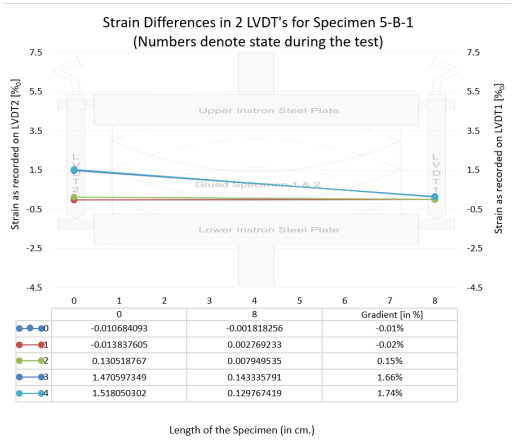

	0	8	Gradient [in %]
0	-0.010684093	-0.001818256	-0.01%
1	-0.013837605	0.002769233	-0.02%
2	0.130518767	0.007949535	0.15%
3	1.470597349	0.143335791	1.66%
4	1.518050302	0.129767419	1.74%

Figure E.25: Failure mechanism in Specimen TG5-B-1

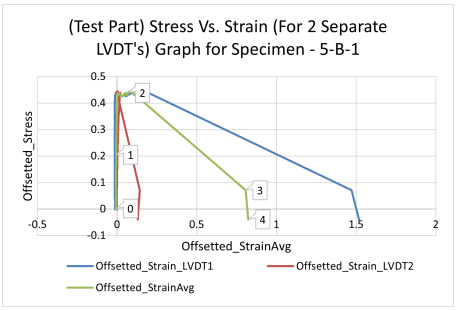

Figure E.26: Stress-strain curve for Specimen TG5-B-1

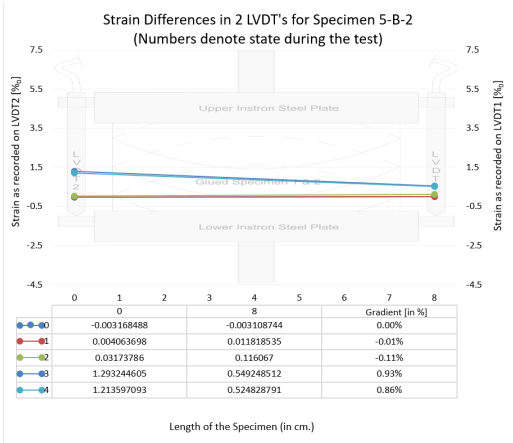

	0	8	Gradient [in %]
0	-0.003168488	-0.003108744	0.00%
1	0.004063698	0.011818535	-0.01%
2	0.03173786	0.116067	-0.11%
3	1.293244605	0.549248512	0.93%
4	1.213597093	0.524828791	0.86%

Figure E.27: Failure mechanism in Specimen TG5-B-2

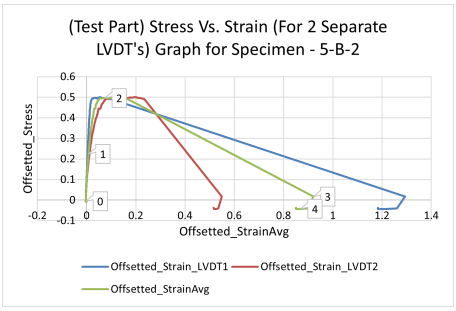

Figure E.28: Stress-strain curve for Specimen TG5-B-2

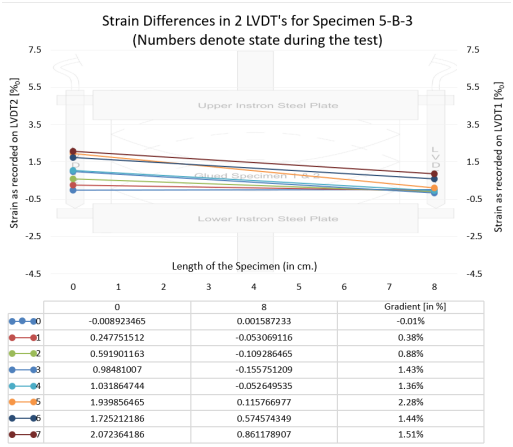

	0	8	Gradient [in %]
0	-0.008923465	0.001587233	-0.01%
1	0.247751512	-0.053069116	0.38%
2	0.591901163	-0.109286465	0.88%
3	0.98481007	-0.155751209	1.43%
4	1.031864744	-0.052649535	1.36%
5	1.939856465	0.115766977	2.28%
6	1.725212186	0.574574349	1.44%
7	2.072364186	0.861178907	1.51%

Figure E.29: Failure mechanism in Specimen TG5-B-3

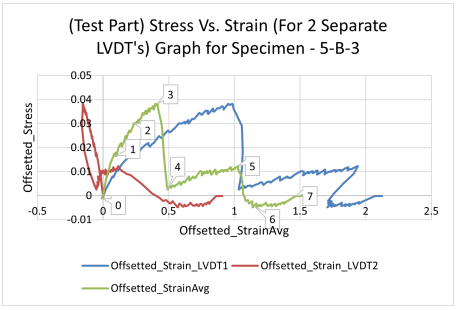

Figure E.30: Stress-strain curve for Specimen TG5-B-3

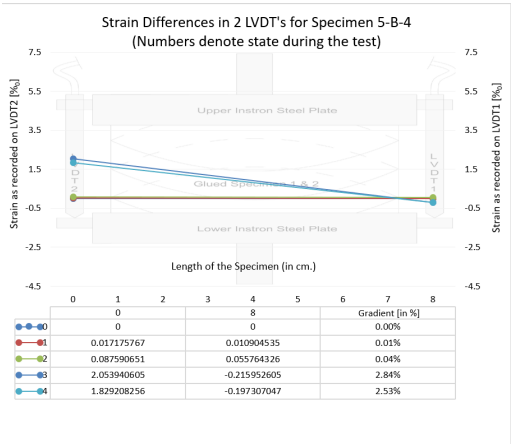

	0	8	Gradient [in %]
0	0	0	0.00%
1	0.017175767	0.010904535	0.01%
2	0.087590651	0.055764326	0.04%
3	2.053940605	-0.215952605	2.84%
4	1.829208256	-0.197307047	2.53%

Figure E.31: Failure mechanism in Specimen TG5-B-4

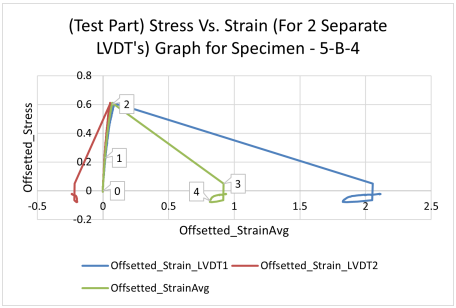

Figure E.32: Stress-strain curve for Specimen TG5-B-4

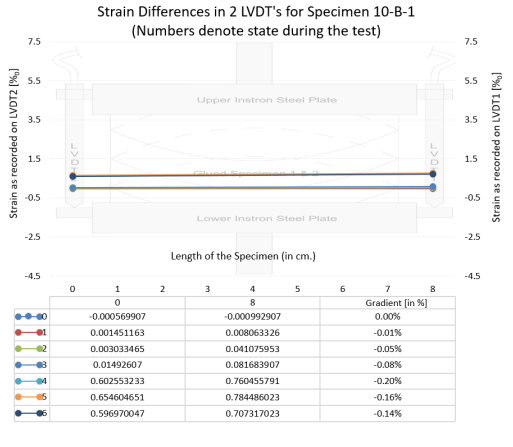

	0	8	Gradient [in %]
0	-0.000569907	-0.000992907	0.00%
1	0.001451163	0.008063326	-0.01%
2	0.003033465	0.041075953	-0.05%
3	0.01492607	0.081683907	-0.08%
4	0.602553233	0.760455791	-0.20%
5	0.654604651	0.784486023	-0.16%
6	0.596970047	0.707317023	-0.14%

Figure E.33: Failure mechanism in Specimen TG10-B-1

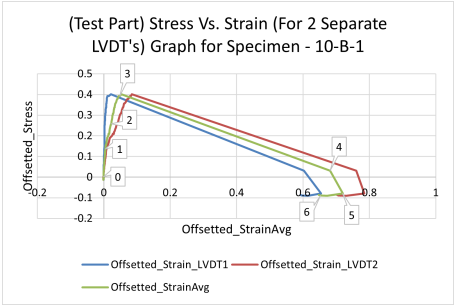

Figure E.34: Stress-strain curve for Specimen TG10-B-1

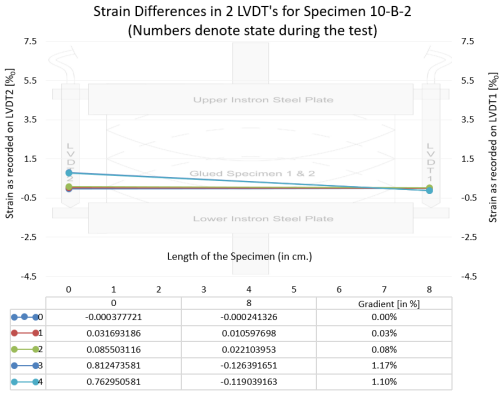

	0	8	Gradient [in %]
0	-0.000377721	-0.000241326	0.00%
1	0.031693186	0.010597698	0.03%
2	0.085503116	0.022103953	0.08%
3	0.812473581	-0.126391651	1.17%
4	0.762950581	-0.119039163	1.10%

Figure E.35: Failure mechanism in Specimen TG10-B-2

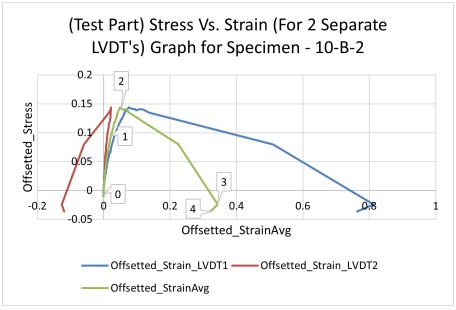

Figure E.36: Stress-strain curve for Specimen TG10-B-2

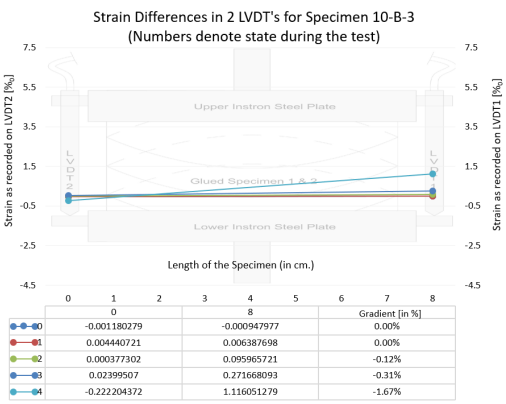

	0	8	Gradient [in %]
0	-0.001180279	-0.000947977	0.00%
1	0.004440721	0.006387698	0.00%
2	0.000377302	0.095965721	-0.12%
3	0.02399507	0.271668093	-0.31%
4	-0.222204372	1.116051279	-1.67%

Figure E.37: Failure mechanism in Specimen TG10-B-3

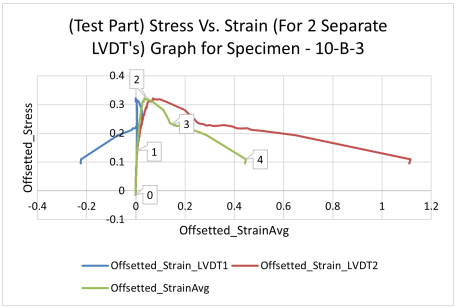

Figure E.38: Stress-strain curve for Specimen TG10-B-3

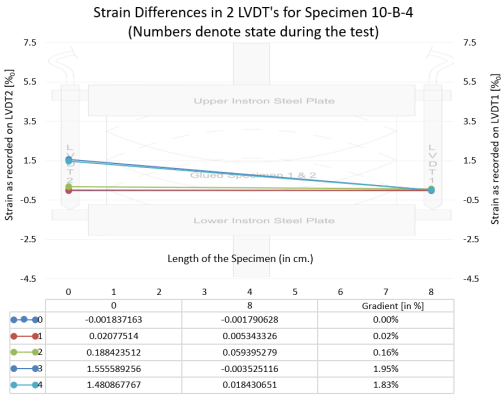

	0	8	Gradient [in %]
0	-0.001837163	-0.001790628	0.00%
1	0.02077514	0.005343326	0.02%
2	0.188423512	0.059395279	0.16%
3	1.555589256	-0.003525116	1.95%
4	1.480867767	0.018430651	1.83%

Figure E.39: Failure mechanism in Specimen TG10-B-4

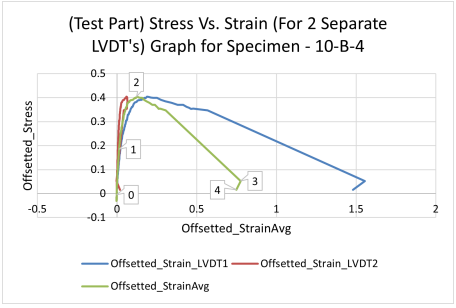

Figure E.40: Stress-strain curve for Specimen TG10-B-4

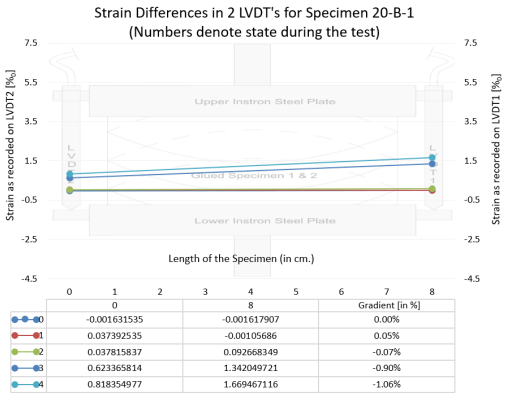

Figure E.41: Failure mechanism in Specimen TG20-B-1

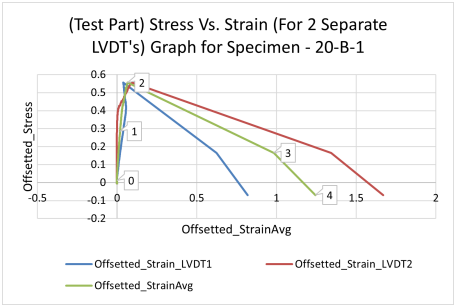

Figure E.42: Stress-strain curve for Specimen TG20-B-1

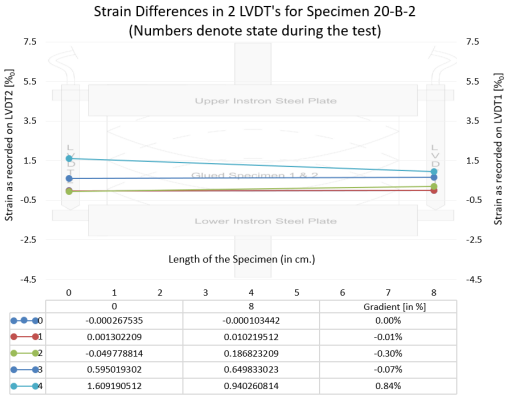

Figure E.43: Failure mechanism in Specimen TG20-B-2

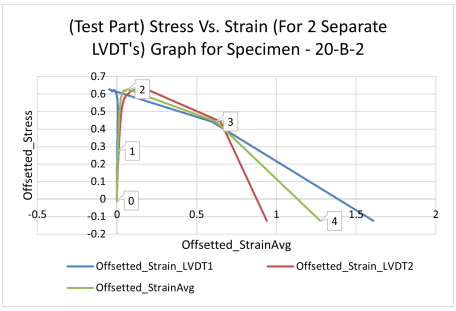

Figure E.44: Stress-strain curve for Specimen TG20-B-2

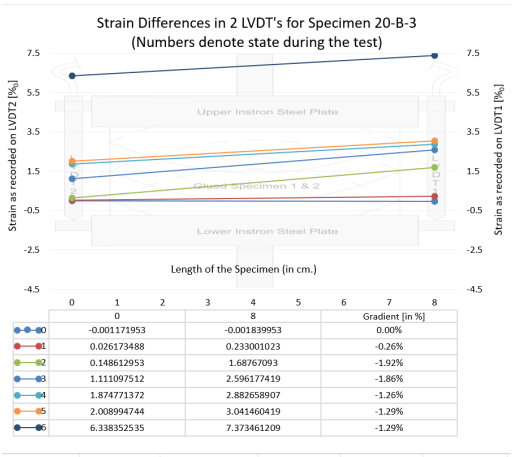

Figure E.45: Failure mechanism in Specimen TG20-B-3

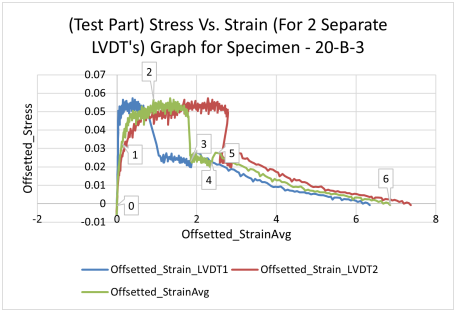

Figure E.46: Stress-strain curve for Specimen TG20-B-3

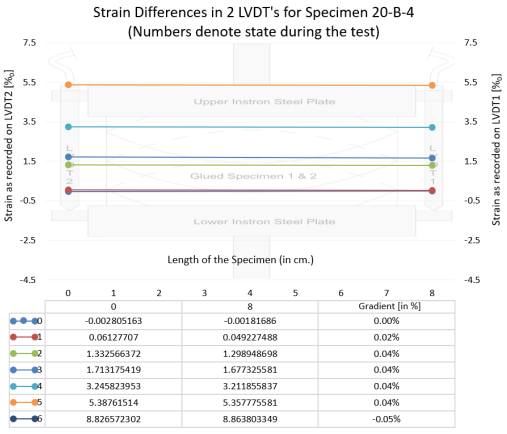

	0	8	Gradient [in %]
0	-0.002805163	-0.00181686	0.00%
1	0.06127707	0.049227488	0.02%
2	1.332566372	1.298948698	0.04%
3	1.713175419	1.677325581	0.04%
4	3.245823953	3.211855837	0.04%
5	5.38761514	5.357775581	0.04%
6	8.826572302	8.863803349	-0.05%

Figure E.47: Failure mechanism in Specimen TG20-B-4

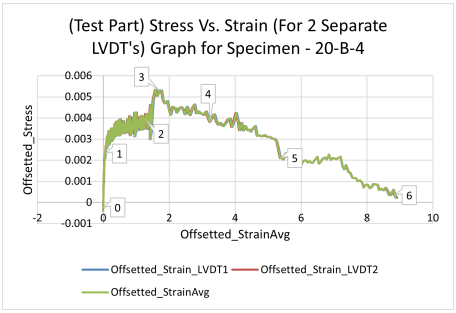

Figure E.48: Stress-strain curve for Specimen TG20-B-4

Specimen Type-C

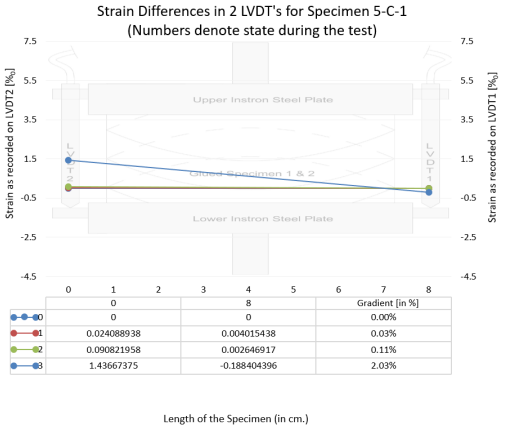

	0	8	Gradient [in %]
0	0	0	0.00%
1	0.024088938	0.004015438	0.03%
2	0.090821958	0.002646917	0.11%
3	1.43667375	-0.188404396	2.03%

Figure E.49: Failure mechanism in Specimen TG5-C-1

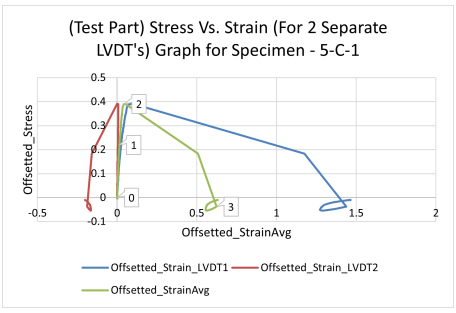

Figure E.50: Stress-strain curve for Specimen TG5-C-1

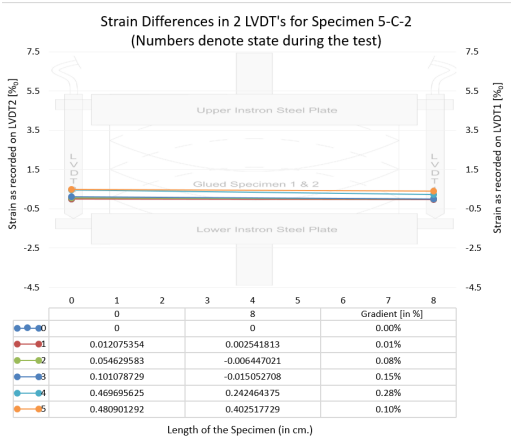

Figure E.51: Failure mechanism in Specimen TG5-C-2

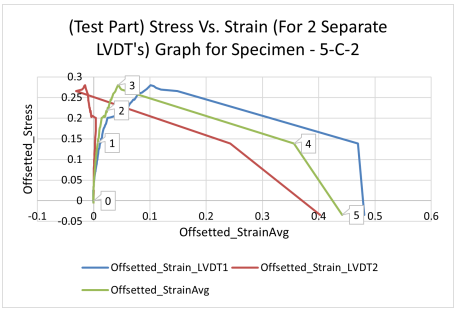

Figure E.52: Stress-strain curve for Specimen TG5-C-2

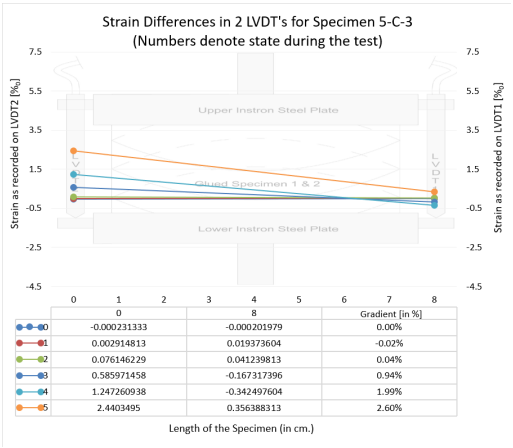

Figure E.53: Failure mechanism in Specimen TG5-C-3

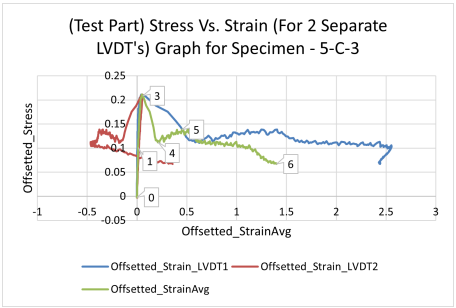

Figure E.54: Stress-strain curve for Specimen TG5-C-3

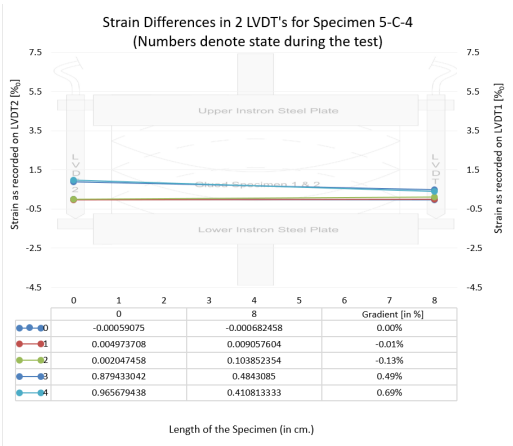

Figure E.55: Failure mechanism in Specimen TG5-C-4

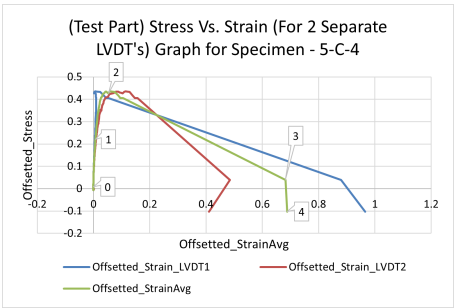

Figure E.56: Stress-strain curve for Specimen TG5-C-4

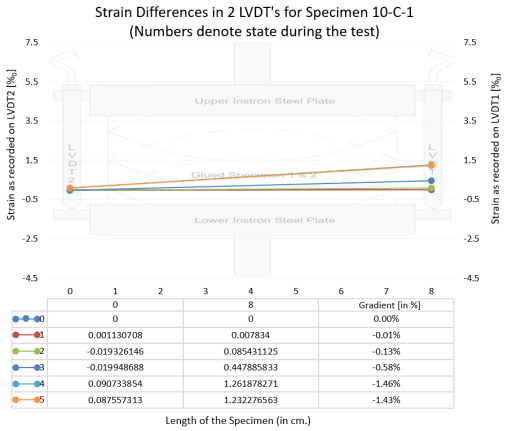

	0	8	Gradient [in %]
0	0	0	0.00%
1	0.001130708	0.007834	-0.01%
2	-0.019326146	0.085431125	-0.13%
3	-0.019948688	0.447885833	-0.58%
4	0.090733854	1.261878271	-1.46%
5	0.087557313	1.232276563	-1.43%

Figure E.57: Failure mechanism in Specimen TG10-C-1

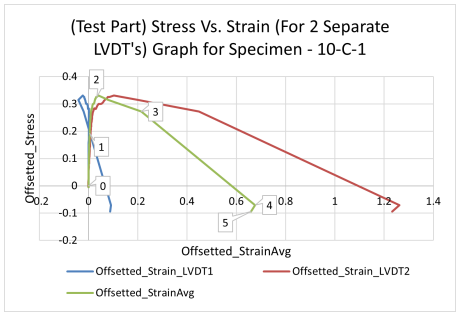

Figure E.58: Stress-strain curve for Specimen TG10-C-1

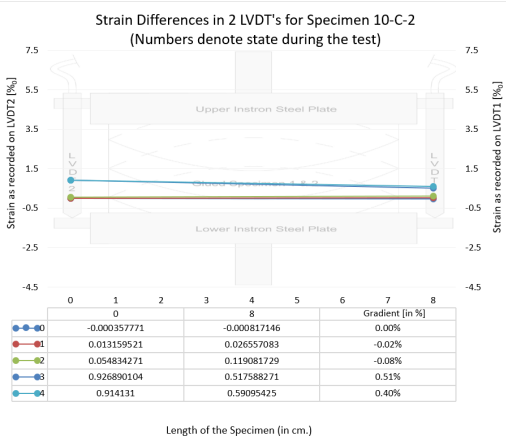

	0	8	Gradient [in %]
0	-0.000357771	-0.000817146	0.00%
1	0.013159521	0.026557083	-0.02%
2	0.054834271	0.119081729	-0.08%
3	0.926890104	0.517588271	0.51%
4	0.914131	0.59095425	0.40%

Figure E.59: Failure mechanism in Specimen TG10-C-2

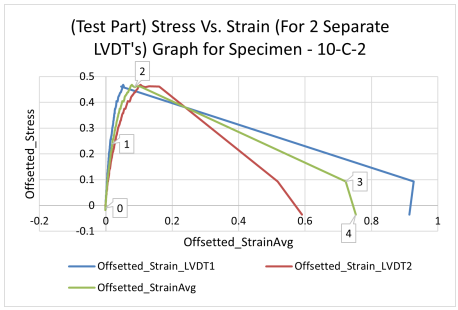

Figure E.60: Stress-strain curve for Specimen TG10-C-2

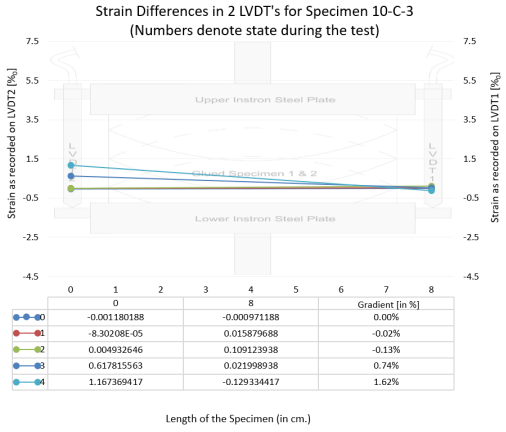

	0	8	Gradient [in %]
0	-0.001180188	-0.000971188	0.00%
1	-8.30208E-05	0.015879688	-0.02%
2	0.004932646	0.109123938	-0.13%
3	0.617815563	0.021998938	0.74%
4	1.167369417	-0.129334417	1.62%

Figure E.61: Failure mechanism in Specimen TG10-C-3

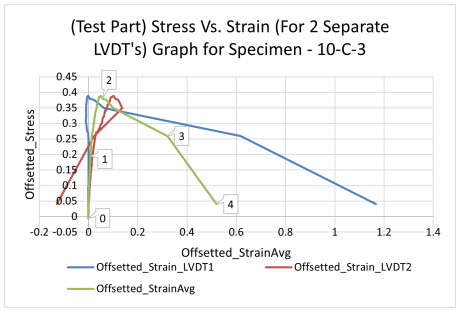

Figure E.62: Stress-strain curve for Specimen TG10-C-3

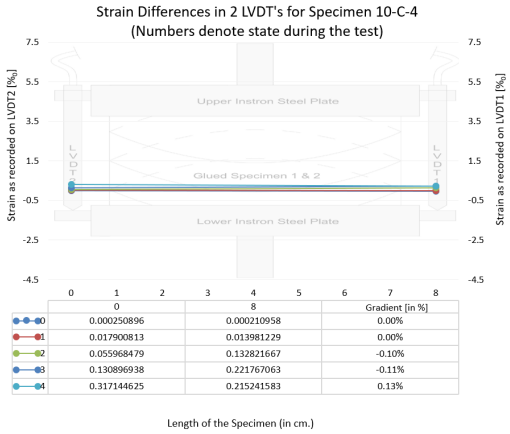

	0	8	Gradient [in %]
0	0.000250896	0.000210958	0.00%
1	0.017900813	0.013981229	0.00%
2	0.055968479	0.132821667	-0.10%
3	0.130896938	0.221767063	-0.11%
4	0.317144625	0.215241583	0.13%

Figure E.63: Failure mechanism in Specimen TG10-C-4

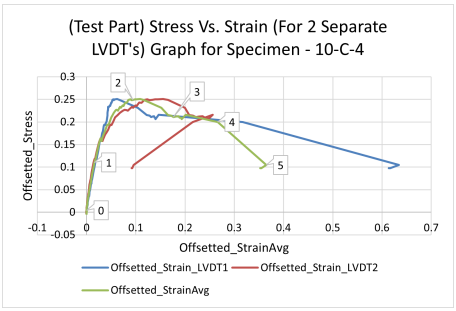

Figure E.64: Stress-strain curve for Specimen TG10-C-4

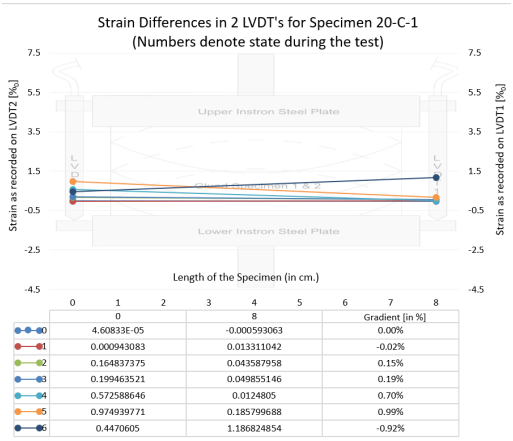

	0	8	Gradient [in %]
0	4.60833E-05	-0.000593063	0.00%
1	0.000943083	0.013311042	-0.02%
2	0.164837375	0.043587958	0.15%
3	0.199463521	0.049855146	0.19%
4	0.572588646	0.0124805	0.70%
5	0.974939771	0.185799688	0.99%
6	0.4470605	1.186824854	-0.92%

Figure E.65: Failure mechanism in Specimen TG20-C-1

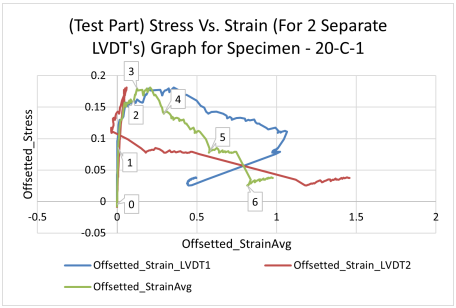

Figure E.66: Stress-strain curve for Specimen TG20-C-1

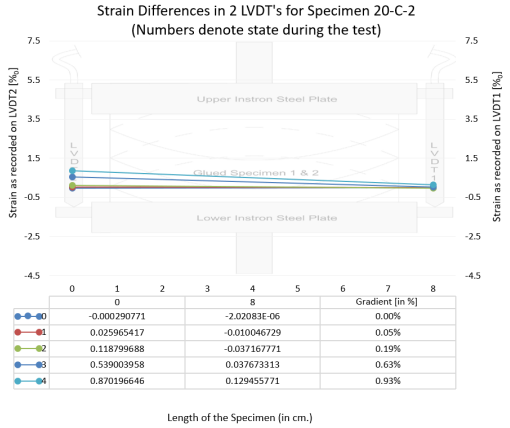

	0	8	Gradient [in %]
0	-0.000290771	-2.02083E-06	0.00%
1	0.025965417	-0.010046729	0.05%
2	0.118799688	-0.037167771	0.19%
3	0.539003958	0.037673313	0.63%
4	0.870196646	0.129455771	0.93%

Figure E.67: Failure mechanism in Specimen TG20-C-2

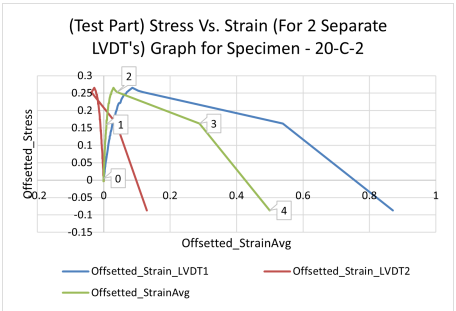

Figure E.68: Stress-strain curve for Specimen TG20-C-2

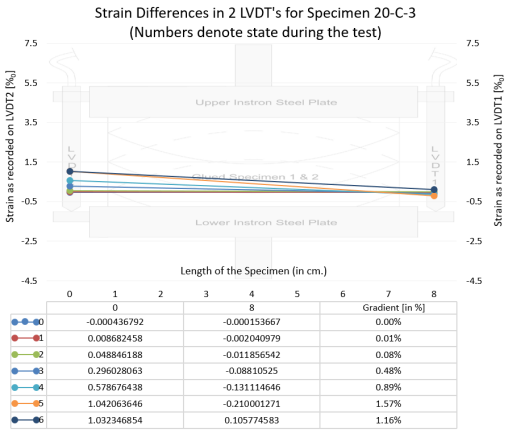

	0	8	Gradient [in %]
0	-0.000436792	-0.000153667	0.00%
1	0.008682458	-0.002040979	0.01%
2	0.048846188	-0.011856542	0.08%
3	0.296028063	-0.08810525	0.48%
4	0.578676438	-0.131114646	0.89%
5	1.042063646	-0.210001271	1.57%
6	1.032346854	0.105774583	1.16%

Figure E.69: Failure mechanism in Specimen TG20-C-3

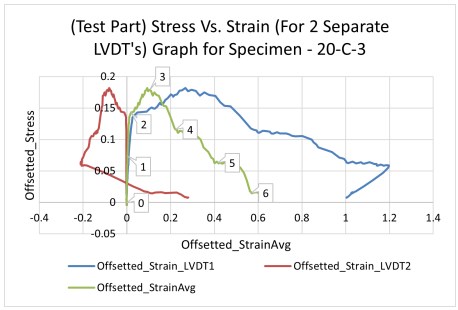

Figure E.70: Stress-strain curve for Specimen TG20-C-3

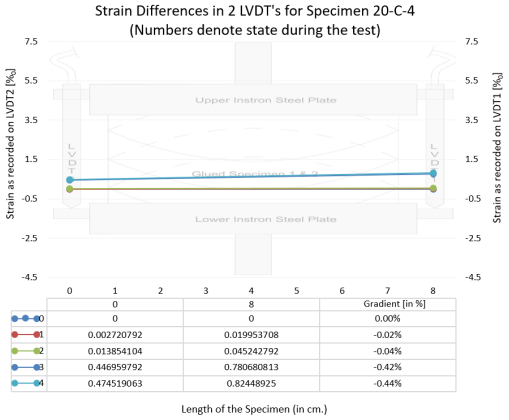

	0	8	Gradient [in %]
0	0	0	0.00%
1	0.002720792	0.019953708	-0.02%
2	0.013854104	0.045242792	-0.04%
3	0.446959792	0.780680813	-0.42%
4	0.474519063	0.82448925	-0.44%

Figure E.71: Failure mechanism in Specimen TG20-C-4

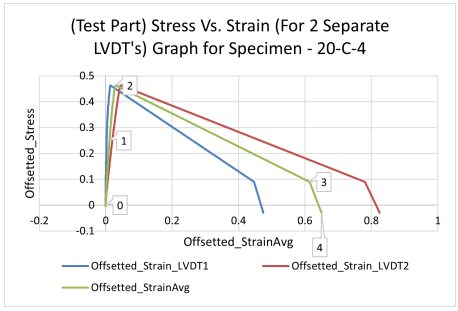

Figure E.72: Stress-strain curve for Specimen TG20-C-4

E.1.2. Failure Mechanism in Mould-Casted-based specimens

Specimen Type-A

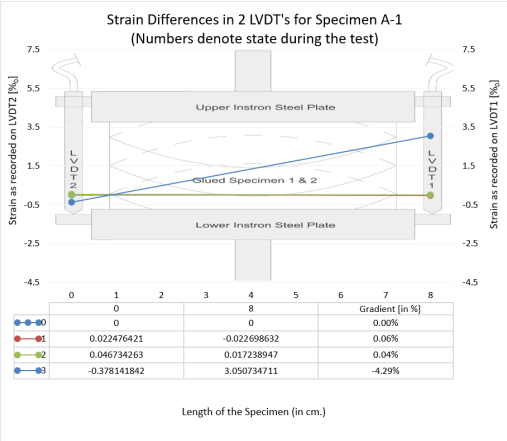

Figure E.73: Failure mechanism in Specimen A-1

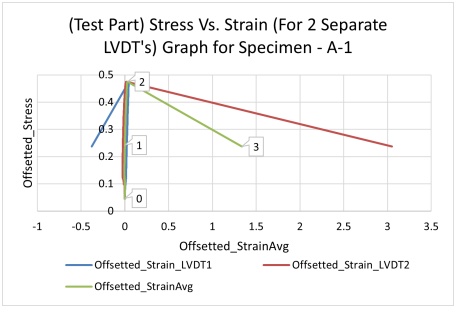

Figure E.74: Stress-strain curve for Specimen A-1

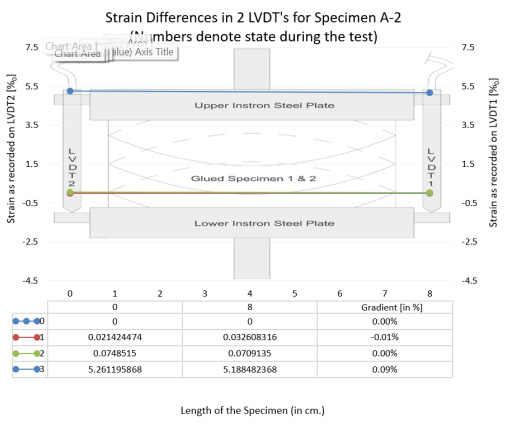

Figure E.75: Failure mechanism in Specimen A-2

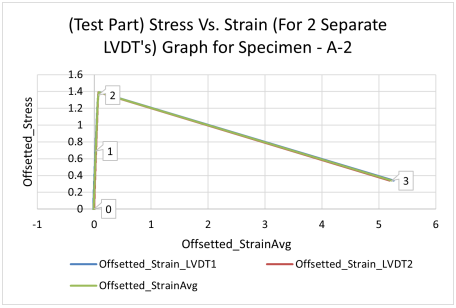

Figure E.76: Stress-strain curve for Specimen A-2

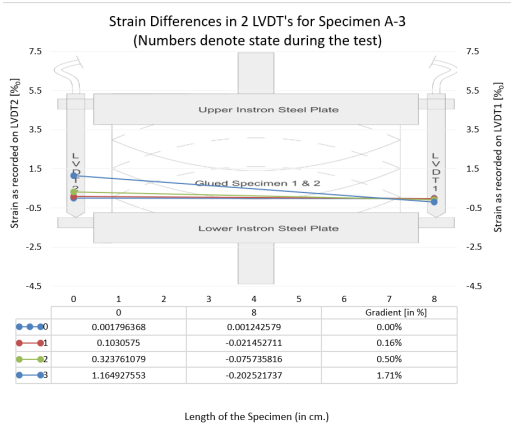

	0	8	Gradient [in %]
0	0.001796368	0.001242579	0.00%
1	0.1030575	-0.021452711	0.16%
2	0.323761079	-0.075735816	0.50%
3	1.164927553	-0.202521737	1.71%

Figure E.77: Failure mechanism in Specimen A-3

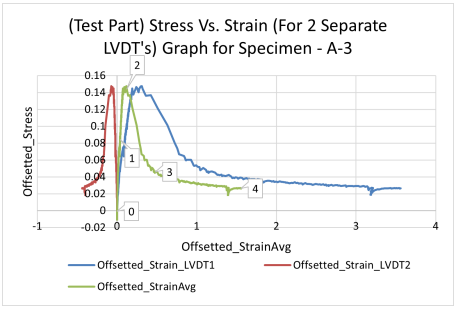

Figure E.78: Stress-strain curve for Specimen A-3

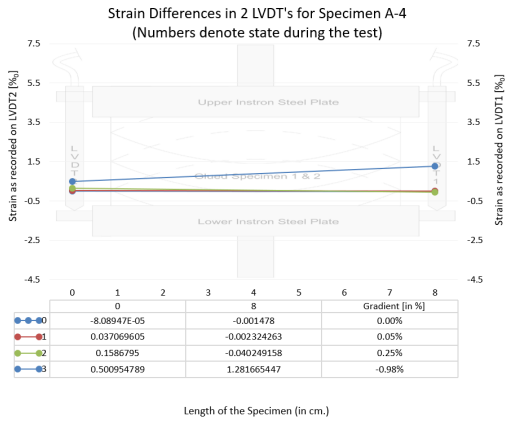

	0	8	Gradient [in %]
0	-8.08947E-05	-0.001478	0.00%
1	0.037069605	-0.002324263	0.05%
2	0.1586795	-0.040249158	0.25%
3	0.500954789	1.281665447	-0.98%

Figure E.79: Failure mechanism in Specimen A-4

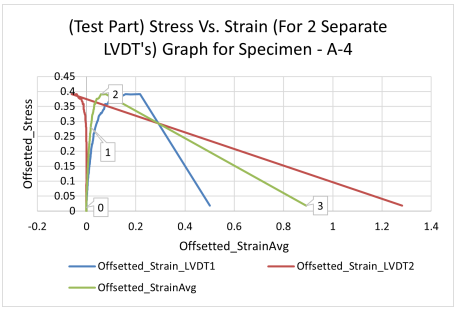

Figure E.80: Stress-strain curve for Specimen A-4

Specimen Type-B

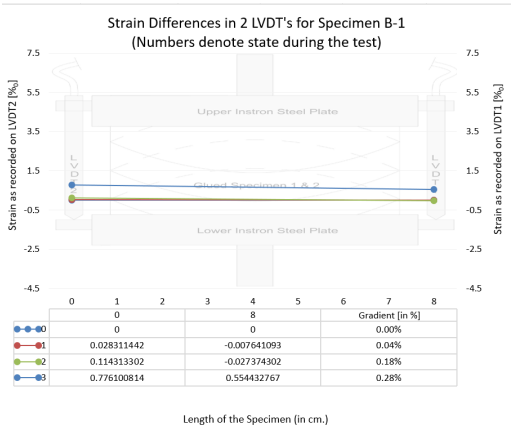

	0	8	Gradient [in %]
0	0	0	0.00%
1	0.028311442	-0.007641093	0.04%
2	0.114313302	-0.027374302	0.18%
3	0.776100814	0.554432767	0.28%

Figure E.81: Failure mechanism in Specimen B-1

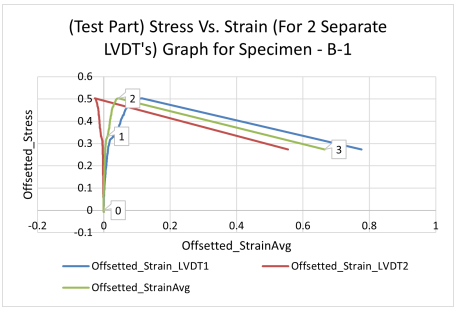

Figure E.82: Stress-strain curve for Specimen B-1

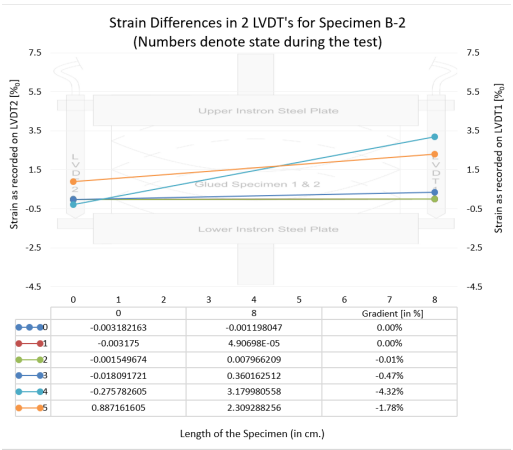

	0	8	Gradient [in %]
0	-0.003182163	-0.001198047	0.00%
1	-0.003175	4.90698E-05	0.00%
2	-0.001549674	0.007966209	-0.01%
3	-0.018091721	0.360162512	-0.47%
4	-0.275782605	3.179980558	-4.32%
5	0.887161605	2.309288256	-1.78%

Figure E.83: Failure mechanism in Specimen B-2

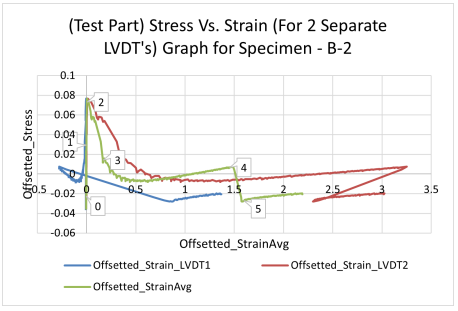

Figure E.84: Stress-strain curve for Specimen B-2

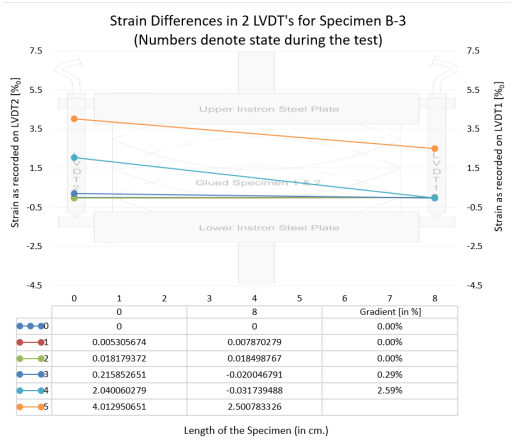

	0	8	Gradient [in %]
0	0	0	0.00%
1	0.005305674	0.007870279	0.00%
2	0.018179372	0.018498767	0.00%
3	0.215852651	-0.020046791	0.29%
4	2.040060279	-0.031739488	2.59%
5	4.012950651	2.500783326	

Figure E.85: Failure mechanism in Specimen B-3

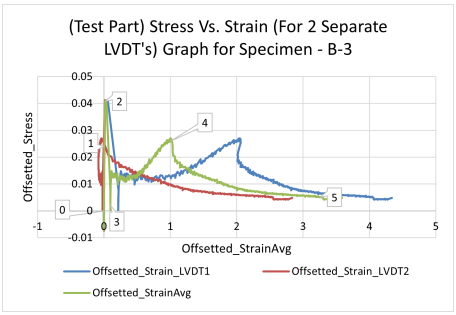

Figure E.86: Stress-strain curve for Specimen B-3

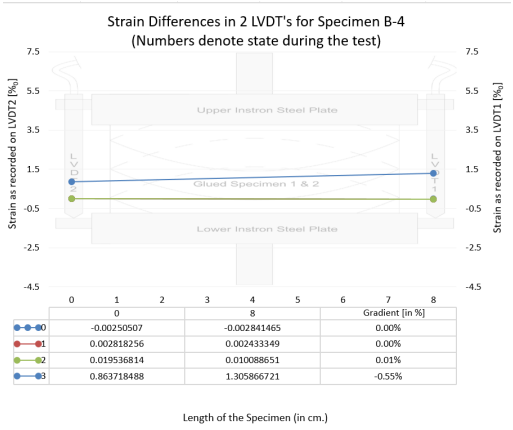

	0	8	Gradient [in %]
0	-0.00250507	-0.002841465	0.00%
1	0.002818256	0.002433349	0.00%
2	0.019536814	0.010088651	0.01%
3	0.863718488	1.305866721	-0.55%

Figure E.87: Failure mechanism in Specimen B-4

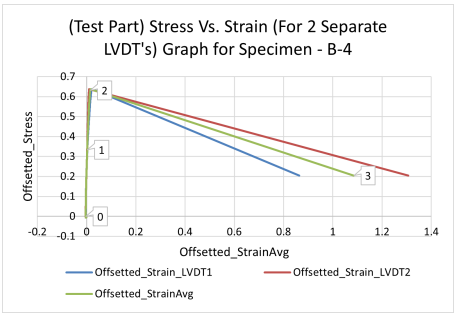

Figure E.88: Stress-strain curve for Specimen B-4

Specimen Type-C

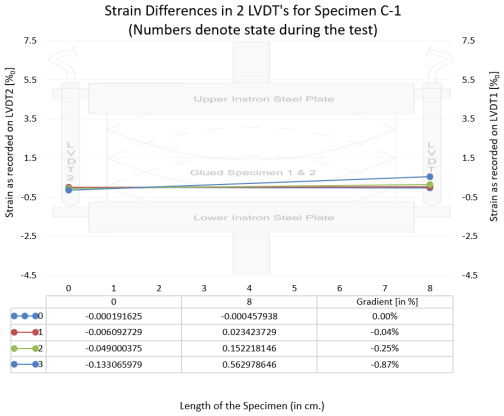

	0	8	Gradient [in %]
0	-0.000191625	-0.000457938	0.00%
1	-0.006092729	0.023423729	-0.04%
2	-0.049000375	0.152218146	-0.25%
3	-0.133065979	0.562978646	-0.87%

Figure E.89: Failure mechanism in Specimen C-1

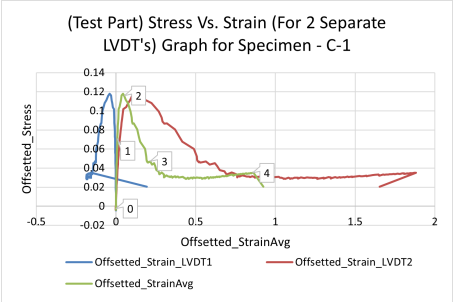

Figure E.90: Stress-strain curve for Specimen C-1

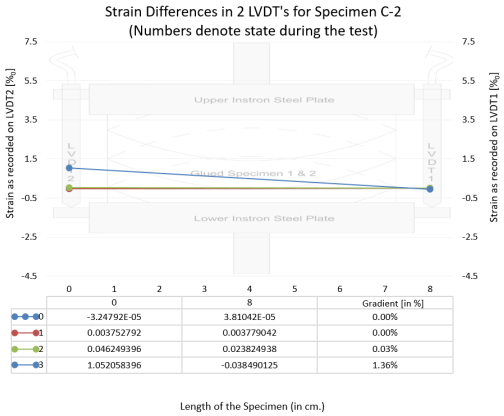

	0	8	Gradient [in %]
0	-3.24792E-05	3.81042E-05	0.00%
1	0.003752792	0.003779042	0.00%
2	0.046249396	0.023824938	0.03%
3	1.052058396	-0.038490125	1.36%

Figure E.91: Failure mechanism in Specimen C-2

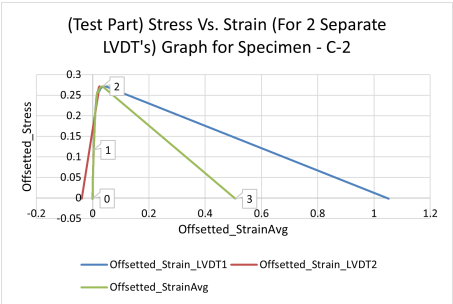

Figure E.92: Stress-strain curve for Specimen C-2

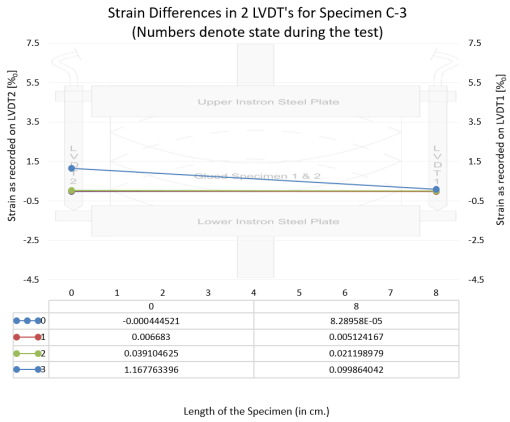

	0	8
0	-0.000444521	8.28958E-05
1	0.006683	0.005124167
2	0.039104625	0.021198979
3	1.167763396	0.099864042

Figure E.93: Failure mechanism in Specimen C-3

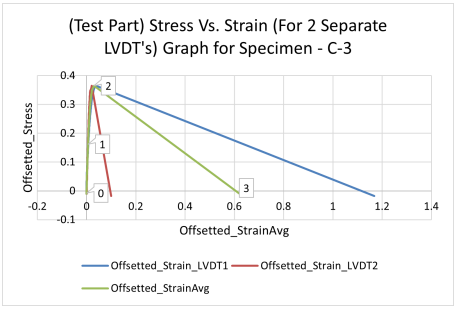

Figure E.94: Stress-strain curve for Specimen C-3

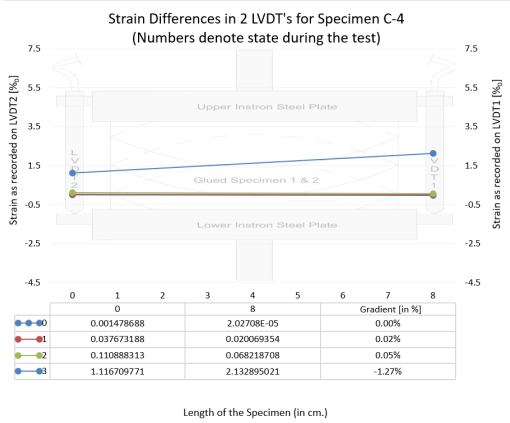

	0	8	Gradient [in %]
0	0.001478688	2.02708E-05	0.00%
1	0.037673188	0.020069354	0.02%
2	0.110888313	0.068218708	0.05%
3	1.116709771	2.132895021	-1.27%

Figure E.95: Failure mechanism in Specimen C-4

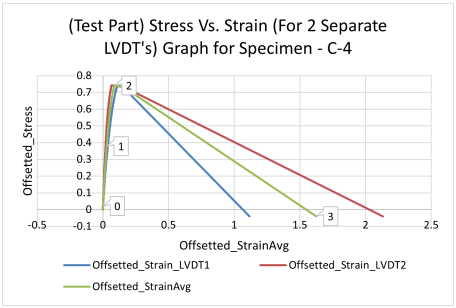

Figure E.96: Stress-strain curve for Specimen C-4